TESLA Technical Design Report

PART V
THE X-RAY FREE ELECTRON LASER

March 2001

Editors: G. Materlik, Th. Tschentscher

List of authors and contributors

M. Abd-Elmeguid[1], B. Adams[2,3], B. Allmann[4], J. Arthur[5], L. Assoufid[2], T. Asthalter[6], K. Attenkofer[3], J. Bahrdt[7], P. Balling[8], F.-J. Balta-Calleja[9], D. Barford[10], A.Q.R. Baron[11], H.D. Bartunik[12], J. Bauer[13], P. Beaven[14], K. Becker[15], U. Becker[16], F. Bell[17], U. Bergmann[18], F. Berg Rasmussen[19], G.F. Bertsch[20], N. Bernhoeft[21], W. Bialowons[22], D. Bilderback[23], U. Bismayer[24], F.J. Börgermann[25], G. Bourenkov[12], T. Brabec[26], M. Brewczyk[27], R. Brinkmann[22], T. Brückel[28], T. Buhrmester[29], E. Burkel[30], J. Chavanne[6], O. Chubar[6], A. Chumakov[6], B.S. Clausen[19], P. Cloetens[6], J. Costello[31], R. Coussement[32], R. Cremer[25], P. Daniels[33] W.H. De Jeu[34], R. Dörner[35], H. Dosch[36], W. Drube[3], H. Dürr[28], W. Eberhardt[28], K. Eidmann[37], E. Eikenberry[38], P. Elleaume[6], U. Englisch[39], V. Engel[40], M. Epple[41], M. Erhard[42], A.I. Erko[7], W. Ertmer[43], B. Faatz[3], G. Faigel[44], R. Feidenhans'l[45], J. Feldhaus[3], K. Flöttmann[22] R. Follath[7], S. Förster[46], R. Frahm[44], H. Franz[3], R. Freeman[48], W. Frentrup[7], A.K. Freund[6], A. Gaupp[7], M. Gavrila[34], R. Gehrke[3], E. Gerdau[49], C. Gerth[3], P. Gibbon[50], E. Gluskin[2], H. Graafsma[6], W. Graeff[3], G. Grübel[6], W. Grünert[51], W. Gudat[7], P. Güertler[3], F. Haaß[29], K. von Haeften[3], U. Hahn[3], J. Hajdu[52], K. Hall[53], P.K. Den Hartog[2], J. Hasting[54], A. Hemmerich[55], C. Hermes[56], J. Heuer[3], D. Holland-Moritz[57], M.R. Howells[18], K. Hradil[58], B.S. Hsiao[59], G. Huber[60], P. Illinski[2], T. Ishikawa[61], S. Jacobi[14], C. Jacobsen[59], J. Jiang[62], R.L. Johnson[49], Z. Jurek[44], R. Kampmann[14], C.H. Keitel[42], U. Keller[63], E. Kennedy[31], S. Kishimoto[64], H. Kitamura[61], U. Klemradt[17], J. Knoth[14], A. Koch[65], A. Kodre[66], P. Konarev[56], J. Krzywinski[67], S. Kuhlbrodt[30], T. Laarmann[3], R.W. Lee[68], G. LeLay[69], O. Leupold[6], T. Limberg[22], I. Lindau[70], D. v.d.Linde[71], P.-A. Lindgård[45], H. Lipkin[72], K.-D. Liss[6], C. Malgrange[73], E. Mandelkow[12], S. Mangold[74], A. Maquet[75], J. Marangos[76], M. Martin[77], G. Materlik[3], T. Matsushita[64], C. McGinley[3], P. McMahon[4], A. McPherson[2], K.-H. Meiwes-Broer[30], R. Menk[78], W. Menzel[79], M. Meyer[80], J. Meyer-ter-Vehn[37], J. Miao[5], D. Mills[2], A. Molenbroek[19], T. Möller[3], L. Moog[2], C. Morawe[6], R. Moshammer[42], J.-P. Mosnier[31], H.G. Muller[34], D. Nagy[44], K. Namikawa[81], T. Nawroth[82], R. Neder[58], M. Neeb[23], J. Neuefeind[3], R. Neutze[52], D. Novikov[3], S. Novikov[83], K. Nugent[4], J.H. Parks[84], A. Patwardhan[76], J. Pflüger[3], M. Pilz[15], R.M. Potvliege[85], W. Potzel[86], H. Poulsen[45], G. Prümper[16], J. Ramirez[87], R. Ramis[87], G. Rapp[3], R. Redmer[30], H. Reichert[36], D. Reis[88], M. Richter[89], C. Riekel[6], D. Riley[90], A. Ringwald[91], I. Robinson[92], R. Röhlsberger[30], J. Rossbach[22], J.-M. Rost[93], J.-E. Rubensson[94], M. Rübhausen[60], R. Rüffer[6], M. Rüter[95], E. Saldin[3], T. Salditt[96], S. Sasaki[2], M. Scheer[7], T. Schlegel[97], I. Schlichting[98], M. Schmitz[99], J.R. Schneider[3], C. Schroer[100], W. Schülke[101], H. Schulte-Schrepping[3], E. Schneidmiller[3], K.-H. Schwalbe[14], H. Schwencke[14], A. Scrinzi[26], O. Seeck[3], F. Senf[7], K. Sengstock[43], S. Shastri[2], Y. Shvyd'ko[49], P. Siddons[102], R. van Silfhout[56], A. Snigirev[6], B. Sonntag[49], D. van der Spoel[52], M. Stamm[103], K. Starke[104], J. Stöhr[5], T. Stoye[95], M. Störmer[14], N. Striebeck[105], W. Sturhahn[2], J. Susini[6], J. Sutter[3], A. Szöke[68], R. Tatchyn[5], K. Taylor[90], S. Techert[106], M. Tischer[3], T. Toellner[2], M. Tolan[107], P.E. Toschek[60], E. Traktenberg[2], A.X. Trautwein[108], R. Treusch[3], D. Trines[91], L. Tröger[2], T. Tschentscher[3], I. Uschmann[50], U. van Bürck[86], M. van Heel[76], I. Vartaniants[92], F. van der Veen[38], E. Vlieg[109], G. Vogl[110], J. Wark[111], E. Weckert[3], H. Weise[99], T. Weitkamp[6], B. Wellegehausen[43], E. Welter[3], J. Wiesmann[14], M. Wilmanns[56], J. Wong[68], G. Wortmann[112], M. Wulff[6], W. Wurth[49], A. Yashishita[64], A. Yonath[72], M. Yurkov[113], H. Zabel[114], P. Zambianchi[2], J. Zegenhagen[6], W. Zinth[17], A. Zuev[33]

1 II. Physikalisches Institut, University Cologne, Germany

2 Advanced Photon Source, Argonne, U.S.A.

3 HASYLAB, DESY, Hamburg, Germany
4 University Melbourne, Australia
5 SSRL, SLAC, Stanford, U.S.A.
6 European Synchrotron Radiation Facility, Grenoble, France
7 BESSY GmbH, Berlin, Germany
8 University Aarhus, Denmark
9 CSIC, Madrid, Spain
10 University Oxford, United Kingdom
11 SPring-8, Harima, Japan
12 MPG-ASMB, Hamburg, Germany
13 Uniwersytet Lodzki, Poland
14 GKSS, Geesthacht, Germany
15 Zeiss, Oberkochen, Germany
16 Fritz-Haber-Institut, MPG, Berlin, Germany
17 Sektion Physik, University Munich, Germany
18 Lawrence Berkeley National Laboratory, Berkeley, U.S.A.
19 Haldor Topsøe A/S, Lyngby, Denmark
20 University Washington, Seattle, U.S.A.
21 DRFMC, CEA, Grenoble, France
22 MPY, DESY, Hamburg, Germany
23 CHESS, Cornell, U.S.A.
24 Dept. of Mineralogy, University Hamburg, Germany
25 Vacuumschmelze AG, Hanau, Germany
26 Technical University Vienna, Austria
27 Uniwersitet Bialymstoku, Poland
28 Institut für Festkörperphysik, FZ Jülich, Germany
29 Dept. of Physical Chemistry, TU Darmstadt, Germany
30 FB Physik, University Rostock, Germany
31 Dublin City University, Ireland
32 University Leuven, Belgium
33 University Karlsruhe, Germany
34 FOM Institute, Amsterdam, The Netherlands
35 Inst. Krist. und Min., University Frankfurt, Germany
36 MPI für Metallforschung, Stuttgart, Germany
37 MPI für Quantenoptik, Garching, Germany
38 Swiss Light Source, PSI, Villingen, Switzerland
39 Dept. of Physics, University Potsdam, Germany
40 University Würzburg, Germany
41 Dept. of Chemistry, University Bochum, Germany
42 University Freiburg, Germany
43 University Hannover, Germany
44 University Budapest, Hungary
45 Risø National Laboratory, Roskilde, Denmark
46 Dept. of Physical Chemistry, University Hamburg, Germany

47 University Wuppertal, Germany
48 University of California, Davis, U.S.A.
49 II. Institut für Experimentalphysik, University Hamburg, Germany
50 University Jena, Germany
51 Dept. of Technical Chemistry, University Bochum, Germany
52 BMC, University Uppsala, Sweden
53 University Leipzig, Germany
54 Brookhaven National Laboratory, Brookhaven, U.S.A.
55 Dept. of Physics, University Hamburg, Germany
56 EMBL, Hamburg, Germany
57 DLR, Köln, Germany
58 Dept. of Mineralogy, University Würzburg, Germany
59 State University New York, Stony Brook, U.S.A.
60 Institut für Laserphysik, University Hamburg, Germany
61 RIKEN Institute, Harima, Japan
62 Technical University, Lyngby, Denmark
63 Eidgenössische Technische Hochschule, Zürich, Switzerland
64 Photon Factory, KEK, Tsukuba, Japan
65 Thomson Tube Electronique, Moirans, France
66 University Ljubljana, Slowenia
67 Academy of Science, Warsaw, Poland
68 Lawrence Livermore National Laboratory, Livermore, U.S.A.
69 University Provence, Marseille, France
70 SLAC, Stanford, U.S.A.
71 Institut für Laser- & Plasmaphysik, University Essen, Germany
72 Weizmann Institute, Rehovot, Israel
73 Universites Paris 6 et 7, France
74 TU Hamburg-Harburg, Germany
75 Laboratoire Chemie et Physique, Paris, France
76 Imperial College, London, United Kingdom
77 Dept. of Chemistry, RWTH Aachen, Germany
78 ELETTRA, Trieste, Italy
79 University Potsdam, Germany
80 Centre Universitaire Paris-Sud, France
81 University Osaka, Japan
82 Dept. of Biochemistry, University Mainz, Germany
83 Rostov State University, Russia
84 Rowland Institute, Cambridge, U.S.A.
85 University Durham, United Kingdom
86 Dept. of Physics, Technical University Munich, Garching, Germany
87 ETSI Aeronauticos, Madrid , Spain
88 University of Michigan, Ann Arbor, U.S.A.
89 Physikalisch-Technische-Bundesanstalt, Berlin, Germany
90 Queen's University, Belfast, Ireland

91 DESY, Hamburg, Germany
92 University Illinois, Chicago, U.S.A.
93 Max-Planck-Institut, Dresden, Germany
94 Dept. of Physics, Uppsala University, Sweden
95 ZM1, DESY, Hamburg, Germany
96 Dept. of Experimental Physics, University Saarbrücken, Germany
97 Technical University Darmstadt, Germany
98 MPI für molekulare Physiologie, Dortmund, Germany
99 MIN, DESY, Hamburg, Germany
100 II. Physikalisches Institut, RWTH Aachen, Germany
101 FB Physik, University Dortmund, Germany
102 National Synchrotron Light Source, Brookhaven, U.S.A.
103 MPI für Polymerenforschung, Dresden, Germany
104 Dept. of Physics, FU Berlin, Germany
105 Inst. für Technische Makromolekulare Chemie, University Hamburg, Germany
106 Max-Planck-Institut, Göttingen, Germany
107 Dept. of Physics, University Kiel, Germany
108 Dept. of Physics, Medical University Lübeck, Germany
109 University Nijmegen, The Netherlands
110 Hahn-Meitner-Institut, Berlin, Germany
111 Clarendon Laboratory, Oxford, United Kingdom
112 University Paderborn, Germany
113 JNIR, Dubna, Russia
114 Dept. of Experimental Physics, University Bochum, Germany

Acknowledgement Many scientists from all over the world have contributed towards the development of free-electron laser theory and technology and also in predicting the inevitable advancement of science when this new light is going to be used to study matter. We have listed above all scientists who have contributed in workshops and working groups directly to this Technical Design Report for the TESLA X-ray free-electron laser. The editors like to express their sincere thanks to all of them for this cooperation which will hopefully lead to the creation of a new type of X-ray source – much brighter than any before.

Contents

1. Preface

For research in natural sciences photons ranging from radio frequencies to hard γ-rays and including visible light, ultraviolet radiation and X-rays provide the most important tool to study nature. From these, X-rays, discovered in 1895 by C.W. Röntgen, have been used for many fundamental discoveries and outstanding applications which were rewarded with many Nobel Prize Awards. They have played a crucial role in basic science and medical diagnostics, as well as in industrial research and development. The main reason for this success is that the X-ray wavelength, which determines the smallest distance one can study with such a probe, is comparable to the atomic dimension.

In spite of the efforts made in building more powerful X-ray tubes, their progress was only moderate for a long time, certainly if seen in the light of the tremendous progress which finally was made with synchrotron radiation sources (Fig. 1.0.1).

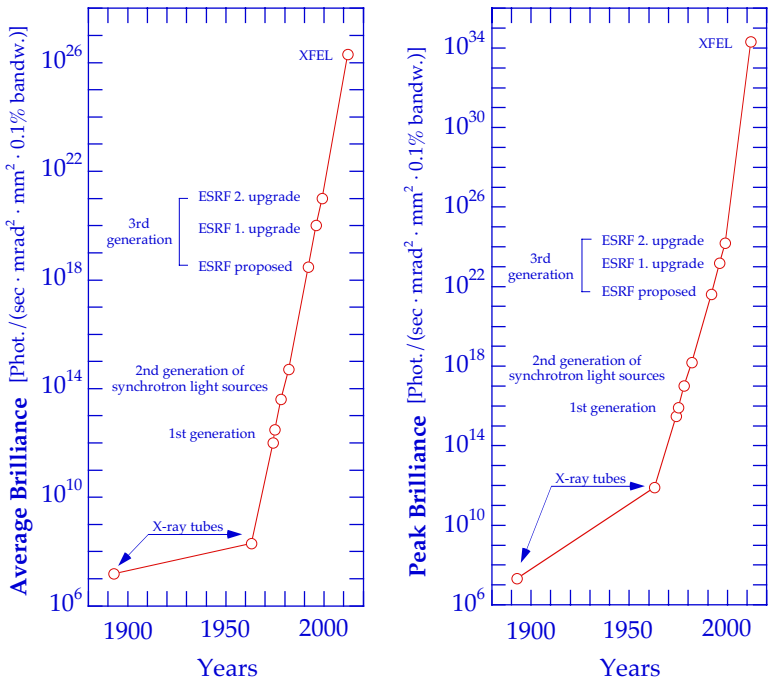

Figure 1.0.1.: *Brilliance development of X-ray sources since the discovery of X-rays by W.C. Röntgen in Würzburg, 1895.*

Synchrotron radiation (SR) has provided over the past thirty years an increase in flux and brilliance by more than ten orders of magnitude. Of course, this opened up fundamentally new areas of research [1]. At DESY scientists began inventing applications based on synchrotron radiation as early as the late 1960's [2] using the DESY synchrotron. The development of storage rings such as DORIS, which were capable of ensuring constant beam conditions, opened the way for systematic scientific studies. The design and construction of storage rings with special magnetic insertion devices, called wigglers and undulators, over the past twenty years has led to third generation machines specially designed for synchrotron radiation research [3], such as the ESRF[1], which by far surpass their design goals. This illustrates impressively how successful accelerator physics has become today.

However, even with these types of brilliant sources, all electrons emit their radiation field without a fixed phase relation leading to an incoherent superposition. The technical challenge is therefore to introduce a constant phase relation between the electrons travelling through an accelerator structure. Already Motz [4] showed in 1951 that an electron bunch travelling through an undulator magnet array can amplify radiation. Philips [5] built in 1960 the Ubitron and started the development of what we now call the "free-electron laser" (FEL). Palmer [6] , Robinson [7] and Csonka [8] continued with further theoretical work. Madey [9] reconsidered the possibilities for building an FEL in the 1970's and finally operated the first one in 1977 at 10 mm radiation wavelength. However, only the idea of self amplified spontaneous emission (SASE) [10]-[22] opened the path to build an FEL as a source for X-rays. Nevertheless, the technical realization remained unlikely throughout the 1980's since a very high 6-dimensional phase space density is required [23]. Only the operation of radio frequency photo-cathode guns [24], emittance compensation methods [25, 26] and successes in accelerator development in the early 90's led to the first proposal [27] that very long undulators coupled to linear accelerators can provide coherent X-rays with true laser properties.

Scientific applications of such a source of coherent laser-like X-rays were discussed in 1992 [28] and 1994 [29] and showed the great research potential it would have. Linac based XFELs should provide transverse coherent X-rays at wavelengths down to 1 Å in pulses of 100 fs duration with dark intervals between pulses ranging from nanoseconds up to seconds in a most flexible way. Peak brilliances would exceed those of third generation SR sources by over ten orders of magnitude (Fig. 1.0.1). Their spectral properties are shown in Fig. 1.0.2.

Discussions on machine related issues started in a workshop at BNL[2] in 1990 [30]. These were continued in discussing fourth generation light sources [31], at the ESRF 1996 [32] and at APS[3] in 1999 [33]. A general consensus was that SASE XFELs will be the most promising new X-ray sources for the future. In parallel to this several workshops were held to specify the scientific case for such a new laser source [34]-[36]. Here it became clear that these new sources are so fundamentally different that they will not replace the 3rd generation sources but will become for many fields a complementary tool and will also open up completely new fields of X-ray science and applications.

Finally two conceptual design studies were presented for an Å-XFEL, the LCLS[4] at

[1] ESRF stands for the European Synchrotron Radiation Facility in Grenoble, France
[2] BNL stands for Brookhaven National Laboratory, New York, U.S.A.
[3] APS stands for the Advanced Photon Source at Argonne National Laboratory (ANL), Illinois, U.S.A.
[4] LCLS stands for Linac Coherent Light Source

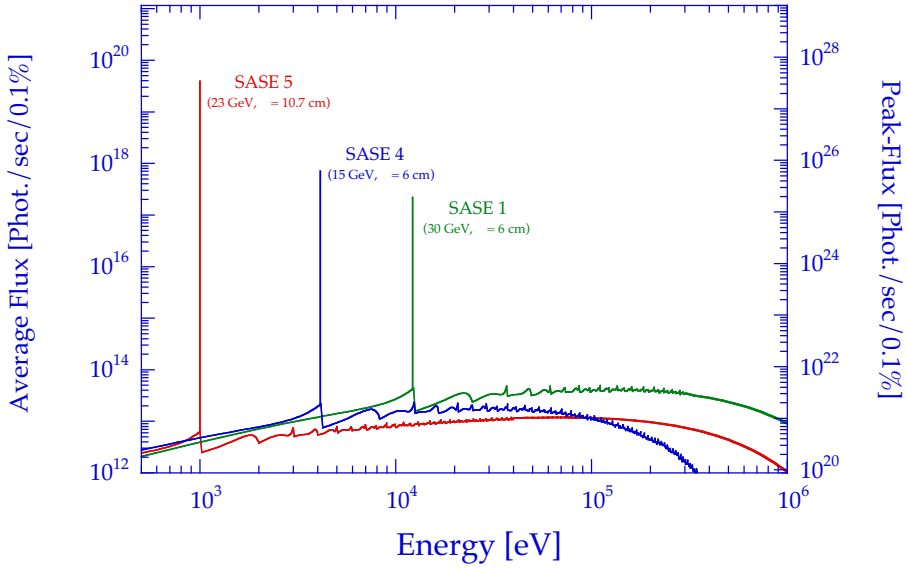

Figure 1.0.2.: *Spectral distribution of angle integrated radiation emitted from three of the SASE-FELs for smallest gap and different electron energies.*

SLAC[1] in Stanford [37] and the TESLA XFEL at DESY [38]. Furthermore two long wavelength projects were started, the TTF[2] FEL with wavelengths between 1000 Å and 60 Å at DESY in 1995 [39] and LEUTL[3] at ANL/APS in the short wavelength part of the visible spectrum in 1996. The goal of these projects was threefold: to prove that the SASE process works as theoretically predicted in these wavelength regions, to provide these SASE FELs for experimental research both in machine physics and scientific applications, and to finally pave the way technologically towards the construction of X-ray SASE FELs. Both experiments were successful in 2000 [40, 41]. TTF FEL showed that SASE works down to a wavelength of 800 Å and LEUTL reached saturation [42] at 5300 Å. Thus these projects are successfully working along with their aim to explore the science and develop the technology for the next generation of synchrotron light sources. Together with these two studies several experiments at longer wavelength showed in the last few years that the measurements agree well with the theoretical predictions for the dependence of exponential growth on electron beam parameters as well as its statistical behavior [43]–[54]. The experience gained in these technical steps and the agreement of SASE FEL theory and measurements form the basis and give us the confidence to propose and to build an XFEL laboratory for the Å wavelength range as proposed in this Technical Design Report for the TESLA XFEL.

Work carried out in a series of scientific workshops and studies (see appendix A for a list of reports) specified the experimental needs for such a source and the connected infrastructure, such as beamlines, photon optics and instruments as presented in this volume. The experience gained at third generation sources has been essential to extrapolate to the new

[1] SLAC stands for Stanford Linear Accelerator Center, California, U.S.A.
[2] TTF stands for TESLA Test Facility
[3] LEUTL stands for Low-Energy Undulator Test Line

requirements. However, in many aspects no straightforward extrapolation has been possible and many of the outstanding photon beam properties need more R & D work in the coming years to finalize constructions and methods.

This requires a worldwide effort which has already begun and needs a very close collaboration in future. The new radiation source will be fundamentally different from a spontaneous undulator in that the emitted radiation causes electron density modulation at the X-ray wavelength within each electron bunch. This leads to coherent emission and full transverse coherence. The result of this process is seen in the spectral shape displayed in Fig. 1.0.2. The coherently emitted XFEL lines appear in addition to the spontaneously emitted undulator spectrum which extends into the MeV regime. Even the time averaged spectral brilliance of the XFEL will exceed by three to four orders of magnitude those of undulators at the third generation synchrotron radiation sources ESRF, APS, and SPring-8[1]. In fact the spectral brilliance of each pulse exceeds the spectral brilliance per second of those sources. In addition, the peak brilliance, as displayed in Fig. 1.0.3, within each 100 fs pulse would be greater by more than 10 orders of magnitude than in third generation synchrotron radiation pulses with more than 30 ps duration. The peak power can reach up to the order of tens of GW. This proposed source with a circular shape could be as small as 100 μm in diameter and with an opening angle as little as 1 μrad. At third generation sources the corresponding values from undulators will typically be $100 \times 100\,\mu\text{m}^2$ with a divergence larger than 10 μrad. For an XFEL this means that even at 1 km distance the beam size increases to only 1 mm. This is a characteristic which relates to the fact that the XFEL source is spatially fully coherent.

In addition the spontaneously emitted synchrotron radiation spectrum is available which extends from the conventional keV range to the MeV regime. Again characteristics exceed the performance of third generation sources in operation today. Although the XFEL photon beam from each device is in principle a single user tool, just like one optical laser, the multi bunch property and the flexible pulse structure provide efficient ways to generate a multi-user facility - very similar to present day synchrotron radiation facilities. In contrast to a storage ring, in a linac each electron bunch will pass the accelerator only once. Therefore it is possible to extract individual bunches from the linear accelerator and guide them alternatively to various undulators. For the TESLA XFEL a part of the long 250 GeV TESLA linac will be available (see Fig. 1.0.4). Extraction lines can be built in parallel, for various electron energies which can be used for producing different X-ray energies in the XFEL laboratory in a quasi-simultaneous manner. This is shown in Fig. 1.0.5. Two such extraction lines for electron energies between 15-25 GeV and 20-30 GeV, respectively, are needed to fulfill the experimental requirements. However, the electron optics in one of the transfer lines can even provide a maximum energy of 50 GeV in case new important scientific applications are discovered in the future which require a higher electron energy. These electron beams are feeding XFEL undulators which in turn will be of different types and change polarization and photon energy range.

At the end of an extraction tunnel, a beam switchyard is foreseen distributing the beams to various undulators. Having left the XFEL, the quality of the electron beam is still high enough for other lower photon energy FEL undulators. Finally, the bunches will be passed

[1] SPring-8 stands for Super Photon Ring - 8 GeV, Harima, Japan

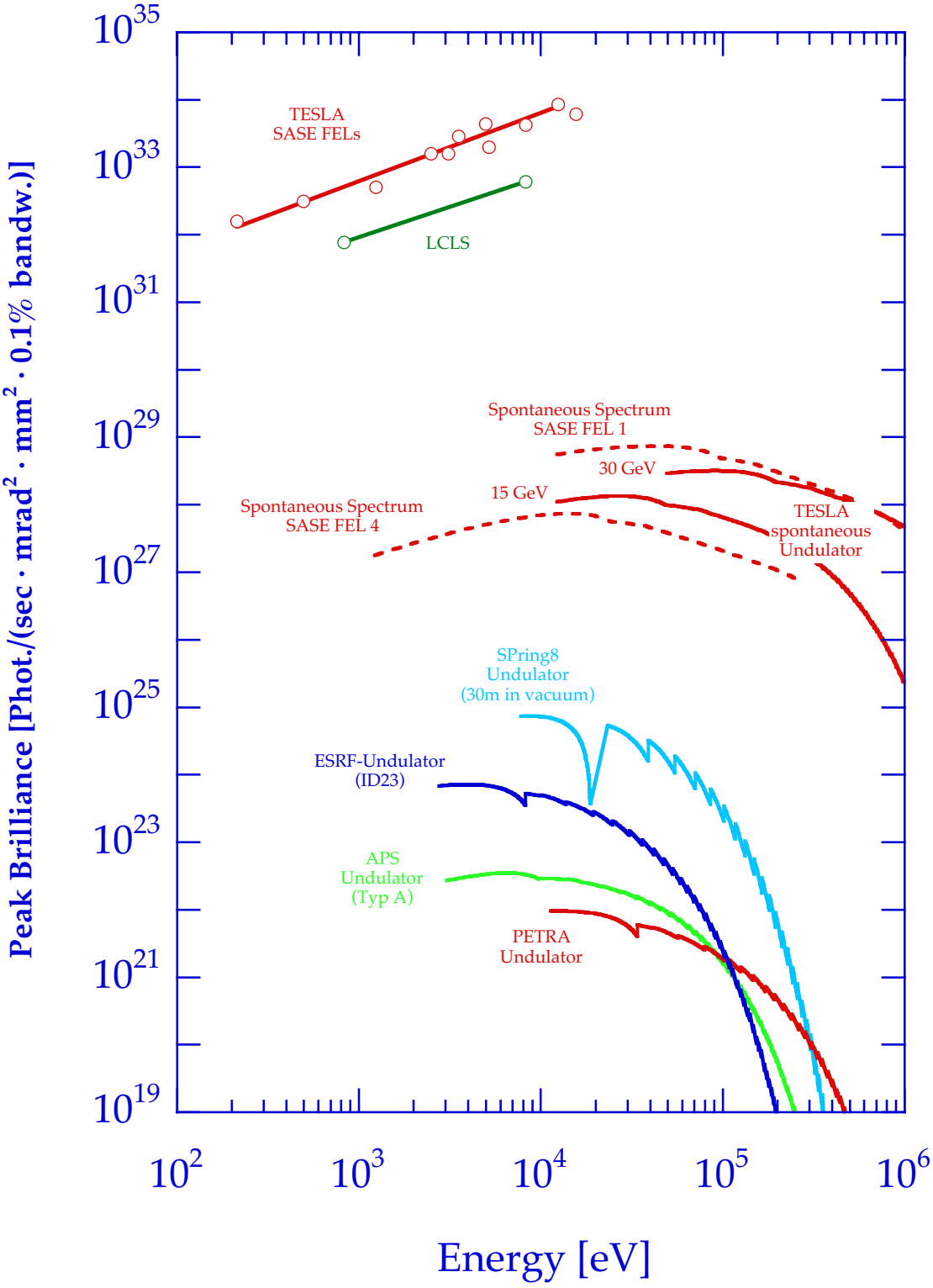

Figure 1.0.3.: *Peak brilliance of the TESLA XFEL devices in comparison to third generation storage ring insertion devices. Red open circles: calculated values for the TESLA XFELs. Note that the photon energy E is related to the wavelength by* $\lambda[\AA] = 12.4/E[keV]$.

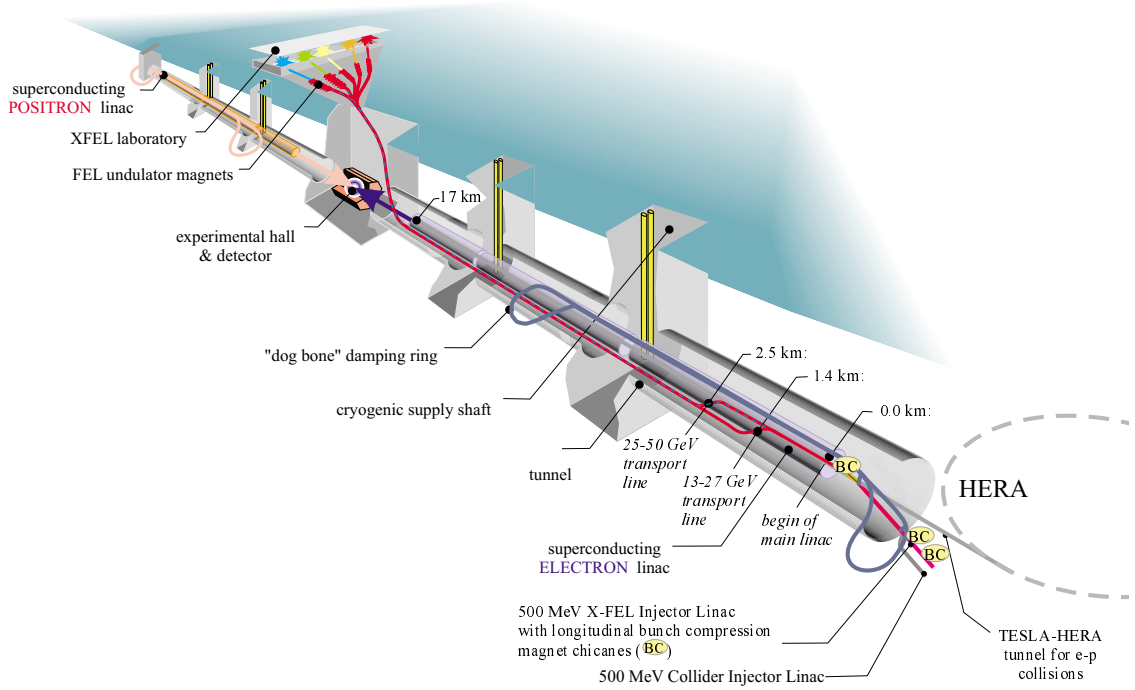

Figure 1.0.4.: *Schematic presentation of the whole TESLA facility.*

through undulators generating spontaneous radiation. The overall length of the XFEL laboratory area is determined by the length of the electron beam switchyard, the length of the FEL undulators and by several hundred meters of drift lines for the intense photon beams. Most important, this long radiation drift lets the SASE beams dilute by natural divergence until the first optical elements can handle the heat loads. In addition, it makes a large demagnification ratio of the X-ray beams possible. And finally, it also assures that the radiation safety requirements in the experimental hall can be realized similar to those in present day synchrotron radiation laboratories.

The discussion in the scientific community over the past decade has produced many ideas for novel applications of the X-ray laser. Brilliance, coherence, and timing down to the femtosecond regime are the three properties which have the highest potential for new science to be explored with an XFEL. The use of linear and circular polarization as well as wavelength tunability with extremely narrow bandwidth are clearly additional, attractive characteristics of this source as is the ideal spontaneous undulator radiation “background”. It is obvious that studies of time dependent phenomena can be tackled for the first time which relate the structural aspects with the transition states of those electrons which are responsible for the formation process of intra-molecular bonds, biologically active macromolecules, clusters, nanoparticles, liquids, solids or even hot dense plasmas. Structure, function and transitions will be seen with a femtosecond time-lens up to human real-time speeds. This can possibly show us directly how matter is formed out of atoms. The high brilliance per pulse is certainly

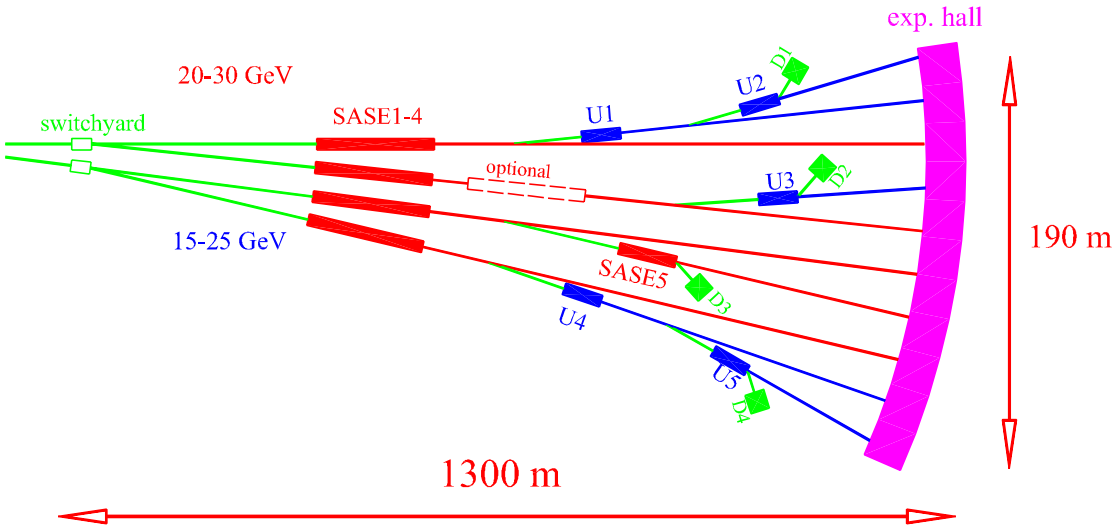

Figure 1.0.5.: *Sketch of the XFEL laboratory. The electron switchyard, SASE XFEL undulators SASE 1–5, undulators U1–U5, beamdumps D1–D4, the photon beamlines in-between, and the experimental hall are shown.*

the most outstanding feature of X-rays from the XFEL. It will make single pulse scattering, diffraction and spectroscopic measurements possible. This scientific and technical case study shows not only the new perspectives for science but also the technical challenges in realizing this outstanding project. The SASE process will be made to work at 1 Å wavelength which requires the generation of an electron beam of unprecedented quality. This beam will be directed through the magnet and accelerating structures such that it produces coherent laser light in very long mechanically precise and stable undulator structures.

Guiding the photons to the experiment requires the development of new beamline components to withstand the high average and peak photon flux, bringing the photon beam tailored to the need of the experiment down onto the sample. In addition, fast detectors with high spatial resolution need to be developed which cope with the expected photon fluxes and count rates to open new time windows from presently available nanosecond sensors down to the femtosecond regime. It is inevitable that these technical developments will lead to corresponding spin-off applications.

Furthermore, it will bring together the development of so-called table-top lasers of different types with the development of accelerator based laser sources (Fig. 1.0.6). Optical, VUV and X-ray table-top sources are needed in pump-probe timing experiments and for home based test and preparation runs. The handling of spatially modulated tiny electron beams will advance today's techniques so far that even beam chirping can become feasible and lead the way to reduce the X-ray bunch duration towards 1 fs. The extremely high power density will open the fully new field of nonlinear X-ray phenomena and start experiments in X-ray quantum optics. It is even suggested that, with the high power levels generated by focusing, one could study the QED vacuum decay in high fields. Plasma physical phenomena will become accessible for the first time in a pressure-temperature region, which up to now cannot

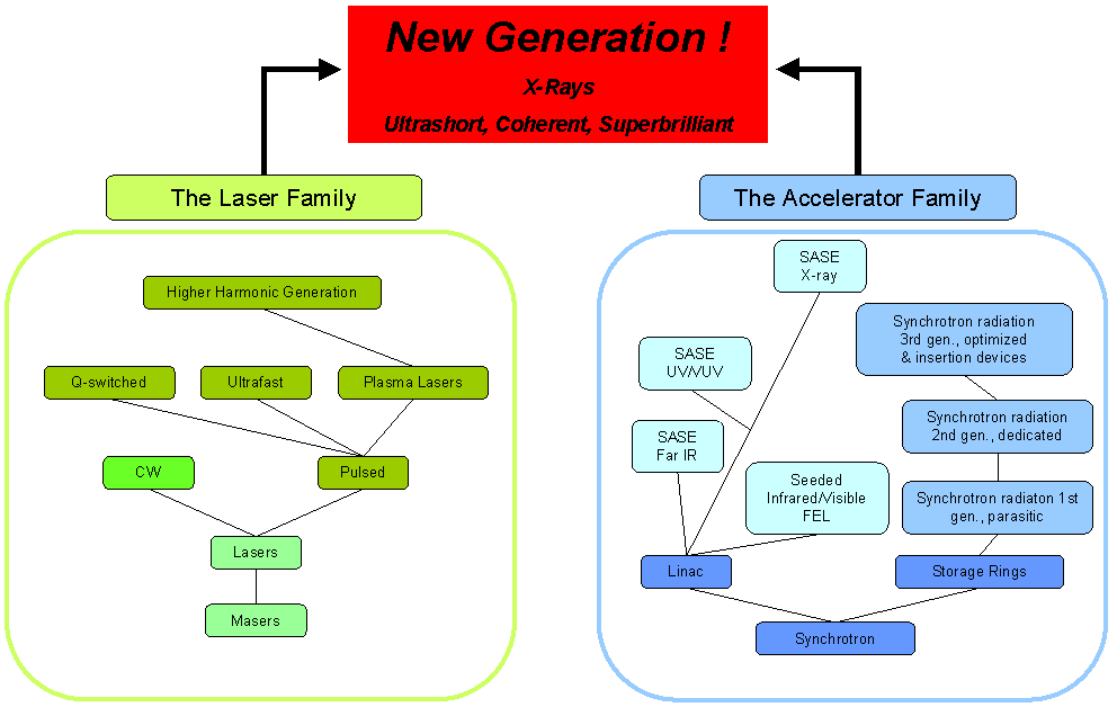

Figure 1.0.6.: *The XFEL will provide the link of two large scientific communities.*

be prepared in the laboratory. The variety of new and exciting experimental possibilities in physics, chemistry, materials science, biology, and industrial applications should in fact lead to the same sort of revolutionary developments in X-ray studies of matter that was triggered in optical studies by introduction of the visible/UV lasers.

In chapter 2 we will give a brief description of the SASE XFEL principle and the main characteristics of the XFEL radiation. Nine different science fields are presented in chapter 3 with proposals and visions for applications of the new laser. In chapter 4.1 and 4.2 we describe the consequences of the scientific proposals with respect to the design of an XFEL laboratory and the characteristics of the XFEL radiation and undulator specification. In chapter 4.3 the realization of the XFEL undulators will then be described. Chapters 5 and 6 deal with the X-ray optical issues for mirrors, lenses and monochromators and the beam line designs together with the experimental techniques. In chapter 7 we briefly describe the civil engineering for the proposed XFEL laboratory and, finally, in chapter 8 a statement on the expected cost can be found. The machine related issues, which provide the basis for the successful operation of these XFELs, are discussed separately in Chapter 9 of Part II of this Technical Design Report. Note that the bibliography is attached to the corresponding chapters. In the scientific case in Chap. 3 we present the bibliography for clarity reasons after each science field. Finally, we note that many more detailed reports are available as an appendix on a CD-ROM.

Bibliography

[1] J. Als-Nielsen and G. Materlik, Phys. Today, 34 (Nov 1995).

[2] R. Haensel and C. Kunz, Z. Angew. Phys. **23**, 276 (1967).

[3] B. Buras and G. Materlik, Nucl. Instrum. Meth. A**246**, 21(1986).

[4] H. Motz, J. Appl. Phys. **22**, 527 (1951); H. Motz, W. Thon, R.N. Whitehurst, J. Appl. Phys. **24**, 826 (1953); H. Motz, M. Nakamura, Ann. Phys. **7**, 84 (1959).

[5] R.M. Philips, IRE Trans. Electron Devices **7**, 231 (1960).

[6] R.V. Palmer, J. Appl. Phys. **43**, 3014 (1972).

[7] K.W. Robinson, Nucl. Instrum. Meth. A**239**, 111 (1985).

[8] P. Csonka, Part. Acc. **8**, 225 (1978).

[9] J.M.J. Madey, J. Appl. Phys. **42**, 1906 (1971); L.R. Elias, W.M. Fairbank, J.M.J. Madey, H.A. Schwettman, T.I. Smith, Phys. Rev. Lett. **36**, 717 (1976); D.A.G. Deacon et al., Phys. Rev. Lett. **38**, 892 (1977).

[10] A.M. Kondratenko and E.L. Saldin, Part. Accelerators **10**, 207 (1980).

[11] R. Bonifacio, C. Pellegrini, L.M. Narducci, Opt. Commun. **50**, 373 (1984).

[12] K.-J. Kim, Nucl. Instrum. Meth. A**250**, 396 (1986).

[13] J.-M. Wang and L.-H. Yu, Nucl. Instrum. Meth. A**250**, 484 (1986).

[14] G.T. Moore, Nucl. Instrum. Meth. A**239**, 19 (1985).

[15] E.T. Scharlemann, A.M. Sessler, J.S. Wurtele, Phys. Rev. Lett. **54**, 1925 (1985).

[16] M. Xie and D.A.G. Deacon, Nucl. Instrum. Meth. A**250**, 426 (1986).

[17] K.-J. Kim, Phys. Rev. Lett. **57**, 1871 (1986).

[18] L.-H. Yu, S. Krinsky, R. Gluckstern, Phys. Rev. Lett. **64**, 3011 (1990).

[19] Ya.S. Derbenev, A.M. Kondratenko, E.L. Saldin, Nucl. Instrum. Meth. A**193**, 415 (1982).

[20] J.B. Murphy and C. Pellegrini, Nucl. Instrum. Meth. A**237**, 159 (1985).

[21] J.B. Murphy and C. Pellegrini, J. Opt. Soc. Am. B**2**, 259 (1985).

[22] K.J. Kim et al., Nucl. Instrum. Meth. A**239**, 54 (1985).

[23] C. Pellegrini, Nucl. Instrum. Meth. A**272**, 364 (1988).

[24] J.S. Fraser, R.L. Sheffield, E.R. Gray, Nucl. Instrum Meth. A**250**, 71 (1986).

[25] B.E. Carlsten, Nucl. Instrum. Meth A**285**, 313 (1989).

[26] X. Qiu, K. Batchelor, I. Ben-Zvi, X.-J. Wang, Phys. Rev. Lett. **76**, 3723 (1996).

[27] C. Pellegrini in [31].

[28] Report on the Workshop on Scientific Applications of Short-Wavelength Coherent Light Sources, W. Spicer, J. Arthur, H. Winick (eds.), SLAC, October (1992).

[29] Workshop on Scientific Applications of Coherent X-rays, J. Arthur, G. Materlik, H. Winick (eds.), SLAC-437, Stanford, February (1994).

[30] Proceedings of the Workshop Prospects for a 1 Å Free-Electron Laser, Sag Harbor, New York, April (1990).

[31] Report on the Workshop on Fourth Generation Light Sources, M. Cornacchia, H. Winick (eds.), SLAC, February (1992), SSRL Report 92/02.

[32] Proceedings of the 10th ICFA Beam Dynamics Workshop on Fourth Generation Light Sources, ESRF, Grenoble, January (1996).

[33] Proceedings of the 17th Advanced Beam Dynamics Workshop on Future Light Sources, APS, Chicago, April (1999).

[34] International Workshop on X-Ray Free Electron Laser Application, DESY, Hamburg, September (1996).

[35] Potential Future Applications in Structural Biology of an X-ray Free Electron Laser at DESY, EMBO Workshop, DESY, Hamburg, July (1999).

[36] SLAC/DESY International Workshop on Interactions of Intense Sub-picosecond X-Rays with Matter, SLAC, Stanford, January (1997).

[37] The LCLS Design Study Group, *LCLS Design Study Report*, SLAC reports SLAC-R-521, Stanford (1998).

[38] R. Brinkmann, G. Materlik, J. Rossbach, A. Wagner, Conceptual Design Report of a 500 GeV e+e- Linear Collider with Integrated X-ray Laser Facility, Vol. II, DESY report, DESY, Hamburg (1997).

[39] T. Åberg et al., Conceptual Design Report of a VUV FEL at the TESLA Test Facility at DESY, DESY Report TESLA-FEL **95-03**, Hamburg (1995).

[40] J. Andruszkow et al., Phys. Rev. Lett. **85**, 3825 (2000).

[41] S.V. Milton et al., Phys. Rev. Lett. **85**, 988 (2000).

[42] S.V. Milton, E. Gluskin et al., *Measured Gain and Saturation of a SASE FEL*, Science, subm. Feb. 2001.

[43] E.L. Saldin, E.A. Schneidmiller, M.V. Yurkov, *The Physics of Free Electron Lasers*, Springer, Berlin-Heidelberg (2000) and references therein.

[44] T. Orzechowski et al., Phys. Rev. Lett. **54**, 889 (1985).

[45] D. Kirkpatrick, Nucl. Instrum. Meth. A**285**, 43 (1989).

[46] J. Gardelle, J. Labrouch, J.L. Rullier, Phys. Rev. Lett. **76**, 4532 (1996).

[47] R. Prazeres et al., Phys. Rev. Lett. **78**, 2124 (1997).

[48] M. Hogan et al., Phys. Rev. Lett. **80**, 289 (1998).

[49] M. Babzien et al., Phys. Rev. E**57**, 6093 (1998).

[50] D.C. Nguyen et al., Phys. Rev. Lett. **81**, 810 (1998).

[51] M. Hogan et al., Phys. Rev. Lett. **81**, 4867 (1998).

[52] L.-H. Yu et al., Nucl. Instrum. Meth. A**445**, 301 (1999).

[53] E.L. Saldin, E.A. Schneidmiller, M.V. Yurkov, Nucl. Instrum. Meth. A**429**, 229 (1999).

[54] A. Tremaine et al., Proceedings International FEL'2000 Conference, Durham USA (2000), Nucl. Instrum. Meth. (in press).

2. The XFEL Principle

A basic description of the FEL process and the photon beam properties is presented. For a detailed description of FEL theory see [1]–[7]. A simplified approach (in German) can be found in [8]. In Chap. 4 specific properties of the TESLA XFELs are discussed.

2.1. FEL vs. Optical Laser

Radiation from a Free Electron Laser (FEL) has much in common with radiation from a conventional optical laser, such as high power, narrow bandwidth and diffraction limited beam propagation. One of the main differences between the two lasers is the gain medium: In a conventional LASER (Light Amplification by Stimulated Emission of Radiation) the amplification comes from the stimulated emission of electrons bound to atoms, either in a crystal, liquid dye or a gas, whereas the amplification medium of the FEL are “free” (unbound) electrons. The free electrons have been stripped from atoms in an electron gun and are then accelerated to relativistic velocities.

While the electrons are propagating through a long, periodic magnetic dipole array – a so called undulator – the interaction with an electromagnetic radiation field leads to an exponential growth of the radiation emitted by the electrons. This amplification of radiation is initiated by an increasingly pronounced longitudinal density modulation of the electron bunch. The initial radiation field can be an external one, e.g. a seed laser, or an “internal” field, i.e. the spontaneous emission of the undulator. In the latter case it is called a SASE (Self Amplified Spontaneous Emission) FEL [9, 10]. Since the electrons in the FEL are not bound to atoms and thus not limited to specific transitions, the wavelength of the FEL is tunable over a wide range depending on accelerator energy and undulator parameters.

For IR, visible and UV FELs, light amplification can be reached in a multi-pass setup, i.e. by using an optical cavity with mirrors on both sides and the electrons passing the undulator as the gain medium in between. With such an arrangement, which – apart from its normally much larger size – exhibits a certain resemblance to optical laser setups, the light from many successive electron bunches is stored and amplified. For VUV and X-ray FELs, mirrors can no longer be applied due to their low reflectivities in normal incidence geometry at these wavelengths and potential mirror deformation/damage due to the high absorbed powers. Since a SASE FEL operates in the high-gain regime, it does not require an optical cavity and it can hence be used to deliver light in the VUV and X-ray regime. In such a "single pass" SASE FEL the full radiation power builds up from spontaneous emission when an electron beam with high phase space density passes a long undulator just once. While FELs in the visible and UV range can also be realized in synchrotron radiation storage rings, there is a consensus that – due to the higher demands on the electron beam properties –

one needs a linear accelerator to generate FEL radiation in the VUV and X-ray range. The most promising approach is the setup of a single pass SASE FEL at a state of the art linear accelerator in combination with a high-performance radio frequency photo-cathode electron gun and longitudinal bunch compression to achieve the required peak current of several kA. Details on the parameters of such an electron gun, the linear accelerator, bunch compressors, etc. can be found in Part II of this report, describing the machine setup for the TESLA project.

2.2. From Synchrotron Radiation to a SASE FEL

The basic principle of the free electron laser can be described within the standard picture for the generation of synchrotron radiation: while travelling with relativistic velocity ($v \simeq c$, $\gamma \simeq 10^2 - 10^5$) through the undulator, the electrons are accelerated in the direction transverse to their propagation due to the Lorentz force introduced by the magnetic field. They propagate along a sinusoidal path and emit SR in a narrow cone in the forward direction. The typical opening angle of the wavelength integrated radiation is

$$\frac{1}{\gamma} = \frac{m_e c^2}{E_e} \,, \tag{2.2.1}$$

where m_e is the electron mass (511 keV/c^2) and E_e the electron energy. In the undulator, the deflection of the electrons from the forward direction is comparable to the opening angle of the synchrotron radiation cone. Thus the radiation generated by the electrons while travelling along the individual magnetic periods overlaps. This interference effect is reflected in the formula for the wavelength λ_{ph} of the first harmonic of the spontaneous, on-axis undulator emission

$$\lambda_{ph} = \frac{\lambda_u}{2\gamma^2}(1 + K_{rms}^2) \,, \tag{2.2.2}$$

where λ_u is the length of the magnetic period of the undulator and K_{rms} is the "averaged" undulator parameter[1]

$$K_{rms} = \frac{e\, B_u\, \lambda_u}{2\,\pi\, m_e c} \tag{2.2.3}$$

which gives the ratio between the average deflection angle of the electrons and the typical opening cone of the synchrotron radiation. B_u is the rms magnetic field of the undulator and e the electron charge.

The interference condition basically means that, while travelling along one period of the undulator, the electrons slip by one radiation wavelength with respect to the (faster) electromagnetic field. This is one of the prerequisites for the SASE process of the FEL. To obtain an exponential amplification of the spontaneous emission present in any undulator, some additional criteria have to be met: One has to guarantee a good electron beam quality and a sufficient overlap between radiation pulse and electron bunch along the undulator. To

[1] Please note that for a planar undulator and a sinusoidal magnetic field, the commonly used undulator parameter K is related to K_{rms} by $K = \sqrt{2} \cdot K_{rms}$ and equation 2.2.3 can be used for K instead of K_{rms} if B_u is replaced by the peak magnetic field B_0.

achieve that, one needs a low emittance, low energy spread electron beam with an extremely high charge density in conjunction with a very precise magnetic field and accurate beam steering through a long undulator.

Oscillating through the undulator, the electron bunch then interacts with its own electromagnetic field created via spontaneous emission. Depending on the relative phase between radiation and electron oscillation, electrons experience either a deceleration or acceleration: Electrons that are in phase with the electromagnetic wave are retarded while the ones with opposite phase gain energy. Through this interaction a longitudinal fine structure, the so called micro-bunching, is established which amplifies the electromagnetic field (Fig. 2.2.1).

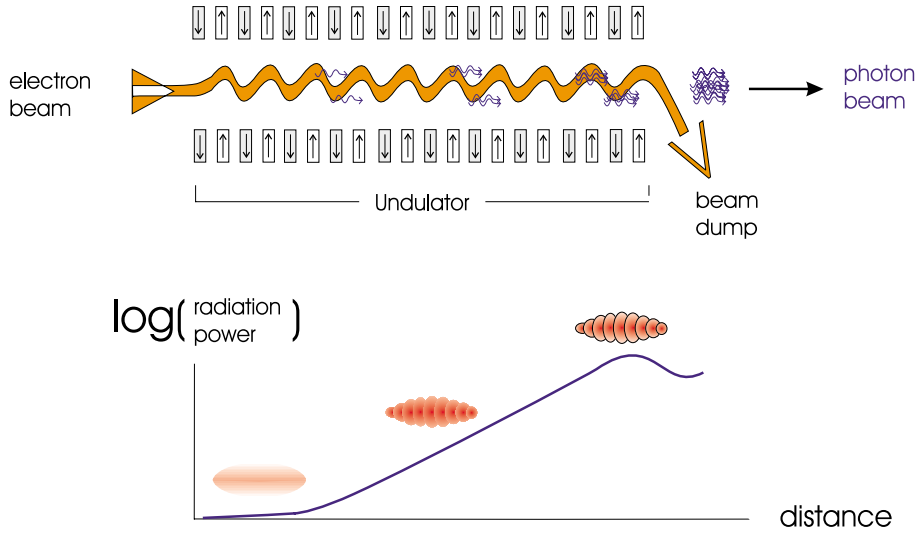

Figure 2.2.1.: *Sketch of the self-amplification of spontaneous emission (SASE) in an undulator resulting from the interaction of the electrons with the synchrotron radiation they emit. In the lower part of the figure the longitudinal density modulation (micro-bunching) of the electron bunch is shown together with the resulting exponential growth of the radiation power along the undulator. Note that in reality the number of micro-bunches is much larger ($\geq 10^5$ for the TESLA XFELs).*

The longitudinal distribution of electrons in the bunch is "cut" into equidistant slices with a separation corresponding to the wavelength λ_{ph} of the emitted radiation which causes the modulation. More and more electrons begin to radiate in phase, which results in an increasingly coherent superposition of the radiation emitted from the micro-bunched electrons. The more intense the electromagnetic field gets, the more pronounced the longitudinal density modulation of the electron bunch and vice versa.

In the beginning – without micro-bunching – all the N_e electrons in a bunch ($N_e \geq 10^9$) can be treated as individually radiating charges with the power of the spontaneous emission $\propto N_e$. With complete micro-bunching, all electrons radiate almost in phase. This leads to a radiation power $\propto {N_e}^2$ and thus an amplification of many orders of magnitude with respect

to the spontaneous emission of the undulator.

Due to the progressing micro-bunching, the radiation power $P(z)$ of such a SASE FEL grows exponentially with the distance z along the undulator [1, 11, 12]:

$$P(z) = AP_{in} \exp(2z/L_g) \tag{2.2.4}$$

where L_g is the field gain length, P_{in} the "effective" input power, and A the input coupling factor. A is equal to 1/9 in one-dimensional FEL theory with an ideal electron beam. For the estimation of the effective input power of the shot noise P_{in} one can use the spontaneous radiation power on the first gain length inside a coherence angle and within the FEL bandwidth. The exponential growth takes place until the electron beam is completely bunched (see Fig. 2.2.2) after which it is overmodulated resulting in saturation.

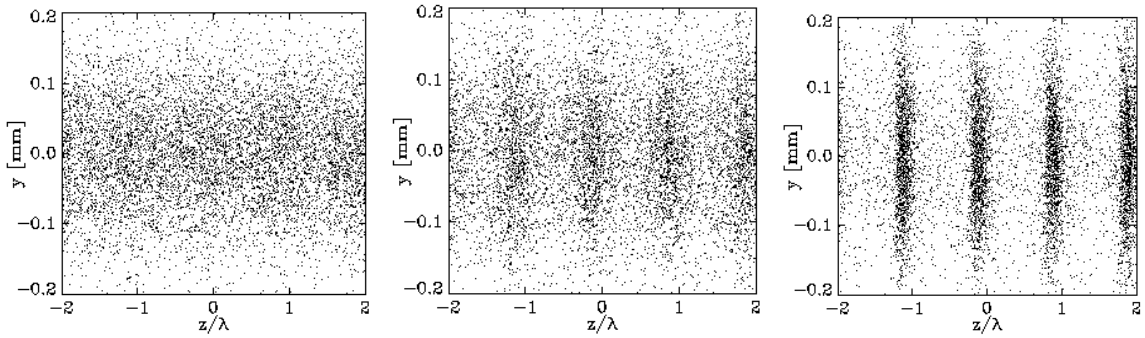

Figure 2.2.2.: *Example of the development of micro-bunching of the XFEL electron beam along the undulator. The electron density is represented by the density of the dots (Left: at the undulator entrance, Middle: in the middle of the exponential growth regime, Right: at the undulator exit, i.e. for saturation). Note that only an enlarged section of the bunch is shown. In reality the number of slices (micro-bunches) is much larger.*

The main properties of the FEL radiation can be simply estimated in terms of the FEL parameter ρ [10]: the field gain length is $L_g \simeq \lambda_u/(4\pi\rho)$, the FEL amplifier bandwidth $\Delta\omega/\omega$ and saturation efficiency (ratio of the output radiation power to the electron beam power) are about ρ. This parameter depends on the parameters of electron beam and undulator and is always much smaller than unity (for the TESLA XFELs ρ ranges between 10^{-3} and 10^{-4}).

The radiation from an X-ray FEL has a narrow bandwidth, it is fully polarized and transversely coherent. The transverse coherence is also reflected in the development of the transverse intensity distribution along the undulator (Fig. 2.2.3) which in the end is nearly Fourier transform limited [1, 13].

On the other hand, compared to conventional optical lasers the longitudinal coherence of an X-ray SASE FEL is rather poor which is a consequence of the start-up from shot noise (see Fig. 2.2.4). The coherence time is defined by the inverse spectral width $\Delta\omega$ and is for XFELs typically much smaller than the electron pulse duration. To improve the longitudinal

coherence length, at best up to the full radiation pulse length, a so called "two-stage SASE FEL" is proposed (see [14] and Chap. 4.2.2), where the final output radiation bandwidth is close to the limit given by the finite duration of the pulse.

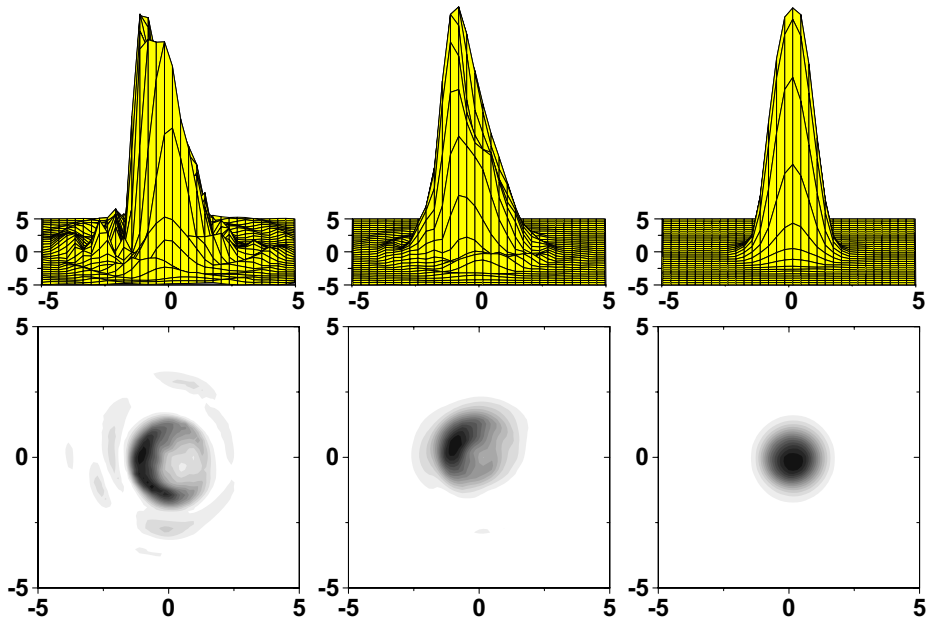

Figure 2.2.3.: *Distribution of the radiation intensity across one slice of the pulse close to the undulator entrance (left), half way through the undulator (middle) and close to saturation (right). The upper figures display the intensity vs. the transverse coordinates, in the lower figures the corresponding polar distribution is shown in units normalized to the radial pulse width* σ_R.

Figure 2.2.4.: *Example of the buildup of coherence along the undulator. The left figure shows the radiation intensity profile half way through the undulator, the figure to the right close to saturation. Please note that for a better visualization of the effect the figures were obtained from a simulation that was made at longer wavelengths and for a coherence length* L_c *which is 10% of the electron bunch length* L_b*, whereas for XFELs the typical ratio is* $L_c/L_b \simeq 10^{-3}$.

Examples of temporal and spectral structure of the radiation pulse from an X-ray FEL are presented in Fig. 2.2.5. The radiation pulse consists of a large number of independent wavepackets which give rise to "spikes". Within one wavepacket, the radiation is transversely and longitudinally coherent. The chaotic nature of the output radiation is a consequence of the start-up from shot noise: since the electron bunch consists of discrete charges randomly emitted from a cathode, the charge density exhibits fluctuations which are random in time and space. As a result, the radiation produced by such a beam has random amplitudes and phases in time and space. These kinds of radiation fields can be described in terms of statistical optics with, e.g., the following parameters: time and spectral correlation functions, transverse correlation functions, probability density distributions of the instantaneous radiation intensity, of its integrals (finite-time and space) and of the energy after a monochromator, coherence time, interval of spectral coherence, coherence area and coherence volume [1].

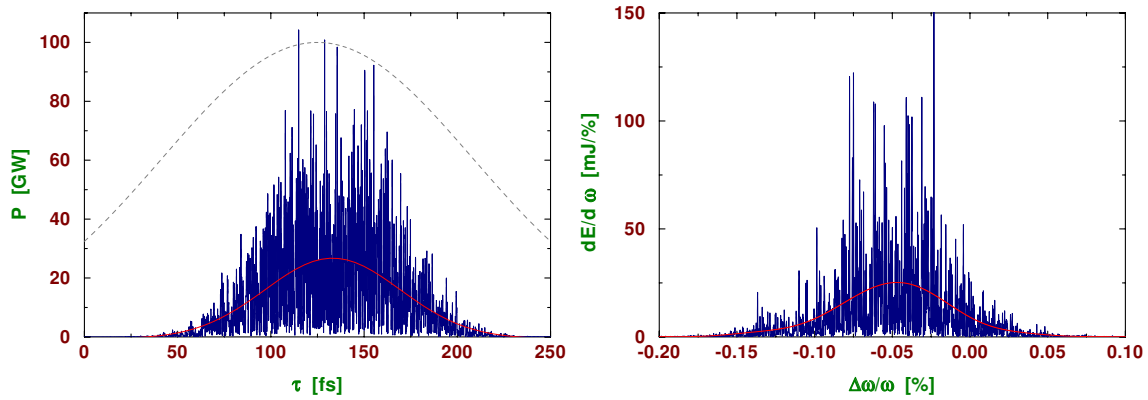

Figure 2.2.5.: *Typical temporal (left) and spectral (right) structure of the radiation pulse from a SASE XFEL at a wavelength of 1 Å. The red lines correspond to averaged values. The dashed line represents the axial density profile of the electron bunch. Note that the growth rate in the electron bunch tail is reduced due to the reduced current. Therefore, the radiation pulse length of 100 fs (FWHM) is about a factor of two shorter than the electron bunch.*

Using a planar undulator, a SASE FEL also naturally generates higher harmonics, since the micro-bunching of the electrons at the fundamental wavelength of the undulator can also drive substantial bunching at the higher harmonics[1]. Simulations yield a significant power output of a high-gain SASE FEL which for the third harmonic amounts to several per thousand up to one percent of the first harmonic output power [15, 16]. Whereas this nonlinear generation of higher harmonics might be quite relevant when extending the FEL operation range to even shorter wavelengths, all quantitative examples in the scientific case

[1] This generation of higher harmonics should not be confused with the so called high gain harmonic generation (HGHG) for FELs. Whereas the mechanism is identical, the HGHG consists of an undulator setup creating a micro-bunching at the first harmonic and a second undulator optimized for a higher harmonic which uses the density-modulated bunch to drive the modulation at this higher harmonic.

and the following chapters are based on the first harmonic of the XFELs.

2.3. Spectral Characteristics

As already mentioned, the characteristics of FEL radiation are high power, short pulse length, narrow bandwidth, spatial coherence and wavelength tunability. In this section, some examples will be given that shed light on the differences between the TESLA XFELs and state-of-the-art synchrotron radiation sources to illustrate the exceptional properties of an FEL. Table 2.3.1 gives an example of some typical photon beam parameters for one of the planned XFELs at TESLA (a detailed discussion of the properties of all XFEL undulators at TESLA can be found in Chap. 4).

	Units	SASE 1
Wavelength*	Å	1–5
Peak power	GW	37
Average power	W	210
Photon beam size (FWHM)**	μm	100
Photon beam divergence (FWHM)***	μrad	0.8
Bandwidth (FWHM)	%	0.08
Coherence time	fs	0.3
Pulse duration (FWHM)	fs	100
Min. pulse separation****	ns	93
Max. number of pulses per train****	#	11500
Repetition rate****	Hz	5
Number of photons per pulse	#	1.8×10^{12}
Average flux of photons	#/sec	1.0×10^{17}
Peak brilliance	B*****	8.7×10^{33}
Average brilliance	B*****	4.9×10^{25}

*Parameters are given for the shortest wavelength.

** Value at the exit of the undulator.

*** Far field divergence.

**** Values determined by the time structure of the electron beam in the accelerator. The average parameters for the SASE-1 FEL are given for the ultimate case when only this beamline is in operation.

***** In units of photons/(sec $\cdot$ mrad^2 $\cdot$ mm^2 $\cdot$ 0.1 % bandwidth).

Table 2.3.1.: *Photon beam properties of the SASE 1 FEL at TESLA. In Chap. 4 photon beam parameters for all FEL devices and also the undulator parameters are presented.*

One of the key parameters to compare different radiation sources is their brilliance[1]. For partially coherent light sources (wigglers and undulators) the brilliance [photons/(sec $\cdot$ mrad^2 $\cdot$ mm^2 $\cdot$ 0.1 % bandwidth)] can be calculated from the spectral flux [photons/(sec $\cdot$

[1]Note: In the US the European "brilliance" is mostly called "brightness".

$0.1\,\%$ bandwidth)] divided by the photon beam's rms radius $\sum$ and divergence $\sum'$ obtained from convolution of the electron beam and photon diffraction parameters as

$$\text{brilliance} = \frac{\text{spectral flux}}{4\pi^2 \cdot \sum_x \cdot \sum'_x \cdot \sum_z \cdot \sum'_z} \tag{2.3.1}$$

$$\text{with} \quad \sum = \sqrt{\sigma_e^2 + \sigma_{ph}^2} \tag{2.3.2}$$

$$\text{and} \quad \sum' = \sqrt{\sigma'^2_e + \sigma'^2_{ph}} \tag{2.3.3}$$

In the case of full transverse coherence (e.g. FELs in saturation) $\sum$ and $\sum'$ are related through

$$\sum\sum' = \frac{\lambda_{ph}}{4\pi} \tag{2.3.4}$$

and Equation 2.3.1 can be transformed into

$$\text{brilliance} = \frac{\text{spectral flux}}{(\lambda_{ph}/2)^2} \tag{2.3.5}$$

This means that the brilliance is simply given by the spectral flux divided by the transverse photon phase space.

As depicted in Fig. 2.3.1 the peak brilliance of the TESLA XFELs surpasses the spontaneous undulator radiation from today's state-of-the-art synchrotron radiation facilities by about eight or more orders of magnitude while the average brilliance is about four orders of magnitude higher (Figure 2.3.2). The peak brilliance is the brilliance scaled to the length of a single pulse while average brilliance is normalized to seconds at the highest possible repetition rate. Figure 2.3.3 shows the number of photons per mode, which can be expressed as

$$\text{No. of Photons/Mode} = \text{Peak Brilliance} \cdot \frac{\lambda_{ph}^3}{4\,c}\,. \tag{2.3.6}$$

Eight orders of magnitude more photons per mode reflect the improved coherence of the FELs compared to the spontaneous emission of third generation SR sources. In summary, extremely short pulses, high intensity and full transverse coherence are the attractive features of the XFEL radiation.

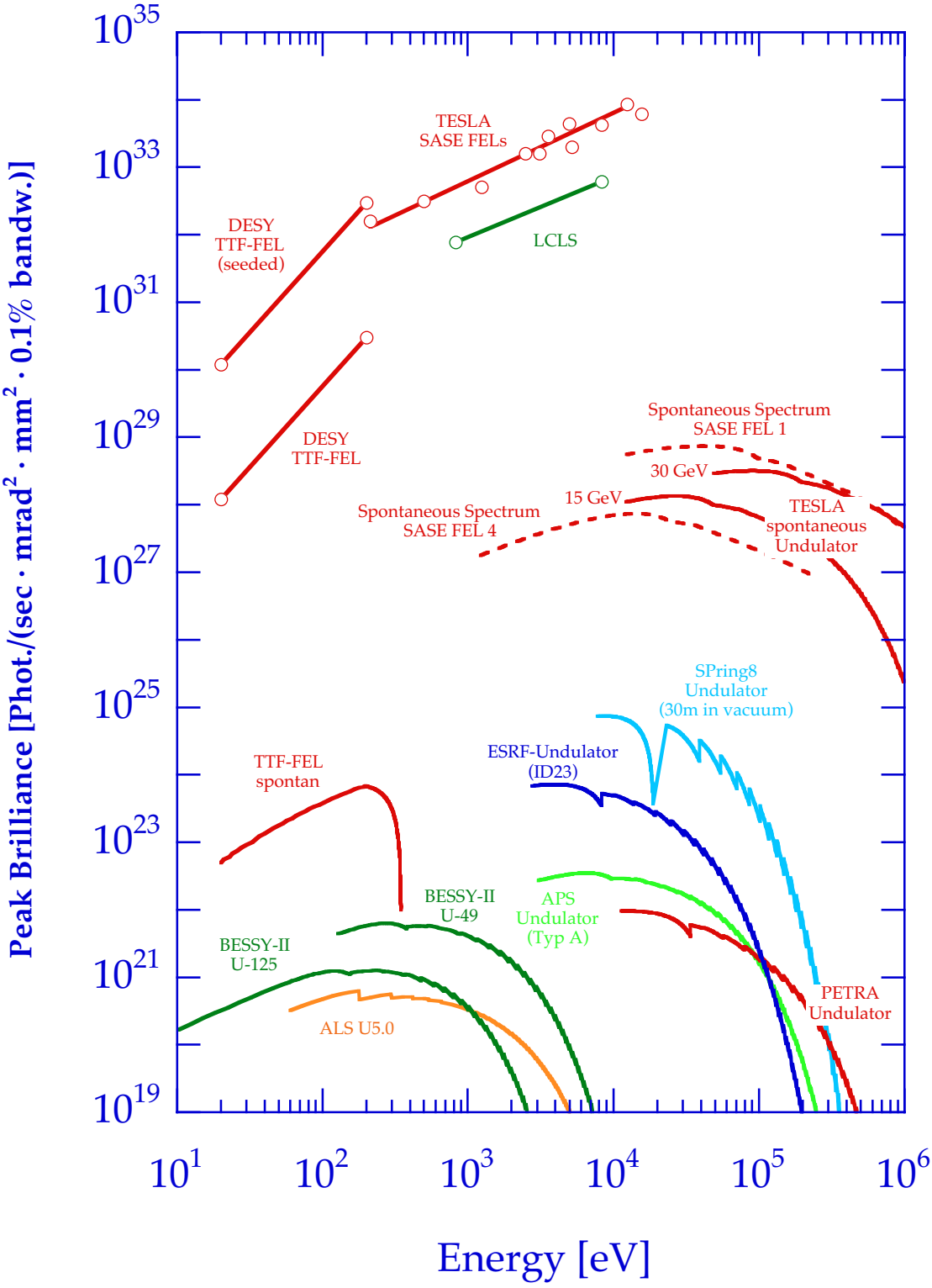

Figure 2.3.1.: *Peak brilliance of XFELs and undulators for spontaneous radiation at TESLA and at the LCLS, Stanford [17], in comparison to the undulators at present third generation synchrotron radiation sources. In addition, also the spontaneous spectrum of an XFEL undulator is shown.*

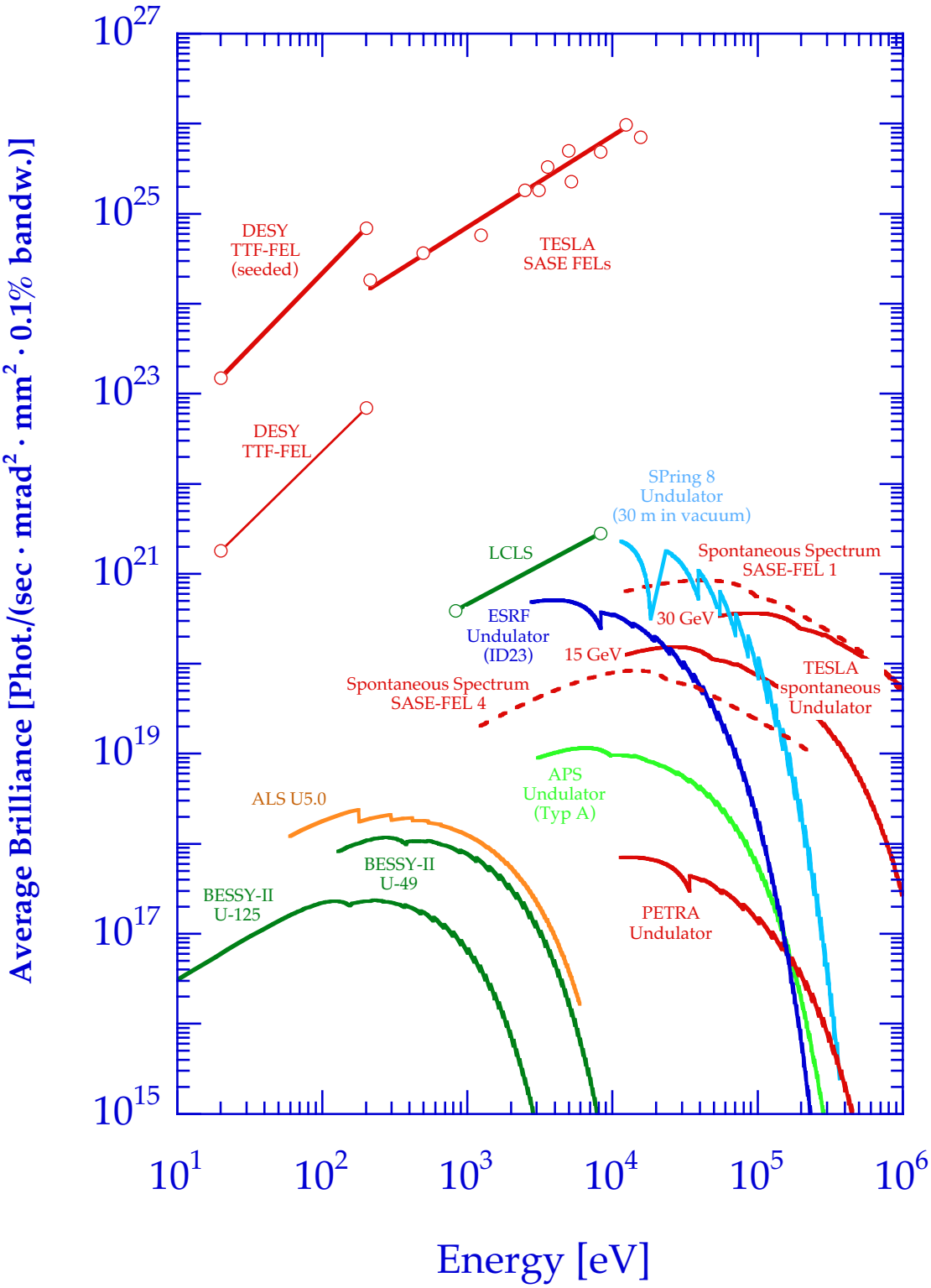

Figure 2.3.2.: *Average brilliance of XFELs and undulators for spontaneous radiation at TESLA and at the LCLS, Stanford [17], in comparison to the undulators at present third generation synchrotron radiation sources. In addition, also the spontaneous spectrum of an XFEL undulator is shown.*

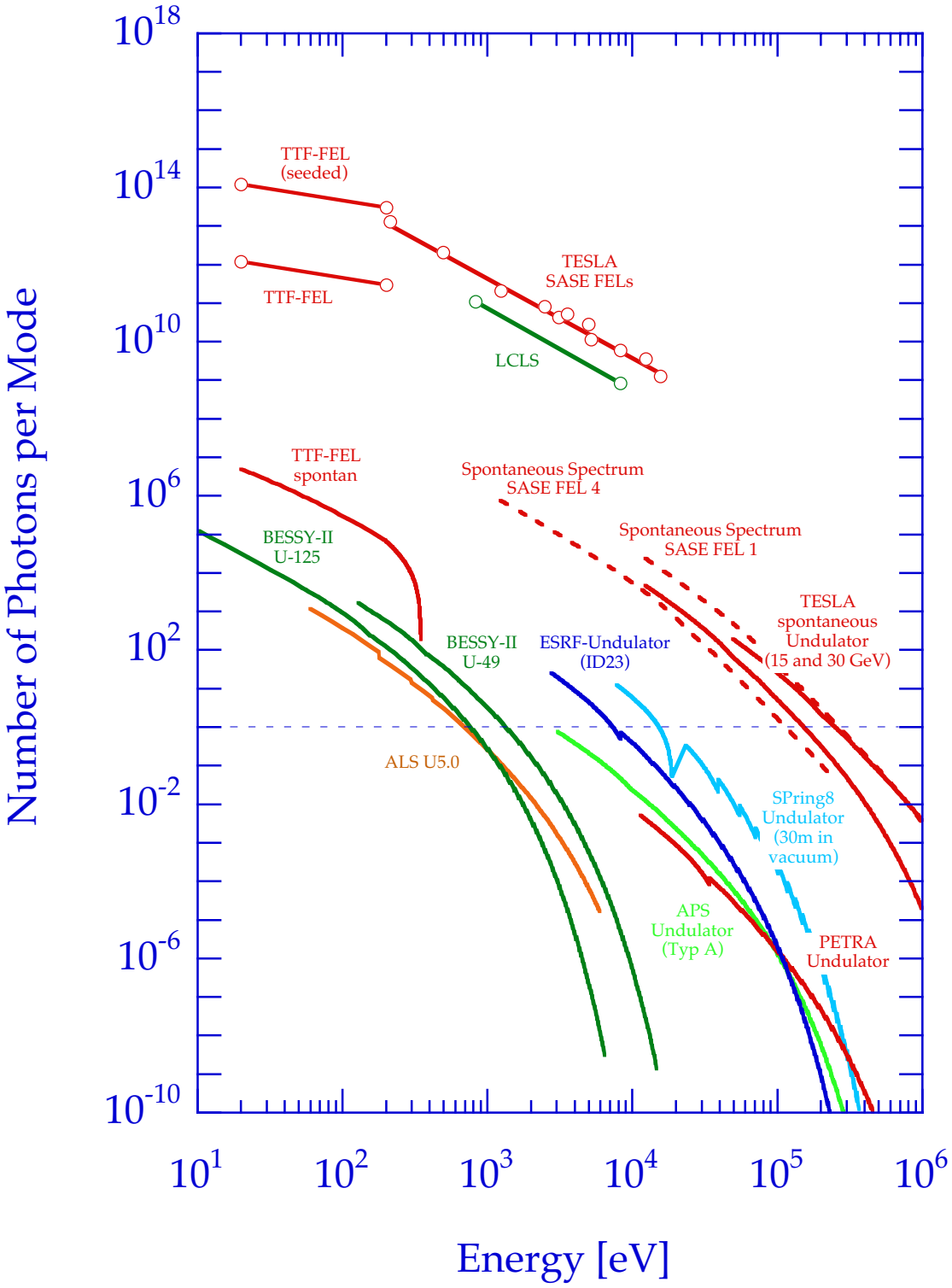

Figure 2.3.3.: *Number of photons per mode for the XFELs and undulators for spontaneous radiation at TESLA and at the LCLS, Stanford [17], in comparison to the undulators at present third generation synchrotron radiation sources. In addition, also the spontaneous spectrum of an XFEL undulator is shown. Please note that these curves were derived using Equation 2.3.6 with a peak brilliance scaled to a bandwidth* $\Delta\lambda/\lambda = 1$.

Bibliography

[1] E.L. Saldin, E.A. Schneidmiller, M.V. Yurkov, *The Physics of Free Electron Lasers*, Springer, Berlin-Heidelberg (2000) and references therein.

[2] T.C. Marshall, *Free Electron Lasers*, MacMillan, New York, NY (1985)

[3] P. Luchini and H. Motz, *Undulators and Free-Electron Lasers*, Oxford Science publications, Oxford (1990)

[4] H.P. Freund and T.M. Antonsen Jr., *Principles of free-electron lasers*, Chapman and Hall, London, UK (1996)

[5] A. Yariv, *Quantum Electronics* (3rd edition), J. Wiley & Sons, New York (1989)

[6] G. Dattoli, A. Renieri, and A. Torre (eds.), *Lectures on the Free Electron Laser Theory and Related Topics*, World Scientific, London (1993)

[7] W.B. Colson, C. Pellegrini, and A. Renieri (eds.), *Laser Handbook*, Vol. 6, North-Holland, Amsterdam (1990)

[8] J. Feldhaus, J. Roßbach und H. Weise, Spektrum der Wissenschaft, Dossier 2/1998: *Laser in neuen Anwendungen*, 106 (1998)

[9] A.M. Kondratenko and E.L. Saldin, Part. Accelerators **10**, 207 (1980).

[10] R. Bonifacio, C. Pellegrini and L.M. Narducci, Opt. Commun. **50**, 373 (1984).

[11] K.J. Kim, Phys. Rev. Lett. **57**, 1871 (1986).

[12] S. Krinsky and L.H. Yu, Phys. Rev. A **35**, 3406 (1987).

[13] E.L. Saldin, E.A. Schneidmiller, M.V. Yurkov, Opt. Commun., in press.

[14] J. Feldhaus, E.L. Saldin, J.R. Schneider, E.A. Schneidmiller and M.V. Yurkov, Opt. Commun. **140**, 341 (1997).

[15] H.P. Freund, S.G. Biedron and S.V. Milton, Nucl. Instrum. and Meth. A **445**, 53 (2000)

[16] Z. Huang and K.-J. Kim, Phys. Rev. E **62**, 7295 (2000)

[17] Values taken from
http://www-ssrl.slac.stanford.edu/lcls/lcls_parms.html

3. Scientific Applications of XFEL Radiation

The idea of an X-ray laser has been around since the invention of the optical laser. X-ray lasers would combine the outstanding properties of laser light with the atomic resolution and the penetration power offered by X-rays. However, right from the beginning it became clear that the simple extrapolation of the inversion and stimulated emission process used in the optical case would not lead to direct success in the Ångstrøm regime. The idea to use free electrons confined in a tiny, micrometer sized bunch has therefore been the most promising step to a successful realization of X-ray lasers - albeit by applying a different physical principle.

Today we are sure that a free-electron laser for X-rays can be build on the basis of the SASE principle. In preparation of the proposal for an XFEL laboratory presented here, many scientific communities were addressed in order to collect proposals for investigations. Of course, when thinking about this, there is always the possibility to extrapolate what we can do today with the best performing X-ray sources, towards the improved parameters available with an XFEL, namely the increased average brilliance, the shorter pulse length, the dramatically higher coherent flux, and the much better collimation. In turn one can achieve in the measurements a better spatial and energy resolution, the time resolution will provide access to new phenomena, and the coherence will allow us to explore new domains of dynamical processes.

But in addition to these already fascinating possibilities with the proposed XFEL, scientists will explore new land. In particular, the dramatically increased peak brilliance will offer a still impossible use of X-rays. The investigation of structural changes on ultra short time scales will become possible, thus complementing femtochemistry with optical lasers. Another application yet unexplored is the possibility to investigate molecular structures without the need of crystallization. This will give access to a vast number of biomolecules yet impossible to crystallize. A new, and maybe most important domain will be the non-linear interaction of X-rays and matter, leading, e.g., to multiphoton processes in atoms and molecules which can not be studied with the present radiation sources. And last not least, by focusing the X-rays to μm^2 and below, one will generate plasmas at still totally unexplored temperatures and pressures.

Although most of the collected proposals are based on extrapolations of today's experience, having a concept of the new source has naturally stimulated the vision of many scientists. Questions like "Can we see the electron dynamics in the bonds?", "Can we see how matter forms and changes?", "Can we take pictures of single molecules?", "Can we make a movie of a chemical reaction?", or "Can we study the vacuum decay in a high field?" have been raised and have found, in many parts, their expression in this report.

In the following sections we have collected ideas going from the simpler systems such as atoms, molecules, and clusters to the more complicated states present in plasma physics,

condensed matter, surfaces, materials, chemistry, life sciences, and finally quantum optics. As will be detailed in the chapter about plasma physics, the high intensity of the XFEL radiation cannot only be used to study systems, but also to generate new states of matter. While this is exciting for scientists studying these new species, it has to be assured for all studies, but especially for solid state samples, that the measurement is not affected by sample damage. Several ways to assure this are proposed in the reports, such as using shorter X-ray pulses, attenuating the beam, using a higher repetition frequency, using samples which can be refurbished or scanned, or going to higher wavelength resolution.

The experimental methods have been separated from these science fields and are collected in chapter 5, which leads over to the beamline proposals. The scientific proposals presented in this chapter and also several proposals of new experimental methods, in chapter 5, were collected through workshops and working groups. Their chairmen together with the coordinators have collected the material in reports which can be found on the attached CD-ROM. From this material the scientific applications of the XFEL in this chapter were put together by the editors. Some redundancy of issues could not be avoided since many themes are common in different fields such as bonding in Physics, Biology and Chemistry. Also, no harmonizing of the different styles has been attempted, among other reasons, in order not to face the danger of modifying the ideas and intentions of the authors. Due to the huge amount of proposed ideas the editors have not been able to verify the technical feasibility of all proposed investigations in detail. In many cases it will only be possible to answer open questions once the new and fascinating light is available for research. The multitude of different ideas collected in this scientific case, however, shows the outstanding opportunities we are looking forward to.

3.1. Atomic, Molecular and Cluster Phenomena

This chapter about atomic, molecular and cluster phenomena is based on contributions to the reports of several workshops held at DESY on "Atom, Molecule and Cluster Physics with a FEL" edited by Th. Möller (HASYLAB, Hamburg) and B. Sonntag (University Hamburg) (see e.g. A.1.1). In these contributions further proposed experiments and details can be found.

The interaction of radiation from an X-ray free electron laser with matter will first of all result in the excitation/ionisation of electrons deeply bound in the atomic/ionic core. The cross corresponding cross sections for the loosely bound valence shell electrons by orders of magnitude. Within femtoseconds the inner-shell holes "bubble up" to intermediate and outer shells via radiative and non-radiative cascades, leaving the atom/ion in a highly ionized state. The detailed understanding of these atomic core-hole creation and decay processes is one of the most important tasks, especially since not only the samples/targets, but also the reflection and diffraction optics necessary to transport the XFEL photon beam, will involve these basic interactions between intense X-rays and atoms/ions.

The interaction of intense XFEL photon beams with matter will differ substantially from that of intense fs-laser radiation in the optical and infrared spectral range. This can be illustrated by estimating the ponderomotive energy. The energy a free electron can gain from the oscillating electromagnetic field $E(\omega)$ given by the ponderomotive potential energy,

$$E_p = e^2E^2/4m_e\omega^2 \ , \tag{3.1.1}$$

is very small at high X-ray frequencies ω. Here e and m_e are the electron charge and mass, respectively, and E is the electric field strength. Focusing the peak power of 30 GW expected for the wavelength of 0.1 nm into a spot of 1 μm diameter results in a power density of 3.8×10^{18} W/cm^2 and a ponderomotive potential energy of 1.8 meV, while in the case of high power infrared and optical lasers it can exceed several keV. The secondary effects caused by these high-energy electrons dominating the processes induced by high-power infrared lasers therefore will not occur in the interaction of matter with XFEL radiation. The XFEL will probe the basic photon-atom interaction undisturbed by ponderomotive effects.

Radiation from an XFEL will open up amazing new possibilities and extend them to a regime where today only predictions and simulations exist. Two types of experiments will be particularly promising :

- The study of the electron dynamics (e.g. multiple core hole formation and multiple photoionization) of atomic, molecular and cluster targets irradiated at different X-ray wavelengths and power levels.

- The investigation of the structure and dynamics of molecules and clusters by the diffraction of intense, femtosecond X-ray pulses. Ideally, a single X-ray pulse would suffice to record a diffraction pattern as indicated in the schematic picture in Fig 3.1.1.

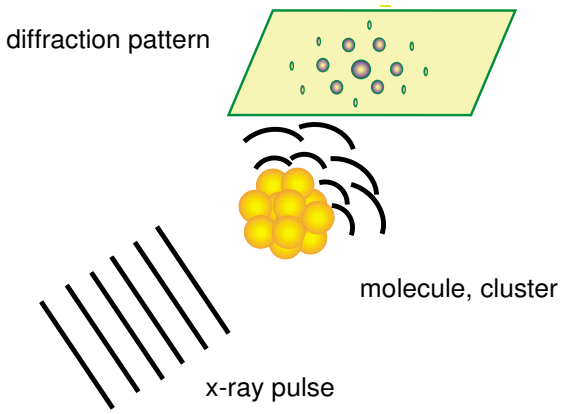

Figure 3.1.1.: *Schematic of diffraction at a molecule or cluster by an ultrashort X-ray pulse. The recorded diffraction pattern will look as shown in Fig. 3.1.5*

3.1.1. Atomic physics

3.1.1.1. Multiple ionization

Photoionization of free atoms is one of the fundamental processes in the interaction of photons and matter. For the ionization of the valence-, subvalence-, and outer core shells, state-of-the-art experimental and theoretical studies have provided deep insight into the dynamics of the excitation and de-excitation processes (see e.g. [1]–[6]). In contrast to this, only a limited number of studies have been performed for deep-inner-shell ionization by X-rays. In most of these cases, only total cross sections have been determined by absorption- or ion yield spectroscopy. The high brilliance and the high flux of XFEL photon beams will allow the limitations set by small cross sections and small number of targets in an atomic beam to be overcome. The simultaneous detection of outgoing ions, electrons and fluorescence photons will yield detailed information on the Auger and fluorescence cascades resulting in highly charged final ions. For example, ions with charges up to 14^+ were observed in Xe ion spectra excited by x-ray photons with energies above the Xe L_1-edge [7].

Although these deep core-hole excitation and decay processes are only weakly modified by the surrounding atoms/ions in molecules, clusters and solids, knowledge and understanding of them is a prerequisite for successful studies with XFEL photon beams.

3.1.1.2. Multiple core hole formation

Besides these decay cascades, electron correlation can give rise to direct multiple core hole formation upon photon excitation or photon ionization, respectively. Since, in the weak field limit the photon interacts predominantly with a single electron, the satellite lines accompanying the main line in the electron- and fluorescence spectra are a clear proof of many-electron interactions and therefore have stimulated great experimental and theoretical efforts. Especially the photo-double-ionization of He (see e.g. [8]) and the photoexcitation of hollow Li atoms (see e.g. [9]) have turned out to be ideal testing grounds for the most advanced many-

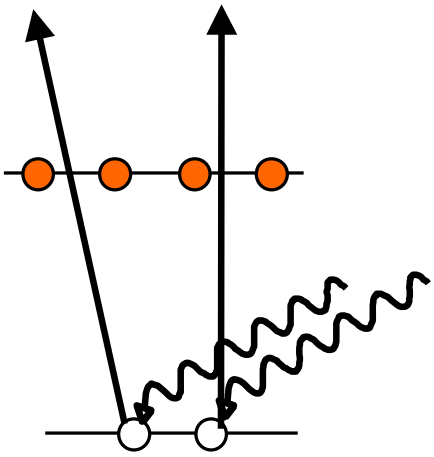

Figure 3.1.2.: *Schematic illustration of a direct multiphoton ionization process. After the absorption of two photons, two innershell vacancies are formed.*

electron theories. Recently, double K-vacancy production in solid molybdenum by X-ray photoionization could be detected [10]. The intensity and brilliance of the XFEL photon beam will allow the extension at these fundamental studies of electron correlation to deep core levels of free atoms. Freeman, Buchsbaum et al. [11] have pointed out that there is a further, very promising process for controlled creation of two vacancies in a core-shell of an atom by a single XFEL photon pulse. For the K-shell of neon atoms, they estimated that there should be a detectable number of atoms that absorb two photons sequentially or simultaneously within a time scale shorter than the core hole relaxation time (see Fig. 3.1.2). Hypersatellites in the electron- or fluorescence spectra provide a reliable means of identifying these processes.

3.1.1.3. Multiphoton ionization of inner-shells

Nonlinear photon-atom interactions have been the domain of laser spectroscopy. For inner-shells, the cross sections for two-photon X-ray photoexcitation/ionisation are too small for those nonlinear processes to be detected even with third generation synchrotron radiation sources. The high-brilliance, high-intensity XFEL photon beams will make studies of two-photon inner-shell processes feasible. As an example, in Fig. 3.1.3, the cross section for the excitation/ionisation of the Ar 1s-shell by two linearly polarized photons calculated by Novikov [12] is presented. The energy range shown covers photon energies close to half of the Ar 1s-ionization energy. The detection of an Ar KLL or KMM Auger electron is a clean signature of the two-photon excitation/ionisation. For reasonable target densities and detection efficiencies, count rates significantly above one Auger electron per laser pulse are expected.

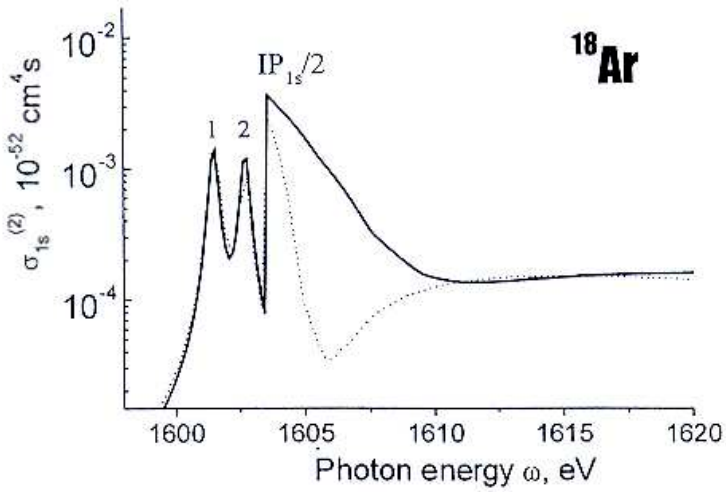

Figure 3.1.3.: *The cross section $\sigma^{(2)}_{1s}$ of the process of excitation/ionisation of the Ar 1s-shell by two linearly polarized photons. The solid line shows the result of the calculation, taking into account the effect of relaxation of the atomic residue in the field of the vacancies being created. The dotted line shows the result without accounting for this effect. (reproduced from [12])*

3.1.1.4. Excitation and ionization of highly charged ions

Ions are ubiquitous in the universe. The knowledge of their interactions with photons is therefore of great importance for many areas of science and technology (e.g. astrophysics, plasma physics). For the X-ray range, experimental data are still scarce, and therefore one often has to rely on calculations. Stringent tests of these calculations are highly desirable. In combination with an electron beam ion trap (EBIT), the XFEL will allow the systematic study of the interaction between X-ray photons and highly charged ions. An EBIT can produce and trap ions ranging from medium nuclear charge Z up to the heaviest systems such as Li-like Uranium. Due to the excellent emittance of this ion source, slow ion beams can be efficiently focused into an interaction chamber equipped with X-ray-, electron- and ion-spectrometry [13].

For He- or Li-like ions the fundamental studies of the few-electron correlation can be extended to strong field systems, e.g. U^{+89}, where relativistic effects, QED and nuclear effects become large.

3.1.2. Molecular physics

Typically, chemical reactions proceed on a fs- to ps- time scale (see also Sec. 3.6.1). Ideal systems for the study of chemical reactions in great detail are small molecules e.g. diatomic and triatomic molecules in the gas phase. The understanding of basic principles and testing of experimental techniques for the investigation of rather simple systems is essential for the application to more complicated systems, e.g. biochemical samples, which will be discussed in Sec. 3.7. Photodissociation of a diatomic molecule AB induced by a fast laser

pulse can be understood on the basis of a wave packet moving on molecular potential curves. In real molecular systems, several electronically excited states are involved in the dissociation process. By going from diatomic to triatomic molecules, the situation becomes even more complicated. Dissociation takes place on a potential surface that sometimes can have saddle points and barriers in the exit channel [14]. Using fs optical lasers, researchers were able to collect a wealth of information on the details of reaction pathways in many molecular systems e.g. I_2, CH_2I_2, and even larger systems [15]. Since all information in optical fs-experiments is obtained from spectroscopic results, e.g. ionization probability or kinetic energy of photoelectrons, a detailed knowledge on the energy surface is required for the interpretation and understanding of the experimental data. An X-ray FEL operating at short wavelength would provide a unique tool for the study of ultrafast reactions. For the first time, direct information on changes in bond length could be obtained. A direct measurement of the atomic separation as a function of the time can be performed with time-resolved photoelectron diffraction or scattering techniques in combination with optical lasers. This will certainly open new fields in fs-chemistry.

3.1.2.1. Multiple ionization, nonlinear effects

The illumination of molecules with intense radiation from a focused XFEL beam will, first of all, involve optical nonlinear processes e.g. multiphoton ionization and multiple core hole formation in their atomic constituents [16]. As a result, one can expect that the molecules break apart and ultrafast dissociation takes place. If several charges are created in the molecule, Coulomb explosion is expected to happen. Such processes have already been observed with optical laser excitation in molecules [17] and clusters [18]. In the optical spectral range, the underlying first step process is either multiphoton or field-mediated ionization. It seems that, in aromatic molecules, the transition to field ionization ('above threshold ionization') takes place at considerably smaller ponderomotive energies than in atoms under similar conditions [19]. The lowered threshold is due to the electronic delocalization in cyclic molecules. The XFEL will allow the study of dissociation processes and Coulomb explosion in molecules being damaged by short-wavelength radiation. Since the chemical composition and the size of molecules can be varied in a very controlled way, it will allow the detailed study of many important radiation-induced processes. The understanding of these processes is one of the most important early tasks. This information is needed, for instance, as a basis for exploring dynamical processes in biological samples, solid state physics, or surface science.

3.1.2.2. Resonant elastic scattering, nonlinear effects

In a first approximation, many excitation and scattering processes can be described in the electric dipole approximation. The validity of the dipole approximation implies that the symmetry of the involved states largely determines the excitation or scattering spectrum. If, for example, the molecule has inversion symmetry, only transitions which change the parity from even to odd (or vice versa), are allowed. At conventional intensities, the symmetry selection rules are strictly valid. Due to vibronic coupling the electronic symmetry may break

during the scattering process, thereby relaxing the selection rules so that 'forbidden peaks' appear in the spectra [20]. Intense radiation from the XFEL will allow the investigation of non-dipole transitions without symmetry breaking by vibronic coupling [21]. Detailed information can be collected by measuring the intensity dependence of the 'forbidden peaks'. In the absence of vibronic coupling, the appearance of 'forbidden peaks' would immediately indicate a departure from the conventional description of scattering processes. The L- and K-shells of many relevant diatomic molecules, e.g. O_2, Cl_2, and Br_2, are within the spectral range of the soft-X-ray beamline of the XFEL. With the high intensity, non-dipole transitions can be easily separated from two-photon processes due to complementary selection rules.

Furthermore, information on the breakdown of the dipole approximation can be obtained from pump-probe experiments combining the XFEL with an optical laser [21]. The optical laser can be used to pre-excite a symmetric molecule. By excitation to high vibrational states, one can appreciably increase the average bond distance in a homonuclear diatomic molecule. Close to the dissociation limit the vibrational wavefunction has a large weight at the classical outer turning point. By performing scattering experiments within initial states that have been pre-excited in this way, one can examine effects beyond the dipole approximation. This approximation is expected to break down when the distance between the atoms becomes longer than the wavelength of the radiation. Through symmetry selection rules, this can be followed experimentally. The breakdown of the dipole approximation can therefore be directly associated with the localization of the core hole to one of the atoms. In other words, the XFEL will allow investigations of fundamental X-ray photon-induced processes in molecules.

3.1.3. Clusters

3.1.3.1. Multiple ionization and Coulomb explosion of clusters

Research on clusters has become a very important and active field of interdisciplinary interest in recent years [22]. Clusters, because they bridge the gap between molecular and solid-state physics, allow one to study how macroscopic properties of matter are determined by the interaction of their microscopic units. The transition from the atom to the solid is not a smooth transition at all, indeed rather interesting variations can occur. The size of the clusters is a new parameter, which can be used to control the variation of their properties, namely geometrical and electronic structure, magnetic properties and chemical reactivity. A thorough understanding of these properties is also of fundamental interest for applications of clusters, since they hold great promise for applications e.g. in microelectronics and photocatalysis [23]. Work on photon–cluster interactions especially has lead to new physics over the past decade. Light-induced processes in clusters can cause photo-fragmentation [24], desorption [25, 26] and Coulomb explosion [27, 28], producing atomic and ion fragments with a few eV of energy. Recently, studies of the photoionization of clusters with high intensity ($> 10^{16}$ W/cm^2) optical fs-laser pulses have shown that superheated plasmas with ion kinetic energies up to 1 MeV can be produced. The clusters (typically rare gas clusters comprising up to 10^5 atoms) are themselves very bright sources for X-rays [29] and act as an active medium for high order harmonic generation [30]. Analogous effects may occur with

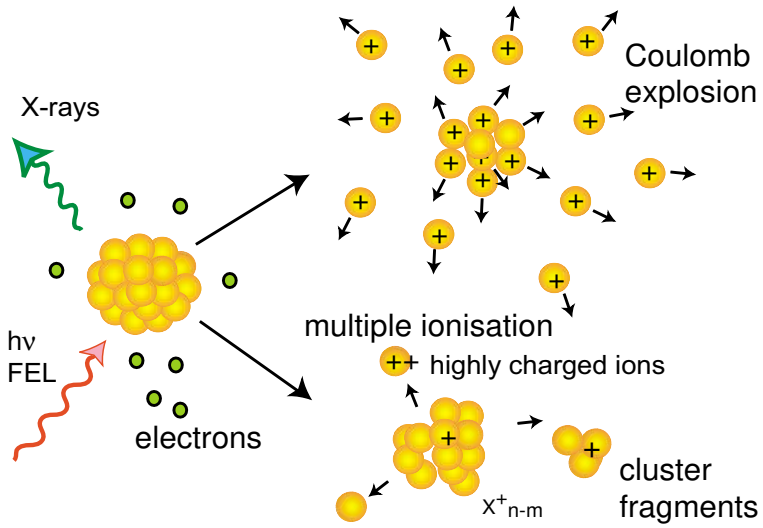

Figure 3.1.4.: *A schematic of dynamical processes in clusters induced by focused XFEL radiation.*

the XFEL beam, however, it can be expected that there are several important differences because the ponderomotive energies are very small compared to the photon energy [11]. Fundamental work on clusters is particularly important, since it can be generalized to studies of radiation damage in bulk materials. The XFEL will be a unique tool for cluster research because of the very high probability of multiple ionization of cluster atoms.

The whole process of cluster excitation and heating with optical fs-lasers is controlled by a movement of electrons in a microplasma driven by the electromagnetic laser field. At X-ray wavelengths, the ponderomotive energy is small, and thus the amplitude of oscillating electrons will be small. As a result, the kinetic energy distribution of electrons emitted from the cluster will contain a signature of the primary processes (photoemission, Auger decay) and of the electron-electron and electron-ion interaction in the cluster. Therefore, in contrast to what optical high-power irradiation permits, the dynamical processes can be analyzed without strong perturbation by the laser field. This situation is illustrated in Fig. 3.1.4.

3.1.3.2. Time-resolved structure determination by X-ray scattering

The geometric structure of clusters is of fundamental importance for the understanding of many other properties, e.g. their electronic structure, reactivity, magnetic and optical properties. While X-ray diffraction has revealed an enormous amount of detailed information on the structure of bulk matter, it yet cannot be applied to clusters, since the particle density of clusters in a beam is very low. Therefore, most information on the geometric structure of clusters comes from indirect methods e.g. mass spectrometry [22], [31]–[33], flow tube measurements [34] and theoretical work [35]. Recently, electron diffraction from trapped cluster ions has provided a means by which the structure and structural phase changes can be observed. Typically, data acquisition requires several minutes because the signal to noise ratio is very low [36]. The acquisition times using conventional X-ray sources are even longer, since the cross section for X-ray scattering is substantially smaller than that for elec-

tron scattering. The intensity of the XFEL offers the possibility to overcome the limits for X-ray diffraction and will open a completely new field of research [37]. The experimental situation is rather similar to that planned for biomolecular imaging [38] (see Sec. 3.7). Estimates show that, under optimal conditions, diffraction patterns of single cluster ions can be recorded within one pulse of the FEL. Here it is assumed that the XFEL radiation can be focused to a spot of 300 nm in diameter. At 0.15 nm wavelength, the estimated flux density will be 3×10^{25} photons/m^2 (corresponding to 3×10^7 photons/nm^2). The clusters will certainly survive under such power levels only for very short time, but with 100 fs X-ray pulses in many cases recording of scattering patterns should be possible before the clusters are destroyed. The destruction of the clusters results from multiple charging and consecutive Coulomb explosion as described in the preceding section. The total number of photons scattered incoherently in 4π by a gold cluster comprising 1000 atoms will be approximately 50000 in a single pulse, if an average scattering angle of 30° is assumed. A particle density of 1×10^7 cluster ions/cm^3 would be needed in order to get one ion per interaction volume, if a volume of 300 nm $\times$ 300 nm $\times$ 10 mm is assumed. This is somewhat higher than what is obtained with radio frequency traps with a rather large volume [36]. On the other hand, one can expect that considerably higher densities could be obtained with ion beams focused into the interaction volume. This will allow the recording of scattering images at the repetition rate of the XFEL, which means every 93 ns. If the density in the ion beam is lower, only part of the photon pulses will be scattered by a cluster. Nevertheless, once the photons are scattered by a cluster the scattering patterns should be of sufficient quality.

Scattering intensities calculated for a single pulse and an ideal cubic gold cluster comprising $21 \times 21 \times 21$ atoms are presented in Fig. 3.1.5 . Some rather intense Bragg peaks can be seen, since the cluster has translational symmetry. In this particular case, structural information can be directly obtained from the scattering pattern. In small or disordered systems, the peaks broaden and get weaker. However, the estimated signal is sufficient in order to obtain information on the orientation of the particle with respect to the photon beam. The structure of the particle can then be derived from the correctly added scattering patterns of identical particles recorded in different shots. Experiments on single small particles offer an important advantage compared to experiments on macroscopic crystals, since phase information can be obtained. The intensity distribution between Bragg peaks contains additional information. This oversampling [39] will enable, for the first time, the determination of precise structural information on mass-selected cluster ions. The accessible size range of clusters depends on the scattering cross section of their constituents. It is expected that, under optimal conditions, clusters comprising 1000 or even fewer atoms can be studied successfully. Particularly interesting are studies on clusters which undergo structural phase transitions like gold clusters [40] or alloyed clusters (e.g. Au_nSi_m), which could provide an opportunity to observe the competition between atomic segregation and stoichiometric mixtures as a function of size and temperature [36]. Furthermore, the time structure of the XFEL will allow the combination of all types of scattering experiments with pump-and probe techniques using optical fs-lasers that can be used to induce well-defined changes in the samples (see Fig. 3.1.6). An experimental scheme fur such measurements is shown in Fig. 3.1.7.

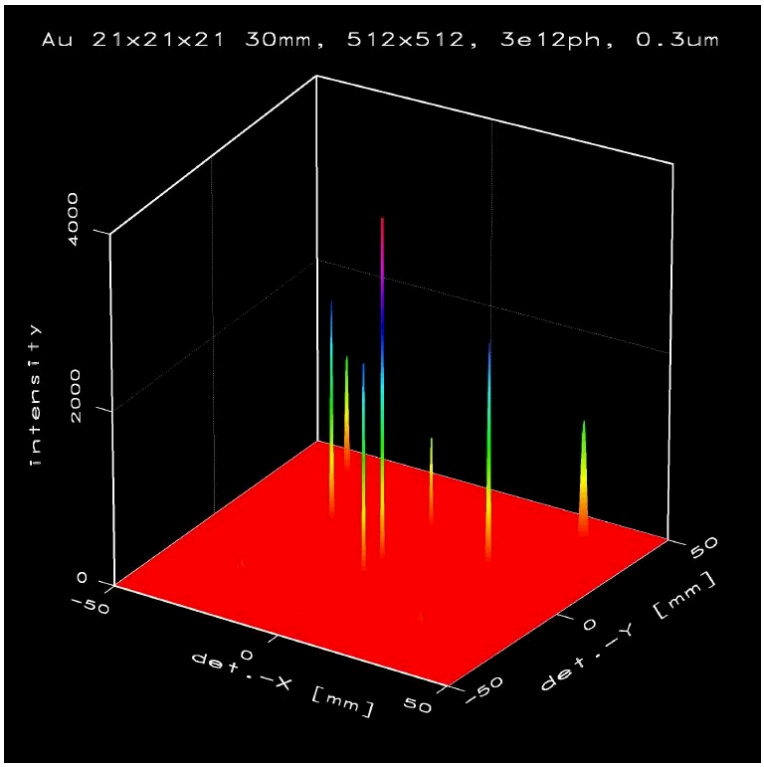

Figure 3.1.5.: *Calculated X-ray scattering pattern of a* $21 \times 21 \times 21$ *atom gold cluster. The two-dimensional intensity distribution is shown for two detector coordinates.*

3.1.3.3. Cluster vibrations and reactions

Clusters have unique electronic, optical and chemical properties that result from their large fraction of surface atoms and the confinement of charge carriers. The topological shape of cluster surfaces differs considerably from the almost perfect surfaces of macroscopic solids, since the atoms try to arrange in low-energy, usually compact and strongly curved structures. As a result, cluster dynamics are expected to differ substantially from those of molecules, surfaces, and bulk solids. In the last few years, substantial progress has been made in the study of the dynamics of electronically excited states in clusters and in molecules, especially vibration and dissociation [41]–[43]. Since many experiments are performed with optical pump-probe techniques, there is no direct information on the nuclear motion. Meanwhile, rather detailed studies are performed on photoreactions and even on solvation dynamics. Usually, information on the nuclear dynamics has to be inferred from spectroscopic information with the aid of potential curves and potential surfaces [15]. In some cases, cluster dynamics, especially surface vibrations, could be studied by inelastic atom scattering [44]. The XFEL will offer very new experimental possibilities, since cluster vibrations and deformations can be observed in real time using pump and probe techniques in combination with optical lasers. Depending on the geometric structure, size, and temperature of the clusters, different vibrational modes can be excited. This will be particularly interesting for systems which show strong variations of the melting temperature with size, as observed for Sn clus-

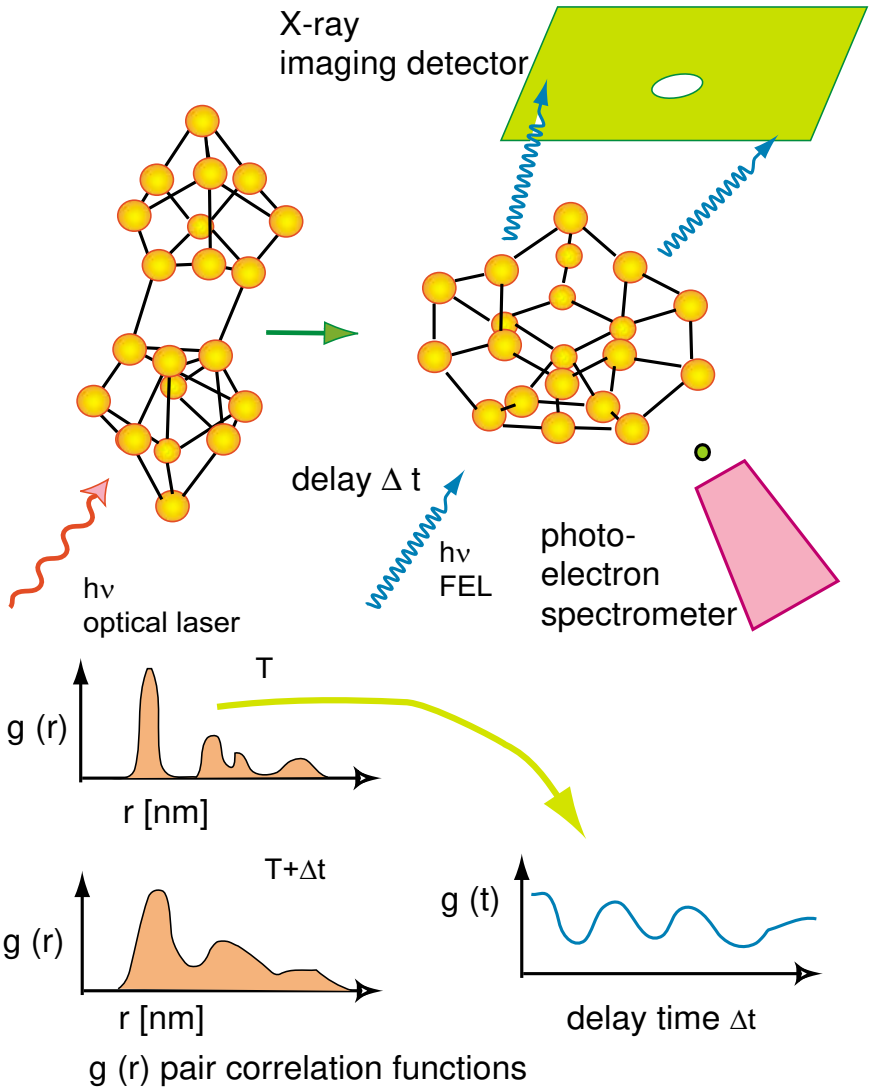

Figure 3.1.6.: *A schematic representation of a time-resolved experiment on phase transition and cluster melting. Small, covalently bound clusters have isomers with rather different geometry [42]. The dynamics can be studied by recording diffraction patterns in combination with pump–probe techniques.*

ters [45]. Furthermore, time-resolved structural studies will allow one to follow the pathway of photo-induced reactions in real space. As a result, dynamical processes can be analyzed without knowledge of the potential surfaces involved. The experiments can be performed as described in the preceding section by recording scattering patterns within one pulse of the XFEL. In addition, if an optical fs-laser is fired to induce a reaction or a phase transition, a scattering pattern can be recorded with the XFEL for variable delays of the optical pump pulse with respect to the XFEL probe pulse. In this way, the change in the cluster structure and the dynamics can be followed on a fs time scale.

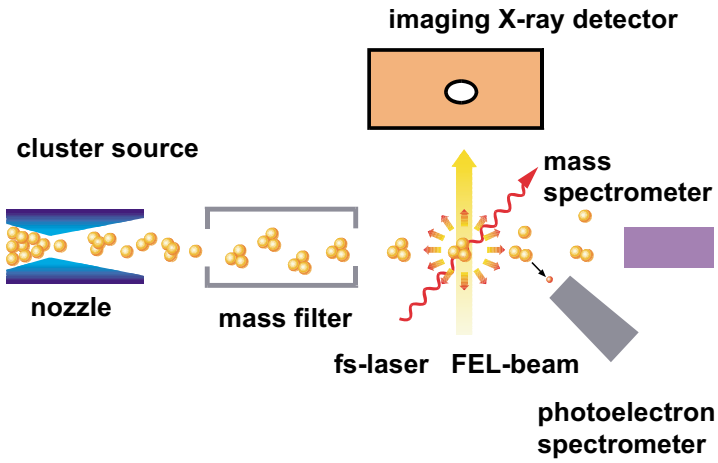

Figure 3.1.7.: *Schematic illustration of an experimental setup for the investigation of nonlinear processes and the electronic and geometric structure of clusters and cluster ions. Time resolved studies may be performed in combination with optical fs-lasers.*

3.1.3.4. Phase transitions and cluster melting

Phase transitions in clusters, especially melting, metal to non-metal and magnetic to non-magnetic transitions are of considerable scientific and technological importance. The reduced dimensions and the small size of the particles give rise to many unusual properties, e.g. a coexistence of liquid and solid phase [46] or strong size-dependent and irregular variations of the melting temperature [47]. Recent work on clusters with unusually high melting points above those of the bulk solid materials point out that very stable isomers with compact shape could be responsible for the experimental findings. The XFEL will offer a unique opportunity to investigate the dynamics of melting and crystallization in clusters and nanocrystals. One could use an optical fs-laser to deposit sufficient energy, so as to induce complete melting. Using the method of time-resolved X-ray diffraction outlined above, it should be possible to study the process of cluster melting in real time. Furthermore, it should also be possible to obtain information about changes in the particle's shape by scattering of X-rays with wavelengths longer than the typical interatomic separations in the cluster (Mie-scattering). The combination of different methods will probably allow one to distinguish between melting at the surface and in the interior of the particle. By choosing suitable wavelengths, the movement of different elements in the particles can be followed. Finally, collective vibrations of liquid clusters, which can be regarded as nanodroplets, can be investigated. Thus, the advent of direct time-resolved structural probes will open new scientific opportunities in this field.

Bibliography

[1] V. Schmidt, Rep. Prog. Phys. **55**, 1483 (1992).

[2] B. Sonntag and P. Zimmermann, Rep. Prog. Phys. **55**, 911 (1992).

[3] U. Becker and D.A. Shirley, *VUV and Soft X-ray Photoionization*, Plenum Press, New York (1996).

[4] W. Mehlhorn, J. Elec. Spec. Rel. Phen. **93**, 1 (1998).

[5] V. Schmidt, *Electron spectroscopy of Atoms using Synchrotron radiation*, Cambridge University Press, New York (1997).

[6] R. Moshammer et al., Phys. Rev. Lett. **84**, 447 (2000).

[7] T. Tonuma et al., J. Phys. B**20**, L31 (1987).

[8] J.S. Briggs and V. Schmidt, J. Phys. B**32**, R1 (1999).

[9] G. Verbockhaven and J.E. Hansen, Phys. Rev. Lett. **84**, 2810 (2000) and references therein.

[10] E.P. Kanter, R.W. Dunford, B. Krässig, S.H. Southworth, Phys. Rev. Lett. **83**, 508 (1999).

[11] R.R. Freeman, P.H. Bucksbaum, K. Kulander, L. Young, R. Falcone, *Atomic Physics Experiments*, in *LCLS : The First Experiments*, Stanford (2000), see also: http://www-ssrl.slac.stanford.edu/lcls/papers/LCLS_experiments_2.pdf.

[12] S. Novikov, *Two-photon excitation/ionisation of atomic inner shells :The 1s-shell of the Ar atom*, private communication.

[13] J.R. Crespo Lopez-Urratia, A. Dorn, R. Mooshammer, J. Ulrich, Physica Scripta **T80**, 502 (1999).

[14] A.H. Zewail, *Femtochemistry: Ultrafast Dynamics in Chemical Bonds, Vol. 1+2*, World Scientific, Singapore (1994).

[15] L. Lehr, M.T. Zanni,C. Frischkorn, R. Weinkauf, D.M. Neumark, Science **284**, 635 (1999).

[16] S.A. Novikov and A.N. Hopersky, J. Phys. B**33**, 2287 (2000).

[17] L. Quaglia and C. Cornaggia, Phys. Rev. Lett. **84**, 4565 (2000).

[18] M. Lezius, S. Dobosz, D. Normand, M. Schmidt, Phys. Rev. Lett. **80**, 261 (1998).

[19] M.J. DeWitt and R.J. Levis, Phys. Rev. Lett. **81**, 5101 (1998).

[20] P. Skytt et al., Phys. Rev. Lett. **77**, 5035 (1996).

[21] J.E. Rubensson and J. Nordgren, *X-ray fluorescence experiments on atoms and molecules using FEL radiation*, in *Proceedings of the workshop on Atomic, Molecular and Clusters Physics at the Free Electron Laser facility*, T. Möller, B. Sonntag (eds.)), DESY Reports TESLA-FEL **2000-23**, Hamburg (2000).

[22] H. Haberland, *Clusters of Atoms and Molecules*, Springer, Berlin (1993).

[23] J.-M. Bonard and A.E. Chatelain, Eur. Phys. J. D**9**, 1 (1999).

[24] T. Baumert, B. Bühler, R. Thalweiser, G. Gerber, Phys. Rev. Lett. **64**, 733 (1990).

[25] R. Pflaum, K. Sattler, E. Recknagel, Chem. Phys. Lett. **138**, 8 (1987).

[26] K. von Haeften et al., Phys. Rev. Lett. **78**, 4371 (1997).

[27] E. Rühl, C. Heinzel, A.P. Hitchkock, H. Baumgärtel, J. Chem. Phys. **98**, 2653 (1993).

[28] L. Köller, M. Schumacher, S. Teuber, J. Tiggesbäumker, K.-H. Meiwes-Broer, Phys. Rev. Lett. **82**, 3783 (1999).

[29] T. Ditmire, T. Donnelly, R. W. Falcone, M.D. Perry, Phys. Rev. Lett. **75**, 3122 (1995).

[30] T.D. Donnely, T. Ditmire, K. Neuman, M.D. Perry, R.W. Falcone, Phys. Rev. Lett. **76**, 2472 (1996).

[31] T.P. Martin, T. Bergmann, H. Göhlilch, T. Lange, Chem. Phys. Lett. **172**, 209 (1990).

[32] R.E. Smalley, *Supersonic carbon cluster beams*, in *Atomic and Molecular Clusters, Vol.* **68** *: Studies in physical and theoretical chemistry*, E.R. Bernstein (ed.), Elsevier, Amsterdam (1990).

[33] H. Haberland, *Clusters of Atoms and Molecules II*, Springer, Berlin (1994).

[34] M.F. Jarrold, Science **252**, 1085 (1991).

[35] U. Röthlisberger, W. Andreoni, M. Parinello, Phys. Rev. Lett. **72**, 665 (1994).

[36] M. Maier-Borst, D.B. Cameron, M. Rokni, J.H. Parks, Phys. Rev. A**59**, R3162 (1999).

[37] S. Krückeberg, D. Schooß, J.H. Parks, *Electron and X-ray scattering from mass selected clusters*, in *Proceedings of the workshop on Atomic, Molecular and Clusters Physics at the Free Electron Laser facility*, T. Möller, B. Sonntag (eds.), DESY Reports TESLA-FEL**2000-23**, Hamburg (2000).

[38] R. Neutze, R. Wouts, D. van der Spoel, E. Weckert, J. Hajdu, Nature **406**, 752 (2000).

[39] J. Miao and D. Sayre, Acta Cryst. A **56**, 596 (2000).

[40] C.L. Cleveland et al., Phys. Rev. Lett. **79**, 1873 (1997).

[41] E. Schreiber, *Femtosecond Real-Time Spectroscopy of Small Molecules and Clusters*, Springer, Berlin (1998).

[42] B. Liu et al., J. Chem. Phys. **109**, 9401 (1998).

[43] A. Assion et al., Science **282**, 919 (1998).

[44] U. Buck and R. Krohne, Phys. Rev. Lett. **73**, 947 (1994).

[45] A.A. Shvartsburg and M.F. Jarrold, Phys. Rev. Lett. **85**, 2530 (2000).

[46] R.S. Berry, Scientific American **263**, 50-56 (1990).

[47] M. Schmidt, R. Kusche, B. von Issendorf, H. Haberland, Nature **393**, 238 (1998).

3.2. Plasma Physics

This chapter has been written on the basis of contributions submitted by:
Richard W. Lee (Lawrence Livermore National Laboratory, U.S.A.),
J. Meyer-ter-Vehn and co-workers (MPI für Quantenoptik, Garching Germany),
R. Redmer (University of Rostock, Germany),
Th. Schlegel (University of Darmstadt, Germany).
Further details and references can be found in the report "Hard condensed Matter Physics" (see A.1.3).

High peak power X-ray FEL radiation deposits energy uniformly in the volume rather than at the surface, in distinction to optical laser light. Exciting possibilities therefore arise for the field of plasma physics, discussed in this chapter. The XFEL will allow small volumes to be heated to unprecedented states of plasma with temperatures up to keV (10^7 K) and pressures in the Gbar (10^{14} Pa) range. After constant-density (isochoric) excitation, the XFEL generated plasma expands hydrodynamically along isentropes cutting into yet unexplored regions of the plasma phase space. The investigation of equation of state (EOS) parameters and, in particular, of the regions of critical points in any kind of solid matter will thus become possible. The 100 femtosecond long X-ray pulses will lead to equilibration at the picosecond timescale. During generation of the plasma a highly non-equilibrium plasma state is created with an abundant K-hole population, of fundamental interest for example to plasma X-ray lasers. Scattering of X-rays provides, in addition, the means to study the microscopic structure of plasmas.

Plasmas at solid-state density, strongly coupled for $\Gamma = \overline{E_{pot}}/\overline{E_{kin}} > 1$, are found in the interiors of the giant planets such as Jupiter or the recently found extrasolar planets [1]. Further, Brown Dwarfs, main sequence stars or compact objects such as White Dwarfs provide other astrophysical examples. The knowledge of the behavior of matter under extreme conditions, especially at these ultra-high pressures, is of fundamental importance to develop improved models for planetary and stellar structure and formation, as well as the evolution of the universe. The behavior of hydrogen and helium (and their mixtures), as the simplest and most abundant elements in nature, is therefore of special interest over a wide range of densities and temperatures. Various methods have been successfully applied to produce dense, strongly coupled plasmas in the laboratory. For instance, strong shock-waves can be generated by chemical explosives [2] or powerful gas guns [3]. Using the technique of fast wire evaporation [4], solid metals can be expanded through the warm fluid region up to hot, dense plasmas. Moreover, the capacity of heavy-ion beams like those available at the GSI in Darmstadt [5], of high-power lasers such as NOVA in Livermore [6], and of ultra-short laser pulses in the femtosecond range [7] can be used to produce strongly coupled plasmas. Many of these capabilities provide the basic ingredients for inertial confinement fusion (ICF), which employs both laser-driven or heavy-ion driven compression of deuterium–tritium capsules [8]. In Fig. 3.2.1 a comparison of astrophysical and earth-based plasma sources in the electron density - temperature phase space has been shown.

A variety of new physical effects has already been obtained at ultra-high pressures using these experimental techniques. For instance, metallic-like conductivities in hydrogen have

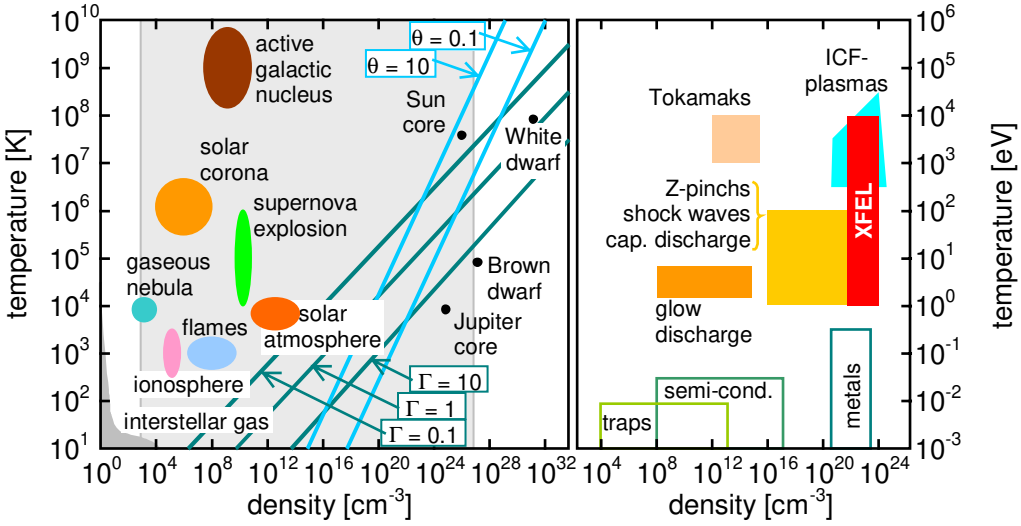

Figure 3.2.1.: *Density–temperature diagram for astrophysical objects (left) and for earth-based plasma generation (right) (after [9]). Lines indicate the Coulomb coupling parameter* $\Gamma = e^2/(4\pi\varepsilon_0 k_B T d)$, d *= mean distance between particles, and the degeneracy parameter* $\Theta = k_B T/E_F$. *The grey shaded area in the left plot corresponds to the area of the right plot.*

been demonstrated for the first time in dense hydrogen fluid around 1.4 Megabar and 2500 K by multiple shock-compression experiments [10]. Figure 3.2.2 compares the experimental data with theoretical models for this nonmetal-to-metal transition, e.g. thermally activated transport of free electrons as well as hopping between atoms [11]. Furthermore, substantial deviations from standard equations of state, e.g. provided by the SESAME library, have been observed from shock-wave experiments driven by the NOVA laser (see Fig. 3.2.3). These deviations have important consequences, e.g., for models of the interior of giant planets and the design of fusion capsules used in the ICF scenario, and have already stimulated many new theoretical efforts to study the properties of strongly coupled plasmas. Some of the most exciting problems to be tackled are the equation of state and its stability behavior, possible phase transitions and the location of critical points, and the impact of reactions such as dissociation and ionization in a plasma. With the XFEL one can access experimentally a regime where the plasma phase transition with a second critical point has been proposed; see e.g. [12, 19, 20].

In addition, fluid metals or alloys are intensively studied in the high-pressure region. These materials are fluids at high temperature, have high heats of evaporation, high electrical, and high thermal conductivities so that they provide optimum high-temperature working fluids in technical equipment for the production, storage, and conversion of energy [21]. The accurate location of the critical points of the liquid–vapor phase transition is known with satisfying accuracy only for some metals, e.g. Cs, Rb, K and Hg [22], while it is uncertain up to a factor of two for metals like Al, Cu, or Mo. Furthermore, a metal-to-insulator transition similar to that occurring in expanded alkali fluids has now been verified in dense metal

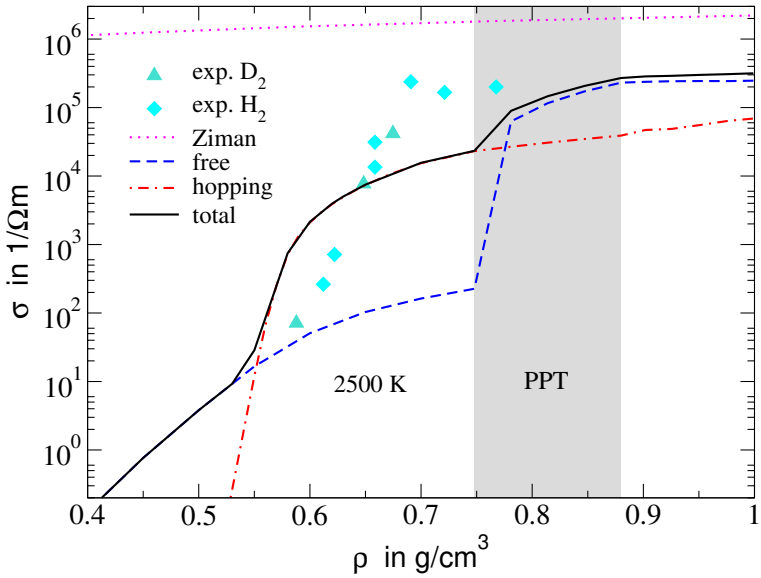

Figure 3.2.2.: *Electrical conductivity of fluid hydrogen at 2500 K: Experiments [10], Ziman curve for a hypothetical fully ionized fluid (dotted line), conductivity of free electrons (dashed line), hopping conductivity between H atoms (dash-dotted line), total conductivity (solid line) [11]. The coexistence region of the plasma phase transition (PPT) is indicated by the shaded area [12].*

vapors of Al and Cu [23]. It will be of particular interest to have new diagnostic methods to determine the equation of state independently of model assumptions.

The continuous increase in available computer capacity has stimulated the development of advanced simulation techniques such as path-integral Monte Carlo (PIMC) [17], quantum molecular dynamics [18], or wave-packet molecular dynamics [24] that are increasingly capable of modelling the quantum nature of an interacting many-body system – in this case of strongly coupled plasmas. Together with standard methods of many-particle theory [25], a more detailed description and understanding of the behavior of strongly coupled plasmas will be possible in the next few years and await its experimental verification. The XFEL will provide here unique possibilities for the generation and diagnosis of dense, strongly coupled plasmas. The behavior of matter in the plasma state produced by the XFEL pulse is related to various fundamental problems, e.g.

- The XFEL interaction will create matter in a wide area of the n-T phase diagram (see Fig. 3.2.1). This area includes interesting values for both Coulomb coupling and degeneracy, allowing detailed studies of extreme plasma states. The versatility of the XFEL permits varying parameters over a wide temperature range at densities at and below solid density, and thus provides the experimental basis for improving theoretical simulations of plasma generation and evolution, including radiation transport and hydrodynamic expansion.

- The detailed study of the interaction between energetic X-rays and cold, warm, and hot

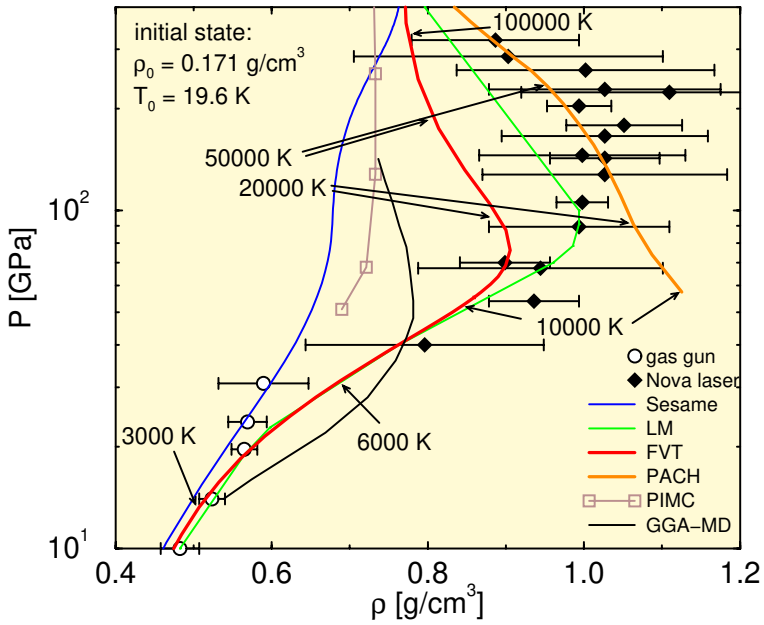

Figure 3.2.3.: *Experimental Hugoniot curve for deuterium D_2 [13] compared with theoretical equations of state [14]: Linear mixing (LM) model [15], fluid variational theory (FVT) [16], fully ionized plasma (PACH), PIMC simulations [17], and quantum molecular dynamics simulations (GGA-MD) [18]. Some temperatures are indicated.*

matter will provide the data for an improved theoretical description. That is, the influence of in-medium effects on the absorption coefficient of X-rays can be studied that will assist many-particle theoretical modelling. Moreover, the generation and behavior of hollow atoms in a dense plasma can be studied, which is of fundamental interest to X-ray laser research.

- The dynamical behavior of strongly coupled plasmas can be investigated. In particular nonequilibrium correlations formed during plasma generation and the relaxation of the nonequilibrium state into an equilibrium state could be studied. Here, the expansion kinetics of the plasma is of interest.

3.2.1. Interaction of X-rays and plasmas

For optical femtosecond lasers one reaches in the focus values of $I\lambda^2 > 10^{10}$ W, where electrons acquire speeds close to that of light, and the relativistic regime of laser plasma interaction is entered [26]. In contrast, XFEL pulses of an intensity of 10^{18} W/cm^2 correspond to much smaller $I\lambda^2 \approx 10^3$ W, and therefore produce far less energetic electrons.

With respect to plasma generation, the difference between X-ray and optical laser beams lies in the interaction. While visible light cannot penetrate into dense matter and is therefore absorbed in surface regions mainly by interaction with free electrons, XFEL photons penetrate into the target. They are absorbed in the wavelength regime of one to several Å pre-

dominantly through photoionization of bound K-shell electrons. The X-rays thus heat solid targets isochorically in the volume, much as do ion beams. The primary electron population has energies of the order of the photon energy and the free electrons equilibrate on typical time scales of 10 to 100 fs. As a consequence, XFEL pulses will generate well-behaved equilibrium plasmas (see discussion in Sec. 3.2.2.2). Optical pulses at intensities above 10^{18} W/cm^2, instead, produce almost collision-free relativistic electrons which self-organize into collimated beams with ultra-high currents and magnetic fields of up to GigaGauss [26].

Plasma generation by X-rays benefits from the high penetration into the whole volume in similarity to heavy-ion beams. However, whereas ions deposit their energy preferentially at the end of their range by collisions with atoms and ions (stopping power), X-rays are uniformly absorbed and therefore also deposit the energy uniformly along their path. This is one of the requirements which enable the isochoric heating of the target by X-ray providing thus plasma generation along isochores.

In addition to the generation of dense plasmas, the diagnosis of plasmas will benefit strongly from the XFEL source. The critical electron density $n_c[cm^{-3}] = 10^{27}(\lambda[nm])^{-2}$, where visible light will not propagate, is $\approx 10^{22}$ cm^{-3}, indicating that all dense plasmas can not be probed. For X-rays this critical density is of the order 10^{29} cm^{-3} well above the plasma frequency at any conceivable density of matter.

3.2.2. Generation of plasmas at solid density

Focused XFEL pulses will convert solid target matter into dense plasma with record temperatures and pressures opening a new branch of dense plasma research. We illustrate this by giving an explicit example of XFEL target heating, using a standard hydrodynamic simulation. As depicted in Fig. 3.2.4, XFEL pulses produce a solid-density plasma with temperatures beyond 100 eV (10^6 K) and pressures close to 1 Gbar.

3.2.2.1. Hydrodynamic response to X-ray pulses

In the following, we discuss heating and hydrodynamic response of a solid gold foil exposed to an X-ray beam at the XFEL. Figure 3.2.4 represent the results of a two-dimensional simulation in terms of temperature and pressure contours for cylindrical symmetry defined by the X-ray beam impinging onto the target at $x = 0.5\,\mu$m. A homogenous beamspot with a diameter of 6 μm is assumed and the y-axis describes the radial distance from the beam center. The FEL X-ray photons are emitted in micro-bunches 90 fs long corresponding to 10^{13} photons per bunch at 3.1 keV photon energy (4 Å wavelength), and lead to an intensity of 5×10^{18} W/cm^2 when focused to a $(1\,\mu\text{m})^2$ spot or even 5×10^{20} W/cm^2, if a focal area of $(0.1\,\mu\text{m})^2$ proves feasible. For the calculation, a pulse of 3.1 keV photons is incident from the right, rising linearly in time over 90 fs to 10^{17} W/cm^2 and then falling in the same way. Although the $0.5\,\mu$m thick disk is heated to 360 eV at its right boundary, implying a pressure of 1 Gbar, it undergoes minimal expansion during the first 200 fs. Strong hydrodynamic expansion, however, is seen at the time of 5 ps, as the target explodes and completely disintegrates. Note that two-dimensional expansion is observed only at the edge of the flat disk, while the central part of the foil is expanding in a purely planar manner. This is a crucial

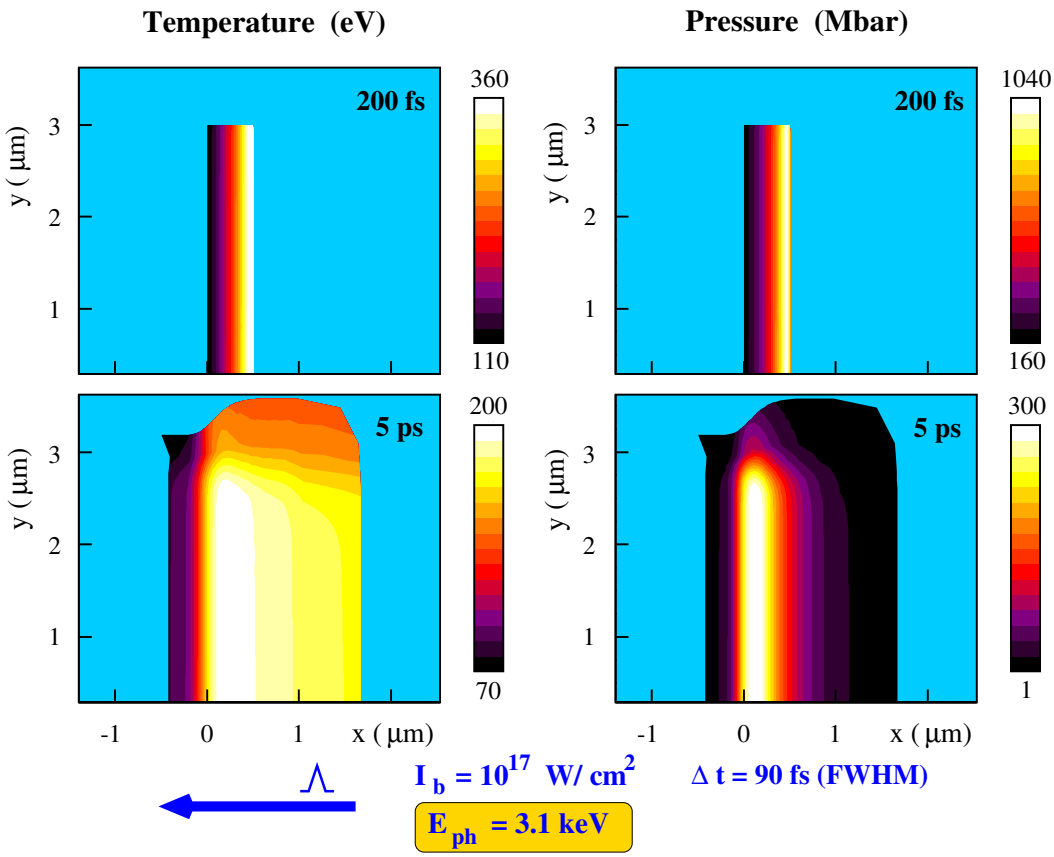

Figure 3.2.4.: *Temperature (in eV, left) and pressure (in Mbar, right) distribution of a gold foil irradiated by* 10^{17} *W/cm*^{2} *of 3.1 keV photons. After 200 fs the foil still has its original size, while after 5 ps it has expanded hydrodynamically.*

condition for quantitative studies.

The simulation results were obtained with the MULTI code [27], which includes beam energy deposition, hydrodynamics, heat conduction and radiative transport. Since hydrodynamic expansion is mainly planar during the first few picoseconds (see Fig. 3.2.4), we restricted ourselves to one-dimensional simulation in the following. Irradiation of thin layers of various materials with 90 fs X-ray pulses were studied. The absorption of the XFEL photons was modelled with Beer's law, using absorption coefficients calculated with the SNOP code [28]. It is important to note that the hydrodynamic simulations assume instantaneous equilibration of the deposited photon energy, such that equations of state can be used. This assumption is adequate for times larger than 100 fs, when the interaction with the XFEL pulse is over. Since hydrodynamic and radiative losses are still small at 100 fs, the deposited internal energy can be calculated at this time in the form $e(\mathrm{J/g}) = I(\mathrm{W/cm^2})\kappa(\mathrm{cm^2/g})\tau(\mathrm{s})$, from the intensity I, the pulse duration τ, and the absorption coefficient κ. Temperature T and pressure p can be calculated using the equations of state $e(T, \rho_0)$ and $p(T, \rho_0)$ from the SESAME library, where ρ_0 is the initial target density. This simple analysis well describes temperatures and pressures just after the pulse and can be used for the initial design of ex-

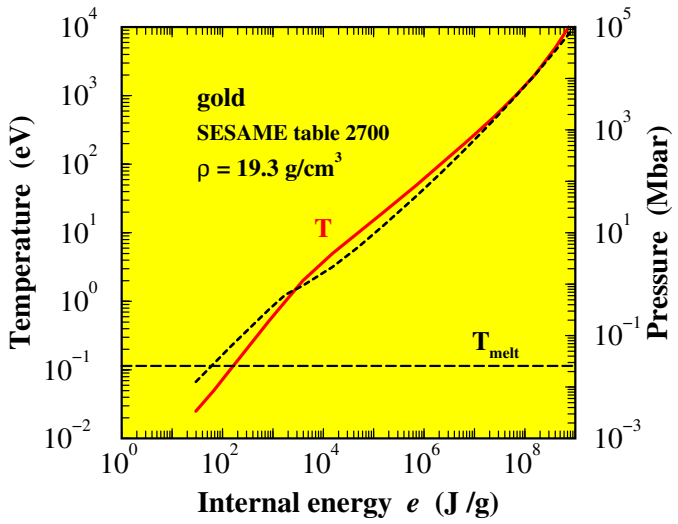

Figure 3.2.5.: *Temperature (red line, left scale) and pressure (short-dashed black line, right scale) versus internal energy at normal density in gold. The melting temperature at normal pressure is also given. For XFEL radiation at 3.1 keV focused to 1 μm^2 we obtain an internal energy for gold of $> 10^7$ J/g, corresponding to a temperature of ≈ 300 eV and a pressure of 1 Gbar.*

periments. For the example of solid gold, temperature and pressure are given as a function of the internal energy e in Fig. 3.2.5. The melting temperature is also indicated. At 3.1 keV a large fraction of the X-ray beam is absorbed in the gold target and the intensity decays exponentially along the X-ray path, leading to gradients in T and p (see Fig. 3.2.4). For targets thin compared to the photon mean free path almost no gradients are generated along the X-ray beam path.

The 1D hydrodynamic response is further illustrated in Figs. 3.2.6 and 3.2.7. We have again chosen the same XFEL beam parameters used to generate Fig. 3.2.4. A 500 nm thick gold layer is illuminated with 3.1 keV photons. The penetration depth of the X-ray photons is given by the inverse mass attenuation coefficient of 0.5 mg/cm^2, and it depends weakly on target density and temperature. In Fig. 3.2.6 the density evolution is shown as a function of space and time coordinate. While almost no hydrodynamic expansion occurs on the heating timescale of 90 fs, rarefaction waves are seen later moving into the heated foil from both surfaces and meet in the middle after 5 ps. At this time, outer layers have expanded over a μm scale, more so on the irradiated right side. Figure 3.2.7 shows temperature profiles at different times and temperature evolution versus time for few foil positions. The highest gas kinetic pressure in the target is reached during laser heating in the region of highest temperature, where values up to a Gbar are predicted.

3.2.2.2. Non-equilibrium plasmas

Transient states of non-equilibrium plasma produced by XFEL micro-pulses will occur during the 100 fs interaction period. An important issue is equilibration of the dense plasma

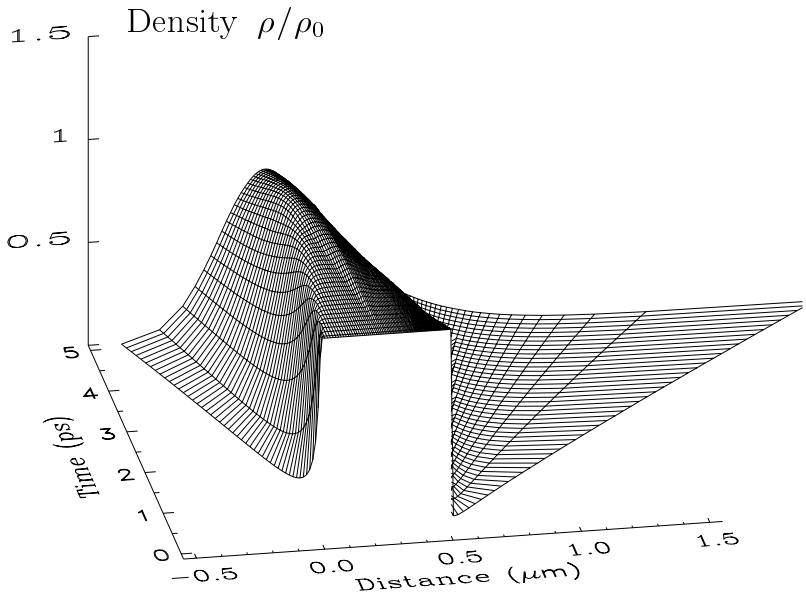

Figure 3.2.6.: *Density versus distance and time. The beam is incident from the side with positive values.*

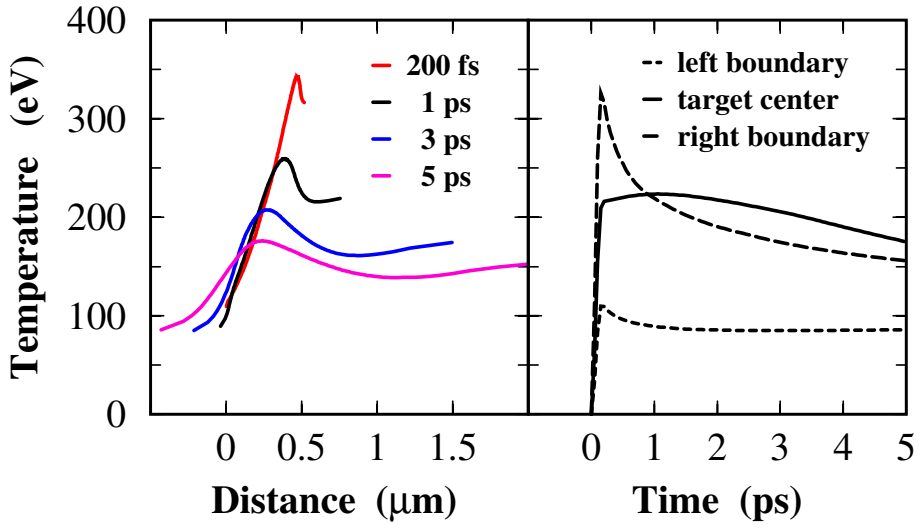

Figure 3.2.7.: *Temperature distribution at different times (left) and temperature evolution for three positions (right). The beam illuminates the target on the right boundary, where also the higher temperatures are produced.*

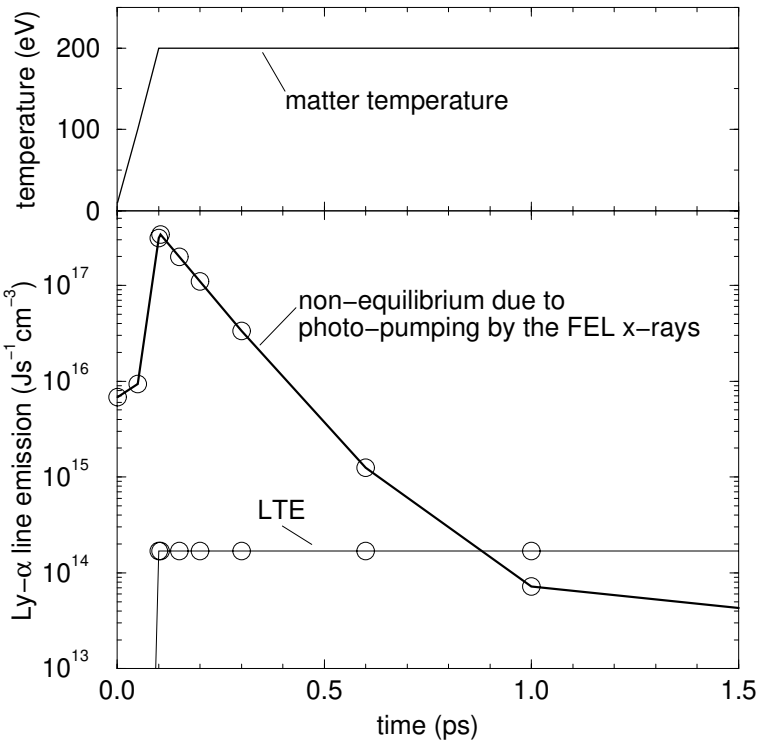

Figure 3.2.8.: *Temporal evolution of Ly-α emission of Al plasma heated by* 10^{17} *W/cm*^{2} *XFEL pulse of 100 fs duration (thick curve, lower part). For comparison, the temperature evolution (upper part) and the corresponding Ly-α emission under equilibrium (LTE) conditions (lower part) are also shown.*

generated by intense FEL X-rays, which depends on the collision times involved. The electron-electron collision time is of the order of femtoseconds for temperatures of a few 100 eV. Thus, one can expect that the free electrons quickly acquire a Maxwellian distribution. In contrast, the characteristic electron collision times for ionization and excitation are in the range of picoseconds. Therefore, the beam-excited matter will be in a state far from local thermal equilibrium (LTE) during the heating period. In particular, photoionization and excitation caused by the X-ray pulse will drive the matter into a state that strongly deviates from LTE. The equilibration between electrons and ions takes place on the picosecond timescale due to the mass ratio m_e/m_{ion}.

The importance of non-equilibrium processes is illustrated by Fig. 3.2.8 showing the emission of Al Lyman-alpha (2p-1s) line at a photon energy of 1730 eV in an Al plasma, heated to 200 eV by a 100 fs pulse. For simplicity, hydrodynamic expansion has been suppressed here, i.e. the density is fixed at solid state density (2.7 g/cm^3), and cooling by expansion is neglected. The heated layer is considered as optically thin for the Al Ly-α photons. By solving the rate equations with an atomic kinetics code [29], the time-dependent variation of the Ly-α emission is calculated. In this preliminary simulation, the layer was heated for 100 fs at a radiation temperature of 1000 eV, corresponding to the energy deposition of

an XFEL beam with an intensity of 10^{17} W/cm^2. A non-equilibrium state strongly deviating from local thermal equilibrium is generated. The strong photoionization and excitation created by the driving radiation causes an overpopulation of the upper states by many orders of magnitude. After the driving pulse is switched off, the overpopulation decays within about 1 ps and approaches a steady state value. This is somewhat below the LTE state, because the Al layer is considered as optically thin and the electron collision frequency is, despite the high density, not high enough to establish LTE.

3.2.2.3. Investigation of warm dense matter

The regime of warm dense matter is accessed in all laboratory experiments where one creates a plasma from solid or near solid density targets. It is, however, difficult to study this part of the plasma creation process in isolation. Rapid temporal variations, steep spatial gradients, and uncertain energy sources lead to indecipherable complexity. Indeed, although there has been much interest in this regime, as evidenced by the literature on strongly coupled plasmas, there has been little progress [30]. The fact that the XFEL will allow the creation and probing of the warm dense matter regime in the laboratory, will provide high quality data that will spark the field. In contrast to other techniques the generation of the warm dense matter along an isochore, i.e. a track of constant density, and subsequent probing along the release isentrope, i.e. a track of constant entropy, will be unique and provide new data for this vast research field. The importance of this data derives from the fact that currently all high quality data derived for warm dense matter is generated by shocking the material. The shock method provides information along the principal Hugoniot, that is, the locus of points in the pressure-density space that are accessed by a single shock - one point for each shock. Although this has been quite useful, it is a very limited set of data providing little information on the general behavior in the warm dense matter regime. Indeed, the amount of data that is now available provides insufficient constraints on theoretical development.

3.2.3. Plasma spectroscopy

3.2.3.1. Plasma diagnosis

Plasma diagnosis first of all will strongly benefit from the penetration power of X-rays, allowing us to obtain information from the volume even for solid-density plasmas. However, in order to obtain important plasma parameters, like temperature, density, charge state, and collective behavior of dense, strongly-coupled plasmas, new spectroscopic tools have to be developed. Very promising here is energy resolved inelastic X-ray scattering to map the velocity distribution of electrons. Furthermore, the density distribution of different ionization stages of atomic species with $Z \sim 20$ can be determined by absorption contrast imaging or X-ray interferometry with the photon energy tuned to the respective absorption edge. The use of X-ray diagnostic tools would provide the first direct measurement of microscopic parameters of solid–density plasma, which could be used to properly interpret measurements of thermal and electrical conductivity, equation of state and opacity found in astrophysical environments as well as in virtually all plasma production devices.

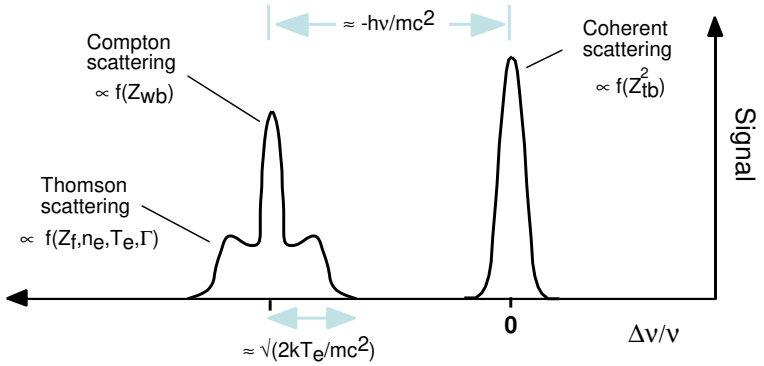

Figure 3.2.9.: *Schematic of an energy resolved X-ray inelastic scattering spectrum, with information provided by each feature noted. The intensity distribution is shown for energies relative to the energy of the probing X-ray beam. For explanation see text.*

Inelastic X-ray scattering Inelastic X-ray scattering can provide information to obtain the ionization state, density, temperature and the microscopic behavior of plasmas. The obtained information can also shed some light on the transport properties. The method is an extension of Thomson scattering using visible light, which is very successfully applied to low density plasmas [31]. Indeed, the corresponding Thomson scattering cross-section is directly related to the dynamic structure factor, $S(k,\omega)$, of the plasma and thus provides insight into the theoretical predictions from different theories [32]. In recent years, it has led to new and important discoveries [33]. Extension of this method to densities above 10^{21} cm^{-3} using visible light will be very difficult. We propose instead to extend the power of spectrally resolved Thomson scattering from the visible light regime to the X-ray regime. However, the preconditions for the interpretation of the scattering data is that there is a valid theoretical model for the $S(k,\omega)$ in the high density regime, which in itself will be a challenge. The tunable X-ray wavelength, the high energy, band width, the short pulse duration and, importantly, the large peak photon flux make this source the only one that can address the X-ray inelastic scattering diagnosis of transient plasmas.

Figure 3.2.9 shows schematically a generic energy resolved spectrum. It contains various contributions providing the means to determine several parameters of the investigated plasma. Coherent scattering from tightly bound electrons (Z_{tb} per atom) will provide an unshifted peak at the probe wavelength (Rayleigh scattering) whose integral intensity is proportional to Z_{tb}^2. Incoherent Compton scattering occurs, in particular, at the weakly bound electrons (Z_{wb} per atom) and will lead to a second peak, which is downshifted in energy by the order of $\hbar\omega/mc^2$ (the Compton shift). The integral intensity of this peak is proportional to Z_{wb}. Thomson scattering from free electrons (Z_f per atom) should provide a dispersed spectrum centered on the Compton peak, with a spectrally integrated intensity varying as Z_f. The form of the spectrum will in general depend on the free electron density, n_e, free electron and/or Fermi temperature T_{Fermi} and electron-ion collisionality ν_{ei}. Hence, by energy resolving the scattered X-rays one gains access, for the first time, to an unparalleled source of information on warm dense matter.

For example, we should be able to infer Z_f, Z_{tb}, and Z_{wb} from the relative contributions of

coherent, incoherent and free electron scattering. This would allow discrimination between different ionization balance models used to define the equation of state of the corresponding plasmas [34]. Using the free electron temperature and density (and hence ionization state since the ion density is effectively hydrodynamically frozen) will shed further light on the equilibrium states of warm dense matter, and the obtained plasma collisionality would allow tests of the validity of various strongly-coupled statistical physics models.

Imaging plasmas The possibility to use coherent X-ray beam from synchrotron radiation to image dense matter quantitatively and thus to observe the density distribution with high spatial resolution of the order of 1 μm^2 has been proven throughout the last years. This technique can be applied for imaging the plasma region and to obtain information about density distribution for all plasmas and/or solids one could produce. The use of interferometers, as done in previous work on plasmas [35], will not be necessary due to the intrinsic coherence of the X-ray beam. New techniques, similar to common point interferometry, can obviate the problem of the statistically varying pulse structure.

We note in closing that there is the intriguing possibility of using part of the beam, for example the spontaneous background, to warm a sample and then use the X-ray pulse to probe it. This is distinct from the idea where we create the plasma using a standard long pulse laser system. The experiments using the XFEL as the heater and probe are much more demanding as the number of free electrons may decrease by at least an order of magnitude. Note that the number of free electrons is a matter of great controversy in this regime as the definition of "free" is open to debate [36]. Further, the need to delay the heater from the probe by X-ray optics creates additional losses. While this may still be possible, and spectral resolution can easily be achieved, the first experiments in both the warm dense matter regime and the plasma X-ray inelastic scattering at higher temperatures should be independently pursued.

3.2.3.2. Investigation of X-ray laser transitions

The difficulty for X-ray plasma lasers is to find inversion schemes that can be populated with high efficiency and enable, therefore, high gain factors. These schemes are developed by simulations, experimentally they are, however, often very difficult to verify. The XFEL will enable for the first time highly efficient photo pumping of specific X-ray laser transitions and therefore offer the possibility to separate the kinetic processes occurring during plasma creation from the pumping of particular transitions used for the laser emission. The XFEL thus could provide a very sensitive test for models of plasma population kinetics. Of further, and particular, interest are those states with a high density of K-vacancies (hollow ions), generated due to the preference in the X-ray interaction for ionizing deeply bound electrons. Such states are of primary interest for so-called gamma-ray lasers. After a consideration plasma kinetics studies two examples are presented, where the XFEL offers new and exciting possibilities.

Investigation of plasma kinetics The importance of the XFEL is that one can use it to pump individual transitions in a plasma, creating enhanced population in the excited states

that can be easily monitored. The idea has been used in lower density plasmas with optical lasers and can, with XFELs, be employed to advance the study of high density plasmas. Furthermore the XFEL will allow pumping of transitions from core states, employed in plasma X-ray lasers. Variations on the idea of pumping individual transitions include the pumping of selected transitions to attempt to understand the inversion mechanisms for the production of laboratory X-ray lasers and the selective pumping of the wings of a line transition to observe redistribution within the line profile. Using the XFEL will therefore allow us for the first time to test theoretical models in the areas of atomic processes, kinetics model creation, line shape formation, and X-ray gain studies.

In order to provide useful data the XFEL radiation must fulfil certain requirements. First, to enable investigation of various transitions the probe must be tunable. This is easily satisfied. Second, the line width of the pump must be such that it can pump entire line profiles and also be capable - for studies of redistribution within line profiles - of pumping parts of the line profile. Again, these conditions are readily met. Finally, one needs to have a pump that can move enough population from one state to another so that the population changes can be monitored. The last requirement can be verified by comparing the pumping rate, R_{lu}, and the spontaneous emission rate, A_{ul}, of the transition being pumped. For systems without non-radiative decay channels the ratio [37]

$$\frac{R_{lu}}{A_{ul}} = 6.68 \cdot 10^{-22} \frac{(\lambda[\text{Å}])^5}{\Delta} \frac{g_u}{g_l} I_0 \left[\frac{W}{cm^2}\right] \tag{3.2.1}$$

of these rates is proportional to the number of photons per mode. The g's are the statistical weights of the upper and lower states, λ and I_0 are the wavelength and intensity. Δ is the smaller value of either the incident bandwidth or transition line width. If we conservatively assume $I_0 \approx 10^{14}$ and $\Delta \approx 0.001$ we find that the ratio is approximately 1 at 10 Å. This number is at least 1000 times larger than can be obtained by using a plasma source to pump a transition. The ratio decreases with decreasing wavelength, and matching, or at least controlling the bandwidth, can have salutary effects.

The He-like Ne scheme A proposed inversion scheme to be used as a plasma laser is shown in Fig. 3.2.10. To obtain the proposed He-like Ne scheme laser transition $(n = 4) \rightarrow (n = 3)$, the $(n = 4)$-state needs to be populated very effectively to achieve inversion. Attempts have been made to study the population kinetics and the laser transition by pumping the $(n = 4)$-state of He-like Ne with an optical laser. The radiating decay of this state was intended to serve as a pump for the He-like Ne $(n = 1) \rightarrow (n = 4)$ transition (see Fig. 3.2.10). Unfortunately, this was not successful due to missing pump power. A particular problem for such pumping schemes of X-ray plasma lasers are hot electrons, which are created in plasmas generated by optical lasers and which lead very efficiently to non-radiative decay.

Using the XFEL tuned to the energy for the transition $(n = 1) \rightarrow (n = 4)$ of He-like Ne, one would very efficiently pump the $(n = 4)$-state, enabling a study of its (de-)population kinetics. The XFEL provides not only a brightness several orders of magnitude higher than the plasma generated He-like Ne pump, it also allows study of the proposed plasma laser system, independent of the difficulties inherent in coupling two separate plasma sources.

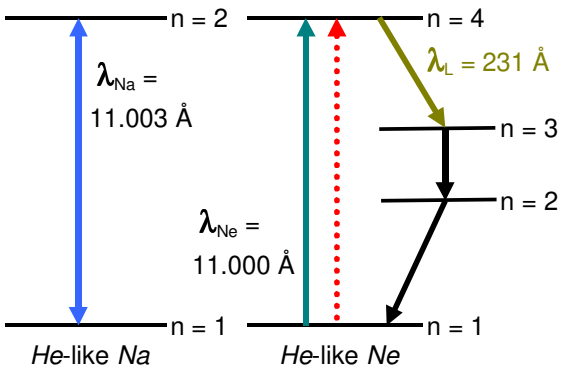

Figure 3.2.10.: *Term scheme for a proposed plasma X-ray laser transition in He-like Ne at 231 Å (right). Instead of using the radiative decay of the He-like Ne* $(n = 4)$*-state for pumping (left) the XFEL offers the possibility for direct pumping of the* $(n = 1) \rightarrow (n = 4)$ *transition of He-like Ne (dotted line), thereby disentangling pumping and (de-)population of the proposed laser state.*

The XFEL thus could fully disentangle the process of pumping the laser transition from the population kinetics of the lasing state.

Redistribution Recent advances in the computation of the radiative properties of complex ions in hot, dense plasmas, made possible by the development of the frequency fluctuation model [38], have resulted in an adequate understanding of the effect of the plasma environment on the emission or absorption process and the shape of the associated spectral lines [39]. The next logical step in understanding the radiative properties of hot dense plasmas is to develop models for the study of the multiphoton response, e.g., the scattering of resonance radiation. One motivation for this study is that for lines with a large optical depth there remain difficult problems involving radiative transfer. Beyond the simplest assumption that the line shape is independent of the radiative redistribution, these problems cannot be understood simply through calculations of the one photon absorption or emission spectrum, but require the development of a computational ability to treat the scattering of near resonant radiation in hot dense plasmas. This means that a theoretical formulation of the two photon plasma spectral properties in the presence of a combination of homogeneous and inhomogeneous broadening processes must be developed. Clearly the creation of an X-ray laser source such as the TESLA XFEL will provide the necessary experimental test bed to evaluate the complex processes that contribute to the redistribution of radiation in a line profile.

As an example we present here a simulation of the radiative redistribution processes of Li-like Fe created in a laser produced plasma. An estimate of the ratio of pumping and spontaneous decay rate at a density $N_e = 10^{22}\,\mathrm{cm}^{-3}$ and temperature $T_e = 500\,\mathrm{eV}$ indicate that the investigation of this pumping process is feasible. In Fig. 3.2.11 simulations of line profiles are shown for two cases. In the absence of XFEL radiation (left-side plot) one observes two emission lines. Stark collisions lead in addition to the appearance of two forbidden emission lines at 1544.6 eV ($4S_{1/2} \rightarrow 1S_{1/2}$) and 1554.7 eV ($4D_{3/2} \rightarrow 1S_{1/2}$). Photo

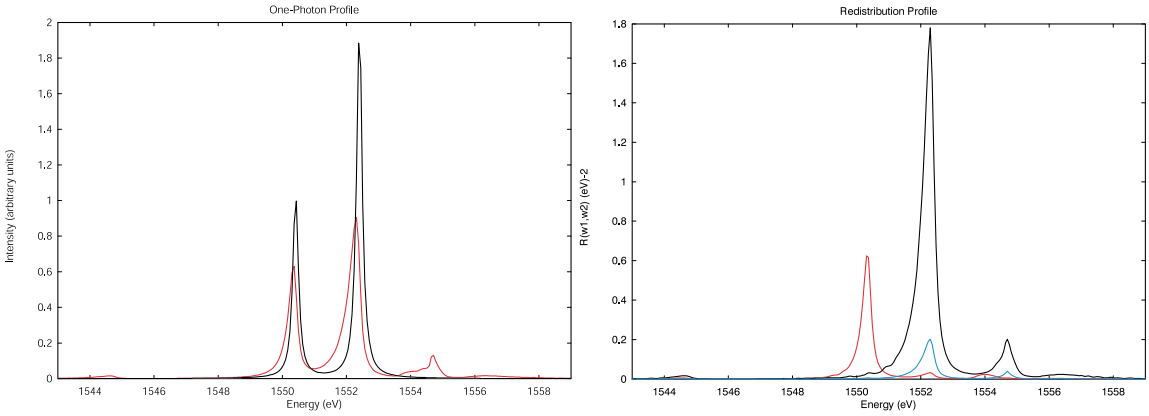

Figure 3.2.11.: *Left: Transitions of Li-like Fe* $(n = 4) \rightarrow (n = 1)$ *at* $T_e = 500\,eV$ *and* $n_e = 10^{22}\,cm^{-3}$. *Only electron broadening (black curve) and electron and ion broadened (red line) have been taken into account. Right : Line profiles including electron and ion broadening after photopumping with the XFEL at three energies: 1550.4 eV (red), 1552.3 eV (black), and 1554.7 eV (blue).*

pumping now with the XFEL at three energies (right-side plot), populating thus different states selectively, leads to line profiles exhibiting far more details. One for example sees that pumping at 1550.4 eV leads to the forbidden $(4D_{3/2} \rightarrow 1S_{1/2})$ transition forming the shoulder at 1554.0 eV. This is a clear indication of redistribution of the excited states within the plasma. A further example for such studies with the XFEL would be aluminum plasma, where similar approaches have already been made [40].

In summary to this chapter, the XFEL opens new possibilities to plasma physics. The generation of dense and strongly coupled plasmas by X-rays that penetrate into the sample and heat it isochorically has the capacity to illuminate the physics of dense plasmas and to study in detail the plasma phase space of many elements. XFEL generated plasmas will cover a wide range of temperatures from warm solids up to hot plasmas at solid density. It will furthermore be important to study equilibration processes occurring in these plasmas and to investigate the plasma kinetics, of interest not only to X-ray laser research. The quality of the XFEL radiation will in addition enable development of new concepts of X-rays based plasma diagnosis, important to study these dense plasmas not accessible by optical means.

Bibliography

[1] D.J. Stevenson, J. Phys.: Condens. Matter **10**, 11227 (1998).

[2] V.E. Fortov, I.T. Iakubov, *Physics of Nonideal Plasmas*, Hemisphere, New York (1990).

[3] W.J. Nellis, S.T. Weir, A.C. Mitchell, Phys. Rev.B **59**, 3434 (1999).

[4] J.F. Benage Jr., W.R. Shanahan, M.S. Murillo, Phys. Rev. Lett. **83**, 2953 (1999); J.F. Benage Jr., Phys. Plasmas **7**, 2040 (2000).

[5] *The HIDIF–Study*, GSI–Report No. 98-06, Darmstadt (1998).

[6] P.M. Celliers et al., Phys. Rev. Lett. **84**, 5564 (2000).

[7] W. Theobald et al., Phys. Rev. Lett. **77**, 298 (1996); G.A. Mourou et al., Phys. Today **51**, 22 (1998).

[8] J. Meyer-ter-Vehn et al., Phys. Fluids B **2**, 1313 (1990).

[9] R. Redmer, Physics Reports **282**, 35 (1997).

[10] S.T. Weir, A.C. Mitchell, W.J. Nellis, Phys. Rev. Lett. **76**, 1860 (1996).

[11] R. Redmer, G. Röpke, S. Kuhlbrodt, H. Reinholz, accepted Contrib. Plasma Phys. **41**, (2001).

[12] D. Beule et al., Contrib. Plasma Phys. **39**, 21 (1999); D. Beule et al., Phys. Rev. B**59**, 14177 (1999).

[13] L.B. DaSilva et al., Phys. Rev. Lett. **78**, 483 (1997).

[14] H. Juranek, R. Redmer, W. Stolzmann, accepted Contrib. Plasma Phys. **41**, (2001).

[15] M. Ross, Phys. Rev. B**58**, 669 (1998).

[16] H. Juranek, R. Redmer, J. Chem. Phys. **112**, 3780 (2000).

[17] B. Militzer, D. Ceperley, Phys. Rev. Lett. **85**, 1890 (2000).

[18] T.J. Lenosky et al., Phys. Rev. B**61**, 1 (2000).

[19] D. Saumon, G. Chabrier, Phys. Rev. Lett. **62**, 2397 (1989); D. Saumon, G. Chabrier, Phys. Rev. A**44**, 5122 (1991); *ibid.* **46**, 2084 (1992)

[20] W. Ebeling et al., Plasma Phys. Control. Fusion **38**, A31 (1996).

[21] R.W. Ohse, *Handbook of Thermodynamic and Transport Properties of the Alkali Metals*, Blackwell, Oxford (1985).

[22] F. Hensel, J. Phys.: Condens. Matter **2**, SA33 (1990).

[23] A.W. DeSilva and H.-J. Kunze, Phys. Rev. E**49**, 4448 (1994); A.W. DeSilva and J.D. Katsouros, Phys. Rev. E**57**, 5945 (1998).

[24] D. Klakow, Ch. Toepffer, P.-G. Reinhard, Phys. Lett. A**192**, 55 (1994); J. Chem. Phys. **101**, 10766 (1994); M. Knaup, P.-G. Reinhard, Ch. Toepffer, Contrib. Plasma Phys. **39**, 57 (1999).

[25] W.-D. Kraeft, D. Kremp, W. Ebeling, G. Röpke, *Quantum Statistics of Charged Particle Systems*, Akademie-Verlag, Berlin (1986).

[26] A. Pukhov and J. Meyer-ter-Vehn, Phys. Rev. Lett. **76**, 3975 (1996); Phys. Plasmas **5**, 1880 (1998); C. Gahn et al., Phys. Rev. Lett. **83**, 4772 (1999).

[27] R. Ramis et al., Comp. Phys. Comm. **49**, 475 (1987).

[28] K. Eidmann, Laser and Particle Beams **12**, 223 (1994).

[29] The FLY code has been used, see R.W. Lee and J.T. Larsen, J. Quant. Spec. Rad. Trans. **56**, 535 (1996).

[30] See the papers in *Strongly Coupled Coulomb Systems*, G.J. Kalman (ed.), Plenum, New York (1998), and the references therein.

[31] H.-J. Kunze, in *Plasma diagnostics*, W. Lochte-Haltgren (ed.), North-Holland, Amsterdam (1968), p. 550.

[32] J. Sheffield, *Plasma Scattering of Electromagnetic Radiation*, Academic Press, New York (1975), and references therein.

[33] S.H. Glenzer et al., Phys. Rev. Lett. **82**, 97 (1999).

[34] F.J. Rogers, Phys. of Plasmas **7**, 51 (2000); D.A. Liberman, Phys. Rev. B**20**, 4981 (1979).

[35] D. Ress et al., Science **265**, 514 (1994).

[36] The controversy on the definition of free versus bound electrons is closely connected with the role of ionization potential depression, continuum lowering, and level shifts near the continuum. See the discussions in Ref. [34]

[37] R.C. Elton, *X-ray Lasers*, Academic Press, San Diego (1990).

[38] B. Talin et al., Phys. Rev. A**51**, 1918 (1995).

[39] A. Calisti, L. Godbert, R. Stamm and B. Talin, J. Quant. Spec. Rad. Trans. **51**, 59 (1994).

[40] C. Back, R. Lee, C. Chenais-Popovics, Phys. Rev. Lett. **63**, 1471 (1989); C. Back, J. Castor, P. Dykema, R. Klein, R. Lee, Phys. Rev. A**44**, 6743 (1991).

3.3. Condensed Matter Physics

This chapter has been written on the basis of contributions to the reports of the workshops "Hard Condensed Matter Physics" edited by Th. Brückel (FZ Jülich) and H. Franz (HASYLAB, Hamburg) (see A.1.3) and "Nuclear Resonant Scattering at the XFEL" edited by U. van Bürck (Technical University, München) and H. Franz (see A.1.7). In these contributions, more detailed description and further references can be found.

Condensed matter comprises a large spectrum of materials, from clusters consisting of only a few atoms only through composites up to macroscopic solids. Objectives of condensed matter research can be described as follows: first is the determination of the atomic, electronic structure and dynamics; second, the determination of the fundamental interactions, third is the relation of the microscopic and mesoscopic structure and dynamics to the macroscopic properties of the materials in question. This field of research thus constitutes a basic pillar of modern material science and engineering applications, described in Sec. 3.5. Historically, solid-state research provides a beautiful example of the application of quantum mechanics and statistical physics to an extreme many-body problem, and has found its greatest success with the theoretical description of simple periodic crystalline materials. This is now standard material in many basic textbooks on solid-state science. Scattering and spectroscopy of X-rays have greatly contributed to our present day understanding of materials on an atomic scale. However, in any real material, deviations from this idealized average perfect structure occur in the form of defects, which can turn out to be decisive for the appearance of certain material properties. The determination of such heterogeneities (dislocations, grains, composites etc.) on a nano- or mesoscopic length scale in bulk materials represents a real challenge for modern condensed matter research. In addition, new materials, such as layered or laterally structured materials created on a nanometer length scale either artificially or by self-organization, have come to the center of attention. This is partly triggered by the fascination of designing materials with certain desired properties, and partly due to previously proven applications. One example is magnetic multilayers, which have found a wide range of application as information storage media or field sensors. New techniques have yet to be developed to study these materials and their dynamic response on wide length and time scales. Besides studies of the geometric structure, another very active field in solid state research is the study of magnetic structures, magnetic excitations and magnetic phase transitions. With the rapidly growing applications of magneto-electronics, the behavior of nanostructured magnetic materials has recently attracted a lot of attention. But also, new bulk materials have appeared with unusual properties resulting from electronic correlations, such as novel superconductors or colossal magnetoresistance manganates. For many problems concerning these novel magnetic materials, traditional probes, such as neutron scattering or X-ray scattering and spectroscopy on present synchrotron radiation sources, face their limit of applicability, e.g. in the observation of ultra-fast response in the femtosecond time regime. Again, the study of such ultra-fast processes is not only of fundamental interest, but bears direct application for magnetic data storage devices, where the times required to switch the magnetization in a nanostructure determine the limitations of the write or read cycles for magnetic memories.

The femtosecond magnetic response discussed above is just one example that shows that not only the static properties, but also the function and performance of devices are governed by the electronic, spin, and vibrational dynamics. Apart from elementary excitations, the time-dependent kinetics of solid-state reactions (e.g. sintering processes in ceramics) or phase transitions play a decisive role for functional materials, such as smart materials. Metastability or nucleation mechanisms for phase transitions are largely unexplored, since local probes capable of resolving fast kinetics have not been available.

As will be shown in the subsections below, for many of the above problems, an XFEL source can provide new insight not attainable with other, more conventional methods. The unique properties of the XFEL source, such as a large degree of lateral coherence, femtosecond time structure, high brilliance, and also the appearance of short-pulse high-energy spontaneous radiation, provide new experimental possibilities and gives access to quantities not attainable at present. It has to be stressed that the XFEL provides not only mere growth, but a qualitative leap promising to make certain observations possible for the first time. Last but not least, the XFEL allows the investigation of materials under extreme conditions, for example, high temperatures, high magnetic field or high pressure.

3.3.1. Magnetism

3.3.1.1. Some open problems in magnetism

Magnetism is a very active and challenging subject of solid-state science, since it represents a typical many-body problem and a complex application of quantum mechanics, statistical physics and electromagnetism. During the last few decades, new discoveries have emerged in this field due to the synthesis of new classes of magnetic materials, due to improved or new powerful experimental techniques or due to advancements in solid-state theory. Let us mention a few examples of materials of current interest: the high-temperature superconductors and the colossal magneto-resistance manganite compounds, both of which have structures derived from the perovskite structure; the rare-earth nickel-boron carbide compounds with a coexistence of magnetism and superconductivity; the large class of Kondo systems and heavy fermion compounds; spin glasses and spin liquids; molecular magnets or new and rather complex hard magnetic materials, just to mention a few. Besides bulk materials, the magnetism of thin films and surfaces has become a topic of great current interest, mainly due to the improved preparation techniques. Driven by pure curiosity, scientists have discovered many fundamental effects in thin film devices, such as oscillating interlayer coupling or giant magneto-resistance. Within less than ten years from their initial discovery, these effects found their applications, for example, in read heads of computer hard disks. A promising new field of application is emerging, so-called magneto-electronics with spin transistors or magnetic random access memories MRAM [1].

Some 3000 years after the discovery of magnetism, fundamental problems remain. The XFEL could contribute significantly to answering the following open questions – a list which is by no means exhaustive:

- Strongly correlated electron systems: How do electronic correlations determine ground state, thermal, or transport properties?

- Molecular magnets: How are the unpaired electrons distributed? What determines the ordering temperatures? How can we *design* materials with the desired properties? What are the time scales for quantum molecular tunnelling?

- Nanostructured materials: What are the magnetic structures, couplings and excitations in magnetic thin films, magnetic quantum wires and quantum dots or nanostructured permanent magnets? What determines time scales for the switching of magnetization in an external applied field?

- Low dimensional magnetism: Do we understand the statistical physics in two and one dimensions with quantum spin plaquettes, spin ladders or spin chains as model systems?

- Magnetism at surfaces and interfaces: What is the magnetic structure at surfaces? Is the magnetism enhanced or reduced as compared to the bulk material? How are the phase transitions altered at the surfaces? How are magnetic and structural roughness related and how do they influence transport or coupling?

- Frustrated and/or disordered spin systems: What is the ground state of highly topologically frustrated systems? Are there new universality classes for the magnetic phase transitions of chiral spin systems? What are the phase diagrams, and the dynamic response of complex, disordered magnets?

Apart from these fundamental questions, solid-state magnetism has become an active area in applied materials science because of the many industrial applications. While it is impossible to predict the progress of science over a decade, it is very likely that similar or related problems in the field of magnetism will be in focus several years from now, when an XFEL source becomes available.

While macroscopic measurements (magnetization, susceptibility, etc.) or local probes such as magnetic resonance imaging or Muon spin resonance give very valuable information, the interpretation of the data obtained with these techniques always relies on model assumptions, which can only be tested by probes with atomic space and time resolution. Since the experiments of C. Shull in 1949, neutron scattering has been the traditional microscopic probe for magnetism. However, within the last decade, various forms of X-ray absorption spectroscopy (linear and circular dichroism, spin sensitive X-ray absorption spectroscopy or related techniques such as Kerr or Faraday effect measurements) as well as X-ray scattering techniques (non resonant magnetic scattering, resonant exchange scattering, magnetic reflectivity measurements, nuclear resonant scattering) have been established and contributed largely complementary information [2]. X-ray scattering provides information on pair correlation functions, and, in contrast to neutron scattering, allows one to distinguish spin and orbital angular momentum [3]–[5]. The high momentum space resolution gives access to larger periods in direct space [3, 5]. By tuning the X-rays to an absorption edge of the magnetic elements, element-specific magnetization [6] or spin pair correlation functions [7] can be determined, giving new insight into the physics of disordered systems. The study of surface magnetism using X-ray methods has been initiated [8, 9]. Recently a magnetic speckle pattern could be observed with the partly coherent beam from a third-generation source [10].

While many of these techniques have become routine, others, such as surface scattering and the full exploitation of coherence or of time resolution on sub-millisecond time scales, await the advent of more powerful X-ray sources.

Considering that magnetic scattering is several orders of magnitude weaker than charge scattering, it is tempting to extrapolate today's X-ray scattering techniques to the possibilities offered by the high peak intensity of the XFEL. This has to be done with extreme caution, since the energy in the XFEL pulse is deposited directly into the electronic system in which magnetism resides. In many cases we will no longer be able to neglect the perturbation by the X-ray beam. Phenomena due to multiple core hole excitations will be studied on the XFEL. First experiments on single atoms investigating electron correlations in double ionization processes have recently been reported [11]. Coherence might play a role in determining electron correlations by multiple excitation processes, but at present, we can only speculate about the implications for magnetic studies. In what follows, we assume that the experimental conditions are such that information on the unperturbed system is obtained (e.g. unfocused monochromatized beam under grazing incidence). The XFEL beam parameters match well the requirements for magnetic studies. The energy range from 0.82 keV to 14.5 keV of the coherent radiation covers all the interesting absorption edges of the actinides (M edges at 3 to 6 keV) and lanthanides (L edges at 5 to 11 keV) used nowadays for resonant magnetic X-ray scattering or magnetic dichroism studies. It would be desirable to push the lower limit down to 0.5 keV in order to cover all of the 3d transition metal L edges. Additional monochromatization down to $\Delta E/E < 10^{-4}$ is indispensable for spectroscopic studies. The spontaneous radiation extends up to several 100 keV and is thus well suited for non-resonant magnetic X-ray diffraction. Clearly, the high inherent degree of polarization is of utmost importance for magnetic studies.

Novel applications result from the coherence, the time structure, and the high brilliance of the XFEL beam. The transverse coherence length will be increased from about 10 μm at a third-generation synchrotron radiation source to the full beam size at the XFEL. This is reflected by an increase in coherent flux of about ten orders of magnitude. The observation of magnetic speckle patterns due to the domain structure of magnetic systems will become routine. Photon time correlation spectroscopy will allow the study of magnetic dynamics in the momentum transfer range Q = 10^{-4} to 10 Å^{-1} and the time range 10^{-3} to 100 s. This method surpasses the possibility of the neutron spin echo technique towards a larger Q and energy range.

3.3.1.2. Magnetic domains, surface and thin films

One application is the study of magnetic thin films or surfaces, where the structural interfaces and the magnetic interfaces will in general have different roughness. The "magnetic" speckle pattern will differ significantly from the "charge" speckle pattern. The interface structure can in principle be reconstructed without model assumptions from such a speckle pattern [12], while the interpretation of reflectivity measurements with incoherent beams always relies on model assumptions for the interface structure. Slow dynamics in the magnetic system at the interface will occur for example in the vicinity of magnetic phase transitions and can be studied without background due to charge scattering by the fluctuating magnetic speckles in

between the static structural or ”charge” speckle peaks. This example demonstrates quite generally how coherence can be used to study magnetic fluctuations in the presence of a much higher charge background and for very small quantities of magnetic material (here just a surface or interface layer!). The method will allow the influence of spatial restrictions to be studied.

With existing sources, it is almost impossible to determine the statistical parameters of magnetic thin-film systems such, as average domain sizes, magnetic roughnesses or relaxation time constants of magnetic fluctuations. Most frequently, there are two ways to investigate magnetic properties: 1) performing two measurements with differently circularly polarized incident beam of opposite helicity and analyzing the normalized difference or 2) illuminating with linearly polarized beam and monitoring the perpendicularly polarized scattering. The first method has the advantage of reasonably high scattered intensity, but definitely prevents time-resolved investigations. Furthermore, in the case of magnetic roughness, the signal scales with the correlation to the charge roughness. Thus, no clean magnetic information is expected. The second method decouples magnetic and charge contributions, but for diffuse scattering the intensity is extremely small.

The FEL source would be capable of doing novel kinds of experiments on the properties of magnetic thin films. Most crucial will be the full coherence and the complete linear polarization of the beam. The high flux is also helpful.

Illuminating the sample surface under grazing incidence causes diffusely scattered intensity, which contains information about the above-mentioned magnetic properties. If the beam is fully coherent, a spiky speckle pattern is expected - see the simulation shown in Fig. 3.3.1. The magnetic speckles with quite weak intensity will be at different positions compared to the charge speckles. (Only if both structures are EXACTLY the same will the patterns match). Both kinds of speckles can easily be distinguished by their direction of polarization if the incident beam is completely polarized.
The following experiments are possible:

- Magnetic X-Ray Photon Correlation Spectroscopy (XPCS). In the case of magnetic fluctuations, the magnetic speckle pattern will change according to the relaxation time. In contrast, the charge speckle pattern remains unchanged. The fluctuating magnetic signal becomes visible in between the charge speckles. Performing a typical XPCS experiment at these positions with polarization analysis will yield the magnetic relaxation times.

- If the magnetic structure is almost static, a scan of the diffuse scattering with polarization analysis yields the complete magnetic speckle pattern. Doing this on different sample positions and averaging the scanned intensities give access to the correlation lengths of the magnetic roughness and domain size in the films.

- Combining the coherence of the XFEL beam for imaging purposes and nuclear resonant scattering techniques, one may obtain 2D or 3D maps of the sample. Using the contrast in the hyperfine structure to obtain two-dimensional images, domain distributions of thin films or surfaces can be investigated at very high spatial resolution. In 3D reconstructions, provided e.g. by holotomography, information on nucleation

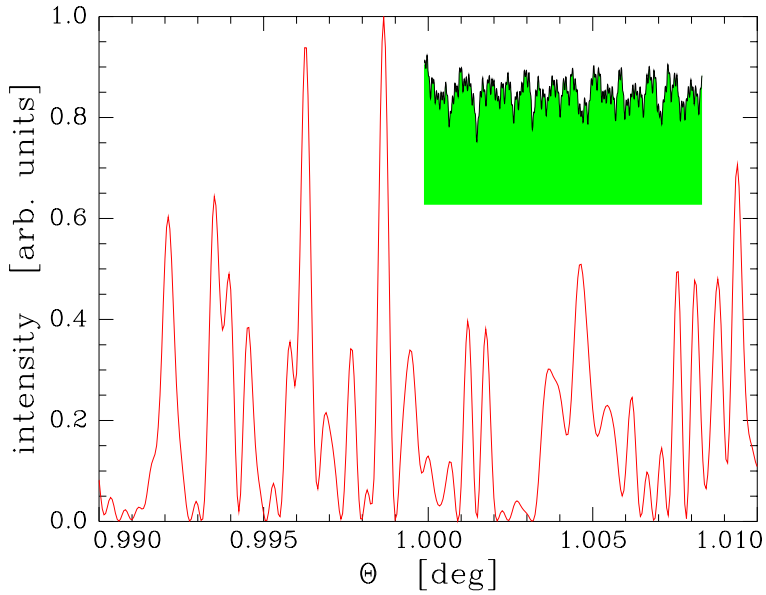

Figure 3.3.1.: *Calculation of a speckle pattern from a rough surface. An incident angle scan with fixed scattering angle ($\phi = 2°$) is shown. The beam size is 20 μm. The distance from the defining pinhole to the sample is 500 mm, as is the distance from the detector to the sample. The wavelength is 1 Å. The inset shows the surface roughness assumed to generate the pattern. The sample size is 0.4 mm, the rms-roughness 5 Å.*

and growth (on a time scale of ms) of magnetic domains or new phases may become accessible. Possible applications of such studies are e.g. the homogeneity of an array of magnetic structures and the response of magnetic nanostructures to external field pulses. Also elements specific surface depth profiles may be reconstructed from dynamical beat maps.

- Magnetism in surfaces and multilayers was studied successfully using nuclear resonance scattering of ^{57}Fe. With the XFEL new isotopes will become available for this kind of study, which has already proven to provide detailed information about magnetic electronic ground states. Of particular interest here are the rare earth isotopes ^{149}Sm, ^{151}Eu and ^{161}Dy, since the 4f-magnetism of the rare earth elements determines many properties of magnetic devices using these elements. As shown by conventional Mössbauer spectroscopy at the ^{119}Sn resonance, non-magnetic Sn is a very useful probe for magnetic samples and also for heavy fermion systems [13].

For most of the above-mentioned experiments a completely coherent and polarized source is needed. A monochromatic beam is necessary (δE = 1 eV, determines the accuracy of the polarization analysis), thus the FEL should be seeded to get the same wavelength for each bunch. The spontaneous emission is small enough if it is about four orders of magnitude less intense than the laser. A well defined time structure is desired. The grazing incidence conditions prevent the damage of the sample by the beam.

Femtosecond magnetism of nanostructures Miniaturized magneto-electronics devices are expected to have a high potential for applications in information technology and as magnetic field sensors. A goal in data storage technology is to develop non-volatile magnetic random access memory (MRAM) nanoscale devices (see Fig. 3.3.2) that can replace present RAM chips. The reduced system dimensions should lead to many new phenomena that are of scientific and technological interest. Although thermodynamically stable magnetization reversal after application of short external field pulses has been achieved, a considerable deficiency exists in our understanding of the spin dynamics and the ultimate timescales on which exchange coupled spins in a solid could eventually be reversed.

RAM devices usually consist of different magnetic and non-magnetic materials that require element-selective measurements of their electronic and magnetic properties. X-ray circular dichroism is to date the only technique that can achieve this. Of special interest is the separation of orbital and spin contributions to the magnetic moment [14]. An example is shown in Fig. 3.3.2.B, where the orbital moment per spin for self-assembled Co dots is plotted as a function of the dot size [15]. The orbital moment links the spins to the crystal lattice and establishes a preferred direction of magnetization [14]. The dramatic increase of the orbital moment in Fig. 3.3.2.B is then indicative of an enhanced spin-orbit coupling with reduced dot size. Such self-assembled magnetic dots can be viewed as prototype systems for nanoscale magnetic storage media. Along with the shrinking bit dimensions, the time scale for read-write operations has to be reduced in order to cope with the increasing storage capacity. In magneto-optical storage media, an intense laser pump-pulse erases the bits. It is expected that enhanced spin-orbit coupling in small devices will help to promote electronic spin-flip scattering leading to faster magnetic switching times [16]. This can be measured in X-ray dichroism experiments utilizing the time structure of an XFEL. A with respect to pump pulse time-delayed femtosecond X-ray pulse would then probe the time evolution of spin and orbital magnetic properties. Such information is unavailable with present femtosecond-laser based techniques [17]. The magnetic switching speed of nanostructures such as MRAM devices (see Fig. 3.3.2.A) could also be measured with such pump-probe techniques. A pump-pulse would then trigger an optical switch and generate an ultra-short current pulse. Combining this method with X-ray [18] or photoelectron emission microscopy [19] would then allow unprecedented studies of the magnetic switching dynamics with femtosecond or picosecond time resolution of small particles and devices.

A second field of interest arises from the understanding of timescales for the demagnetization of RAM elements. Today most experiments on ultrafast magnetization processes employ visible light lasers with time resolution below 50 fs. In these pump–probe experiments, valence electrons are excited, and the probe yields information on the induced local changes in electron temperature and average spin direction. The latter is obtained magneto-optically, either by measuring Kerr rotation (and/or ellipticity) or by using second-harmonic generation [20]. Experiments on Ni clearly suggest that a reduced average spin direction ("transient demagnetization") is established already ≈ 250 fs after the excitation. This is the same timescale on which electrons reach a new thermal equilibrium [20]. However, this picture has been disputed on the basis of time-resolved magneto-optical Kerr experiments which reveal clear differences between Kerr rotation and ellipticity during the first few 100 fs [21]. The results rather support the notion that a true demagnetization cannot be achieved faster

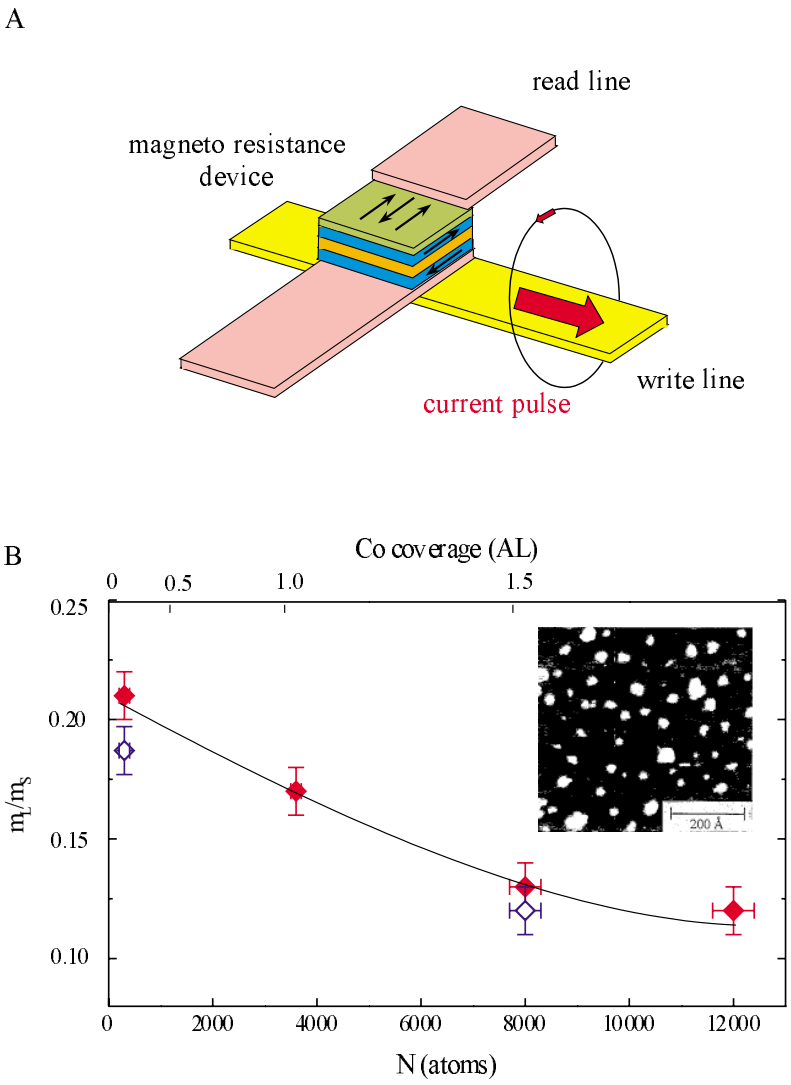

Figure 3.3.2.: *A) Schematic diagram of a magnetic random access memory (MRAM) unit consisting of a giant magneto-resistance device. The free ferromagnetic layers can be switched by the magnetic field of a short current pulse propagating along a write line. The changing magneto-resistance caused by an (anti)parallel alignment with another ferromagnetic layer can be detected via a read line. The magnetic moment of the second layer is pinned through exchange biasing with an adjacent antiferromagnet. B) Orbital magnetic moment per spin, m_L/m_S, for various Co dot sizes N measured with magnetic circular X-ray dichroism below (red symbols) and above (blue symbols) the blocking temperature. The dots were self-assembled on an Au(111) surface by controlling the Co coverage. A scanning tunnelling microscopy image is shown in the inset.*

than in a few picoseconds, i.e. on the time scale of electron-phonon relaxation. This finding is supported by the argument the demagnetization timescales should be comparable with electron-phonon equilibration because the lattice is needed as a 'reservoir' to maintain angular momentum conservation during the de-magnetization (spin flip), but also ultrafast spin dynamics has indeed been predicted theoretically [16]. To resolve the experimental discrepancy it has been argued that the high excitation densities in second harmonics generation "dichroic bleaching" affects the reflectivity of the probe pulse during the first few 100 fs. Such vast conceptual discrepancies show that research on spin dynamics is obviously in its infancy.

The aim of the proposed project is to perform a series of basic pump-probe experiments on the spin dynamics in itinerant and localized magnetic systems, employing 100 fs short X-ray pulses of circular polarization from the XFEL. While current pump-probe experiments in the (near) visible involve transitions between valence bands (with small spin-orbit parameters $\zeta_{s.o.}$ of a few 0.1 eV), the large $\zeta_{s.o.}$ of core levels give rise to a rich multiplet structure of low-spin and high-spin core-hole states, which allows one to tune the photon energy to individual lines such that an electron with a well-defined spin is excited into the 'magnetic' 3d (or 4f) shell. This so-called Fano effect has been the basis of many successful X-ray magnetic dichroism experiments. Starting from simple ferromagnetic Fe and Gd films , we propose to investigate the timescales at which magnetization reversal occurs in itinerant (Fe) and localized (Gd) spin systems. Through comparison of these two prototype cases (Stoner-type versus Heisenberg-type system) we expect to elucidate the role of the valence-band electrons, which either carry the magnetic moment (Fe) or mainly just mediate the coupling between the localized 4f moments (Gd).

It is the unique possibility of an X-ray pump-probe experiment that one can reverse the spin of the optically excited electron, just by a small change of the photon energy from one multiplet line to another. (This is principally not possible for transitions in the visible owing to the much smaller valence-band $\zeta_{s.o.}$ parameters.) Through this 'pumping' of a spin-polarized electron into the 'magnetic' shell, we aim at an experimental separation between postulated optical effects (dichroic bleaching) and true, possibly ultrafast demagnetization processes on the order of 100 fs, well beyond electron-phonon equilibration times. The magnetic state after excitation will be probed via time-resolved X-ray magneto-optical Kerr effect, i.e. by measuring the reflectivity of the circularly polarized probe pulse [22].

For investigations of magnetic materials, the XFEL offers an energy range covering all relevant core levels from the heavier 3d-transition metal $L_{2,3}$ edges ($2p \rightarrow 3d$ excitations) to the lanthanide $M_{4,5}$ edges ($3d \rightarrow 4f$). The measurements on RAM compounds make use of the 100 fs time structure and the coherence of XFEL X-ray pulses. In addition, the XFEL has to be interfaced with an optical femtosecond pump laser. In order not to damage the often delicate nanostructures, it would be necessary to reduce the peak X-ray power and instead increase the number of electron bunches to achieve an average photon flux of about 10^{12} - $10^{13}\,s^{-1}$.

3.3.1.3. Bulk magnetism

The investigation of hyperfine fields in rare earth elements has been an active field for many years. Other methods aside conventional Mössbauer spectroscopy and nuclear forward scattering (NFS) have contributed to the understanding of magnetism in such systems. NFS proved to particularly useful when the brilliance of a synchrotron radiation beam could be used; i.e. in studies of thin films and under high pressure [23].

The XFEL will open new possibilities in this field also. The time structure enables study of the large hyperfine splitting in ordered Dy ($H \approx 600\,T$). This corresponds to a beating of $\approx$ 100 ps in bulk as well as in thin films. Also multilayer systems of Fe and Dy will be an interesting system to study. The high brilliance will for the first time give access to studies of phononic excitations in films or under high pressure for both elements.

Collective magnetic excitations The high brilliance is indispensable for inelastic magnetic studies. Since monochromatization to $\Delta E/E \approx 10^{-7}$ is required for meV energy resolution, the remaining flux does not pose a severe "heat load problem" for the sample. At third-generation sources, phonons can be conveniently measured with meV resolution. Due to the increase in average brilliance by five to six orders of magnitude, the same will be possible for magnetic excitations at the XFEL, in particular at high energy transfers, where excitations are broader and the energy resolution can be relaxed. This is of particular interest for steep, high energy excitations in strongly correlated magnets, which are at the limit or beyond the possibilities of neutron scattering. By means of resonance exchange scattering or nuclear resonant scattering, the magnetic fluctuations of one specific species can be studied. Inelastic tensor scattering (Templeton scattering) will become accessible and will, for example, allow the study of the dynamics of orbital order. Critical dynamics close to the magnetic phase transition can be investigated using the coherence of the XFEL beam. The method will allow the study of the influence of spatial restrictions for all universality classes in combination with the above topic.

Magnetic collective excitations (magnons) have not yet been accessible to X-ray studies due to the very small excitation energy. Using nuclear resonant scattering techniques at the XFEL it will be possible to enable the investigation of inelastic processes with energy transfers of the order 1 μeV. By exploiting the q-dependence of the scattering, the scattering function $S(\overrightarrow{q},\omega)$ can be studied. This would allow the observation of the spin dynamics and the determination of magnon dispersion curves.

3.3.1.4. Relaxation phenomena of magnetic states

Relaxation of magnetic phenomena after short pulse initiation is a new class of experiments not accessible today for the study of magnetism with X-rays. Exploiting the bunch structure of the XFEL, one can apply an external field pulse in the 200 ms between two bunch trains and study the relaxation phenomena in the μs to ms time domain by stroboscopic (cyclic) measurements. With a pulsed magnetic field, the behavior of magnetic materials in fields up to 100 T can be studied, while the present limit for static diffraction measurements is 15 T. In the same way, electric field pulses, temperature pulses, or pressure pulses can be

applied. One example is the investigation of systems having a non-magnetic ground state, but a magnetic excited state, such as singlet ground state systems or organic molecules in a diamagnetic matrix. The molecule Pentazen can be excited into an spin S = 1 state by application of an optical laser pulse. The life time of the excited states ranges between 50 μs and 830 μs, so that the decay of the excited state takes place during one XFEL bunch train. In nanostructured devices, of particular interest for applications in magneto-electronics, time constants for magnetic switching are in the femtosecond regime.

Another investigation of great technical relevance for the development of high-speed magnetic storage devices and spin electronics is the dynamics of magnetization reversal. For example, long-lived (milliseconds) electronic states in Eu compounds can be excited by laser light and their relaxation followed with extreme time resolution using nuclear resonant scattering. This would give simultaneously information on the decay and on the magnetic properties of these states, or the symmetry around the Eu atom. The envisaged time structure of the XFEL source fits perfectly to such experiments, enabling one to synchronize the excitation of the electron shell at the start of one bunch train and monitor the physical properties during the decay. The long distance between bunch trains helps to avoid over-heating of the system. The experimental method proposed here offers the possibility to study magnetic phenomena with an outstanding time resolution, in particular for the rare-earth magnetism (see above). The theory of nuclear resonant scattering in the presence of hyperfine-field switching has already been developed and tested to a great extent [24, 25].

3.3.2. Phase transitions

Phase transitions present interesting possibilities and problems for condensed matter and material science physicists. Fundamental and universal aspects make a deep understanding interesting for all scales of physics from sub-nuclear to astronomic scales [26] where often one particular case is given, but no experimental data are available. The endless variety of condensed matter samples and the enhanced capacities offered by the XFEL, notably the high q-resolution and adjustable coherence, will make possible the study of unsolved fundamental questions and cases, such as the nature of quantum transitions and many others.

More mundane material aspects will be considered in the following, which are nevertheless important for producing self-organized micro- or mesostructured materials. At a phase transition, or more generally at phase separation conditions, a material is particularly susceptible to external influences. Related to this is the fact that most real materials are not in an equilibrium state, but only in a metastable, though perhaps very useful state. A much better understanding of metastability and of nucleation mechanisms for phase growth is seriously missing at present due to a lack of experimental methods which probe the correct space and time regime. Here the XFEL promises to be very important with respect to the possible time resolution of phenomena from the pico- to the millisecond scale also. It further offers possibilities to carry out *in-situ* experiments under extreme conditions, such as high pressure. Problems in the field of phase transitions range from understanding the freezing or glass formation of water, through instrumental goals such as assisting protein folding, to understanding and controlling the growth of nanostructured bulk or surface crystalline materials.

3.3.2.1. Smart materials

As a more detailed example, let us look at the so called smart materials, which are the inorganic representatives for functional materials, with built-in special abilities, not occurring in nature spontaneously. Smart materials constitute a group of materials, usually metals or metallic alloys of two or more metals, which crystallize in the open *bcc* phase at high temperatures and condense into a more closed packed phase (*hcp, fcc,* ω-phase etc.) at low temperatures. The latter phase is textured, and if it is possible to generate one or a few of the symmetry-allowed crystalline variants (domains), it is possible to use the characteristic shape and anisotropy changes in technologically important applications. The materials exhibit 'shape-memory' and are called 'smart' because they can be 'trained' to exhibit a certain property (by repeated forced cycling through a desired operation). What actually happens in the 'training' process is not known in any detail, and further information about it would be highly significant. It is supposed to be related to nucleation and growth of particular variants at defects in the crystal. A further knowledge of spontaneous or fixed nucleation centers is crucial. Typical materials include NiTi or NiAl alloys and brass-like materials as CuZnX alloys (X= Al or Be for example), pure metals as Ti and Zr, and of course Fe.

The martensitic transformation is a first-order transition accompanied by large strain effects [27]. Therefore, the transition (upon cooling) starts at a temperature M_s and ends at a significantly lower temperature M_f (the process exhibits hysteresis effects, and the corresponding temperatures upon heating,called A_s and A_f, are higher). The process can be stopped at any intermediate temperature in a partially developed intermediate state, probably a *self-organized critical* state, stabilized by the induced strain. Ultrasound and calorimetric measurements indicate that the transition in the intermediate phases proceeds with avalanches of domain growth [28], which is quite reproducible, and which can be detected by the energy release, the Barkhausen noise. However, a more detailed understanding is missing.

Here, time-resolved X-ray scattering in the nanosecond range would be highly useful. It is a relatively simple experiment in which the time evolution of Bragg peaks from the textured sample must be followed. A possible accurate measurement of the peak position would in addition give a direct microscopic evaluation of the strain build-up and release. The technical difficulty rests in getting sufficiently fast counters to resolve the time evolution.

One could also see a possible use of the good spatial coherence up to over $100 \times 100\,\mu m^2$ that the XFEL may offer. This allows essentially a perfect Fourier-transformed picture of the investigated volume, or a snap shot of the actual structure. Hence a detailed 'speckle' pattern will result. Although difficult to interpret in detail, it might be useful as a time- and temperature-dependent 'finger print' of the structure. This would for example allow one to see whether the nucleation occurs at the same positions during a memory cycling. Phase coherence is a well known feature in Monte Carlo simulations, and considerable effort is usually made to obtain proper ensemble averages (which average out the speckle peaks). As an example is shown the simulated speckle pattern [29] of the oxygen ordering in $YBa_2Cu_3O_{6+x}$, Fig. 3.3.3. The pattern does not change at low temperatures because the domain pattern, which gives rise to it, changes very slowly. Clearly, the two speckle patterns to the right contain much more information than the simple Bragg peak plus diffuse back-

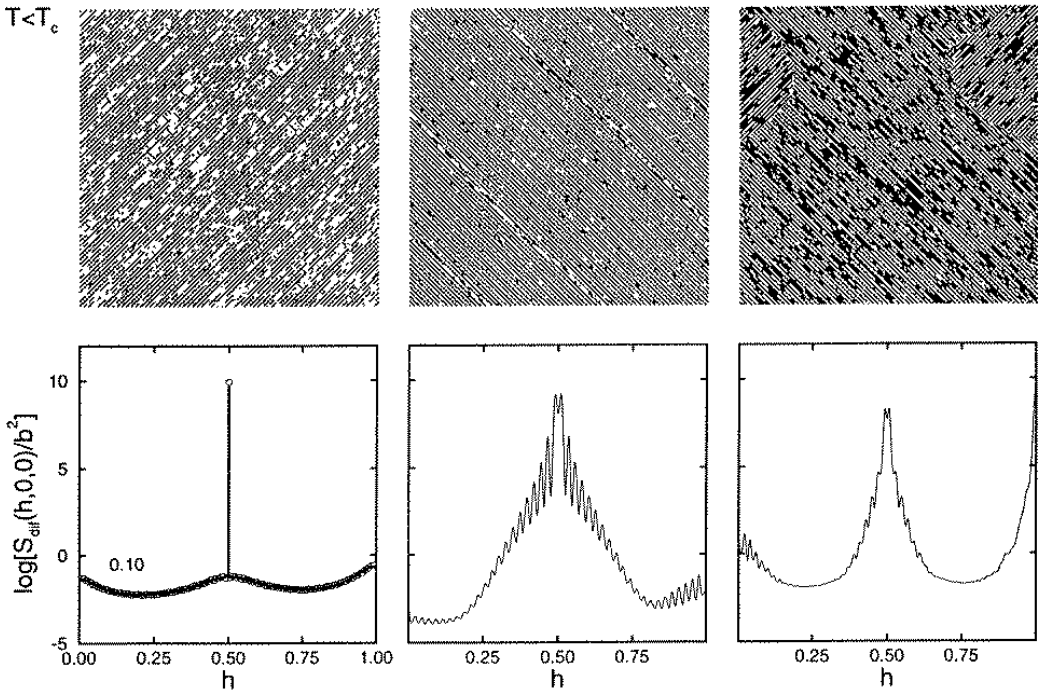

Figure 3.3.3.: *Real space pictures of the simulated oxygen configuration in* $YBa_2Cu_3O_{6+x}$ *below the ordering temperature for oxygen stoichiometries* $x = 0.4$ $x = 0.5$ *and* $x = 0.6$*, from left to right. The effect of domain structures is most clearly seen in the corresponding structure factors at* $x = 0.5$ *and* $x = 0.6$*, showing a pronounced speckle pattern even when averaged over long time at the low temperatures (log[S(***q***)] plotted along the (h,0,0)* **q***-direction in reduced units). The simulated system is 3D (*$256 \times 256 \times 16$*) corresponding to a top plane of a spatial extent of about* $0.1 \times 0.1\ \mu m^2$.

ground to the left. The task will be to utilize such information. Clearly, examples on phase transitions should not be restricted to 'hard' condensed matter. Many current problems exist in the 'soft' matter realm. One could mention polymer mixtures, behavior of surfactants, (poly)electrolytes, suspensions of (charged)colloidal particles, protein folding, etc. The advantage of the XFEL for the study of polymer systems is enormous and is discussed in Sec. 3.5 in this report.

3.3.2.2. Dynamics in the vicinity of phase transitions

Possible applications of the proposed XFEL laboratory for the study of disordered crystals are introduced in this section: Many crystalline materials show deviations from the average perfect structure, and a wide range of defects exist from individual atoms to large clusters and even to microscopic aggregates of a different phase [30, 31]. The defects can be distributed at random, or may show short-range order. Often the physical properties are decisively shaped

by the type and distribution function of the defects. The exact composition of many materials undergoes local fluctuations. These fluctuations may be due to local changes in the chemical composition, extended domains, or even different crystal structures embedded in the matrix of the host crystal. As a consequence of the compositional variation, the local structure will change. The local chemical variations may be gradual or abrupt, in the latter case forming domains. Often, the average structure does not change significantly due to the change in composition. Locally, however, a change can be expected to display a variation of bond lengths, coordination numbers and, most significantly, local defects. A prominent class of materials that may be expected to display this type of behavior are decagonal quasicrystals. Here, a significant change of the diffuse scattering is observed for samples that display chemical differences as little as 1 atom percent. The changes observed include intensity variations of the different diffuse scattering phenomena and even the reversal of satellite vectors [32].

An experiment at an XFEL beam line should utilize the specific properties of the X-ray laser. Thus, the use of a coherent X-ray beam, the time structure and last but not least the primary beam intensity and its relation to sample stability must be discussed. Coherent X-ray diffraction has up to now been used in studies of surfaces and dynamical changes, mostly in amorphous solids [33]-[41]. LeFloc'h et al. [42] and Brauer et al. [43] studied intensity fluctuations in crystalline Fe_3Al near the phase transition. Studies of the local structure by coherent X-ray diffraction should be a very promising experimental field at an XFEL beam line. Fully coherent scattering experiments on disordered materials will allow the study of precursor phenomena near phase transitions and local variations of the disorder. The peak intensity of diffuse scattering is typically four to six orders of magnitude less than the peak intensity of Bragg reflections. The integral intensity of the diffuse scattering in highly disordered materials, however, may be close to that of the Bragg reflections, and the information contained in the diffuse scattering is essential to fully understand the real structure of materials. Presently, large samples and, consequently, large incoherent beams are used to study diffuse scattering. By use of a well focused coherent beam, small sections of the samples can be analyzed. The modifications of the expected "speckle" pattern will yield information on the variation of the local structure.

Systems of particular interest are materials undergoing second-order phase transitions. Here, distinct differences can be found for the high-temperature phase and the low temperature phase for specific atoms of the unit cell. In the case of lead phosphate, $Pb_3(PO_4)_2$, a ferroelastic phase transition occurs at 453 K [44], exhibiting at temperatures above the transition an intermediate regime with excitations between different ferroelastic orientation states inside monoclinic clusters of short-range order. In pure lead phosphate, these excitations are fully dynamical, whereas they can be frozen in diluted systems (e.g. for phosphate arsenate $Pb_3(P_{1-x}As_xO_4)_2$ [45]). The micro-domains are of the order of 50 Å and show different temperature stability depending on the orientation. Three orientations have been found. In the vicinity of the phase transition, the orientations start fluctuating and it would be interesting, and has not yet been accessible to experimental investigation, to see the dynamics of this fluctuation. Such investigation would provide new insight in the dynamical precursor processes leading to phase transition. It is expected that characteristic time scales range from nanoseconds to microseconds. A series of coherent diffraction patterns covering the

full time range will offer an exciting new insight in the time-dependent development of local structures.

These investigations create several experimental requirements which have to be fulfilled. First, the coherence of the beam is of crucial importance, and no elements can be introduced into the photon beam that reduce the nearly perfect degree of transverse coherence from the source. This requirement will put a strong constraint on the focusing or collimating elements inserted to achieve beam spots at the sample in the order of $\approx 1\,\mu$m. As one intends to investigate sample dynamics on variable time scales from picoseconds to milliseconds, it is important to preserve the sample during the exposure and to avoid heating effects. For the lead phosphates, a stability range of typically 100 K can be expected. A possibility to select the primary photon energy is important in order to control for different elements the absorption in the sample and therefore the deposited power. It may be necessary to use in addition to the basic harmonic of the undulator its third harmonic. Suitable means for intensity absorption of the primary beam are also needed. For detection, two-dimensional CCD detectors will be used. As these detectors do not offer enough time resolution, a monitoring of the primary beam is crucial for normalization. The variable filling pattern of the bunch train offers for the experiment the possibility to select a bunch distance according to the investigated time delay. Time delays in the range from 100 ns to 1 ms in steps of 100 ns can be achieved using the structure of the bunch train. For shorter delays, it will be necessary to apply split and delay techniques for the photon beam. Longer time scales from 1 ms to 200 ms will not be easily provided by the proposed TESLA XFEL.

3.3.3. Liquids and disordered systems

The glass transition from a liquid to a glassy state has already been mentioned in the former section on phase transitions. Despite the fact that glass production is a fairly old technique developed empirically over many centuries, the scientific understanding of the glass transition is poor. An open question for example is whether the transition from a glass to a liquid happens via a two-phase intermediate or rather as a homogeneous process. Closely connected to this is the discussion on a diverging length scale (cooperativity length) at the transition. Finally not even the transition temperature itself is defined in a generally accepted manner.

The study of the *dynamics* of undercooled or supercooled liquids will be and is already the key to the understanding of this transition. Inelastic neutron scattering experiments have supplied the bulk of information on which modern theories are based. The XFEL will allow to determine the dynamical structure factor $S(\vec{q},\omega)$ with unprecedented resolution in both variables. In particular using nuclear resonance scattering an extreme energy resolution in the order of few neV can be achieved. Combined with an extraordinary $\vec{q}$ resolution, X-ray spectroscopy with an XFEL will allow to map out $S(\vec{q},\omega)$ over a range that is not accessible with any other technique. In addition, the coherence together with the high spectral brilliance would allow to map the relaxations in an undercooled liquid on a μm length-scale. This will lead to new information on low-energy excitations (slow dynamics).

The study of structural relaxation in disordered systems and diffusion jumps require inelastic scattering at rather high momentum transfer not attainable with present day sources.

With such experiments new information can be obtained about the scaling behavior of relaxations. At the XFEL time domain interferometry (TDI) using nuclear resonant scattering could be utilized as a standard method for the study of dynamics. TDI has the option to extend the q-range of present high resolution inelastic scattering techniques. While neutron spin echo covers the range of low–momentum transfer with similar (neV) energy resolution this technique is limited to $\approx 2\,\text{Å}^{-1}$ in q–space. TDI will be able to go out to $q \approx 12\,\text{Å}^{-1}$.

Inelastic scattering with very small momentum transfer and extremely high momentum resolution is of particular interest for the study of systems that are confined in large structural units. Those rather complex samples are currently used to investigate the question concerning cooperativity effects at the glass transition [46]. Besides that such experiments may help to understand the interaction of the liquid with a surface, important for example for the understanding of friction or catalysts. In particular element specific methods are helpful in this case as they allow to suppress the signal from the matrix.

Another open question is connected to the boson-peak, a low-energy (few meV) excitation found in disordered systems [47]. Extremely high energy resolution and momentum resolution are mandatory here to unambiguously decide whether the excitation exhibits dispersion or not or whether it couples to other excitations. Only under those conditions it is possible to resolve the nature of that particular excitation, i.e. if it is propagating or localized. The same holds true for experiments tackling the problem of phonon damping in disordered systems. Presently the rather poor energy resolution of inelastic X-ray scattering experiments (or neutron experiments at high momentum transfer) prevents accurate line shape analysis.

3.3.4. Materials under extreme conditions

3.3.4.1. High pressure and temperature phases

High pressure investigations, often also connected with high temperatures, are of utmost interest to geosciences and related mineralogy [48] as well as to materials sciences [49]. For the former in particular the understanding of the earth's interior (compare Fig. 3.3.4) is the driving force whereas for the latter field aspects of materials behavior under extreme load such as high pressures or temperatures present the focus of interest.

High pressure studies have received a great deal of attention at the third generation synchrotron sources due to the high brilliance of the beam and the possibility of using diamond anvil cells which explore completely new regimes for X-ray based structure determination in high pressure research. This field will benefit largely from the XFEL as the possibility to focus hard X-rays in the range of 10 to 200 keV down to a beam size of $1\,\mu\text{m}^2$, which enables unprecedented studies of smallest samples in diamond anvil cells, also at highest temperatures by Laser heating (even temperature/pressure profiles in a pressurized sample can be studied). The "classical" high-pressure X-ray diffraction studies, using the energy dispersive [50] or the angle dispersive [51] mode, have reached with diamond anvil cells, at maximum and not simultaneously, up to 4 Mbar and about 3000 K and 5000 K with static and pulsed Laser heating, respectively. New methods have developed rapidly at 3rd generation SR sources. For instance, inelastic X-ray scattering has been applied for sound velocity measurements up to 1.1 Mbar [52]. By X-ray emission spectroscopy (analyzing the K_β fluo-

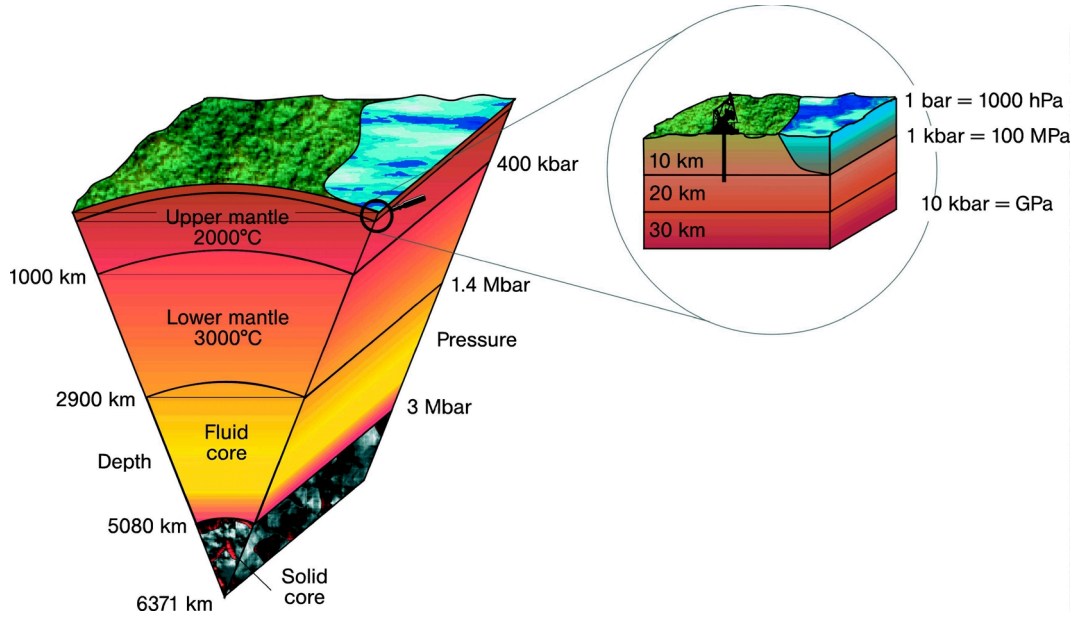

Figure 3.3.4.: *Schematic of the earths crust and indication of several temperatures and pressure estimates. For a better understanding of the processes in the earth interior one has to determine the equation-of state by experiments, because no direct access is possible. This means one needs to measure the p-V-T phase diagram for all relevant materials. Up to now only the outer part (≈ 2900 km below surface) is understood in sufficient detail.*

rescence of iron), the depression of magnetic moments has been studied in FeO at pressures up to 1.4 Mbar [53]. Wide new applications are presently developed with nuclear resonant scattering. Using elastic nuclear forward scattering, magnetism and valence transition can be studied in the Mbar range [54, 55]. Nuclear inelastic scattering provides a unique tool to study phonon densities-of-states (DOS) and vibrational excitation on minute samples under high pressure [56]. The phonon-DOS in the hcp phase of iron (e-Fe) was studied up to 1.53 Mbar, the derived thermodynamic and elastic parameters (like the sound velocities) are of utmost geophysical interest [57].

At the XFEL all established and new methods would profit from the increased flux and brilliance of the source. More importantly, however, is the use of the time structure of the XFEL for new types of high-pressure studies. For instance to study the impact of a shock-wave, which has the same time scale as an XFEL bunch train, on various properties of the compressed sample. These experiment are described in the next section. Here we want to mention that static high-pressure experiments can be combined with pulsed Laser population of excited electronic levels (e.g. 4f-multiplets) with drastic modifications of the electronic and magnetic properties. With pulsed Laser heating, which allows for higher temperatures than with continuous heating, one can study at multi Mbar pressures samples at temperatures exceeding the present upper limits around 3000 K, so arriving at the conditions of the Earth's core and approaching that of larger planets.

Shock-wave high pressure states In shock waves, produced by implosive techniques [58] or by intense Laser pulses [59], extreme high pressures (up to 20 Mbar) and, simultaneously, high temperatures (up to 10000 K) may be reached within a very short time window. The properties of the compressed matter are derived from the shock-wave velocity u_s and the particle velocity u_p, which are, up to now, mostly monitored by optical methods (e.g. streak cameras). From the measured velocities, using conservation laws for mass, momentum and energy, one obtains the volume V, the pressure p and the internal energy E in the compressed material [58], the derived p-V relation represent the Hugoniot curve for the material. Evaluation of isothermal p-V data from shock wave measurements require additional information about the equation of state of the material. It is not surprising, because of many assumptions involved in the evaluation of the shock-wave data, that thermodynamic and elastic properties derived from shock-wave and static high-pressure experiments often differ. For iron at conditions of the Earth's core, there are large differences in the derived sound velocities (which deliver direct information from the Earth core) and the melting temperature at the solid-liquid boundary [59]. Also recent ab-initio calculations differ from each other and from the experimental results [60]. Conventional shock-wave studies provide little information on structural phase transitions. Recently, different groups have used laser generated shock waves (1 ns pulse) and recorded diffraction patterns from a compressed sample (Si crystal and LiF powder) with a 100 ps pulse of X-rays. The results indicate that time-resolved diffraction measurements of the lattice parameters can be made on Laser shock-waves in crystals. This is promising for future combined optical and diffraction studies that may allow not only "one pulse", but a series of pulses within the bunch sequence of the XFEL, from which detailed information on the p-V-T variation within the shock-wave can be derived. It is obvious that with this technique pressure and/or temperature induced phase transitions, including their kinetics, can be studied in an unique way.

Other methods for high-pressure studies are applicable in similar ways. For instance, the suppression of a magnetic moment as function of p,T can be followed using K_β-fluorescence or by nuclear scattering. Inelastic nuclear scattering may provide, as demonstrated for iron [56, 57], a complete picture of the dynamic properties, including sound velocities and Debye temperatures, from which melting curves could be determined independently from theoretical models.

Shock-wave generation It should also be noted that the broad band X-ray beam can be directly used to apply a shock-wave. As already shown in Sec. 3.2 on plasma physics the X-ray beam can produce enormous pressures of up to Gbar (10^{14} Pa). This transient state will have only a very short life-time. Investigations may be carried out using pulse split-and-delay techniques.

3.3.5. Excitations

3.3.5.1. Electron relaxation processes

The ultimate goal and experimental challenge for our understanding of electronic transitions leading to molecular reactions or phase transitions is the time dependent measurement of

the electronic wavefunction forming the bonding configuration. These processes occur on the femtosecond to sub-femtosecond timescale. The XFEL offers a unique possibility to perform such experiments which are at the frontier of condensed matter studies as well as of molecular science in biology, chemistry and physics.

Optical spectroscopy with ultrashort laser pulses has already given deep insights into the nature of chemical reactions. Its limitation is however the long wavelength at optical frequencies which does not permit any spatial resolution of the molecules that are probed. Ultrashort X-ray pulses offer a possibility to achieve spatial resolution within chemical bonds and to obtain information on changes of the electron density at the sites of specific elements by X-ray spectroscopic methods. Whereas the reorganization of the nuclei happens at timescales from few 10 fs to several 100 ps or longer, the fundamental processes of electron charge redistribution leading to the chemical reaction occur in the sub-femtosecond regime. Here the atomic time unit is ~ 0.024 fs [61] which derives from the circulation frequency of the electron in the hydrogen model. This is considerably less than optical oscillation periods but should be attainable with X-rays.

X-ray diffractive and spectroscopic studies of changes induced by optical excitations, especially if used together, provide insights into the electron dynamics, relaxation, multiparticle effects, etc. which cannot be obtained with present day techniques: X-ray diffraction gives spatial resolution on the atomic scale and X-ray spectroscopy is element specific and provides a reference energy level which is missing in optical spectroscopy.

Lattice dynamics and melting Optical excitation of a crystal with ultrashort laser pulses produces the phenomenon of nonthermal melting: The electrons in the bands (or chemical bonds, depending on the point of view) heat up while the nuclear motion still shows a velocity distribution that reflects the original temperature of the sample. However, the nuclei become free to move because of massive breakup of chemical bonds. A statistical and isotropic velocity distribution of the cores leads to a progressive reduction of the structure factor of an X-ray reflex within a few picoseconds as is indicated schematically in Fig. 3.3.5. Any anisotropies in the structure factor decay will thus directly reflect an anisotropic velocity distribution of the cores due to the phonon dispersion in thermal equilibrium, or due to coherent phonon excitation by another short laser pulse.

These processes are presently subject of intense study [62], using X-rays from a plasma that is generated by the same laser pulse that triggers the changes in the sample. Such a plasma based X-ray source has the brilliance of a very small X-ray tube and is not well matched to diffractive techniques. Conventional ring-based X-ray sources, as used in the study of coherent phonon excitation [63] by intense laser pulses, have a much larger time-integrated brilliance but the number of photons provided within a few femtoseconds is also rather low. The best X-ray source for these studies would be an XFEL, providing highly brilliant ultrashort pulses.

Electron dynamics and relaxation in crystals Whereas so far, diffractive studies of optical excitations can be based only on the changes in the structure factor due to motion of the atom cores, the XFEL would permit to study the changes in band occupancy which occur within few femtoseconds after the optical pulse. These changes have a much weaker

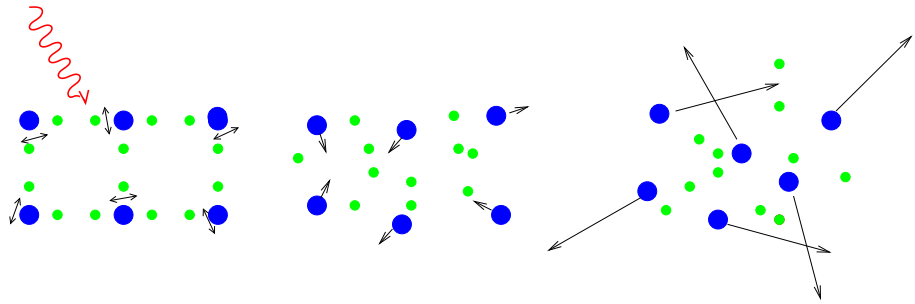

Figure 3.3.5.: *Three stages of nonthermal melting: Left: Atoms in a crystal oscillate around their equilibrium positions with a thermal energy given by room temperature as an intense laser pulse hits the crystal, middle: The chemical bonds are broken and the electrons have high velocities, the atom cores still have low velocities but are beginning to move away from their rest positions, right: Many picoseconds later some energy has been transferred from the electrons to the cores.*

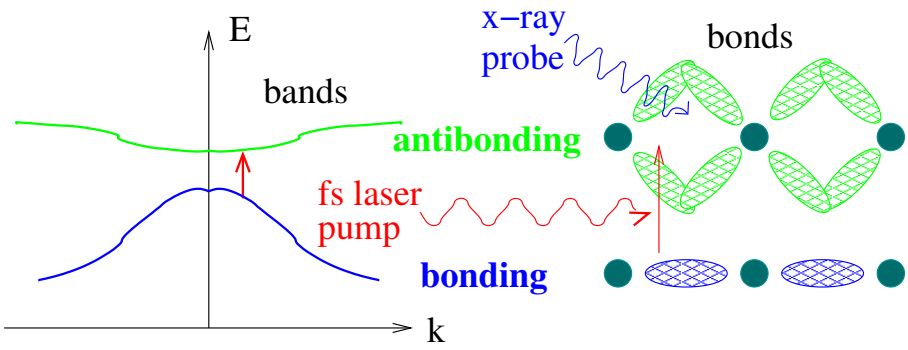

Figure 3.3.6.: *Change of the structure factor of X-ray scattering by electronic excitation from the valence to the conduction band (left), i.e. from bonding to antibonding orbitals (right). Because no movement of the atom cores is involved, the change in structure factor occurs within femtoseconds.*

effect on the structure factor, even more so if the excitation stays below the melting limit, and are not visible with the present low-brilliance ultrashort X-ray sources (see schematic in Fig. 3.3.6) .

It has been demonstrated in various recent experiments that femtosecond time-resolved photoelectron spectroscopy is a valuable technique for the study of dynamical processes in e.g. molecules [64]–[67]. Performing such experiments with a combination of visible pump/X-ray probe pulse offers several advantages over the use of visible laser pulses only.

Investigations of chemical shifts Femtosecond pump excitation in the visible regime results in electronic excitation of molecules. Due to the broad spectral width of the ultrashort pulses, nuclear wave packets are created in excited electronic states and thus the nuclei experience new intramolecular interactions. This, in turn, induces geometrical changes which are

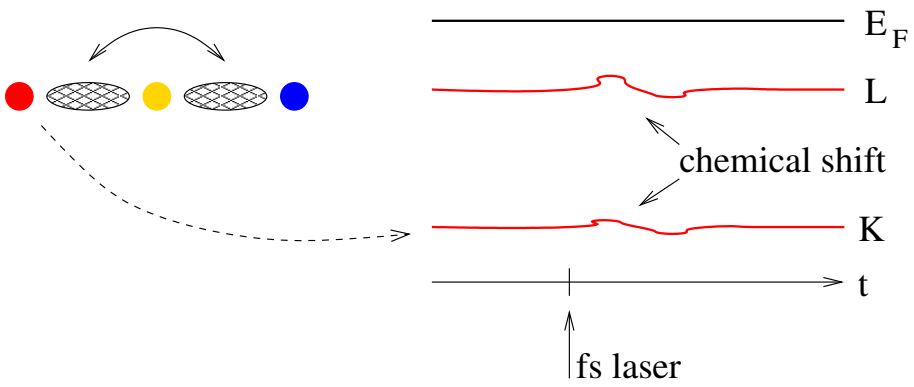

Figure 3.3.7.: *Schematic representation of the excitation of wavepackets in chemical bonds of a molecule, leading to time-dependent chemical shifts at element specific sites. These can be probed by spectroscopic means with sufficiently short pulses (a few fs) of X-rays.*

connected to internal vibrational motion or chemical reactions [68, 69]. Such time resolved experiments probe the energy difference between the intermediate and final electronic state [70] of the system under consideration and thus are not sensitive to the dynamics of particular atoms. Much more detailed information can be obtained by use of an X-ray probe and monitoring the time-dependent chemical shifts in photoelectron or photoabsorption spectroscopy. This might even be carried further to obtain information on the electron dynamics immediately following the pump excitation, and before any nuclear motion sets in: A coherent superposition of excited states leads to oscillating wavepackets in chemical bonds and correspondingly to an oscillating electron density near the atom cores. This should result in a chemical shift in X-ray spectroscopy (XAFS, Auger, photoemission, etc., see Fig. 3.3.7) just as much as that due to nuclear motion within a molecule. Information can thus be obtained on the electron dynamics and relaxation after an optical excitation at element specific sites in a molecule or crystal.

Furthermore, X-ray spectroscopy provides a reference energy level. Whereas optical absorption spectroscopy alone can probe only the combined density of initial and final states, a combination of optical photons and X-rays can deconvolute this combination because it provides the initial state of the X-ray process as a reference.

Dynamics of core-excited states Femtosecond pump-probe experiments in the visible study molecular dynamics in valence-excited electronic states. Completely different dynamics are to be expected if core-excited states [71] are prepared by coherent X-ray excitation. As an example, molecular Auger processes may be induced which take place on various time scales. A particularly interesting situation is encountered if the characteristic time constant for the Auger decay is comparable to the time-scale of the vibrational motion. In this case a strong coupling of the electronic and nuclear degrees of freedom is to be expected.

Up to now, there is no time-resolved spectroscopic information about the dynamics of nuclear and electronic wave packets in core-excited states, the reason for this is obviously

lack of brilliance. Coherent X-ray-visible probe spectroscopy is a unique tool for investigating such elementary processes. In a possible experiment, the optical probe excitation could produce photoelectrons to be detected as a function of their kinetic energy and pump/probe delay, see above.

Visible Pump, X-ray Probe: Separation from Parasitic Processes A decisive advantage of visible pump/X-ray probe over visible pump and probe experiments is that due to the large difference in photon energies, the pump-probe processes under consideration can be separated easily from what might be called parasitic processes which are based on interaction with several photons from the pump or from the probe beam only. A typical experiment [72] would be to couple two electronic states $|1\rangle, |2\rangle$ resonantly by a femtosecond pump-field at a frequency ν_1 in the visible range. This interaction prepares nuclear wave packets in each state. The dynamics is then probed by time-delayed ionization and detection of the photoelectron spectrum as a function of delay time. In order to detect the ground state motion in $|1\rangle$, a resonant transition via $|2\rangle$ is necessary to achieve sufficient electron yields (disregarding super intense field ionization). In the simplified picture of Fig. 3.3.8 this fixes the probe frequency ν_2 to be equal or close to ν_1. However, this means that the photoelectron spectrum obtained by two-photon ionization from $|1\rangle$ falls into the same energy range as the spectrum obtained by one-photon ionization from state $|2\rangle$. As a consequence the dynamics in both states cannot be separated. Obviously, as is illustrated in Fig. 3.3.8, the use of a probe pulse at shorter wavelength solves the problem since now the spectra fall in different energy regions, i.e. are well separated. A theoretical treatment can be found in Ref. [73].

3.3.5.2. Multiphoton excitations in condensed matter

Multiphoton absorption is a commonly investigated phenomenon in outer shells using low photon energies, especially in the optical region and usually using conventional laser sources. In contrast, multiphoton absorption of inner shells is a quite unexplored new area of X-ray physics (see also Sec. 3.1). The XFEL will open the possibility of examining hitherto inaccessible excited atomic states, and allow sensitive tests of core-hole screening theories, important in wide-band materials such as oxide insulators and superconductors.

Two effects make multiphoton absorption very difficult to observe especially for the most fundamental 1s-shell. First, absorption cross-sections are typically by some four to six orders of magnitude lower with corresponding reduction in absorption probability of the first photon. Second, lifetimes of the excited states are shorter, making the absorption of a second photon by the excited atom less probable. The theory of the simplest multiphoton process, the two-photon absorption from the ground state A to a resonant state B, gives for the transition rate [74]

$$\tau = (\frac{r_0^2}{\omega^2})|m^{-1}\sum_I \frac{(\vec{p}\hat{\varepsilon})_{BI}(\vec{p}\hat{\varepsilon})_{IA}}{E_I - E_A - \hbar\omega}|^2 \delta(E_B - E_A - 2\hbar\omega) j_{ph}^2 \ ,$$

where r_0 is the electron radius, m the electron mass, ω the photon frequency and j_{ph} the beam number density. Summation over all intermediate states I makes the calculation unwieldy even for the simplest atoms, and has caused substantial difficulties in the theory of optical

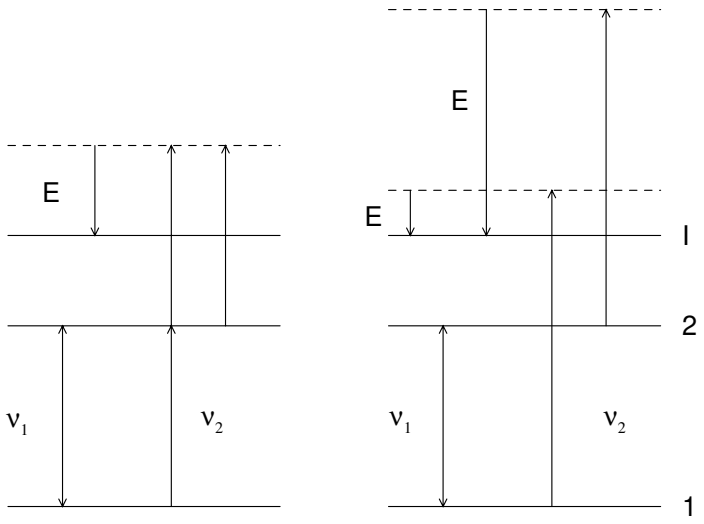

Figure 3.3.8.: *Schematic ionization scheme for pump–probe ionization in the visible wavelength regime (left part) and for visible pump/X-ray probe transition (right part). In both case the pump pulse at frequency ν_1 couples the electronic states $|1\rangle$ and $|2\rangle$ coherently. If the probe frequency ν_2 is similar to ν_1, photoelectrons are created with average energy E in the ionic state $|I\rangle$ via a two-photon ionization process from $|1\rangle$ and via a one-photon ionization process from $|2\rangle$. If the probe frequency is chosen much higher, then the two processes can be separated since the photoelectrons have very different kinetic energies.*

multiphoton absorption [75]. For simplicity, the consecutive photoabsorption of two photons can be considered as a limiting case where the intermediate state is in the same energy shell and the energy denominator reduces to the lifetime width.

As an example, two-photon excitation of the K-shell of copper is estimated. Assuming $5 \cdot 10^{12}$ photons/bunch focused into a spot of $1\,\mu m$ diameter $\approx$ 15 photons/atom will be absorbed. The short K-shell lifetime (≈ 0.2 fs) thus leads to ≈ 0.04 photons absorbed per atom per lifetime, which is a weak effect. A much higher effect is obtained for argon (0.36 photons/atom/lifetime), with factors of ≈ 3 gained in both the cross-section and the lifetime. Evidently, this hypothetical case represents the threshold of observable two-photon absorption, but the effect would be significant to allow investigation of some of the important phenomena. The expected non uniformity in the radiation within a bunch should increase the multiphoton absorption rate. Also, if extreme focusing can be used (≈ 100 nm), the number of absorbed photons per atom per lifetime can be drastically increased.

Element specific X-ray absorption spectroscopy by itself is a versatile and widely used method for the characterization of materials. The position, the shape and the polarization dependence of X-ray absorption edges contain important information about the electronic structure, the chemical composition as well as about the magnetic properties of samples. The cross section for the absorption process is usually governed by a dipole matrix element

between initial and final state and by the density of empty states available for the transition. Since the dipole selection rules for optical transitions require a change of angular momentum $\Delta l = \pm 1$ between initial and final states the investigation of empty d-states is usually only possible through the excitation of p-levels. Since these empty d-states close to the Fermi level turn out to be very important for the properties of many materials this is a severe restriction.

However, for two-photon photoabsorption the respective selection rules are $\Delta l = 0, \pm 2$ which would for example allow the investigation of s-d or d-d transitions. Hence, if two-photon photoabsorption experiments which are quite common for conventional laser sources would become possible in the X-ray regime through the use of FEL radiation this would greatly increase the flexibility of X-ray absorption spectroscopy. The aim of this project is to investigate the possibility of correlated two photon photoabsorption to obtain unique spectroscopic information on the properties of selected materials. Possible candidates for first experiments could be high Z-elements like tungsten or platinum.

For these investigations high photon flux together with very low background is needed. The detection of the two photon photoabsorption process shall be performed through the detection of secondary decay processes i.e Auger electrons emitted in the decay of the core hole created by the photoabsorption processes. Possible spin analysis of the emitted electrons would in addition allow the investigation of magnetic properties of materials.

3.3.5.3. Collective excitations

The development of advanced new materials and their engineering on nanoscopic length scales will be an important key technology in the new millennium. The technological properties of these materials are determined not only by their structure but also by their electronic and vibrational dynamics. Examples of technological relevance are friction accompanied by phonon excitation, heat transfer in microelectronic devices, and magneto-elastic effects in magnetic microstructures or electronic excitations in band-engineered semiconductors. The more that dynamical properties are expected to govern the function and performance of future devices, the more important are efficient methods for their characterization.

Synchrotron radiation has become an ideal tool in this field in recent years. The high brilliance of third-generation synchrotron radiation sources initiated enormous progress in established X-ray methods and enabled the development of completely new types of spectroscopies for the study of condensed matter dynamics.

Electronic and ionic excitations can be studied by the observation of the electron distributions and their fluctuations in space and time. In addition, it is also possible to study the dynamics of the nuclei directly by inelastic nuclear absorption spectroscopy [76]–[78].

The strengths of these methods are the access to very small amounts of materials and the possibility of working on a mesoscopic length scale. This allows new insight into the dynamics of ordered and disordered systems. New aspects in systems with reduced dimensionality, confined geometry or under high pressure can be studied [55, 56].

At present, few dedicated beamlines are available for inelastic X-ray scattering spectroscopy studies at synchrotron radiation facilities. However, these techniques will improve in quality when radiation from the XFEL becomes available.

The measured quantity in inelastic X-ray scattering spectroscopy is the dynamic structure

factor $S(\vec{q},\omega)$ of the scattering electron system, the Fourier transform in space and time of the time-dependent expectation value of the density-density correlation function. Therefore this technique offers the most direct experimental access to the correlation in a Fermi liquid, a problem that, even for simple metals, has not been solved theoretically with sufficient accuracy. Because of the low cross section of inelastic scattering, together with the problem of high photon absorption cross section when going to higher-Z elements, the application of inelastic scattering with radiation from third-generation synchrotron radiation sources to the study of electron correlation was limited to elements with Z below 20. Thus, the study of most of the interesting new materials, such as high-T_c superconductors or heavy fermion systems, by means of inelastic X-ray scattering was not possible, in spite of the fact that electron correlation plays the crucial role for many physical properties of these materials.

One can easily predict that the flux of XFEL radiation, useful for inelastic X-ray scattering investigations, will be two orders of magnitude larger than that for synchrotron radiation sources of the third generation. This will shift the application of inelastic X-ray scattering in investigations of electron correlation to the end of the periodic table. These experiments will be a real step into a new quality, rather than a quantitative step in the sense of *faster, higher accuracy* etc. Moreover, the high collimation of the XFEL radiation makes feasible coherent inelastic scattering, where the quantum interferences of excitation amplitudes from two coherently coupled plane waves deliver information about the full spatial distribution of the correlation function without any restriction with respect to the atomic number Z.

For the studies of ionic dynamics with inelastic scattering, the use of radiation from the XFEL will allow the limit of the energy resolution expected for crystal optics in the range of 0.3 meV to be reached. In addition, the improved flux will allow smaller solid angles for the detection of the scattered photons, thus improving the spatial resolution drastically. Improved resolution curves will be obtained by multiple reflections at the analyzer crystals. This will be of enormous advantage in the studies of the dynamics of disordered systems like liquids or glasses, where it is important to measure at small momentum transfers and low energy transfers to gain further insights into the dynamics within the mesoscopic regime. The dynamics of such systems including high-Z elements will easily be studied under extreme conditions as high pressure and/or high temperature, too.

Due to the gain in photon flux at the XFEL, the inelastic scattering technique can also be applied in grazing incidence geometry. This will lead to depth sensitivity and, thus, to the study of the surface influence on the bulk phonon dynamics, such as soft modes for instance, interesting in the case of invar alloys. The already very successful technique of nuclear resonant absorption for the determination of partial density of the vibrational states will also gain by the improved energy resolution possible at the XFEL source. This method is an ideal tool to study the influence of reduced dimensionality or confined geometry on the vibrational spectrum to get more insight into the unusual mechanical properties of such systems. Phonons are influenced in their propagation in nano-sized structures. Topological disorder caused by impurities or rough boundaries leads to a reduced lifetime compared to perfect crystals. For the studies of thin films, interference effects in grazing incidence geometry can be used to enhance the intensity of inelastic nuclear absorption significantly.

Currently there is no X-ray spectroscopic technique available that covers the range from a few μeV to a few meV with μeV resolution. On the other hand, vibrational excitations

in this energy range have recently attracted considerable attention. For instance, vibrational spectra of disordered solids exhibit a universal feature around 4 meV, the so-called boson peak, that is presently not fully understood [47]. Further examples are magnons, two-level systems, phasons in quasicrystals, rotational excitations in liquids, soft phonons, etc. While these excitations have been studied by neutron scattering in the past, the use of X-rays opens conceptually new possibilities :

- Due to the high brilliance of the synchrotron radiation from an XFEL, regions of phase space become accessible that cannot be reached by other methods. Due to the high angular resolution of crystal optics, the range of very small momentum transfers can be studied with extremely high momentum resolution. This range is of particular interest for the study of dynamics in disordered systems with low-energy excitations that are confined in large structural units.

- While these advantages can already be exploited to some extent at third-generation facilities, the XFEL will push this field into new areas of research : The momentum resolution can be expected to be an order of magnitude better than allowed by existing sources, and the average flux will be 2 – 3 orders of magnitude larger. This pushes the sensitivity limit down by about the same order of magnitude so that dynamical properties of very dilute systems can be studied.

Spin excitation in Si–Ge heterostructures Modern and future semiconductor devices will be engineered by tailoring monolayers and two-dimensional heterostructures. Si-Ge heterostructures are for example presently used in high-frequency wireless communication transistors and other high-speed applications. The most ambitious projects involving Si-Ge heterostructures, however, are devices for quantum computation. In many present solid-state approaches to quantum computers, it is proposed to generate the basic two-bit quantum gate by a tunable Heisenberg exchange interaction between different spins (see e.g. [79] and references therein). Besides quantum dots and donor-atom nuclear spins, both electron spins and nuclear spins in $Si - Ge$ heterostructures are being considered for that purpose. Electron-spin-resonance transistors based on Si-Ge heterostructures have recently been proposed for quantum computing [80]. In these devices a stack of epitaxial layers of different compositions $\mathrm{Si}_{1-x}\mathrm{Ge}_x$ is essential both for tuning the spin-resonance frequency (due to different g-factors in Si and Ge) and for band-structure engineering in order to control the extension and overlap of the wave-functions for the exchange interaction. Another recent proposal aims at computation via nuclear spins incorporated in $\mathrm{Si/Si}_{1-x}\mathrm{Ge}_x$ heterojunctions [81]. Here the two-dimensional heterojunctions operated in the quantum Hall effect regime are essential for detection and control of the nuclear spins via their hyperfine interaction with the electron spins. Since Si and Ge have only one isotope each with non-zero spin, the variation of the isotopic composition will permit the engineering of heterostructures with tailored concentrations of nuclear spins.

In such systems the observation and monitoring of hyperfine interactions and phononic excitations by means of nuclear resonant scattering on the Mössbauer isotope ^{73}Ge, $E_\gamma = 13.3$ keV, which will be feasible at the XFEL, seems to be a fascinating possibility. It will

become possible to investigate extremely thin layers or quantities of Ge in these devices and the ^{73}Ge Mössbauer isotope can be employed as a high-resolution local probe to study electric field gradients and magnetic fields in semiconductor devices containing Ge. Three types of experiments can be envisaged.

- nuclear forward scattering which gives the most detailed information on hyperfine fields but will face low count rates,
- incoherent elastic nuclear scattering, which will be a high count rate experiment, giving access to hyperfine splitting in the excited state
- inelastic scattering yielding the partial phonon density of states of the Ge probe [82].

Bibliography

[1] See e.g. *Technologieanalyse Magnetismus Vol. 2: XMR-Technologien*, VDI Technologiezentrum

[2] S.W. Lovesey and S.P. Collins, *X-ray Scattering and Absorption by Magnetic Materials*, Oxford University Press, Oxford (1996).

[3] D. Gibbs, D.E. Moncton, K.L. D'Amico, J. Bohr, B.H. Grier, Phys. Rev. Lett. **55**, 234 (1985).

[4] V. Fernandez, C. Vettier, F. de Bergevin, C. Giles, W. Neubeck, Phys. Rev. B**57**, 7870 (1998).

[5] J. Strempfer et al., Eur. Phys. J. B**14**, 63 (2000).

[6] P. Fischer et al., J. Synchrotron Rad. **6**, 688 (1999).

[7] D. Hupfeld et al., Europhys. Lett. **49**, 92 (2000).

[8] G.M. Watson et al., Phys. Rev. Lett. **77**, 751 (1996).

[9] S. Ferrer et al., Phys. Rev. Lett. **77**, 747 (1996).

[10] F. Yakhou et al., ESRF Newsletter **32**, 12 (1999).

[11] Th. Weber et al., Nature **405**, 658 (2000).

[12] M. Tolan, *X-Ray Scattering from Soft-Matter Thin Films*, Springer Tracts in Modern Physics **148**, Berlin (1999).

[13] M.M. Abd-Elmeguid, Hyperfine Inter. **113**, 11 (1997); D.D. Koelling, B.D. Dunlap, G.W. Crabtree, Phys. Rev. B**31**, 4966 (1984).

[14] D. Weller et al., Phys. Rev. Lett. **75**, 3752 (1995).

[15] H.A. Dürr et al., Phys. Rev. B**59**, R701 (1999).

[16] G.P. Zhang and W. Hübner, J. Appl. Phys. **85**, 5657 (1999).

[17] H. Regensburger, R. Vollmer, J. Kirschner, Phys. Rev. B**62**, 14716 (2000) and references therein.

[18] T. Eimüller et al., J. Appl. Phys. **87**, 6478 (2000).

[19] G. Schönhense, J. Phys. C**11**, 9517 (1999).

[20] J. Hohlfeld et al., Phys. Rev. Lett. **78**, 4861 (1997).

[21] B. Koopmans, M. van Kampen, J.T. Kohlhepp, W.J.M. de Jonge, Phys. Rev. Lett. **85**, 844 (2000).

[22] K. Starke et al., submitted to Phys. Rev. Lett.

[23] R. Lübbers, G. Wortmann, H.F. Grünsteudel, Hyperfine Inter. **123/124**, 529 (1999).

[24] Yu.V. Shvyd'ko et al., Phys. Rev. Lett. **77**, 3232 (1996).

[25] Yu.V. Shvyd'ko, Phys.Rev. B**59**, 9132 (1999).

[26] H.E. Stanley, Rev. Mod. Phys. **71**, S358 (1999); R.E. Slusher, *ibid*, S471; C. Schmidhuber, Am. J. of Phys. **65**, 1042 (1997).

[27] See e.g. *Phase Transitions, Material Science and Technology Vol. 5*, P. Hansen (ed.), VCH, Weinheim (1991); *European Symposium on Martensitic Transformation and Shape Memory Properties*, G. Guénin /ed.), J. de Phys. Colloque C**4**, Paris (1991); *IIIrd European Symposium on Martensitic Transformations*, A. Planes, J. Ortín, Ll. Mañosa (eds.), J. de Phys. Colloque C**2**, Paris (1995).

[28] E. Vives et al., Phys. Rev. Lett. **72**, 1694 (1994).

[29] T. Fiig, N.H. Andersen, P.-A. Lindgård, J. Berlin, O.G. Mouritsen, Phys. Rev. B**54**, 556 (1996).

[30] T.R. Welberry and B.D. Butler, Chem. Rev. **95**, 2369 (1995).

[31] F. Frey, Z. Krist. **212**, 257 (1997).

[32] K. Hradil, E. Weidner, R.B. Neder, F. Frey, B. Grushko, Phil. Mag. A **79**, 1963 (1999).

[33] S.B. Dierker, R. Pindak, R.M. Fleming, I.K. Robinson, L. Berman, Phys. Rev. Lett. **75**, 449 (1995).

[34] I.K. Robinson et al., Phys. Rev. B**52**, 9917 (1995).

[35] I.A. Vartanyants, J.A. Pitney, J.L. Libbert, I.K. Robinson, Phys. Rev. B**55**, 13193 (1997).

[36] A. Malik et al., Phys. Rev. Lett. **81**, 5832 (1999).

[37] A.C. Price et al., Phys. Rev. Lett. **82**, 755 (1999).

[38] I.K. Robinson et al., Phys. Rev. B**60**, 9965 (1999).

[39] T. Thurn-Albrecht et al., Phys. Rev. E**59**, 642 (1999).

[40] G. Grübel, D.L. Abernathy, D.O. Riese, W.L. Vos, G.H. Wegdam, J. Appl. Cryst. **33**, 424 (2000).

[41] A.M. Lindenberg et al., Phys. Rev. Lett. **84**, 111 (2000).

[42] D. Le Floc'h et al., Phys. Rev. Lett. **81**, 2272 (1998).

[43] S. Brauer et al., Phys. Rev. Lett. **74**, 2010 (1995).

[44] U. Bismayer, R.W. Röwer, B. Wruck, Phase Transitions **55**, 169 (1995).

[45] U. Bismayer et al., Mineral. Mag. **64**, 233 (2000).

[46] B. Frich, R. Zorn, H. Büttner (ed.), *Proceedings of the Int. Workshop on Dynamics in Confinement*, J. Phys. IV **10** (2000).

[47] W. Schirmacher, G. Diezemann, C. Ganter, Phys. Rev. Lett. **81**, 136 (1998).

[48] *Ultrahigh-Pressure Mineralogy: Physics and Chemistry of the Earth's Deep Interior*, R.J. Hemley (ed.), Reviews in Mineralogy, Vol. 37, (1998).

[49] *Science and Technology of High Pressure*, Proc. AIRAPT-17, Hawaii (1999), M.H. Manghnani, W.J. Nellis, M.F. Nicol (eds.), Universities Press, Hyderabad, (2000) Vol. 1-2.

[50] H.-R. Wenk et al., Nature **405**, 1044 (2000).

[51] L.S. Dubrovinsky et al., Phys. Rev. Lett. **84**, 1720 (2000); see also ESRF Highlights 1999, p.73; U. Schwarz et al., Phys. Rev. Lett. **83**, 4281 (1999); M. Hanfland, K. Syassen, N.E. Christensen, D.L. Novikov, Nature **408**, 174 (2000).

[52] G. Fiquet, J. Badro, F. Guyot, H. Requardt, M. Krisch, Science **201**, 468 (2001)

[53] J. Badro et al., Phys. Rev. Lett. **83**, 4101 (1999); J.-P. Rueff et al., Phys. Rev. Lett. **82**, 3284 (1999).

[54] G. Wortmann, *Study of Magnetism in the Megabar Range by Nuclear Resonance Scattering of Synchrotron Radiation*, Ref.[49], p.52-57.

[55] R. Lübbers, G. Wortmann, H.F. Grünsteudel, *High-Pressure Studies with Nuclear Scattering of Synchrotron Radiation*, in *Nuclear Resonant Scattering of Synchrotron Radiation: Principles and Applications*, E. Gerdau, H. de Waard (eds.), Baltzer Science Publ. (1999), p. 529 ff. and Hyperfine Interactions **123/124**, 529 (1999).

[56] R. Lübbers, H.F. Grünsteudel, A.I. Chumakov, G. Wortmann, Science **287**, 1250 (2000).

[57] H.K. Mao et al., Science (in print).

[58] W.L. Nellis, Scientific American (May 2000, p. 84)

[59] L. Stixrude and J.M. Brown, Ref. [48], p. 261.

[60] D. Alfe, M.J. Gillan, G.D. Price, Nature **401**, 462 (1999); A. Laio et al., Science **287**, 1027 (2000); see also: S. Scandolo, G. Chioretti, E. Tosatti, Physics World **13**, 31 (2000).

[61] T. Brabec and F. Krausz, Rev. Mod. Phys. **72**, 545 (2000), p. 584.

[62] K. Sokolowski-Tinten, D. von der Linde, Phys. Rev. B**61**, 2643 (2000).

[63] A.M. Lindenberg et al., Phys. Rev. Lett. **84**, 111 (2000).

[64] J.A. Davies, J.E. LeClaire, R.E. Continetti, C.C. Hayden, J. Chem. Phys. **111**, 1 (1999).

[65] V. Stert, W. Radloff, C.P. Schulz, I.V. Hertel, Euro. Phys. J. D**5**, 97 (1999).

[66] V. Blanchet, M.Z. Zgierski, T. Seideman, A. Stolow, Nature **401**, 52 (1999).

[67] T. Frohnmeyer and T. Baumert, Appl. Phys. B**71**, 259 (2000).

[68] J. Manz, L. Wöste, *Femtosecond Chemistry*, VCH, Weinheim (1995).

[69] A.H. Zewail, J. Phys. Chem. A**104**, 5660 (2000).

[70] See e.g. *Atomic, Molecular, and Optical Physics Handbook*, G.W.F. Drake (ed.), AIP press, Woodbury (1996).

[71] See e.g. *Handbook on Synchrotron Rad., Vol. 1A*, E.-E. Koch (ed.), North Holland, Amsterdam (1983).

[72] A. Assion, M. Geisler, J. Helbing, V. Seyfried, T. Baumert, Phys. Rev. A**54**, R4605 (1996).

[73] C. Meier and V. Engel, Chem. Phys. Lett. **212**, 691 (1993).

[74] J.J. Sakurai, *Advanced quantum mechanics*, Addison-Wesley, New York (1977).

[75] E. Karule, in *Multiphoton Processes*, J.H. Eberly, P. Lambropoulos (eds.), J. Wiley, New York (1978).

[76] E. Burkel, *Inelastic Scattering of X-Rays with very High Energy Resolution*, Springer Tracts in Modern Physics **125**, Berlin (1991).

[77] W. Schülke, *Inelastic Scattering by Electronic Excitations*, in *Handbook of Synchrotron Radiation, Vol. 3*, G. Brown, D.E. Moncton (eds.), Elsevier, Amsterdam (1991), page 565.

[78] E. Burkel, Rep. Prog. Phys. **63**, 171 (2000).

[79] D.P. DiVicenzo et al., Nature **408**, 339 (2000).

[80] R. Vrijen et al., Phys. Rev. A**62**, 12306 (2000).

[81] I. Shlimak et al., to be published in Proc. Int. Conf. Phys. Semiconductors ICPS-25, Osaka (2000); submitted to Semicond. Sci. Technol.

[82] R. Rüffer and A.I. Chumakov, Hyperfine Inter. **128**, 255 (2000).

3.4. Surface and Interface Studies

This chapter has been written on the basis of contributions to the report of the workshop "Surfaces, Interfaces and Nanomaterials" edited by H. Dosch (MPI Metallforschung, Stuttgart) and W. Drube (HASYLAB, Hamburg) (see A.1.9). In these contributions, more detailed description and further references can be found.

The equilibrium structure, the structural changes, and the associated properties of surfaces and interfaces have been in the focus of scientific interest for the last 30 years. Most static structures of the simple metal and semiconductor surfaces are known today on the atomic level and their range of stability has been studied in detail [1]. Surface sensitive X-ray diffraction techniques have been key techniques in unravelling surface reconstructions [2, 3] and surface disordering phenomena [4]. These studies have become possible because of the availability of highly brilliant synchrotron radiation provided by synchrotron radiation facilities of the so-called second and third generation.

Future research in condensed matter physics and chemistry will face new challenges in the investigation of surfaces and interfaces: The rapid development in nanotechnology produces systems and devices which contain small-sized materials with a high density of surfaces and interfaces. Today's microelectronic and micromechanical devices are composed of micrometer-sized structures of all kinds of materials, ranging from semiconductors through metal alloys to polymers. The future trend is to reduce the typical length scale in such devices significantly below the micrometer size and to increase the speed of their performance. Functional properties of materials such as electrical conductivity, magnetic susceptibility or thermal conductivity become increasingly sensitive to the size of the system and to its boundaries, when the linear dimensions of the system fall short of a critical length. Further reduction of the device size will raise new scientific challenges to understand and control the influence of the size on their properties. With the increased speed of performance, it also will become essential to understand how these modified properties behave on various length and time scales.

Almost all interactions with materials in technology and in our everyday life is mediated via the surface: Selective catalytic reactions, oxidation and corrosion processes, or the tailored reactivity of surfaces to special organic and inorganic molecules in sensor technology are examples of solid-gas and solid-liquid reactions which are of paramount importance. Another far-reaching field which is highly relevant for future technologies is the microscopic understanding of friction and lubrication between gliding and rolling surfaces. From everyday experience we know that a liquid film confined between two solid surfaces acts as a lubricant. Such films, as they reduce friction and wear, are of significant economical importance. It is well-established that even fluid films of only a few monolayers thickness may reduce the friction between sliding objects substantially [5]. A microscopic description of "boundary lubrication" [6] is needed for a directed search for materials and conditions yielding maximum lubrication and minimal wear. In all these examples, the challenge is to understand the dynamics of the structural changes associated with these surface phenomena.

Liquid and soft-matter surfaces and interfaces have been extensively investigated in the past decades [7]–[11]. In our daily life, soft-matter films and liquid/solid interfaces are play-

ing a more and more important role: Thin polymer films are used as coatings in many technological applications. The variety extends from their simple use as protection of surfaces against corrosion to the use of ultra-thin films in semiconductor technology. Organic multilayers are promising materials for biosensors, and liquid films are present in many obvious contexts.

The microscopic understanding of surface properties is also of fundamental interest: The symmetry breaking at surfaces and interfaces poses a serious challenge to theory which strives for quantitative models with predictive power. This holds particularly for co-operative phenomena (like electronic correlations and magnetic order), which are crucially affected by the size of the system and by the presence and detailed structure of its surfaces and interfaces. In thin films, liquids and organic macromolecules may be confined in a quasi-two-dimensional geometry. The state of soft-matter (fluids, complex mixtures, polymers, self-organized assemblies, proteins) confined between two solid surfaces at spacings comparable to the size of the supramolecular structure or even to the size of single molecules is expected to be totally different from the respective bulk behavior [12]–[14].

The intense ultra-short X-ray pulses from the XFEL offer novel opportunities to study these phenomena in a coherent and time-resolved manner. In the following, we selectively discuss intriguing scientific problems of current and future interest which can be attacked with experiments specifically utilizing the unique properties of the XFEL. They are subdivided into time-resolved X-ray diffraction from surfaces (Sec. 3.4.1), X-ray diffraction from liquid and soft surfaces (Sec. 3.4.2) and from collective excitations in low dimensional systems (Sec. 3.4.3).

3.4.1. Time-resolved X-ray diffraction from surfaces

The study of the temporal evolution of surface and interface structures on very short time scales is particularly important for a fundamental understanding of dynamic properties. A challenging task ahead is the experimental access to atomic motions during rapid structural changes and the correlation of these dynamics with the short-time properties of surfaces and interfaces. Taking $\mathrm{k_B T} = 50\ \mathrm{meV}$ as a typical thermal energy and $\mathrm{a_o} = 0.1\ \mathrm{nm}$ as the typical microscopic distance in condensed matter, the thermal velocity is $\mathrm{v_{therm}} = \sqrt{(2\,\mathrm{k_B T/m})} = 1000\ \mathrm{m/s}$, implying a typical "thermal time scale" $\mathrm{t_{therm}} = 100\ \mathrm{fs}$. A unique way to study these short-time dynamics associated with structural changes, phase transitions and irreversible processes is given by pump-probe X-ray scattering and X-ray spectroscopy experiments. In such experiments (Fig. 3.4.1), the surface under investigation is exposed to a short laser, pressure, or gas pulse ("pump") that triggers certain reactions at the surface and/or in the subsurface regime, which are subsequently monitored by a synchronized X-ray pulse ("probe"). Essentially all established X-ray methods which today effectively use the high brilliance of synchrotron radiation may enter the ultra-short (eventually single-pulse) time domain as pump-probe X-ray techniques, such as pump-probe surface crystallography using truncation-rod scattering and evanescent scattering, pump-probe X-ray diffuse scattering, pump-probe coherent X-ray diffraction, pump-probe magnetic X-ray diffraction, pump-probe X-ray spectroscopy (magnetic and nonmagnetic, EXAFS) and pump-probe X-ray imaging.

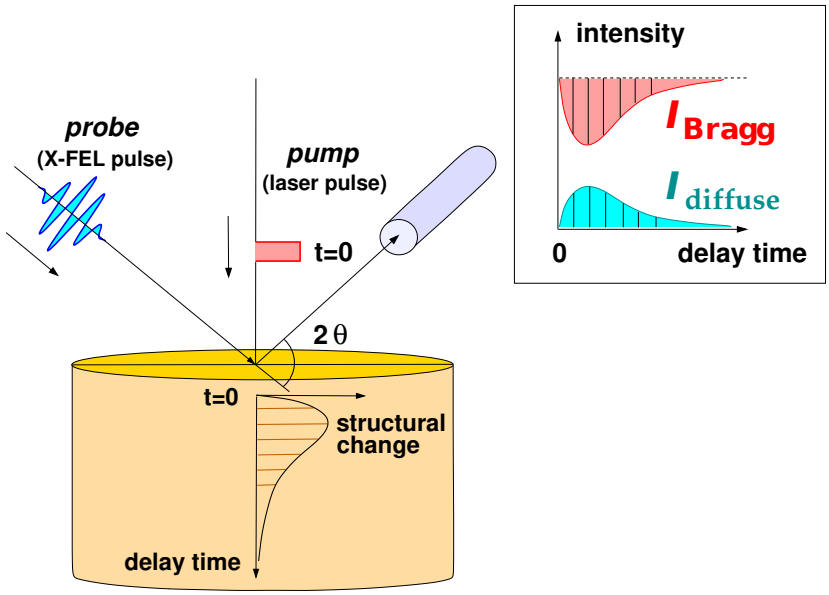

Figure 3.4.1.: *Schematic view of pump-probe experiments.*

3.4.1.1. Short-time transients during phase transformations

Novel non-equilibrium structures and phases of condensed matter can be expected in a short time interval after a sudden temperature change: In order to understand the origin of such transient structures, consider a system in an initial equilibrium state given by the initial free energy $F_i = E_i - T_i S_i$. After a heat pulse the system will arrive at a final equilibrium state $F_f = E_f - T_f S_f$. Notice that the internal energy involves only nearest and next-nearest neighbor interaction and thus readjusts fast, while the entropy maximization requires long-ranging rearrangements of atoms, which necessarily proceeds in a more sluggish manner. Consequently, new transient states will be able to emerge on a short time scale that are governed by the minima of the local energy (Fig. 3.4.2) and not by the free energy. These short-time structures can potentially have a hitherto unknown effect on the microscopic details of the final equilibrium structure which forms from these transients.

3.4.1.2. Nature of melting and stability of solid phase

Melting and freezing are phase transitions of first order which are accompanied by a latent heat. In order to promote the solid-liquid transformation in either direction, the formation of a critical nucleus of the metastable phase is a prerequisite, leading quite generally to undercooling and overheating phenomena. While, however, one can undercool a liquid quite considerably, the overheating of a solid is not observed, at least if its boundary is a free surface. One thus is forced to assume that the free surface necessarily sparks the melting of the solid. Several experiments have unravelled this so-called "surface melting phenomenon" in various systems [15, 16]. The detailed structural changes during the formation of this quasi-liquid surface layer upon heating are greatly unknown up to now, but are crucial for the understanding of both the stability of the solid phase and the melting process.

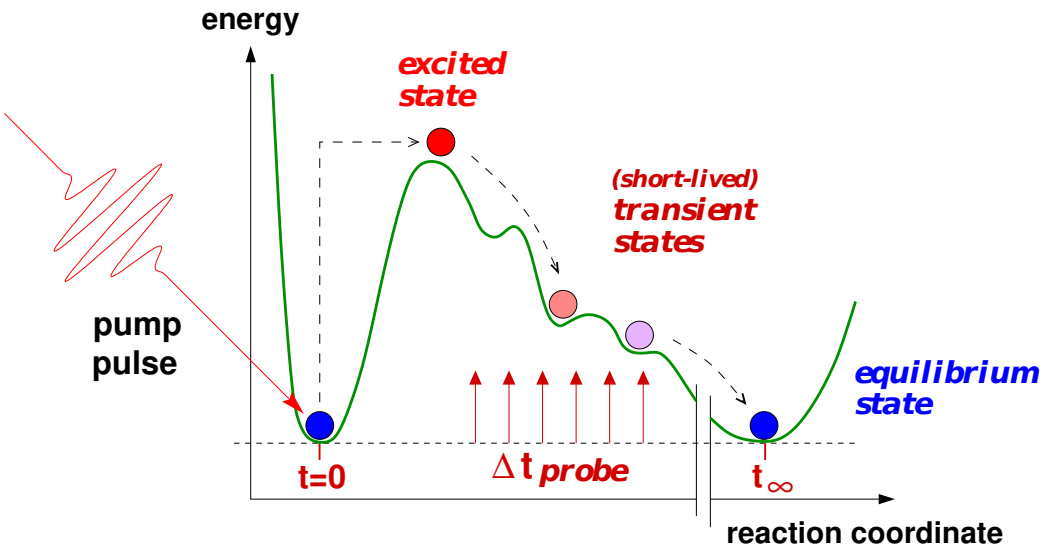

Figure 3.4.2.: *Illustration of transient states.*

When a solid is exposed to a short laser pulse, the energy is deposited in the electronic system. It is commonly assumed that "thermal melting" occurs, after the energy is transferred from the electronic to the ionic system via electron-lattice relaxation processes. However, there is increasing experimental evidence for a second, completely different melting process, called "electronic melting": A long-range ordered structure may be disrupted on a sub-picosecond time scale if an impinging electromagnetic wave promotes a critical portion of the binding electrons from the valence band into the conduction band. Several time-resolved X-ray experiments give an indirect evidence for this non-thermal melting process [17, 18]. The most recent one by Siders *et al.* [19] investigated the temporal behavior of a Bragg intensity in Ge within a sub-nanosecond time window after laser heating (see Fig. 3.4.3). The nature of the disorder which emerges within a 100 fs time scale is unknown, but could ideally be investigated with the XFEL using its unique time structure and the high number of photons per pulse.

3.4.1.3. Time-resolved structural studies of lubrication and friction

Eminently suited for studies of boundary lubrication is the surface force apparatus pioneered by Israelachvili *et al.* [20]. In this instrument, the area and the spacing of the contacting surface areas are well defined, allowing for quantitative measurements of normal forces and shear forces as a function of the gap distance. As the gap between the confining surfaces decreases to a few molecule or particle diameters, the confined fluid film is generally found to attain an apparent viscosity much higher than that of the bulk fluid, to the point that the surfaces may get stuck. It has been conjectured that the stickiness is related to an ordered, solid-like, state of the fluid film, induced by the presence of the confining surfaces [21] (Fig. 3.4.4). If a shear force is applied, the film becomes fluid again, allowing the surfaces to slip. By use of coherent X-ray scattering, time-dependent structural investigations of confined fluids can be performed. The XFEL brilliance can be exploited for studies in gaps down to

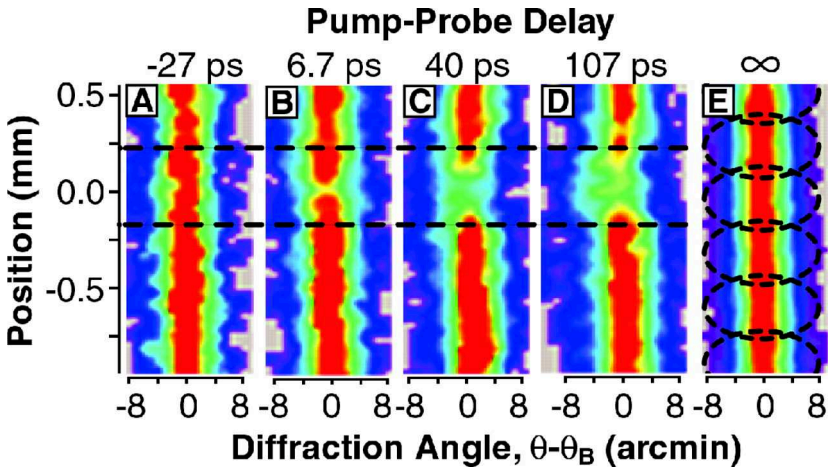

Figure 3.4.3.: *Images obtained from a photon-counting X-ray area detector for five pump-probe time delays. The horizontal axis corresponds to the diffraction angle, shown relative to the Bragg angle for Ge. The vertical axis corresponds to the position on the semiconductor wafer. The optical pump photoexcites only a portion [indicated by dotted lines in (A) through (D)] of the entire X-ray-probed area. The image at infinite time delay (E), including six single-pulse damage regions (indicated by dotted circles), was taken nonrastered and with the optical pump blocked during the exposure. (Figure and caption reproduced from [19])*

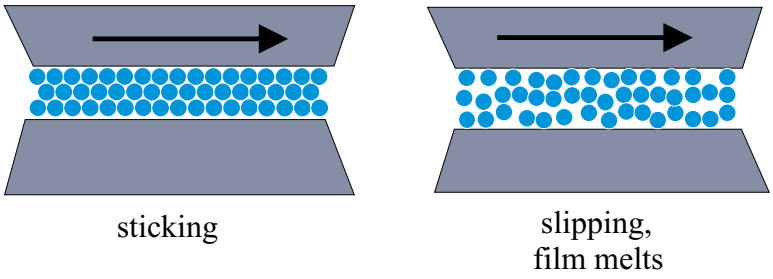

Figure 3.4.4.: *Schematic representation of the stick-slip phenomenon in a lubricated system. In the sticky state, the confined fluid is ordered into a solid-like state. Such ordering is thought to occur whenever an integer number of closed-packed layer of molecules (or particles) exactly matches the gap width. A melted (slippery) state corresponds with a non-matching condition.*

only a few nanometers. The beam is directed into the gap along a direction nearly parallel to the plates, using the system as a waveguide [22]. As the guided waves have their maximum amplitude within the fluid and a rapidly decaying amplitude within the confining plates, the scattering contribution from the plates is minimized. Studies of fluids in gaps down to only a few nanometers require the use of ultra-smooth crossed cylinders of controlled shape as the confining surfaces (see Fig. 3.4.5). Structure determinations are based on the far-field detection of guided modes as well as non-guided modes which partly travel through the confining medium. Using the above method, one may measure, in the presence and absence of shear

motion, the density profile in the fluid across the gap between the surfaces [23] and correlate the measured density profiles directly to the changes in viscoelastic properties as determined from simultaneous measurements of the friction force. Systems of interest include confined colloids, lubricants of alkane molecules, emulsions, grafted polymer brushes, dry lubricants (nanoparticles) and confined granular media.

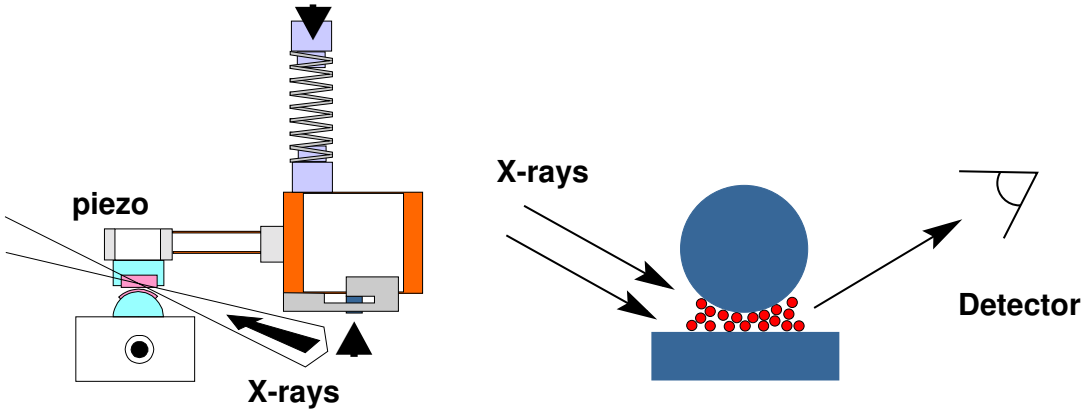

Figure 3.4.5.: *Schematic of the crossed cylinder geometry with approach mechanism (left). The X-ray beam is incident at a glancing angle along the long axis of the lower cylinder. The lower cylinder can be sheared sideways. The upper cylinder is spring-loaded, allowing force measurements. Right: side view of scattering geometry. Angles and distances are not to scale.*

By measuring the scattered intensity as a function of parallel momentum transfer, i.e. in the plane perpendicular to the confining direction, one determines the structure factor $S(q_{\parallel})$ of the confined liquid, which is expected to differ from that of the bulk fluid. The dynamics of colloids or emulsions in confined geometry are also of considerable interest. Using fully transverse coherent beams, one may extend the above studies to the time domain, applying X-ray photon correlation spectroscopy (XPCS). Time correlation functions can be measured for scattering vectors $q_{\perp}$ perpendicular to the confining surfaces and as a function of $q_{\parallel}$ parallel to the surfaces. Such measurements, if performed for different gap widths, should reveal the anisotropic effect of confinement in the diffusion constant. The modified dynamical properties of fluids in confinement have important implications for many technological applications. The XFEL brilliance should also enable studies of the rheological properties of liquids in nanometer-sized cylindrical pores. The response of the fluid to the application of shear to one of the surfaces leads to density fluctuations whose time correlation spectrum can also be measured by XPCS. Within granular systems, avalanche effects should readily be detected. Present-day synchrotron sources deliver X-ray intensities that are just sufficient for time-averaged small-angle scattering experiments on planar fluid films confined within nanometer gaps (e.g., 5 nm vertical x 10 μm horizontal). For scattering studies at larger momentum transfers, as well as for XPCS over a wide range of $q_{\parallel}$, the available intensity is too low by at least three orders of magnitude. A *single* 100 fs XFEL pulse (12.4 keV with rela-

tive bandwidth of 2 x 10^{-5}) will deliver 1.4 x 10^{8} coherent photons onto a 5 nm x 1 μm area (assuming a 60:1 demagnifying focussing lens), which is two to three orders of magnitude higher than presently obtained *per second*. This high flux would even enable time-dependent fluctuations in the coherently scattered signal to be measured on the time scale of the bunch spacing, i.e. 100 ns. Novel two-dimensional pixel detectors (2000 x 2000 pixels) are currently in development [24]. In these, each pixel operates in single photon counting mode and is connected to a read-out chip containing a preamplifier, a discriminator and a counter. Although present read-out times of the entire 2D-array are too long, fast frame buffer schemes may be developed which meet these requirements.

3.4.1.4. Short-time X-ray monitoring of laser-induced processes

In current and future Si technology, it will become increasingly important that the Si crystallization from α-Si can be carried out such that a crystalline Si layer is produced with a low density of structural defects, and that the underlying structures and devices are not degraded. One of the current problems is intimately related to the fact that pulsed-laser induced melting and the subsequent crystallization are first-order phase transitions far from equilibrium that lead to a copious nucleation of stable and metastable phases. Consequently, a small-grain polycrystalline structure containing many structural defects emerges after laser treatment. In order to produce a crystalline Si film with a low defect density, it is mandatory to understand and control not only the mere thermodynamic aspects of the solid-liquid transformation, but in particular the microscopic details regarding the transition kinetics. One avenue to obtain large-grain single-crystal Si films is to multiply irradiate the α-Si layer with such an energy dose that melting is achieved with solid Si islands in between which act as nucleation seeds ("super-lateral growth", see e.g [25]). Pump-probe X-ray diffraction studies are a prerequisite to fully understand the structural evolution of such technologically relevant films after pulsed laser treatment.

3.4.2. Liquid and soft interfaces

Many fundamental properties of the structure and dynamics of liquid and soft interfaces have been discovered with synchrotron radiation from second- and third-generation machines (see e.g. Refs. [26]–[28]). The next major step, the investigation of fast dynamics down to nano- and picoseconds in combination with atomic resolution, requires more advanced X-ray sources such as the XFEL. Only the special coherence properties of this machine, in combination with the extreme brilliance, will allow the solution of a wide range of key questions in life sciences, electrochemistry, lubrication, and interface physics in general.

Obviously, not all real-space techniques with atomic resolution, such as STM and AFM, work with liquid or soft surfaces. Also, these techniques cannot deliver nanosecond time resolution of dynamic processes at interfaces. Therefore, X-ray scattering techniques are mandatory in order to obtain the desired information.

Probes for the investigation of the structure and dynamics of such systems have to be sensitive to the vertical length scale. Laterally, on one hand, quite large length scales (> 10 μm, requires very high q-resolution) have to be covered, since soft-matter materials and liquid

surfaces may possess long-range correlations, for instance, capillary wave fluctuations [29]–[32], on their surfaces. On the other hand, many fundamental properties are expected to be dominated by the regions close to the soft-matter/solid interface, i.e. atomic resolution is needed for their investigation.

Here it becomes clear that the requirement of atomic resolution in real space, ultrahigh resolution in q-space, and nanosecond time resolution can only be fulfilled with a new tool, namely the XFEL, whose short wavelengths yield atomic resolution and whose extreme coherence properties are required for the q-resolution and the spectroscopy on short time scales.

3.4.2.1. Biological systems

Functional biological systems on solid substrates are an important emerging field of research, including topics such as the coupling of nerve cells to semiconductor chips, biocompatible implants, drug delivery systems, biosensors, and biotechnological processing [33]–[35]. Generally, proteins adsorb and denature at solid interfaces, and therefore have to be shielded by appropriate intermediate layers. For instance, composites of lipid bilayers and biopolymers could make up the interface between the biofunctionalized system and the solid substrate. They can conveniently be deposited on the substrate by self-assembly techniques with typical thickness values in the nanometer range. Apart from the technological implications, such systems can provide a controlled setup to study biomolecular interactions and the self-assembly of supramolecular structures under well-defined constraints of geometry and external fields (temperature, pressure, chemical potential, electric field).

Structure, elasticity and dynamics in such layers are important issues, which can be uniquely studied by surface-sensitive X-ray scattering and spectroscopy techniques, combining the advantage of high resolution and compatibility with very soft systems (for a sketch of such an experiment, see Fig. 3.4.6). Furthermore, they allow for a wide range of in-situ controlled parameters. However, to date the amount of structural information is often limited in strongly disordered systems due to low ratios of signal to noise, and time-resolved studies are only possible in the limit of very slow dynamics. The advent of the XFEL leads to significant quantitative and qualitative improvements, in particular to new techniques of probing the dynamics of proteins and biomolecules in well-defined environments of solid-supported, lipid bilayers and biopolymer networks. Photon correlation spectroscopy, nuclear resonant scattering, time-resolved reflectivity, and inelastic scattering are among the techniques which have currently been developed but cannot successfully be applied to the systems of interest mentioned above. Using more conventional techniques, the supramolecular structure could be elucidated with unprecedented accuracy, even in the absence of full crystallographic ordering, due to the presence of highly aligned samples (interfaces) and highly brilliant radiation.

A big challenge in structural biology is raised by the need to visualize large molecular assemblies and machineries inside a cell at molecular resolution. To date, a large gap exists between the high-resolution X-ray structures at the level of macromolecules and the understanding of the functional organization of the cell (e.g. as derived from advanced optical microscopy techniques). A combined in-situ approach, which would allow molecular reso-

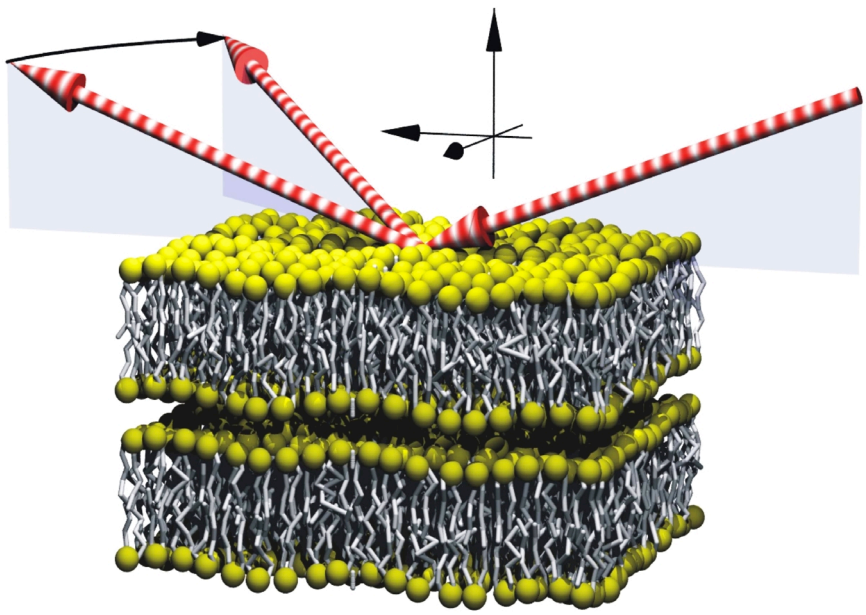

Figure 3.4.6.: *Sketch of a surface scattering and diffraction experiment from a disordered biomembrane layer stack. Radiation damage is drastically reduced if grazing angles below the critical angle of the soft materials are used.*

lution in the cellular environment with many intervening length scales, is still lacking. Such a goal could be achieved in the future by novel X-ray diffraction, spectroscopy and imaging techniques, using a fully coherent beam of an XFEL.

3.4.2.2. Free-standing soft-matter films

A field where the XFEL can provide unique results is the investigation of the dynamics of fluctuations of freely suspended smectic liquid crystalline films or membranes. Smectic phases occur in monomeric as well as polymeric systems. Stacks of surfactant membranes also show smectic ordering. The simplest type is the smectic-A phase, which can be described as a stack of liquid layers in which the distribution of the centers of mass of the elongated molecules is given by a 1D density wave. Smectic liquid crystals can be suspended over an opening in a solid frame. Such freely suspended membranes have a high degree of uniformity and a controlled thickness ranging from two to many hundreds of layers (each typically 3 nm thick) [36]. Moreover, thanks to the absence of a substrate, these freely suspended membranes are remarkably insensitive to radiation damage.

Freely suspended smectic membranes are model systems of low-dimensional order. Their reduced dimensionality leads to strong thermal fluctuations of the smectic layers, resulting in an algebraic decay of the static density-density correlation function. Fundamental questions regarding the dynamic critical behavior of such systems have been addressed theoretically [37, 38] (effects of finite size, of non-zero surface tension and of viscous dissipation). Re-

cently the possibilities of dynamic light scattering have been extended with coherent X-rays to perform XPCS on smectic membranes [39, 40]. However, with present third-generation synchrotron sources, serious limits are encountered at (sub)microsecond timescales and in coherent intensities. The coherence properties and the brilliance of the radiation from an XFEL allow the experimental investigation of the dynamics of monomeric and polymeric smectic membranes, as well as of cationic lipid membranes incorporating DNA chains down to molecular length scales.

Stacks of surfactant membranes in solution can lead to a highly swollen lamellar phase. Examples are hydrated phospholipids, where lipid bilayers alternate with water layers, and ternary systems of surfactants, water and oil, where surfactant monolayers separate layers of water and oil. A wide range of periodicity can be found (1-100 nm), which can be tuned by a proper adjustment of the dilution. In these systems, the neighbors limit the space available for fluctuations, causing an entropic membrane repulsion (Helfrich effect). This effect depends strongly on the intermembrane distance [41]. It is of fundamental interest to measure its dynamics with an XFEL which could cover the required time and wave number scales.

Smectic ordering plays a role in the ordering of DNA chains in lipid membranes. Linear DNA chains and cationic liposome mixtures can self-assemble into a coupled 2D smectic phase of DNA chains imbedded between a 3D smectic phase of lipid layers [42, 43] (see Fig. 3.4.7). These systems are of interest because they mimic certain characteristics of nat-

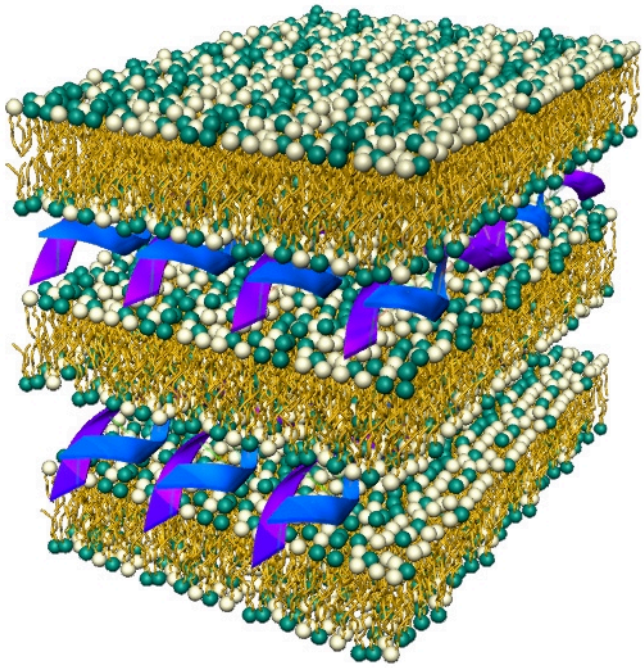

Figure 3.4.7.: *Diagram of a DNA-membrane complex (from Ref. [41], see http://www.aip.org/physnews/graphics/html/dna_memb.htm).*

ural viruses in transporting extracellular DNA across the cell membrane. Moreover, if the membranes' bending rigidity is lowered, an inverted hexagonal phase can be found with a strongly enhanced tendency for membrane fusion. Also, new theoretical models for the ordering in these DNA-cationic lipid complexes have recently been developed [44]. Once the dynamic behavior of the simpler systems is clarified, the dynamics of these and related biologically relevant membrane systems provide a fascinating and still completely open field to explore with an XFEL.

3.4.2.3. Liquids and liquid films

The structure and dynamics of bulk liquid and liquid thin-film surfaces are of fundamental and practical importance. From the fundamental point of view, classical hydrodynamics may be tested down to nanometer length scales with surprising results. Recently it has been shown by X-ray scattering techniques that the surface tension has to be substantially modified if lateral length scales of a few nanometers are probed [32, 45] (see Fig. 3.4.8). In

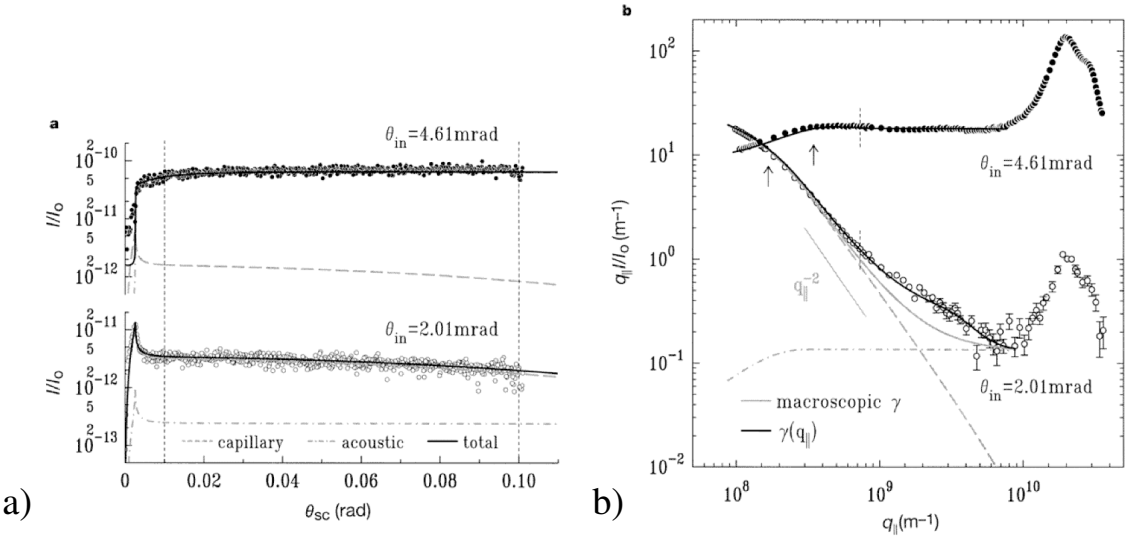

a) b)

Figure 3.4.8.: *Off-specular X-ray scattering data as a function of the lateral wavevector transfer (symbols) from a water surface for different incident angles* θ_{in} *above and below the critical angle. The lines are fits where a new theory for the surface tension was used (reproduced from [32]).*

addition, the wetting behavior of liquid thin films is of great practical interest for many applications, among which painting is of course the most prominent. However, many of the more complicated wetting processes that occur in nature and daily life are at best only partially understood.

There are three major questions concerning the structure and dynamics of liquid surfaces and the solid/liquid interface:

1. The influence of a solid substrate is expected to modify the solid/liquid interface. While this situation has been extensively studied theoretically in the past, only a few experiments have been carried out so far (this point will be addressed in the next section).

2. The liquid/vapor interface is also of fundamental interest. Calculations of the intrinsic liquid/vapor density profile have been done for many fluids (see e.g. Refs. [46]–[48]). Many aspects of capillary waves at the liquid/vapor interface, and the question of how these capillary waves on liquid thin films are altered by the background potential due to the substrate, have been the focus of a large body of theoretical work too (see e.g. Refs. [45, 46, 49, 50, 51]).

3. The *dynamics* of surface fluctuations have been measured only by dynamic light scattering so far [52]. Thus, the dynamics of fluctuations on liquid surfaces at nanometer length scales are not explored experimentally yet.

From the experimental point of view, it is quite difficult to investigate liquid surfaces on a nanometer scale. On the one hand, they are difficult to prepare, and on the other hand, direct probes such as AFM and STM cannot be used to get structural information. Thus scattering techniques are mandatory. The structure of the liquid/vapor interface has been extensively investigated by X-ray scattering methods in the past [29]–[32]. However, the investigation of the dynamics of liquid surfaces by X-ray photon correlation spectroscopy has only recently been achieved [53] (Fig. 3.4.9). But these investigations have suffered from the insufficient coherence properties of micron-sized beams produced with pinholes. Thus it will be impossible to extrapolate these experiments towards atomic dimensions by using conventional synchrotron sources. For the test of hydrodynamics on nanometer length scales, a perfectly coherent X-ray beam, such as will be delivered by the XFEL, is of eminent importance.

The freezing of liquids undergoing the glass transition is a field that is still controversial. Many groups have performed experiments that show how the microscopic motion freezes in the bulk (see e.g. refs. [54]–[57]). No quantitative studies which monitor the freezing of liquid surfaces at molecular length scales exist so far. The X-ray photon correlation spectroscopy data shown in Fig. 3.4.9 were obtained for a lateral length scale of $\approx 50\ \mu$m. It has been estimated that this result may be extended with third generation synchrotron sources down to a few microns [53]. Monitoring the freezing at the molecular level is clearly beyond the scope of today's experiments. However, this field is of fundamental interest, since it is not clear if the glass transition is altered at a surface, i.e. if the transition temperature may be a function of the depth in a material [58]–[61]. The answer to this question would also have an economic impact, since the microscopic structure of a glass could be designed so as to minimize light scattering, which is the main reason for using these materials. The entire field of "glass physics and chemistry" would dramatically benefit from the coherence properties of the XFEL.

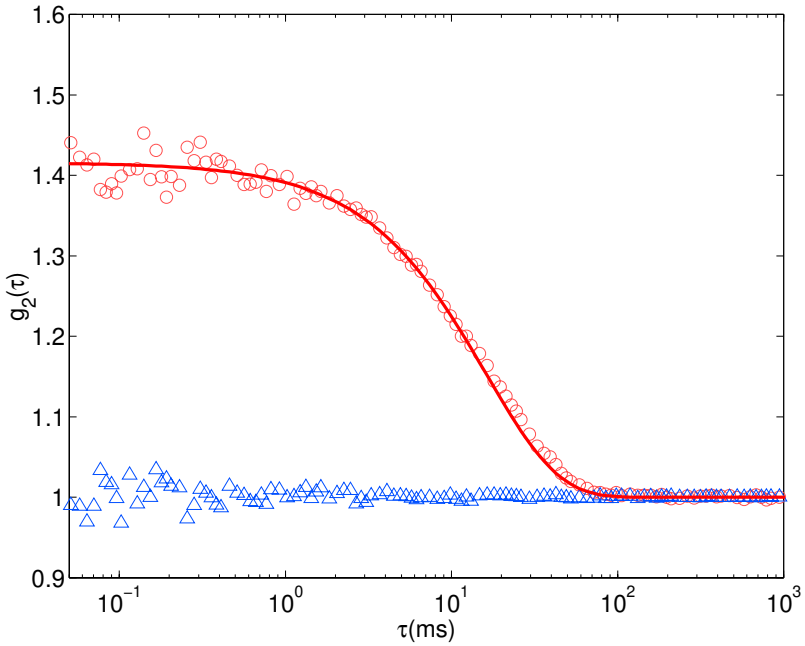

Figure 3.4.9.: *X-ray photon correlation spectroscopy data from a glycerol surface. The intensity-intensity correlation function $g_2(\tau)$ at $T = 253\,K$ is shown (open circles). The length scale that was probed is $x_0 = 56\,\mu m$. The correlation function of the monitor signal is given by the open triangles. The solid line is a fit according to $g_2(\tau) = g_0 \exp(-\tau/\tau_0) + 1$, from which the two parameters g_0 (contrast) and τ_0 (time constant of overdamped capillary waves) are obtained.*

3.4.2.4. Confined liquids

Liquid films on solid substrates and liquid films confined between two solid surfaces (a sketch is shown in Fig. 3.4.10) have attracted great attention in the last few years, since their structural properties have become accessible with third-generation synchrotron sources. Such films are not only important for the understanding of fundamental concepts in basic research. They also play an increasing role in applications such as lubrication of metal surfaces. The microscopic dynamics of such films on molecular length scales, e.g. the sliding friction, have mostly been theoretically investigated by molecular dynamics simulations [62]–[65]. The lack of experimental data is due to the limitations of the available probes. Most suitable are scattering methods with high energy photons ($> 10\,keV$) using synchrotron radiation. But even the best third-generation sources have only very restricted possibilities to look at the dynamics of sliding. The investigation of the static structure of such films is already a great challenge because they are only a few Angstroms thick and covered by solid surfaces. Such a configuration inherently leads to a low signal-to-noise ratio in scattering experiments [12, 14, 28, 66].

The XFEL does provide major advantages for the investigation of confined fluids: The extremely high brilliance allows a collimation to spot sizes of only a few nanometers with sufficiently high flux. In this way, a controlled illumination of the thin films from the side

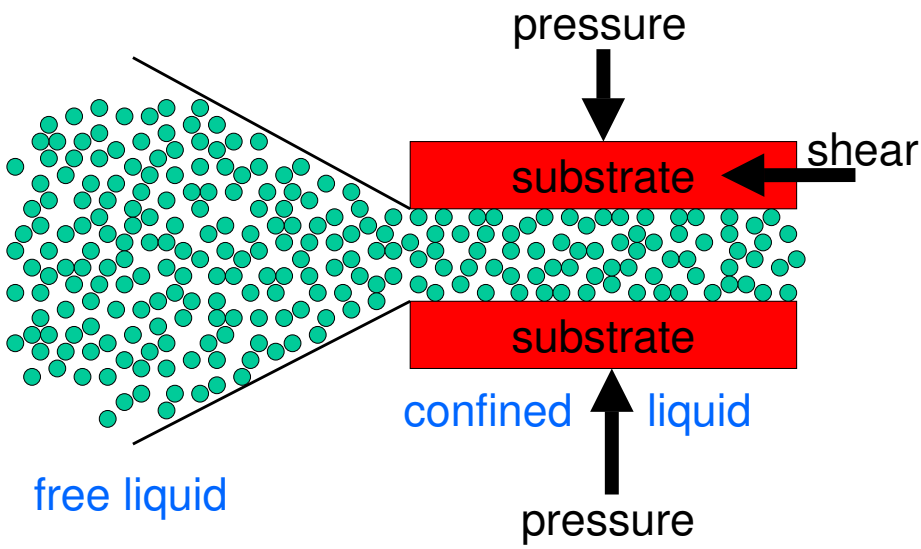

Figure 3.4.10.: *Sketch of a confined liquid. The bulk liquid (left side) is constrained between two substrates with a gap distance of only a few molecular diameters of the liquid. Shear or pressure may be applied to investigate the effect of the confinement.*

(and not as usual from the top through one solid substrate) would become possible. The setup would act as a perfect waveguide structure that captures a large amount of the incoming photons. The structural information of the confined liquid is thus considerably magnified and could be extracted from the scattered radiation [67].

The liquid films exhibit different states of disorder, depending on the film thickness and the kind of sliding along the interfaces. An X-ray beam which is perfectly coherent in the transverse direction will give rise to speckle patterns. Those speckles sensitively depend on the order or disorder in a region. Thus the time-dependent measurement and interpretation of speckle patterns could resolve structural properties at the interfaces of the films [68]–[74].

The dynamics of confined liquids involves very short time scales. A resolution of 10 nanoseconds up to microseconds is required. The time structure of the XFEL would make such scales accessible. The starting point is a static setup. After initializing a sliding of one surface, the confined liquid is expected to change its structure and degree of order. The in-situ monitoring of such structural and even phase behavior changes at interfaces is a big challenge that is of decisive importance for the microscopic understanding of sliding friction. The extreme brilliance and the coherence properties of an XFEL beam would provide microscopic information about this important topic that could otherwise not be obtained.

3.4.2.5. Electrolytic interfaces

Another important field of applied and basic research which would strongly benefit from an XFEL source is electrochemistry. Electrochemistry plays an important role in our daily life. Even disregarding the above-mentioned field of life sciences, the impact in inorganic materials science is already large. Corrosion and galvanic plating processes are of major economic

relevance. In the semiconductor industry, wet chemical processes are a significant part of the production line. Many recipes for process control such as particular etching solutions, for instance brighteners (for plating) or inhibitors (for corrosion), have been developed over the years, yet a deeper knowledge and understanding, in particular about structural processes on the atomic scale, is largely missing. Deposition, stripping, and particularly corrosion are reaction processes at interfaces. They may occur close to equilibrium, if controlled by an external potential, or far off equilibrium in other cases. There is little knowledge about accompanying structural changes, although this situation is slowly improving owing to scanning probes and advanced X-ray techniques. The decisive structural transitions occur within the inner Helmholtz layer, where oppositely charged layers of atoms/molecules are separated by atomic distances.

However, there is no information at all available on the kinetics of the reaction, e.g., how an ion loses or acquires the solvation shell. The timescale of these processes reaches down to the picosecond range. Thus, the time structure of the XFEL is ideally suited to study such processes in-situ. Many potential-controlled adsorption (deposition) and desorption (stripping) processes can be carried out reversibly, and need not be single-pulse experiments. Suitable experimental techniques could be X-ray diffraction, for instance, the observation of the time evolution of a fractional order peak for some underpotential deposits; time-dependent crystal-truncation-rod scattering; or X-ray standing-wave studies.

3.4.2.6. Experimental schemes

Photon correlation spectroscopy, nuclear resonant scattering, time-resolved reflectivity, and inelastic scattering are techniques which are expected to benefit strongly from the XFEL in order to investigate the dynamics on atomic length scales at interfaces. These techniques are being steadily improved at all third-generation synchrotron sources. However, despite the already impressive developments achieved so far, they cannot be successfully applied to the systems and time scales of interest which are addressed in the above-mentioned examples because they are limited either by the degree of coherence and/or by the brilliance of conventional sources (for a typical setup of an experiment using coherent X-rays on third-generation synchrotrons see Fig. 3.4.11). The supramolecular structure of soft-matter molecules at interfaces could be elucidated with unprecedented accuracy, even in the absence of any order in the crystallographic sense, with an XFEL.

The problem of radiation damage in connection with soft-matter experiments may be solved either by single-pulse experiments or by applying special scattering geometries, e.g. the use of grazing incidence angles, where radiation damage is drastically reduced [53]. The required instrumentation would consist of a diffractometer that would allow a very high resolution (for instance, by a long incident beam side and a long detector arm). High resolution is needed, since the size of the speckles is inversely proportional to the length of the respective objects in real space (large molecules at interfaces in this case). In addition, the diffractometer's mechanics must be very precise, since a typical XFEL experiment will deal with micron-sized X-ray beams. For time-dependent measurements those as X-ray photon correlation spectroscopy (XPCS), ultrafast detectors are needed to push the time resolution into the nanosecond range. It is not unreasonable to assume that such detectors will be available

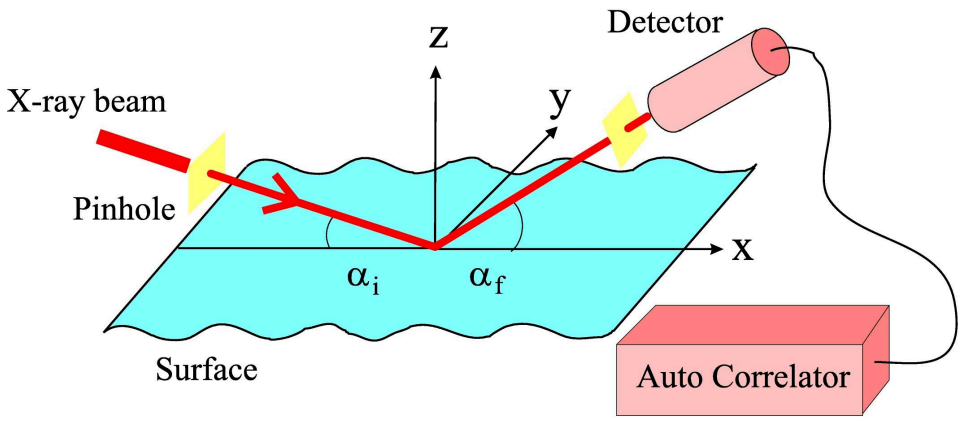

Figure 3.4.11.: *Sketch of the setup for a surface X-ray photon correlation spectroscopy experiment on a third-generation synchrotron. The pinholes deliver a partially coherent X-ray beam. With the XFEL, a perfectly coherent beam is inherently produced which can be used to investigate the dynamics of liquid surfaces at atomic length scales.*

by the time the XFEL is operational.

3.4.3. Collective excitations in low dimensions

The investigation of collective excitations in reduced dimensions by means of advanced X-ray scattering techniques will be an important contribution of the XFEL to the field of artificially structured materials, in particular such of nanoscale dimensions. "Band gap engineering" has been applied very successfully in the past decade to create and improve an enormous variety of devices based mainly on thin films, which allow the precise control of electronic and optical properties. With further progress in deposition and structuring techniques (including also self-assembly methods etc.), it is very likely that the variety of materials as well as their complexity will greatly increase in the future. Such systems will exhibit great deviations from bulk behavior. Whereas most structural properties can be sufficiently characterized at present-day X-ray sources, there is a strong need for efficient spectroscopic methods to study dynamical properties of low-dimensional systems. The XFEL offers unique opportunities for the investigation of those collective excitations that lie at the heart of novel functional properties, e.g. the precise control of response functions to external fields. The use of X-ray energies will give access to buried interfaces, for which no alternative technique is currently available.

In the following we will focus specifically on vibrational excitations. Phonons are a good example for quasiparticle excitations that can be significantly modified by interfaces [75] and artificial superlattices [76]. The tailoring of phononic spectra for specific purposes will be of increasing importance in the future, and a field of "phonon engineering" can be envisaged with many similarities to "band gap engineering". Since only a fundamental understanding of vibrational properties under the influence of interfaces will ensure full tunability, basic research and applications will be intimately related. The following fields of materials physics

are anticipated to play a key role:

3.4.3.1. Smart materials based on lattice instabilities

Smart materials possess the ability to respond autonomously to external stimuli. Functional materials of this type are sensor/actuator combinations based on structural phase transitions, which allow the material to modify its domain structure or the band structure to respond to external parameters like temperature, pressure, electric or magnetic fields [77]. The underlying physics of these phase transitions is intimately related to lattice instabilities with soft phonon modes.

Figure 3.4.12 schematically shows one transverse optic (TO) and one transverse acoustic (TA) phonon branch of a hypothetical crystal with several types of phonon anomalies labelled I - IV. The softening of an infrared-active mode at the zone center (I) is well known to be the driving force of ferroelectric transitions of usually (nearly) second-order character. The elastic analogue is found in ferroelastic transformations; it is closely related to the famous Zener instability of bcc lattices. Its signature is a soft shear modulus with a small slope in the acoustic limit and the upward curvature at the zone center (II). Phonon anomalies of type III and IV are frequently found in shape memory materials, where the minima at finite wave vectors represent intracell atomic displacements that essentially "freeze" at the phase transition [78].

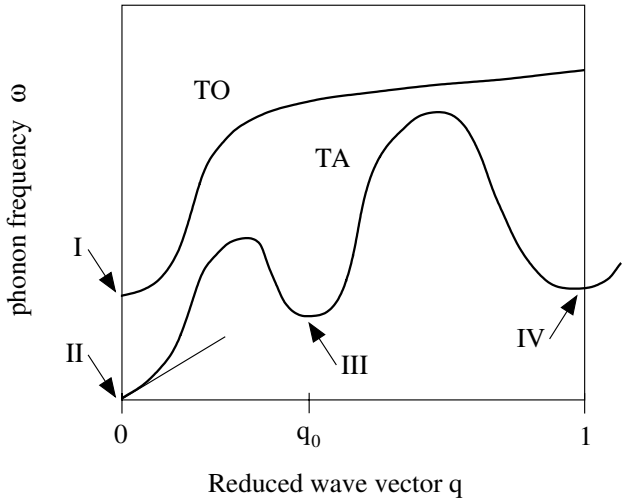

Figure 3.4.12.: *Schematic of phonon branches with various soft phonon anomalies associated with lattice instabilities (reproduced from [79].)*

It must be emphasized that meV-resolution is required to investigate such phonon anomalies. Currently, this is only possible for bulk materials using inelastic neutron and X-ray scattering, and for free surfaces using inelastic electron or helium scattering. However, in the future, materials with new transformation behavior based on strongly modified dispersion

relations will emerge. This is particularly anticipated for the following fields :

- Ferroelastic/martensitic transformations are associated with the shape memory effect and other unusual properties of metals and ceramics, e.g. superelasticity and rubber-like behavior [80]. There is a strong interest in these systems for on-chip applications like microactuators and micropumps/valves in microelectronic mechanical systems technology [81]. During the next decade, further miniaturization will bring this systems into the 100 nm regime, since the efficiency increases with decreasing actuator size. It will be important to determine the physical limits of this process.

- Phase-transforming materials with their high ratio of work per unit volume are of particular interest if they can be switched electromagnetically. Structural distortions associated with ferroelectric phase transitions can be used to generate actuator effects in conjunction with the permanent electric polarization. The actuator effect in ferroelectrics, albeit one order of magnitude smaller than for metallic alloys, can be switched by electric fields and is therefore several orders of magnitude faster compared to thermal switching [82]. This effect will allow similar applications as described above. The ferroelectric transition depends on the phonon behavior, which has already been demonstrated to exhibit unexpectedly strong modifications in thin films [83].

3.4.3.2. Incipient lattice instabilities and high-density integration

The vicinity of phase transitions related to the phonon spectrum will modify response functions significantly. This can be used to enhance certain response functions of the paraelastic / paraelectric phase by several orders of magnitude (or even into the non-linear regime). For example, this effect will play an important role for future tailoring of high-ϵ dielectric structures for high-density integration purposes [84]. Furthermore, the envisaged widespread application of nanostructured ferroelectric materials as non-volatile, random access memory materials [85, 86] will necessitate detailed basic research on ferroelectric transitions in ultrathin films and dots in particular [87].

3.4.3.3. Nanoscale tribology

The phenomenon of friction, discussed above in the context of time-resolved X-ray experiments, results from dynamical processes: The density of vibrational states at a particular frequency determines how much energy can be dissipated into that mode. The design of solids with a vibrational frequency gap within a critical region could prevent energy losses through friction. Since these processes are naturally located at buried interfaces, inelastic X-ray scattering spectroscopy with its great penetration power and high surface sensitivity is the ideal tool for this purpose.

3.4.3.4. Thermal transport in microstructures

In a confined geometry, the vibrational spectrum is altered if the film thickness or the multilayer period is comparable to the phonon mean free path. This leads to novel features like

phonon zone-folding in periodic layer structures like superlattices and *phonon confinement* due to the restriction of phonon propagation to certain layers. Such size effects in the vibrational properties will be of particular technical relevance in thin films that are part of micromechanical and microelectronic devices, because thermal properties like heat capacity and thermal conductivity become more and more critical with increasing power level and decreasing time scales of electronic and mechanical processes in those devices [88, 89]. In Sec.5.3.5, it will be shown that the XFEL enables spectroscopic investigations that are not feasible at existing sources and thus provides an ideal tool for the aforementioned purposes.

3.4.3.5. Experimental schemes

While *coherent* inelastic X-ray scattering has been a well established technique since the early eighties [90], *incoherent* inelastic nuclear resonant absorption was introduced only a few years ago [91, 92]. The former method allows the determination of the dispersion relation of vibrational excitations, while the latter technique is highly specific to vibrations of Mössbauer nuclei and allows direct derivation of the vibrational density of states of the resonant atoms. Therefore, the combination of both techniques allows complementary information about excitations in the sample to be obtained. In the following we discuss the new options that the XFEL is offering for both methods.

Inelastic Nuclear Resonant Scattering Since this method yields the *partial* vibrational density-of-states of the Mössbauer atoms in the sample, it opens the unique possibility to selectively obtain the vibrational properties of nanoparticles and thin films that contain the resonant isotope. There is no need to discriminate against inelastic signals from surrounding materials. The sensitivity of the method to thin films has been proven already in a number of experiments [93]–[95]. However, the statistical quality of the data that can be obtained at present-day sources does not allow the investigation of single monolayers. On the other hand, flux estimates for the SASE line of the XFEL at 14.4 keV indicate that a vibrational spectrum from a single monolayer of ^{57}Fe could be obtained in a few minutes. This opens the possibility to selectively introduce δ-doping layers in the sample and obtain vibrational properties with atomic resolution. It is an inherent advantage of X-ray spectroscopy over other methods like inelastic electron or He–scattering that dynamical properties can be probed inside solids, i.e. at interfaces or grain boundaries. At the XFEL, several Mössbauer isotopes will become accessible for these studies of equilibrium lattice dynamics of thin films.

Furthermore, using pump-probe schemes, non-equilibrium thin film lattice dynamics can be investigated by this method. As an example, we consider highly monochromatic phonons with lifetimes of several 100 ns, created by coupling the laser pulse to impurity resonances that decay via electronic relaxation [96]. The decay of such non-equilibrium phonon states provides valuable information about the thermal transport properties of the sample. The spectral and temporal evolution of these phonon states can then be determined by tuning the photon energy of the X-ray probe pulse around the nuclear resonance. For a fixed pump-probe delay, one obtains the phonon spectrum that has developed during this time interval, and by tuning the pump-probe time delay at a fixed off-resonance X-ray energy, one can monitor the time evolution of particular vibrational states. The time resolution is given by

the pulse length. Note that the energy resolution ΔE and the time resolution Δt are linked according to $\Delta E \Delta t > \hbar$ = 0.66 meV $\cdot$ ps. Using a meV monochromator, it should thus be possible to study non-equilibrium lattice dynamics on a ps time scale. Time resolution well below 1 ps can be obtained by sacrificing energy resolution, taking full advantage of the short-pulse XFEL time structure. An immediate application would be to study the dynamics of heat-transfer on nanoscopic length scales, as mentioned above. Due to the isotopic sensitivity of the absorption process, an extremely high spatial resolution can be obtained by the use of probe layers, making this technique a rather XFEL specific application.

Coherent Inelastic X-ray Scattering In general, the application of this method to thin films suffers from the difficulty of separating the inelastic signal of the film from the signal of the adjacent layers and the substrate. A certain control of this effect can be achieved by adjusting the angle of incidence, but this does not offer a perfect solution since one cannot restrict the radiation field to single layers exclusively. The XFEL opens a very interesting option to solve this problem using meV in-line monochromators [97] as analyzers. This approach offers a number of significant advantages over the spherically bent crystals used presently. With the application of in-line monochromators, one is not restricted to the energies determined by the Si back reflections. It is then possible to perform inelastic scattering at (almost) arbitrary energies, e.g., around the absorption edge of a particular element. This allows to discriminate the inelastic signal from this element by using the anomalous dispersion around the absorption edge. The subtraction of two measurements above and below the edge yields the inelastic signal from that particular element. If that element is confined to the film, the difference signal is free of contributions from the adjacent layers, and one obtains the vibrational modes of just those atoms. Thus, a similar elemental sensitivity as in the case of nuclear resonant scattering is obtained, and vibrational properties of single films and particles can be studied. Selective δ-doping of the film can be used to access vibrational properties of buried interfaces with atomic resolution.

Momentum transfers of $q = 0.006$ Å^{-1} have to be employed for the investigation of correlations on length scales of about 100 nm. This range is of interest for the study of dynamics in disordered systems with low-energy excitations that are confined in large structural units. Extremely high energy resolution and momentum resolution are mandatory, e.g., to unambiguously decide whether a low-energy excitation exhibits a dispersion or not. Only under those conditions it is possible to resolve the nature of that particular excitation, i.e., propagating or localized. It should be noted here that, for X-ray inelastic scattering, there are no kinematical restrictions as there are for neutron scattering. Energy resolution and momentum resolution are therefore completely decoupled. Thus, arbitrary energy transfers can be probed even at the smallest momentum transfers.

Bibliography

[1] See e.g. *Physical Structure*, in *Handbook of Surface Science, Vol 1*, N.V. Richardson and S. Holloway (eds.), Elsevier, Amsterdam (1996).

[2] R. Feidenhans'l, Phys. Rep. **10**, 105 (1989).

[3] I.K. Robinson and D.J. Tweet, Rep. Prog. Phys. **55**, 599 (1992).

[4] H. Dosch, Springer Tracts in Mod. Phys. **126**, Heidelberg (1992).

[5] See: Proc. of the Workshop on the Physical and Chemical Mechanisms of Tribology, Bar Harbor, Maine, USA (1995), Langmuir **12**, 4482 (1996).

[6] B.N.J. Persson, *Sliding Friction*, Springer Series in Nanoscience and Technology, Springer, Berlin (1998), page 1 ff.

[7] J. Als-Nielsen, D. Jacquemain, K. Kjær, F. Leveiller, M. Lahav, Phys. Rep. **246**, 251 (1994).

[8] M. Deutsch and B.M. Ocko, *X-ray and Neutron Reflectivity*, in: *Encyclopedia of Applied Physics, Vol. 23*, Wiley-VCH, Weinheim (1998), page 479.

[9] See e.g. *X-ray and Neutron Reflectivity*, in *Lecture notes in physics M58*, J. Daillant, A. Gibaud (Eds.), Springer, Berlin–Heidelberg (1999).

[10] I. Mellanby and B.M. Ocko, Synchrotron Rad. News **12** (1999).

[11] M. Tolan, *X-ray Scattering from Soft-Matter Thin Films*, Springer Tracts in Modern Physics Vol. **148**, Springer, Berlin–Heidelberg (1999).

[12] W.J. Huisman et al., Nature **390**, 397 (1997).

[13] S. Granick, Physics Today **7**, 26 (1999).

[14] A.K. Doerr, M. Tolan, J.-P. Schlomka, W. Press, Europhys. Lett. **52**, 330 (2000).

[15] J.W.M. Frenken and J.F. van der Veen, Phys. Rev. Lett. **54**, 134 (1985).

[16] J.F. van der Veen, Surf. Sci. **433-435**, 1 (1999).

[17] B.C. Larson, C.W. White, T.S. Noggle, D. Mills, Phys. Rev. Lett. **48**, 337 (1982).

[18] C. Rischel et al., Nature **390**, 490 (1997).

[19] C.W. Siders et al., Science **286**, 1340 (1999).

[20] J.N. Israelachvili and P.M. McGuiggan, J. Mater. Res. **5**, 2223 (1990).

[21] P.A. Thompson and M.O. Robbins, Science **250**, 792 (1990).

[22] M.J. Zwanenburg et al., Phys. Rev. Lett. **82**, 1696 (1999).

[23] M.J. Zwanenburg, J.H.H. Bongaerts, J.F. Peters, D.O. Riese, J.F. van der Veen, Phys. Rev. Lett. **85**, 5154 (2000).

[24] Ch. Brönnimann, S. Florin, M. Lindner, B. Schmitt, C. Schulze-Briese, J. Synchrotron Rad. **7**, 301 (2000).

[25] J.S. Im et al., phys. stat. sol. (a) **166**, 603 (1998).

[26] O.M. Magnussen et al., Phys. Rev. Lett. **74**, 4444 (1995).

[27] M.J. Regan et al., Phys. Rev. Lett. **75**, 2498 (1995).

[28] C.-J. Yu, A.G. Richter, A. Datta, M.K. Durbin, P. Dutta, Phys. Rev. Lett. **82**, 2326 (1999).

[29] M.K. Sanyal, S.K. Sinha, K.G. Huang, B.M. Ocko, Phys. Rev. Lett. **66**, 628 (1991).

[30] B.M. Ocko, X.Z. Wu, E.B. Sirota, S.K. Sinha, M. Deutsch, Phys. Rev. Lett. **72**, 242 (1994).

[31] A.K. Doerr et al., Phys. Rev. Lett. **83**, 3470 (1999).

[32] C. Fradin et al., Nature **403**, 871 (2000).

[33] E. Sackmann, Science **271**, 43 (1996).

[34] D. Beyer et al., Angew. Chemie-internatl. Engl. Edit. **35**, 1682 (1996).

[35] P. Fromherz and A. Stett, Phys. Rev. Lett. **75**, 1670 (1995).

[36] E.A.L. Mol, J.D. Shindler, A.N. Shalaginov, W.H. de Jeu, Phys. Rev. E**54**, 536 (1996).

[37] A. Ponierewski et al., Phys. Rev. E**58**, 2027 (1998).

[38] A.N. Shalaginov and D.E. Sullivan, Phys. Rev. E**62**, 699 (2000).

[39] A.C. Price et al., Phys. Rev. Lett. **82**, 755 (1999).

[40] A. Fera et al., Phys. Rev. Lett. **85**, 2316 (2000).

[41] R.S. Safinya, E.B. Sirota, D. Roux, G.S. Smith, Phys. Rev. Lett. **62**, 1134 (1989).

[42] T. Salditt, I. Koltover, J.O. Rädler, C.R. Safinya, Phys. Rev. Lett. **79**, 2582 (1997).

[43] G.L. Wong, Y.L. Koltover, C.R. Safinya, Appl. Phys. Lett. **73**, 2042 (1998).

[44] C.S. O'Hern and T.C. Lubensky, Phys. Rev. Lett. **80**, 4345 (1998).

[45] K.R. Mecke and S. Dietrich, Phys. Rev. E**59**, 6676 (1999).

[46] F.P. Buff, R.A. Lovett, F.H. Stillinger, Phys. Rev. Lett. **15**, 621 (1965).

[47] R. Evans, Adv. Phys. **28**, 143 (1979).

[48] S. Iatsevitch and F. Forstmann, J. Chem. Phys. **107**, 236 (1997).

[49] S. Dietrich and M. Napiórkowski, Physica A**177**, 437 (1991).

[50] S. Dietrich and A. Haase, Phys. Rep. **260**, 1 (1995).

[51] S. Dietrich, J. Phys.: Condens. Matter **8**, 9127 (1996).

[52] See e.g. *Light Scattering by Liquid Surfaces and Complementary Techniques*, D. Langevin (ed.), Marcel Dekker, New York (1992).

[53] T. Seydel, A. Madsen, M. Tolan, G. Grübel, W. Press, Phys. Rev. B**63** (2001), in press.

[54] J. Wuttke, W. Petry, G. Coddens, F. Fujara, Phys. Rev. E**52**, 4026 (1995).

[55] F.J. Bermejo, A. Criado, A. de Andres, E. Enisco, H. Schober, Phys. Rev. B**53**, 5259 (1996).

[56] P. Lunkenheimer et al., Phys. Rev. Lett. **77**, 318 (1996).

[57] F. Fujara, W. Petry, R.M. Diehl, W. Schnauss, H. Sillescu, Europhys. Lett. **14**, 563 (1991).

[58] J. Jäckle and K. Kawasaki, J. Phys.: Condens. Matter **7**, 4351 (1995).

[59] J. Baschnagel and K. Binder, Macromolecules **28**, 6808 (1995).

[60] J.A. Forrest, K. Dalnoki-Veress, J.R. Stevens, J.R. Dutcher, Phys. Rev. Lett. **77**, 2002 (1996).

[61] Y.C. Jean et al., Phys. Rev. B**56**, R8459 (1997).

[62] M.W. Ribarsky and U. Landman, J. Chem. Phys. **97**, 1937 (1992).

[63] J. Gao, W.D. Luedtke, U. Landman, J. Chem. Phys. **106**, 4309 (1997).

[64] R. Hentschke and R.G. Winkler, J. Chem. Phys. **99**, 5528 (1993).

[65] R.G. Winkler, R.H. Schmid, A. Gerstmaier, P. Reineker, J. Chem. Phys. **104**, 8103 (1996).

[66] A.K. Doerr, M. Tolan, T. Seydel, W. Press, Physica B**248**, 263 (1998).

[67] M.J. Zwanenburg et al., Phys. Rev. Lett. **82**, 1696 (1999).

[68] M. Sutton et al., Nature **352**, 608 (1991).

[69] D.L. Abernathy et al., J. Synchrotron Rad. **5**, 37 (1998).

[70] S.K. Sinha, M. Tolan, A. Gibaud, Phys. Rev. B**57**, 2740 (1998).

[71] S.B. Dierker, R. Pindak, R.M. Fleming, I.K. Robinson, L. Berman, Phys. Rev. Lett. **75**, 449 (1995).

[72] T. Thurn-Albrecht et al., Phys. Rev. Lett. **77**, 5437 (1996).

[73] S.G.J. Mochrie et al., Phys. Rev. Lett. **78**, 1275 (1997).

[74] G. Grübel, D.L. Abernathy, D.O. Riese, W.L. Vos, G.H. Wegdam, J. Appl. Cryst. **33**, 424 (2000).

[75] V.V. Kokorin, Phase Transitions **54**, 143 (1995).

[76] D.-Y. Xing and C.-D. Gong, Chinese Physics **3**, 721 (1983).

[77] M.V. Gandhi and B.S. Thompson, *Smart Materials and Structures*, Chapman and Hall, London (1992).

[78] S.M. Shapiro, B.X. Yang, G. Shirane, Y. Noda, L.E. Tanner, Phys. Rev. Lett. **62**, 1298 (1989).

[79] J.A. Krumhansl and G.R. Barsch, Proc. of the Int. Conf. on Martensitic Transformation, Monterey Inst. of Advanced Studies, Carmel, CA (1992), page 25.

[80] X. Ren and K. Otsuka, Nature **389**, 579 (1997).

[81] K. Bhattacharya, A. DeSimone, K.F. Hane, R.D. James, C.J. Palmstrom, Mat. Sci. Eng. A**273-275**, 685 (1999).

[82] K. Uchino, in: *Shape Memory Materials*, K. Otsuka, C.M. Wayman (eds,), Cambridge Univ. Press, Cambridge (1999), chap. 8.

[83] I.A. Akimov, A.A. Sirenko, A.M. Clark, J.-H. Hao, X.X. Xi, Phys. Rev. Lett. **84**, 4625 (2000).

[84] S.R. Summerfelt, in: *Ferroelectric Thin Films*, R. Ramesh (ed.), Kluwer, Netherlands (1997), chap. 1.

[85] J.F. Scott and C.A.P. de Araujo, Science **246**, 1400 (1989).

[86] B. Xu, Y. Ye, L.E. Cross, J.J. Bernstein, R. Miller, Appl. Phys. Lett. **74**, 3549 (1999).

[87] M. Alexe et al., Appl. Phys. Lett. **75**, 1158 (1999).

[88] M.I. Flik, B.I. Choi, K.E. Goodson, J. Heat Transfer **114**, 666 (1992).

[89] T.Q. Qiu and C.L. Tien, J. Heat Transfer **115**, 842 (1993).

[90] E. Burkel, Rep. Prog. Phys. **63**, 171 (2000).

[91] M. Seto, Y. Yoda, S. Kikuta, X.W. Zhang, M. Ando, Phys. Rev. Lett. **74**, 3828 (1995).

[92] W. Sturhahn et al., Phys. Rev. Lett. **74**, 3832 (1995).

[93] R. Röhlsberger et al., Physica B**263-264**, 581 (1999).

[94] W. Sturhahn et al., J. Magn. Magn. Mat. **198-199**, 590 (1999).

[95] R. Röhlsberger et al., J. Appl. Phys. **86**, 584 (1999).

[96] W.A. Tolbert, W.M. Dennis, W.M. Yen, Phys. Rev. Lett. **65**, 607 (1990).

[97] T.S. Toellner, Hyperfine Interactions **125**, 3 (2000) and references therein.

3.5. Materials Science

This chapter has been written on the basis of contributions to the reports of the workshops "Hard Condensed Matter Physics" edited by Th. Brückel (FZ Jülich) and H. Franz (HASYLAB, Hamburg) (see A.1.3), "Nuclear Resonant Scattering at the XFEL" edited by U. van Bürck (Technical University, München) and H. Franz (see A.1.7), "Surfaces, Interfaces and Nanomaterials" edited by H. Dosch (MPI Metallforschung, Stuttgart) and W. Drube (HASYLAB, Hamburg) (Part-V A.1.9), and "Chemistry Applications of an XFEL" edited by M. Epple (University Bochum) and E. Welter (HASYLAB, Hamburg) (see A.1.2). In these contributions, more detailed description and further references can be found.

In contrast to solid state physics, where physical phenomena are often studied on simple model systems, materials research deals with complex materials. Minute changes of their chemical composition or mesostructure can lead to large effects with respect to physical and/or mechanical properties. The goal is to correlate the macroscopic properties of applied materials with atomic and mesoscopic properties. Examples are alloys with many constituents and complicated precipitate structures, ceramics, materials with intergranular stresses, glasses, artificial fibers, composite materials and magnetic compounds. Finally, interfacial properties are gaining more and more attention, with broad implications for protective coatings and corrosion, lubrication and adhesion, functional layers, and biocompatibility. Some of these aspects have already been discussed in Sec. 3.4. In order to understand and control the properties of certain materials their production process has to be studied in real time. Time-resolved diffraction using hard X-rays in the 100 keV range is the preferred tool to accomplish this task.

Today synchrotron radiation has a very important impact on materials science. In the determination of electronic properties like band structures or band gaps, which essentially determine the function of all devices in information technology, spectroscopy with synchrotron radiation is unrivalled. Resonance scattering has granted new element specific insights into the magnetic properties of matter. In a more general sense, resonant scattering allows for contrast variation in diffraction experiments by tuning the incident photon energy through an absorption edge. This has been very successfully used in studies of alloys by means of X-ray small angle scattering. Time-resolved studies of phase transitions have been performed with synchrotron radiation; however, in most cases only ground state properties have been investigated so far. The temporal resolution provided by the XFEL and by the spontaneous undulator radiation (SUR) will open the possibility to study matter in non-equilibrium states excited by shock waves, by very high pulsed magnetic fields, or by heat waves produced by high power optical or IR laser pulses.

For studies of bulk properties of matter, the limited penetration power of X-rays in the 1 Å wavelength range, varying between ten and some hundred micrometers, is insufficient. However, with the SUR today very intense beams of photons with energies around 100 keV are available which have penetration powers in matter of the same order as thermal neutrons and which are already today used to study bulk properties like local texture and strain deep inside larger components. With the intense hard SUR emitted spontaneously by the XFEL

undulators or special insertion devices, non-equilibrium bulk states can be studied with the intrinsic time resolution defined by the SUR pulse length of 188 fs.

In this materials science section of the TDR the possibilities to apply XFEL radiation to technological and engineering problems is discussed for a variety of substance classes; starting with hard materials (Sec. 3.5.1), then polymer materials (Sec. 3.5.2), and finally nanomaterials (Sec. 3.5.3). In the section on hard materials, we also discuss the possibility of time-resolved investigation of dynamical materials processes in a more general way (Sec. 3.5.1.2). Proposals of such studies for a specific sample system can also be found in other sections. Furthermore, at the end of each section about hard, polymer, and nanomaterials, experimental schemes are described, as these vary quite substantially.

3.5.1. Hard materials

Modern science based developments of materials and processing technologies save time and costs, and this is of central importance for industry in increasingly competitive global markets. Comprehensive characterizations of materials and components are the essential basis to correlate structures with mechanical properties and to reliably assess components at service conditions for their whole lifetime [1]–[3]. For example, novel light weight components made of e.g. Mg, Al and Ti–alloys or intermetallic Ti–Aluminides are being developed for advanced transportation systems to save fuel and costs as well as to protect the environment [4]. Figure 3.5.1.a shows high pressure compressor blades made of Ti-Aluminide. During hot-processing, dynamic recrystallization occurs and a specific texture is generated. In Fig. 3.5.1.b the fine grained microstructure formed by dynamic recrystallization during isothermal forging is seen. After annealing, a fully lamellar microstructure is formed which shows a good creep behavior. Between the constituent phases of the lamellar microstructure, a lattice misfit is present, resulting in high residual stresses of the second and third kind.

In many cases, e.g. during deep drawing or forging of materials, or the optimization of the superconducting properties of high–T_c superconducting ceramics, the control of orientation of grains, the texture, is of crucial importance [5] for physical and mechanical properties. Here hard X-ray diffraction has major advantages, including the ability to follow the evolution of texture of bulk samples during recrystallization at elevated temperature in real time. The properties of most engineering materials depend strongly on the specific microstructure, and hard X-ray diffraction can provide a variety of information over spatial ranges from 1 nm to 10 μm that is important to materials designers as well as process engineers. Relevant systems include precipitates and pores in metallic alloys, ceramics or membranes and particle size dispersion in colloids and aerosols.

The use of hard X-rays above 80 keV enables the investigation of materials without sectioning and therefore provides the possibility to investigate not only grain structures but also dynamical processes, as will be shown below. Even today high resolution diffractometry with very small gauge volumes of $\approx 5 \times 5 \times 50\,\mu\text{m}^3$ has provided information for optimizing processing technologies and for revealing stress related problems. Using the XFEL SUR, high resolution diffraction of selected grains in critical areas, e.g. in welded joints and around crack tips or pores, can be performed for determining the variation of the stress tensor even within grains. Element selective 3D-imaging by absorption or phase contrast

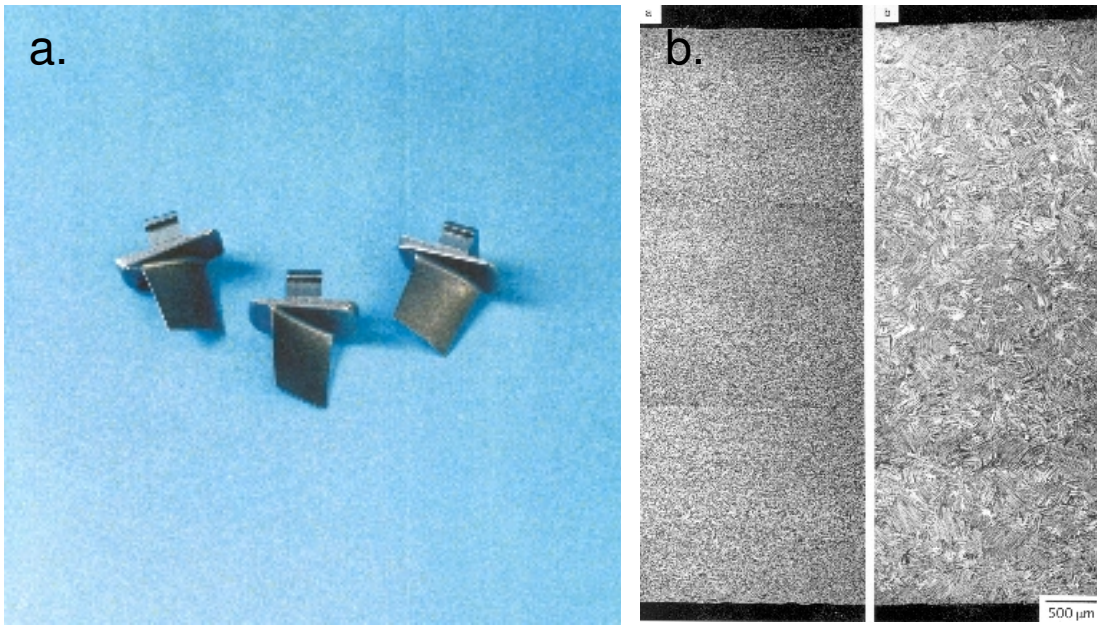

Figure 3.5.1.: *a. High-pressure compressor blades for an aero engine made from a* Γ*-TiAl alloy. The blades were produced by hot extrusion followed by closed-die forging and electro-chemical milling. b. Microstructure of a compressor turbine blade in different stages of processing: A duplex microstructure formed by dynamic recrystallization during isothermal forging at* $1150\ ^\circ C$ *(left) and a fully-lamellar microstructure formed by subsequent annealing at* $1360\ ^\circ C$ *and furnace cooling.*

tomography with micrometer spatial resolution and the study of precipitates and pores by small angle scattering methods are further applications. Hard X-ray reflectometry is beginning to be exploited for the study of interfaces in the bulk of materials, and it has a high potential for analyzing protective layers and coatings, as well as other surface related engineering applications. For hard materials, no other experimental technique may contribute such comprehensive analysis in the bulk and near the surface, and a new quality of data sets will allow for tremendous improvements of finite-element models which are crucial for more intelligent component development.

3.5.1.1. 3D structural characterization of mesoscale systems

Investigating the meso- or nanoscale properties of hard materials has become a focus of the hard condensed matter community. In contrast to the atomic and macroscopic scale, our understanding of the structure on this scale is less mature. In particular, models tend to be based on average properties, despite the fact that the materials often are very heterogeneous on this scale. As an example, the macroscopic properties of metals such as strength or fatigue are governed by the properties of grains and dislocation structures and the neighboring relationships between these objects. The properties of the objects vary by orders of magni-

tude depending on factors such as size and crystallographic orientation. Present structural techniques cannot characterize this heterogeneity. For a summary of this field see [6]. Neutron diffraction and X-ray diffraction with conventional sources lack the spatial resolution for observing the "building blocks". Electron microscopy, on the other hand, probes only the surface. As such it can be used only for "post mortem" analysis. As a result, only static and statistical data are provided. The dynamics thus cannot be probed, and the interactions between objects cannot be observed directly. Also, heterogeneous structures tend to be truly three-dimensional, and sections can be misleading. It is for this reason we propose to investigate structural properties of mesoscale systems in three dimensions at a spatial resolution of $100 \times 100 \times 200\,\mathrm{nm}^3$. Some application to metal and ceramic systems are described in the next two paragraphs.

Metals Typical metal structures are displayed in Fig. 3.5.2, displaying the four inherent length scales: Grain structures in well annealed metals have typical sizes of 1 - 100 μm and are very homogeneous, as can be seen in Fig. 3.5.2.a . Application of stress leads to deformation and the formation of individual dislocations at length scales 0.1 - 1 μm (Fig. 3.5.2.b). Increasing the deformation leads to dislocation structures at the few micrometer scale (Fig. 3.5.2.c). Upon annealing, new nuclei are formed which grow from the matrix and show no dislocations (Fig. 3.5.2.d). The processes of deformation and annealing are important in every materials 'life' and it is evident that dynamic, e.g. time-resolved, data will help in understanding the underlying processes. Such data can only relate to the bulk of the material, as the surface is non-representative due to stress relaxation, dislocation migration, pinning on surface grooves, etc.. The following specific questions of vital interest motivate such 3D structural investigations to include :

- How do dislocation structures emerge from individual dislocations?
- How do grains and dislocation structures deform?
- Nucleation: Where in the deformed material do nuclei form, and what are the orientation relationships between nuclei and the sites at which they form? What is the nucleation mechanism?
- Growth: How do the nuclei grow - what are the kinetics as a function of the relative orientations of the nuclei and the surrounding dislocation structures? Does the morphology of the dislocation structure play a role? How are the various types of dislocation structures actually absorbed into the moving interface of the nuclei?

These topics have been addressed in much detail by traditional means, but answers have been elusive. The XFEL SUR should be able to provide answers to some of these questions. Furthermore, combined dynamic investigations will be possible on three of the inherent length-scales: those of the sample, grain and dislocation structure. Hence, such data will be instrumental in the development of global models that bridge the length scales; in other words, in anchoring the macroscopic properties of interest to engineers to the mesoscale properties. The case for (industrial) alloys is similar, with the addition that the simultaneous

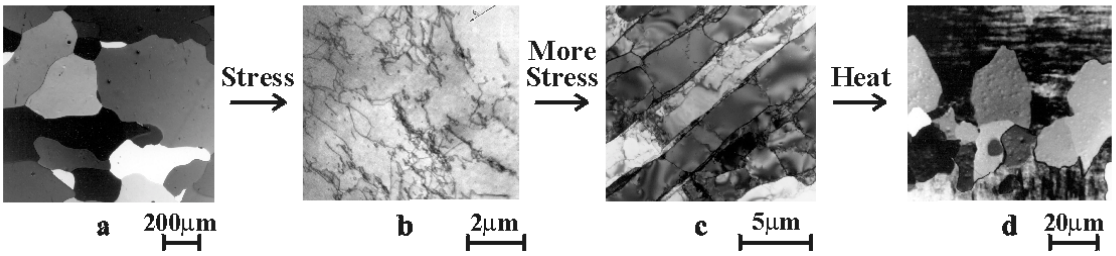

Figure 3.5.2.: *Typical metal structures seen in traditional microscopes. This set of micrographs is snapshots in time of what is seen at different and random locations after exposure to stress and heat. No direct information about dynamics can thus be obtained using this method. (a) A well annealed grain structure shows evidence of tangled dislocations after some deformation (b). With more deformation these form into dislocation structures (c). Upon annealing new nuclei form and grow from this deformed matrix (d).*

use of tomography will be helpful in mapping and identifying secondary phases, inclusions, etc..

Ceramics Modern ceramics tend to be heterogeneous partly because non-equilibrium parts of phase diagrams are used and partly because function/cost considerations dictate the use of several components (multilayers, inclusions). The kinetics of the reactions, phase transformations, etc. depend on the local environment of the grains, whether in the form of powders or sintered pellets. Again, surface studies are non-representative as the diffusion mechanisms are different. By providing local-scale information, ceramics processing will take a major step away from the present state of trial-and-error.

The study of grain dynamics with the XFEL SUR will allow the kinetics of the individual grains to be observed without locating the grains exact positions. This will be a substitute for conventional in-situ powder diffraction. "Single crystal" structure refinements are applied here. In this way, a statistical study can be performed based on groups of grains with specific volume, orientation and/or stoichiometric properties. Furthermore, reactions between neighboring grains can be observed directly by high resolution mapping. The resolution of 100 nm fits well with the grain size of many powders. The combination of diffraction and imaging is particularly attractive in this case, since structure and density of the various grains often are unknown.

3.5.1.2. Dynamic processes and time-resolved investigation

The understanding of reactions during materials processing will be founded on a new basis if it will be possible to provide experimental data and correspondingly refined modelling at spatial resolution below 1 μm and temporal resolution below 1 μs. Real time small angle X-ray scattering analysis may further be performed to analyze dissolution or coarsening of precipitates or pores with sizes smaller than $\approx 1\,\mu$m, whereas the opening and closing of larger pores formed e.g. during creep or close to a crack tip may be measured using radio-

graphy for varying external load. Thus, comprehensive 3D pictures of local microstructures may be derived with an information content close to that obtained by the use of electron microscopy. A few examples from prominent areas have been selected below and indicate that time-resolved hard X-ray measurements at the XFEL can improve to a great extent the present-day knowledge of processing technologies. This applies equally to techniques not mentioned yet, like extrusion, powder processing, sintering, cutting, carburizing, rapid solidification, and joining. Even extremely fast processes like brittle cracking or fast deformations of materials by shock waves can be analyzed.

Analysis of turbine blades under load Analysis of stresses within grains, even in rapidly rotating components such as compressor and turbine blades of aero-engines, will become feasible. Measurements may start with high resolution 3D mapping of grains within selected volume elements with the component being at rest. Afterwards, the variation of lattice spacings at high rotation frequency may be followed in selected grains through the use of adequate wavelengths and detector positions. Taking the proposed time structure for the XFEL (see Sec. 4.1) with the high repetition rate within bunch trains, distances between gauge volumes in the range of 1 μm may be realized even in the case of very high rotation frequencies of up to 30000 min^{-1}. Changes of stress fields, movements of grain boundaries, and the formation of pores during creep testing may be analyzed *in-situ*. This also holds for the much more complicated structural changes in front of crack tips.

Real-time investigation of welding The high intensity and repetition rate of XFEL SUR pulses will further allow to novel real time analysis of fast materials processing. It will, for example, be feasible to study in-situ fast formation and deformation of grains as well as precipitation reactions during welding. This will tremendously increase our basic understanding of formation of microstructures in welds, which is regarded as an excellent basis for improving this joining technology. Time-resolved hard X-ray measurements at the XFEL laboratory are expected to greatly improve our knowledge of further processing technologies.

Precipitates and pores The anticipated time resolution will allow the analysis of extremely fast growth and shrinkage of precipitates or pores. These effects may occur, for example, near crack tips, during melting, during solidification and fast cooling of droplets in powder processing, or during laser treatments of surfaces with local melting and fast cooling afterwards. Further novel analysis will be based on the extreme intensity of beams with areas even less than 1 $\mu\mathrm{m}^2$ which may allow tomographic small angle X-ray scattering investigations to be performed. These may be performed simultaneously with grain mapping so that spatial variations of sizes and number densities of precipitates and pores may be derived. Such analysis will, for example, significantly improve our basic understanding of failure mechanisms of materials around crack tips or the incoherent formation of creep pores in alloys and ceramics [7].

Diffusion at grain boundaries It is generally believed that properties of polycrystalline materials are determined by grain-boundary diffusion rather than in-grain diffusion. Diffusion from grains and grain-boundaries can be measured and separated in nuclear resonance scattering experiments. Here, only slow dynamics, i.e. movements on a timescale longer than typical vibration times (ps range) are considered. In this area, transport of matter via diffusion or long range relaxation modes is of major interest. Deformation or degradation of materials is governed by such processes. Also, coarsening phenomena in polycrystalline materials is a topic of technical relevance. Quasi-elastic nuclear forward scattering [8], which allows the study of the dynamics of resonant nuclei, and time domain interferometry [9], which allows the measurement of the intermediate scattering function of non-resonant samples, are current techniques to study diffusive motion using synchrotron radiation. Focussing in the μm range at the XFEL will allow single grain properties in polycrystalline material to be studied. This gives access to detailed information of jump-vectors and frequencies without the need to use single crystals (which may be difficult or even impossible to grow). Similar information may be gained by using imaging techniques. In particular, diffusion at grain boundaries could be studied in a unique way.

Ultra-short pulse laser interactions with matter The interactions of high power, short-pulse lasers with materials have recently aroused a lot of interest in both the scientific community [10, 11] and the technological arena [12]–[15]. One the one hand, understanding of the fundamental processes and basic mechanisms such as energy transfer from laser field to material, energy transport and subsequent athermal or thermal modifications in the material are largely lacking on one hand. On the other, technological processes such as laser drilling [16] and cutting, machining [15] and peening, and laser ablation for thin film deposition [12] have now been developed as alternative and replacing technologies for conventional processes. Laser damage in optical materials [16] present technological roadblocks to high-tech processing of materials.

Given the femtosecond time structure and extremely high brilliance of XFEL sources, the dynamics of ultra-short pulse laser interaction with matter may now be explored experimentally by using a variety of time-resolved and spatially resolved techniques. These include diffraction, imaging, and a whole host of spectroscopic methods to capture and record modifications in crystal structure, phase transformation [17, 18], morphology, and microstructure evolution which occur during the time the material "sees" the laser light. Such dynamical data will in turn help to verify existing models and to construct new and better models of laser-matter interaction processes. These advances will further our basic understanding of laser based technologies and help us to improve and develop them for future material processing and fabrication.

3.5.1.3. Experimental schemes

The 3D XRD microscope at ESRF for 50-100 keV X-ray energy [19] is a suitable instrument for the presented investigations. Under favorable conditions, a complete mapping of bulk material on the grain scale can already be done, but investigations at of the dynamics at nanoscales remains impossible. We propose to establish a 3D microscope dedicated to three

dimensional nanoscale investigations of structural properties using XFEL SUR. The aim is a simultaneous mapping of the pertinent features: identification, morphology, orientation, and strain. This is to be performed in depth and with a speed that allows in-situ studies under standard processing conditions. There exist superior options for nano-focusing of hard X-rays. With a focal distance of several meters - allowing large sample auxiliaries for processing experiments - and a beam divergence matching the requirements for strain analysis, a spot-size of 100×100 nm^2 should be feasible at 100 keV. (Also, the minimal beam size that can be defined by a slit is $\Delta = 0.62\sqrt{\lambda R}$, where R is the slit-to-sample distance. With the high flux available up to 1 MeV, a 100 nm beam could possibly be produced by slits.) The longitudinal resolution should be 200 nm.

The combination of high resolution imaging by phase contrast tomography and diffraction studies will be possible. Its value is perhaps best illustrated by analogy to electron microscopy, where the two techniques have merged completely. As one example of an area that would obviously benefit from the combination, we mention fatigue, where imaging can be used to visualize crack fronts and diffraction to measure the strain field around them. Instrumentally, the merge is considered unproblematic, as techniques for X-ray tracing and holotomography are quite similar.

For the investigation of dynamical processes, one notes that radiographs may be produced with photons from one bunch, corresponding to an exposure time of ≈ 200 fs. They will allow any moving object to be imaged with a spatial resolution in the submicron range without any spatial smearing. New perspectives will thus arise for real time radiological investigations of for example solidification and segregation processes in metallurgy and materials science, rapidly rotating engines, surface treatments of materials, or chemical reactions to name a few. Hard X-ray radiography, high resolution diffractometry and small angle scattering investigations may be combined for fast and comprehensive analysis of materials processing or failure mechanisms. New perspectives are thus expected for in-situ investigations on e.g. formation kinetics of pores and phases in metal foams, dynamic recrystallization and formation of textures, formation of creep and fatigue pores, and local plastic deformation and pore formation near crack tips.

3.5.2. Polymers

Polymers play an important role as materials. The macroscopic properties of a polymer material, such as mechanical strength, are determined by its microscopic structure down to the atomic length scale. Experiments with synchrotron radiation are able to reveal the relations between the processing conditions of a polymer material, like applied temperature programs or mechanical elongation, and its response in terms of structural changes and consequently of the macroscopic properties. Therefore, such studies can help to find the processing conditions which lead optimally to structures having the desired macroscopic properties of the material. By knowing the relationship between processes and structural changes on one hand and between structure and macroscopic properties on the other, the problem of finding the optimum processing conditions is no longer a question of trial and error, but can be solved on the basis of principal knowledge.

Polymers and biopolymers are the most representative examples of soft condensed mat-

ter. The classical aspects of polymer science cover mainly the behavior of bulk polymer materials. During the last few years, new aspects have entered the field of polymer science. These deal with the functional properties of systems based on polymers. Keywords for these exciting new developments are, for example, electrically conducting polymers, photo- and electroluminescence, laser emission, thin- and ultra-thin polymer membranes, interfaces between polymers and other materials, and micro- and nanostructured polymer systems. This research is stimulated by the idea to use polymers as functional components in molecular electronic devices, in membranes for specific filtering applications on a molecular scale, polymer light-emitting diodes for electronic display applications, in polymer laser diodes, or in optical data storage media (see e.g. [20] for an overview). For these new fields, the study of bulk materials does not play a major role anymore. Therefore, new techniques came to the focus of interest.

During the past twenty years, synchrotron radiation has established itself as a powerful tool for research on synthetic polymers . X-ray scattering techniques using synchrotron radiation in the wide and small angle X-ray scattering regimes were used to study processes of crystallization, phase separation, and chain orientation in a wide variety of polymer systems (see e.g. [21]). Many of these experiments were carried out under real-time *in-situ* conditions on a time scale of a few seconds. Such experiments would not have been possible without the help of synchrotron radiation because most soft condensed matter systems (colloids, liquid crystals, synthetic polymers, functional materials, etc.) are extremely weak scatterers of X-rays. The results of the experiments had great impact on understanding fundamental relations between thermal and mechanical treatment of polymer materials and the resulting structural changes like phase formation, changes of structure within the phases, and phase orientation [22]. Additionally, in real-time experiments the dynamics of these changes could be studied. These investigations have provided important insights into fundamental laws of the mechanics and thermodynamics of polymer systems. Besides this aspect of basic research, preferably carried out on model substances, there is also the aspect of applied research.

Concerning the use of synchrotron radiation in this field, there are especially two new methods: Scattering using a microfocus beam, and scattering at surfaces and interfaces under grazing incidence. In recent years, the first attempts have been made to use grazing incidence scattering and X-ray reflectivity measurements to study interfaces and thin polymer films down to monomolecular layers. Another effort has been made to use microfocus beams to perform scattering experiments on distinct microphases within a sample and to use this technique to scan along the sample to reconstruct sample images based on the information obtained from the scattering patterns. At present, even at the most powerful instruments, this technique suffers from a lack of intensity. Since the X-ray beam has to be significantly focused a strong increase of beam divergence follows making it difficult to realize a scattering set-up with the desired angular resolution. If, on the other hand, a small divergence is maintained by means of collimation, the intensity left in the microbeam becomes very low. Therefore sources with small beam cross section and divergence are mandatory and even present state-of-the-art undulator sources at third generation storage rings still place severe restrictions on this kind of experiment. The same applies for the use of coherence. In recent years, a couple of attempts were made to use synchrotron radiation from undulator sources

for X-ray photon correlation spectroscopy on polymer systems [23]. This technique could be useful to study critical fluctuations near phase transitions of multi-component systems or the molecular mobility in the vicinity of interfaces. Useful information about diffusive mobility within the sample could be obtained with this technique. But the required degree of coherence has to be obtained by strong collimation of the beam, which severely reduces the intensity.

Up to now time-resolved experiments with synchrotron radiation in polymer science were typically carried out on time scales from seconds up to a few hundred seconds. This is sufficient for studying processes like crystallization, melting, phase separation, and reorientation, where thermal conductivity or other factors within the sample limit the speed of the process. There are other processes which cannot be investigated this way. For instance, microstructural changes in highly oriented polyethylene, involving details larger than 100 nm, have been recently studied using ultra small angle scattering [24]. The time resolution of such experiments is well above the hundred second scale due to the very long sample detector distance. Other examples would be reorientation of segments in liquid crystalline polymers as a result of rapidly changing external electrical fields, phase changes due to rapid heat deposition by short laser pulses, conformational changes of photoactive sites in polymers caused by short laser pulse excitation, and fast diffusion of polymer segments on the atomic length scale. This kind of time-resolved experiments on time scales down to the femtosecond regime will become especially important when one studies the new functional polymer systems mentioned above. These problems cannot be addressed even with the most sophisticated synchrotron sources presently available, but many of these experiments would be feasible at the XFEL laboratory.

3.5.2.1. Structural changes

Phase formation An inhomogeneous sample is scanned on a one- or two-dimensional raster of μm spatial resolution (see Sec. 5.3.3.3 for details). Certain information in the scattering patterns is used to reconstruct an image of the sample which visualizes the spatial distribution of structural properties. One application of this is the observation of structural changes along the cross section of a polymer fiber during melt spinning. Present techniques allow only scattering patterns which average over the whole cross section to be obtained. Surface effects on the structure formation cannot be distinguished [25]. If a periodic line scan is performed across the fiber during the continuously running fiber spinning experiment, a 100 μm thick fiber could be spatially resolved into about 100 distinct regions which give information on structural differences (crystalline structure, chain orientation) between the material in the center of the fiber and that close to the surface. In addition, the distance between the extruder nozzle and the X-ray beam can be varied to study in detail how the structures are formed after the melt has left the nozzle. Such investigations are of great value for the development of optimized processes to produce fibers with special desired properties.

In the case of homogeneous samples, raster scanning can be used during structural changes on the nanosecond or microsecond time scale to obtain time-resolved scattering patterns of these changes in real-time, as will be discussed in Sec. 5.3.3.3. The shortest time resolution is given by the time distance between two adjacent pulses in the bunch train, i.e.

93 ns at minimum. On the other hand, the longest time available to observe the process is given by the duration of a complete bunch train, i.e. 1 ms at maximum. This technique becomes necessary if irreversible processes are involved or if radiation damage caused by a single-shot exposure does not allow stroboscopic or pump-probe experiments. It allows the study of the early stages of phase formation in polymers, like crystallization or the growth of latex particles during the polymerization process.

3.5.2.2. Dynamics of polymers

Reorientation of polymers Using the XFEL radiation two-dimensional scattering pattern is acquired with one single bunch pulse. After this exposure, sufficient time is available to read out the detector contents. With this kind of experiment conventional integrating detectors like CCD cameras or image plate detectors can be used. Due to the short exposure time of about 100 fs, snapshots of rapidly changing structures can be obtained this way, as the scattering patterns are not averaged over time when structural changes on a picosecond time scale or above are involved. If the structural changes are reversibly periodic, like segment reorientation in liquid crystalline polymers in response to a periodically changing external electric field, like changes during rapidly oscillating external mechanical forces, or like laser induced conformational changes at optically active polymer sites, stroboscopic or pump-probe techniques could be used to resolve the course of these changes over time. The moment at which the exposure takes place has to be synchronized to the phase of the external field or to the moment of external excitation. In this way a series of scattering patterns can be obtained as a function of the phase of the external field or of the elapsed time after excitation. This technique could be used to study the behavior of new polymer systems which are candidates for fast data storage, display applications, or molecular electronic devices [26].

Crystallization, growth, nucleation Crystallization could be initiated by heat deposition in an initially amorphous material by means of a short laser pulse immediately followed by the observation of the time dependence of the X-ray scattering. Up to now only the late stages of a crystallization process have been accessible, while the nucleation and early growth are below the available time scale [27]. But these processes which take place within the first millisecond determine to a great extent the phase formation behavior on the longer time scale and consequently the properties of the finally formed material. Therefore, these early processes of nucleation and growth are of great importance and have not been well understood up to now. Another example covers the field of high strength polymer fibers. These light weight fibers are generally soft and flexible at low deformation rates but become extremely strong under high impact rates (>50 m/s). This new class of high performance polymer materials includes morphologically different systems like gel-spun ultra-high molecular polyethylene or nanocomposites of carbon nanotubes in a polymer matrix [28]. The structure/property relationship under the high deformation rates is not well understood. X-ray investigations of these materials require the observation of X-ray scattering during ultra-fast deformation processes with time resolution in the μs-range.

Fast diffusion Investigations of phase fluctuations in polymer multiphase systems will be possible using X-ray Photon Correlation Spectroscopy (XPCS). Depending on the time regime of interest this measurements can be done using the normal pulse sequences of the XFEL or by split-and-delay techniques as is outlined in Sec. 5.3.2.2. It is of special interest to study these fast fluctuations at conditions (e.g. temperatures) at which the sample approaches a phase transition. This can reveal useful insights into the dynamics of the local diffusion processes on which the phase transition processes are based.

XPCS allows to investigate the diffusive motion of polymer molecules which take place on time scales down to picoseconds and on length scales down to about 0.1 nm. It would thus become possible to probe the local dynamics of polymers which are directly related to its macroscopic dynamic mechanical properties, e.g. elastic response at short times and viscous flow behavior at long ones. The basic theoretical description of the chain diffusion in an entangled environment is given by the reptation model [29] where a single chain performs a random walk along a tube formed by temporary entanglements with neighboring chains. The relaxation within this tube was verified by neutron spin-echo investigations [30], the reptative relaxation could not be addressed with this method because the delay times in neutron spin-echo measurements are too short for this processes. The reptation model predicts that compositional fluctuations at wavevectors which are large compared to the polymer radius of gyration should show a relaxation rate which is independent of the wave vector and is given by the inverse of the time the polymer needs to reptate out of its original tube [31]. XPCS with XFEL sources should be able to verify this behavior by probing polymer motions on length scales comparable to or smaller than the polymer radius of gyration and on time scales comparable to the disentanglement time.

Of special interest are collective diffusion mechanisms in restricted chain environments, like in membrane layers and composite materials or in entangled polymer systems. The measurements will allow to test the dynamic random phase approximation which predicts collective dynamics of polymer blends and mono-disperse entangled melts of flexible polymers from single-chain motions.

3.5.2.3. Materials properties

Fatigue of polymers In some cases structures are formed which are randomly distributed in the sample. An example is the formation of micro-cracks (crazes) during elongation of a polymer sample [32]. This craze-formation is the early stage of fatigue of a polymer material. Scattering experiments with a micro-focus beam allow to observe a single craze and the time course of its formation. However, the problem is that one does not know the locations at which crazes will appear. Rapid periodic scanning along a line can help to solve this problem. With the scanning scheme discussed in Sec. 5.3.3.3, each point in the line-scan can be observed with a time resolution of about 10 μs. In this experiment, the sample can either be elongated continuously or subjected to a periodic external force.

3.5.3. Nanomaterials

Due the increasing miniaturization of device structures, mainly of integrated circuits in the semiconductor industry, but also of magnetic, optical and biological sensors, there has been a tremendous interest recently in the manufacturing and the characterization of structures on a nanometer size scale. Besides the interest in miniaturization, there is an even more important aspect to the use of nanostructures in modern technological applications.This is the fact that the material properties of nanostructures can be tailored by changing the size of the structures. Tailoring material properties by exploiting quantum size effects promises to lead to a technological breakthrough similar to the introduction of semiconductor heterostructures, which has been awarded with the Nobel prize for physics in the year 2000.

There has been a tremendous impact on our current understanding of the growth and the structural properties of nanostructures through the use of scanning microscopy techniques which enable us to achieve atomic resolution in real-space structural determinations. However, similar experimental techniques to obtain element specific electronic structure information on a nanometer scale are still lacking.

3.5.3.1. Nanoscale spectroscopy

Coherent FEL radiation has unique properties (high photon flux, high resolution, variable polarization, element specificity, surface sensitivity, sensitivity for chemical and magnetic properties) that enable it to overcome this gap and provide a photon beam of sufficient quality for the spectroscopic investigation of nanostructured materials. The aim of the project is to built a photoelectron spectrometer to perform element specific high-resolution core level photoelectron spectroscopy with a spatial resolution in the range of a few nanometers. This should provide unique information on the electronic structure and the chemical composition of single nanostructures or even large single organic molecules. To achieve this goal it is planned to combine the technologies developed for scanning microscopy with photoelectron spectroscopy. Due to the high coherent photon density of the FEL radiation, it should be possible through the use of special optics based on photon sieves to illuminate only sample areas in the nanometer range with a sufficient amount of photons to perform spectroscopic investigations. A prototype instrument is currently under construction and will be tested at the Tesla Test Facility VUV-FEL.

3.5.3.2. Structures of nanocrystals

Despite the fact that nanoparticles obtain many of their fascinating properties only as an ensemble of many particles, it may be of interest to study properties of a single particle. This would be of particular interest for in-situ studies of catalytic or magnetic behavior. Alternatively, investigating ensembles requires non-interacting particles with exactly the same size in order to obtain information about a single particle. In the following a possible applications of the proposed XFEL laboratory for structural investigations of nanocrystalline compounds in the form of single particles are presented.

Rough estimates show that single exposures of nanocrystalline materials with diameters of 100 nm will be possible within 1 s. The proposed XFEL facility will therefore be of great

interest for structural studies of two different classes of nanocrystalline materials. The first class includes all materials commonly known as nanocrystals i.e. materials with particle size in the range up to some 50 nm and in many cases a lack of translation periodicity. Important groups of these materials are metal alloys and special ceramics based on oxides [33]. A common trend in modern material science is the adsorption of organic and metal-organic molecules onto the surface of nanocrystalline particles. The second class of materials comprises the extremely fine particles of clays and clay minerals. These materials usually do show translation periodicity; however, they are in many cases highly disordered.

Due to their finite size, these materials can not at present be investigated by single crystal X-ray diffraction techniques. At the same time, powder diffraction data are affected by the lack of translation periodicity, the finite size of the particles, the high defect density, the particle size distribution and the variation of structure and defect density of the different particles. As a result, powder diffraction patterns do not show sharp Bragg reflections and consist of an incoherent ensemble average not suitable for detailed structural determination.

To collect diffraction data the sample has to be manipulated with extreme resolution and present-day technology of AFM microscopes will be useful to fulfill the diffractometer requirements. One should consider the option of not preparing individual particles at all. The particles could be blown through the X-ray beam in a highly diluted gas stream. New techniques will have to be developed to synchronize the movement of such small particles with the X-ray beam and the detection system. One would obtain a series of diffraction patterns at random orientation of different particles, each recorded with a fully transversely coherent X-ray beam. Analytical techniques, that have been established for electron diffraction will have to be applied here to analyze the diffraction patterns in order to obtain structural information about the samples.

For the detailed structural analysis of single crystals, it is important to obtain integral Bragg intensities with high reliability. Therefore, it is necessary to establish a highly precise monitoring system for intensity, coherence and wavelength. To record in addition time-dependent diffuse data, similar monitoring is needed, and comparable intensities in time intervals from milliseconds to several seconds have to be provided. An estimate of the sample sizes and exposure times that takes sample damage into account, based on a rough comparison to experiments at the ESRF, shows that for a crystal of $100 \times 100 \times 100\,\mathrm{nm}^3$ size and an exposure time of 1 s, diffracted intensities would provide a signal allowing the structure to be solved with sufficient accuracy. The information obtained from these data will be sufficient to determine accurately the structure (Bragg peaks) and the degree of disorder (continuous diffuse scattering). (Note that different to the example of clusters discussed in Sec. 3.5.3.3, this estimate extrapolates conventional X-ray diffraction.)

If sample degradation due to radiation induced damage turns out to be tolerable, much smaller samples will be feasible, offering the exciting prospect of studying individual single nano-crystalline particles with X-ray diffraction techniques. With increasing sample size and respective beam diameter, the time scale is reduced correspondingly. If for example 1 μm resolution is considered sufficient for the determination of the local structure fluctuation, a thin needle or flat sample of larger overall dimensions can be sampled with a primary beam size of 1 μm diameter. In this case an exposure of 600 ns is sufficient to record the diffuse scattering in a single orientation.

Particularly, for single crystal diffraction of crystals with strongly fluctuating properties, the sample stability is of crucial importance. Whether samples will be stable under the intense XFEL beam can not at present be answered with any degree of certainty. The experience with clay minerals studied at the micro-focus beamline at the ESRF shows that purely inorganic samples are stable under the present conditions. Organic samples and intercalates of organic molecules into clay minerals are much less stable even at low temperature. Data collection with protein crystals requires a shift of the sample normal to the X-ray beam along the spindle axis of the diffractometer to gain access to undisturbed sections of the sample. These types of samples can be expected to suffer serious radiation damage within short exposures, possibly even during a single bunch. Diffraction studies on well crystallized materials can rely on a series of exposures using several crystals, although the mounting and preparation time would greatly reduce the efficiency gained from the extremely high source brilliance. Translation of the crystals to expose different areas is a second, far less time consuming possibility. On the other hand, disordered samples will vary from specimen to specimen, so that fully coherent radiation exposures of two samples are not immediately comparable. This situation will become even more complicated for nanocrystalline materials without translational symmetry. Structural investigations on these samples will have to be carried out on a single crystal.

Diffraction experiments that require very high scattering vectors, such as electron density studies and the determination of the pair distribution function, will not use SASE FEL radiation, but have to rely on the spontaneous radiation available for the hard X-ray regime. The use of very hard X-rays offers unparalleled access to very long scattering vectors, which in turn will give very high resolution electron density distributions and pair distribution functions.

3.5.3.3. Imaging of small objects

One potential of the XFEL lies in the ability to measure the time-evolution of transient structures on the 100 ns time-scale of the XFEL pulse spacing. The 100 fs exposure time of a single bunch might catch a spontaneous fluctuation on that time scale. It is estimated that crystalline objects 10 nm across would give measurable diffraction patterns, and objects 100 nm across would be measurable during a single XFEL pulse. This type of application requires all the special properties of the XFEL: a coherent beam for the imaging, intensity because of the object size, and intensity and time structure for time-resolved experiments.

Consider a crystal surface with an area of only a few square micrometers. The coherent XFEL produces enough photons to fully characterize such an area in one bunch train, thus in 1 ms. It will thus be possible to see step dynamics on the time scale of these bunch trains (200 ms). The dynamics can be caused either by statistical fluctuations or by growth or etching. This imaging would not only be faster than is currently possible, but could also be applied to systems under high gas pressure or at high temperature, or to surfaces buried under a solid or liquid, for which there are no alternative techniques. On a much slower time and larger length scale, a silicon wafer has been imaged in this way during the etching of the native oxide [34].

Of considerable scientific interest are the spontaneously nucleated clusters of a crys-

talline solid in an aqueous solution close to saturation. Time-resolved experiments with the XFEL would permit testing of the microscopic theory of classical nucleation, which has not been possible before. According to theory, solute molecules randomly associate into clusters with a thermodynamic equilibrium distribution, so that the largest clusters are the scarcest (Fig. 3.5.3). Once a cluster exceeds the critical nucleus size, it becomes thermodynami-

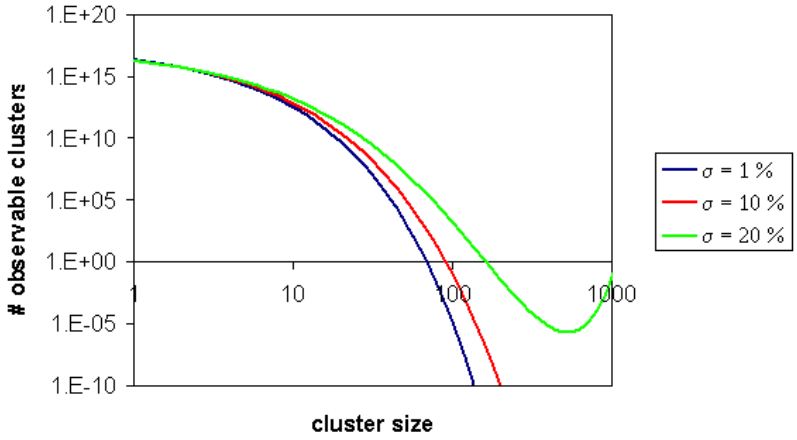

Figure 3.5.3.: *An estimated cluster-size distribution as a function of supersaturation σ according to standard nucleation theory. Only few clusters exist at a appreciable size.*

cally stable and grows into a macroscopic crystal. In standard nucleation theory, a smooth size distribution of small crystallites is assumed to be present up to the critical nucleus size. However, one can imagine that in reality the size distribution is not smooth, but that certain sizes are preferred. In the case of 2D nucleation on metal surfaces, such magic clusters have been observed using STM [35]. The sub-critical nuclei may also have a shape or structure that deviates substantially from that of the bulk crystals that eventually grow out of them.

X-ray diffraction from a small object is *inherently coherent* diffraction. Figure 3.5.4 shows a theoretical example of such a pattern. Since it is a continuous function of reciprocal space, it is invertible into a real-space image of the object under investigation. Methods to perform this inversion are still under development, but we are confident that this will be possible by the time the XFEL radiation will be available. Since we are interested in atomic scale fluctuations upon a large background of parent material, it is advantageous to concentrate the beam onto a reasonably small sample volume of the order of a 1 μm^3 so as to improves the statistics. Since the source is diffraction-limited, it is inherently coherent and would not be expected to limit the ability to invert the diffraction patterns obtained.

Imaging and coherent diffraction from surfaces and clusters The XFEL source size and divergence are suitable for this purpose, so long as the focussing can be achieved faithfully, and with a reasonable demagnification (around 100:1). The instrumentation re-

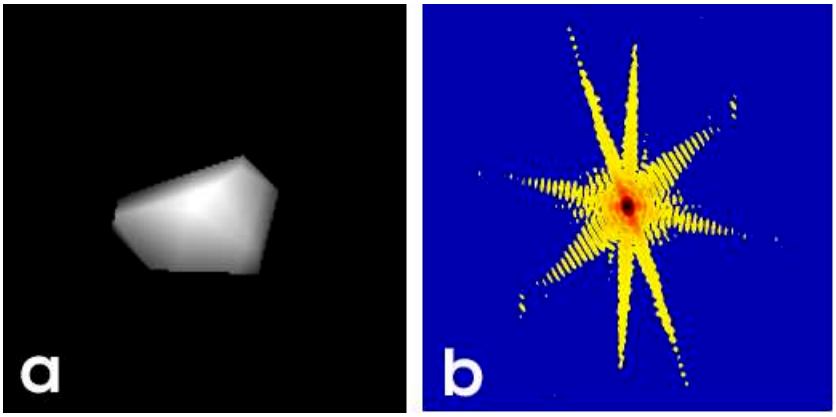

Figure 3.5.4.: *(a) Computer-generated model of a small crystal with randomly chosen facet directions. The grey scale denotes the thickness of the crystal.*
(b) Simulation of the coherent diffraction pattern of the small crystal. Note that the streaks are crystal truncation rods corresponding to the facets seen in (a). Where two facets oppose each other, the streaks become strongly modulated in intensity.

quired would be a diffractometer with a very long detector arm, able to reach the two-theta angles for diffraction from small-unit-cell crystals. The length of the arm needed depends upon the pixel size of the detector. It is necessary to have several pixels within each "speckle" of the diffraction pattern. The speckle size is the inverse of the particle size under investigation, so the length of the detector arm can be used to adjust the angular acceptance for each pixel. If the pixels are a few millimeters in size (see below), the arm may have to be tens of meters long. Most of the technical difficulties envisaged concern the detector. To have a 2D array with 100 ns time resolution is the goal. Energy resolution, although desirable, is a lower priority because a monochromator can be used before the sample. It is not believed that a CCD will be developed with sufficient readout speed, although this might be possible with a 1D linear array shifted at high speed into a 2D readout array. A better solution would be to develop a new detector based on scintillator or avalanche photodiode pixels, each with an electronic readout chain. To accept very high count rates, the measurement should be analog, proportional to the number of photons reaching the detector during the 100 ns between pulses. The detector would need to operate in at least two different modes. In the first it would measure the temporal correlation function, pixel by pixel, without storing the full time sequence. The second mode would be triggered by an "event" as a particle-physics detector would be. The event would be either a larger-than-threshold intensity caused by a fluctuation in the sample or else an external trigger produced by an irradiating ion. Full frames of pixels would only need to be saved around the time of the triggering event for later analysis. Since the experiments envisaged require seeking a small signal on a high background, the background subtraction should be an integral part of the signal processing in each pixel.

Bibliography

[1] F. Appel and R. Wagner, Mat. Sci. Eng. R**22**, 187 (1998).

[2] H. Clemens and H. Kestler, Advanced Engineering Materials **2**, 551 (2000).

[3] W.T. Marketz, F.D. Fischer, H. Clemens, Z. Metallkd. **90**, 588 (1998).

[4] G. Sauthoff, *Intermetallics*, VCH, Weinheim (1995).

[5] R.W. Cahn, *Measurement and Control of Texture*, in *Materials Science and Technlogy, Vol. 15*, R.W. Cahn, P. Haasen, E.J. Kramer (eds.), VCH, Weinheim, (1991).

[6] See e.g. Proc. of Risø Int. Symp. on Mat. Science **1-21**.

[7] H. Riedel, *Fracture Mechanisms*, in *Materials Science and Technlogy Vol. 6*, R.W. Cahn, P. Haasen, E.J. Kramer (eds.), VCH, Weinheim (1992).

[8] B. Sepiol, A. Meyer, G. Vogl, H. Franz, R. Rüffer, Phys. Rev. B**57**, 10433 (1998).

[9] A.Q.R. Baron et al., Phys. Rev. Lett. **79**, 2823 (1997).

[10] B.C. Stuart et al., Phys. Rev. Lett. **74**, 2248 (1995).

[11] B.C. Stuart et al., Phys. Rev. B**53**, 1747 (1996).

[12] B.C. Stuart et al., J. Opt. Soc. Am. **13**, 459 (1996).

[13] J. Neev et al., IEEE, J. Selected Topics in Quan. Electron. **2**, 790 (1996).

[14] M. Feil et al., Appl. Surface Science **127-129**, 869 (1998).

[15] M.D. Perry et al., J. Appl. Phys. **85**, 6803 (1999).

[16] For example, see Proc. 30th Ann.Conf. in Laser Damage in Optical Materials, SPIE vol. 3578, (1999).

[17] C.W. Siders et al., Science **286**, 1340 (1999).

[18] M. Rouhi, C&EN, Nov. 15, (1999).

[19] D. Jul Jensen et al., Mat. Res. Soc. Symp. Proc. **590**, 227 (2000).

[20] G. Wegner, Acta Mater. **48**, 253 (2000).

[21] *Characterization of Polymers in the Solid State II : Synchrotron Radiation*, in *X-Ray Scattering and Electron Microscopy Advances in Polymer Science, Vol. 67*, H.H. Kausch, H.-G. Zachmann (eds.), Springer, Heidelberg (1985).

[22] A. Gottwald, D. Jehnichen, D. Pospiech, P. Friedel, A. Janke, J. Macromol. Sci.–Phys. B**38**, 549 (1999).

[23] D. L. Abernathy et al., J. Synchrotron Rad. **5**, 37 (1998).

[24] F. Ania, D.R. Rueda, F.J. Balta Calleja, G.V. Krosigk, J. Mater Sci. **35**, 5199 (2000).

[25] J.M. Samon et al., J. Polym. Sci. Phys. **37**, 1277 (1999).

[26] V. Cimrova, D. Neher, S. Kostromine, T. Bieringer, Macromolecules **32**, 8496 (1999).

[27] F. Ania, M.E. Cagiao, F.J. Balta Calleja, Polymer Journal **31**, 735 (1999).

[28] B. Vigolo, et al., Science **290**, 1331 (2000).

[29] P.G. de Gennes, J. Chem. Phys. **55**, 572 (1971).

[30] P. Schleger et al., Phys. Rev. Lett. **81**, 124 (1998).

[31] P. Pincus, J. Chem. Phys. **75**, 1996 (1981).

[32] S. Minko et al., J. Macromol. Sci.–Phys. B **38**, 913 (1999).

[33] H.J Freund et al., Crystal Research and Technology **33**, 977 (1998).

[34] I.K. Robinson et al., Phys. Rev. B**60**, 9965 (1999).

[35] G. Rosenfeld et al., Phys. Rev. Lett. **69**, 917 (1992).

3.6. Chemistry

This chapter has been written on the basis of contributions to the report of the workshop "Chemistry applications of an XFEL" edited by M. Epple (University Bochum) and E. Welter (HASYLAB, Hamburg) (A.1.2). In these contributions, more detailed description and further references can be found.

A major impact of the XFEL in chemistry is foreseen in the areas of reaction kinetics, heterogeneous catalysis, solid state chemistry/crystallography, materials chemistry, and analytical chemistry. Examples for the possible use of an XFEL laboratory in chemical research will be highlighted in this chapter. Most important, the investigation of ultrafast structural changes during chemical reactions will be described in the section on femtochemistry. In this area the new X-ray source will have a big impact due to the possibility of combining X-ray structural determination and femtosecond time-resolution for the first time to an extent that enables the investigation of structural changes during reactions in complex systems from chemistry and other scientific areas. Further benefits come from the coherence of the beam which will enable the study of dynamics processes in liquids and soft matter important for many open questions in chemistry. The extreme brilliance will allow us to focus the X-ray beam well below 1 μm and, in combination with spectroscopic techniques, open completely new areas of spatially resolved investigations to be explored.

In addition to the scientific areas presented in the following sections further areas of research in chemistry will benefit from the advent of XFEL radiation, e.g. polymer chemistry, materials chemistry, synthetic chemistry (inorganic and organic chemistry), colloid and surface chemistry, food chemistry and biochemistry.

3.6.1. Femtochemistry

While picosecond experiments are of considerable importance, the breakage and formation of bonds happen on the femtosecond time scale, and this time scale is not currently accessible for detailed structural studies. Structural experiments in this time domain will be possible with the radiation from the XFEL, and will lead to a synthesis of femtosecond spectroscopy and femtosecond structural methods. Such studies cannot be imagined without the planned XFEL facility.

The fastest chemical processes happen in femtoseconds. Mechanical perturbations are essentially localized on a time scale of 100 fs within a molecule. Consequently, structural perturbations in a system will be much better characterized in the femtosecond time regime than in longer time regimes. The best synchrotron sources allow structural studies to be performed in a few tens of picoseconds, much too long for the observation of intrinsic electronic processes. In addition, a femtosecond light excitation may synchronize molecules in the sample for a short time (a couple of picoseconds). This phenomenon offers amazing new possibilities for structural investigations with femtosecond X-ray pulses through the observation of coherent reaction dynamics. On this time scale, real synchronism could be achieved among molecules in the sample before the structures enter the Maxwell-Boltzmann regime. Planned experiments with the XFEL will allow the very first observation of transition states

in three dimensions. On longer time scales, e.g. in the Maxwell-Boltzmann regime, chemical reactions do not proceed synchronously. Here, intermediates may be present simultaneously, but they are vibrationally uncoupled and thus unsynchronized. The interpretation of all time-resolved experiments outside the femtosecond domain is invariably compromised by this factor today.

Structural investigations of ultrafast phenomena will only be enabled by XFEL sources. The resolving power of X-rays for the determination of structural properties is at XFEL machines combined with ultrashort pulses of the order 100 fs. In addition, the number of X-ray photons within one single pulse will enable the observation of structures at very high resolution. Both achievements, the high peak flux and the short pulse length, make these machines an outstanding tool for femtosecond structural investigations in comparison to existing sources. Femtosecond structural investigation will lead in various scientific areas to completely new information about the system under investigation. In the following, examples from the area of (bio)chemical reactions and condensed matter are selected. In other sections of the scientific case many other examples are discussed.

A hundred years after the first observations of quantum-mechanical effects quantum chemistry dictates many features in modern physicochemistry. One of the most successful applications of quantum effects leads to the spectroscopy in the optical regime with which it was and is possible to precisely characterize stationary and dynamic optical and electronic properties of matter. However, the correctness and precision of a method is always limited by the approximations, which are made in the basics of a theory describing experimental investigations. If just these approximations have to be questioned in their validity - due to their break-down in describing new experimental effects - it is not only necessary to develop new theories but also to develop new experimental techniques, which from another point of view (like a new energy window) give systematic reference data on which actual theories can be developed and tested to lead to a better understanding of nature.

Two fundamental approximations of optical spectroscopy are the Born-Oppenheimer approximation and the Franck-Condon principle [1]. Nearly all data in optical or ultrafast spectroscopy are based on strategies built on these fundamental approximations. According to the Born-Oppenheimer approximation electronic energy and the internal energy of the nuclei are separable (due to the different masses of the electrons and nuclei) so that electrons always nearly instantaneously follow the nuclear motions. Vice versa, this approximation means that by determining the energy of the electrons from the fast spectroscopic shifts, statements about structural changes can be made.

The award of the 1999 Nobel Prize in Chemistry to Ahmed Zewail reflects the high maturity attained in the area of ultrafast spectroscopy [2]. Nonetheless, a detailed knowledge of the potential energy surfaces of the ground and all accessible excited states is required for interpreting any spectroscopic signal [3]. Since in optical experiments it is the energies of binding electrons that are probed, it is impossible to deduce the atom positions during structural transitions without pre-knowledge of the potential energy surface. In the required precision this knowledge is - at present - available only via computer simulations. This condition presents severe challenges as the system of study increases in complexity, and emerging X-ray based methodologies provide new approaches, in particular to ultrafast phenomena, complementing the information accessible through ultrafast spectroscopy

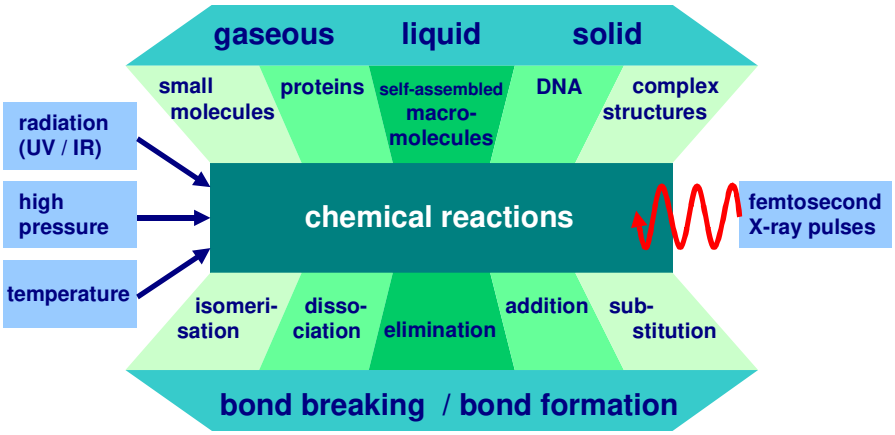

Figure 3.6.1.: *Applications for time-resolved investigation of chemical reactions. Systems in different phase (top) can undergo various chemical processes (bottom), which can be triggered by a variety of methods (left) and investigated by femtosecond X-ray pulses (right).*

alone[4, 5]. Here in particular, the combination of femtosecond spectroscopic methods with femtosecond structural methods is expected to provide new results.

Angstrom wavelength radiation in combination with photon pulse length in the order of 100 fs provides a unique tool for the study of ultra-fast chemical and biological phenomena. A setup where an ultra-fast optical laser pulse initiates a photo-reaction which can be probed with the X-ray laser pulse enables to follow ultra-fast structural changes due to e.g. structural rearrangements, bond breaking, and bond formations. These are the processes essential for chemical and biological reactions. These structural changes can occur in cyclic and non-cyclic compounds and can be triggered by a wide variety of mechanisms.

Fig. 3.6.1 summarizes possible experiments with respect to applications in the area of material science as well as classical chemistry (organic, inorganic, physical) or biochemistry. After the initiation of a chemical reaction, the mechanism of the chemical reaction (e.g. dissociation, isomerization, substitution, elimination and / or addition) can be followed with one X-ray pulse or a time series of X-ray pulses. Due to the high flux of the X-ray laser, the time-resolved behavior of small molecules as well as DNA can be examined in the different phases (gaseous, liquid and solid).

Light-triggered time-resolved studies with 100 ps resolution are now frequently performed at synchrotron sources [6, 7]. But only with the availability of pulses 1000 times shorter and 10^6 times more intense will it be possible to investigate phenomena in the time range below 1000 ps down to several 10 fs. This is exactly the timescale for structural reorganization processes of chemical reactions e.g. in liquids. Not only will the time window be extended by three orders of magnitude, but also the increased number of photons per pulse will yield far better photon statistics in any single experiment. This is particularly important when considering ultra-fast phenomena, as the magnitude of the structural motions which arise on the fs time-scale are likely to be smaller by far than those arising on slower time-scales, necessitating higher quality and higher resolution data.

An even broader range of chemistry occurs with reactions on a slower time scale, that are not triggered by light, but by temperature-jump or pressure-jump experiments. Currently the insufficient X-ray flux does not allow non-cyclic reactions on the nanosecond and microsecond time-scale to be followed. With the XFEL it will become possible to perform time-resolved X-ray diffraction and absorption experiments on non-cyclic systems. This will enable chemical, thermal and pressure triggering protocols to be utilized, in particular for systems with complex structural response characteristics like self-assembled macromolecules, proteins or DNA. In combination with a flexible bunch-to-bunch time structure of the XFEL linac, there will be sufficient X-ray photons per pulse to yield high quality structural information from a single exposure. This approach will open windows into a huge domain of dynamic chemical phenomena which structurally cannot be characterized with current X-ray sources or classical spectroscopic tools.

Capturing nuclear motions on the excited state energy surface - reversible photo-reactions In the upper part of Fig. 3.6.2, one example of a fundamental photochemical reaction - the trans/cis isomerization of stilbene - is shown [8]. After initiation of the reaction with an optical photon pulse (starting at the trans product, 180° the system undergoes a relaxation process via a photochemical funnel to the trans (180°) and cis (6°) product states. The relaxation process is determined mainly by the isomerization coordinate, which is the torsional angle between the two phenyl moieties. In the lower part of Fig. 3.6.2, a simulation of the diffuse scatter signal of stilbene for the different configurations during the isomerization is shown. The time scale for this relaxation process is about 4 ps.

Figure 3.6.3 shows another example of a photo-induced relaxation process, the configurational rearrangement of N,N-dimethylaminobenzonitrile (DMABN) induced by an electron transfer process. In literature DMABN is widely discussed with special emphasis on the possible relaxation mechanisms during photo-excitation. The discussions focus mainly on the torsional motion of the amino moiety around the phenylic plane, as sketched in Fig. 3.6.3. Information about the picosecond to subnanosecond dynamics of this system was recently obtained by time-resolved powder diffraction at the ESRF [7]. However, with the state of the art apparatus, the resolution of the data is relatively low due to the lack of X-ray photons. This would dramatically change with an XFEL. With the new device it would be possible to follow ultra-fast relaxations like structural reorganizations of and in the liquid phase.

Capturing nuclear motions on the excited-state energy surface - irreversible photo-reactions Another proposed irreversible reaction might be a photo-induced elimination reaction of phenylester in a direct comparison between the solid state and the liquid phase: in the crystal, eliminated groups can dock transiently, migrating back to the bonding side in a diffusion controlled process and re-forming the initial educt state (Fig. 3.6.4). However, in the liquid phase this "solvent cage" is looser, so that the products can escape the cage forming dissociated states. Depending on the solvent, solvent cages with different properties might be formed, leading to product distributions typical for the solvent. Since most of the preparative chemistry - inorganic as well as organic - is performed in the liquid phase, it will give new information about the reaction mechanism and the influence of these mechanisms

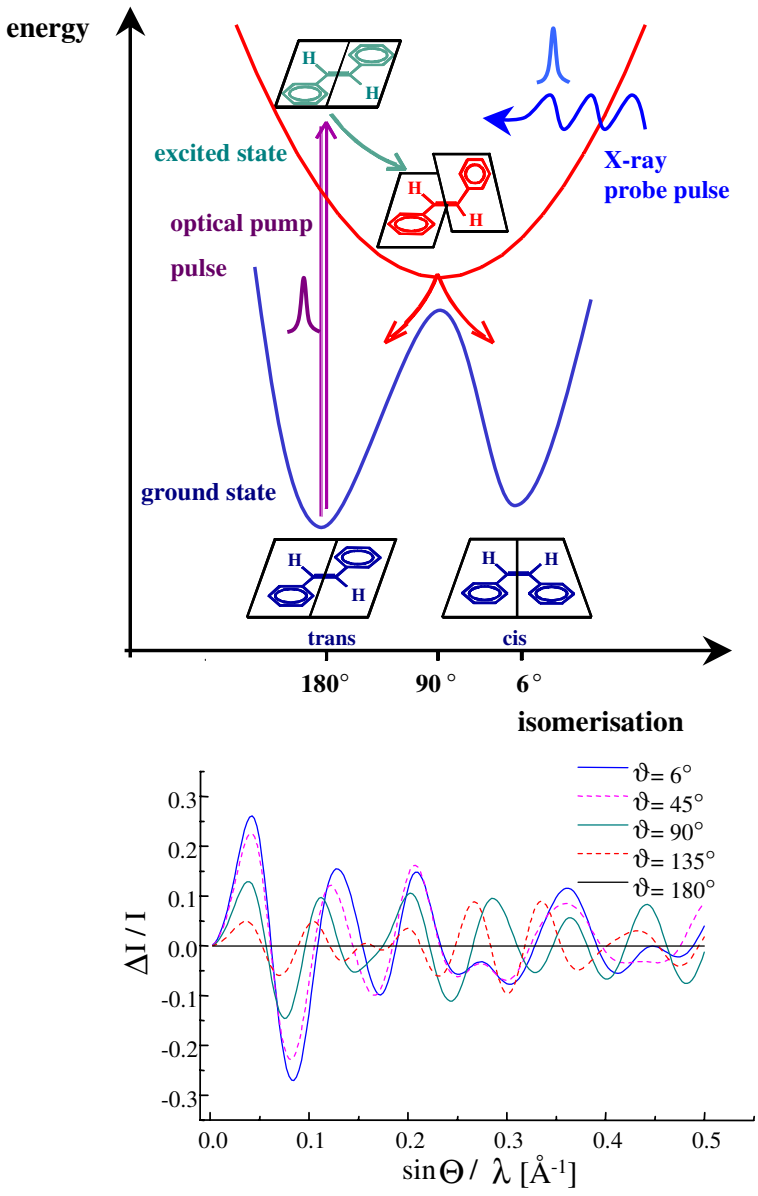

Figure 3.6.2.: *Top: Simplified reaction scheme of the trans-cis isomerization of trans-stilbene. Bottom: Change of the diffuse scattering signal of stilbene during the photo-isomerization. A photo-excitation level of 30 % was assumed.*

by structural properties. Due to the time resolution and the high flux of the XFEL, these experiments should become possible.

Photochemical reactions It is further proposed to obtain during the course of a photochemical reaction direct time resolved information on the changes in the electronic and the geometric structure. A promising candidate for pioneering experiments would be the photo-

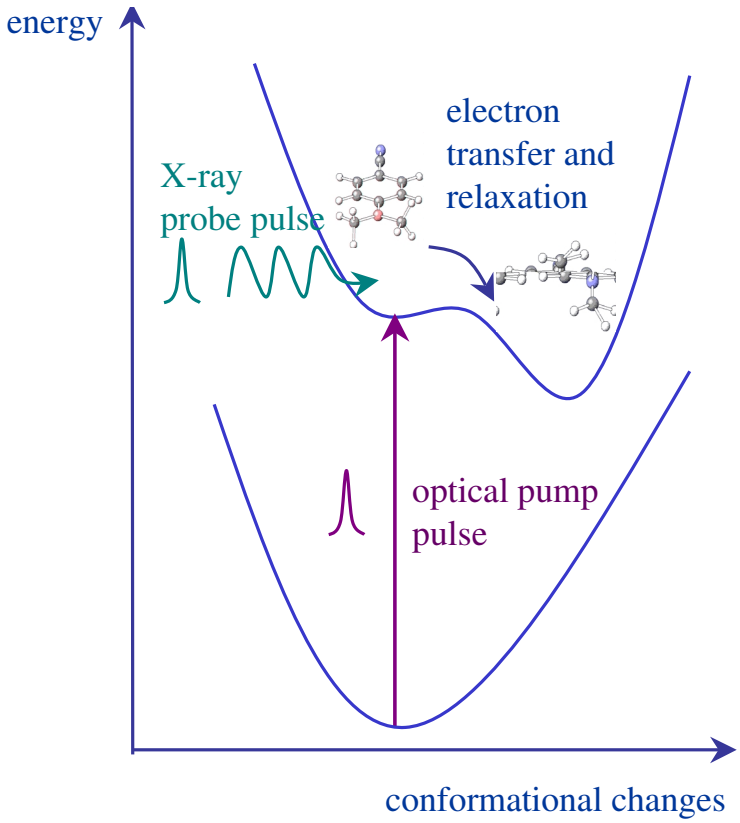

Figure 3.6.3.: *Configurational rearrangements of a photo-excited molecule (N,N-dimethylamino-benzonitrile) induced by an electron transfer process.*

chemical dissociation of Br_2 or I_2 molecules through excitation using an optical femtosecond laser pulse at 400 nm, or 480 nm wavelength, respectively. Subsequent investigation of the L (Br_2) or M (I_2) X-ray absorption with a FEL pulse with variable delay with respect to the initial laser pulse would provide information about the dynamical processes. If the absorption cross section is measured at a fixed photon energy above the absorption edge, one should be able to observe oscillations in the absorption cross section with increasing time delay due to the increase in the intramolecular distance in the dissociation process.

3.6.2. Analytical solid state chemistry

The synchrotron radiation of second and third generation storage rings has found widespread application in the area of (environmental) analytical chemistry over the last few years. One aim is the determination of chemical bonding forms of metals in either real or synthetic environmental samples. The latter investigations aim at the exploration of the interaction of metals of interest with single important constituents of environmental samples like clay, iron and manganese minerals or different organic compounds. In either case the concentration of the analyte is normally small. That means that all data, usually from absorption spectroscopy experiments used to obtain information about the chemical state and the nearest neighbors

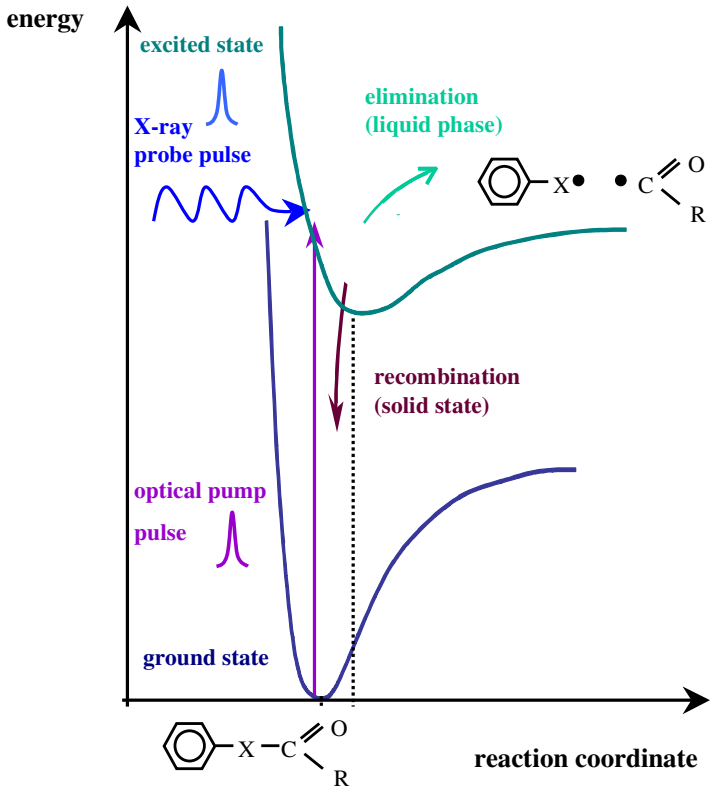

Figure 3.6.4.: *Photo-induced elimination reaction of phenylester. In the solid state the system reacts back to the educt state. In the liquid phase, the formed radicals can escape the solvent cage and follow further reaction pathways.*

of the species under investigation, have to be obtained from fairly diluted samples. But although the bulk concentration may be small there are often regions (particles) where the analyte is enriched or even pure. These particles are usually small. Figure 3.6.5 shows an electron microscope image of soil containing lead particles. In the backscattered electron detector image, the areas containing Pb appear bright, and several of these structures become visible. The lead content of these particles, initially not bound, does go into solution upon weathering and partially binds to matrix constituents. The analysis of the chemical bonding form of the bound lead is a prerequisite for the development of successful and economical soil cleaning procedures. Further examples for speciation analysis can be found in the literature [9, 10]. The analytical technique most often used in these investigations is X-ray absorption spectroscopy (XAS).

3.6.2.1. 2-D elemental-mapping, 3-D tomography with nanometer spotsize

The proposed investigations are a further miniaturization of the experiments that are performed at third generation sources. While the spatial resolution at these sources is limited to $\approx 1\,\mu$m, the use of an XFEL source with its much higher photon beam quality will give

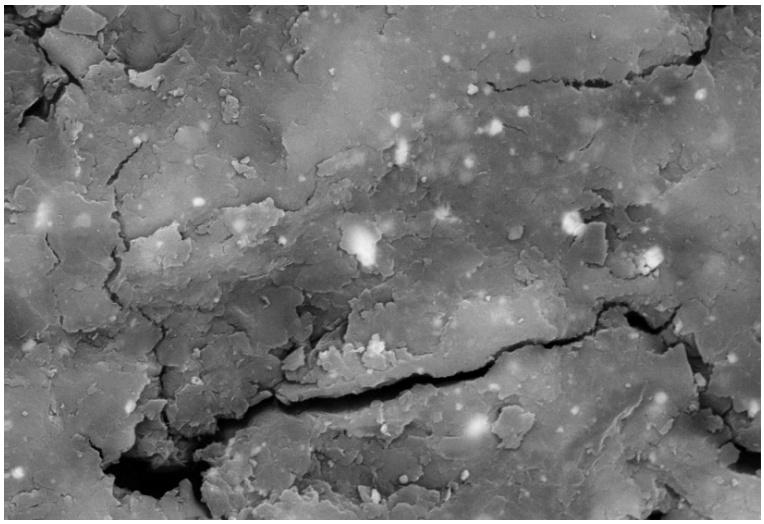

Figure 3.6.5.: *Electron microscope image, obtained by back-scattered electron detection, of a Pb containing soil sample. Areas containing lead appear bright.*

a substantially increased spatial resolution for the hard X-ray regime. It will be possible to reach 100 nm spot sizes with 1 Å, radiation at an XFEL source. Such resolution allows new types of samples like single colloidal particles to be investigated. Possible applications of imaging and mapping techniques are :

- *μ-tomography* can be used in materials science to obtain deeper insight into the structure of materials. Of special interest here are inclusions of impurities or regional demixing of alloys, which severely affect the (mechanical) strength of materials. Figure 3.6.6 shows a state of the art reconstructed image obtained at a third generation source (ESRF) from a uranium fuel particle found in Chernobyl soil. This particle was emitted during the Chernobyl nuclear reactor accident. The image corresponds to a spatial resolution of $\approx 1.6 \times 1.6 \mu m^2$ [11]. It shows cavities which were probably formed during the normal reactor operation by volatile nuclear fission products.

- *μ-XANES* : At present the spatial resolution of μ-XANES is limited by spotsizes $>$ 1 μm. The method is used to determine the distribution of the different oxidation states of elements in a wide variety of samples. Examples of scientific areas of pursuit that might profit from μ-XANES are [12]:

  - Determination of redox states and mineralogical associations of toxic species in natural and contaminated soils and sediments or waste encapsulation materials. These investigations are aimed towards providing information about the long-term behavior of elements sorbed at mineral phases. One possible area of use is the investigation of the interaction between actinides from nuclear disposal and minerals (clay, Fe-phases, Mn-phases etc.). An example from a recent investigation is a μ-XAS study of sorbed Pu on tuff [13]. It was performed at an APS

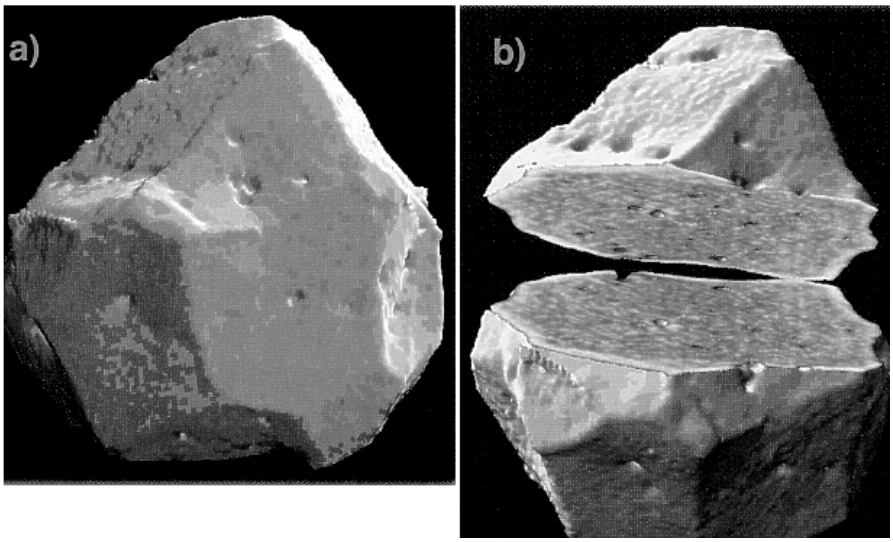

Figure 3.6.6.: *μ-tomographic reconstruction of a uranium fuel particle taken from Chernobyl soil, taken at the ESRF beamline ID22 (reproduced from [11]).*

undulator beamline (station ID-C), using a Kirkpatrick-Baez optics to focus the beam. The spatial resolution was limited to $4 \times 7\mu m^2$ by the photon source size.

- Oxygen fugacity determination based on partitioning of elements in specific valence states between coexisting phases in earth and extraterrestrial materials.
- Redox state of the Earth's interior based on valence determinations on microcrystals within diamonds from the mantle.
- Redox chemistry of manganese and other metals at the root-soil interface of plants and its role in agriculturally relevant plant diseases.
- Distribution of elements in different oxidation states in micro electronic devices.
- Mapping and chemical characterization of heavy metals within single cells and the binding domains of the biological films. These films are in almost all cases present at water/mineral surfaces and are believed to play a very important role in the binding of heavy metals in soils and sediments.
- Characterization of single colloidal particles: It is believed that a major part of the transport of sparingly soluble substances is mediated by submicron particles (colloids). These colloids mainly consist of mineralogic components (FeOOH, clay, precipitates) or NOM (refractive or biologically available organic acids) which absorb toxic elements [14].

3.6.2.2. Investigations of low Z elements

Element specific investigations of low-Z elements under ambient conditions or within *in-situ* environments will be enabled only if X-rays can be utilized which provide far higher

penetration power than the photon energies characteristic of the corresponding absorption edges. The XFEL will open the way for a solution to this problem by enabling X-ray Raman spectroscopy to investigate low Z element absorption edges. In the following, active research topics from three quite different areas are listed:

- Measurement of the XAS spectra from light elements in semiconductor materials. At present these studies have to be performed in the soft X-ray region. Materials of interest are III/V semiconductor materials such as Mg or Si doped GaN or AlGaN and InGaN alloys [15]

- An interesting experiment would be the combination of X-ray Raman spectroscopy with the imaging techniques mentioned before. This would enable a three-dimensional mapping of light elements and their chemical bonding forms in thick particles where the penetration depth of edge energy photons is much too small. One scientifically and economically interesting field of application for this method includes semiconductors, especially B and N containing III-V semiconductors (see above).

- The use of X-ray Raman spectroscopy in catalyst research will make it possible to perform *in-situ* experiments looking, not from the reactive (metal) center of a catalyst, but from the substrate molecule on the chemical reaction mechanism.

Experimental scheme In non-resonant X-ray Raman spectroscopy, a sample is irradiated with a beam of fixed energy. The transmitted or reflected radiation will be investigated spectroscopically. In the case of non-resonant edge absorption, a photon will be scattered with an energy difference corresponding to the energy of the absorption edge of the absorbing atom species. The energy distribution of the scattered photons shows the same oscillation which is found in the corresponding absorption spectra (compare Fig. 3.6.7). In the X-ray regime the method does have a high cross-section for low-Z elements like carbon, nitrogen or oxygen, and offers the possibility of measuring for the first time XAS spectra of these elements in thick samples under environmental conditions, whereas experiments at present-day X-ray sources suffer from long measurement time, e.g. about 1 h for bulk samples.

Tohji and Udagawa [17] used measurement times between 24 h and 72 h to measure X-ray Raman spectra of pure carbon compounds (diamond and graphite) at a bending magnet beamline of the Photon Factory, KEK, Tsukuba, Japan. They estimated the flux to be 10^{11} photons/s. The line width of the incident monochromatic X-rays was estimated as 2 eV (FWHM). Using an XFEL source will reduce the time necessary to measure a spectrum to several seconds and will for the first time enable the measurement of X-ray Raman spectra from diluted systems like environmental samples. For the XFEL, the spectral flux from one bunch at 7.8 keV is estimated to be 5×10^{12} photons, thus the number of photons per bunch is comparable or even slightly larger than the number of photons per second available today. A very important factor with respect to an XFEL is that these experiments are performed at constant incident photon energy. Therefore Raman spectroscopy can make use of the high brilliance and relatively small energy bandwidth of the XFEL beam emitted by the SASE undulators. Nevertheless, in order to achieve sufficient energy resolution in the detection

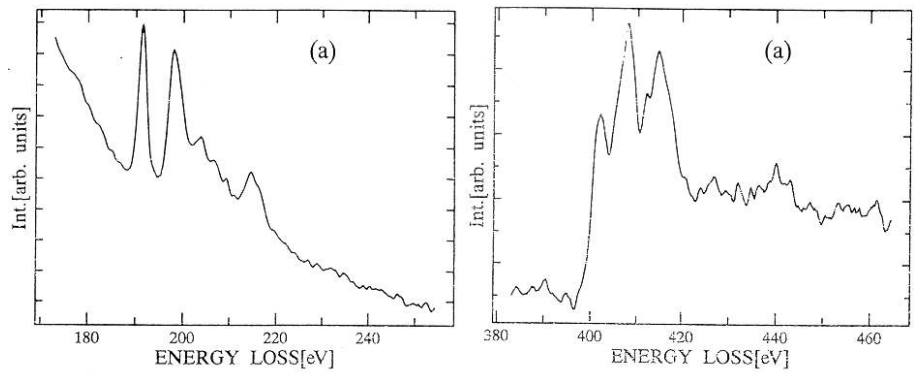

Figure 3.6.7.: *Examples for K-edge spectra from boron (a.) and nitrogen (b.) in different BN samples, obtained by X-ray Raman spectroscopy. The data have been obtained at the wiggler beamline BL16X of Photon Factory, KEK, Tsukuba, Japan at an incident flux of 10* ^{13} *photons/s and a spectral width of 1.1 eV(FWHM) at 6 keV. The time needed for data collection per spectrum was several hours (reproduced from [16]).*

system, the bandwidth of the laser line is too broad to be used without further monochromatization.

3.6.3. Heterogeneous catalysis

3.6.3.1. New approaches in photoelectron spectroscopy

Photoelectron spectroscopy is one of the most frequently used techniques for the physico–chemical characterization of heterogeneous catalysts [18, 19]. This is due to its ability to provide information about the chemical properties of the near-surface region. The chemical composition of the analyzed region (almost all elements can be detected without hindrance) and the chemical state of the elements traced can be described.

This analytical potential serves the needs of heterogeneous catalysis very well. However, severe disadvantages remain such as the required ultrahigh-vacuum environment during the measurements, that prevents *in-situ*-studies, the long data acquisition time and the low spatial resolution (for imaging instruments in the mm range). Nowadays, progress in basic catalyst research is strongly expected from studies of the catalyst under operation conditions, i.e. during interaction with a gas phase. Such studies are not possible with the present-day XPS technique. The usually long data acquisition times have up to now prevented any real effort to establish mapping methods for catalysts. Such methods would be of considerable interest, since real catalyst preparations are mostly powders with inherent particle-to-particle fluctuations of properties. Mapping XPS could become a useful tool in an effort to optimize catalyst preparation methods that provide powders of highly homogeneous distribution of critical properties.

SASE FEL radiation will permit XPS to be performed at unprecedented speed. This should allow the introduction of new approaches into the analysis of catalysts by XPS - both time-resolved and laterally resolved XPS (mapping). Due to the inhomogeneities inherent in

real catalyst preparations, spatial resolution is not required in studies in which surface properties are related to reactivity properties, since these are accessible only as an average over the particle array. However, these spatially averaged measurements can now be performed with time resolution. On the other hand, the fluctuation of properties between particles or within larger particles may themselves be studied by introducing "mapping" methods that may probe different spots on a catalyst granule or compare a large number of powder particles. These two strategies (averaged, mapping) have different requirements for avoiding the radiation damage problem or beam focusing for example.

Apart from the analysis of catalyst surfaces, which should be near to present-day methods, fast data acquisition will give the means to realize a new approach to the XPS study of catalysts under in-situ conditions. This approach combines the pulse-wise XPS analysis with pulse-wise exposure of the catalyst surface to the reactants in order to collect information about surface intermediates of short lifetime. This should be most relevant to catalysis, and to changes of the surface induced by this process. In this setup, the catalyst surface is periodically exposed to reactant pulses. The interaction of the reactant with the surface is probed by photoelectron spectroscopy with single bunch trains admitted at known time lags relative to the reactant pulses. This approach, which is a subdivision of the average strategy, will be labelled "*in-situ*-XPS". In modern basic research in heterogeneous catalysis much emphasis is laid on application of spectroscopic characterization techniques in-situ, i.e. on the working catalyst. XPS, which is generally a technique well adapted to the needs of catalysis research, has great problems in coping with the in-situ requirement since it is an in-vacuum technique. In general, good "post-mortem" analysis is the best that can be done today. Direct dosing of reactants during data acquisition is limited to very low partial pressures (10^{-6} mbar) to avoid damage of the electron detectors. Attempts to construct differentially pumped flow cells, out of which XPS spectra could be taken, have not been successful. When rapid XPS analysis is available, it should however, be possible to analyze surface species relevant to catalysis and the perturbations they cause on the surface in a pulse mode. The approach proposed is inspired by the "Temporal Analysis of Products" (TAP) method [20]. A typical application is shown in Fig. 3.6.8 (from [21]). The left panel shows the response of a V-Sb-O mixed oxide catalyst when propylene and ammonia are pulsed simultaneously. It can be seen that acrolein leaves the catalyst earlier than acrylo nitrile, which indicates that the former is an intermediate in the formation of the latter. The right panel shows pump-probe experiments, where propane was pulsed with the indicated time lags (in s) after ammonia. The acrylonitrile formation decays with the length of the time lag. This shows that a short-lived intermediate is formed from ammonia, which plays a major role in acrylonitrile formation. There is at present no way to identify this short-lived intermediate.

Mapping inhomogeneities in catalyst preparations For averaging measurements, the photon beam has to illuminate a large number of particles (mm scale) so that the spectrum is representative for the whole powder sample. The high primary intensity will allow very fast data collection (typically within seconds). In order to fully benefit from the short measurement time and to avoid the limitation of sample exchange, one can imagine investigating many samples in a combinatorial way (see section 3.6.3.5). In the mapping strategy, the photon beam will be focused on individual spots of a larger particle or on small individ-

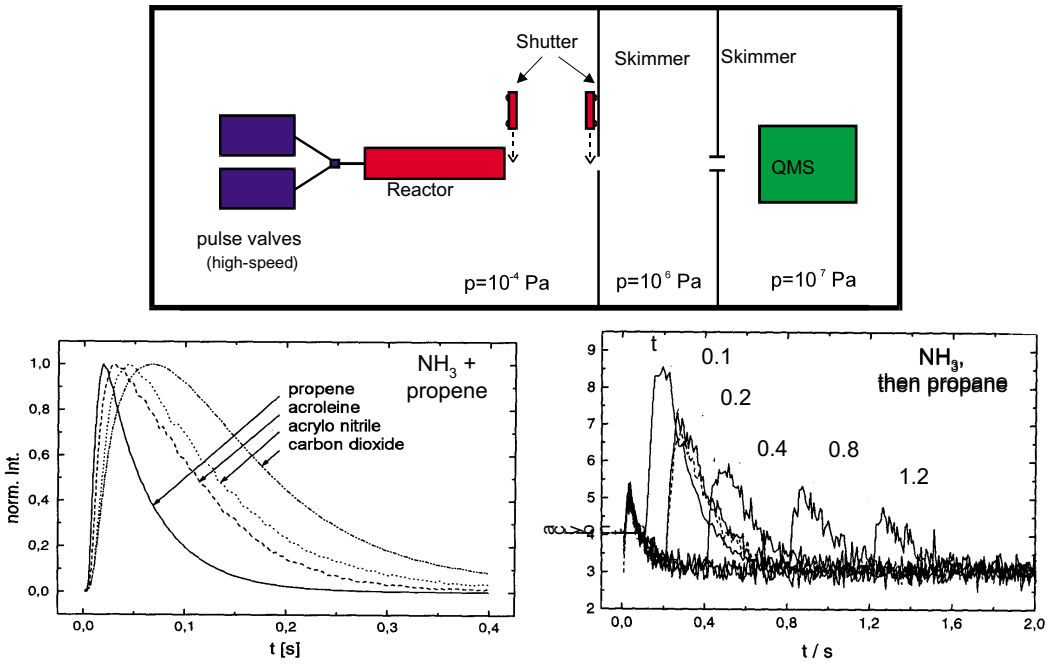

Figure 3.6.8.: *The "Temporal Analysis of Products" Technique (TAP). The upper panel shows a schematic representation of a TAP setup and the lower panel an application of TAP. Here, on the left the identification of a reaction intermediate is shown (acrolein, in the ammoxidation of propene to acrylonitrile over a V-Sb-O catalyst), and on the right the detection of a reactive intermediate from the interaction of NH_3 with V-Sb-O by a pump-probe technique is demonstrated (reproduced from [21]).*

ual particles of the sample, which are analyzed separately. A manipulator technology will have to be applied that moves the sample rapidly in a defined way in order to scan the photon beam over the sample surface in order to bring individual particles into the focus. If mapping is performed on one large granule, sample damage must be avoided. For mapping of individual powder particles, sample damage is unlikely provided that photoelectron detectors are available which analyze the required binding-energy range simultaneously (one-shot measurement). The short measurement time for each investigated surface particle allows the investigation of many particles in a time still short compared to a single particle measurement at a present-day small-spot XPS facility. The investigation of many particles is important for demonstrating that the obtained data is representative of the catalyst studied.

3.6.3.2. Phase composition of real catalysts

The analysis of the elemental concentrations of solid catalysts on the micrometer scale is carried out routinely in an automated mode by electron probe micro-analysis. Concentration profiles of cross sections of catalyst pellets can be obtained by the analysis of X-rays excited by an electron beam. One of the disadvantages of the electron micro-probe analysis is that the sample has to be put into vacuum, so that the changes in elemental composition during a

catalytic reaction cannot be determined. Even in a so-called environmental scanning electron microscope, a pressure above a few mbar is not attainable [22]. Probing a catalyst by X-rays does not restrict the environment to vacuum, so in-situ measurements at high temperature and high pressure are possible. Here, we propose a study of the phase composition distribution and oxidation states on a cross section of catalyst pellets by scanning an XFEL beam with a size of a few micrometers over the sample.

A complete X-ray diffraction pattern can be collected for every position of the beam on the sample. Quantitative phase information and average crystallite sizes can be obtained with a lateral resolution of $10 \times 10 \mu\text{m}^2$ by performing Rietveld refinements for example on the powder diagrams. Similarly, XAS spectra can be obtained as a function of the position of the beam on the sample. Coordination numbers, oxidation state and interatomic distances can be obtained over a cross section of a catalyst pellet or even along a reactor. In this way information about oxidation or reduction, phase transformation, sintering and deactivation of the active catalyst during reactions can be obtained. This method could be used to study a catalyst during preparation (e.g.impregnation) and/or operation. Here it has been observed by microprobe analysis that the catalyst composition of the outer shell differs significantly from that of the inner parts. If the characterization is performed directly after the preparation of the catalyst, as for example by cutting a cylindrical pellet into two cylinders, then the phase composition of the inner plane at the cut may be studied radially. It is expected that the outer few 100 μm have a significantly different composition, which might also change during operation of the catalyst. The obtainable information will give a significant enhancement compared to present possibilities where one needs to use a relatively large (several square millimeters) beam in order to get a sufficient count rate [23].

3.6.3.3. Catalyst reactions

Time-resolved *in-situ* characterization methods have become increasingly important in catalysis research in order to obtain insight into the relationship between structure and activity. The ultimate goal in catalysis with respect to time resolution is to follow catalytic reactions while they occur. Studies of chemical reactions, bonding, and bond-breaking take place on the 10 to 100 fs timescale. Femtosecond chemistry is a rapidly developing field, and nowadays it is possible to perform experiments at optical wavelengths at femtosecond time scales. The 1999 Nobel prize in chemistry was awarded to Ahmed Zewail for "showing that it is possible with rapid laser technique to see how atoms in a molecule move during a chemical reaction" [24]. Transition states and intermediate phases can be probed in order to get insight into the breaking and formation of chemical bonds. In practice, a powerful ultra-fast pump laser is used to excite molecules or adsorbates at surfaces, while a probe pulse with a variable time delay is used to monitor structural changes. Fast X-ray pulses can be used as probe pulses as well. By using femtosecond pulses produced by the XFEL, the time scale to probe reactions can be reduced by several orders of magnitude in comparison to third generation synchrotrons. Thus it should be possible to probe fast reactions, such as :

- the hydrodesulferization (HDS) of oil fractions on CoMoS and $NiMoS$ catalysts supported on alumina particles. In these, the bonding of the sulfur containing compounds (such as tiophenes and benzothiophenes) to the active sites, which are most probably

the promoted Ni and Co edge sites, could be probed under realistic reaction conditions [25].

- steam reforming of methane over Ni/$MgAL_2O_4$ or Ni/MgO catalysts. Here the bonding between C, O and Ni could be probed. The pre-exponential factor of the conversion of methane and water to CO and H_2 is on the order of 10^9 reactions/s [26].

- the synthesis of methanol over Cu/ZnO based catalysts. Here the elementary reaction may be probed by observing the CO and CO_2 bonding to the Cu surface.

Reaction kinetics is described by the Arrhenius law containing a pre-exponential factor and an exponential term. The pre-exponential factor, in units of s^{-1}, can be used to classify the reaction as 'fast' or 'slow'. In general only the investigation of reactions occurring on very short time scales is of interest for studies at XFEL sources. Slow reactions may equally well be investigated by other means. Pre-exponential factors for reactions can be estimated from transition state theory. Here fast reactions are classified as $Langmuir - Hinshelwood$ type reactions ($A^* + B^* \rightarrow C^* + D^*$). Their pre-exponential factors vary, depending on whether the surface species are mobile or not, between 10^8 and 10^{13} reactions/s. Furthermore, molecular desorption processes ($A^* \rightarrow (A^+)^*$) and associative desorption reactions ($2A^* \rightarrow A_2 + 2^*$) have pre-exponential factors of the order of 10^{13} reactions/s [27] and therefore are of potential interest to these studies.

The energy spread of a single SASE line is sufficiently small (0.2 % bandwidth) to perform diffraction directly without monochromatization or focusing. However, the energy spread is at the same time large enough to do spectroscopy. Using a dispersive XAFS setup and a position sensitive detector, a XANES spectrum of 20 eV width can be obtained at 10 keV. This is sufficient to probe the pre-edge and near-edge region close to e.g. a Cu K-edge. In this way, the oxidation state of Cu atoms can be monitored during a chemical reaction, e.g.the oxidation or reduction of Cu.

3.6.3.4. Characterization of colloidal particles

The characterization of colloidal particles in a suspension can be performed by dynamic light scattering (DLS) in a laboratory setup. With a coherent X-ray source, the small q-range available for optical lasers can be extended and the transparency of the suspension is a less severe limit. Particle sizes, aggregate size distribution and dynamics of aggregates can be obtained. Here we propose to study aluminum hydroxide (AlOOH) samples suspended in water. AlOOH is used as a precursor for highly porous transition alumina, which is used as a carrier for several types of industrial catalysts [28]. The characterization of AlOOH and transition alumina is performed routinely by various techniques e.g. (ultra) small angle X-ray scattering (U)SAXS, XRD, SEM, TEM, and DLS. Time-dependent autocorrelation functions can be obtained from X-ray photon correlation spectroscopy (XPCS) directly on the as-prepared AlOOH aggregate. Dilution of the samples to a very low dry-matter content, as is necessary for DLS, is not necessary for XPCS. As the high porosity of the AlOOH aggregates gives rise to a strong small angle X-ray scattering signal, they are well suited for XPCS. The extremely high coherence of the XFEL beam has the advantage over third generation

synchrotron beams that the cross section of the beam has not to be reduced to micrometer size. At a distance of 500 m, the size of the fully coherent beam is approximately 0.5 mm. This is close to the size of the glass capillary tubes that will be used to enclose the sample. XPCS using the fully coherent XFEL beam thus increases the size of the beam at the sample with at least three orders of magnitude. As the scattered intensity increases correspondingly, a new range of measurements not presently possible at synchrotron radiation will be opened.

3.6.3.5. Combinatorial approach to catalyst research

With the development of fast mechanical devices, it would become possible to investigate libraries of samples or to perform experiments on ensembles of samples having different compositions. Short exposure times would enable the methodological scanning of these libraries within a short period of time. Exposure times of approx. 10 - 15 min are necessary to achieve good signal to noise ratios at present. With the more intense source, single shot exposures are sufficient, so that within one bunch train a series of samples could be investigated. Thus the number of samples can be drastically increased. For studies on reaction kinetics of catalytic systems, it is necessary to observe reactions evolving under conditions similar to real catalysis conditions. Even if the sample is in a non-equilibrium state after exposure, it would be feasible to tune to another sample in the library and continue to investigate the time dependent reaction. For this type of experiment it would be necessary to have a detector with fast readouts. By preparing the experiments in double detection setup, i.e. simultaneous transmission and fluorescence measurements, as well as a diffraction experiment with a large curved position sensitive detector, the amount of information would be increased in a way that diffraction and spectroscopy information from exactly one defined state could be collected.

Bibliography

[1] G. Herzberg, *Molecular Spectra and Molecular Structure*, R.E. Krieger Publishing, Malabar, Florida (1991).

[2] A.H. Zewail, J. Phys. Chem. A**104**, 5660 (2000).

[3] T. Elsässer, J.G. Futjimoto, D.A. Wiersma, W. Zinth, *Ultrafast Phenomena XI*, Springer, Berlin (1998).

[4] J. Manz and L. Wöste, *Femtosecond Chemistry*, VCH, Weinheim (1995).

[5] C. Rulliere, *Femtochemistry*, Springer, Berlin (1999).

[6] F. Schotte et al., *Recent Advances in the Generation of Pulsed Synchrotron Radiation Suitable for Picosecond Time-Resolved X-ray Studies*, in *Handbook of Synchrotron Radiation, Vol. 5*, D. Mills (ed.), Wiley and Sons, New York to appear (2001).

[7] S. Techert, F. Schotte, M. Wulff, Phys. Rev. Lett. **86**(9), (2001) in press.

[8] D.H. Waldeck, Chemical Reviews **91**, 415 (1991).

[9] A. Manceau et al., Environ. Sci. Technol. **30**, 1540 (1996).

[10] E. Welter, W. Calmano, S. Mangold, L. Tröger, Fresenius J. Anal. Chem. **364**, 238 (1999).

[11] B. Salbu et al., ESRF Highlights 1999, 24 (2000).

[12] S.R. Sutton, S. Bajt, J. Delaney, D. Schulze, T. Tokunaga, Rev. Sci. Instrum. **66**, 1464 (1995).

[13] M.C. Duff et al., J. Synchrotron Rad. **6**, 350 (1999).

[14] F. v.d.Kammer and U. Förstner, Water Science & Technology **37**, 173 (1998).

[15] M. Katsikini, T.D. Moustakas, E.C. Paloura, J. Synchrotron Rad. **6**, 555 (1999); M. Katsikini et al., J. Synchrotron Rad. **6**, 558 (1999).

[16] N. Watanabe, H. Hayashi, Y. Udagawa, K. Takeshita, H. Kawata, Appl. Phys. Lett. **69**, 1370 (1996).

[17] K. Tohji and Y. Udagawa, Phys. Rev. B**39**, 7590 (1989).

[18] See e.g. *Spectroscopy of Transition Metal Ions on Surfaces*, B.M. Weckhuysen, P. Van Der Voort, G. Catana (eds.), Leuven University Press, Leuven (2000).

[19] G. Moretti, in *Handbook of Heterogeneous Catalysis*, G. Ertl, H. Knözinger, J. Weitkamp (eds.), VCH, Weinheim (1997), p. 632 ff.

[20] J.T. Gleaves, J.R. Ebner, T.C. Kuechler, Catal. Rev.-Sci. Eng. **30**, 49 (1997).

[21] H.-W. Zanthoff and S. Buchholz, Catal. Lett. **49**, 213 (1997).

[22] G.D. Danilatos, in *In-situ microscopy in materials research*, P.L. Gai (ed.), Kluwer Academic Publishers, Dordrecht (1997), Chap. 2.

[23] B.S. Clausen, Catalysis Today **39**, 293 (1998).

[24] S. Pedersen, J.L. Herek, A.H. Zewail, Science **266**, 1359 (1994).

[25] H. Topsøe, B.S. Clausen, F.E. Massoth, *Hydrotreating Catalysis*, Springer, Berlin (1996).

[26] J.R. Rostrup-Nielsen, *Catalytic Steam reforming*, Springer, Berlin-Heidelberg (1984).

[27] J.A. Dumesic, D.F. Rudd, L.M. Aparicio, J.E. Rekoske, A.A. Trevino, Annual report ACS, 40 (1993).

[28] C.N. Satterfield, *Heterogeneous Catalysis in Practice*, McGraw-Hill, New York (1980).

3.7. Life Sciences

This chapter has been written on the basis of contributions to the report of the workshop "Life sciences" edited by J. Hajdu (University Uppsala) and E. Weckert (HASYLAB, Hamburg) (see A.1.4). In these contributions, more detailed description and further references can be found.

3.7.1. Introduction

The most interesting new properties of XFEL radiation for life sciences are the extremely short pulse width (≈100 fs) and the very high peak brilliance. For some experiments, the coherence and the increased average brilliance will also be very valuable. Possible life sciences XFEL experiments can be divided into two categories:

1. Totally new experiments which exploit the unique features of XFEL radiation. It will be through these experiments that the greatest impact of the XFEL is to be expected. Since our knowledge of the interaction of such extreme radiation pulses with matter is incomplete, predictions about these experiments are difficult and expectations might be both over as well as underestimated.

2. Experiments that are already feasible today but which can be performed under very much improved conditions. The expected results for these experiments can be extrapolated into the new regime in an almost straightforward manner.

Of course, any discussion on applications of the XFEL has to take into account the expected rapid developments of life sciences and of those fields that are relevant for the status reached at the time XFEL radiation will become available.

Recent developments such as the genome projects, together with technical improvements in the structure determination process (availability of synchrotron radiation, protein expression, MAD/SAD phasing[1]), make it likely that the exponential increase of structures solved and deposited at the protein data bank (PDB) will continue [1]. Despite this rapid progress, it is also foreseeable that many challenges in structural biology will remain the same. These include systems that are difficult to crystallize, such as membrane proteins and large multicomponent complexes, of which only a few have been solved by now.

The natural environment of membrane proteins is composed of two-dimensional lipid bilayers (see Fig. 3.7.1). Therefore, these molecules have almost no tendency to form three-dimensional crystals which are mandatory for a crystallographic structure determination. As a matter of fact, the three-dimensional structure at close to atomic resolution, which is the key for all investigations concerning structure-function relationships, of only a very small number of membrane proteins is known up to now. About 30% of the proteins encoded in the human genome are membrane proteins. They are the targets for 70% of all known drugs. The knowledge of the structure and function of membrane proteins is scientifically of extreme importance not only for the understanding of biochemical and biological processes but also for social and economic reasons due to their importance for physiology. Any method

[1] MAD: Multi wavelength anomalous diffraction; SAD: single wavelength anomalous diffraction.

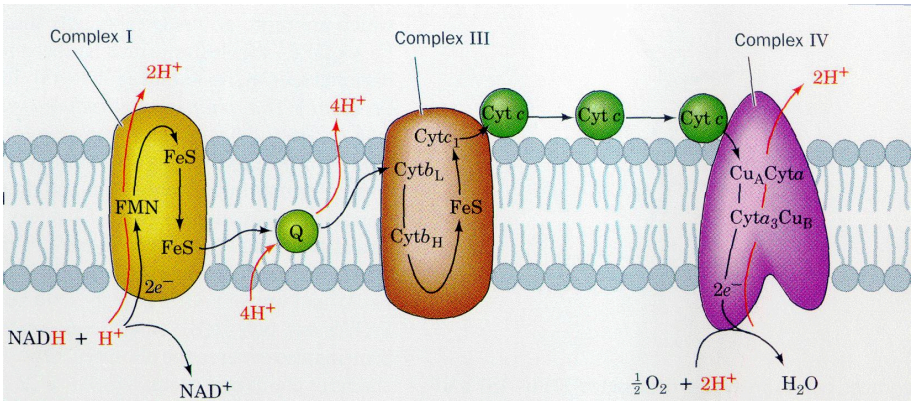

Figure 3.7.1.: *Example of the arrangement and function of membrane proteins; diagram of the mitochondrial electron transport chain indicating the pathway of electron transfer (black) and proton pumping (red). Electrons are transferred between complexes I and II by the membrane-soluble CoQ and between complexes II and IV by cytochrome c (reproduced from [2]). Apart from complex I, the structure of all components is known in this chain. However, the structure and function of the vast majority of membrane proteins is unknown.*

providing means to solve the structure of membrane proteins more easily would have an enormous impact in this field. Here the XFEL radiation in conjunction with new techniques can form the basis of such methods.

Quite recently the structure of the ribosome (see Fig. 3.7.2) has been solved to high resolution [3, 6]. This is an example of a very large but relatively stable protein-RNA assembly from which we learn how the information contained in the genetic code is read and used to synthesize the corresponding protein chains. The study of the structure of such large macromolecular assemblies is one of the keys to gaining insight into the interplay of different proteins and will facilitate the understanding of biological processes on a molecular or even atomic level. This addresses the fundamental question : How does biology work on a molecular scale? The crystallization of these large assemblies is difficult. Therefore, what has been said above for the investigation of membrane proteins is also valid for these complexes. Other targets for such investigations would be, for example: signal transduction complexes, the anaphase promoting complex, transcription factors, DNA repair/replication/remodelling systems, splicing factors and chaperons.

Even if diffraction size crystals can be grown from these large macromolecular assemblies, the solution of their structure is by no means straightforward, since standard phasing techniques can often not be applied. The ribosome structure was solved using the anomalous signal from large heavy metal clusters. However, there is an alternative approach possible with XFEL radiation. The nuclear anomalous signal of a single ^{57}Fe atom is in the same order of magnitude. This alternative for phasing, however, requires a seeded XFEL in order to have a sufficient number of photons within the extremely small wavelength bandwidth required.

In recent years the solution of quite a number of difficult macromolecular structures, for which only extremely small crystals could be grown, became feasible due to the existence

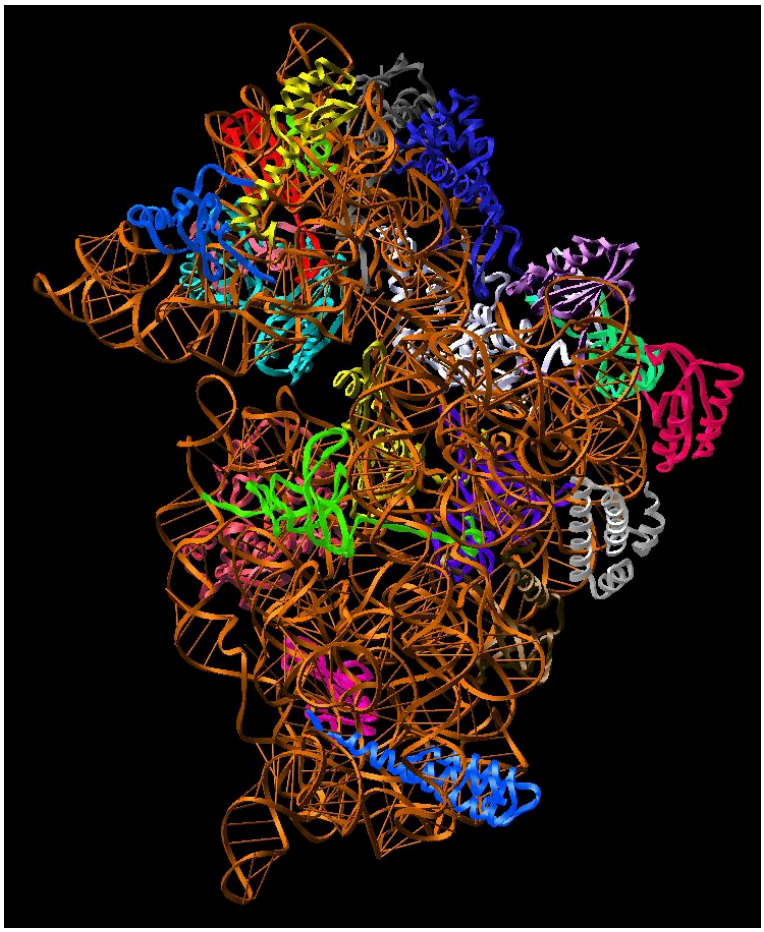

Figure 3.7.2.: *Example for a large macromolecular assembly: Schematic drawing of the small 30S-subunit of the Thermus Thermophilus ribosome; the RNA is shown in brown, other colored objects represent the attached proteins (courtesy: MPG-Arbeitsgruppe Ribosomenstruktur, Hamburg).*

of microfocus beamlines at third generation synchrotron radiation sources. XFEL radiation provides the potential to go far beyond what is possible in that direction today. A single focused pulse already provides enough intensity for diffraction from a two-dimensional layer of macromolecules or form sub-micrometer crystals.

XFELs can provide X-ray flashes with pulse durations of less than 100 femtoseconds and peak brilliance of 10-12 orders of magnitude higher than what is available from the best synchrotron radiation sources today. The predicted radiation tolerance to X-rays in the femtosecond time regime is several orders of magnitude higher than the theoretical limits in conventional X-ray experiments [7]. Therefore, the possibility to record diffraction images from single virus particles and large macromolecular assemblies without the need to amplify scattered radiation through translational repetition of the individual units leading to Bragg reflections come into reach.

With the existing and future X-ray sources in mind, the following exemplary fields of research in structural biology are considered to play a very important role for progress in life sciences:

1. Structure of the viral genome: No genome structure is known in three dimensions today, and structure-function relationship studies at the gene/genome level are missing. Single particle scattering experiments on individual viral particles offer a possibility to overcome this limitation.

2. Nanocluster technology: Assembling proteins of choice into regular nanoclusters for subsequent structural studies for novel X-ray diffraction experiments is a key development. This will include the specific attachment of target proteins onto the surface of regular templates. Such nanoclusters can be used for structural studies on both soluble and membrane proteins to obtain structures of proteins which do not crystallize.

3. Time-resolved diffraction methods and computer modelling of biological function: A functional understanding of biological macromolecules and complexes requires observations in four dimensions (x,y,z,t) (see example in Fig. 3.7.3). Time-resolved structural studies on biomolecular function are coming of age. The focus has shifted from studies on "systems of opportunities" to a more problem-oriented approach addressing significant questions in biology and chemistry [8]. The combination of diffraction methods with spectroscopic techniques in the experiments provides a means to correlate electronic transitions with structural transitions in the sample, eliminating much of the guess-work from experiments.

The knowledge of the dynamic properties of a number of macromolecules is the key for the understanding of their function. In past years, nuclear scattering experiments have successfully been applied to study some of these phenomena. At third generation sources, these experiments take very long, since the energy resolution required is extremely high, leaving few photons for the experiment. These experiments would benefit enormously from the extremely high spectral brilliance of the XFEL, especially after the seeding option has been implemented.

Even if the structure of all possible macromolecules and macromolecular assemblies were known, there would still be the question of how they are arranged in the cell and how they interact at different stages of the cell's life cycle. Cellular functions are carried out by modules of interacting molecules. Understanding how such modules work and interact with each other is a key aim for understanding the organization and function within a cell, and ultimately, in life. The answer to this basic question would bridge the gap between the molecular and the macroscopic level of our biological knowledge. At present, soft X-ray microscopes are able to achieve a resolution of about 20 nm with frozen hydrated samples. Since XFEL radiation will be coherent in the transverse direction, direct or holographic images of whole cells with a significantly higher resolution should in principle be possible. This might even be feasible within a single pulse,and suitable techniques/optics have to be developed.

At this place a more technical remark concerning the XFEL time structure seems appropriate: Whereas the bunch train structure of TESLA allows for a lot of flexibility in adapting

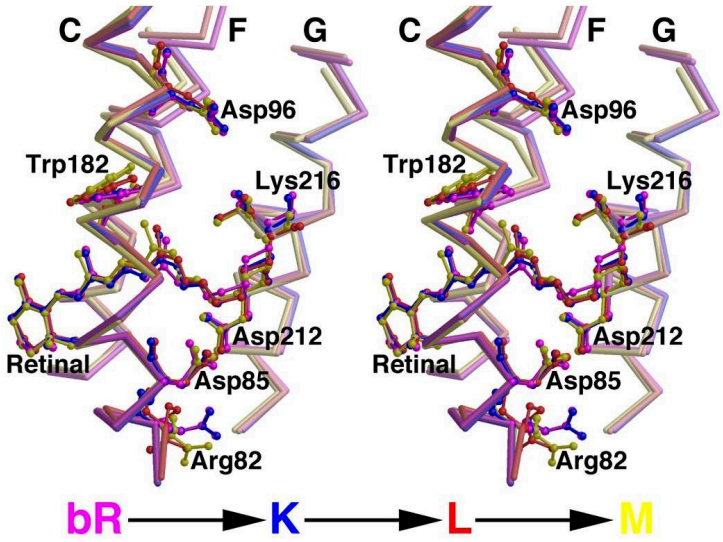

Figure 3.7.3.: *Light induced structural changes during the photocycle of bacteriorhodopsin. The ground state model (in purple) is shown with the K (blue), L (red) and M (yellow, D96N mutant) intermediate structures overlaid. Retinal isomerization from the all trans to a 13-cis geometry induces a sequence of movements in the surrounding residues. Pronounced movements of the main chain and side chain of Lys 216, which is covalently bound to the retinal, are visible in all three intermediate structures.*

the pulse sequence to the needs of the experiments discussed, for continuous sampling of data it is not optimal. This is because sample manipulation speed is limited and today's 2D CCD detector readout rates are at best only up to the kHz regime and effectively only a fraction of the available pulses in a bunch train can be used for exposures. In the following, a number of XFEL experiments addressing the scientific questions presented above will be discussed in more detail.

3.7.2. Macromolecular assemblies without translational symmetry

Today, limits in atomic resolution structural studies on biological systems are set by the requirement for crystals. This restricts the scope of detailed structural analysis to macromolecules and macromolecular assemblies which can be crystallized. Many biologically important systems are difficult or impossible to crystallize. As a consequence, there are large, systematically blank areas in structural biology. This has implications for current efforts in functional genomics. In particular, there are only a handful of membrane protein structures known today, structural studies on large assemblies are problematic, and there is no hope of reaching high resolution with currently available methods on non-repetitive and non-reproducible structures (e.g cells).

An X-ray FEL could offer the possibility to overcome this major limitation, and to open

up new avenues to explore the structure and dynamics of complex biological systems with unprecedented detail. This cannot be done with traditional methods due to radiation damage affecting the sample during data collection (see above). Any method capable of retrieving three dimensional structural information without the need for diffraction quality crystals will have important influence on the field. For small macromolecules (<30 kDa), NMR offers an alternative [9], and for very large assemblies like viruses and ribosomes, cryo electron microscopy is able to provide information at low and intermediate resolution [10, 11]. In both cases up to now, the accuracy can not compete with an atomic resolution X-ray crystal structure determination. In cryo electron microscopy are technical problems like lens transfer function corrections from particles at a-priori-unknown defocus positions in single-particle averaging techniques. In addition, radiation damage limits the maximum dose on the sample and hence the statistical signal, which translates directly to structural information in the form of the achievable resolution [12].

Because of the extremely short pulses of the XFEL, first calculations show that there is the possibility to extend this damage barrier for objects that provide a sufficient signal from a single 100 fs XFEL pulse. This is because neither secondary radiation decay processes nor heat transport have time to develop during the exposure being an extremely short photographic flash pulse [7, 8]. Molecular dynamics calculations of a macromolecule during its interaction with an focused XFEL photon pulse, which take into account all damage creating inelastic photon scattering effects, came to the following conclusions [7]:

1. There is a certain flux density which a sample can withstand during the duration of a pulse. Beyond that flux density (which depends on pulse length; see Fig. 3.7.4), the molecule will begin to be affected in a way that changes its diffraction pattern significantly.

2. The shorter the X-ray pulse, the higher the flux density for which the sample can remain relatively undistorted for the duration of the pulse. Inertial forces delay the Coulomb explosion.

3. Since all damage processes which are slower than the X-ray pulse can be neglected (e.g. diffusion of free radicals, transport of heat), significantly higher radiation doses can be applied compared to experiments with longer exposure times.

4. A single focused XFEL pulse is sufficient to cause enough ionization events to initiate the Coulomb explosion (see Fig. 3.7.5); however, these events do not manifest themselves during the passage of the pulse through the sample if the pulse is short enough.

These four statements have been obtained under the assumption that the results obtained for a single small macromolecule in Ref. [7] can be scaled to larger assemblies. The calculations of the effect will be further refined including the inelastic interactions of emitted Auger electrons due to the decay of K holes. According to our present knowledge for 100 fs long X-ray pulses, molecules consisting mainly of low-Z atoms can stand about $3 \cdot 10^{10}$ photons/pulse focused into $0.1\mu m$, which should be achievable by the time the XFEL is

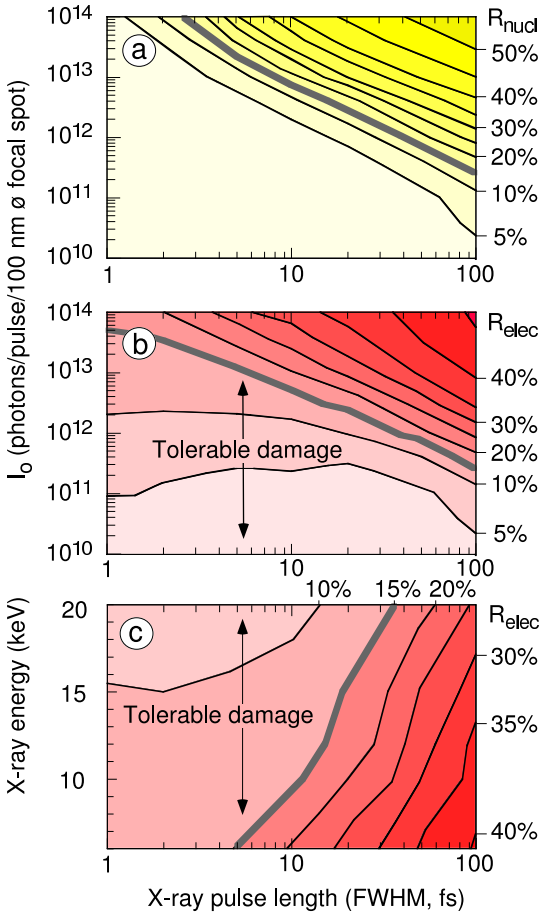

Figure 3.7.4.: *R-factor contour levels as function of the photon intensity (a.,b.), photon energy (c.) and radiation pulse duration (reproduced from [7]). The thick lines indicate the maximum tolerable sample damage. Only photo inelastic effects have been considered; R gives the confidence level in comparing data and model assumption and is defined by* $\sum|\sqrt{I_i^o} - k\sqrt{I_i}|/\sum\sqrt{I_i^o}$. I_i^o*: pixel intensity of the undisturbed object;* I_i*: actual pixel intensity;* k*: scale factor; the sum runs over all detector pixels.* R_{elec}*: R value based on scattering from the actual electron configuration,* R_{nucl}*: neglecting changes in the electronic configuration of the atoms, it represents a measure for the distortion of the positions of the nuclei during the exposure.*

scheduled to operate[1]. Under these conditions, the capsid of a large virus (e.g. blue tongue virus (BTV) [13]) will scatter significantly only in the low resolution regime (Fig. 3.7.6). Hence, a single diffraction image of such a capsid will not contain enough information to retrieve detailed structural information. However, as soon as a single diffraction image contains enough information to enable the alignment of images of randomly orientated objects, averaging techniques similar to those developed for cryo electron microscopy image reconstruction can be applied. The achievable resolution can therefore be enhanced significantly by using a large number of diffraction images. The resolution will finally be determined by

[1]The number of photons per pulse varies from 10^{12} to 10^{13} depending on photon energy (compare Tab. 4.2.4).

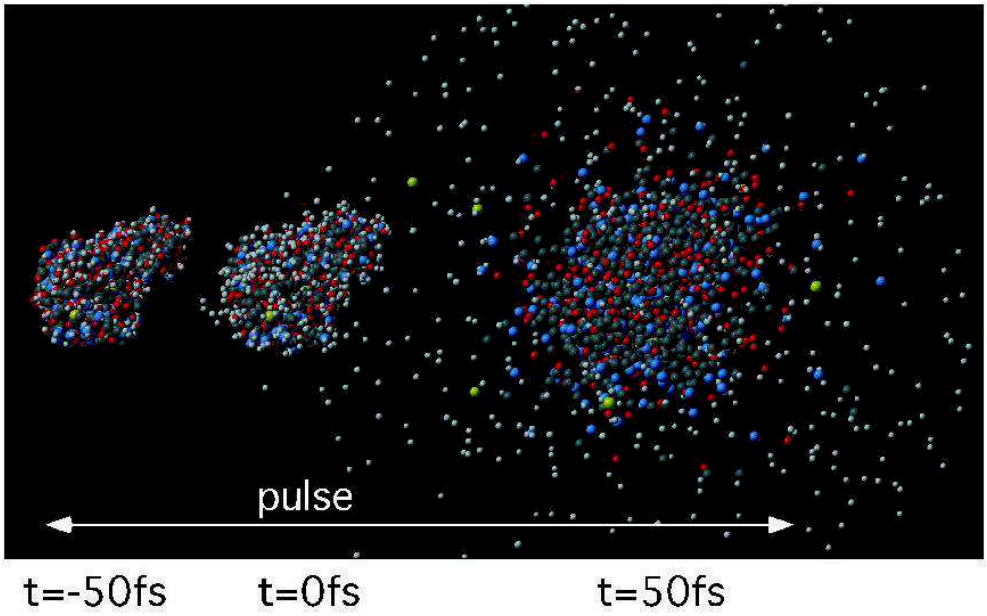

Figure 3.7.5.: *Coulomb explosion of a T4 lysozyme molecule (H: white; C: grey; N: blue; O: red; S: yellow) induced by the radiation damage caused by a* 3×10^{12} *photon per* $(0.1\ \mu m)^2$ *pulse of 12.4 keV energy. The FWHM of the pulse was 50 fs. The molecule is shown at the beginning, in the middle and after the pulse. Even after half of the pulse has passed, the distortions are small. After the pulse the Coulomb explosion is under way [7]. The distortion of the molecule during the time of the pulse is considerably smaller for lower flux densities during the pulse (see also Fig. 3.7.4).*

the reproducibility of the individual samples (e.g. virus particle), the number of exposures, and the statistical accuracy achieved during the numerical alignment procedure.

The result of such measurements will be the continuous distribution of the scattering amplitude in reciprocal space. Opposite to a crystalline scattering pattern information becomes available continuously in reciprocal space and not only in the direction of the Bragg reflections. This so-called molecular transform is the Fourier transform of the object's electron density. It is considerably oversampled compared to what is measured in a crystal when only Bragg spot are measured. This is demonstrated in Fig. 3.7.7 showing the pattern of scattering intensities for a molecule versus a crystal. In the case of the molecular transform, the phase problem can be circumvented, since methods exist already to retrieve the scattering density (electron density) in real space from an oversampled transform [14]–[16]. Present-day estimates indicate that a non-translationally periodic object with a mass comparable to a single BTV capsid scatters sufficiently to allow for numerical alignment needed for repetitive measurements. To demonstrate this in Fig. 3.7.8 the correlation between different images is given, as obtained by simulations.

In order to investigate a protein, one could attach it to the surface of some core molecule of known structure serving as a scaffold, e.g. an icosahedral virus capsid. The molecule might bind tightly and adapt the symmetry of the scaffold molecule. In this case, the struc-

ture could be determined by holographic reconstruction methods [17], since the scattered wave from the known scaffold structure would serve as a reference wave. In principle any reproducible object of known structure which can bind molecules in a defined orientation can serve as a scaffold for unknown macromolecules. The rapidly developing field of nanotechnology can be anticipated to provide means to assemble such structures [18]. The scattering experiments have to be carried out in vacuum so as to reduce any source of background. With ultrasmall samples, new procedures for sample selection, characterization, and handling will need to be developed. Work is progressing to develop novel "container-free" methods based on spraying techniques [19]–[24] in order to select and rapidly inject single hydrated molecules, nanoclusters of molecules and larger particles, e.g. viruses, ribosomes, protein nanoclusters, nanocrystals, or even small living cells, into an intense X-ray beam. The sample entering the vacuum chamber is in random orientation, encapsulated in a micro-droplet, and would spend only a few microseconds in the instrument. The micro-droplets can be dried to a desired level before interacting with the X-ray beam. A beam of molecules/particles can thus be injected into the pulse train of the X-ray source. This introduction system can provide a 'gentle' environment for the analysis of proteins such that surface water molecules can be retained in these complexes [19, 20]. Recent experiments have also demonstrated that virus particles retain their three-dimensional structure and remain capable of infection after electrospray ionization and collection [21]–[23]. Intact ribosomes may be analyzed this way.

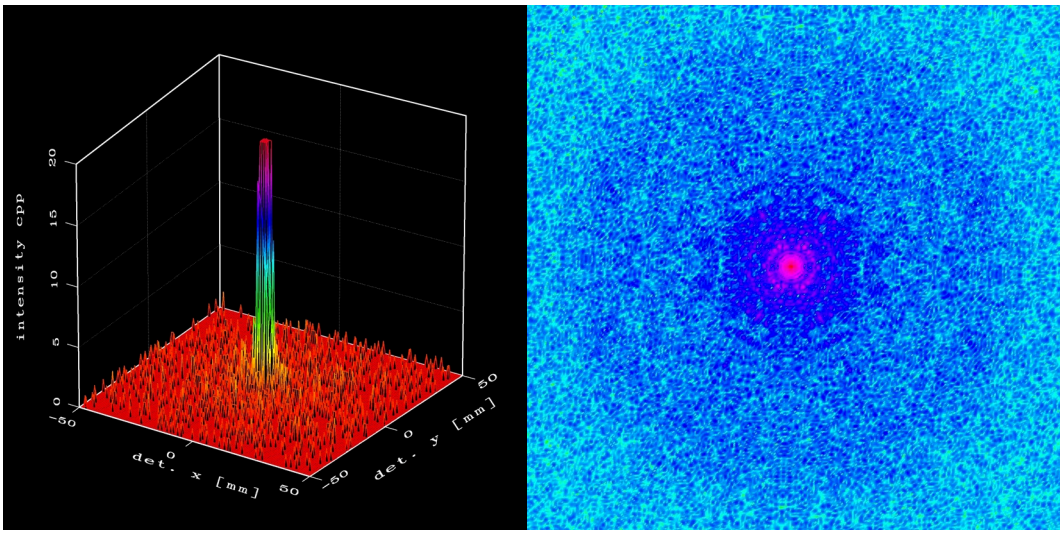

Figure 3.7.6.: *Left: Diffracted intensity of a single blue tongue virus (BTV) capsid from a single* $\approx 3 \cdot 10^{10}$ *photon pulse focused into* $0.1\ \mu m$*. The rim of the detector corresponds to about 2.2 Å resolution. There is a statistically significant signal only at extremely low resolution. However, this is sufficient to align diffraction images of randomly oriented particles in order to average a large number of exposures to reconstruct the scattering distribution in reciprocal space. Right: Plane section of the molecular transform of BTV. The rim of the image corresponds to about 8 Å resolution.*

Experiments with electrospray techniques coupled to orthogonal time-of-flight mass spectroscopy technology could provide high sensitivity and a potentially unlimited molecular weight range. By fine tuning the drying conditions and the path lengths that the particles undergo before they meet the radiation pulse, one could use similar techniques for introducing small living cells into intense photon beams. Results so far suggest that conditions in the spray can be made similar to conditions in electron cryo-microscopy (low temperature, high vacuum, hydrated samples). However, mass spectrometry has the potential to select large samples based on mass differences of a few Daltons. The marriage of structural methods with mass spectrometry will open up new horizons for studies of structure function relationship, solvation, and reaction dynamics in both biology and chemistry.

When such techniques can be applied, single particle imaging at atomic resolution using radiation from an XFEL would be a significant advance in structural biology because it would provide means to obtain structural information of large macromolecular assemblies that can not be crystallized. Preferred targets for such investigations would be membrane proteins.

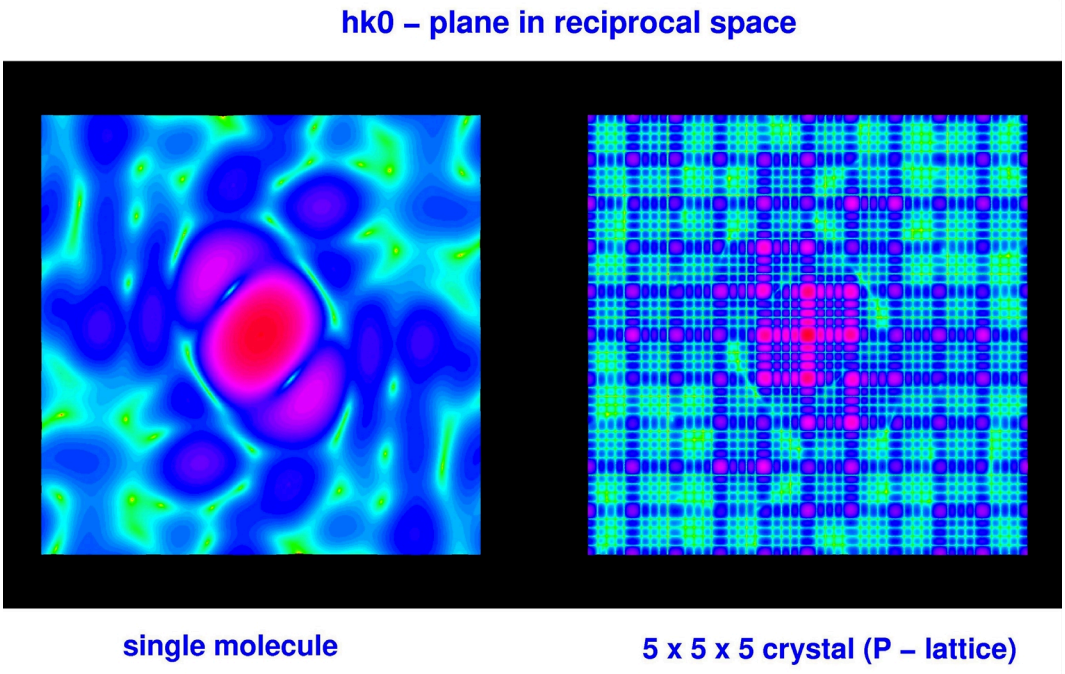

Figure 3.7.7.: *Comparison of the Fourier transform of a single macromolecule (left) and that of a* $5 \times 5 \times 5$ *primitive crystal of the same molecule in the same orientation (right). The colors represent a logarithmic scaling with green the lowest and pink/red the highest modulus. The maximum intensity on the right side is about 15000 time higher. In a crystal the Fourier transform of a molecule or unit cell can only be sampled in the directions of Bragg reflections, which determine the scattering pattern. For larger crystals the intensity between the reflections disappears almost totally due to destructive interference.*

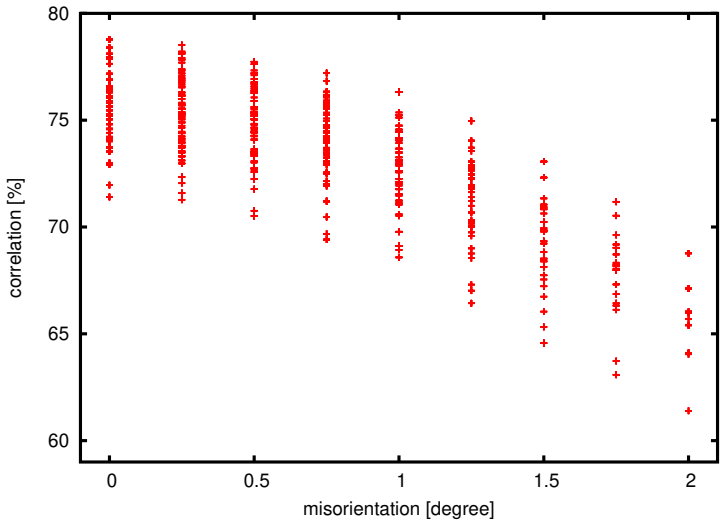

Figure 3.7.8.: *Correlation coefficient between images of different misorientation with respect to an ideal image of no misorientation. Diffraction images were calculated for the known structure of the BTV virus capsid assuming a pulse with* 3×10^{10} *photons focused to* $0.1\ \mu m$*. The scatter of the data points for the same misorientation originates from the applied Poisson noise.*

3.7.3. Micro- and 2D crystals

Up to now only a very few three-dimensional crystals have been grown from membrane proteins. Therefore, our knowledge about this physiologically very important class of proteins shows vast blank regions. However, many membrane proteins, like bacteriorhodopsin, already form two-dimensional crystals in their natural environment. Therefore, XFEL radiation might allow to study these molecules in 2D crystals [25]. Estimates show that, given a $20 - 25\,\mu m^2$ two-dimensional protein crystal, a single pulse of an XFEL focused to approximately this size will provide diffraction rods of reasonable intensity (see Fig. 3.7.9).

Since the sample will not survive significantly longer than the pulse duration, many small 2D crystals will be needed to obtain a complete intensity data set. The challenging objective is to design a support which will produce tolerable additional background. These efforts are probably minor in relation to the benefit yielded by a method that would help to solve the structure of a larger number of membrane proteins.

From crystal growth studies using e.g. atomic force microscopes, it is known that proteins very often form micrometer size crystals but do not continue to grow. In these cases, the experimental procedures for the non crystalline objects described in section 3.7.2 can be envisaged for microcrystals also. Microcrystals of protein molecules are already large enough to show distinct Bragg reflections (see Fig. 3.7.7). For this reason, the determination of the orientation from the diffraction patterns of randomly oriented crystals should be easier than of non-periodic objects. However, in order to derive a meaningful intensity data set, the size distribution of the microcrystals has to be narrow in order to be able to average and merge a large number of diffraction patterns from different crystals.

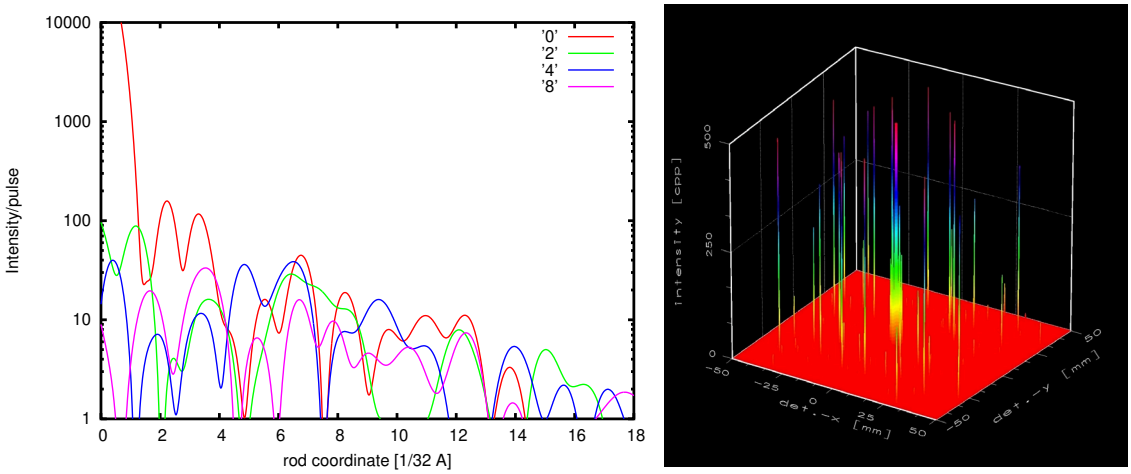

Figure 3.7.9.: *Left: Intensity for a single XFEL pulse along (0 h) rods (the h index is given in the figure) of a hypothetical 2D crystal of a small macromolecule (lysozyme) of about 25 μm^2 size (1500 x 1500 molecules). The XFEL beam was assumed to be focused in order to provide 400 ph/Å^2 (10^{12} photons focused to 25 μm^2). At this flux density, about 0.5% of all non-H atoms will have suffered photo ionization. Right: Theoretical diffraction pattern of 50×50×50 lysozyme molecules placed on a primitive cubic lattice of 38 Å periodicity using a single XFEL pulse (3×10^{10} ph/$(0.1\mu m)^2$). The intensity scale was truncated at 500 counts per pixel (cpp). The detector rim corresponds to about 2 Å resolution.*

3.7.4. Function of biomolecules

The time scale of reactions, charge transport, translocation of ions, conformational changes, etc. in biological macromolecules extends from several femtoseconds to seconds, minutes and longer (see Fig. 3.7.10). At present, a time resolution in the ns range is accessible for strongly scattering crystals of relatively small macromolecules with stroboscopic pump-probe techniques [26]–[28]. Since the pulse width of an XFEL (≈ 100 fs) will be about three orders of magnitude shorter than that provided by present day sources, it should be possible to achieve a considerable higher time resolution. This requires reversible reactions that show small conformational changes, that can be triggered fast enough, that yield a sufficiently high population of the state to be investigated [29, 30], and that can be repeated several times reproducibly in order to be able to sample a representative region of reciprocal space. In the time regime pertinent to possible XFEL experiments, reactions that can be triggered by a fast laser pulse are the most suitable, e.g. reversible photo dissociation or isomerization of small groups. Possible targets include all proteins containing a chromophore, like heme or retinal. The short pulses of an XFEL would enable one to observe structural changes in atomic detail with sub picosecond time resolution, thus providing a better understanding of the very early stages of the mechanisms of these processes.

Mechanical perturbations are essentially localized in a molecule on a time scale of 100 fs [31]. Consequently, structural perturbations in a system will be much better characterized in the femtosecond time-regime than on longer time scales. This phenomenon will give ac-

cess to many important processes which are inaccessible today. In addition, a femtosecond excitation may synchronize molecules in the sample for a short time (a couple of picoseconds). This phenomenon offers amazing new possibilities for structural investigations with femtosecond X-ray pulses through the observation of coherent reaction dynamics. On this time scale, real synchronization could be achieved among molecules in the sample before the structures enter the Maxwell-Boltzmann regime. Planned experiments with the XFEL will allow the very first observation of transition states in three dimensions. On longer time scales, e.g. in the Maxwell-Boltzmann regime, chemical reactions do not proceed synchronously. Here, different intermediates may be present simultaneously, but they are vibrationally uncoupled and thus unsynchronized. The interpretation of all time-resolved experiments outside the femtosecond domain is invariably compromised by this factor today [32].

As these studies rely mainly on the time structure of the XFEL, the spontaneous radiation could in principle be used for well scattering samples. Depending on the system and the number of possible reversible repeats, highly focused and divergent monochromatic, quasi monochromatic or limited bandwidth diffraction techniques could be applied to collect the intensity data [33]–[35].

Reaction initiation, either with photons or by the diffusion of reactants, can be a limiting factor in structural kinetics. Time-resolved structural studies on diffusion-triggered processes

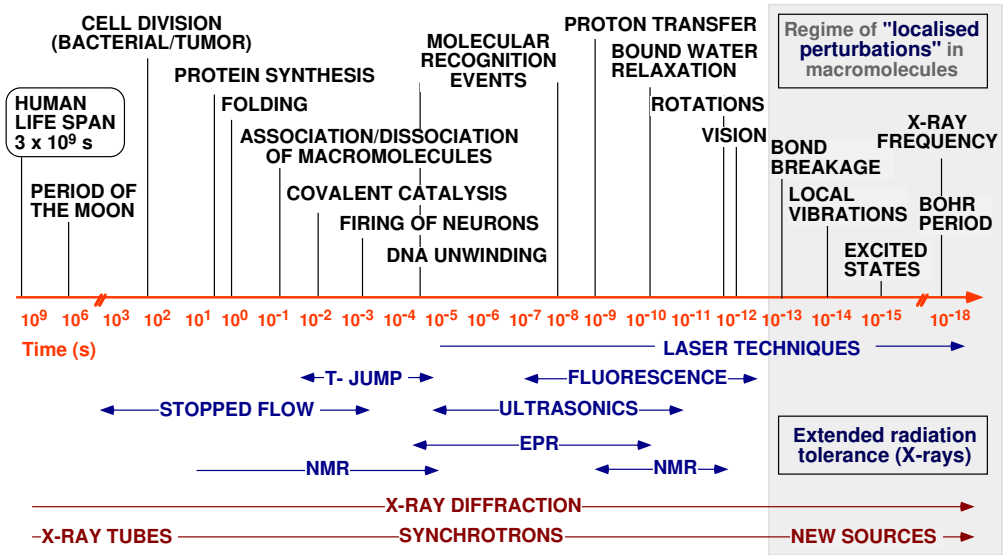

Figure 3.7.10.: *Relevant time scale of a number of biochemical processes and instrumental techniques to investigate them. With present day sources, time scales down to* 10^{-9} *seconds are accessible.*

could be extended to a much wider range of systems if one could lower the diffusion barriers. One obvious possibility for lowering diffusion barriers is to reduce the sample size and to use nanoclusters or nanocrystalline enzyme assemblies of micron or submicron dimensions for time-resolved structural studies. With very small samples, the vast majority of solution techniques (e.g. stopped flow methods) would become available for time-resolved structural investigations.

Reactions that result in large conformational changes either disrupt the crystalline order or are kinetically hindered by the energy barrier associated with crystal packing contacts. In these cases the molecules have to be studied in solution by small angle scattering.

3.7.5. Dynamics of macromolecules

The function of many biological macromolecules depends critically on the molecules' inherent flexibility. For example, in the well studied case of myoglobin, the static structure does not show any path on which the ligand (O_2, CO or NO_x) could access the heme group [36]. This is only possible due to dynamic changes of the molecule's structure. Standard crystallographic diffraction experiments are used to evaluate the time average of the ensemble of all molecules inside the whole crystal. However, for a detailed understanding of the function of proteins, the knowledge of the dynamical behavior is as important as the three-dimensional static structure. One possibility to study dynamics is nuclear inelastic scattering (NIS) which directly determines the spectrum of the phonons to which the Mössbauer nucleus is coupled. Further techniques have been developed in order to obtain the total phonon density of states even in crystals free of a Mössbauer nucleus [37, 38]. These reveal important information about the crystals' and the molecules' dynamical behavior. In addition, information on the chemical and magnetic surroundings of the Mössbauer nucleus can be derived from the hyperfine interaction [39, 40] determined by nuclear forward scattering (NFS) experiments.

These experiments benefit from XFEL radiation in several ways: (i) the short pulse length would provide a possibility to measure almost immediately after the very short excitation, enabling better access and interpretation of fast relaxation processes, (ii) the high pulse intensity is an advantage at longer decay times because it gives better signal for slow relaxation processes, and (iii) even very small sample volumes can be analyzed rapidly using a single pulse. The tailorable bunch population within a 1 ms macro bunch train provides the possibility for a variety of time delayed nuclear scattering experiments.

Biologically relevant Mössbauer nuclei are ^{57}Fe (14.4 keV), ^{61}Ni (67.4 keV) and ^{67}Zn (93.3 keV). In order to make use of the latter two nuclei, higher harmonics of the laser line have to be used. An alternative is the spontaneous undulator radiation, which still has the advantage of pulses 1000 times shorter than those of third generation synchrotron sources.

3.7.6. Cellular structure

The understanding of biological structures on a sub-cellular level requires knowledge of the three dimensional structure of cells or organelles at the highest possible resolution. The XFEL may take us also there. Light microscopes are limited in their resolution by the wavelength of the light used and the numerical aperture of the optical system. Various techniques

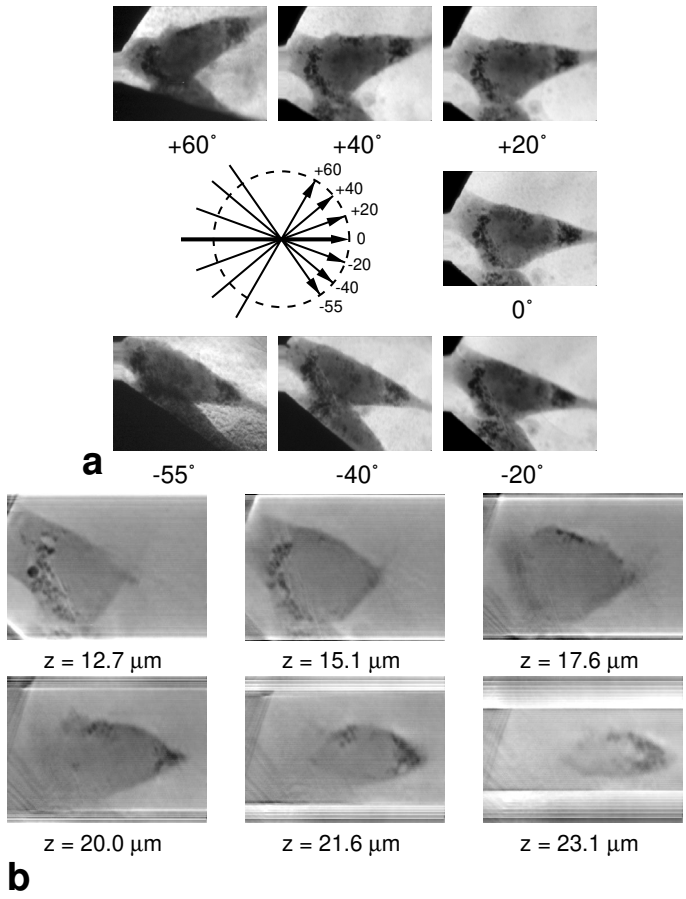

Figure 3.7.11.: *Cryo scanning transmission X-ray microscope; a: images of frozen hydrated 3T3 fibroblast tilted by different angles. b: slices at different z of the 3D reconstruction from the images in a); final resolution* $100 \times 100 \times 250\, nm^3$ *(reproduced from [50]).*

have pushed the limits significantly (see e.g. [41]–[43]). Electron microscopes and electron tomographic reconstruction techniques can provide 3D resolution of 10 nm or better on frozen hydrated specimens [44]. They are limited, however, to a specimen thickness of about 1 μm due to the inelastic mean free path of electrons in ice. Soft X-rays can provide a means for high resolution imaging of frozen hydrated specimens up to about 10 μm thickness [45]–[47], allowing one to study a larger range of intact cell types. Such specimens can be imaged with microscopes using zone plate optics with a resolution of about 30 nm in present-day work [48, 49]. In fact, a 30 nm resolution image of a 10 μm thick object will have considerable problems with overlapping features. To resolve this problem, tomographic reconstruction in soft X-ray microscopy has been applied successfully [50, 51] (see Fig. 3.7.11).

However, the depth of focus of a Fresnel zone plate of outermost zone width δ_{r_N} is about $8\delta_{r_N}^2/\lambda$ (see e.g. [50]). For a 30 nm lateral resolution at 520 eV, the depth of focus is only about 3 μm, and it decreases to 1 μm at 20 nm lateral resolution. This is a disadvantage when thicker ($\simeq 10\,\mu$m) samples are imaged. One alternative is to use phase contrast [52] at higher

photon energies (e.g. 8 keV), though one might then be faced with a problem of phase unwrapping unless the cumulative phase were kept below $\pi/2$, in which case the contrast of small structures would be quite low. Another alternative is to use diffraction tomography [53], where a complex object can be reconstructed from the measurement of intensity at a plane beyond the sample in each projection. Experiments to use diffraction tomography, with a zone plate used to transfer a magnified version of downstream intensity distributions to a CCD camera, are now under development; however, the anticipated exposure time for a tilt series using existing synchrotron sources is on the order of a day, during which time the specimen is usually altered by ice buildup in the cryo system. The X-FEL's ability to provide high time-averaged brilliance would allow this type of experiment to reach its full potential.

By exploiting the coherence of XFEL radiation, direct holographic schemes using an additional reference wave could also be envisaged to image larger biological objects like cells. Presently, the resolution of in-line Gabor type holography is limited by the spatial resolution of the detector being much larger than the wavelength/numerical aperture ratio. Fourier type holography is limited by the size of the point source used to generate the spherical reference wave (e.g. the focus of a zone plate [54]). However, even rather complex objects that are not pointlike can be used to generate a complex reference wave [16, 17]. In this case the resolution is limited by the accuracy to which the reference scatterer is known [55, 56]. Suitable reference objects could, for example, be fabricated by nanotechnological methods [18]. These experiments would allow the use of currently impossible methods to image objects like whole cells with high resolution. It may even be possible to obtain several holograms for different observation angles within a single pulse [57].

The application of these techniques will enable one to investigate the arrangement and interplay of different constituents of biological objects in three dimensions at high resolution. This should provide a better understanding of biological processes. The ultimate goal would be to investigate the temporal evolution of these processes.

3.7.7. Alternative phasing method

The multiple wavelength anomalous diffraction (MAD) method [58] has gained significant importance for the phasing and the solution of macromolecular structures due to the availability of stable and tunable synchrotron beamlines. The anomalous signal is derived from atoms that show strong anomalous scattering. In large complexes, the phasing power of a single metal atom is in general too small for a successful application of MAD. Therefore, atoms with stronger phasing power would be helpful. As an alternative, the anomalous signal of derivatives with large clusters of heavy metal atoms is used at present. An exciting alternative that might become feasible with the advance of XFEL radiation is the use of the anomalous signal provided by nuclear scattering of a Mössbauer nucleus [59]. One single Fe atom provides an f'-value equivalent to 440 electrons [60]. The application of this method requires an interference of the promptly scattered radiation from the atom's electrons with the delayed emitted photons of the Mössbauer nuclei. Therefore, the exciting radiation's longitudinal (temporal) coherence must be of the order of the time delay of the nuclear scattering. This can be achieved by using an extremely narrow bandpass nuclear scattering monochro-

mator. At an energy resolution of 10 neV, the XFEL would provide about 10^7 photons per second in a 0.1 x 0.1 mm^2 spot. This intensity could be increased by roughly a factor of 500 using the high resolution seeding option (see A.2.2), which is intended to provide a laser line with 20 meV energy resolution. Since the number of photons in the required bandwidth interval (5×10^9 per second) is still limited even at an XFEL, the maximal structure size that can be determined by nuclear anomalous scattering from ^{57}Fe is not determined by the magnitude of the Bijvoet differences but by the time that is needed to collect the intensity data with sufficient statistical significance. First estimates show that, within a week's beam-time, an intensity data set for a molecule of the size of the BTV capsid ($\approx$ 40 MDa) could be measured. The radiation damage for a given significance of the anomalous signal will be considerably smaller in the case of nuclear scattering due to the smaller number of incident photons required for the same signal.

Bibliography

[1] http://www.rcsb.org/pdb/holdings.html.

[2] D. Voet and J.G. Voet, *Biochemistry*, Wiley, New York (1995).

[3] F. Schlunzen et al., Cell **102**, 615 (2000).

[4] B. Wimberly et al., Nature **407**, 327 (2000).

[5] J.H. Cate et al., Science **285**, 2095 (2000).

[6] N. Ban et al., Science **289**, 905 (2000).

[7] R. Neutze, R. Wouts, D. van der Spoel, E. Weckert, J. Hajdu, Nature **408**, 752 (2000).

[8] J. Hajdu, Curr. Op. Struct. Biol. **10**, 569 (2000).

[9] K. Wüthrich, Acta Cryst. D **51**, 249 (1995).

[10] F. Mueller et al., J. Mol. Biol. **298**, 35 (2000).

[11] C. M. Spahn, P.A. Penczek, A. Leith, J. Frank, Structure **8**, 937 (2000).

[12] R. Henderson, Q. Rev. Biophys. **8**, 171 (1995).

[13] J.M. Grimes et al., Nature **395**, 470 (1998).

[14] J. Miao and D. Sayre, Acta Cryst. A **56**, 596 (2000).

[15] J. Miao, J. Kirz, D. Sayre, Acta Cryst. D **56**, 1312 (2000).

[16] A. Szöke, Chem. Phys. Letters **313**, 777 (1999).

[17] J. Somoza et al., Acta Cryst. A **51**, 691 (1995).

[18] K. Soong et al., Science **290**, 1555 (2000).

[19] C.V. Robinson et al., Nature **372**, 646 (1995).

[20] C.V. Robinson et al., J. Amer. Chem. Soc. **118**, 8646 (1996).

[21] D. Despeyroux, R. Phillpotts, P. Watts, Rap. Commun. Mass Spect. **10**, 937 (1996).

[22] G. Siuzdak et al., Chem. Biol. **3**, 45 (1996).

[23] M.A. Tito et al., J. Am. Chem. Soc.**122**, 3550 (2000).

[24] A.A. Rostom et al., Proc. Natl. Acad. Sci. USA **97**, 5185 (2000).

[25] M. Becker, *Considerations on the possibility of using hard X-rays from a Free Electron Laser to determine structures of membrane proteins in 2-dimensional crystals.*, EMBO Workshop: Potential Future Applications in Structural Biology of an X-ray free Electron Laser at DESY, Hamburg, (2000) 184–198.

[26] V. Šrajer et al., Science **274**, 1726 (1996).

[27] B. Perman et al., Science **279**, 1946 (1998).

[28] K. Moffat, Nature Struct. Biol. **5**, 641 (1998).

[29] I. Schlichting and R. Goody, *Triggering Methods in Kinetic Crystallography*, in *Methods in Enzymology, Vol. 277*, Academic Press, (1997), pages 467–490.

[30] I. Schlichting, Acc. Chem. Res. **33**, 532 (2000).

[31] A.H. Zewail, J. Phys. Chem. A **104**, 5660 (2000).

[32] J. Hajdu et al., Nature Struct. Biol. **7**, 1006 (2000).

[33] Z. Ren et al., J. Synchrotron Rad. **6**, 891 (1999).

[34] M. Wulff et al., Nucl. Instrum. Meth. A**398**, 69 (1997).

[35] D. Kosciesza and H.D. Bartunk, J. Synchrotron Rad. **6**, 947 (1999).

[36] A. Ostermann, R. Waschipky, F. Parak, G. Nienhaus, Nature **404**, 205 (2000).

[37] C. Keppler et al., Europ. Biophys. J. **25**, 43 (1996).

[38] H. Grünsteudel et al., Inorganica Chimica Acta **70**, 917 (1998).

[39] H. Paulsen et al., Phys. Rev. B**70**, 975 (1999).

[40] C. Keppler et al., Eur. Biophys. J. **29**, 146 (2000).

[41] W.A. Carrington et al., Science **268**, 1483 (1995).

[42] S.W. Hell, M. Schrader, H.T.M. van der Voort, Journal of Microscopy **187**, 1 (1997).

[43] M.G.L. Gustafsson, D.A. Agard, J.W. Sedat, Journal of Microscopy **195**, 10 (1999).

[44] R. Grimm et al., Biophysical Journal **74**, 1031 (1998).

[45] D. Sayre, J. Kirz, R. Feder, D.M. Kim, E. Spiller, Ultramicroscopy **2**, 337 (1977).

[46] C. Jacobsen, R. Medenwaldt, S. Williams, *A perspective on biological x-ray and electron microscopy*, in *X-ray Microscopy and Spectromicroscopy*, J. Thieme, G. Schmahl, E. Umbach, D. Rudolph (eds.), Springer, Berlin (1998).

[47] G. Schneider, Ultramicroscopy **75**, 85 (1998).

[48] S. Spector, C. Jacobsen, D. Tennant, Journal of Vacuum Science and Technology **B15**(6), 2872 (1997).

[49] D. Weiss, M. Peuker, G. Schneider, J. Appl. Phys. **72**, 1805 (1998).

[50] Y. Wang, C. Jacobsen, J. Maser, A. Osanna, Journal of Microscopy **197**, 80 (2000).

[51] D. Weiß et al., Ultramicroscopy **84**, 185 (2000).

[52] G. Schmahl, D. Rudolph, G. Schneider, P. Guttmann, B. Niemann, Optik **97**, 181 (1994).

[53] M.H. Maleki and A.J. Devaney, Opt. Eng. **33**, 3243 (1994).

[54] I. McNulty et al., Science **256**, 1009 (1992).

[55] A. Stroke et al., Phys. Lett. **18**, 274 (1965).

[56] M. Howells, B. Calef, C. Jacobsen, J. Spence, W. Yun, *A calculation of the performance of a scheme for imaging macromolecular assemblies by diffraction tomography*, Book of Abstracts: 7th International Conference on Synchrotron Radiation Instrumentation, Berlin (2000), Pos1–125 (submitted for publication).

[57] M. R. Howells, C. Jacobsen, S. Lindaas, *Possibility for one-shot tomography using a high-gain free-electron laser*, Proc. of the Workshop on Scientific Applications of Coherent X-rays (J. Arthur, G. Materlik, and H. Winick, eds.), no. NTIS CONF-940250, Washington, D.C.: National Technical Information Service, Feb. 1994., SLAC-SSRL 0066, Stanford, California.

[58] W. Hendrickson, Science **254**, 51 (1991).

[59] F. Parak, R. L. Mössbauer, U. Biebl, Z. Physik **244**, 456 (1971).

[60] J. Hannon and G. Trammell, *Resonant γ-ray scattering and coherent excitations of nuclei*, in *Resonant Anomalous X-Ray Scattering*, G. Materlik, C. Sparks, K. Fischer (eds.), (1994), pages 565–587.

3.8. Nonlinear Processes and Quantum Optics

This chapter has been written on the basis of contributions to the reports of the workshop "Non-Linear Optics, Quantum Optics and Ultrashort Phenomena investigated with an XFEL" edited by G. Huber (University Hamburg) and B. Adams (APS, Chicago) (see A.1.6). In these contributions, more detailed descriptions and further references can be found. A. Ringwald (DESY) has contributed Sec. 3.8.2.

Nonlinear optics is well established in the visible spectral region and covers fundamental aspects as well as industrial applications. Its development was based largely on advances in visible light lasers. A somewhat analogous development can be expected with the XFEL. Whereas present day X-ray sources largely have the characteristics of thermal light, the XFEL produces highly coherent X-rays at high power densities. Both of these properties are required to exploit nonlinear optical effects, the former to achieve accurate phasing and the latter specifically to reach the nonlinear regime.

The specific properties of X-rays that make their application in quantum optics interesting are the high photon energy, facilitating single photon detection at high quantum efficiency and low noise level, and the high photon momentum, which is favorable for achieving well separated regions in phase space in photon-atom interactions. The XFEL will offer a time structure with pulses of about 80 fs duration, i.e. ca. 1000 times shorter that those available from contemporary synchrotron radiation sources. By use of pulse compression or pulse slicing techniques, even shorter pulses should become possible. This is the time scale on which the elementary steps of chemical reactions and of some phase transitions take place. In conjunction with ultrashort laser pulses, the X-rays from the XFEL will offer information on the dynamics of chemical reactions with atom-sized and element-specific resolution.

3.8.1. Nonlinear optics and quantum optics

The refractive index for X-rays in any kind of matter is rather close to unity, and therefore nonlinearities are exceedingly small. The nonlinearity of the vacuum itself is even smaller, and probably not even accessible with the XFEL. Nonlinear optical effects are classified according to their order n. The total number of photons created and annihilated is $n = m+1$. Furthermore, the parity of inversion symmetry of the nonlinear material must be different from the parity of the order of the nonlinear process considered. Generally speaking, even-order nonlinear effects (such as frequency doubling) require an acentric material, while odd-order effects do not. In the visible spectral region, the even-order optical nonlinearities normally have their origin in asymmetries and anisotropies of chemical bonds. Because the energy of a chemical bond is typically in the energy region of a few eV, chemical bonds do not play a big role for X-rays unless the X-ray energy is chosen to lie very close to an absorption edge. Even order nonlinear processes from atoms or ions will therefore require a chemical bond or a strong external field that breaks the centrosymmetry *plus* an X-ray energy close to an absorption edge. If the strong external field is of oscillatory nature, we are actually considering an odd-order effect.

3.8.1.1. Free electrons

A totally different type of nonlinearity is based upon quasi-free electrons (i.e. with binding energies well below the X-ray photon energies). It is of noncentrosymmetric character and therefore permits even-order nonlinear effects (see A.2.1 for further details) and can be described by an expansion of the radiating current density of a distribution of free charges that is subjected to several electromagnetic plane waves. In a nonrelativistic approximation, we simply iterate the Lorentz equation. Higher order terms come about because (i) the oscillating electrons sample the electromagnetic field at locations other than their respective rest positions, (ii) the oscillatory velocity gives rise to a $\mathbf{v}\times\mathbf{B}$ term and also (iii) to a displacement current.

The first order simply describes Thomson scattering. In second order, effects such as second harmonic generation, optical sideband generation or spontaneous down conversion appear. Among the many effects that are conceivable in third order, the most important ones for our purposes are probably four wave mixing involving either all X-rays or one X-ray and two optical photons. The orders of magnitude are given by the following expressions:

$$\begin{aligned} \text{2. order:} \quad \Phi_f &= \sum \Gamma \frac{137\pi r_e^4}{4\omega_i} \Phi_i \Phi_j \\ \text{3. order:} \quad \Phi_f &= \sum \Gamma \frac{137^2 \pi^2 r_e^6}{\omega_i \omega_j} \Phi_i \Phi_j \Phi_k \ , \end{aligned} \tag{3.8.1}$$

where Γ is a geometry and polarization factor in summary representation of the projection factors that arise from different combinations of wave vectors and polarization directions in the contributions to the nonlinear current. The sums in Eqs. 3.8.1 are to be taken coherently, i.e. including all interference terms. The incident photon fluxes Φ_i, Φ_j, Φ_k are in units of photons per unit time and area, and the radiated photon flux is in units of photons per unit time and solid angle. A cross section relating the incident flux Φ_i to the outgoing flux Φ_f can be defined by $\Phi_f = \sigma\Phi_i$ by assigning to σ everything on the right hand sides in Eqs. 3.8.1 except Φ_i itself, but including Φ_j and Φ_k.

The nonrelativistic approximation is valid if the dimensionless light amplitude eA/mc^2 is less than unity, where A is the amplitude of the vector potential. Converted to power density, this reads

$$\mathcal{P} < \frac{[mc^2]\omega^2}{8\pi c r_e} \ . \tag{3.8.2}$$

At a photon energy of 1eV, the limit is $\approx 10^{22}\,\mathrm{W/m^{-2}}$. This value is surpassed by orders of magnitude with state-of-the-art short pulse lasers. In contrast, the limit for X-rays of 12.4 keV is ca. $10^{30}\,\mathrm{W/m^{-2}}$ which is out of reach for an XFEL, even if focused to 0.1 μm^2. Generally speaking, a relativistic calculation will yield the same or considerably larger optical nonlinearities of free electrons as in the nonrelativistic and ultrarelativistic cases, respectively. The order of magnitude estimates given in this text are therefore realistic for processes involving X-rays only and are underestimates where high power visible laser pulses are involved.

3.8.1.2. Photon addition and subtraction

At moderate intensities, processes occur which can generally be described by a transformation of several photons into several others. Table 3.8.1 shows an overview of possible processes which may be described this way. A distinction between X-ray and visible (i.e. infrared – UV) photons is made for mostly practical reasons.

type	X-ray in	visible in	X-ray out	visible out	discussed in section
harmonic generation	> 1	0	1	0	3.8.1.2
spontaneous down conversion	1	0	2	0	3.8.1.2
sidebands	1	> 0			3.8.1.2
atomic multiphoton scattering	> 1	> 0	> 1		
atomic multiphoton absorption	≥ 1	≥ 0	0		3.8.1.2

Table 3.8.1.: *Types of X-ray multiphoton processes with coherence between in- and outgoing beams. As the power density increases, these multiphoton processes merge into parametric processes, such as induced or self phase modulation, see Sec. 3.8.1.3*

.

Sidebands The energy of an X-ray photon can be augmented or diminished in distinct steps by addition or subtraction of visible laser photons in a nonlinear medium. Experimental evidence of such a process has been obtained in a pioneering experiment [1] by K. Namikawa, exploiting resonance enhancement of the X-ray interaction. The nonlinear material was GdGa garnet and the X-rays were tuned to an L edge of Gd. Two optical photons were subtracted from the X-ray photon as shown in Fig. 3.8.1, leading to energy- and momentum-shifted X-rays which appeared as a small satellite to an X-ray reflection.

Despite the small nonlinearity of free electrons, it should be possible to observe and exploit visible sideband generation to X-rays with an XFEL. With the large power available from short pulse optical lasers, the conversion cross section can be driven to values not far below or even on par with the Thomson scattering cross section. Although the effect is only linear in the incident X-ray flux, the XFEL with its equally short pulses is much better suited to these experiments than ring based sources. The following examples illustrate this:

Second order processes: We mix one visible photon of energy $\hbar\omega_v$ to one X-ray photon of energy $\hbar\omega_x$ to generate one photon of energy $\hbar(\omega_x \pm \omega_v)$. The nonlinear medium is a solid, which need to be crystalline , or a dense gas of light elements (frozen hydrogen would be a good choice). The density has to be high enough to make the wavenumber of the visible light considerably larger than its vacuum value. Otherwise, the wavevectors $\mathbf{k}_x$ and $\mathbf{k}_v$ in the wave vector matching scheme shown in Fig. 3.8.2 would be almost collinear, which would make the geometry factor Γ rather small (see A.2.1). For the visible light laser we assume a power of 10^{15}W on 1 mm^2, keeping us below the relativistic limit. According to Eqs. 3.8.1, the conversion cross section (see definition of σ just below Eqs. 3.8.1) for the X-rays is then

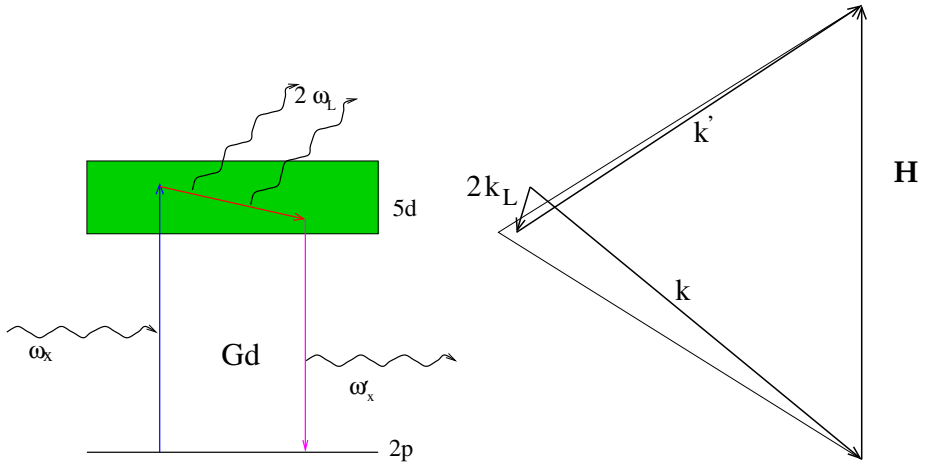

Figure 3.8.1.: *Left: Energy diagram for resonant subtraction of visible photons from an X-ray photon [1]. Right: The corresponding wave vector matching.*

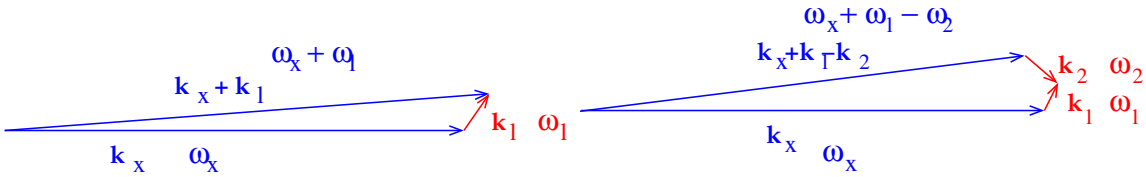

Figure 3.8.2.: *Wavevector matching for optical sideband generation in second (left) and third order (right).*

of the order of $10^{-3} r_e^2$, i.e. about 1/10 of a percent of the Thomson scattering cross section.

Third order processes: To gain more freedom in both the wavevector matching geometry, and the range of sideband frequencies that are achievable, we go to the third order and mix two visible light photons with one X-ray photon. With the same laser power density as above, Eqs. 3.8.1 yields a conversion cross section of the order of $10^{-4} r_e^2$. The relative sideband frequency tuning range extends from zero to several times 10^{-4}.

Possible applications of optical sideband generation with resonance similar to Namikawa's experiment are spectroscopic applications to study the band structure and electronic dynamics of materials. Other applications include correlation of X-ray and visible light intensities, timing control in visible/X-ray pump-probe type experiments, and precise relative frequency shifts to X-rays in Mössbauer and inelastic X-ray scattering from zero to several times 10^{-4}.

Harmonics The effect of harmonic generation of X-rays would probably be useful at an XFEL for two reasons: It might be used for intensity correlation measurements, and, if the efficiency is high enough, shorter wavelength photons could be provided for experiments. For the sake of this discussion, we will restrict ourselves to plane waves, i.e. we combine n

photons of energy $\hbar\omega$, and wave vectors $\mathbf{k}_1, \mathbf{k}_2, \ldots$ into one photon of energy $n\hbar\omega$ and wave vector $\mathbf{k}_n$, possibly with the additional momentum contribution $\hbar\mathbf{q}$ from a crystal.

Out of the nonlinear processes for X-rays the absorption edge based ones are probably out of the question for two reasons: Heavier elements with absorption edges in the X-ray region will absorb the X-rays so heavily that only very small volumes of matter may be used. Furthermore, the ionization due to X-ray absorption will remove the very absorption edges that the harmonic generation would be based upon. This leaves the nonlinearity of free electrons, which luckily is also the easiest to predict.

According to Eqs. 3.8.1 and the more detailed discussion in A.1.6, the cross section for second harmonic generation in a second order process with an X-ray beam of 10 GW, focused to a spot of 100 nm diameter, is $\approx 10^{-9} r_e^2$.

Apart from the requirement of a sufficiently strong nonlinearity, means must be found to match the wavevectors that are involved in the process. Because the refractive index for X-rays in any kind of matter is close to unity, the wave vectors $\mathbf{k}_i, i = 1 \ldots n$ must either be almost collinear with $\mathbf{k}_n$, or a crystal must be employed to supply sufficient momentum. For the latter to work, the incident power must either be limited to considerably less than the above 10 GW on 100 nm^2, or the X-ray pulse duration must be limited to a few optical oscillation periods, i.e. to the order of about one attosecond. From the experience gained with few-cycle visible laser pulses a mainly unimpeded nonlinear oscillation with low disturbance from competing dissipative processes then occurs. The idea of producing such short pulses may seem rather far fetched but should not be totally discounted.

From the points discussed above, it seems that the only way to achieve harmonic generation of X-rays is in a gas or plasma of light elements. Because the refractive index of any matter for X-rays is very close to unity, the wavevectors of the incident photons must be nearly collinear. However, normal dispersion of the refractive index will always make the sum of the wavevectors for the longer wavelengths slightly shorter than the wavevector for the shorter wavelength. This is indicated in Fig. 3.8.3. We can consider several ways out of

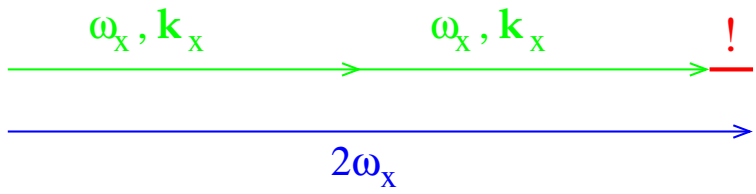

Figure 3.8.3.: *Wavevector matching for second harmonic generation.*

this problem:

- The refractive index can be tuned by using an admixture of a small amount of an element with an absorption edge close to the energy of the incident wavelength. This, however, will bring up the problem of absorption and is also insufficient by itself for reasons discussed below. However, fine tuning after exploiting the other means might be achieved this way.

- Higher order processes in which several incident photons combine into more than one outgoing photon leave a rather large parameter space to tune with. The weakness of the nonlinearity does not favor this solution.

- One might assist the harmonic generation with an intense optical laser pulse. The power of this pulse can compensate for the order of magnitude penalty due to the higher order of the process. Another reason that favors this solution is given below.

The expression for the nonlinearity of free electrons contains vectorial products which go to zero for collinear incident waves. For this reason, it will be necessary either to use to a process beyond second order in which several incident photons combine into several outgoing ones (which seems to be difficult because of the small nonlinearity) or to provide an intense optical laser pulse coming from a different direction. The cross section for visible laser assisted harmonic generation is rather low (see A.2.1 and A.1.6). If, for example, 10 GW of X-rays at a wavelength of 1 Å are focused to a spot of 1 μm^2, and a visible laser pulse at a wavelength of 1 μm and a power of 10^{16} W is focused to a spot of 1mm^2 around the XFEL focus, then the cross section for second harmonic generation in third order is about $10^{-19} r_e^2$. Tighter focusing of the visible laser would push up the cross section at the expense of less well defined wave vector matching.

Multiphoton absorption In most cases, multiphoton absorption can be treated by perturbation theory of the appropriate order. In the case of the absorption of multiple X-ray photons there are generally no intermediate resonant states available. Therefore, the cross sections are rather low. A possible breakdown of the perturbational treatment in the high power density in a focused XFEL beam concerns the stability of atoms in intense fields.

A special case of multiphoton absorption is the so-called laser assisted X-ray absorption near an absorption edge. This process, involving one X-ray photon and one or more visible light photons, can nevertheless be treated in first order perturbation theory by introduction of a modified Volkov wave function for the final state [2]. It includes the electromagnetic field of the visible light laser, which thus need not be taken into account by perturbation.

Z-Scan A rather simple method to determine the optical nonlinearity of a material is the so-called z-scan. The harmonic generation efficiency or the multiphoton absorption is monitored while a sample of the material is moved along a focused beam. With a homogeneous sample, all linear effects are independent of the sample position, leaving modulations of the signal to be attributed solely to the nonlinearity. Similarly, harmonic generation from or multiphoton absorption in a sample of known nonlinearity can be used to locate the focus of an X-ray optical assembly.

Spontaneous Down Conversion Spontaneous down conversion, also known by the name of parametric down conversion, is the spontaneous decay of photons into pairs of highly correlated photons whose energies add up to that of the incident one. The effect can be described as nonlinear mixing of real photons with vacuum fluctuations, resulting in two real photons for each incident one. Because only one incident X-ray photon is required for

each event, the effect is linear in the incident intensity. The high power density of vacuum fluctuations in the X-ray regime compensates for the small optical nonlinearity, making it possible to observe the effect at present day X-ray sources. Several recent publications [3, 4] corroborated the findings of Eisenberger's pioneering experiment [5]. The highest event rate observed to date is about 0.1/s at a third-generation source (see A.1.6). Simple extrapolation of the experimental parameters leads to up to 10/s to 100/s at a third-generation source.

The TESLA FEL, offering about 10000 times higher X-ray flux will make it possible to use the pairs of nonclassically correlated photons from spontaneous down conversions for a number of applications (see A.1.6), some of which are given below:

- Sub-Poisson Statistics : This is a rather simple application of the pairs of correlated photons from spontaneous down conversion, making use only of the property that if there is one photon in a pair, there must be another one. No use is made of phase correlation. The basic idea is that instead of splitting off part of the photons in a beam incident on a sample, pairs of correlated photons are used, one going to the sample and the other one to a reference detector. Thus, in principle the number of photons hitting the sample is known exactly and not only within the Poisson statistics inherent in the process of taking some of the photons out of the incident beam.

- Two Photon Interferometry, tests of the quantum theory : Instead of making a single photon probe two interfering paths, one might also employ two-photon states in interferometry. A great variety of experiments have been tried out with visible photons, showing both amplitude and intensity or only intensity contrast [6]–[8].

These experiments have been done for such purposes as probing the extent of a wavepacket belonging to one photon [9] (see Fig. 3.8.4), or measuring a possible violation of Bell's inequality [10]–[13]. Any deficiency in the quantum efficiency of the photon detectors employed in tests of the quantum theory (such as Bell's inequality) is equivalent to influences of external degrees of freedom on the pure quantum states that are under investigation. Use of X-rays for these experiments would make nearly 100% detection efficiency available.

Apart from testing the quantum nature of the electromagnetic field, higher order interferences can also be used to obtain information about a sample. A possible setup to probe correlations in a sample is shown in Fig. 3.8.5. The two photons can be made to have different energies, for example above and below the absorption edge of a species in the sample.

3.8.1.3. Parametric amplification

Processes in which a parameter, such as the refractive index, changes in time are called parametric processes. They result generally in frequency mixing. The difference from the multiphoton processes, as it is discussed in Sec. 3.8.1.2 is mostly one of taking a different point of view. Speaking more basic, a time dependence of the refractive index of an optical medium induces spectral broadening in radiation that traverses it. The Fourier components of the refractive index contribute directly to the spectral components of the radiation. An application of this effect is found in the generation of ultrashort laser pulses: In order to

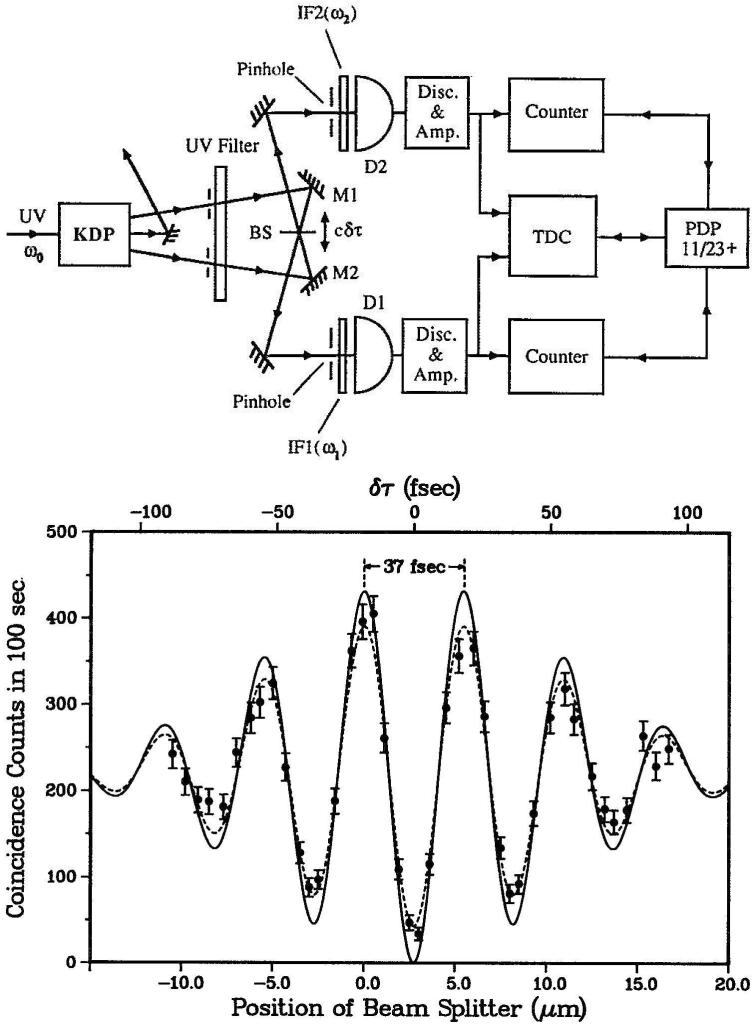

Figure 3.8.4.: *Experiment to probe the extent of wavepackets associated with photons in two arms of an interferometer (reproduced from [9]). The two correlated photons from a spontaneous down conversion process are recombined in a beamsplitter (BS) (top panel) such that each photon can reach either detector by being transmitted through or reflected from the BS. Being coherent with each other, the two photons interfere, producing a contrast of coincidences of events in the two detectors which depends on the position of BS (bottom panel). The envelope is given by the energy bandpass of the filters in front of the detectors, i.e. the longitudinal coherence length of the two photons.*

broaden the spectrum beyond the gain bandwidth of the laser amplifier and thus to shorten the pulse, self phase modulation [14] is employed: The refractive index of an optically non-linear medium is changed by the radiation and this change contributes to a coherent spectral broadening.

It is conceivable that a similar effect can be put to use to compress pulses of X-rays that are tuned to an absorption edge of some atomic species. Both saturation and the AC Stark

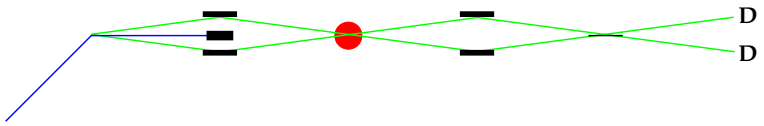

Figure 3.8.5.: *Two-photon interferometry to probe correlations in a sample. The two photons from a spontaneous down conversion traverse a sample and are recombined by mirrors and are brought to interference in a beamsplitter.*

shift would contribute to a rapid change in the refractive index.

X-rays induce another effect that is similar to a rapid change of the refractive index but has no direct analogue in the visible regime. A rapid change in some Fourier component of the electron density in a crystal can induce coherent spectral broadening and frequency shifts of X-rays that are traversing it under conditions of dynamical diffraction. Because such a change of a Fourier component corresponds to a redistribution of electrons over tiny distances in real space on the order of those between atoms, the change of the structure factor that is relevant for diffraction can occur very rapidly. It could be brought about by a massive optical excitation of the valence electrons in the crystal by use of a short pulse laser. Use of this effect for switching, compressing, and analyzing X-ray pulses has already been proposed (see A.1.5 and A.1.6). A detailed theory to predict the spectral changes of X-rays diffracting under rapidly changing conditions will have to be worked out. It could be based on the Takagi-Taupin theory.

3.8.2. Fundamental high-field science

In addition to the immediate applications in material science and biology, the XFEL may also be employed to study some physics issues of more fundamental nature. In this context, ultrahot matter creation, coherent γ-ray generation, violent acceleration and "event horizon physics", as well as non-linear effects ("vacuum decay") in quantum electrodynamics (QED) have been discussed in the literature [15]–[18]. These are high-field science applications of the XFEL: They make use not only of the high energy and transverse coherence of the X-ray beam, but also of the possibility of focusing it to a spot with a small radius, hopefully in the nanometer range. In this way it is possible to obtain very large power densities and electric fields (compare also Tab. 3.8.2), larger than those obtainable with any other laser.

Realistically speaking, the study of the high-field science applications mentioned above requires ultrahigh power densities, typically in the $\mathcal{O}(10^{30})$ W/m^2 range. Such values are far above the ones reachable with presently available technology (see Tab. 3.8.2). Intensive development in technical areas, particularly in that of X-ray optics, will be needed in order to achieve such ultrahigh power densities. It should be pointed out, however, that even though progress to achieve such a lofty goal is rather slow and laborious, the rewards that may be derived in this unique regime are so extraordinary that looking into XFEL's extension to this regime merits serious considerations. There will be unprecedented opportunities to use these intense X-rays in order to explore some issues of fundamental physics that have eluded man's probing so far [15].

XFEL Parameters				
		SASE 5	Focused [19]	Fiction [16]
Wavelength	λ	0.4 nm	0.4 nm	0.15 nm
Photon energy	$E_\gamma = hc/\lambda = \hbar\,\omega$	3.1 keV	3.1 keV	8.3 keV
Peak power	P	110 GW	1.1 GW	5 TW
Spot size (rms)	σ	26 μm	21 nm	0.15 nm
Coherent spike length (rms)	τ	0.04 fs [19]	0.04 fs [19]	0.08 fs
Derived Parameters				
Peak power density	$S = P/(\pi\sigma^2)$	5×10^{19} W/m^2	8×10^{23} W/m^2	7×10^{31} W/m^2
Peak electric field	$E = \sqrt{\sqrt{\mu_0/\epsilon_0}\,S}$	1×10^{11} V/m	2×10^{13} V/m	2×10^{17} V/m
Peak electric field/critical field	$\Upsilon = eE\lambda\!\!\!^{-}/(m_e c^2)$	1×10^{-7}	1×10^{-5}	0.1
Photon energy/Rest mass of e	$\epsilon_\gamma = E_\gamma/(m_e c^2)$	0.006	0.006	0.02
Adiabaticity parameter	$\gamma = \hbar\omega/(eE\lambda\!\!\!^{-}) = \epsilon_\gamma/\Upsilon$	6×10^4	5×10^2	0.1
Pair production rate	w	$\mathcal{O}(10^{-17063})$/(m^{3}s)	$\mathcal{O}(10^{-105505})$/(m^{3}s)	1×10^{43}/(m^{3}s)
Pulse space-time volume	$V\tau = \pi\sigma^2 c\tau^2$	1×10^{-33} m^3 s	7×10^{-40} m^3	1×10^{-37} m^3

Table 3.8.2.: *Parameters relevant for estimates of the power density and the electric field strength that can be reached at the XFEL. The column labelled "SASE 5" displays the XFEL design parameters (Tab. 4.2.4). The column labelled "Focused" assumes that the SASE 5 X-ray beam can be focused to a rms spot size of $\sigma \simeq 50$ nm with an extraction efficiency of 1 %, which is achievable with present day methods [19]. The column labelled "Fiction" shows parameters which might be theoretically possible by increasing the energy extraction of the FEL (by the tapered undulator technique) and by a yet unspecified method of diffraction-limited focusing of X-rays [16].*

The subject of fundamental/high-field science at an X-ray FEL is still in its infancy and in a development phase. Besides the issues mentioned above, which are nicely reviewed in Ref. [15], there might be even more applications. In the following, we shall concentrate on the study of nonlinear effects in QED, which are theoretically well established. We shall discuss in particular the possibility of obtaining an electric field so high that e^+e^- pairs are spontaneously produced in vacuum [16, 17].

3.8.2.1. QED "vacuum decay" in a laser field

In a seminal work, published already in 1951, Schwinger demonstrated that in the background of a static uniform electric field, the QED vacuum is unstable and, in principle, "sparks" with spontaneous emission of e^+e^- pairs [20]. Particle creation from vacuum by an external field ("vacuum instability" in an external field) ranks among the most intriguing nonlinear phenomena in quantum field theory. Its consideration is theoretically important, since it requires one to go beyond the scope of perturbation theory, and its experimental observation would verify the validity of QED in the domain of high fields. Moreover, the Schwinger mechanism plays a very prominent rôle in various aspects of quantum field theory, ranging from black hole physics to particle production in QCD (see e. g. Ref. [21] for a list of references).

At small electric field strengths E,

$$E \ll E_s = \frac{m_e c^2}{e\lambda\!\!\!^{-}} = 1.3 \times 10^{18}\ \mathrm{V/m}, \tag{3.8.3}$$

for which the work of the field on a unit charge e over the Compton wavelength of the electron $\lambda\!\!\!^{-} = \hbar/(m_e c)$ is much smaller than the rest energy $m_e c^2$ of the electron. The Schwinger mechanism of e^+e^- pair production can be understood as a non-perturbative tunnelling process in QED. Correspondingly, its probability per unit time and unit volume is exponentially small [20],

$$w \simeq \frac{c}{4\pi^3 \lambda\!\!\!^{-4}} \left(\frac{E}{E_s}\right)^2 \exp\left(-\pi \frac{E_s}{E}\right) . \tag{3.8.4}$$

Because ordinarily available field strengths are typically much smaller than the Schwinger critical field E_s in Eq. 3.8.3, e^+e^- pair production in a (quasi-)static field has never been directly observed under laboratory conditions up to now.

In the beginning of the 70's, the question was raised whether the focus of a coherent optical laser could be employed to study the Schwinger mechanism of e^+e^- pair production in an electromagnetic field [22]. A first semi-quantitative treatment of this issue was presented in Ref. [23]. As a quasi-realistic picture of the electromagnetic field of a laser, a pure electric field oscillating with a frequency ω was considered, under the assumption that the field amplitude E is much smaller than the Schwinger critical field, and the photon energy is much smaller than the rest energy of the electron,

$$E \ll E_s \,, \qquad \hbar\omega \ll m_e c^2 \,; \tag{3.8.5}$$

conditions which are well satisfied at realistic X-ray lasers (see Tab. 3.8.2). It was found that the ratio γ of the energy of the laser photons over the work of the field on a unit charge e over the Compton wavelength of the electron,

$$\gamma = \hbar\omega/(eE\lambda\!\!\!^{-}) \,, \tag{3.8.6}$$

plays the rôle of an adiabaticity parameter. As long as $\gamma \ll 1$, i. e. in the high-field, low-frequency limit, the non-perturbative Schwinger result (Eq. 3.8.4) for a static uniform field applies. On the other hand, for large γ, i. e. in the low-field, high-frequency limit, the essentially perturbative result

$$w \simeq \frac{c}{16\pi^2 \lambda\!\!\!^{-4}} \left(\frac{eE\lambda\!\!\!^{-}}{m_e c^2}\right)^2 \left(\frac{eE\lambda\!\!\!^{-}}{2\hbar\omega}\right)^{4m_e c^2/\hbar\omega} \tag{3.8.7}$$

is obtained for the pair production probability.

In Tab. 3.8.2 we have summarized the relevant parameters and the estimated pair production probabilities for the XFEL. We conclude that the power densities and electric fields which can be reached with presently available technique (column labelled "Focused" in Tab. 3.8.2) are far too small for a sizeable effect. On the other hand, if the XFEL technology can be further improved and/or the energy extraction can be increased considerably and the focus can be improved, leading to a spot size in the 0.1 nanometer range, as has been argued to be possible at least theoretically [16], then there is ample room (c. f. column labelled "Fiction" in Tab. 3.8.2) for an investigation of the Schwinger pair production mechanism at the XFEL [24].

3.8.3. Atom optics

In atom optics the roles of light and matter are reversed as compared to usual optics. Light beams are used to cool, move, or otherwise manipulate atoms. Light-induced coherent superpositions of atoms offer a host of interesting phenomena due to the rich variety of internal degrees of freedom in atoms. The field has been opening up in the last decade and can be considered rather mature and close to practical application. X-rays from an XFEL could extend the possibilities of coherently manipulating atoms. They would offer the specific advantage of large momentum transfer and maybe even of being able to address the additional degrees of freedom associated with nuclear transitions.

3.8.3.1. Dipole forces, Atom lattices

The AC Stark effect from laser light tuned to a few linewidths away from an optical transition in an atomic or molecular species can provide potentials and corresponding forces on the respective species. The sign of the potential depends on the excitation state of each atom or molecule. The simplest example for such an effect is a state selective optical mirror for atoms [25], operating on the dependence of optical dipole forces on the detuning from the nearest transition. In a similar manner, dipole forces based on nuclear transitions might be used for isotope separation. It may seem to be rather inefficient to operate a whole XFEL beamline for such a task. There are, however, two fields where this would make sense:

- In nuclear physics experiments where either atoms of a short lived isotope species are created in situ and must be quickly separated from the rest of the experiment, or separation of nuclei in an excited metastable state that is dipole resonant with some other state from those nuclei of the same isotopic species that are in the ground state. Typically, the energy of the metastable nuclei is just a few MeV above the ground state, making mass separation rather difficult. Examples would be the Hf isotopes ^{176}Hf, ^{178}Hf, and ^{180}Hf [26].

- For the separation of other isotopes, a monochromator is employed that takes a narrow band out of the XFEL beam and passes the rest on to another experiment.

Standing wave patterns of various types of linear and elliptical polarization have been used to create periodic potentials for atoms which, together with a dissipative effect, lead to a spatial density modulation of these atoms [27]–[29]. It was demonstrated some years ago that such a lattice can Bragg reflect light of a shorter wavelength than which was used in its generation [30]. This effect might be used to provide an indestructible optical element [31] in an XFEL beamline, see Sec. 3.8.5.

3.8.3.2. Atom interferometry

Atom interferometry is interesting for both fundamental studies, and practical applications. The large number of internal degrees of freedom in an atom (as compared to neutrons, for example) provides many means to manipulate the particles in one branch of the interferometer and to thus produce a dynamical or topological phase which shows up in the interference.

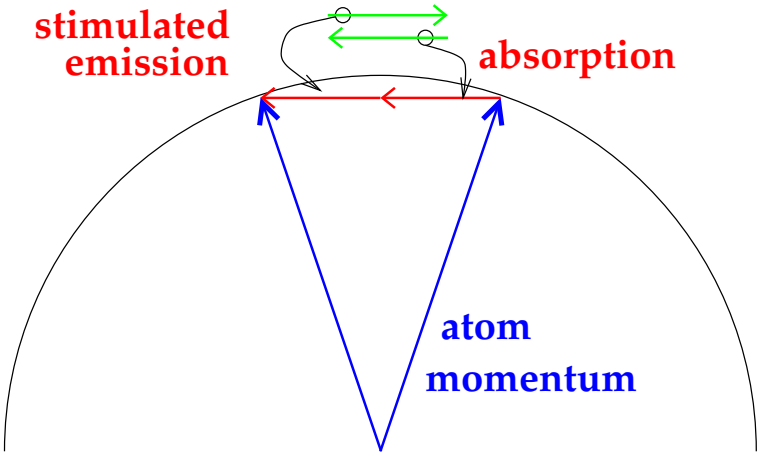

Figure 3.8.6.: *Energy-conserving momentum transfer to an atom in a standing light wave: Two photon momenta are exchanged, one by absorption from one running wave component, the other by stimulated emission into the other running wave.*

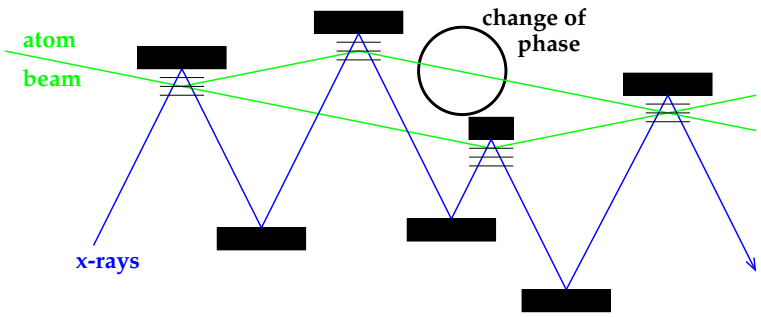

Figure 3.8.7.: *A possible layout of an X-ray-beamsplitter based atom interferometer. The large beam separation permits introduction of an apparatus (interaction zone, resonator, etc.) that induces a dynamical or topological phase shift in the atoms traversing it.*

Absorption and stimulated emission of photons can be used to split and recombine atom beams or clouds coherently. The conceptually most simple approach [32] is to transfer momentum to atoms in an atomic beam by absorption and stimulated emission as indicated in Fig. 3.8.6.

The physical separation of the atomic beams depends on the ratio of photon recoil momentum to longitudinal momentum in the atom beam. With present day techniques, it is rather hard to achieve a separation that is larger than the transverse size of the beams. The much larger recoil with X-ray photons will provide a beam separation that permits manipulation of the atoms in one beam only (see Fig. 3.8.7). A complete atom interferometer with X-ray based atom beam splitters might consist of four single crystals adjusted to Bragg-reflect X-rays of an energy that is matched to an X-ray transition in the respective atomic species.

The atoms traverse the interferometer at rather low velocity. Therefore it will be necessary to employ X-ray pulses from different bunches in the FEL. Because there is no definite phase relationship between them, a reference interferometer has to be operated in parallel to provide the phase relationship of each set of X-ray pulses used for splitting the atomic beams. A novel type of atom interferometer might be based on a laser-cooled cloud of atoms which is split and recombined coherently with X-ray pulses. The cloud may stay in the split state for an almost indefinitely long time, thus allowing plenty of time for manipulation of internal degrees of freedom. The X-ray interaction that leads to the splitting and recombination might be based on a nuclear resonance.

3.8.4. Phase conjugation

Optical phase conjugation is used in a variety of applications such as automatic correction for imperfections in imaging systems, improvement of laser beam quality, realization of reflectivity above 100%, or optical data processing. Interesting theoretical questions arise, such as how spontaneous emission from an atom is modified if it is sitting close to a phase conjugating mirror [33, 34]. Whereas a normal mirror converts an incident wave into its mirror image with respect to the spatial dependence, a phase conjugating mirror creates a time-reversed wave, i.e. if the eikonal representation of the incident wave is $A(\mathbf{r})e^{iS(\mathbf{r},t)}$, the phase conjugate wave is $A(\mathbf{r})e^{iS(\mathbf{r},-t)}$.

Two distinctly different effects are used for phase conjugation in the visible regime: Degenerate four wave mixing (also called dynamic holography) and stimulated Brillouin scattering. Four wave mixing involves the simultaneous creation and readout of a holographic grating, is created by interference of the incident wave with one pump wave, leading to a pattern of the refractive index in an optically nonlinear medium, and is read out by diffraction of another pump wave from it. The reflected power has its origin in the pump wave and can therefore be larger than the power of the incident wave. Stimulated Brillouin scattering relies on the buildup of density fluctuations in the mirror material, originating from initial random density fluctuations, and being enhanced by an electrostrictive effect that maps out the intensity distribution of the interference pattern of incident and scattered waves.

Possible applications of phase conjugation with the XFEL lie in X-ray imaging systems and in ways to improve the coherence properties of the XFEL itself. These will all rely, though, on sufficiently nonlinear X-ray optical materials.

3.8.5. Novel X-ray optical elements

Some of the effects to be discussed in this section have already been mentioned previously in this text. Here, emphasis shall be put on their application for novel X-ray optical elements. These could be classified into two categories: X-ray optical elements whose properties are not influenced by the X-rays (‘linear’ in X-rays) and ones in which the X-rays themselves modify the operation (i.e. truly nonlinear or ‘incoherently’ nonlinear in the X-rays - this distinction will become clear below).

3.8.5.1. Linear in X-rays

This category involves all kinds of ideas that first somehow improve the XFEL radiation for some specific application and second could in principle work with any X-ray source, but work better with an XFEL due to reasons of duty cycle or coherence.

Switching X-rays with an optical laser A concept that has recently been tried is the coherent phonon Bragg switch [35]. An intense and short laser pulse generates a coherent superposition of highly occupied optical phonon states. This results in a periodic modulation of the lattice and thus gives rise to superstructure reflections. The modulation can be removed by application of a properly phased second pulse. The switching time constants are given by the phonon oscillation periods, i.e. ca. 100 fs for GaAs as switch material.

It should be possible to achieve even faster switching timescales by exploiting effects that rely only on electron dynamics (i.e. without requiring any motion of atom cores). Such a device could potentially reach the sub-femtosecond regime. A class of devices has been proposed, operating on the principle of a change of the dispersion sheets in dynamical diffraction by laser-induced massive transfer of electrons from the valence to the conduction band in a semiconductor crystal.

Atomic lattices It has been demonstrated [30] that a lattice of atoms held in place by an optical potential in a standing wave of laser light can give rise to Bragg reflection of light in the first reflection order. Similarly, it should be possible to obtain Bragg reflection of X-rays in the first reflection order (i.e. at very small angle) from such an atomic lattice. This effect could be used to couple a small amount (up to maybe 10^{-6}) of the radiation out of the main XFEL beam. Thus, several experiments which do not need the full intensity but other properties such as the time structure or the coherence could be served by one undulator. It might also be used to return a small part of the radiation to the undulator input in a regenerative amplifier free electron laser (RAFEL).

Although the high power in the XFEL beam will probably destroy the lattice in the interaction, it is recreated within a few ms. Even better would be to channel atoms of a transversely cooled atomic beam into lattice planes [36]. Because of the thermal velocity of the atoms, a fresh part of the lattice moves into the FEL beam within the ca. 100 ns spacing of the pulses from the TESLA XFEL (see Fig. 3.8.8).

3.8.5.2. Nonlinear in X-rays

Self-terminating diffraction The high peak power of the XFEL beam is mostly seen as a problem with regard to the stability and performance of optical components. One might, however, also exploit the power loading of a diffractive element to achieve a self-termination of the diffraction and thus to obtain ultrashort pulses of X-rays. The electrons in the diffracting crystals are heated by the incident X-rays through photoelectron emission etc., and thus the structure factor of a Bragg or Laue reflection is reduced progressively (or rather spike-by-spike of the X-ray intensity) throughout a bunch from the XFEL. This has the effect of a temporal modification of the beam path under diffractive conditions.

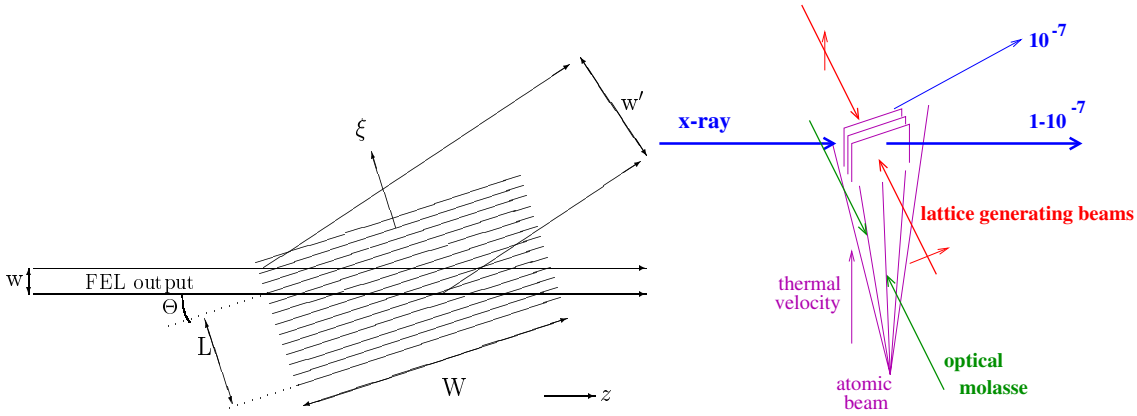

Figure 3.8.8.: *An atomic beam (for example Cs) moves upward at thermal velocity. It is first cooled transversely in an optical molasse, then channelled by the optical potential of a standing light wave into lattice planes of optical wavelength spacing. These are oriented such that the X-ray beam from the FEL is Bragg reflected in a low order, i.e. at small angle.*

We consider the following example, using Bragg geometry (an analogous scheme could be set up in Laue transmission geometry as well): A combination of two crystals in (almost) nondispersive configuration and with different reflection curve widths is detuned slightly relative to each other such that the rocking curves just barely overlap. Such a combination could be, for example, diamond (111) and Ge (220). The second crystal, being composed of heavier atoms, is much more susceptible to heating by the X-rays. As it is heated, the structure factor of the X-ray reflection is reduced, so that the reflection curves do not overlap any more in the heated regions. As is indicated in Fig. 3.8.9, this results in greater penetration and thus in a displacement of the reflected beam (also, of course in attenuation) which progresses with time. Placing a slit in the exiting beam, or simply relying on the increased attenuation of the deeper penetrating beam, will thus reduce the duration of the reflected pulse. Or one might use a position sensitive detector in the exiting beam to record the temporal dependence of the X-ray intensity. This might be called a self-activated streak camera. The strength of the effect can be tuned by the degree of focusing, by the choice of diffracting material, and by the choice of the reflection. The process can be very fast because it relies on electron heating and not on nuclear movement.

Saturable absorber A saturable absorber could be used for the correlation of X-ray pulses from the XFEL. Take, for example, X-rays tuned just above the K absorption edge of some element. When such an atom has become photoionized by the X-rays, then removal of the second K electron requires more energy, and thus the K absorption edge would be shifted upward. Therefore, a gas cloud of such atoms would absorb the X-rays strongly until, after receipt of a certain radiation dose, most atoms would be ionized. In a correlator setup with X-ray beams crossing each other in the saturable absorber, each beam would thus be absorbed strongly if it came first and weakly if it came behind (see Fig. 3.8.10).

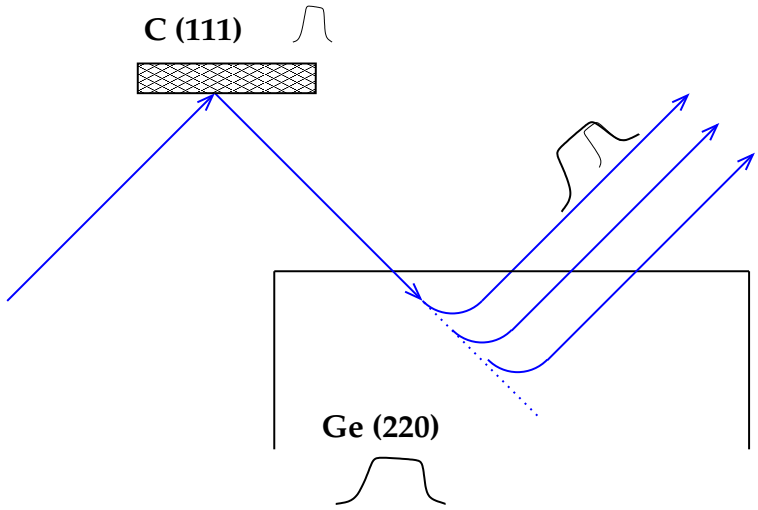

Figure 3.8.9.: *Self-terminating Bragg diffraction used as a pulse cutter, for example with the combination of diamond (111) and Ge (220) (details, see text).*

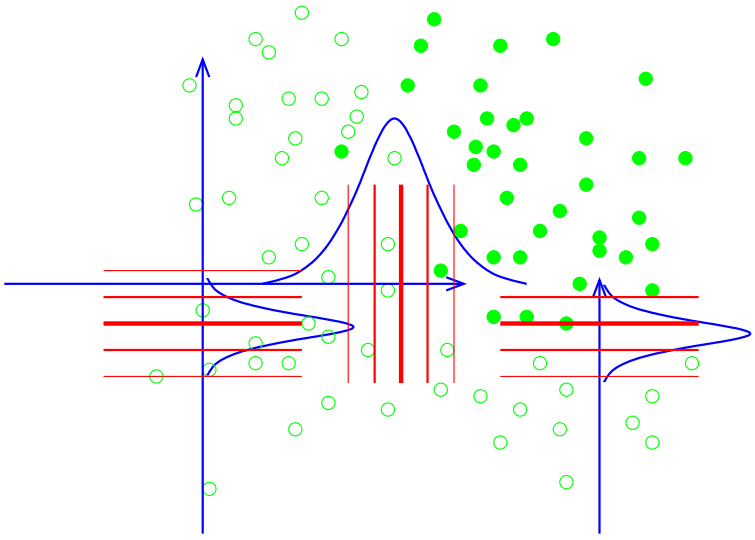

Figure 3.8.10.: *An X-ray correlator based on a saturable absorber. X-rays (indicated by line profiles) are tuned to an absorption edge in a gas. An X-ray pulse comes from the left and photo-ionizes the gas atoms (open circles) whereas the atoms not yet reached by the pulse (full circles) are still neutral. Another X-ray pulse, coming from below, can pass the gas cloud (left) where it arrives after the passage of the pulse from the left, whereas the part of it that hits the not-yet ionized atoms (right) gets stopped.*

3.8.6. Experimental schemes

The experiments and techniques discussed in this text all depend crucially on the properties that set an XFEL apart from present day X-ray sources: The transverse coherence, short pulse duration, and high peak power. Here is a list of these experiments showing which of the source properties are most important for them and where improvement would be desirable:

- Nonlinear optical phenomena with X-rays only become barely visible with an XFEL, whereas there is no hope of reaching the necessary intensity with any other source. Because intensity is really crucial, tight focusing and pulse compression are key issues.

- Experiments like optical sideband generation, in which one X-ray photon is mixed with one or several visible light photons, are in principle linear in the X-ray intensity. The advantage of the XFEL over present day sources lies mostly in its short pulse duration which is ideally matched to the short pulses of high power lasers. In contrast, only one part in 1000 of a bunch from a third-generation source could interact with a pulse from a Ti:Sapphire laser. However, in order to obtain ideal matching of the XFEL pulses to those from state-of-the-art high power lasers, the bunch pattern should be quite different from what is presently proposed for the TESLA facility (see Fig. 4.1.2). The Ti:Sapphire TW lasers output pulses at one to several kHz repetition rate, and this is very hard to change. The ideal bunch pattern for optical sideband generation - and, much more importantly, for pump-probe experiments - would therefore be continuous with at least one kHz repetition rate.

- The manipulation of atoms with light-induced forces is a well developed field in the visible spectral region. The XFEL will provide sufficient intensity and coherence to do the same with X-rays, thus gaining on the side of momentum transfer in the atom-light interaction. In order to achieve sufficiently strong interaction for beam splitters, etc., a very high intensity is necessary. That can be delivered only by an XFEL. The timescales of experiments with cooled atoms in a gas or a beam are much longer than the duration of a single XFEL pulse. It is therefore necessary either to have some device to determine the phase relationship between successive pulses (like a reference atom interferometer or an X-ray interferometer with an optical delay line), or to provide phase coherence between successive pulses with seeding techniques.

- The intrinsic pulse duration of the XFEL output is already much less than that of present day synchrotron light sources and is short enough for the study of all but the very fastest dynamics in condensed matter physics and in chemistry. The potential is there to obtain pulses of sub-femtosecond duration by any one of many possible pulse compression or pulse shaping techniques. This would permit us to go right down to the fundamental processes of chemistry and electron dynamics in crystals. Because of the great scientific significance of the XFEL contribution to that field, it seems justified to exert a major effort on research and development in the areas of pulse compression down to ca. 0.1 fs, or more generally in phase control of the XFEL output and in control and measurement of the timing of X-ray vs. visible light pulses. The ideal

bunch pattern for pump-probe experiments was mentioned above in the section on optical sideband generation.

Bibliography

[1] K. Namikawa, results published in workshop proceedings only

[2] P. Kalman, Phys. Rev. A **38**, 5458 (1988).

[3] Y. Yoda, T. Suzuki, X.-W. Zhang, K. Hirano, S. Kikuta, J. Synchrotron Rad. **5**, 980 (1998).

[4] B. Adams et al., J. Synchrotron Rad. **7**, 81 (2000).

[5] P. Eisenberger and S.L. McCall, Phys. Rev. Lett. **26**, 684 (1971).

[6] R. Ghosh and L. Mandel, Phys. Rev. Lett **59**, 1903 (1987).

[7] C.K. Hong, Z.Y. Ou, L. Mandel, Phys. Rev. Lett. **59**, 2044 (1987).

[8] X.Y. Zou, T. Grayson, G.A. Barbosa, L. Mandel, Phys. Rev. A **47**, 2293 (1993).

[9] Z.Y. Ou and L. Mandel, Phys. Rev. Lett. **61**, 54 (1988).

[10] P.G. Kwiat, A.M. Steinberg, R.Y. Chiao, Phys. Rev. A **47**, R2472 (1993).

[11] P.R. Tapster, J.G. Rarity, P.C.M. Owens, Phys. Rev. Lett. **73**, 1923 (1994).

[12] M. Michler, K. Mattle, H. Weinfurter, A. Zeilinger, Phys. Rev. A **53**, R1209 (1996).

[13] W. Tittel, J. Brendel, H. Zbinden, N. Gisin, Phys. Rev. Lett. **81**, 3563 (1998).

[14] T. Brabec and F. Krausz, Rev. Mod. Phys. **72**, 545 (2000)

[15] T. Tajima, *Fundamental Physics with an X-Ray Free Electron Laser*, Comments on Plasma Physics and Controlled Fusion (2001), to be published.

[16] P. Chen and C. Pellegrini, *Boiling the Vacuum with Intense Electromagnetic Fields*, in *Quantum Aspects of Beam Physics*, Proc. 15th Advanced ICFA Beam Dynamics Workshop on Quantum Aspects of Beam Physics, Monterey, Cal. (1998), Pisin Chen (ed.), World Scientific, Singapore, (1998), p. 571.

[17] A.C. Melissinos, *The spontaneous breakdown of the vacuum*, in *Quantum Aspects of Beam Physics*, Proc. 15th Advanced ICFA Beam Dynamics Workshop on Quantum Aspects of Beam Physics, Monterey, Cal. (1998), Pisin Chen (ed.), World Scientific, Singapore, (1998), p. 564.

[18] P. Chen and T. Tajima, Phys. Rev. Lett. **83,** 256 (1999).

[19] See A.1.5 for a status report.

[20] J. Schwinger, Phys. Rev. **82**, 664 (1951).

[21] S.P. Gavrilov and D.M. Gitman, Phys. Rev. D**53**, 7162 (1996).

[22] F. Bunkin and I. Tugov, Soviet Physics Doklady **14**, 678 (1970).

[23] E. Brezin and C. Itzykson, Phys. Rev. D**2**, 1191 (1970).

[24] A. Ringwald, in preparation.

[25] V.I. Balyakin, V.S. Latokhov, Y.B. Ovchimikov, A.I. Sidorov, Phys. Rev. Lett. **60**, 2137 (1988).

[26] E. Gerdau, private communication.

[27] A. Hemmerich, D. Schropp, Jr., T.W. Hänsch, Phys. Rev. A**44**, 1910 (1991).

[28] S. Friebel, C. D'Andrea, J. Walz, M. Weitz, T.W. Hänsch Phys. Rev. A**57**, R20 (1998).

[29] A. Hemmerich and T.W. Hänsch, Phys. Rev. Lett. **70**, 410 (1993).

[30] M. Weidemüller, A. Hemmerich, A. Görlitz, T. Esslinger, T.W. Hänsch, Phys. Rev. Lett. **75**, 4583 (1995).

[31] B. Adams, in *Free Electron Lasers*, Procs. of 18th Int. FEL Conf., North-Holland, New York (1997), p. II-26.

[32] P.J. Martin, B.G. Oldaker, A.H. Miklich, D.E. Pritchard, Phys. Rev. Lett. **60**, 515 (1988).

[33] B.H.W. Hendriks, and G. Nienhuis, Phys. Rev. A **40**, 1892 (1989).

[34] E. Bochove, Phys. Rev. Lett. **59**, 2547 (1987).

[35] P.H. Bucksbaum and R. Merlin, Solid State Commun. **111**, 535 (1999).

[36] C. Salomon, J. Dalibard, A. Aspect, H. Metcalf, C. Cohen-Tannoudji, Phys. Rev. Lett. **59**, 1659 (1987).

4. XFEL Sources and Spontaneous Emitters

4.1. Design Specifications and Performance Goals

To define in this chapter the parameters for the FEL undulators and the spontaneously emitting undulators we will first describe the requirements which follow from the collection of the scientific proposals presented in the previous chapter. The implications of the scientific case for the design layout of the XFEL laboratory and its undulators will be described first. We further summarize those parameters of the TESLA electron accelerator design which are important for the XFEL design.

4.1.1. Implications from the scientific case

The proposals for investigations using XFEL radiation presented in Chap. 3 are based on key properties of this radiation. Namely, on the ultra short photon pulse length of approximately 100 fs, on the high degree of coherence, on the outstanding peak brilliance, and last not least on the average brilliance. It is one of the main tasks of designing the layout of the XFEL laboratory and the undulator systems to provide X-ray beams which preserve these superior properties and enable their use in the experiments.

For the design of the XFEL laboratory and the undulators the requirements with respect to photon energy range and tunability are important. It was concluded that most experiments which are not interested in particular resonance effects will benefit from using photon energies close to 1 Å. One has to note here that due to quantum fluctuations 1 Å is close to the smallest wavelength to be obtained from the SASE FEL process in its fundamental line. A design was conceived that enables to obtain XFEL radiation at or close to 1 Å wavelength at four of the five SASE undulators simultaneously. The TESLA accelerator delivers electrons to the XFEL switchyard by means of two transfer lines with different electron energy acceptance of 13 to 27 GeV and 20 to 50 GeV. At the beginning of either branch fast switches distribute the electrons alternatively to two SASE undulators. These, in total, four SASE undulators (SASE 1 to SASE 4) are the beginning of the four electron tracks, each ending in an electron beam dump (see Fig. 4.1.1). To operate these devices at the requested photon energies two energy ranges of the electron beams of 15 to 25 GeV and 20 to 30 GeV are needed. Due to the stringent requirements to the electron phase space volume, SASE undulators can be placed behind each other only at the condition that the second undulators radiates at least four times longer wavelength (see Sec. 4.2.1.2). In contrast, spontaneously emitting undulators can be placed without problems behind SASE FELs.

The distribution of electrons is achieved on the basis of bunch trains and it is possible to serve one electron track with up to 5 Hz. Switching within bunch trains will not be possible

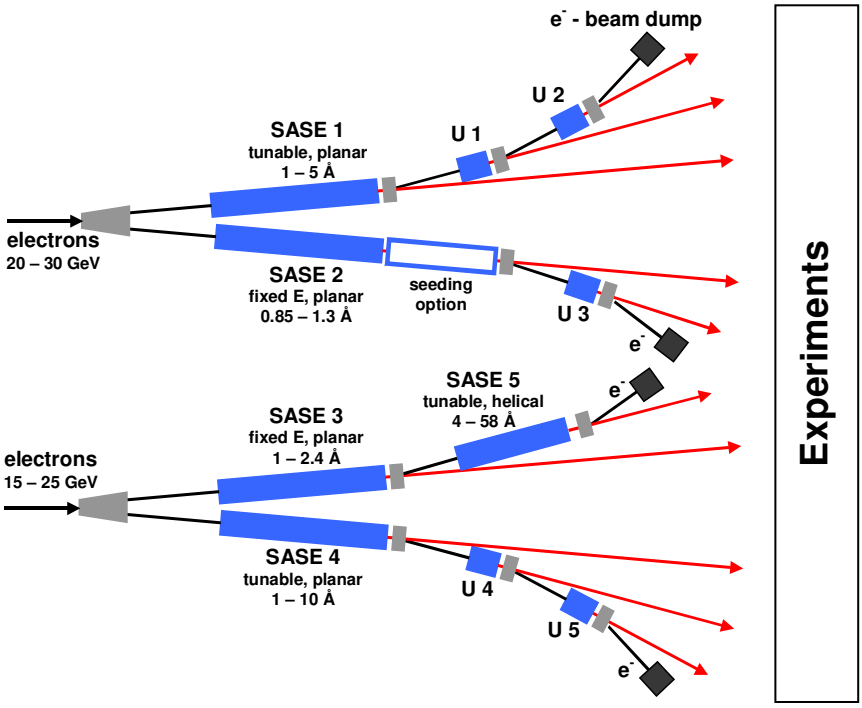

Figure 4.1.1.: *Design of the XFEL switchyard showing schematically the electron distribution and X-ray beamlines (red arrows). SASE undulators SASE 1 to SASE 5 and spontaneously emitting undulators U 1 to U 5 are indicated. Photon wavelength ranges are given for the SASE devices of different specification concerning tunability and magnetic field. Parameters for U 1 to U 5 can be found in Tab. 4.3.1.*

in the present design. The energy acceptance of the accelerator of typical $\pm 3\%$ will allow to apply electron energy variation of this amount within one bunch train or from bunch train to bunch train. Larger changes of the electron energy are possible by tuning the accelerator, but take a longer time. It follows that simultaneous usage of photon energies around 1 Å and 10 Å or even longer wavelength will be possible in the same branch only if the undulators operate at similar electron energy. For this reason the concept of placing a low photon energy SASE undulator behind a SASE undulator for the Ångstrom regime is highly advantageous. In this scheme it will be possible to provide in parallel hard and soft X-rays for two beamlines.

Energy tunability is provided for all five SASE and five spontaneously emitting undulators. Firstly, the energy in each electron branch can be tuned. This will be a rather slow tuning and does further apply to all undulators in the corresponding electron track, thus may lead to interferences of different experiments. It will, however, be the method of choice to select the photon energy for two so-called *fixed gap* undulators. The *fixed gap* mode requires shorter SASE undulators (see Sec. 4.3.3.4.C for explanation) and one device is foreseen in each electron branch. Secondly, magnetic gap tuning at the second SASE undulator in each electron branch will enable rather independent energy selection of both SASE devices and also faster energy tuning. The spontaneously emitting undulators have gap tunability and

provide photon energies up to several 100 keV at their third or fifth harmonic (see Sec. 4.2.3 for details).

Another design specification is the circular polarization. From the scientific proposals the necessity was raised to provide over the whole energy range the possibility for varying the polarization of the X-ray beam, in particular to provide linear and circular polarized X-rays. Considering crystal optics for generation and variation of the polarization it was concluded that for the soft X-ray regime the undulator itself has to provide variable polarization (see Chap. 5 for more details). Furthermore the high power of the X-ray beam and the strong collimation requires large distances between the source and the optics. Other properties, like e.g. coherence, will lead to constraints in the beamline design in order to preserve this characteristics, but do not have influence on the design of the general layout. With respect to the X-ray pulse length the layout of the XFEL is not critical.

For time-resolved measurements the length of the photon pulse as well as a precise knowledge of its arrival are important. For a time resolution better 1 ps the length of ~ 100 fs is excellent but particular attention has to be paid to the time jitter of arrival of the photon pulse at the experiment. At present it will not be possible to reach this specification for the arrival of the electron bunch at the undulator. In order to achieve a time resolution better than 1 ps therefore post-synchronization methods have to be applied. For several investigations of ultra short phenomena and of biomolecules a X-ray pulse length even shorter than 100 fs has been requested. This field is open to research but yet no solution to compress the pulse width or to efficiently cut a slice out of the 100 fs pulse has been foreseen. An ultimate time resolution could be achieved using the substructure of the FEL photon bunch with characteristic times of 0.2 fs in correlation experiments. Table 4.1.1 lists performance values for characteristic properties of XFEL radiation which have served as the basis for the scientific case. These values are the target to be reached at the TESLA XFEL laboratory. Their fulfillment in particular requires excellent electron beam properties.

Parameter	Unit	Performance values			
Photon energy	keV	0.5	4	12.4	14.4
Photon wavelength	Å	25	3.1	1	0.85
Tunability		yes	yes	yes	yes
Pulse length (FWHM)	fs	100	100	100	100
Linear polarization	%	100	100	100	100
Circular polarization	%	100	100	-	-
Photons/pulse		10^{13}	10^{13}	10^{12}	10^{12}
Peak brilliance	*	10^{32}	10^{32}	10^{33}	10^{33}
Average brilliance	*	10^{24}	10^{24}	10^{25}	10^{25}

* In units of photons/(sec mrad^2 mm^2 0.1% bandwidth).

Table 4.1.1.: *Performance values of characteristic XFEL radiation parameters for four photon energies.*

The electron part of the XFEL is described in detail in Part II, Chap. 9. Some operation

characteristics which are important for the XFEL are estimated and predicted as follows: The electron energy stability is $\Delta E/E \sim 5 \times 10^{-4}$ which corresponds to a photon wavelength stability of 2%. The spiky structure determines the lower level for the intensity fluctuation from pulse to pulse namely 3%. The time jitter for the electron pulse is $\simeq 1$ ps with a bunch length stability of $\sim 10\%$. The pointing stability of the photon beam needs to be smaller than 10% of the divergence since the experiments and optical elements are very far from the source.

In order to reduce intensity fluctuations of the XFEL radiation and to increase the peak and average brilliance, a seeding option has been proposed (see A.2.2). Seeding has also been requested by several science proposals and its advantages are discussed in Sec. 4.2. In the layout of the XFEL switchyard seeding is foreseen as a future option for FEL SASE 2 (see Fig. 4.1.1).

4.1.2. Design specifications

Photon energy range The FEL laboratory will provide intense photon beams in the X-ray regime. Within the present upper limit for generation of XFEL radiation at ~ 15 keV a wide range of photon energies has to be provided. At 14.4 keV the resonance of the Mössbauer isotope ^{57}Fe is situated, which will be the upper energy target to be reached by XFEL radiation in its fundamental harmonic. In the proposed design, usage of higher harmonic XFEL radiation is not taken into account. The lower energy cutoff is partially determined by the availability of other sources, in particular the DESY TTF VUV-FEL facility which is foreseen to deliver FEL radiation with photon energies up to 600 eV ($\cong 2$ nm) in its third harmonic. Providing a certain overlap between the two FEL laboratories the lower energy cutoff will be around 400-500 eV. This energy range corresponds to a wavelength range from 3 nm to 0.08 nm for the TESLA XFEL.

Since in the beginning only a use of the undulator fundamental is foreseen, for above 15 keV spontaneously emitted radiation must be considered. Although the specific brilliance advantages of XFEL radiation will be lost in the spontaneous radiation, the pulse length smaller than 200 fs, the small divergence, the small photon source, and the high degree of coherence make the spontaneous radiation very valuable for investigations with hard X-rays, produced both from the SASE undulators and spontaneously emitting undulators.

Photon pulse delivery X-ray pulses of full width half maximum length of 100 fs are generated in the SASE process out of the 188 fs (FWHM) long electron bunch (see Fig. 2.2.5 for an explanation). The temporal structure for the electron delivery is sketched in Fig. 4.1.2 and shows the overall time structure of the TESLA accelerator with bunch trains for the XFEL and the particle physics experiments. For the FEL each bunch train has up to 11500 electron bunches carrying 1 nC of charge each. The generic time distance between electron bunches is 93 ns, defined by the RF system of the accelerator. In fact smaller distances would lead to a chirp of the electron energy along the bunch train. The total length of the bunch train is ~ 1 ms and the energy acceptance of the accelerator provides the possibility for defined, fast electron energy tuning of ± 3 %, thus a wavelength tuning of ± 6 %, within the bunch train or between bunch trains.

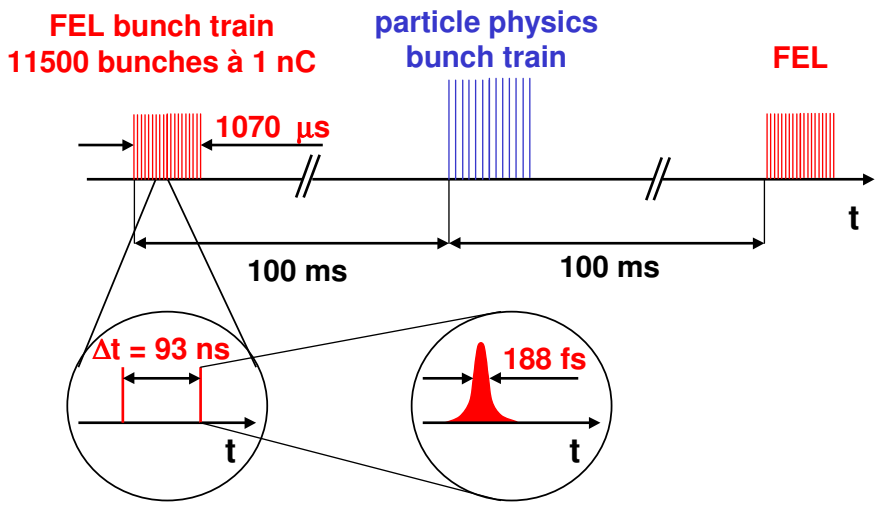

Figure 4.1.2.: *Electron bunch pattern as provided by the TESLA accelerator. For details about the bunch train for particle physics see Part II. The FWHM width of the electron bunch of 188 fs corresponds to* $\sim 56\,\mu m$ *in length.*

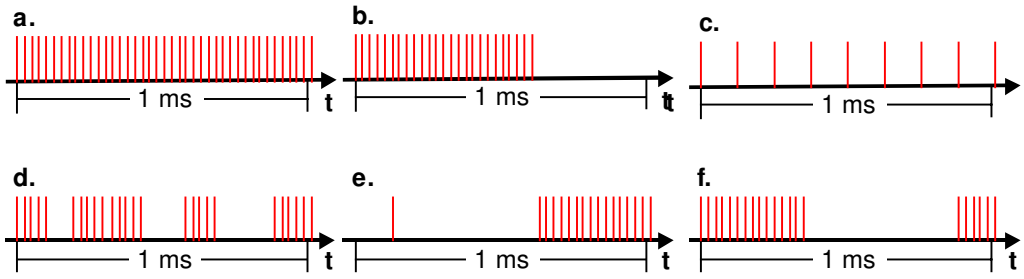

Figure 4.1.3.: *Fill pattern of the electron bunch train. a. corresponds to a homogenous filling (11500 bunches). Fill patterns with fewer bunches (b.) or larger bunch distance (c.) are possible. Several groups of bunches may be selected (d.) or a preceding bunch for timing purposes (e.). Also pump and probe experiments using one bunch train (f.) are feasible.*

Furthermore, as one electron bunch train will basically serve one SASE undulator and the XFEL radiation will be used only by one experiment at a time, it is feasible to realize special fill patterns of the electron bunch train. In Fig. 4.1.3 six proposed fill patterns are presented schematically. To achieve stability of the electron beam by means of position feedback control these nominal pulses may have an advanced electron pulse carrying reduced charge, thus not reaching SASE amplification.

4.2. Generation of SASE and Spontaneous Radiation

4.2.1. Choice of the SASE FEL parameters

In the previous section the design requirements, as they follow from the scientific case, have been described. The most important parameter of choice here is the wavelength, and this section deals with the optimization of the various parameters in order to obtain best performance for all SASE FELs at TESLA covering the wavelength range from 1 to 25 Å. The starting point of the optimization of FEL parameters is a combination of technical constraints, such as achievable electron beam parameters and undulator quality, and the desired wavelength. The electron beam parameters that can be obtained and optimized for the FEL, as well as their growth along the accelerator, bunch compressors, and transfer line, are given in Part II, Sec. 9.1.5 of the TDR. Similar constraints on undulator parameters are described in Sec. 4.3. Here, the final parameters at the undulator entrance are quoted in Tab. 4.2.1.

Electron beam energy, $\mathcal{E}$	13 – 50 GeV
Peak current, I	5.0 kA
rms bunch length, σ_z	25 μm
rms normalized emittance, ϵ_n	1.6 mrad mm
rms energy spread, σ_E	2.5 MeV
Bunch train duration	1070 μs
Bunch separation	93 ns
Max. number of pulses per train	11500
Repetition rate	5 Hz

Table 4.2.1.: *Electron beam parameters at the entrance of the TESLA X-ray FEL undulators.*

With these electron beam parameters, the goal is to design a user facility which minimizes the length of all undulator beamlines while maintaining a large wavelength range. Also a flexibility of operation modes has to be guaranteed to assure that different experimental requirements can be fulfilled simultaneously. An additional constraint is that the energy of the ^{57}Fe Mössbauer line can be reached with at least one of the SASE beam lines (see Sec. 4.1). The wavelength can be changed by changing the electron beam energy or by changing the gap of the undulators. Thus, the strategy is that one electron beam line supplies electrons to two different SASE undulator beam lines, one with a fixed gap, the other with variable gap. The wavelength required for the fixed gap device determines the electron beam energy. The wavelength in the second undulator is then set by setting the undulator gap. With two electron beam lines, four undulators can deliver FEL radiation independently at four desired wavelengths. The electron beam, after generating radiation in the short wavelength range, can still be used to generate spontaneous radiation or SASE radiation at longer wavelengths. Therefore, additional wigglers are placed behind the four SASE undulators, one of which is a SASE undulator for longer wavelengths.

The optimization process has been performed with a combination of analytical param-

eterization, linear and nonlinear steady state and time dependent simulation codes. The remainder of this section is dedicated to the optimization process and the underlying physics that went into the simulations.

4.2.1.1. Calculation of the FEL process

The optimization of SASE undulators and the calculation of output characteristics have been done using the electron beam parameters presented above.

The focusing system will provide a nearly uniform focusing of the electron beam in the undulator, so X-ray FELs have been optimized using the axially symmetric model of the electron beam (the validity of the model was checked later with the actual focusing structure, using a non-axially symmetric model). It is assumed that the transverse distribution function of the electron beam is Gaussian, so the rms transverse size of the beam is $\sigma = \sqrt{\epsilon\beta}$, where $\epsilon = \epsilon_{\rm n}/\gamma$ is the rms beam emittance with $\epsilon_{\rm n} = 1.6\,$mrad mm and β is the focusing beta-function. The energy spread is also assumed to be Gaussian with rms deviation $\sigma_{\rm E}$. The electron beam is assumed to have a Gaussian axial profile with rms bunch length $\sigma_{\rm z} = 25\ \mu$m and a peak value of the current of 5 kA.

The operation of the FEL amplifier is described by the following parameters [1, 2]: the gain parameter Γ, the diffraction parameter B, the efficiency parameter $\rho_{3D} = \rho B^{1/3}$ (where ρ is the one-dimensional efficiency parameter [3]), the space charge parameter $\hat{\Lambda}_{\rm p}^2$, the energy spread parameter $\hat{\Lambda}_{\rm T}^2$, the betatron motion parameter $\hat{k}_\beta$, and the number of cooperating electrons $N_{\rm c}$:

$$\begin{aligned}
\Gamma &= \left[I\omega^2\theta_{\rm s}^2/(I_{\rm A}c^2\gamma_{\rm z}^2\gamma)\right]^{1/2} , \\
B &= 2\Gamma\sigma^2\omega/c\,, \qquad \rho_{3D} = c\gamma_{\rm z}^2\Gamma/\omega\,, \\
\hat{\Lambda}_{\rm T}^2 &= (\sigma_{\rm E}/\mathcal{E})^2/\rho_{3D}^2\,, \qquad \hat{k}_\beta = k_\beta/\Gamma\,, \\
N_{\rm c} &= I/(e\omega\rho_{3D})\,, \quad \hat{\Lambda}_{\rm p}^2 = 2c^2/(A_{\rm JJ}\theta_{\rm s}\sigma\omega)^2
\end{aligned} \tag{4.2.1}$$

Here $\omega = 2\pi c/\lambda$, I is the beam current, $I_A = mc^3/e \simeq 17$ kA is Alfven's current, $\gamma_{\rm z}^2 = \gamma^2/(1+K^2)$, $k_\beta = 1/\beta$, and $\theta_{\rm s} = K/\gamma$. The factor $A_{\rm JJ}$ is equal to 1 for a helical undulator, and to $J_0(K^2/2(1+K^2)) - J_1(K^2/2(1+K^2))$ for a planar one, where J_0 and J_1 are the Bessel functions of the first kind. The peculiarity of the parameter space of an X-ray FEL at TESLA is that the optimization of the FEL parameters can be performed by taking into account only diffraction effects, the energy spread in the electron beam, and the effects of betatron motion. There exists one more factor complicating the optimization of FEL parameters, namely, quantum fluctuations of the incoherent undulator radiation. When the electron beam moves in the undulator, it also emits incoherent radiation [4]. The mean energy loss of each electron into incoherent radiation is given by:

$$d\mathcal{E}/dz = 2r_e^2\gamma^2 B_{\rm u}^2(z)/3 \quad , \tag{4.2.2}$$

where $B_{\rm u}$ is the magnetic field in the undulator and $r_e = e^2/m_e c^2$. If the energy loss of the electron $\Delta\mathcal{E}_{\rm SR}$ is about

$$\frac{\Delta\mathcal{E}_{\rm SR}}{\mathcal{E}} \simeq \rho_{3D} B^{-1/3}\,, \tag{4.2.3}$$

the undulator should be tapered in order to compensate this effect and to keep the resonance condition.

A fundamental limit on the minimal achievable wavelength is imposed by the growth of the uncorrelated energy spread in the electron beam due to the quantum fluctuations of undulator radiation. The rate of energy diffusion is given by the expression (for $K \gg 1$):

$$< d(\delta\mathcal{E})^2_{\rm qf}/dz >= 55e\hbar\gamma^4 r_e^2 |B^3_{\rm u}(z)|/24\sqrt{3}m_e c \quad . \tag{4.2.4}$$

This effect grows drastically with energy and imposes a principle limit on achieving very short wavelengths. Even in the case of zero initial energy spread, the minimal achievable wavelength is about [5]:

$$\lambda_{\rm min} \simeq 45\pi \left[\lambda\!\!\!^{-}_{\rm c} r_{\rm e}\right]^{1/5} L_{\rm u}^{-7/15} \left[\epsilon_n^2 \frac{I_A}{I}\right]^{8/15}\,, \tag{4.2.5}$$

or, in practical units

$$\lambda_{\rm min}[\text{Å}] \simeq 4\frac{\pi\epsilon_n[\text{mrad mm}]}{\sqrt{I[\text{kA}]L_{\rm u}[\text{m}]}}\,, \tag{4.2.6}$$

where $\lambda\!\!\!^{-}_{\rm c} = \hbar/m_e c$ and $L_{\rm u}$ is the undulator length.

The amplification process in the FEL amplifier passes through two stages, linear and nonlinear. The linear stage lasts over a significant fraction of the undulator length, so the main resources for optimization of the undulator length are in the optimization of the field gain in the linear regime. Optimization of parameters of X-ray FELs has been performed in several steps, of which the first was a thorough study of the linear stage. In the linear high-gain limit, the radiation emitted by the electron beam in the undulator can be represented as a set of modes. The radiation power P emitted by the electron beam is given by

$$P \;=\; \left| \int \mathrm{d}\omega \exp[i\omega(z/c - t)] \times \sum_{n,k} A_{nk}(\omega)\Phi_{nk}(r,\omega)\exp[\Lambda_{nk}(\omega)z + in\phi] \right|^2 , \tag{4.2.7}$$

where $\mathrm{Re}(\Lambda_{nk}) > 0$ and ϕ and n are the azimuthal angle and number, respectively.
During amplification, the mode configuration in the transverse plane remains unchanged, while the amplitude grows exponentially with the undulator length. Each mode is characterized by the eigenvalue $\Lambda_{nk}(\omega)$ and the field distribution eigenfunction $\Phi_{nk}(r,\omega)$ in terms of transverse coordinates. With sufficient undulator length, the fundamental Φ_{00} mode gives the main contribution. Thus, the first step of optimization was to choose parameters of the FEL in order to maximize the gain of the fundamental mode. This step has been performed via a numerical solution of the corresponding eigenvalue equations, taking into account all the effects (diffraction, energy spread and emittance) [2, 6]. The value of interest is the field gain length of the fundamental mode, $L_{\rm g} = 1/\mathrm{Re}(\Lambda_{00})$, which gives a good estimate for the

expected length of the undulator needed to reach saturation, $L_{\rm sat} \simeq 10 \times L_{\rm g}$. Calculations performed at this step allow one also to fix tolerable deviations of the electron beam parameters from the project values given in Tab. 4.2.1. The dependence of the gain length on the peak value of the beam current is not a critical one (see Fig. 4.2.1). The tolerable initial energy spread in the electron beam at the undulator entrance can also be larger than the project value of 2.5 MeV (see Fig. 4.2.2). The most critical parameter is the emittance, as illustrated in Fig. 4.2.3.

The second step of optimization of the FEL parameters was the solution of the initial-value problem, i.e. calculations of coefficients $A_{nk}(\omega)$ appearing in Eq. 4.2.7. This has been done by means of a technique developed in [7]–[9]. At this stage, the degree of transverse coherence of the radiation from the SASE FEL is calculated [9]. Calculations show that the degree of transverse coherence of the output radiation in the end of the linear regime is close to 100% for all X-ray FELs in this project.

The final stage of the FEL calculations was to simulate the FEL process with nonlinear codes. The calculations have been performed with the three-dimensional, time-dependent simulation codes FAST and Genesis 1.3 [10, 11], which were run in steady-state and time-dependent modes. Both codes allow one to simulate rigorously the start-up from shot noise, an arbitrary axial profile of the electron bunch, and an energy chirp along the bunch induced by wakefields. The influence of wakefields on the SASE FEL operation has two different aspects. The first one is the energy chirp along the electron bunch induced before the beam enters the undulator. It results in a frequency chirp along the SASE radiation pulse but does not suppress the output power. Thus, the only effect of wakefields induced in the accelerator and transfer line (see Part II, Sec. 9.7) is the broadening of the spectral distribution of the

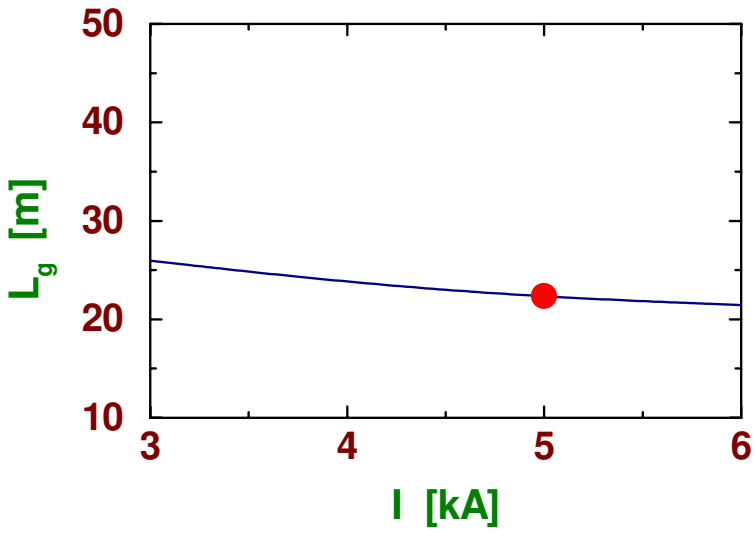

Figure 4.2.1.: *Field gain length versus peak current for the SASE 1 FEL operating at a wavelength of 1 Å . The nominal value of the normalized rms electron beam emittance is 1.6 mrad mm. The calculations take an increase of the energy spread due to quantum fluctuations of incoherent radiation into account. The dot corresponds to the project value of* $I = 5$ *kA.*

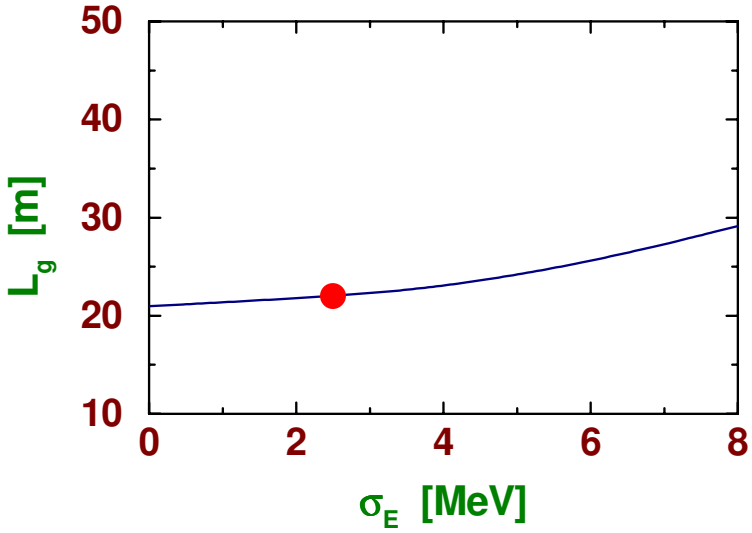

Figure 4.2.2.: *Field gain length versus initial energy spread at the undulator entrance for the SASE 1 FEL operating at a wavelength of 1 Å . The nominal value of the normalized rms electron beam emittance is 1.6 mrad mm. The calculations take an increase of the energy spread due to quantum fluctuations of incoherent radiation into account. The dot corresponds to the project value of* $\sigma_{\rm E} = 2.5$ *MeV.*

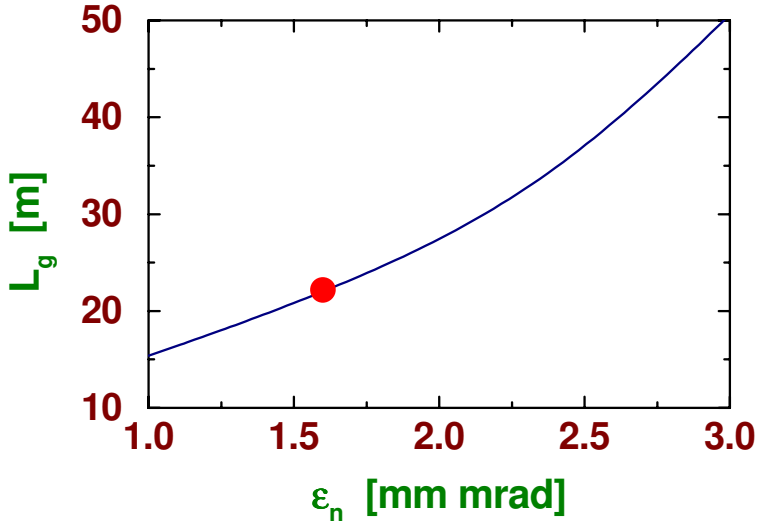

Figure 4.2.3.: *Field gain length versus emittance for the SASE 1 FEL operating at a wavelength of 1 Å. The initial energy spread at the undulator entrance is equal to 2.5 MeV. The calculations take an increase of the energy spread due to quantum fluctuations of incoherent radiation into account. The dot corresponds to project value of* $\epsilon_{\rm n} = 1.6$ *mrad mm.*

radiation. The simulation of this effect in SASE 1 with the code FAST for 1 Å shows an increase of the spectral width by less than a factor two. The second aspect is a different energy change of each longitudinal slice in the electron beam induced by the wakefield inside the vacuum chamber while moving through the undulator. This effect can in principle lead to a significant suppression of the radiation pulse energy (see [12]). The magnitude depends on the choice of vacuum pipe diameter and material (see also Sec. 4.3.2.1 and Part II, Sec. 9.7). In the wakefield calculations, an aluminum vacuum pipe with 10 mm inner diameter has been assumed, resulting in a minimum undulator gap of 12 mm. Aluminum has been chosen as the worse of two appropriate materials. For the design, copper coated stainless steel is chosen since it will even exceed the wakefield properties of aluminum. The effect of surface roughness and resistive wall wakefields for SASE 1 at 1 Å leads to a reduction of the output power by a factor of 2.5 compared to a simulation not including wakefields. The main reason for the power reduction is the relative energy loss of approximately 10^{-3} in the central part of the electron beam, which can be compensated by applying an additional tapering to the undulator. With the appropriate taper, i.e. keeping the center of the bunch in resonance with the electromagnetic wave, the results with wakefields are within a few percent the same as those without wakefields.

The results of simulations for different undulators are compiled in Tabs. 4.2.2 and 4.2.3 together with the main undulator and electron beam parameters. General properties of the output radiation are described in Sec. 4.2.2.

	Units	SASE 2			SASE 3	
β-function	m	45			45	
Magnetic period	mm	45			45	
Magnetic gap*	mm	12			12	
Magnetic field	T	0.95			0.95	
K-value		4			4	
Electron energy**	GeV	30	25	20	23	15
Photon wavelength	Å	-	0.85	1.33	1	2.4
Saturation length	m	-	210	155	185	115
Total undulator length	m	311.1			274	

* No gap tunability is provided, but adjustment of gaps for undulator tuning and beam alignment will be possible.

** SASE 2 is in the electron branch with tuning range 20-50 GeV electron energy, but energies above 25 GeV are used only in SASE 1; SASE 3 is in the other branch with 13-27 GeV range.

Table 4.2.2.: *Parameters of the fixed-gap* SASE FELs at TESLA.*

4.2.1.2. Results of optimization of FEL parameters

For the shortest X-ray wavelength of 0.85 Å in the branch with electron energies between 20 and 50 GeV, an undulator with a fixed gap of 12 mm is planned (SASE 2). For this gap, the wakefield effects are tolerable (see previous section). The optimum energy versus undulator

	Units	SASE 1			SASE 4		SASE 5	
β-function	m		45		45		15	
Magnetic period	mm		60		60		107	
Electron energy*	GeV	30	25	20	25	15	23	15
Magnetic gap**	mm	19-12	22-12	22-13	22-12	21-12	35-12	35-12
Magnetic field	T	0.82-1.33	0.66-1.33	0.66-1.25	0.66-1.33	0.7-1.33	0.38-0.96	0.38-0.96
Photon wavelength	Å	1-2.5	1-3.5	1.5-5	1-3.5	3-10	4-25	10-58
K-value		4.6-7.5	3.7-7.5	3.7-7.0	3.7-7.5	3.9-7.5	3.8-9.6	3.8-9.6
Saturation length	m	220-150	220-120	175-100	220-120	125-80	120-60	95-50
Total length	m		323.5		323.5		176.9	

*SASE 1 is in the electron branch with tuning range 20-50 GeV electron energy; SASE 4 and SASE 5 are in the other branch with 13-27 GeV range.
**Gap tuning range at the various electron energies. The following lines show the corresponding parameters.

Table 4.2.3.: *Parameters of the gap-tunable SASE FELs at TESLA.*

period, keeping the radiation wavelength fixed, results in an electron beam energy of 25 GeV and an undulator period of 45 mm (see Tab. 4.2.2 for details). For higher energies, the saturation length increases due to the larger energy spread caused by quantum fluctuations. For lower energies, the geometrical emittance increases the saturation length. In order to change the wavelength of a second undulator (SASE 1) supplied with electrons by the same electron beam line, this undulator has a variable gap. With the gap opened (and therefore with a reduced magnetic field on axis) a minimum wavelength of 1 Å can be obtained by using an undulator period of 60 mm. For this period, the wavelength of SASE 1 can be varied by a factor of 3.5 for energies up to 25 GeV. In principle, one could also use a beam of 30 GeV, with a somewhat smaller tuning range (see Tab. 4.2.1), but with larger peak powers. However, for this energy, undulator SASE 2 in the other track of this electron branch does not reach saturation anymore.

For the lower energy branch of the TESLA user facility (from 13 to 27 GeV), a similar strategy is chosen. Because here the optimum choice of undulator period is almost the same, it has been chosen as in the high energy part, i.e. 45 mm (SASE 3, fixed gap) and 60 mm (SASE 4, variable gap). See Tables 4.2.2 and 4.2.3 for details. Behind SASE 3, a second undulator is placed (SASE 5). It uses the electron beam with the rather large induced energy spread. However, going to longer wavelength, the acceptable limit on the energy spread increases. Therefore, the beam can still be used in this undulator as long as the wavelength is a factor of 3 to 4 larger, which is always the case, independent of the undulator gap setting of SASE 5. For this undulator as well as for all undulators discussed previously, tapering is necessary because of the large energy loss of the electron due to incoherent undulator radiation.

Finally, a few remarks should be made concerning the choice of the β-function. As can be seen in the tables, an energy-independent β-function of 45 m has been chosen. For the highest energy, this is close to the optimum. In addition, for this value, the quadrupole strength is still moderate, which makes the beam less sensitive to imperfections (e.g. alignment, see Sec. 4.3.3.4.D and Part II, Sec. 9.8.3). For lower energies, the kicks by quadrupoles of given strength are larger. Therefore, reducing the quadrupole strength proportional to energy, thus keeping the β-function constant, will partly compensate this effect. The increase in gain length due to the larger electron beam radius (reduced current density) is moderate and of minor importance because the undulator length is needed for the highest energies in any case.

4.2.2. Details of SASE FEL radiation

The radiation from an X-ray FEL has a narrow bandwidth, it is always totally polarized and transversely coherent [1, 9]. Due to the latter property, the (peak or average) brilliance B of the X-ray FEL is simply given by $B = 4\dot{N}_{ph}/\lambda^2/(\Delta\omega/\omega)$, with $\dot{N}_{ph} = P/(\hbar\omega)$ as the photon flux, and P as the FEL (peak or average) power. An important characteristic of the output radiation is the degeneracy parameter, i.e. the number of photons per mode, that can be expressed in terms of the of the peak brilliance as $B\lambda^3/(4c)$. Plots of (average and peak) brilliance and of the number of photons per mode were shown in Figs. 2.3.1, 2.3.2 and 2.3.3. The main parameters of the radiation are given in Table 4.2.4.

	Units	SASE 1	SASE 2*	SASE 3	SASE 4	SASE 5**
Wavelength***	Å	1-5	0.85-1.33	1-2.4	1-10	4-58
Peak power	GW	37	19	22	30	110-200
Average power	W	210	110	125	170	610-1100
Photon beam size (FWHM)****	μm	100	110	120	110	60-90
Photon beam divergence (FWHM)*****	μrad	0.8	0.7	0.7	0.7	3.3-19
Bandwidth (FWHM)	%	0.08	0.07	0.08	0.08	0.29-0.7
Coherence time	fs	0.3	0.3	0.3	0.3	0.3-1.8
Pulse duration (FWHM)	fs	100	100	100	100	100
Min. pulse separation$^+$	ns	93	93	93	93	93
Max. number of pulses per train$^+$	#	11500	11500	11500	11500	11500
Repetition rate$^+$	Hz	5	5	5	5	5
Number of photons per pulse	#	1.8×10^{12}	8.2×10^{11}	1.1×10^{12}	1.5×10^{12}	$2.2 - 58 \times 10^{13}$
Average flux of photons	#/sec	1.0×10^{17}	4.6×10^{16}	6.4×10^{16}	8.3×10^{16}	$1.2 - 33 \times 10^{18}$
Peak brilliance	B^{++}	8.7×10^{33}	6.2×10^{33}	5.9×10^{33}	7.0×10^{33}	$18 - 1.0 \times 10^{32}$
Average brilliance	B^{++}	4.9×10^{25}	3.5×10^{25}	3.3×10^{25}	3.9×10^{25}	$10 - 0.5 \times 10^{24}$

* After upgrade to a two-stage FEL, the bandwidth decreases and the brilliance increases by a factor of 500.
** Uses electron beam coming out of SASE 3.
*** Parameters are presented for the shortest wavelength of each beamline, except for SASE 5 where parameters for the extreme wavelengths are given.
**** At the exit of the undulator.
***** Far field divergence.
$^+$ Time structure of the beam in the accelerator. The average parameters for SASE FELs are presented for an ultimate case when only one beamline is in operation.
$^{++}$ In units of photons/(sec·mrad^2·mm^2·0.1 % bandwidth).

Table 4.2.4.: *Photon beam properties of the SASE FELs at TESLA*

Typical temporal and spectral structures of the radiation pulse from the X-ray FEL are presented in Fig. 4.2.4. The radiation pulse consists of a large number of independent wavepackets. The radiation within one wavepacket is transversely and longitudinally coherent. The chaotic nature of the output radiation is a consequence of the start-up from shot noise. The shot noise in the electron beam causes fluctuations of the beam density that are random in time and space. As a result, the radiation produced by such a beam, has random amplitudes and phases in time and space. These kinds of radiation fields can be described in terms of statistical optics with, e.g., the following parameters: time and spectral correlation functions, transverse correlation functions, probability density distributions of the instantaneous radiation intensity, of its integrals (finite-time and space), and of the energy after the monochromator, coherence time, interval of spectral coherence, coherence area, and coherence volume [1].

The FEL amplifier, operating in the linear regime, filters the input signal-shot noise in the

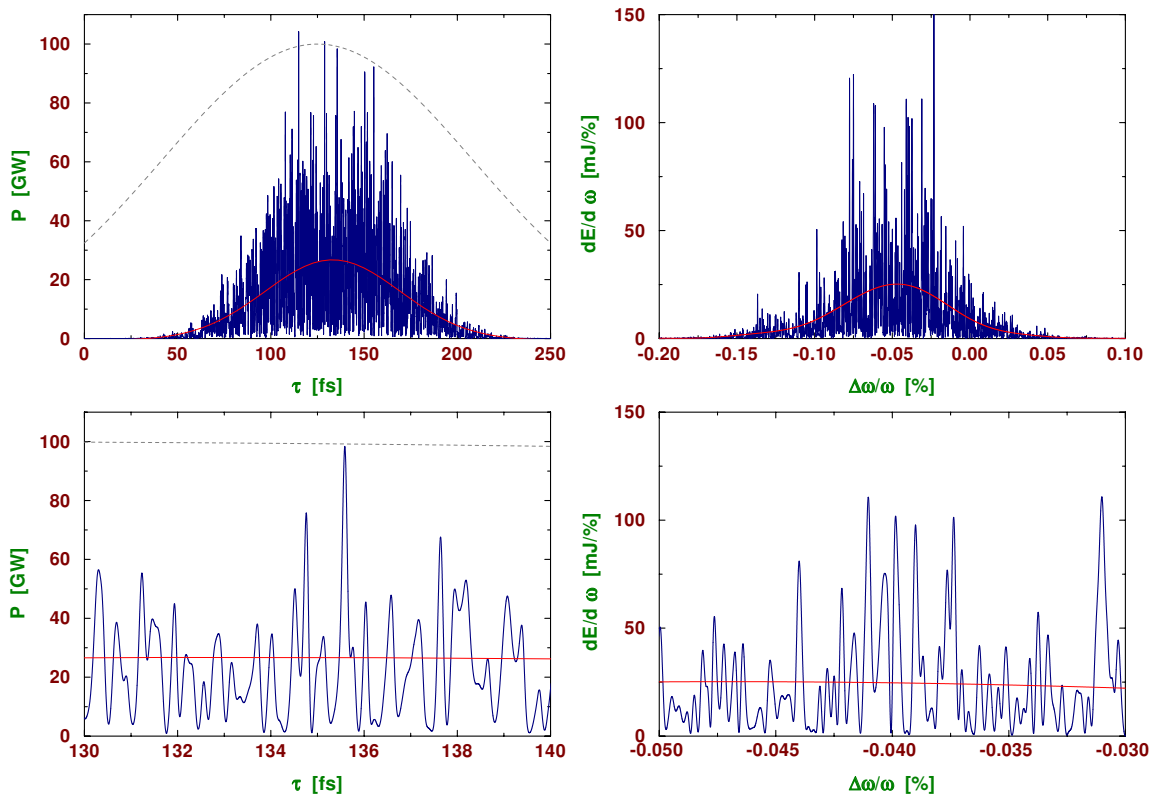

Figure 4.2.4.: *Temporal (left) and spectral (right) structure of the radiation pulse from the SASE 1 FEL operating at a wavelength of 1 Å . The bottom figures show an enlarged section of the central part of the pulse. The undulator length is 200 m. The red lines correspond to averaged values. The dashed line gives the axial profile of the electron bunch.*

electron beam. As a result, the output radiation is a Gaussian random process and we can define its general statistical properties without any calculations. For instance, in the case of the SASE FEL, the instantaneous radiation intensity fluctuates in accordance with the negative exponential distribution, and the energy in the radiation pulse fluctuates in accordance with the gamma distribution. We can also state that the spectral density of the radiation energy and the first-order time correlation function should form a Fourier transform pair (Wiener-Khintchine theorem). Also, the higher-order correlation functions (time and spectral) can be expressed in terms of the first-order correlation functions. These properties are well known in statistical optics as properties of completely chaotic polarized radiation.

The coherence time of SASE FEL radiation which is defined by the inverse spectral width $\delta\omega$, is for an X-ray FEL much shorter than the pulse duration (see Table 4.2.4). To significantly increase the longitudinal coherence, at best up to the full length of the radiation pulse, the so-called two-stage SASE FEL is proposed [13]. The scheme consists of two undulators and an X-ray monochromator located between them (see Fig. 4.2.5). For the Å wavelength range, the monochromator could be realized using Bragg reflections from crystals [14]. The first undulator operates in the exponential gain regime well below saturation. The monochro-

mator selects a narrow band (optimally the inverse pulse duration) from the SASE radiation pulse coming out of the first undulator. Due to an energy spread in the electron beam the micro-bunching induced in the first undulator is suppressed when the beam goes through a bypass. Saturation is reached in the second undulator which operates with the fully coherent radiation as an input signal (its power has to be much larger than the effective power of shot noise). The two-stage FEL, an option for which space is reserved behind SASE 2, is optimized for a photon energy of 14.4 keV. The spectral bandwidth of the radiation from two-stage SASE FEL (20 meV) is defined by the finite duration of the electron pulse. The shot-to-shot fluctuations of the energy spectral density are dramatically reduced in comparison with the 100 % fluctuations in a SASE FEL [15]. The peak and average brilliance are by three orders of magnitude higher than the values which could be reached by a conventional X-ray SASE FEL.

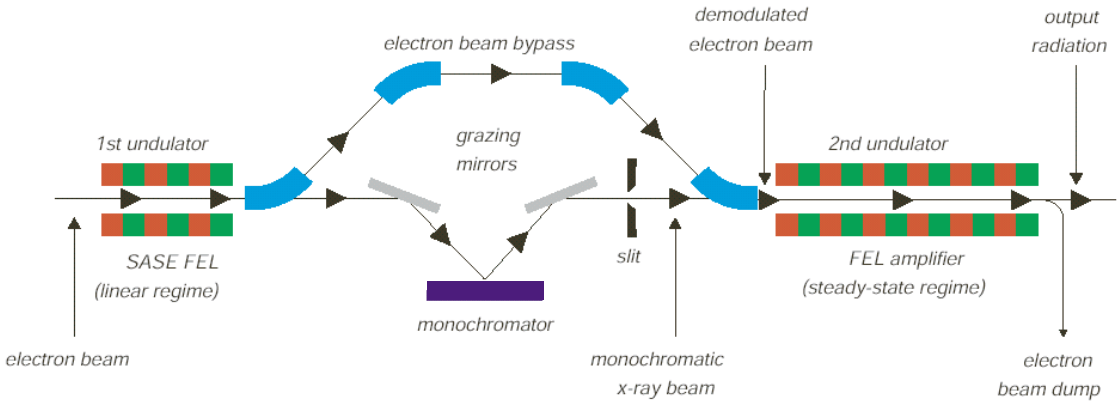

Figure 4.2.5.: *Basic scheme of a two-stage FEL providing full longitudinal and transverse coherence of the output radiation.*

4.2.3. Details of spontaneous radiation

As already mentioned, it is planned to place long undulators for spontaneous emission behind the SASE FELs. Although the electron beam performance is degraded by the SASE process, the beam has still a high quality compared to storage rings for example. The energy spread induced by wakefields is no problem for spontaneous emission. Therefore, the minimum undulator gap has been reduced to 6 mm. Due to the small magnetic gap, high fields and consequently large K-values are possible. That means the angle-integrated spectrum of these undulators covers a large spectral range up to the MeV region. On axis, the spectrum consists of the well-known peaks of the odd harmonics. By variation of the electron energy and the magnetic gap, the energy of these harmonics can be varied. Of course the central brilliance of these lines is several orders of magnitude lower than that of the SASE lines, but their spectral range reaches much higher photon energies, and the photon beam has the same outstanding

timing properties.

Like any normal undulator, the SASE FEL undulators will also emit a spontaneous spectrum. Although the brilliance and spectral flux of the spontaneous emission are several orders of magnitude smaller than the laser values, it might be of advantage that the angle integrated spectrum is nearly a continuum and extends to much higher energies. Combining the five proposed undulator designs with the possibility of varying the electron energy between 15 and 30 GeV, one is able to cover the spectral range from 1000 eV up to about 1 MeV with nearly constant spectral flux of about 10^{13} Phot./sec/0.1%. This is shown for some of the SASE devices in Fig. 4.2.6.

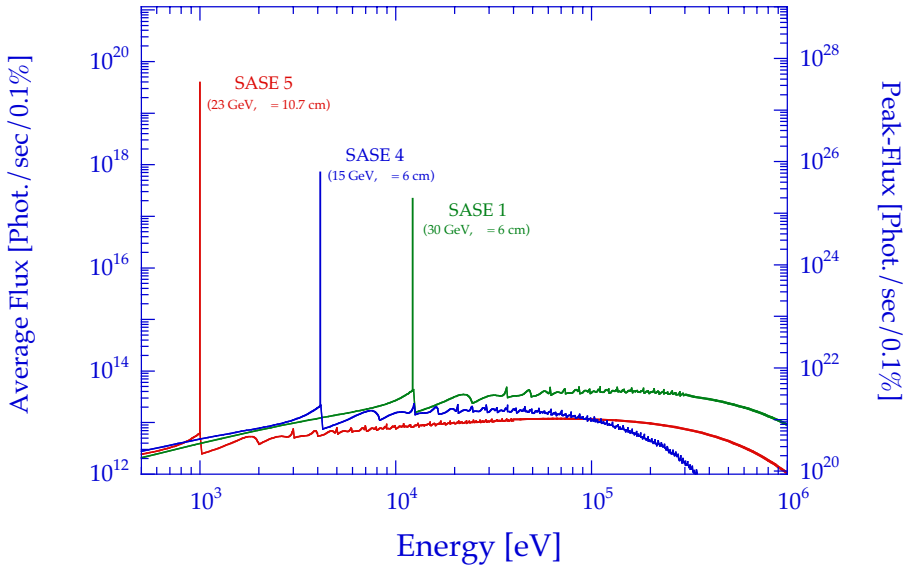

Figure 4.2.6.: *Spontaneous angle integrated flux from three of the SASE FELs for smallest gap and different electron energies*

The spectral flux is 4 to 7 orders of magnitude below that of the FEL spectral line, but the total flux integrated over the whole spectrum is comparable. Correspondingly, this is also true for the power emitted by the spontaneous radiation, which is for certain designs much higher than the power emitted into the laser line. Another important difference between the induced and the spontaneous radiation is the angular divergence. Whereas the laser line is extremely well collimated with an angular divergence of some μrad, the angular divergence of the total, wavelength integrated spontaneous radiation is about 100 μrad. Therefore it is in principle possible to separate the laser beam by passing it through an aperture of some μrad acceptance.

Only one spontaneous undulator type is proposed, because it covers already a large spectral range. The undulator properties are listed in Tab. 4.2.5, and the photon beam properties arising from these devices are listed in Tab. 4.2.6. The angle-integrated spectral flux emitted by such a device at fixed gap is shown in Fig. 4.2.7. It corresponds to the sum over all har-

	Units	30 GeV	15 GeV
Photon Energy	keV	49	12.3
Gap	mm	6	6
Length of Period	cm	3.0	3.0
Number of Periods	#	1666	1666
Magnetic Field	T	1.1	1.1
K-Value	#	3.1	3.1
Beam Size (RMS)	μm	35	50
Beam Divergence (RMS)	μrad	0.78	1.10

$I_{average}$ = 57 μA, I_{peak} = 5000 A, length 50 m, β = 45 m

Table 4.2.5.: *Parameters of the undulators for spontaneous emission for electron energies of 30 and 15 GeV*

	Units	U-1*		
Photon energy	keV	20	50	200
Peak power	MW	2.72	8.77	18.95
Average power	mW	31	100	220
Photon beam size (FWHM)	μm	120	80	80
Photon beam divergence (FWHM)	μrad	5	3	2
Bandwidth (FWHM)	%	0.2	0.15	0.07
Pulse duration (FWHM)	fs	188	188	188
Pulse separation**	ns	93	93	93
Number of pulses per train**	#	11500	11500	11500
Repetition rate**	Hz	5	5	5
Number of photons per pulse	#	2.2×10^8	2.5×10^8	1.4×10^8
Average flux of photons	#/sec	1.0×10^{13}	1.3×10^{13}	0.7×10^{13}
Peak brilliance	B***	1.3×10^{28}	2.9×10^{28}	2.1×10^{28}
Average brilliance	B***	1.5×10^{20}	3.3×10^{20}	2.4×10^{20}

* Only one undulator structure will be used to obtain radiation at various photon energies by varying the electron energy and the undulator gap. In this table, no reference to the undulator status is made, but only averaged beam properties at selected energies are given.

** Time structure of the beam in the accelerator. The average parameters for SASE FELs are presented for single beamline operation.

*** In units of photons/(sec· mrad^2· mm^2· 0.1 % bandwidth).

Table 4.2.6.: *Beam properties for spontaneous radiation at TESLA. See text for description of the flux calculation based on the accepted fan of spontaneous radiation.*

monics at each energy. Also shown in this figure are the spectra of the first, third and fifth harmonic, produced by varying the magnetic gap of the undulator.

On the other hand, the angular pattern of one harmonic optimized for a given photon energy is much better suited for an experiment than the total sum over all harmonics, because it has its maximum on-axis, and higher harmonics contribute only at larger angles. The angular pattern of the sum spectrum consists of concentric rings of intensity with nearly no radiation on axis. This behavior is qualitatively shown in Fig. 4.2.8 (a) and (b) for photon

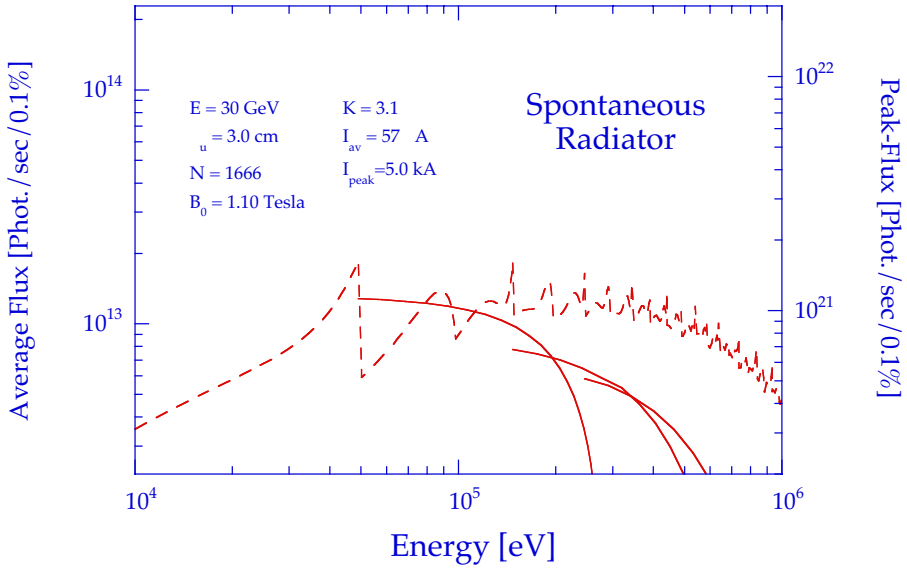

Figure 4.2.7.: *Angle-integrated flux from the spontaneous emission undulator shown as the sum over all harmonics at the smallest gap (dashed line) and for the first, third and fifth harmonics as scanned from the smallest gap to larger values.*

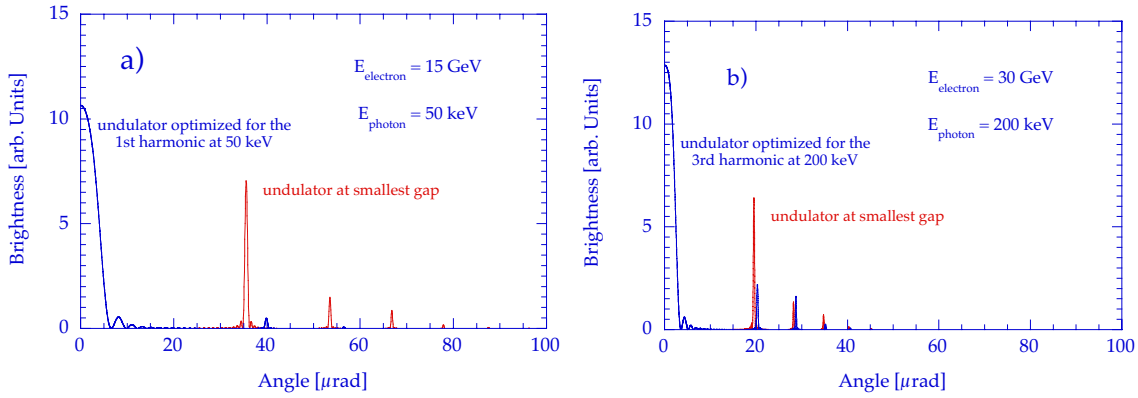

Figure 4.2.8.: *Angular pattern of undulator radiation for the spontaneous emission at smallest gap and optimized for the respective energy:. (a) spectra at 15 GeV and optimized for the first harmonic at 50 keV; (b) spectra at 30 GeV and optimized for the third harmonic at 200 keV.*

energies of 50 and 200 keV, respectively. For the chosen parameters, the intensity of the sum spectrum is mainly concentrated in a ring 40 or 20 μrad off axis, whereas the spectrum optimized for the first harmonic at 50 keV (a) or the third harmonic at 200 keV (b) has a nice peak on axis. The average and peak brilliance of the SASE FELs as well as the spontaneous emission undulators in comparison with conventional third-generation storage ring sources were shown in Fig. 2.3.1 to 2.3.3. Even though the average brilliance of the spontaneous emission undulator is comparable to that of storage ring devices, the peak brilliance surpasses that of these devices by several orders of magnitude.

4.3. Undulator Systems

4.3.1. Introduction

The undulator is at the heart of any FEL. It provides the periodic magnetic field which induces the FEL process. As seen best from Eq. 4.2.6 and in figures 4.2.1 and 4.2.3, the emittance ϵ and the peak current I which can be realized for the electron bunch determine the length of undulators. Thus, using the values $\epsilon = 1.6$ mrad mm and I = 5 kA requires very long SASE undulators. As discussed in Sec. 4.2 the saturation length for 1 Å X-rays is of the order 200 m and additional length must be provided for technical reasons, as is discussed in this section. The electron beam parameters allow for a so-called 'separate function' undulator, where the generation of the periodic magnetic field and the strong focusing are physically separated. The 'undulator system' thus consists of 'undulator segments' and separated strong focusing quadrupoles and phase adjusters, beam correctors, position monitors etc. For the TESLA project five SASE FELs are planned in total. In addition there will be five spontaneous devices, which will use the spent electron beam of three of the SASE FELs. There is no fundamental difference between a SASE and a spontaneous undulator system. Therefore, in the following, no special distinction is made, and all undulator systems are treated in the same fashion. The spontaneous undulator systems are chosen to have lengths of 50 m in order to provide enough average flux. A schematic arrangement of the undulator systems is shown in Fig. 4.1.1. In Tab. 4.3.1 the parameters of the SASE FEL and spontaneous devices are summarized.

The undulators, which will be described in this section, are very long systems when compared to presently installed devices. Many components have to work together in a complex way. The most delicate and also the most expensive items are the magnetic structures. Fortunately, there has been a tremendous development of insertion device technology since undulators have come into use as intense sources of SR 20 years ago. Considerable progress has been made in the design, construction and optimization of these devices. There are now well-established techniques to produce insertion devices with properties that are very close to perfect and meanwhile, these techniques have become fully established. Design and construction of the TESLA undulator systems will certainly take full advantage of these achievements. One striking difference to a third generation X-ray source such as the APS, ESRF or Spring8 is, however, the total length of installed insertion devices. For these sources it is about 110 m. For the TESLA XFELs, in contrast, the total length of undulator systems is 1714 m. The construction of this large number of undulator segments in sufficient quality, in reasonable time and at reasonable cost has to be assured.

4.3.2. Choice of parameters

4.3.2.1. Choice of gaps

The gap size is one of the critical parameters of an insertion device, irrespective of the magnet technology that is used. Generally, the smaller the gap, the shorter the undulator may be at otherwise constant properties. In a SASE FEL, the smallest gap is, however, determined by wakefields induced by the bunched electron beam due to the resistive vacuum wall and

its surface roughness. Wakefields are treated in detail in Part II, Sec. 9.7. Their impact on FEL physics is treated in Sec. 4.2 . Following the results of this analysis is was decided to use vacuum chambers with circular cross section made of copper coated stainless steel with an rms surface roughness of about 0.1 μm and an inner chamber radius of 5 mm, see Sec. 4.3.3.4.F. Such chambers result in an acceptable wakefield level which does not degrade the FEL process. As a consequence, a minimum gap of 12 mm is chosen.

4.3.2.2. Magnet technology

In principle, undulators may be built using superconducting magnets, room-temperature electromagnets, or permanent magnets (PM). These technologies were investigated and discussed in Refs. [16, 17]. At present, there is no alternative to permanent magnet technology for the large-scale use in undulator systems, like for TESLA. The permanent magnet technology is based on either SmCo or NdFeB material. The two principal magnet design concepts for planar structures have both been proposed by Halbach in the early 1980's. One of them uses only permanent magnets [18]. The field quality in this case is fully determined by the magnet material properties. The other, also called 'hybrid design' uses permanent magnets and soft iron parts which concentrate the magnetic flux [19]. In this case the errors are strongly determined by the machined pole faces. In order to produce circularly polarized light, a modified planar pure permanent magnet structure was proposed by Sasaki [20]. There have now been almost 20 years of development on undulator technology based on permanent magnets. Permanent magnet devices are used in large numbers in all SR sources throughout the world. Techniques for error compensation have been developed. At DESY, numerous insertion devices based on this technology have been built for DORIS-III [21], PETRA [22, 23], and for the VUV-FEL [24]. Technologically, all problems related to manufacturing of large numbers of these devices are solvable :

- Manufacturing techniques are well established, extensive experience exists.
- The magnet structures are planar, allowing for excellent access for magnetic field measurements and for the insertion of vacuum chambers.
- Helical undulators can be built as planar devices as well.
- Numerous high-precision magnetic field measuring techniques are available.
- Control of field errors can be done using shims or field fine-tuning [25] – [27].

The design proposal for the undulator systems for the TESLA FEL will be based exclusively on PM technology.

4.3.2.3. Radiation damage

A severe problem is the potential radiation damage of the permanent magnet material due to electron, neutron, and hard X-ray bombardment. Extensive experience exists only for IDs in storage rings, where a very high transmission and therefore a very low loss rate is enforced by the requirement of long lifetime of the stored electron beam. Under normal

operating conditions, no significant radiation damage has been observed [28, 29]. Deviation from these conditions, such as missteering of the beam during injection, may lead to severe degradation [30, 31].

In contrast, not much is known about how PM undulators behave in the radiative environment of a high duty-cycle Linac such as TESLA. Here the situation is completely different. Although the emittance and beam size are smaller than in storage rings, there might be a significant amount of beam halo and dark current far outside the phase space covered by the transverse and longitudinal electron beam emittance. A well-designed collimator system that has to protect the undulators from being hit by electrons is therefore mandatory. It is described in detail in Part II, Sec. 9.1.9 and 9.6.4. Experience at TTF has shown that a well-working collimator system may reduce the radiation level in the direct vicinity of the beam pipe inside the undulator systems to a level below 20 Gy per week.

At the TTF the radiation doses were continuously measured without interruption in a meticulous way over the whole operation time of the undulator at 15 positions equally spaced over the length of the device. The total accumulated doses over 18 months vary from 6000Gy near the undulator entrance to about 120Gy in the 3rd undulator segment. For optimum collimator adjustment radiation doses always show this pattern. They were always highest near the entrance and decay rapidly along the undulator. A coarse lifetime estimate for the magnet material has been made. It is described below and based on the following assumptions:

- We take the result of Okuda [32] who observed a 9% loss of demagnetization of NdFeB material for an absorbed dose of 2.5 MGy after electron irradiation, equivalent to 1% for 0.28 MGy.
- At TESLA the RF pulses are about a factor of 2 longer than at TTF leading to an increased dark current. There is a strong correlation between dark current levels and radiation doses.
- We assume a factor of 50 for increased availability of TESLA as compared to TTF.
- We take the low dose levels at the undulator end for comparison thus considering the first two segments as additional shielding elements.

Extrapolating for TESLA this leads to an expected annual dose of 8000 Gy. This is a worst case estimate. Expected radiation at TESLA will be even lower, which is supported by the following arguments:

- At TESLA there will be phase space as well as "energy" collimation. Dark current therefore cannot hit the undulator. In addition unlike the TTF the electron beam in the collimator does not point towards the undulator. See Part II, Sec. 9.1.9 and 9.6.4. for more details.
- The TTF doses are integrated over the whole previous life. They include runs with missteered electron beam, high dark current levels or non optimum collimator adjustments as well. Such conditions contribute significantly to irradiation doses. At TESLA beam conditions like these can be avoided.

- The gap of the TTF undulator is fixed. At TESLA it can be opened for commissioning and beam optimization. Thus the irradiation at these operation modes can be avoided.
- Online dosimeters [33] and loss monitors [34] will be installed at TESLA, which give a clear signal, if the dose level inside the undulator region becomes too high.

The resulting worst case life time estimate for 1% demagnetization is 35 years. It does not include the above relieving arguments. As a result NdFeB should be fully sufficient for the use in the TESLA undulators. However, permanent magnet material based on Samarium and Cobalt may be used as a fallback solution in the unlikely event that even increased radiation hardness its needed. As compared to NdFeB the improvement is more than factor of 20 [32]. The penalty would be a reduced magnetization by about 10% and a 30% increase in cost for the permanent magnet material. At the TTF the dosimetry program will be continued and extended. As more experience will be made during TTF operation and upgrade a well substantiated decision can be made.

4.3.2.4. Device parameters

The radiation wavelength of an FEL is given by the basic relations

$$\lambda_R = \frac{\lambda_U(1+K_{rms}^2)}{2\gamma^2}\ ; K_{rms} = \frac{eB_{rms}\lambda_U}{2\pi m_e c}\ ; B_{Max}[T] = a_1 exp\left\{a_2\frac{g}{\lambda_U} + a_3\left(\frac{g}{\lambda_U}\right)^2\right\}\ . \tag{4.3.1}$$

Here e is the electron's charge, m_e its mass, γ its kinetic energy in units of its rest mass and c the speed of light. λ_U is the undulator period length, g the undulator gap. Rms and maximum values for magnetic field or K-parameters are connected by :

$$(B,K)_{rms} = \frac{1}{\alpha}(B,K)_{Max} \tag{4.3.2}$$

with $\alpha^2 = 2$ for planar structures having a sinusoidal field and $\alpha^2 = 1$ for helical structures. The constants $a_1 - a_3$ depend on a specific magnet design. They are usually determined by fitting to calculated results. Some representative and illustrative examples for different magnet structures may be found in [17]. For a state-of-the-art hybrid undulator made of NdFeB, a_1=3.694, a_2=-5.068, and a_3=1.520 are used. The assumption is valid for NdFeB for $0.1 < g/\lambda_U < 1.0$. By means of these equations, the undulator period length λ_U can be determined as a function of the magnetic gap g at given γ and magnet structure (constants a_1 - a_3) for a desired radiation wavelength λ_R. For a given gap, 12 mm in the case of the TESLA FEL undulators, λ_U is determined this way.

Table 4.3.1 shows an overview and a collection of parameters over the SASE and spontaneous devices based on the layout presented in Sec. 4.1, which is the result of vivid discussions with the potential user community. There will be two transfer lines delivering electrons from the main TESLA linac into two branches with different electron energy range. Within their ranges the electron energy in each branch can be freely selected. In each branch electrons then are split onto two beamlines with SASE FEL devices named SASE 1 to SASE 4. It is proposed to install one SASE FEL (SASE 5) as a second in a row using the spent beam

Device	Type	E_e [GeV]	Wavelength [nm]	Photon Energy [keV]	λ_U [mm]	ρ^+ [10^{-4}]	K_{min}-K_{max}	B_{min}-B_{max} [T]	Gap [mm]	β [m]	L^*_{sat} [m]	L^{**}_{tot} [m]	F^{++}_{mag} [kN]	Segm. $^{+++}$
SASE 1	planar	30	0.1-0.25	12.4-4.9	60	4.3-5.9	4.6-7.5	0.82-1.33	19-12	45	220-150	323.5	26.7-70.2	53
		25	0.1-0.35	12.4-3.5		4.2-6.3	3.7-7.5	0.66-1.33	22-12		220-120			
		20	0.15-0.5	8.25-2.5		5.1-7.7	3.7-7.0	0.66-1.25	22-13		175-100			
SASE 2	planar	25	0.085	14.4	45	3.6	4.0	0.95	12	45	210	311.1	35.8	51
		20	0.13	9.3		4.1	4.0	0.95	12		155			
SASE 3	planar	23	0.1	12.4	45	3.8	4.0	0.95	12	45	185	274.5	35.8	45
		15	0.24	5.2		4.1	4.0	0.95	12		115			
SASE 4	planar	25	0.1-0.35	12.4-3.5	60	4.2-6.3	3.7-7.5	0.66-1.33	22-12	45	220-120	323.5	26.7-70.2	53
		15	0.3-1.0	4.1-1.24		7.1-10.3	3.9-7.5	0.70-1.33	21-12		125-80			
SASE 5	circular	23	0.4-2.5	3.1-0.5	107	14.5-26.8	3.8-9.6	0.38-0.96	35-12	15	120-60	176.9	11.5-73.2	29
		15	1.0-5.8	1.2-0.21		19.2-35.7	3.8-9.6	0.38-0.96	35-12		95-50			
U 1/U 5	planar	50	0.003-0.009	420-140(1.harm)	30	-	0-3.1	0-1.1	∞-6	45	50 ***	61.0	0-51.6	10
		30	0.0083-0.025	150-50(1.harm)										
			0.0028-0.0083	450-150(3.harm)							total	total		total
		15	0.033-0.1	37-12(1.harm)							250	305		50
			0.0123-0.033	111-37(3.harm)										
										Sum	1405	1714.1		281

*The saturation length is taken as the net magnetic length of the undulator.

**The total length of an undulator system includes the saturation length plus 1.1 m for intersections (Quadrupoles, phase shifters, correctors, diagnostics, pumps, etc.) and 20 % contingency for field errors, misalignment, etc. For the spontaneous undulators, no contingency for the device length is considered.

***For the spontaneous undulators U 1 – U 5, the "saturation length" represents the assumed magnetic length of each device. The summation in the bottom line includes 5 devices.

$^+$For SASE 1 to SASE 4 a normalized emittance ϵ_n of $1.6 \cdot 10^{-6}$ m, an energy spread of 2.5 MeV and a peak current of 5000 A is used. For SASE 5, due to the spent beam, an energy spread of 6.0 MeV is used.

$^{++}$A pole width of 40 mm and an undulator segment length of 5.0 m is assumed. Load values for max./min. gaps are given. The total magnetic length including 20 % contingency is 1405 m, the total undulator length, including the intersection is 1714.1 m.

$^{+++}$Length assumptions : Undulator segment 5.0 m, Intersection 1.1 m, cell length 6.1 m

Table 4.3.1.: *Overview over the undulator systems planned for the TESLA XFEL.*

of SASE 3. SASE 5 is optimized at a longer wavelength range of 0.4 - 2.5 nm at 23 GeV and, therefore, has a much larger ρ parameter. It can tolerate the increased energy spread caused by SASE 3 leading to a saturation length of 120 m.

All SASE FELs will have possibility to tune the photon energy, but only SASE 1, SASE 4 and SASE 5 will enable tuning of the photon energy by changing the gap. Their tunability range is 3.5 asking for longer saturation length since the shorter wavelengths are at larger gaps and correspondingly smaller peak fields. The saturation lengths of SASE 1-4 undulators reaches 220 m. Gap tuning for SASE 2 and SASE 3 is not provided, but the photon energy can be changed by changing the electron energy. They are designed to operate at a wavelength of 0.085 nm and 0.1 nm at an electron energy of 25 and 23 GeV, respectively. In addition, two spontaneous undulators can be placed behind the SASE FEL undulators SASE 1 and SASE 4. Behind SASE 2 optional space for a future seeding scheme for 0.85 Å is kept and one further spontaneous undulator is placed thereafter.

Devices SASE 1 to SASE 4 and the spontaneous undulators will be built in planar technology providing radiation linearly polarized in the horizontal plane. They will cover the wavelength range from 0.085 to 0.4 nm. In this range circular polarization, needed for many experiments, can be most flexibly produced using X-ray optical methods. The technique of $\lambda/4$ wave plates (see also Chap. 5) is quite robust and much easier to implement than a helical undulator. It further allows higher flexibility, better control of polarization, and fast and precise switching of the polarization state [35]. For the long wavelength device SASE 5 the situation is different, as no quarter wave plates in this wavelength range exist. Circularly polarized light therefore has to be produced with a helical undulator. The APPLE design proposed by Sasaki [20] is planned for SASE 5. More details will be given in Sec. 4.3.3.4.B . SASE 5 needs a large period length and a correspondingly large K parameter in order to produce radiation at these long wavelengths.

The total length of the undulator systems is much higher than the bare saturation lengths. First, space has to be provided for intersections to accommodate quadrupoles, phase shifters, correctors, beam diagnostics, etc. (see next section). Second, a contingency reserve of undulator length is needed for field errors, alignment errors, etc. which all have a negative impact on the SASE process and increase the saturation length. The assumptions made for the calculation of the total system length are mentioned in the footnotes of Tab. 4.3.1. For the spontaneous undulators the gap limitations imposed by wakefields do not apply. Therefore, they are designed with a 6 mm gap.

4.3.2.5. Influence of undulator errors

The main requirements on the quality of the undulators are related to the increase of the saturation length caused by a poorer overlap between radiation field and electron beam. An additional restriction is that the resonance condition has to be maintained along the entire interaction length. The requirement on overlap can be translated into an upper limit on the second magnetic field integral [36, 37, 38].

$$I_{2,\mathrm{rms}}[\mathrm{T\,mm^2}] < 0.65\sigma_r E_b\,, \tag{4.3.3}$$

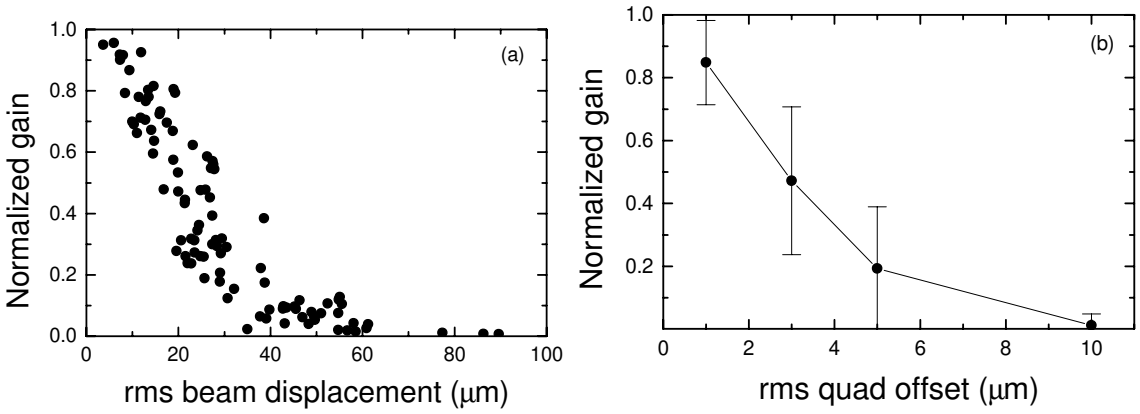

Figure 4.3.1.: *a. Gain reduction as a function of the rms orbit displacement caused by field errors in the undulator. b. Gain reduction due to different rms quadrupole offsets without orbit correction applied. For each data point 50 random samples of quadrupole offset distributions have been taken and their scatter determines the error bar.*

with σ_r the beam radius given in μm and E_b the beam energy in GeV. As an example for the TESLA X-ray FEL, Fig. 4.3.1.a shows the gain reduction for different undulator error distributions for a beam energy of 25 GeV. With a beam radius of $35\,\mu$m, this results in an upper limit of $I_{2,\mathrm{rms}} < 550\,\mathrm{T\,mm^2}$. Such an upper limit for the second field integral deviation can easily be guaranteed. The rms beam offset related to this field integral is

$$\Delta x_{\mathrm{rms}}[\mu\mathrm{m}] = 0.3\frac{I_{2,\mathrm{rms}}}{E_b}\,. \tag{4.3.4}$$

For the above values, this results in an rms-value of the beam orbit deviation of less than $7\,\mu$m. Both, undulator errors and quadrupole offsets contribute to this rms beam offset. Even with perfectly aligned quadrupoles, a small non-zero second field integral results in a kick by the quadrupoles that grows along the undulator. Therefore, the second field integral has to be as close as possible to zero at the end of each undulator segment. An analysis on the electron beam alignment is given in Part II, Sec. 9.8.3. With perfect undulator segments assumed, the kicks by the individual quadrupoles have been studied separately. Results are shown in Fig. 4.3.1.b.

As can be seen, the upper limit for quadrupole misalignment without application of error corrections would be about $1\,\mu$m. As this level of alignment is not feasible, a beam-based orbit correction procedure will be applied as described in Part II, Sec. 9.8.3. The calculations of field error influences are representative for all undulator systems and a more detailed study can be found in Ref. [38]. One concludes that the rms deviation of the second field integral is not a problem. It is more difficult to get the second field integral small enough at the end of each undulator segment and to correct quadrupole offsets. Both can be done by means of steerer coils, as described in Sec. 4.3.3.4.C and in Part II, Sec. 9.8.3.

4.3.3. Hardware setup

4.3.3.1. Introductory remark

The extent of the undulator systems has already become visible in Fig. 4.1.1 and Tab. 4.3.1. For the whole FEL laboratory, their total length is 1714 m. This huge length, with as much as 281 segments, calls for standardization and an economic design, that is optimized for the production of large quantities. Several aspects play a role in long undulator systems for SASE FELs. They have been discussed in Ref. [24]. The total length of an undulator system is much longer than the optimum β-function for largest FEL gain. External strong focussing is therefore needed to keep the β-function within limits acceptable for the FEL process. The undulator system may be separated into undulator segments and strong focussing quadrupoles.

On SASE 1, SASE 4, SASE 5 and the spontaneous undulators U 1 - U 5 the radiation wavelength will be tuned by changing the gaps. This increases the saturation length, requires tunable phase shifters and may induce gap dependent field errors. In this section a design proposal for a representative undulator system is made which deals with these aspects. Mechanical and magnetic design, vacuum system, control system, and requirements on temperature stability are treated in detail.

4.3.3.2. Cellular structure

The undulator system for an X-ray FEL is a long periodic array of undulator segments and intersections. It is therefore quite obvious to compose the undulator system out of individual and identical units which we call undulator cells. Each cell consists of one undulator segment and the components in the intersections such as a phase shifter, correctors, a quadrupole, and BPMs. For gap tunable devices gap dependent phase control is mandatory.

4.3.3.3. Standardization

Only four different types of magnet structures are needed. This situation resembles the requirements in small SR facilities. But the total magnetic length of SASE 1 plus SASE 4 is 530 m, that of SASE 2 plus SASE 3 is 480 m, that of SASE 5 is 145 m, and that of U 1 through U 5 is 250 m. For the design and construction, one should take advantage of the large numbers by using standardized components wherever it is possible. Items which will contain as many identical components as possible are:

1. The gap separation drive systems, motion control components, motors, servos
2. Girders
3. Components inside the undulator interruptions, such as phase shifters, corrector magnets and their power supplies, quadrupole magnets, and beam position monitors (BPMs)
4. Control systems for gap motion and gap dependent excitation of coils, readout of BPMs, etc.
5. Vacuum chambers and other vacuum equipment

Instead of optimizing the components for different undulators individually, they will be designed for the most demanding case. For example, mechanical gap separation drive systems and girders will be designed for maximum magnetic forces occurring at the most critical undulator and then adopted for all of them. Phase shifters should be designed to meet the phase shifting requirements at the longest wavelength. This standardization policy leads to most economical solutions in terms of production, prototyping, operation and maintenance.

4.3.3.4. Description of an undulator system

A. Segmentation, focusing

A periodic focusing of the electron beam is important for the FEL process. The choice of the focusing scheme has an impact on the undulator design and determines the length of the undulator segments. In a FODO lattice, consisting of a periodic arrangement of focusing and defocusing quadrupole magnets, the optical β-function (determining the size of the beam envelope) varies between a minimum and a maximum value given in thin lens approximation by:

$$\beta_{Max,Min} = \overline{\beta}(1 \pm \sin\frac{\mu}{2}) \; ; \; \overline{\beta} = \frac{\lambda_{FODO}}{\sin\mu} \; ; \; \sin\frac{\mu}{2} = \frac{\lambda_{FODO}}{4f} \; ; \; \frac{1}{f} = ceL_Q\frac{g_Q}{E} \qquad (4.3.5)$$

λ_{FODO} is the FODO period length as depicted in Fig. 4.3.2. f is the focal length of the quadrupole magnet, L_Q its magnetic length, g_Q its field gradient and μ is the betatron phase advance per FODO period. E is the kinetic energy of the electrons. For constant λ_{FODO} and $\mu < 90°$, the ratio β_{Max}/β_{Min}, i.e. the variation of the beam cross section decreases with increasing $\overline{\beta}$. If it is small enough, it has only a minor effect on the FEL process. For TESLA, optimum FEL performance calls for average β values above 14 m, so that a quadrupole distance can be chosen which allows a separated function design with quadrupole magnets every 6.1 m and 5 m long undulator segments in between. SASE 5 has the smallest $\overline{\beta}$ value of 15 m, corresponding to $\mu = 54°$, (see Tab. 4.3.1). For a quadrupole distance of 6.1 m, the ratio β_{Max}/β_{Min} is 2.68 (see below) and requires for L_Q = 0.2 m a gradient g_Q of 62 T/m which can easily be realized using quadrupoles with 15 mm bore. For $\overline{\beta}$ larger than 15 m, as required in most of the undulators, the quadrupole gradient will be smaller. Girders of 5 m length can be manufactured with sufficient accuracy and at reasonable cost. The choice

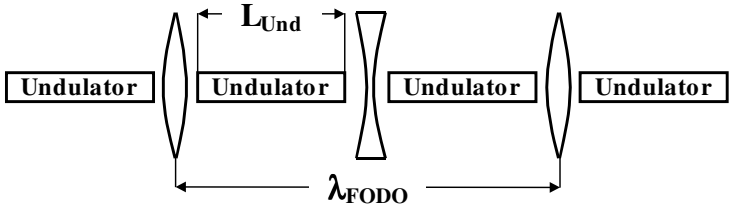

Figure 4.3.2.: *Schematic layout of a separated focusing undulator. The quadrupole separation of a FODO lattice is large enough so that an undulator segment of length L_{Und} can be installed.*

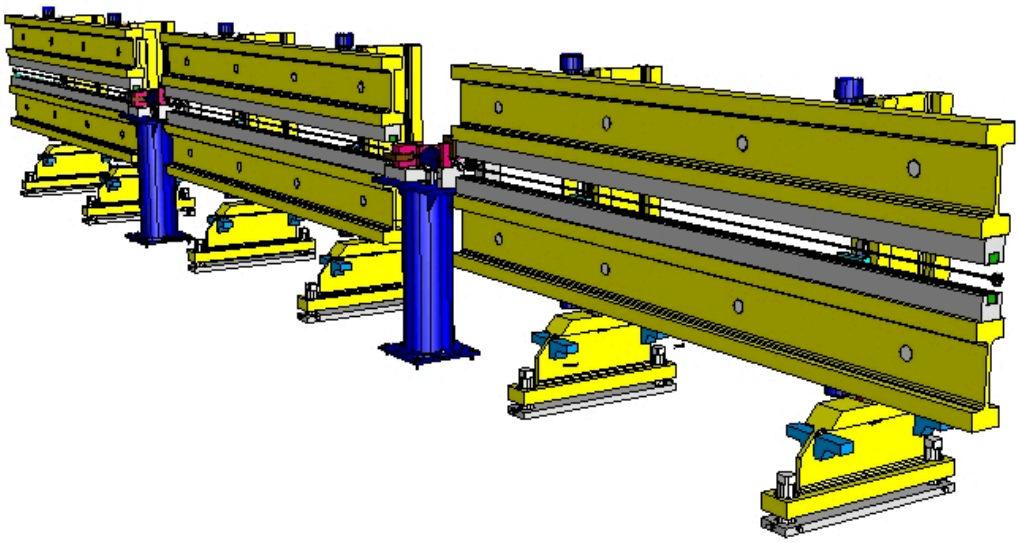

Figure 4.3.3.: *3D view of three cells of the undulator system showing the 5 m long undulator segments and 1.1 m long intersections for phase shifters, beam correctors, quadrupoles, BPMs, vacuum pumps, etc.*

of 5 m segment length is also reasonable in terms of manufacturing and girder deformation caused by magnetic forces, which is proportional to the fourth power of the overall length, (see Sec.4.3.3.4.B below). Figure 4.3.3 illustrates the segmentation principle in a 3D view.

B. Undulator segment

Mechanics A standard gap separation drive and support system has been developed in a conceptual design study [42]. It considers the principles of economic manufacturing of large quantities while tough requirements on mechanical accuracy have to be maintained. Figure 4.3.4 shows in a 3D view how these ideas can be realized. The length of a segment is 5.0 m. For the girders, an I-beam profile with dimensions $550 \times 200 \times 100$ mm^3 is used. They are supported on four points rather than two to reduce deformation due to magnetic loads. In order to keep girders under changing load conditions (gap change) flat within ± 4 μm this large girder profile, with a correspondingly large moment of inertia and a four-point support, is needed. The same profile is also used for the vertical support column and consequently avoids a welded box type structure. From the point of stability and deformation, there is no penalty as compared to a box structure. Large profiles like these cannot be ordered off the shelf. For sufficiently large quantity, they have to be produced on special request by a steel mill. This is unproblematic, since more than 4700 m with a total weight of about 2000 tons of this profile will be needed for the TESLA support systems. Their use becomes economic since it avoids welding, and only minimal machining is required on the columns.

Standard guiding elements, which can be ordered off the shelf are used for precise gap motion. There are four individual motors which are appropriately synchronized by a control

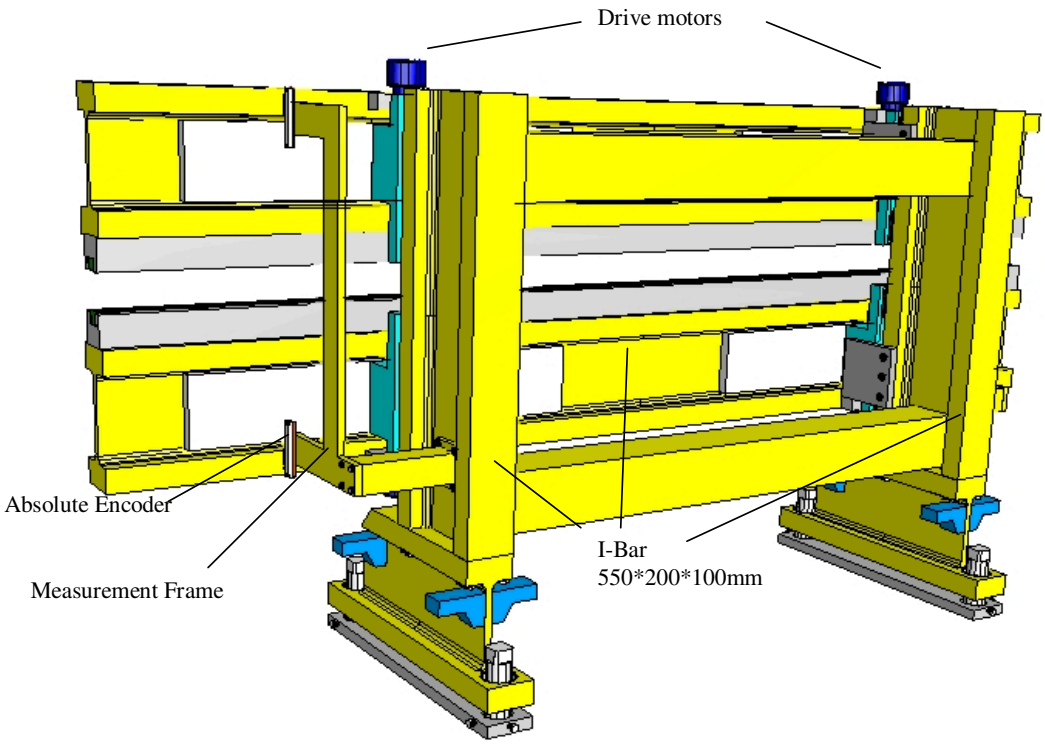

Figure 4.3.4.: *3-D View of a standard undulator segment.*

unit. Motors and their motion control units are part of the control system (see Sec. 4.3.3.4.E below). In order to get accurate gap information with micrometer accuracy separate frames are used to support absolute length encoders. In this way, the exact girder position close to the motor can be measured without errors induced by deformation of the girder support or the support structure. Gap adjustment accuracy is better than $\pm 2\,\mu$m. For more information see [42].

Linear magnetic structure A magnet design based on NdFeB PM hybrid technology has been developed for a prototype structure for the SASE 1 undulator [43]. Its parameters are those of SASE 1/SASE 4 given in Tab. 4.3.1. The period length is 60 mm. The width of poles and magnets was determined such that a transversal good-field region of ± 1 mm results in which the relative field variation is less than the ρ parameter, i.e. $4 \cdot 10^{-4}$ in the open gap position. This is the most restrictive case. In this way horizontal alignment requirements on the undulator segments are reduced, and the FEL process is not affected by poor field homogeneity. Thus the proportions of magnets and poles have been optimized in terms of a sufficiently wide good-field-region and, simultaneously, the required magnet volume has been minimized. Figure 4.3.5.a illustrates the dependence of the peak field on the ratio of magnet to pole length. A maximum value $B_{Max} = 1.33$ T at 12 mm gap is obtained for a pole length of about 8 mm. The iterative optimization results in a pole geometry of $40 \times 8 \times 55$ mm^3 (width $\times$ length $\times$ height) and $70 \times 22 \times 65$ mm^3 for magnets. This corresponds to a magnet volume of 400 cm^3 per period or a demand for 13.3 tons magnet material for the 53 segments for SASE 1.

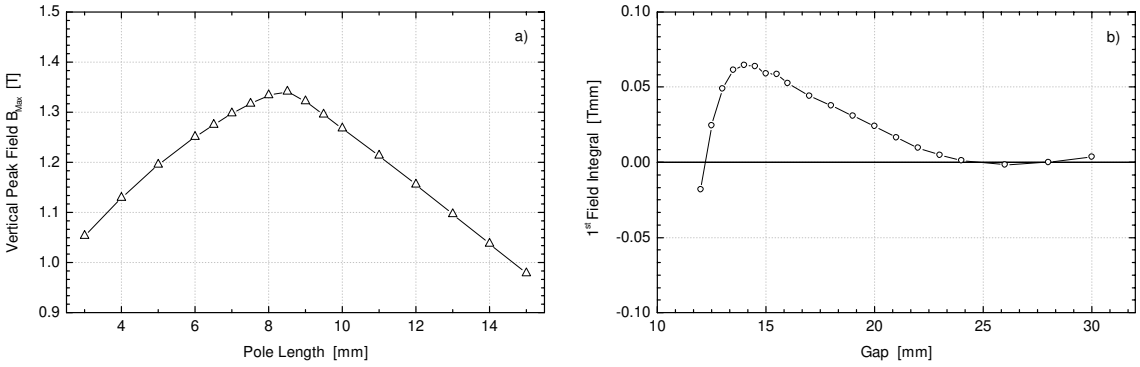

Figure 4.3.5.: *a. Peak field as a function of pole length at constant period length. b. Gap dependence of the first field integral.*

The end pole configuration of multi-segmented devices is a critical issue in the magnet design. Residual field integrals should be compensated for all gaps, preferring passive elements. The field of the undulator segment is symmetric with respect to the center plane so that the second field integral is cancelled once the first field integral is tuned to zero. There is a wide range of possibilities for reducing and trimming the field integral gap independently by means of choosing proper dimensions for the last poles and magnets [26]. In this study the length and vertical position of the last magnet, the height of the last pole, and the width of the second last pole are used to tune the first field integral. The gap residual dependence of the first field integral has been calculated and is depicted in Fig. 4.3.5.b. The exponential increase of the peak field B_{Max} with decreasing gap (Eq. 4.3.1) complicates the field integral adjustment in the small gap range. A maximum residual field integral of 0.05 T mm is induced at 13 mm gap while for short photon wave length, i.e. large gaps, a value < 0.005 Tmm is achieved. The remaining gap dependence can be compensated by means of shims which so far have not been included in the calculation. Also, more sophisticated solutions in the end pole optimization including a modification of the pole shape may be elaborated. There are horizontal and vertical correctors, which are needed to correct quadrupole alignment errors (see Part II, Sec. 9.8.3) which also represent an active way to tune the field integral by changing the excitation of the correctors as a function of the gap.

Planar helical magnetic structure For SASE 5 a helical structure is planned. The following criteria have to be fulfilled:

1. The structure should allow lateral access for high precision magnetic characterization and the insertion of vacuum systems.

2. Peak field and polarization properties should be adjustable.

A helical structure following Sasaki's APPLE design is proposed [20]. This type of magnet structure offers the highest fields and greatest variation of polarization characteristics found in literature. As seen from Figure 4.3.6, it is based on a pure PM structure that is sliced along the electron beam axis in four parts: Upper Front/Back and Lower Front/Back. The

Upper Back and Lower Front are kept fixed. The Upper Front and Lower Back can be moved independently along the beam axis by an amount D, that is limited to $\pm\lambda_0/4$. If D=0 the

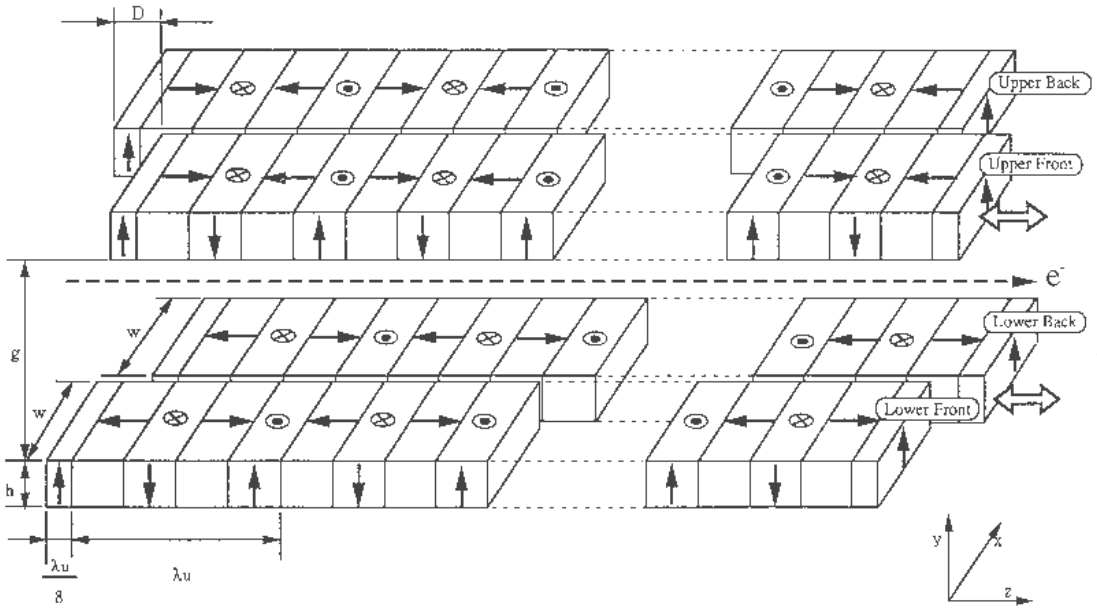

Figure 4.3.6.: *Magnet design principle of a Sasaki's APPLE undulator. It is a planar helical structure with adjustable polarization properties.*

structure is a equivalent to a standard pure PM structure producing light linearly polarized in the horizontal plane. If D=$\pm\lambda_0/4$ and Upper Front and Lower Back are moved in the same direction, right/left handed circularly polarized light is produced. In between there is elliptical polarization. If Upper Front and Lower Back are moved in opposite directions, linearly polarized light with an inclined plane of polarization is produced. Two additional independent drive systems are required to shift the Upper Front and Lower Back girder. Typically it takes several seconds to go from right to left polarization. At BESSY-II, several of these devices, up to 3.2 m long, are in operation or under construction. A comprehensive experimental study of their magnetic as well as emission properties has been made by Bahrdt et al. [44].

A design study for a Sasaki-type undulator for SASE 5 has been made by Bahrdt et al. [45]. A Sasaki-type undulator with adjustable properties requires considerably more mechanical effort than a planar one. The SASE 5 undulator system has a total length of 177 m. While changing polarization properties, one half of the upper and lower magnet structure

needs to be shifted along the entire length and has to be equipped with suitable drive systems. There are no soft iron parts in this device. Thus its magnetic field quality depends completely on the quality of the PM material. Great care is needed in the characterization and selection of the magnets. Also iron parts for the support beams have to be avoided. The experience at BESSY II shows nevertheless that such a device can be built and operated with high perfection.

C. Gap tunability, phase matching, beam correctors

For three of the SASE, as well as for the spontaneous devices gap tuning is required. This has three consequences:

1. Since the longest SASE saturation length is expected at the shortest wavelength at which the FEL is to operate, the required undulator length is determined by the comparatively weak magnetic field at the upper gap position. Thus the undulator must be longer than needed for a fixed (i.e. 12 mm) gap device optimized for short wavelength.

2. The matching of the phase of the photon beam originating from different undulator segments becomes gap dependent. This is likewise true for the SASE and spontaneous devices. For segmented fixed gap undulators such as the ones at the TTF (DESY) or at LEUTL (APS) the phasing is most easily done by properly choosing the distance between individual undulator segments so that the radiation emitted by both segments interferes constructively on axis. If the undulator gap, and therefore the radiation wavelength is changed, the interference condition is changed too. Changing the inter-segment distances is not possible in a undulator system with a large number of segments. Instead the electron beam has to be slightly delayed as compared to the photon beam. This is done by a suitably designed magnetic chicane called a phase shifter. A prototype phase shifter for the SASE 5 undulator system, which is the most demanding one, is described in [46]. It may also be used for the other undulator systems. It uses electromagnets at an excitation level which is low enough so that water cooling is not needed. Its tuning range is large enough, so that SASE 5 can be operated over the full range from 0.4 to 2.5 nm at 23 GeV. Figure 4.3.7 shows the phase shifter magnets embedded in the other components needed inside the intersection described below.

3. The third consequence relates to field errors. In a tunable undulator, field integral errors, which might be fully compensated at one specific gap can still have some effect at different gap values. Especially in hybrid structures this effect could occur (see Fig. 4.3.5b for illustration). These residual errors are expected to be below 0.05 T mm. To compensate for this effect horizontal and vertical correctors are planned, which can be excited with gap dependent current settings. For horizontal correction one of the chicane magnets can be used simultaneously. The same type of magnet, rotated by 90° is used to steer the beam vertically. The corrector magnets also provide correction for quadrupole misalignment which are independent of the gap (see Sec. 4.3.3.4.D below).

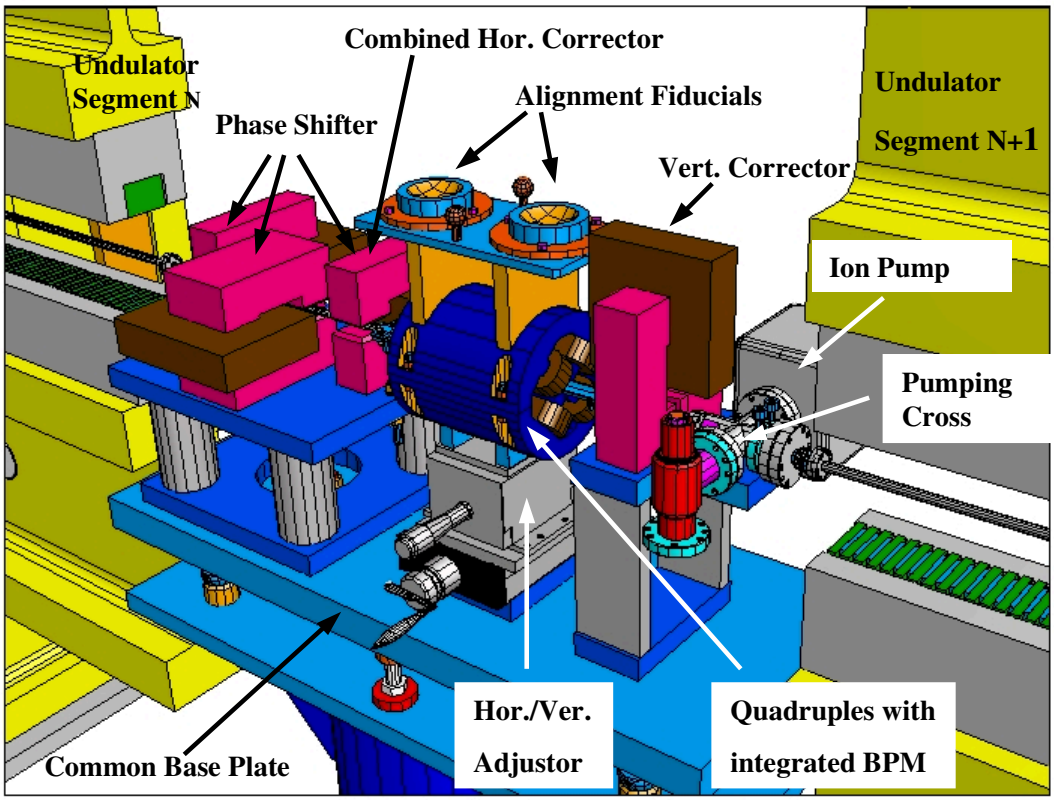

Figure 4.3.7.: *3D view of an undulator intersection.*

Figure 4.3.7 shows a 3D view of an undulator intersection embedded between two neighboring undulator segments. The phase shifter is seen at the left. It consists of three horizontal magnets. The length of the center one is doubled because it needs twice the strength. The vertical corrector is seen at the right. In between, there is a quadrupole with a 15 mm bore, which is capable of producing a maximum gradient of 100 T/m. Its magnetic length is only 0.2 m. With such quadrupoles, an average β-function of 12 m at 25 GeV can be generated, which is even smaller than what is needed for SASE 5 (see Tab. 4.3.1) and thus gives sufficient room for later empirical optimization. The total length of an intersection is 1.1 m. SASE 1, SASE 4, SASE 5, and the spontaneous devices are gap tunable. In contrast, SASE 2 and SASE 3 are operated at the minimum gap only. However their gaps should be made adjustable too for the following reasons:

1. The radiation wavelengths of different segments have to be tuned with an accuracy better than the ρ parameter, which is in the order of 4×10^{-4}. In order to adjust peak fields of different segments with this accuracy, the required gap control accuracy consistent with this requirement is $\Delta g \leq \pm 2\mu$m [42]. This accuracy cannot be preserved in a truly fixed gap device. Although the field might be precisely adjusted in the lab it is hard to preserve this level of accuracy. So some possibilities for fine adjustment have to be provided.

2. In order to compensate for the average energy loss of the electron beam by synchrotron

radiation and wakefields induced in the vacuum chamber (see Sec. 4.2.1.1) a taper has to be applied. It increases FEL efficiency and maximizes the output intensity. Such a taper could be implemented as a step taper from one segment to the next. Gap adjustable devices would allow very fine control over the amount of taper. Suitable modes of operation are planned. (see also Sec.4.3.3.4.E)

3. By opening the gap of a segment, one can effectively switch it off. So the effective length of the undulator system can be varied. For diagnostic reasons this option might become very important. A photon beam based alignment procedure is outlined in Sec. 5.1 and Part II, Sec. 9.8.3. Starting at the entrance the spontaneous radiation emitted by each segment, one by one, is detected in a diagnostic station in the photon beam line. The electron beam may be steered such that all the radiation spots overlap completely. In this way the beam may be threaded through the undulator system. The proper phasing can also be checked and updated using this method.

4. Experience at TTF has shown that high radiation levels may be created if the beam is missteered. Although this must not occur during routine operation it nevertheless might happen during machine setup or commissioning. The maximum gap to which the TESLA undulators can be opened is 200 mm, reducing the radiation hazard considerably. See also the discussion in Sec. 4.3.2.3.

D. Alignment

The great advantage of separating undulator and focusing in the TESLA undulator systems is that only moderate requirements on the alignment of the undulator segments have to be fulfilled. The fields and the field integrals of individual segments are well tuned and adjusted, they behave almost like drift spaces for the 13-50 GeV electron beam. For obtaining good overlap between electron and photon beam the quadrupoles play the dominant role. They need very stable supports. With no further means of correction, their centers would need to be adjusted with an accuracy of about 1 μm in both directions over the full length of an undulator system [38] (see also Sec. 4.3.2.5), which is way beyond the capability of even the most sophisticated alignment techniques. There is also no way to measure and align the magnetic centers of the quadrupoles with this accuracy. Instead, the method of beam based alignment (BBA) has to be used. Two steps are needed: There will be a coarse alignment to about ± 0.3 mm using conventional optical alignment techniques. Fine alignment is done using BBA in conjunction with the horizontal and vertical corrector magnets in the intersections [47]-[49]. Their strength is sufficient to compensate for a quadrupole misalignment of about ± 0.4 mm. To correct this error in a 0.2 m long quadrupole with a gradient of 100 T/m a corrector field integral of ± 8 Tmm is required. This is well within the capacity of the magnets used for the phase shifters. See also Part II, Sec. 9.8.3 for more details on BBA. The tolerance on uncorrected misalignment determines, however, the time scale at which the orbit correction has to be repeated due to mechanical motion of the quadrupole supports. A rough estimate of this time, based on orbit measurements at HERA (see Part II, Sec. 3.2.3.3 in for details), results in a few hours.

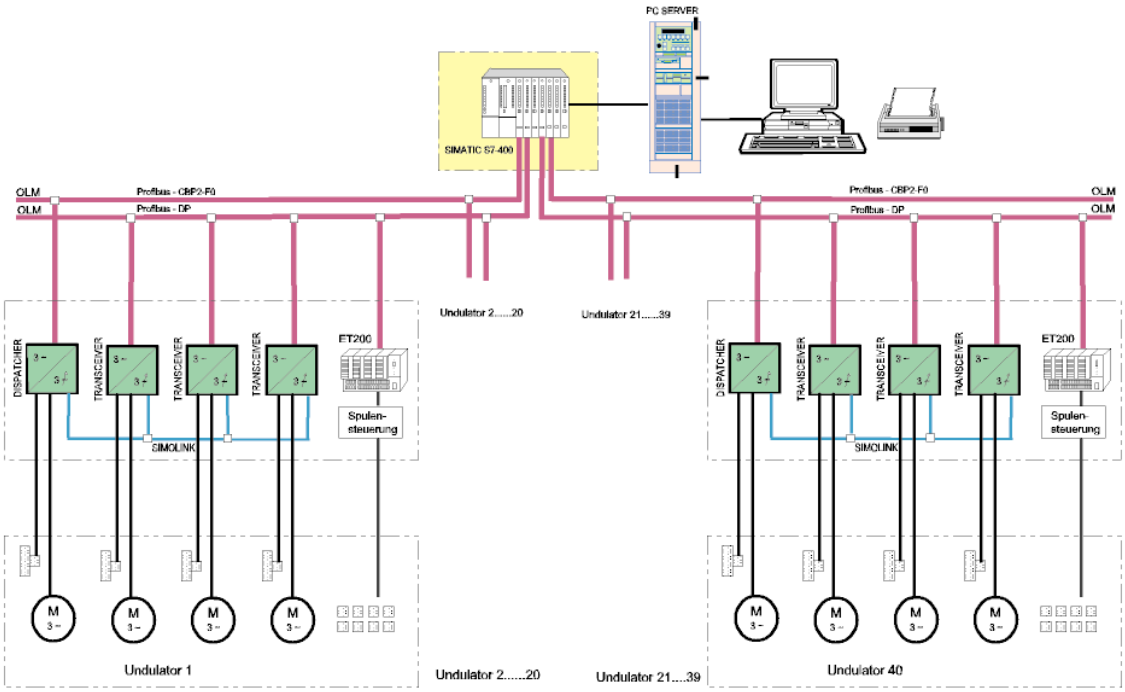

Figure 4.3.8.: *Control concept of an undulator system based on SIMATIC components.*

E. Control system

Each undulator system needs its own control system. It has to fulfill the following tasks:

- synchronize the motors of the whole system for gap motion,
- provide gap dependent corrector current settings,
- provide great flexibility to allow for numerous special operation modes.

The control system is most effectively organized in a cellular way in an analogous fashion to the mechanical setup (see Fig. 4.3.8). For the control system, each cell consists of the four drive motors for the gap separation drive and related components, such as encoders, switches etc. which are needed for an undulator segment. The corrector coils of that segment which in general need current settings depending on the actual gap value of that segment also belong to that cell. Each cell is an individual unit, and an undulator system is a periodic array of up to 64 of these cells.

A study for the realization of such a control system using industrial SIMATIC components has been made [50]. Its layout is shown in detail in Fig. 4.3.8. In each cell there are four servo motors and their control units that use the absolute length encoders as feedback. They are connected using a cell internal synchronization bus called SIMOLINK. There is an ET 200 programmable logic controller (PLC) in each cell, which generates the gap dependent current setting for the power supplies. Three power supplies are assumed per cell: one for

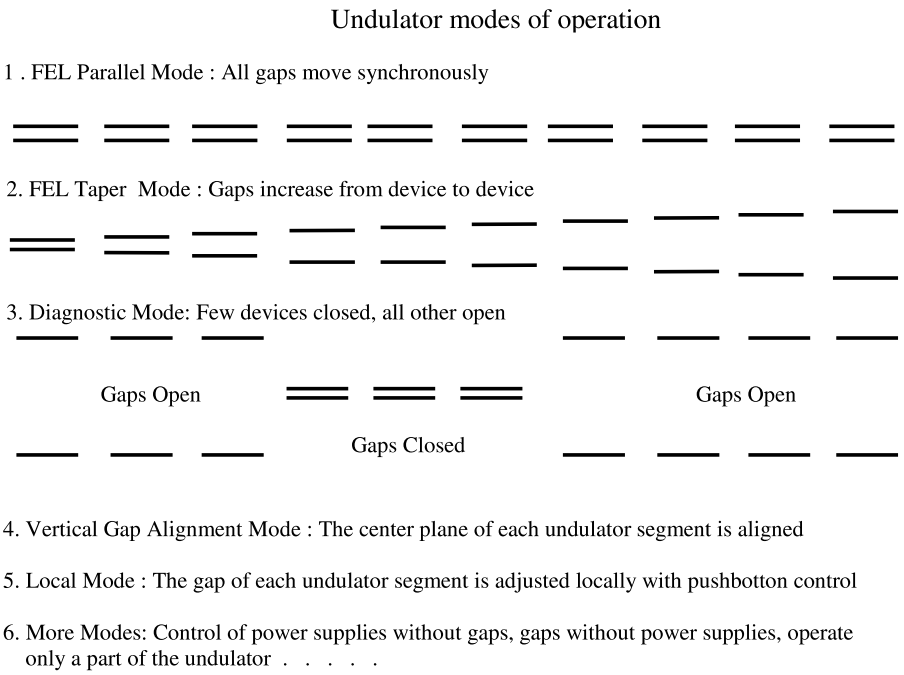

Figure 4.3.9.: *Different operational modes which can be realized with the undulator control system.*

the phase shifter, one for the horizontal and one for the vertical corrector. The motion controllers guarantee a highly synchronous gap movement within one cell. A SIMATIC S7-400 unit is used as a master controller for the cells of an undulator system. It may be accessed by external computer systems via suitable interfaces or alternatively through a dedicated control station as shown in Fig. 4.3.8. The PLCs provide properly synchronized current settings.

In order to avoid hardware limitations there are 2 separate pairs of Profibus-DP / Profibus CBP2 systems. Each one can address up to 32 cells. In this way, the maximum number of cells is 64. The Profibus DPs, with a transmission rate of 1.5 Mbit/s, is used for standard communication such as transmission of set values, error status etc. The Profibus CBP2 is a very fast bus with a transmission rate of 12 Mbit/s. It provides real time synchronization between the cells. In this way synchronous movement of all motors of an undulator systems is possible. The explicit intention of the conceptual design study in Ref. [50] is to have a system, that allows for easy and modular extension of cells and that avoids constraints thus allowing for great flexibility for future use. Some potential modes of operation are explained in Fig.4.3.9. They also include the diagnostic mode mentioned at the end of Sec. 4.3.3.4.C.

F. Undulator vacuum

Several features determine the layout of the undulator vacuum system:

- the minimum gap size of the undulator,
- the material of the vacuum chamber,
- wakefield effects,
- the required average pressure, and
- the operational needs.

The vacuum system has the same segmented periodic structure as the undulators system. Here we discuss the vacuum system for one undulator segment, representative for the others.

Layout of the undulator vacuum system There will be different gaps for the FEL and the spontaneous undulators: The five XFEL structures will use a minimum gap of 12 mm. For the five spontaneous undulators, the gap will be as low as 6 mm. The reason for this different choice is the presence of resistive wall and surface roughness wakefield effects, as has been described in Sec. 4.2.1.1 and Part II, Sec. 9.7. They limit FEL performance, but do not play a role for the spontaneous undulators. The vertical vacuum aperture is limited to about 10 and 4.5 mm, respectively. A distributed pumping geometry has to be adapted to the undulator geometry. There will be no pumping inside the undulator segments. Pumps are localized inside the 1.1 m long intersections between two undulator segments only. For the FEL's, the pumping cross section has to be designed to minimize wakefield effects. In Fig. 4.3.7 the arrangement of the ion pump in the intersection is shown. Figure 4.3.10 shows the pumping cross. For pumping the beam pipe is perforated with 1 mm wide slots, which extend along the beam direction. A 20 l/s noble diode ion pump, which is not shown in Fig. 4.3.10 is connected to the CF63 flange. At one side the pumping cross is designed as a fixed point for the undulator vacuum tube. The other side is connected via flexible RF shielded bellows. The bellows allow for a thermal expansion of the tube in the order of a few millimeters.

For the FEL's, the inner diameter of the beam pipe is 10 mm. For the spontaneous devices it is 4.5 mm. The resulting wall thickness is 0.5 and 0.25 mm, respectively. The pressure distribution $P(x)$ along the beam pipe can be calculated analytically using the formula given in Ref. [51]:

$$P(x) = au\left(\frac{2L}{S} + \frac{x}{C} - \frac{x^2}{2CL}\right) \tag{4.3.6}$$

Here L is the length of a vacuum segment (in cm), u is the perimeter (in cm), a the specific desorption rate (in mbar l/(s cm^2)), S the pumping speed (in l/s) and C the conductance of the whole beam pipe (in l/s). The equation assumes a constant gas load along the beam pipe. The conductance C for a 2.5 m long segment with an inner diameter of 10 mm is 0.048 l/s. By integration of Eq. 4.3.6, the average pressure P$_{ave}$ can be calculated:

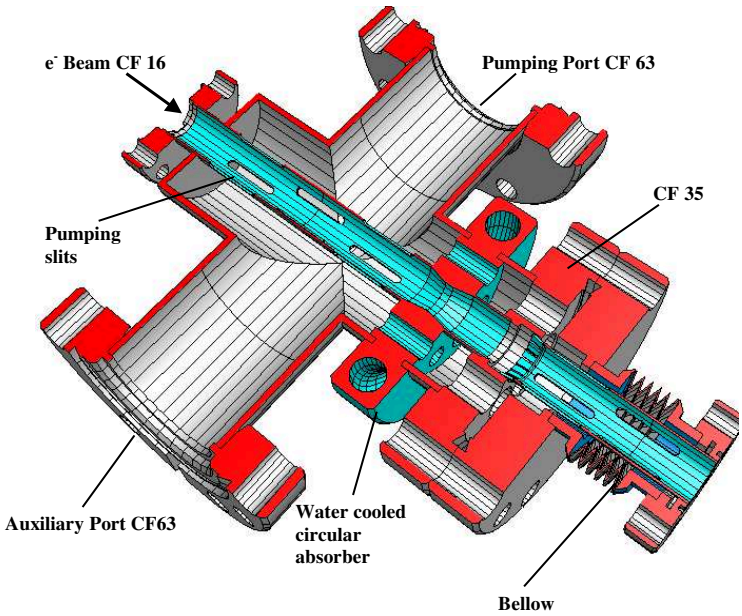

Figure 4.3.10.: *3D cross section of the pumping cross showing the beam pipe with RF pumping slots and water cooled circular synchrotron radiation absorber.*

$$P_{ave} = \frac{auL}{C}\left(\frac{2C}{S} + \frac{1}{3}\right) \tag{4.3.7}$$

P_{ave} inside the beam pipe becomes practically independent of the pumping speed for $C \ll S/6$. Assuming again an inner diameter of 10 mm, a pumping speed higher than 1 l/s will not significantly reduce the average pressure, which is mainly defined by the gas load and the conductance of the beam pipe. The conductance is defined by the diameter, which in turn is determined by the gap size. To reach low average pressure, the gas desorption has to be minimized. The gas load of the undulator vacuum system originates from thermal and photo desorption. The spontaneous undulator radiation hits only the water cooled circular absorber (see Fig. 4.3.10). This increases the gas load locally through photo desorption and necessitates additional pumping. Figure 4.3.11 shows a plot of the average pressure as function of the beam pipe diameter for two different pumping speeds. For the calculation a thermal desorption rate of 2×10^{-11} mbar l/(s cm^2) and pumping speeds of 1 l/s and 0.1 l/s are assumed. For the 10 mm tube the resulting average pressure is $P_{ave} \cong 5 \times 10^{-7}$ mbar. For UHV processed copper coated stainless steel as used for the PEP-II project, thermal desorption rates are reported which are two orders of magnitude lower [52]. With these tubings an average pressure in the 10^{-9} mbar range could be achieved.

The FEL radiation is assumed not to hit a vacuum chamber wall and therefore does not contribute to photo desorption. This is not true for the spontaneous part of the undulator radiation. For a worst case estimate, we chose the SASE 1 undulator at the minimum gap of 12 mm. With a magnetic field of 1.33 T and an average current of 57 μA, an average radiation power of 8.3 kW with an opening angle of 0.22 mrad FWHM is emitted. At closed gap, the

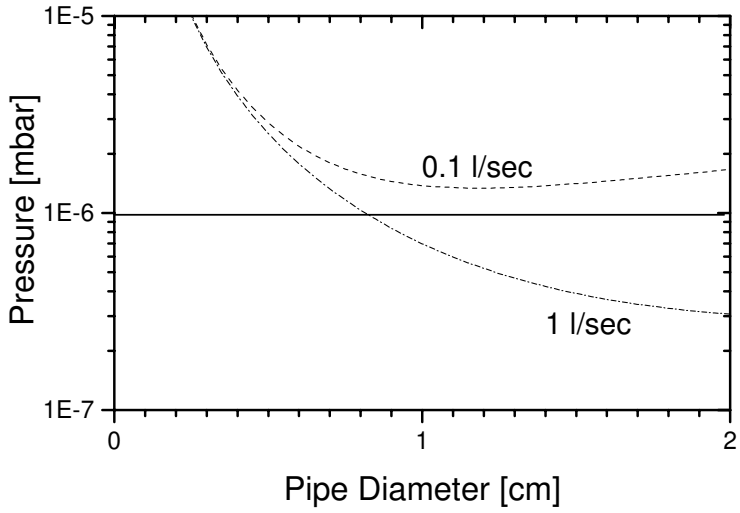

Figure 4.3.11.: *The average pressure as function of the tube diameter for different pumping speeds.*

saturation length of SASE 1 is about 170 m. The angle defined by this length and the vacuum chamber aperture is 0.055 mrad. About 75% of the radiation will hit the internal absorber and contribute to the pressure by photo desorption. Using the critical energy of the device (796 keV) we get an average photon number of $\approx 1.7 \times 10^{15}$ photons/s on one single internal absorber. By using the molecular desorption yield of 5×10^{-3} molecules/photon given in Ref. [53], one gets a photo desorption rate of 3.2×10^{-7} mbar l/s. This is about ten times the assumed gas load by thermal desorption of the vacuum chamber. The gas load created locally by photo desorption at the water cooled aperture is pumped directly through the slots (see Fig. 4.3.10). These allow for an effective pumping speed of 8 l/s for air at the aperture. The resulting pressure will be 4×10^{-8} mbar. Thus the average pressure is not affected. This estimate is valid for the 12 mm gap size only. For the narrow gap spontaneous emission devices we propose to use chambers with a horizontally larger aperture and a longitudinal slit for continuous pumping according to the chamber developments at the Advanced Photon Source [54].

Radiation background due to bremsstrahlung Bremsstrahlung, i.e. hard X-rays with energies which can be as high as the electron beam energy, are produced if electrons collide with residual gas molecules. The average pressure in the undulator vacuum system defines the amount of background radiation at the experimental stations. It is closely collimated around the direction of the electron beam. Simulations on this subject have been published [55]. An estimate of the expected dose for an XFEL beamline can be scaled to experience made at DORIS, where 30 cm of lead at the position of the beam stop is used. An equivalent shielding for the XFEL can be determined. The dose H due to Bremsstrahlung is related to geometry of a beamline by an empirical formula [56] :

$$H = I \frac{s}{x_0} \frac{P}{P_0} \frac{1}{C_R F} \tag{4.3.8}$$

with beam current I, conversion factor C_R, length of the straight section s, area irradiated by Bremsstrahlung F, scattering length in air x_0 at pressure P_0 and pressure in the straight section P. The following formula gives the pressure relation for Bremsstrahlung doses at DORIS and TESLA beamlines :

$$\frac{P_{TESLA}}{P_{DORIS}} = \frac{I_{DORIS}}{I_{TESLA}} \frac{s_{DORIS}}{s_{TESLA}} \frac{C_{50GeV}}{C_{5GeV}} \frac{F_{50GeV}}{F_{5GeV}} \tag{4.3.9}$$

Comparing TESLA with DORIS one has to consider the following facts:

- The energy is 10 times higher,
- the average beam current is 3000 times smaller,
- the straight sections are 30 times longer,
- C_R is smaller by a factor 2, though to be on the safe side it is taken as unity, and
- the irradiated area is about the same: At the XFEL the opening angle, proportional to $1/\gamma$, is 10 times smaller, but the beam lines are at least 10 times longer, so that the irradiated area stays about constant.

In order to have approximately the same Bremsstrahlung background, the pressure ratio $P_{TESLA}/P_{DORIS} \simeq 100$ has to be fulfilled. For DORIS, a typical operational pressure is 5×10^{-9} mbar so that for the TESLA XFEL an average pressure of 5×10^{-7} mbar is needed. This average pressure can be reached as has been shown above.

Chamber material Surface roughness and surface conductivity of the undulator vacuum chamber have a large impact on beam quality, as they give rise to resistive and surface roughness wakefield effects. This has been treated in Part II, Sec. 9.7 and 4.3.2.1 of this section. These effects can deteriorate FEL performance by inducing a coherent energy spread along the electron bunch. For the spontaneous undulators, this effect needs not be considered. In order to keep the resistive wall wakefield effects small, the surface of the vacuum chamber has to be made from highly conductive material i.e. copper or aluminum, which are comparable in terms of wakefield effects. Therefore only chambers with an aluminum or copper surface will be further discussed. Surface roughness wakefields require smooth surfaces. Extruded tubes from aluminum, copper or stainless steel are available with good surface quality ($R_a \sim 200$ nm (rms)). Developments for the semiconductor industry, which has a strong interest in ultra-pure gas systems, have lead to seamless stainless steel tubings (e. g. Type 1.4429 (316-L)) with very clean and smooth inner surfaces. These tubes are extruded, cleaned and then electro-polished to R_a values in the 100 nm (rms) range. Such tubes have to be coated with a thin layer of copper. Some R&D effort has to be invested to find the best surface treatment which fulfills roughness and vacuum requirements. The surface roughness issue becomes more critical for SASE FEL undulators with narrow gaps. There are also practical reasons to choose stainless steel: Aluminum has the disadvantage of an oxide surface layer which makes a surface treatment very difficult. Also the common available flange systems use stainless steel. If aluminum or copper is used for the chamber, special transition

pieces between tube and flanges have to be designed. Copper coated stainless steel tubes are very suitable for vacuum processing without loosing the mechanical properties. They achieve the lowest thermal desorption rates.

Beam position monitors Beam position monitors are mandatory to align the electron beam to the axis of the undulators. There is a variety of monitors in operation in the FEL undulators at the TTF. The different beam-focussing scheme and the variable-gap undulators for the XFEL will allow stripline monitors [57] for a precise beam position measurement. These monitors can easily be integrated in the quadrupole vacuum chamber installed between the undulators. See Fig. 4.3.7 for details. Every quadrupole will get a monitor in its center. These monitors will allow the application of beam based alignment techniques (see Sec. 4.3.3.4.D for details). At additional places wire scanners, successfully used at TTF [34], will be installed for beam position and beam profile measurements. Special photon diagnostic stations (compare section 5.1) in the photon beamline will be used for beam diagnostic and undulator alignment. The installation of electron beam optics between the undulators requires a very stable and carefully designed foundation for quadrupoles and integrated beam diagnostics. Alignment precision and stability of all components in the μm range are mandatory. This has been taken care for in the floor stand, the adjustable base plate and the adjustments for the quadrupoles shown in Fig. 4.3.7.

G. Temperature control

Permanent magnet material has a reversible temperature coefficient. For NdFeB it is $-0.1\%/^\circ$ C. For SmCo it is by a factor of three smaller. This means, that the field of a NdFeB structure is increased by 0.1% if the temperature is lowered by 1° C. This has consequences for the temperature control of the undulator system. The FEL band width is of the order of the ρ parameter. In order to preserve this condition, the peak field of an undulator segments B_i must not deviate from the average by more than:

$$\frac{|\overline{B} - B_i|}{\overline{B}} = \eta \cdot \Delta T \leq \rho \tag{4.3.10}$$

where $\eta = 10^{-3}/^\circ$ C is the reversible temperature coefficient for NdFeB. For $\rho = 4 \cdot 10^{-4}$, one obtains a maximum allowed temperature deviation for adjacent undulator segments of: $\Delta T \leq 0.4^\circ$ C. This defines the specification of the air conditioning which has to be fulfilled over the whole length of the system.

4.3.4. Industrial manufacturing

4.3.4.1. Problem description, experience and analysis of present manufacturing

The underlying problem and challenge with the undulator systems for the TESLA FELs is the production of the large number of segments at sufficient quality in reasonable time and at reasonable cost. This requests a close collaboration with industry which will be of paramount

importance. For many synchrotron radiation laboratories large parts or even complete undulators have already been built by industry. At HASYLAB, encouraging experience exists for the undulators for DORIS III, PETRA and the FEL at the TESLA Test Facility. A typical situation found in SR laboratories is that usually only a small number (<10) of devices is needed at a time. Often it is only one and rarely more than two of them that are identical so that there was no need to streamline the design. Typically, the mechanical part, the manufacturing of the gap support, drive systems, and girders is commissioned out to mechanical workshops with appropriate machining capacities. In some laboratories, such as DESY or the ESRF, good experience has been had in having the magnetic structures manufactured at companies such as UGIMAC, VACUUMSCHMELZE or WIDIA. These companies are manufacturers of PM material, but they also produce "magnetic systems". Such systems are, for example, magnetic separators, torque clutches, special rotors for direct drive motors, synchronous motors or multipole magnet systems. Complete magnetic structures for wigglers and undulators have been built this way as well. The companies take care of producing the magnets, pole pieces and non-magnetic holder parts, as well as mounting tools if needed, and do the magnetic assembly of the magnetic structures on the girders. In the case of wigglers, magnetic measurements and subsequent magnetic shimming or fine tuning have been done so far at the SR laboratories themselves. There were at least two reasons to do so: First, expensive equipment and highly experienced staff is required for this purpose. Second, the performance of the devices depends critically on these measurements. It is more reliable to have them done in house. Also, final assembly, electric and motion control engineering and all the many things which have to be done to get a device ready for installation are done at the laboratory. A large fraction of the work is thus still done by the SR facility. For the large number of devices needed for TESLA a 'Turn Key Ready' concept is proposed in order to avoid the setup of production facilities and a large staff at TESLA, both of which needed only during the construction phase. This implies a much deeper involvement of industry than has been the case so far. In this paragraph, the impact of this concept on the logistics of the whole project is investigated.

4.3.4.2. Research and development program

Presently, insertion devices are built in the way described above using state of the art magnet material available on the market. There are a number of problems to be solved before the production of the large amounts of segments could be started. Many of them have a straightforward solution, which in principle does not differ if one or 100 or more items have to be built. For example, mechanic, electric/electronic or magnetic design, prototyping etc. However, the magnetic structures are the most expensive and delicate items. Their production technique deserves the most attention and offers a big potential for optimization. An analysis of the production process has shown that these are two major points where a resolute R&D effort is needed, which may have a large economical impact [58]:

1. All insertion device activities using permanent magnets so far content themselves with magnet material qualities, which are readily available on the market and do not vary too much from manufacturer to manufacturer. The quality requirements so far are dictated by the predominant use of the magnet material in industry, for example, all

kind of electro-motors, voice coil motors (VCM) positioning systems for hard disk drives and linear motors. The sales quantities for these purposes are many times larger than those for insertion devices. For the TESLA undulator systems about 100 tons of permanent magnet material are required. This quantity should be large enough for a demand for new quality standards. The goal should be to improve present quality standards by at least a factor of 10. An analysis of the production process shows that this is feasible.

Real permanent magnet material is inhomogeneous. A measure is the so called North-South effect, i.e. the difference in field level on geometrically equivalent positions, which may amount to several percent. Its magnetization deviates from its nominal magnitude by $\pm(1-2)$ % and its orientation by $\pm(1-2^{\circ})$ from its nominal direction. These are typical values for commercially available high quality material used for IDs today. The consequence of these imperfections for manufacturing of insertion devices so far was that extensive single block handling was needed: The magnetic moment, its deviation from the nominal direction and its North-South effect has to be measured and recorded for each single block. The data are then used for sophisticated sorting procedures such as simulated annealing [59, 60]. According to these sorting schemes the structures are assembled in an ordered manner, which of course requires addressing and finding the single blocks again. For large undulator systems, a large number of blocks, typically several thousand, have to be dealt with. In addition, the magnet material needed for one TESLA FEL undulator system is in the order of 15 metric tons. This is much more than the maximum lot size for production, which typically is only 1-2 tons. The magnets for one system originate from different lots and thus include additional errors. Sorting procedures work better as the number of magnets increases. The best procedure would be to take all magnets of a system, which are up to ~ 18000 pieces. Even if this number is subdivided into several sub-tasks, several thousand magnets are still needed for the procedure to work. This requires a lot of additional internal logistics of storage and retrieval of the magnets. This is very time consuming and cost intensive. It is obvious that improvements in magnet quality would simplify the production of the magnet structures significantly and, if sufficient, allow single block handling to be omitted completely. Therefore, a program to improve magnet material properties has to be initiated. This can only be done in close collaboration with a magnet manufacturer. Such a program should address the following two points: First, the powder metallurgical process should be improved in order to make the magnetic properties more predictable and thus reduce the deviations between different lots. Second, the process of magnetic orientation of the powder during the pressing process should be improved and optimized. Presently, the field of a single loop coil is used even for quite large magnet blocks. This makes the orientation of the magnet powder very sensitive with respect to the exact position and alignment in the coil but also creates inhomogeneities in the edge regions of the magnets where the field of the orienting coil diverges. This could be the reason for the North-South effect. Optimizing the coil geometry, for example, by using a Helmholtz coil type geometry, could improve the situation considerably.

Estimates made in [58] show that the errors could be reduced by about one order of magnitude. Thus magnetization and North-South errors could be in the order of a very few tenths of a percent, while angular orientation errors would not exceed $\pm(0.1 - 0.2^{\circ})$. It is characteristic for the present quality situation that the magnetic field measurement techniques in use for the characterization of permanent magnet single blocks also have to be refined to cope with these improved qualities. If successful, single block treatment and sorting could be omitted. This would greatly simplify the manufacturing procedure of undulator structures and reduce their production effort.

2. Magnetic characterization of insertion devices has been developed to a high degree of perfection in many labs. Although a number of standard techniques have been established and are used throughout the world each lab has its own specific way of doing the measurements. The measurement systems and software packages are made by experts for experts and are not straightforward to use. Using them requires special skills and is very specific to a laboratory. The same statement also holds for techniques used for the fine tuning of magnetic structures. In order to allow a potential manufacturer to do the magnetic measurements and the fine tuning, well tested and approved measuring benches, test stands and data evaluation software have to be provided to them. It is important to design these systems so that they can be operated by trained and skilled technical personnel. Instructions by the software, for example in the placement of shims, have to be clear and unambiguous. In this way it is possible to include all measurement techniques.

These two points are the most important ones. They need considerable R&D work, as they have quite some impact on the price for the whole system. There are, of course, also the other topics already mentioned above, which require extensive R&D work as well. They are, however, more obvious and need less explanation. All these activities should be concentrated in a 'Prototype Phase'. They are summarized below:

- Optimization of insertion device technology (as described above):
  - Improvement on magnet material quality
  - Development of magnetic measuring and tuning techniques for industrial use.
- Magnet design optimization for the planar and helical structures
- Mechanical design and optimization of the gap separation systems
- Mechanical design and optimization of planar and helical structures
- Mechanical design of intersections
- Motion control engineering
- Design of control system
- Design of the phase shifter magnets, with special emphasis on very low hysteresis

- Heavy prototyping of mechanic design, control system, magnetic structures, phase shifters, intersections, test of measurement techniques and fine tuning
- Planning of the production capacities

At the end of the prototype phase everything is ready for production. Well prepared and documented drawings exist, production procedures are described and the properties of the items to be manufactured are well specified. According to this material, the production of the undulator systems may be started immediately.

4.3.4.3. Production phase

A. Introductory remark

After the successful end of the prototype phase, the production of about ∼280 undulator segments may start. Consequently, this part of the project will be called the 'Production Phase'. Of great importance will be a tough and effective organization of the whole production phase so that they can be delivered 'Turn Key Ready' , within cost and on time. This section will show how the setup of the undulator systems can be effectively organized. Here the term 'Project' will be used for the production of the whole ensemble of undulator systems.

B. Project organization

At this stage it is too early to present a full project organization chart for the complete manufacturing of the undulator systems. However, the ideas developed in this chapter can exemplify an organization structure for the production of the main component, the 281 undulator segments needed for the TESLA XFELs. A potential organization chart of this sub-task is shown in Fig. 4.3.12. The 'Production Management' takes full control over these activities. Its responsibilities and duties can be described as:

- Monitoring and control of all activities
- Enforcement and supervision of time schedule
- Cost control
- Guarantee of Quality Assurance and Quality Control (QA/QC) of all sub-components as well as of the final undulator segments
- Organization, coordination and synchronization of sub-delivery of components. For example it organizes the sub-delivery and assembly of mechanical and electronic components in time, and guarantees that they comply with QA/QC standards.
- Documentation of the production

Manufacturing should quite naturally be split into three parts, which may be placed in different production facilities:

1. Mechanical manufacturing : Machining of the gap support drive, girders, mechanical assembly, etc.

2. Electric / Electronic manufacturing : Production and assembly of the cabinets for motion control equipment, power supplies, cables, etc.

3. Production of the magnetic structures

The Organization chart for the mass production is shown in Fig. 4.3.12. The red items mean, that the production management is involved. For example, after mechanical production, the gap support drive units need to be equipped with motors, encoders, limit switches, cables etc. so that a working gap support unit results, as indicated in the organization chart in Fig. 4.3.12. In the next step, the support units need to be combined with the magnetic structures. This will most likely happen at the magnet manufacturer's site, so that there is now a working undulator segment ready for magnetic measurements and tuning. The organization of all these activities, QA/QC, cost control and timeliness is the responsibility of the production management which can but does not need to be done by TESLA staff. There are engineering companies, having expertise in planing and building large and complex production plants. Such a company could work on behalf of TESLA or act as a prime contractor and thus take full responsibility for the whole production phase. In this case it would guarantee that all quality standards are met. On one hand, it is obvious that very good documentation, description and specification of the work to be done is a prerequisite; this work needs a lot of care. On the other hand the TESLA staff directly involved in the production of items can be kept small.

C. Manufacturing considerations of the magnetic structures

The manufacturing of the magnetic structures is the most expensive part in the whole manufacturing process, it requires substantial resources. A study was carried out to estimate the effort to build the magnetic structures and to do the final assembly and magnetic optimization for $\sim$280 segments within the TESLA time frame [58]. About one year has to be estimated for setting up the production facilities. Production capacities have to be adapted to the TESLA schedule. Considering a production rate of $\approx$ 1.5 segments per week or 6 per month, the first SASE FEL will be completed within one year after production has started. In this estimate, corresponding to a completion of the entire ensemble of TESLA undulator systems after four years, some assumptions were made, which are described within the R&D development goals in Sec. 4.3.4.2:

1. No single block handling! This assumes successful improvement of material quality.

2. Magnetic measurement and tuning must not need more than three working weeks per segment.

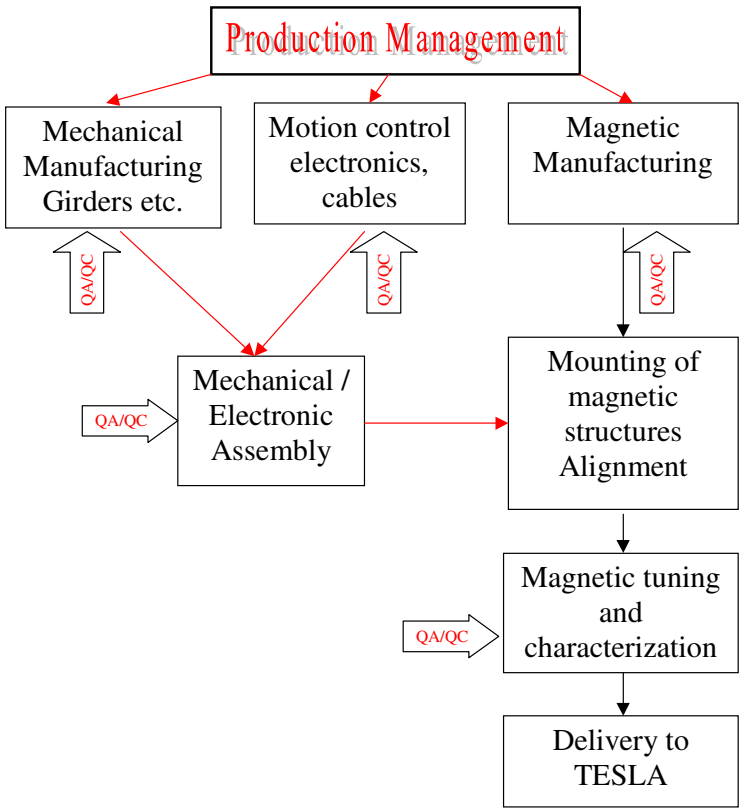

Figure 4.3.12.: *Organization chart for the mass production of the undulator segments.*

3. Assembly effort is the same as for the magnetic structures for the TESLA Test Facility.

4. Manufacturing extends to the production of the magnetic structures , the final assembly with the drive systems as well as magnetic measurements and fine tuning.

5. Drive systems and girders are sub delivered from external suppliers.

6. The magnets are pressed, sintered and machined externally. They are delivered unmagnetized.

7. The size of the magnetic measurement facilities is based on DESY experience.

A preliminary layout of such a production facility for magnetic structures has been worked out in collaboration with a manufacturer of magnetic systems [58]. It is shown in Fig. 4.3.13. Compared with the organization chart in Fig. 4.3.12, these activities correspond to the rightmost column. The bottle neck lies in the magnetic field measurements. To achieve the production rate, at least 4 magnetic benches, which have to work in parallel, are needed. With the assumptions made above, the capacity of the benches is at the limit, but within errors margins. The whole production may be enclosed in a hall with an area of $1500\,\mathrm{m}^2$. Air conditioning is required for magnetization and magnetic measurement facilities. There is a large central mounting area where girders and drive system are combined. This area

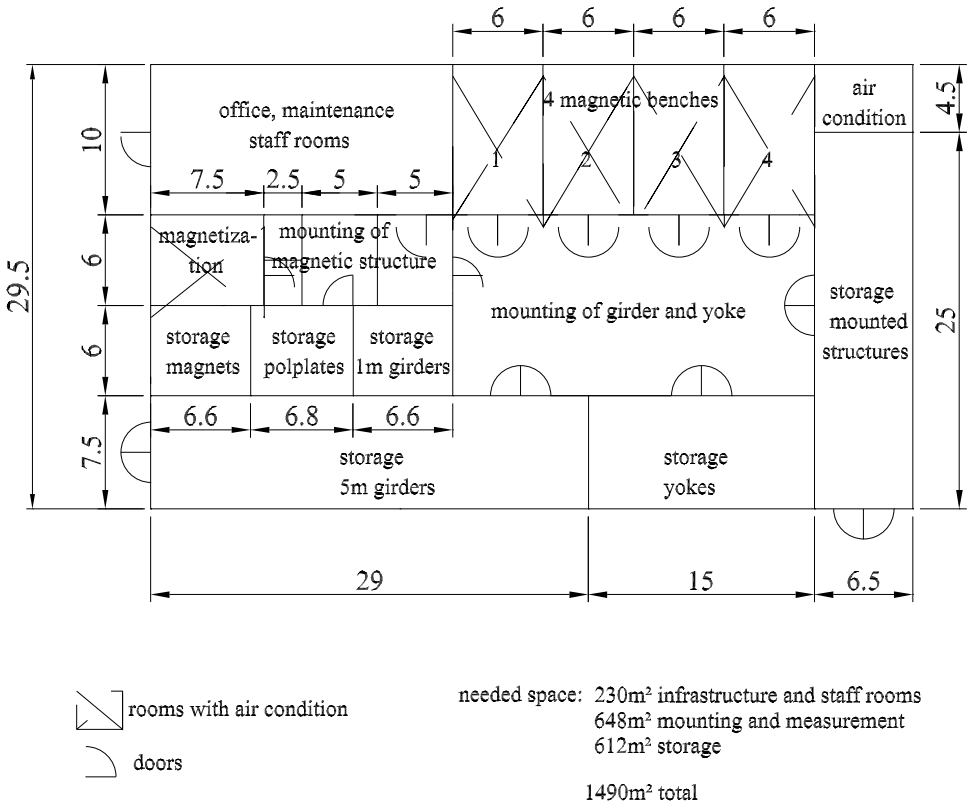

Figure 4.3.13.: *Preliminary layout of a production facility for the production of the magnetic structures, the final assembly of undulator segments and for making magnetic measurements.*

needs a 5 ton crane. Outside this area, and also into the measurement rooms, the undulator segments will be moved on castors, as described in [42]. These castors will also be used later to transport undulator segments within the TESLA FEL tunnel. Sufficient storage area is provided for all steps of the production process.

4.3.5. Summary

The setup of the undulator systems has been described in detail. A total magnetic length of 1405 m is needed. Only four different types of magnetic structures have to be built. They will be subdivided into a total of 281 segments of 5 m length each. Key issues for the production are: Standardization and production on an industrial basis to allow the system to be built with the required quality and within time and cost frame. The whole project is subdivided into a prototype and a production phase. The prototype phase includes a resolute R&D program as a prerequisite to an effective manufacturing of undulator segments as well as design and heavy prototyping activities. Present state-of-the-art undulator technology is used. Industrial manufacturing of undulator segments has been investigated in a feasibility study. First ideas on project organization and production management have been presented.

Bibliography

[1] E.L. Saldin, E.A. Schneidmiller, M.V. Yurkov, *The Physics of Free Electron Lasers*, Springer, Berlin-Heidelberg (2000) and references therein.

[2] E.L. Saldin, E.A. Schneidmiller, M.V. Yurkov, *The general solution of the eigenvalue problem for a high-gain FEL*, Proc. FEL'2000 Conference, Durham, USA, (2000), Nucl. Instrum. Meth. A, in press.

[3] R. Bonifacio, C. Pellegrini, L. Narducci, Opt. Commun. **50**, 373 (1984).

[4] Ya.S. Derbenev, A.M. Kondratenko, E.L. Saldin, Nucl. Instrum. Meth. A**193**, 415 (1982).

[5] J. Rossbach, E.L. Saldin, E.A. Schneidmiller, M.V. Yurkov, Nucl. Instrum. Meth. A**374**, 401 (1996).

[6] M. Xie, Nucl. Instrum. Meth. A**445**, 59 (2000).

[7] K.J. Kim, Phys. Rev. Lett. **57**, 1871 (1986).

[8] S. Krinsky and L.H. Yu, Phys. Rev. A**35**, 3406 (1987).

[9] E.L. Saldin, E.A. Schneidmiller, M.V. Yurkov, Opt. Commun. **186**, 185 (2000).

[10] E.L. Saldin, E.A. Schneidmiller, M.V. Yurkov, Nucl. Instrum. Meth. A**429**, 233 (1999).

[11] S. Reiche, Nucl. Instrum. Meth. A**429**, 243 (1999).

[12] S. Reiche, *Numerical Studies for a Single Pass High Gain Free-Electron Laser*, Thesis (1999) DESY, Hamburg, Germany.

[13] J. Feldhaus, E.L. Saldin, J.R. Schneider, E.A. Schneidmiller and M.V. Yurkov, Opt. Commun. **140**, 341 (1997).

[14] E.L. Saldin, E.A. Schneidmiller, Yu.V. Shvyd'ko, M.V. Yurkov, *X-ray FEL with a meV Bandwidth*, Proc. FEL'2000 Conference, Durham, USA, (2000), Nucl. Instrum. Meth. A, in press.

[15] E.L. Saldin, E.A. Schneidmiller and M.V. Yurkov, Nucl. Instrum. Meth. A**445**, 178 (2000).

[16] *Conceptual Design of a 500GeV Linear Collider with Integrated X-ray Laser Facility Vol. II*, R. Brinkmann, G. Materlik, J. Rossbach, A. Wagner (eds.), DESY reports DESY **1997-048**, Hamburg (1997), Sec. 5.4.3.4.

[17] P. Elleaume, J. Chavanne, B. Faatz, *Design considerations for an 1 Angstroem SASE undulator*, DESY reports TESLA-FEL **2000-16**, Hamburg (2000); see also A.3.6; and Nucl. Instrum. Meth. A**455**, 503 (2000).

[18] K. Halbach, Nucl. Instrum. Meth. **187**, 109 (1987).

[19] K. Halbach, J. de Physique C**1**, C1-211 (1983).

[20] S. Sasaki, Nucl. Instrum. Meth. A**347**, 719 (1991).

[21] J. Pflüger, Rev. Sci. Inst. **63**, 295 (1992).

[22] J. Pflüger, Conf. on electron sources of high brightness radiation, San Diego, USA (1993), SPIE Vol. 2013.

[23] K. Balewski, W. Brefeld, U. Hahn, J. Pflüger, R. Rosmanith, Proc. of the particle accelerator conference, Dallas, USA (1995).

[24] J. Pflüger, Nucl. Instrum. Meth. A**445**, 366 (2000).

[25] J. Chavanne and P. Elleaume, Synchrotron Radiation News **8**, 18–22 (1995).

[26] I. Vasserman and E.R. Moog, Rev. Sci. Instr. **66**, 1943 (1995).

[27] J. Pflüger, H. Lu, T. Teichmann, Nucl. Instrum. Meth. A**429**, 386 (1999).

[28] J. Pflüger, G. Heintze, I. Vasserman, Rev. Sci. Instr. **66**, 1946 (1995)

[29] E.R. Moog, P.K. Den Hartog, E.J. Semones, P.K. Job, Proc. of the 10th National US conference on Synchrotron Radiation Instrumentation (1997), CP417, 219.

[30] J. Chavanne, P. Elleaume, P. van Vaerenberg, ESRF/MACH-ID/96-01, Grenoble (1996).

[31] P. Colomp, T. Oddolaye, P. Elleaume, ESRF/MACH-ID/93-09, Grenoble (1993).

[32] S. Okuda, K. Okashi, N. Kobayashi, Nucl. Instrum. Meth. B**94**, 227 (1994).

[33] H. Henschel, M. Körfer, K. Wittenburg, F. Wulf, *Fiberoptic radiation sensing system for TESLA*, DESY reports TESLA **2000-26**, Hamburg (2000).

[34] G. Schmidt and U. Hahn, *Wire scanners*, Proc. FEL'2000 Conf., Durham, USA, (2000), Nucl. Instrum. Meth. A, in press.

[35] C. Giles et al., Rev. Sci. Instr. **66**, 1518 (1995).

[36] B. Faatz, J. Pflüger, P. Pierini, Nucl. Instrum. Meth. A**375**, 441 (1996).

[37] B. Faatz, J. Pflüger, Y.M. Nikitina, Nucl. Instrum. Meth. A**393**, 380 (1997).

[38] B. Faatz and J. Pflüger, *Field accuracy requirements for the undulator systems of the X-ray FELs at TESLA*, DESY reports TESLA-FEL **2000-14**, Hamburg (2000); see also A.3.5.

[39] S.V. Milton et al., Nucl. Instrum. Meth. A**407**, 210 (1998).

[40] B. Faatz and J. Pflüger, Proc. FEL'2000 Conf., Durham, USA (2000), Nucl. Instrum. Meth. A, in press.

[41] B. Faatz, *Influence of different focusing solutions for the TESLA X-ray FELs on debunching of the electron beam*, DESY reports TESLA-FEL **2000-15**, Hamburg (2000); see also A.3.4.

[42] M. Rüter and J. Pflüger, *Conceptual design of the gap separation drive for the undulators of the TESLA XFELs*, DESY reports TESLA-FEL **2000-07**, Hamburg (2000); see also A.3.7.

[43] M. Tischer and J. Pflüger, *Magnet design of a prototype structure for the X-ray FELs at TESLA*, DESY reports TESLA-FEL **2000-12**, Hamburg (2000); see also A.3.9.

[44] J. Bahrdt et al., *Elliptically polarizing insertion devices at BESSYII*, Proc. SRI'2000, Berlin, Germany (2000), to be published in Nucl. Instrum. Meth. A.

[45] J. Bahrdt, A. Gaupp, U. Englisch, W. Frentrup, M. Scheer, *Conceptual Design of a planar helical undulator for the TESLA SASE FEL*, DESY reports TESLA-FEL **2000-11**, Hamburg (2000); see also A.3.3.

[46] J. Pflüger, M. Tischer, *A prototype phase shifter for the undulator systems at the TESLA X-ray FEL*, DESY reports TESLA-FEL**2000-08**, Hamburg (2000); see also A.3.1.

[47] T. Tennenbaum, D. Burke, R. Helen, J. Irvin, P. Raimouch, , SLAC-PUB 95-6769 (1995).

[48] P. Castro, B. Faatz, K. Flöttmann, Nucl. Instrum. Meth. A**427**, 12 (1999).

[49] K. Flöttman, B. Faatz, E. Czuchry, J. Rossbach, Nucl. Instrum. Meth. A**416**, 152 (1998).

[50] H.H. Radszuweit, J. Krunkowski, J. Pflüger, M. Tischer, *Ein SIMATIC basiertes Kontrollsystem für die Undulatoren des TESLA Röntgenlasers*, DESY reports TESLA-FEL **2000-09**, Hamburg (2000); see also A.3.10.

[51] J. Delafosse and G. Mongodin, *Les Calculs de la technique du vide*, edite par la societe francaise des ingenieurs et techniciens du vide (1961).

[52] D. Behne, *Outgassing Test Results from PEP-II Standard Straight Section Vacuum Chambers* (1997), see also SLAC report R-521 (1998).

[53] C.L. Foerster, Synchrotron Radiation News **11**, 20 (1998).

[54] E.M. Trakhtenberg, E. Gluskin, and S. Xu, Rev. Sci. Instr.**66**, 1809 (1995).

[55] J.C. Liu, W.R. Nelson, K.R. Kase, Health Physics **68**, 205 (1995).

[56] K. Tesch, private communication.

[57] C. Magne and M.Wendt, *Beam Position Monitors for the TESLA Accelerator Complex*, DESY reports TESLA **2000-41**, Hamburg (2000).

[58] R. Cremer, F.J. Börgermann, J. Pflüger, M. Tischer, *Manufacturing Considerations of the magnetic structures for the Undulators for the XFEL at TESLA*, DESY reports TESLA-FEL **2000-10**, Hamburg (2000) ; see also A.3.2.

[59] S. Kirkpatric, C.D. Gelatt, M.P. Vecchi, Science **220**, 671 (1983).

[60] B. Faatz and J. Pflüger, *Sorting strategy for the TTF-FEL undulator magnets*, DESY reports TESLA-FEL **99-01**, Hamburg (1999); see also A.3.11.

5. X-ray Optics and Experimental Techniques

This chapter has been written on the basis of contributions to the report of the workshop "Methods and Instrumentation for an XFEL" edited by J. Hastings (BNL Brookhaven) and Th. Tschentscher (HASYLAB, Hamburg) and of experimental details of scientific proposals presented in Chap. 3. In the report (see A.1.5), more detailed description and further references can be found.

In the following, the X-ray optical issues for mirrors, lenses and monochromators in XFEL beamlines as described in section 6.1 are presented. Additionally, special requirements for experimental techniques besides the elements included in the generic beamline design are discussed.

5.1. Photon-Beam-Based Alignment

An X-ray diagnostic station is planned for each of the XFEL undulator beamlines. The primary purpose of the X-ray diagnostics is to have an additional tool for alignment and commissioning of the numerous undulator cells along an XFEL beamline independent of the electron beam–based alignment procedure. For obvious reason the method presented in the following is called photon beam–based alignment. Both methods will complement each other. The X-ray diagnostic data will be an essential input to the undulator control system described in Sec. 4.3.

The diagnostic station with a crystal monochromator as a principal instrument is located about 180 m downstream from the undulator (see 6.1). The spatial distribution of the spontaneous radiation of individual or several consecutive undulator segments is imaged and analyzed in order to optimize angle and position of the electron beam trajectory, to verify the magnetic gap and to adjust the phase match between two undulator segments (Fig. 5.1.1). The two latter purposes cannot achieved by electron beam-based alignment. As all undulators will be equipped with a gap drive, individual segments can be selected for diagnosis by switching off, i.e. opening the gap, of all the other segments. This concept of one common diagnostic station for all (~ 50) undulator cells in one beamline avoids a multiple installation of identical diagnostic devices [1], which all would have to be calibrated against each other. It rather facilitates a precise alignment and setup of the undulator. A second instrument of the X-ray diagnostic will be a calorimetric tool to determine the integral power of the photon beam.

The X-ray diagnostic station should resolve a trajectory misalignment of $< 0.5\,\mu$rad and gap variations on the μm scale. First step in the setup procedure is the alignment of the

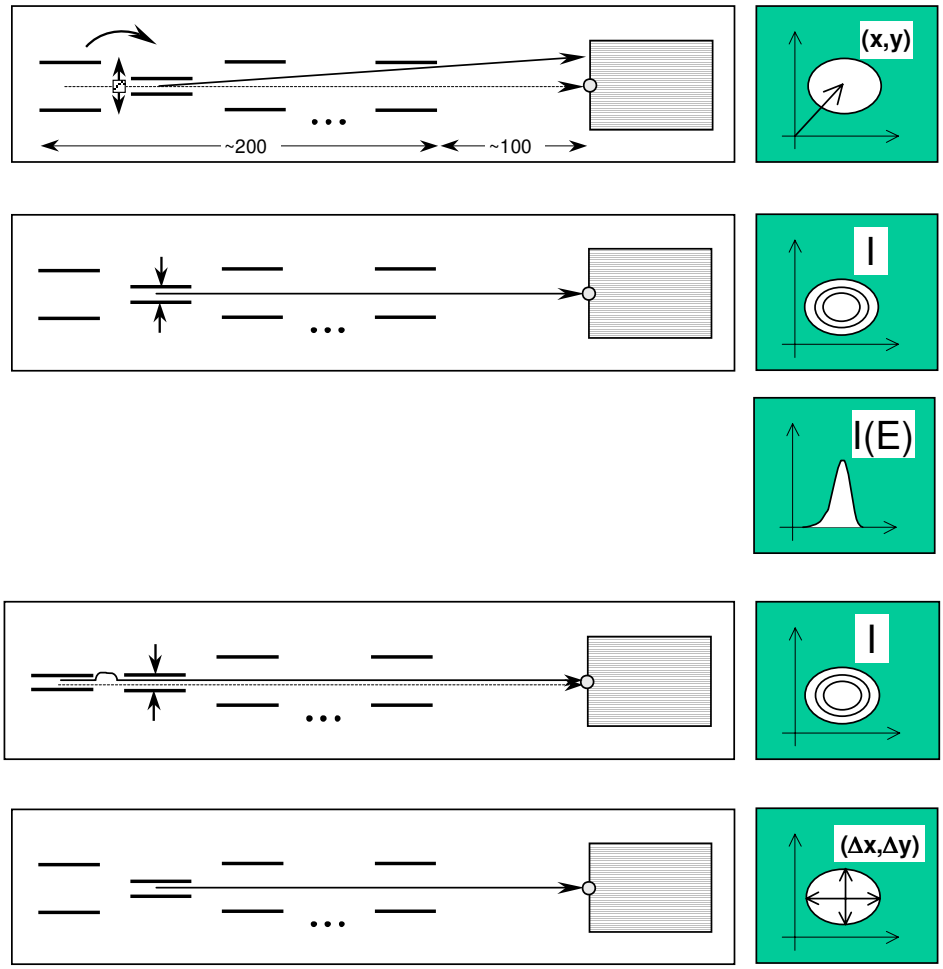

Figure 5.1.1.: *Illustration of photon beam-based alignment scheme for the undulator. In the uppermost panel a scheme for individual successive alignment of the electron beam trajectory in position and angle is sketched. Below, gap tuning relative to a reference segment and possibly detection of the spectral distribution I(E) is shown. The third panel shows the setup for measurement of phase matching and the lowest panel sketches emittance measurements.*

individual trajectory within each undulator cell. The center of the spontaneous synchrotron radiation cone will be recorded and matched onto a reference point by means of steering coils in the intersection module upstream of the specific undulator segment. Two beam position monitors in the diagnostic station serve to distinguish angular misalignment and transversal offset. Once the trajectories of all segments lie on the same axis, the gap, i.e. photon energy, of each segment can be fine-tuned and calibrated to a selected energy by maximizing the radiation intensity. Finally, the phase match of successive cells can be optimized by monitoring the photon intensity as function of the phase shift in the intermediate intersection.

5.2. X-ray Optical Elements

5.2.1. Requirements

The optical elements in the XFEL photon beam will have to fulfill certain requirements which go beyond what is customary today. In particular, it is required to preserve the high degree of transverse coherence and the time structure of the SASE FEL radiation. For extreme focusing the surface roughness and angular errors will have to be further decreased. In addition, the optical elements in the XFEL beam will have to withstand a high power load. Here, in particular the peak load imposed by the short pulse length of 100 fs does require further understanding of the fundamental interaction mechanisms of highly intense, short X-ray photon pulses with solid matter. In addition, the optical elements will have to fulfill the requirements already indispensable at current sources, like high and ultra-high monochromatization, preservation of polarization, possibility of changing the polarization, stability and others.

5.2.1.1. Preservation of the time structure

The advent of fast laser flash X-ray sources and of fast crystal based X-ray spectroscopy has stimulated first developments of a time-dependent dynamical diffraction theory [2, 3], using different formalisms. Recently, a comparison of experimental and theoretical data obtained for diffraction with bent single crystals yielded good agreement [4], further details are discussed in A.1.5. In addition, various schemes have been proposed to delay, superimpose or compress X-ray pulses in analogy to methods used for current lasers, to overcome the machine-limited pulse length of storage ring sources and to shorten pulses even on the sub-picosecond time scale. These proposals (e.g. ref. [5]) must still be further refined and experimentally validated in more detail.

For an XFEL, the X-ray pulse duration is smaller than or in the order of the time needed to traverse an extinction length (for perfect crystals) or an absorption length (for mosaic crystals). Therefore, pulse broadening can occur. By definition of Bragg's law, the path difference of an X-ray beam is precisely one wavelength per lattice plane with respect to the beam reflected at the crystal surface. Thus the time delay per lattice plane is λ/c where c is the speed of light. It follows that, e.g. for the silicon (111) reflection, the total pulse length of typically 100 fs remains unchanged, but the microbunch sub-structure ($\ll 1$ fs) within one pulse will be affected. The influence of the crystal diffraction on the microbunch structure must therefore be investigated in more detail. A widening of 2.5 fs is obtained for a δ-like excitation and the transient response shows a temporal beating [6]. For the (444) reflection $\Delta t = 60$ fs. This broadening is in agreement with the limit given by the uncertainty principle $\Delta E \Delta t \geq h/2\pi$.

Because the microbunch sequence is not periodic but stochastic, both in time and in amplitude, strong intensity fluctuations will occur from bunch to bunch that can be enhanced after crystal reflection. In fact, the energy spectrum obtained by the Fourier transform of the temporal spectrum shows a similar spiky structure that changes from bunch to bunch. Simulations of the reflection of a XFEL bunch by a single and a double crystal monochro-

mator (non-dispersive setup) have been performed [7, 8]. The result from [7] shows that the spiky structure is both smoothed out and stretched in time. For the (111) double-reflection the intensity fluctuations are still significant, but for the (444)-reflection an almost Gaussian profile is obtained. This finding differs from [8], where it is shown that the monochromatization by a crystal does not change the statistics of the outgoing beam. Here the amplitudes normalized to the average amplitude follow the same statistical law as the incident beam, namely the Rayleigh distribution. A crystal reflection has a much narrower energy acceptance for a fixed incident angle and consequently a broader response in the time domain. In this picture the monochromatization by a crystal will not broaden the duration of the whole bunch (100 fs), but change its spiky structure to a longer time scale (2-3 fs).

With asymmetric Bragg reflections it is possible to produce a time-space chirp, where the isochrones and isophases that are parallel before the reflection form an angle after the reflection. Simultaneous combinations of the time-space and energy-angle chirps could also be envisaged. Extremely grazing incidence can be used at XFEL sources, leading to a spectral resolution of $\Delta E/E \approx 1 \cdot 10^{-3}$. If the beam is initially 100 μm wide, it will be stretched to about 60 mm. More elaborate investigations, in particular pulse stretching and the superposition of wavefields excited by subsequent pulses inside an extinction volume, will require refinements of the mathematical treatment. They also have to include the time-dependent transmission through an arrangement of several crystals, similarly to what is presently possible by ray -tracing in the stationary case. It would also be very helpful to use graphic schemes such as DuMond diagrams that contain the time coordinate. Finally, full phase space analysis of FEL beam conditioning by real crystals including time and describing the mutual interdependence of all beam parameters must be conducted, a complex and challenging but truly exciting and rewarding task.

The SASE XFEL pulse duration of 100 fs corresponds to 30 μm in space, yielding a spatial stability requirement for the X-ray path length. This is in particular relevant for reflection at high angles. In order not to introduce instability, the X-ray beam path should be stable to better than 3 μm. This only applies to the 100 fs FWHM length of the X-ray pulse. In order to also preserve the pulse substructure with a characteristic width of few 100 as (attosecond), all requirements mentioned above have to be improved by a factor of 1000.

5.2.1.2. Preservation of coherence

Experience at third generation synchrotron radiation sources has shown that the beam coherence is reduced by optical elements that introduce inhomogeneous phase shifts. For experiments exploiting the transverse coherence, like X-ray photon correlation spectroscopy or imaging techniques, such optical elements have to be avoided. In particular, this affects the choice of monochromator crystals. Whereas Si crystals are highly perfect and do preserve the beam coherence, diamond which is the preferred material in terms of power load stability, is not yet available with sufficient crystal perfection.

The *spatial coherence length* l_s is commonly defined as half the wavelength λ times the angle ϕ under which the radiation is seen at a distance D from the source: $l_s = \lambda\phi/2$ [9, 10]. If the source size S is smaller than $\psi \cdot D$ where ψ is the "natural" emission angle, i.e. beam divergence, of the synchrotron or FEL beam, the angle ϕ is given by D/S, otherwise

$\phi = \psi$. For a 100 μm source and a divergence of 1 μrad, $D/S = \psi$ at a distance of 100 m which can be considered as optimal in terms of an intensity vs resolution compromise. In the symmetric Bragg case, perfect crystals fully preserve the spatial coherence in the sense that they preserve both beam divergence and source size, both for a single reflection and multiple reflections in non-dispersive geometry.

Because the *temporal coherence length* l_t is given by $\lambda/2(\Delta\lambda/\lambda)$ [9, 10], monochromator crystals can be used to control (usually increase) the longitudinal coherence. The extinction depth, normally of the order of μm (see above), can become very large and finally is limited by absorption which in turn determines the highest obtainable spectral resolution. It should be noted at this point that even a single perfect crystal reflection can be used to modify the spatial coherence. This is not new, but should be taken into account here more explicitly. Indeed, by projecting the extinction depth $t_e = (2/\pi)Nd_H$ onto a direction normal to the X-ray beam, an "extinction width" $(4/\pi)t_e cos(\theta_B) = (2/\pi)\lambda/\omega_H$ is obtained that corresponds to the crystal-induced spatial (i.e. lateral) coherence length, l_c. This shows that crystal diffraction controls both spatial and temporal coherence at the same time and that both quantities are correlated, in a manner different from other optical elements such as pinholes used to create spatial filtering affecting only spatial coherence. The conditioning of spatial coherence by crystals has been experimentally verified quite recently [11].

Mosaic or imperfect crystals may strongly affect coherence. The effect of the angular mosaic block distribution can be expressed as an increase of the source size by $\Delta S = 2D_{sc}\eta$ where D_{sc} is the source-to-crystal distance and η is the width of the mosaic distribution. In the diffraction plane this effect can be compensated by reflection from a second, identical mosaic crystal, but in the sagittal plane this is not feasible. In practice, however, it is almost impossible to find crystals with absolutely identical mosaic structure. In the kinematical limit the penetration depth is determined by absorption. It ranges from about ten to a few hundred μm or even more for low Z materials such as beryllium or graphite. Secondary extinction effects limit the penetration depth to values somewhere between the primary extinction depth and the absorption depth. This relaxes the perfection requirements of diamond single crystals, which would otherwise limit the coherence of the monochromatized beam. Furthermore, crystals with a lattice spacing gradient, due to bending or substitution of elements, might find very interesting applications, in particular for monochromatic focusing and for the modification of the time structure. To our knowledge the effect of crystal curvature and lattice spacing gradients on coherence has not been studied up to now.

In the asymmetric Bragg case, the diffraction planes form an angle with the surface, and the beam can either be expanded or compressed. In both cases coherence is affected (both laterally and longitudinally), because diffraction effects change the beam divergence and the energy resolution. Moreover, refraction has a dispersive effect such that different energies are reflected into different directions. In fact, the whole scattering process can be imagined as a superposition of diffraction and refraction. It would be interesting to envisage experiments where the energy-dispersive effect (energy-angle chirp) could be applied. This has not been done yet to our knowledge. The influence of asymmetric Bragg reflection on the coherence properties has been studied both experimentally and theoretically [12, 13]. At very small angles of incidence, approaching the angle of specular reflection, the low energy part of the beam is reflected by specular reflection and much less power is absorbed by the crystal. This

could be interesting to reduce power load at the XFEL without changing the beam coherence.

In the Laue case, the diffraction patterns strongly depend on the crystal thickness. Maximum reflectivity is obtained for a given wavelength and a corresponding thickness. The rapidly oscillating Pendellösung fringes can have dramatic effects on coherence and have to be taken into account. This applies in particular to photon delay lines, which would use Laue crystals as beam splitters. In conclusion, the influence of crystal diffraction on the coherence properties of X-ray beams is quite well understood. Interesting new applications may become possible with XFEL beams, in particular when asymmetric reflections are used.

5.2.2. Monochromatization

5.2.2.1. Soft X-ray monochromator

At the XFEL, the SASE 5 undulator covers an energy range from 500 eV to 3100 eV with an intrinsic line width of $\approx 0.5\%$. Below , a suitable monochromator design is briefly described; a more detailed design study is found in A.2.3.

For many experiments and spectroscopies, the required spectral resolution is higher than that provided by the intrinsic SASE line width. Therefore, the spectral bandwidth has to be reduced by a monochromator which should achieve a resolving power $E/\Delta E \approx 10.000$ across the entire spectral range with relatively high transmittance. The specified energy range (500 to 3100 eV) is challenging for both monochromator types in consideration, for grating as well as for crystal monochromators. The efficiency of gratings usually decreases drastically for energies approaching 2000 eV and beyond, whereas single crystals with sufficient reflectivity and beam power stability are only available above 2100 eV (Si).

A further challenge is the high brilliance of the SASE beam. The optical elements will be exposed to tremendous photon densities. In the XUV energy range, atoms exhibit a high absorption cross section which could lead to a continuous evaporation of surface atoms. On the other hand, taking advantage of the high brilliance, very small angles of incidence can be chosen at still tolerable lengths of the optical elements. In addition, the large distance between the FEL and the first optical element reduces the density to a reasonable level. Also, the grating problem can be solved by using the same advantage of the FEL along with appropriate coatings. However, requesting a good performance in the desired energy range at FEL photon densities and total amount of absorbed power pushes the proposed design to the limits of existing technology.

A plane grating monochromator following the designs of BESSY II [14] is proposed. In contrast to operation with collimated light, for the XFEL the first mirror will be used to generate a convergent beam with a demagnification of 5:1. Two gratings with line densities of 600 l/mm and 1200 l/mm have been optimized to cover the energy ranges of 500–1200 eV and 1200–3100 eV, respectively.

Due to the extremely high photon densities and corresponding heat loads on the optical elements, the thermal properties of the mirror substrate and coating material are of crucial importance for the performance of the beamline. Experience at high energy third generation light sources with crystal monochromators shows that cryogenic cooling (present designs use liquid nitrogen cooled silicon) is best suited to cope with high heat loads. Even absorbed

power densities of several W/mm^2 did not degrade the performance of crystal monochromators [15]. The slope errors induced by the thermal load seemed to be far below 1 arcsec. Moreover, at lower photon energies and for grating applications, silicon single crystal material is already well established. Thus we propose to use silicon as bulk material and a cryogenic cooling technology for the mirrors and gratings of the XUV-FEL-monochromator as well.

The bulk silicon material has to be covered with an appropriate thin-film coating in order to avoid a strong absorption at its K-edge at 1840 eV. Two coating materials seem to be optimal, carbon and chromium. Chromium is a well-proven coating material, which forms very smooth layers, adheres very tightly to the bulk material, and is often used as contact layer. Its disadvantage are strong absorption edges at 574 eV and 584 eV. Carbon shows no absorption edges above 285 eV (K-edge). It has excellent thermal properties when used in its diamond modification. On the other hand, the coating quality of diamond layers on silicon is not yet as good as for chromium. Generally, the reflectivity of carbon in total external reflection is somewhat higher than for chromium, but for chromium the cutoff energy for a given incidence angle is much higher. If diamond is used as coating material, grazing angles smaller than 0.5° have to be used, requiring an inclined beam geometry. For photon energies above 3000 eV and in case of insufficient diamond surface quality, chromium should be reconsidered.

For power considerations, the penetration depth of the radiation is very important. In the regime of total external reflection, the penetration depth $d_{1/2}$ perpendicular to the surface, in which the intensity drops to half of its initial value, can be calculated according to

$$d_{1/2} = \frac{\lambda}{4\pi} \frac{\ln 2}{\sqrt{\cos^2\phi / \cos^2\phi_c - 1}} \,, \tag{5.2.1}$$

where ϕ_c is the critical angle of total external reflection for wavelength λ. ϕ_c is related to the index of refraction by $n = \cos\phi_c$. For carbon coatings a penetration depth of 2.4 nm at 500 eV is obtained, leading to the deposition of a significant amount of energy into a thin surface layer at a time scale where thermal conductivity does not take place. It is therefore important to know whether the surface atoms will stay in place or will ablate. As a rough estimate, we can calculate the number of atoms N_A, that absorb a photon by assuming that half of the absorbed photon flux is absorbed within the penetration depth $d_{1/2}$.:

$$N_A = \frac{\mathrm{n} \cdot d_{1/2}}{0.5 \cdot \Phi_{abs}} \tag{5.2.2}$$

where *n* denotes the particle density in the layer material (n $\approx 1 \cdot 10^{20}/\mathrm{mm}^3$ for carbon). It follows that an average number of 2200 atoms absorbs one photon per bunch, yielding approximately 0.22 eV per atom. The bunch separation of 93 ns should be long enough to thermalize this energy deposition, so that even the most critical optical element should withstand the peak power deposition within 100 fs.

5.2.2.2. Crystal monochromators

Monochromatization by crystal diffraction will be used to decrease the 0.1 % bandwidth of the FEL line for various applications, in particular for spectroscopy. The crystal-dependent

relative energy resolution $\Delta E/E = \epsilon_H = 2/\pi N \approx (1/N)$ is typically $1.4 \cdot 10^{-4}$ for the silicon (111)-reflection and $6 \cdot 10^{-5}$ for the diamond (111)-reflection. It can be as small as a few 10^{-9} for high-order reflections and is limited by the accuracy with which the crystal lattice constant is defined (perfection limit for silicon), except when using nuclear resonance where still higher resolution is achievable. In the following, silicon and diamond crystals will be described, as they have shown the highest ability to fulfill the requirements for XFEL sources. Whereas silicon crystals can be nearly perfect, diamond has the advantage of high heat conductivity and high damage threshold, thus achieving good performance at high power loads.

Silicon and diamond crystals Comparing diamond and silicon single crystals, one finds that the diamond (111) data are very close to those of silicon (220) except for the absorption thickness, which is more than one order of magnitude larger for diamond [16]. Therefore, not only are the reflection properties of diamond better, i.e. the peak reflectivity is (slightly) higher, but also less heat is absorbed. Beryllium is still superior in this respect; however, it can not presently be grown as a dislocation-free crystal but has in the best case a mosaic spread of 200 μrad. Silicon is absolutely dislocation-free, while diamond single crystals are only locally perfect [17]. The silicon (111) reflection provides a good matching ($\omega_H = 35\,\mu$rad at 8 keV) for synchrotron beams, but none of its possible reflections has a Darwin width small enough to match the XFEL beam divergence. This means that the reciprocal space element selected by a perfect crystal out of a spectrally wide, but well collimated beam will be anisotropic, typically with its long axis parallel to the beam direction. This situation is radically different from laboratory or even synchrotron radiation conditions.

Silicon (111) gives about twice as much flux than the diamond (111) reflection, but also half the resolution: at 8 keV, $\Delta E/E = 1.35 \cdot 10^{-4}$ for silicon and $0.60 \cdot 10^{-4}$ for diamond crystals. Furthermore, its 1.5 times larger lattice spacing permits silicon to reflect correspondingly longer wavelengths, which is of advantage in certain cases. On the other hand, the reciprocal space of diamond crystals is 3.5 times less dense than that of silicon crystals, reducing the probability of parasitic reflections (*glitches*) by the same factor. This is an advantage, in particular for X-ray absorption spectroscopy. The choice between silicon and diamond will depend on the degree of crystal perfection that is needed, the actual heat loads, and radiation damage compatibilities, as discussed below. Both materials are also used as very efficient half- or quarter-wave plates to control polarization (see below).

While it is obvious that diamond is the ultimate monochromator material to be used at XFEL's, it is also very important that the crystal quality of diamond will be further improved. Fig. 5.2.1 illustrates the state-of-the-art quality showing the distribution of lattice tilts inside a 10×12 mm^2 diamond (111) crystal plate. The darker blue areas represent the zones where the crystal reflects according to dynamical theory and the FWHM corresponded to the instrument resolution, which was even smaller than the Darwin width. Efforts are under way to grow even better crystals with a mosaic spread of about 2 arcsec.

Heat load simulations It is well known that when a crystal or mirror plate is cooled from the rear or the side, the thermal deformation results in a slope error composed of a bending and a bump component, and in a change of lattice constant for a crystal. Briefly, the amount of thermal deformation is proportional to the quantity $P_a \alpha_{th}/\kappa$ where P_a is the

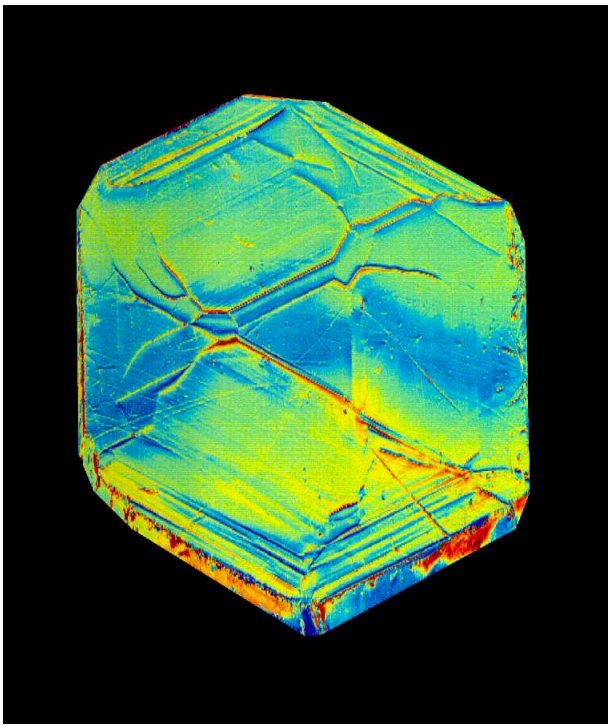

Figure 5.2.1.: *Distribution of lattice tilts of a* $10 \times 12\,mm^2$ *diamond (111) crystal determined by the spatially resolved rocking curve technique (for details see Ref. [17]).*

absorbed X-ray power, α_{th} is the linear thermal expansion coefficient, and κ the thermal conductivity of the material. With $P_a = P_o e^{-(\mu t/sin\theta_B)}$ for the symmetric Bragg case, where P_o is the incident power, μ the linear X-ray absorption coefficient, and t the crystal thickness, and considering $t_e < t < t_a$ in the ideal case, one can define the relevant figure-of-merit as being $\kappa/(\mu\alpha_{th})$. Here, t_e and t_a denote the extinction and absorption depth, respectively. Even if $t > t_a$ the fact that the power is absorbed in the bulk rather than close to the surface is an advantage favoring small absorption. It is evident that diamond single crystals are by far the best material from this point of view. At room temperature its figure-of-merit is more than one order of magnitude better than that of silicon at low temperature. Cooling techniques such as cryogenic cooling of Si or inclined crystal geometries have become standard at third generation sources and water-cooled diamond crystals are used in many beamlines worldwide. The present limit of total power is about 1 kW for cryogenic cooling. Present sources can reach power densities up to 350 kW/cm^2 and a total power of several 100 W [16]. Cryogenic cooling of diamond has been tried [15, 18] but more technological developments are needed, in particular for mounting.

Finite element calculations of edge-cooled diamond crystals show the response to the X-ray beam in terms of temperature distributions (see A.1.5 for details). At 1 Å an average power of 210 W at the undulator exit corresponds to a normal incidence power density of 288 W/mm^2 at a distance of 1000 m from the undulator for a beamsize (FWHM) of 0.8 mm. This time-averaged power and power density at a large distance from the SASE undulator

is comparable to that of third generation synchrotron radiation sources. However, since the XFEL time structure is radically different, the thermally relevant time scale is 93 ns for the bunch-to-bunch separation and one millisecond for the complete bunch train. Fig. 5.2.2 illustrates the results of a simulation for a 100 μm thick cryogenically cooled diamond crystal. Each bunch heats up the crystal by $\approx$1 K and the full bunch train of 11500 bunches deposits 1.2 J within 1 ms. The temperature rises steeply to $\approx$ 200 K within the first 0.2 ms of the bunch train and then saturates. At the end of the bunch train the temperature drops with a similar time constant.

These results were obtained for a geometry where a Laue-case reflecting diamond disc is surrounded by a solid diamond cylinder acting as a heat sink. The outer surface of this cylinder is cooled with liquid nitrogen. The results of the simulation indicate that liquid nitrogen cooled diamond crystals are well suited as monochromator crystals in XFEL applications. The time structure of the XFEL bunch train modulates the temperature of the crystal in an unusual way compared to present sources. During a bunch train, the temperature of the crystal rises and drops on a millisecond timescale. The absolute value of the temperature rise depends on the crystal thickness. In the assumed geometry, the temperature at the interface is roughly 10 K above the liquid nitrogen temperature, which imposes no risk of boiling the liquid nitrogen.

$\lambda/4$-plates Quarter wave plates (QWP) - well known in optics - are crystals which have different indices of refraction for two orthogonal directions of the electric field. The thickness of a QWP is such that the induced phase shift between those two orthogonal electric fields is 90°. If they are adjusted in a way that these directions make a 45° angle with the linear polarization of an incident beam, they transform the linear into circular polarization, right-handed or left-handed depending on the sign of the 90° phase shift. Non-cubic crystals are birefringent in the visible range, but not at X-ray wavelengths. Birefringence for X-rays occurs in perfect and good crystals at and near Bragg diffraction. The most convenient and versatile way to take advantage of this birefringence is to use the forward-diffracted (i.e. transmitted) beam outside the reflection range.

The principle works in Laue and Bragg diffraction geometry, both symmetric and asymmetric. For a given reflection and wavelength, one has to optimize the beam path in the crystal with respect to phase shift and transmission. It is in general necessary to use a crystal with as little absorption as possible. Diamond crystals are the best choice here [19].

As an illustration, Fig. 5.2.3 (left) shows the beam path, the corresponding offset for a 90° phase shift, and the Darwin width as a function of wavelength for a diamond crystal with 30% transmission. The minimum acceptable value of the thickness is evaluated to be twice the Darwin width, which explains why 3.8 Å has been considered as the maximum wavelength for which a diamond phase plate works with a good transmission. Beyond 4 Å it is possible to use very thin silicon crystals with several disadvantages, in particular low transmission. Fig. 5.2.3 (right) shows the beam paths allowing a transmission of 10^{-3} and 10^{-4} and the corresponding offsets for a 90° phase shift. Considering an offset of at least twice the Darwin width, a beam path of the order of 25 μm is suitable for wavelengths between 4 and 5 Å if a transmission in the 10^{-4} range is acceptable.

In conclusion, QWPs can probably be used to transform the linear polarization delivered

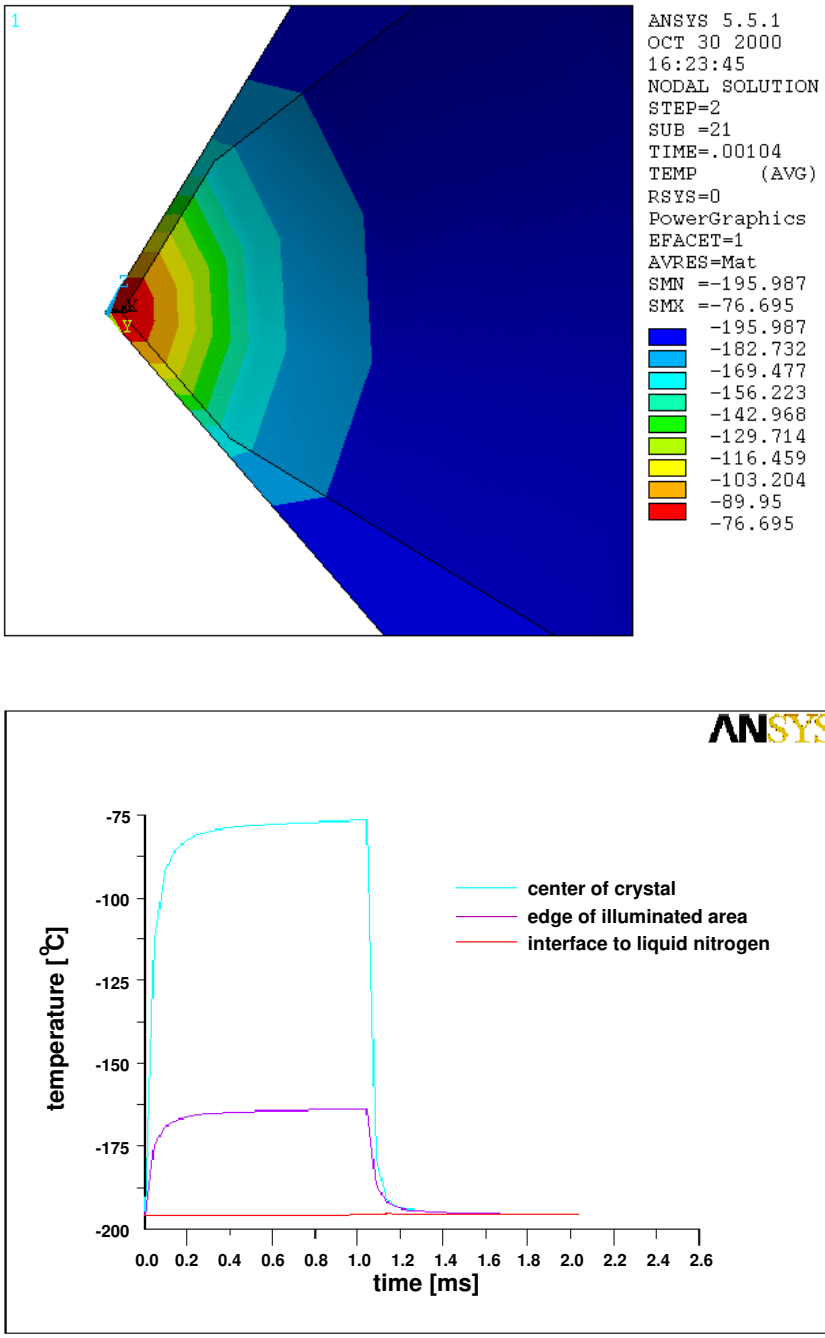

Figure 5.2.2.: *Top : Temperature distribution in a cryogenically cooled diamond crystal (thickness 100 μm) after passage of one bunch train. Bottom: Temperature development in a 100 μm thick crystal over 2 ms calculated at the center and edge of the illuminated area, and at the interface to liquid nitrogen.*

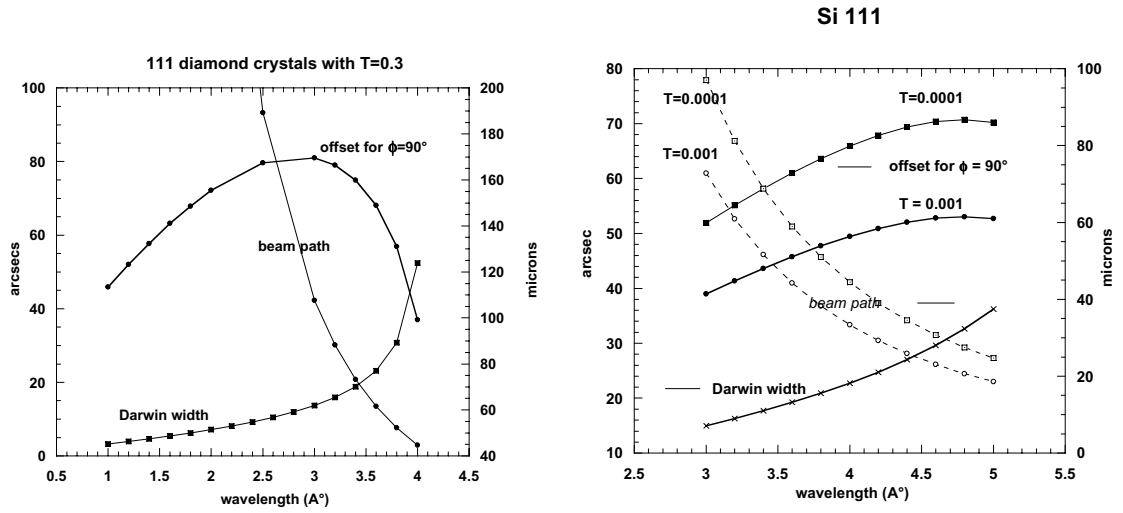

Figure 5.2.3.: *Beam path t and offset $\Delta\Theta$ giving a phase shift of 90 ° in diamond (left) and silicon (right) as a function of the wavelength, calculated to obtain a transmission T = 0.3 (diamond) and 0.001 and 0.0001 (silicon). The Darwin widths are also shown.*

by a planar XFEL undulator into circular polarization without any major difficulty. The heat load problem, however, has to be investigated, but it is much less crucial than for monochromators since the QWP is located downstream from the monochromator and does not operate at the exact Bragg position. Without further discussion here, it is mentioned that since the QWP device uses the forward-diffracted beam outside a Bragg peak it is unlikely to affect the time structure of the XFEL pulse. Compared to specially designed undulators delivering circular polarization, there are some advantages of using QWPs: the transfer of polarization by monochromators need not be considered, the switching of the polarization handedness is easily done by small rotations of the crystal and therefore very easy to handle, the cost is much lower than for a corresponding undulator. On the other hand, QWPs have the important disadvantage of a limited spectral range. They are well suited only from 1 Å to 3.8 Å. From 3.8 Å to 4 Å the efficiency is lower, resulting in lower transmission. From 4 Å to 5 Å thin silicon crystals can still be used but with very low transmission. QWPs cannot be used at wavelengths > 5 Å because of absorption. It is therefore concluded that for wavelengths longer than ≈ 4 Å, circular polarization has to be provided by undulators directly.

5.2.3. Focusing

Focusing the already highly collimated XFEL radiation to a small spot at the sample position is needed by many scientific applications. Although in most cases a moderate demagnification of 1:1 to 10:1 is sufficient, some applications aim towards focal spot sizes below 100 nm in both lateral directions, corresponding to a demagnification > 1000:1. As focusing devices, we will only consider mirrors and refracting lens optics.

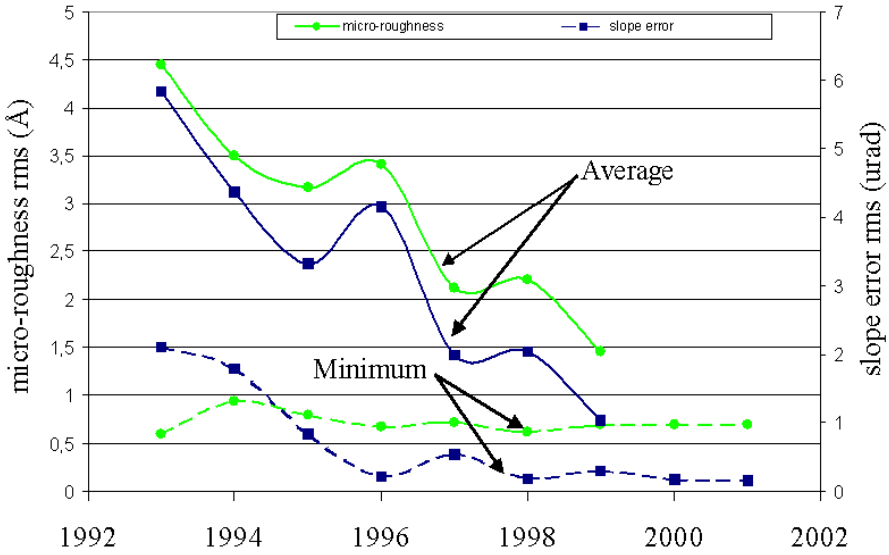

Figure 5.2.4.: *Development of micro roughness and slope error of mirrors over the last 10 years. The best achieved and measured [20] values settle at RMS values of 0.7 Å and 0.15 - 0.17 murad, respectively, measured over a length of a perfect mirror area of 160 and 400 mm.*

5.2.3.1. Mirrors

Mirrors will be used at the XFEL for several purposes: focusing, low-pass filtering, and deflection in order to discriminate spontaneous radiation from Bremsstrahlung background. Due to the long straight optics sections at the XFEL, it is envisaged in the generic beamline layout to use two mirrors in a (+,–) double -bounce geometry. In the following, some aspects of mirror layout, design, and fabrication are discussed. For extreme focusing, which will be possible at the XFEL due to its small source size and highly collimated beam, Kirkpatrick-Baez geometry is favorable, which has already proven to give the best focusing results at longer wavelengths. State-of-the-art polishing of long flat mirrors (1 m) achieves around 1 μrad rms slope error. The impressive development of micro roughness and slope error of mirrors over the last 10 years is shown in Fig. 5.2.4. The best achieved values at present settle at 0.7Å and 0.15 - 0.17 μrad, respectively, for mirrors with a perfect area with a length of 160 and 400 mm. The average quality curve shows a distinct trend towards these values. The currently used ion beam figuring (IBF) and metrology capabilities to achieve this mirror quality have been developed for lithography optics with a diameter of 40 cm. It is therefore anticipated that 0.1 μrad for a 1m long mirror is a reasonable R&D goal.

Shorter mirrors can even be bent into elliptical shapes with similar (1 μrad) accuracy. For an elliptical bending of larger mirrors, an accuracy of $\approx$ 31 μrad over 60 cm has been achieved [21]. Toroidal mirrors, on the other hand, do not give good images except close to 1:1 magnification. They are also harder to manufacture than flats and spheres. Thus it is suggested, that for micro-focusing, Kirkpatrick-Baez mirror pairs will be used. The mirrors can be manufactured as flats and formed into any shape, including an elliptical cylinder, by bending. For strong demagnification with long optical elements, the accuracy of the shape is

very important, and dynamical bending is easier to implement and more accurate than direct fabrication of a rigid spherical shape, especially in the hard X-ray regime where the radius is large (>200 m) and the mirror is long (> 0.5 m).

Optical tolerances for extreme focusing An analysis of the required optical tolerances has been carried out based on the formalism proposed by Church and Takacs [22]. In particular, the effect of surface errors on the image quality, in terms of the Strehl factor and the image width, has been considered. Finally, several mirror layouts have been compared based on a commercial mirror produced by Carl Zeiss that represents a benchmark quality below which mirrors *can be produced at reasonable cost and in reasonable time* and above which they *are difficult to produce and special characterization and polishing tools are required which might still have to be developed* [23]. One extremely important result of this comparison is that current state-of-the-art mirrors are acceptable for almost all cases if ultra grazing angles are used. One of the reasons is that the ultra grazing geometry makes the performance of the mirror more forgiving of roughness errors. The analysis further showed that for "normal" grazing incidence and state-of-the-art mirrors, focusing will be limited to 10:1 demagnification. It is clear that the use of ultra grazing incidence increases the mirror length and therefore may have strong implications for the detailed design of the XFEL optical systems. Even for plane mirrors, adaptive optics schemes will be necessary to keep the mirror surface in a plane shape.

Dose reduction by ultragrazing geometry The heat load problem is a central issue for mirrors also. The average power load is very reasonable (less than 0.1 W/mm^2 or even less than 0.01 W/mm^2). Cooling will be required to satisfy tight tolerances and avoid thermal gradients. Internal cooling could be favorable here as it is more efficient and reliable than indirect (side) cooling schemes. While the average power is moderate, the peak power on the mirrors may be in the GW range. At these values, the principal problem may no longer be thermal distortion, but rather the possibility of plasma formation at the mirror surface, which affects the reflection efficiency and may even cause permanent damage. Formation of a plasma will depend on the radiation dose per pulse, which we will quantify as the energy absorbed per atom per pulse.

In the X-ray range, grazing angles of a few mrad or less are commonly used to obtain good reflection efficiency and the added benefit of reduced power per unit area on the mirror surface. The induced heatload, however, is related to the deposited energy per unit volume, i.e. the dose. This quantity becomes small only at incidence angles significantly smaller than the critical angle α_c for two reasons: First, the penetration of the field into the mirror becomes roughly independent of the angle and no longer compensates the increasing size of the beam footprint. Second, the mirror also starts to reflect efficiently. Because the beam footprint and the reflectivity increases linearly with decreasing α, the dose scales roughly with α^2. Figure 5.2.5 shows the dose per atom for several interesting mirror materials [24]. The onset of the advantageous α^2 dependence for all materials occurs near half the glancing angle α_c. It is evident that beryllium has a clear advantage over gold ($> 10^2$ at X-ray energies) in terms of the atomic dose required to reflect a given energy at a given angle. If we adopt 0.01 eV/atom as a tentative value for the limiting dose per pulse, then the estimate gives

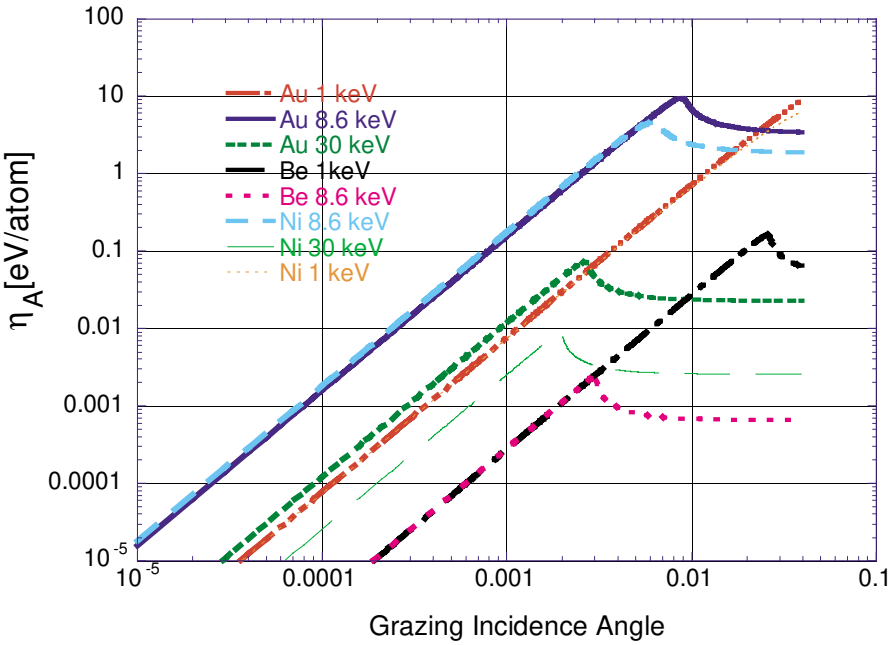

Figure 5.2.5.: *Dose per atom as function of grazing incidence angle α for various materials and photon energies [24]*

.

about 1.2×10^2 J/cm^2 as the limiting energy density for a beryllium mirror at 8 keV at normal incidence. The same limit applies for any angle down to $\alpha_c/2$ apart from the small region around the bump at α_c. This suggests that beryllium or carbon coated mirrors operating at grazing angles of a fraction of a milliradian will be useful for XFEL applications.

In summary, in terms of dose as a measure for the heat load, it is only for grazing angles below $\alpha_c/2$ that grazing incidence provides any advantage at all. This implies that mirrors exposed to the high peak-power of the XFEL beam have to be operated at ultra-grazing angles. It is interesting to note that the use of very low grazing angles is also highly beneficial in reducing the effects of optical surface errors on the mirror performance. To conclude this part about mirrors, it can be stated that the variation of the grazing angle does provide a possibility to reduce the absorbed dose per atom and therefore improves the radiation tolerance of mirrors. Furthermore, low grazing angle geometry improves the error tolerance in focusing applications. It is clear that due to the resulting mirror lengths, the R&D program needs to emphasize the accuracy improvement of long mirrors. Additionally feasibility limits have to be discussed.

5.2.3.2. Refraction optics

A recently developed technique to build X-ray refractive lenses provides a new and promising optical element not only for focusing but also for imaging applications [25]. Compared to mirrors, the beampath is straight and much larger demagnification is possible. With a parabolic shape, the lens is free of spherical aberration. In practise, an X-ray refractive lens

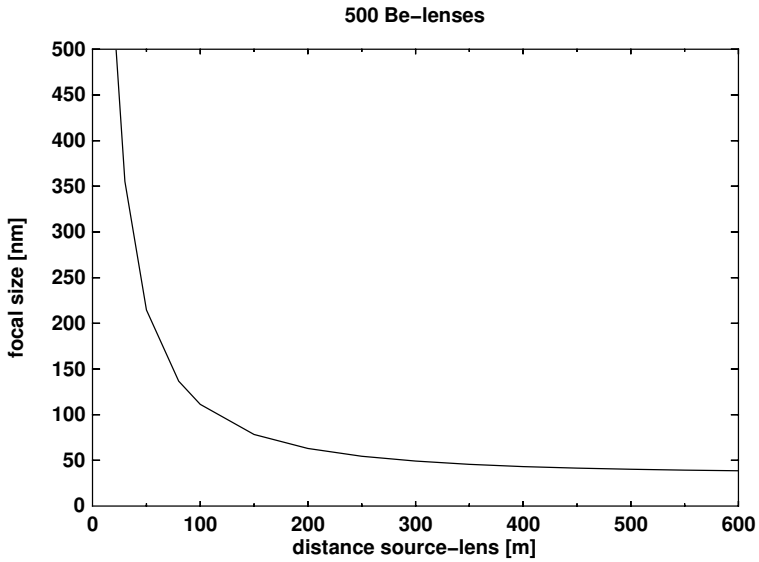

Figure 5.2.6.: *Size of the focused XFEL beam obtained with a stack of 500 refractive Be lenses. The calculation includes the effects of diffraction and Compton scattering, but neglects small-angle scattering.*

is a compound device: single refractive lenses with long focal lengths are arranged in a stack to form an effective lens with short focal length. This compound refractive lens will have a focal length that can be adjusted by adding or removing lens elements in the lens stack. Due to its small size and short focal length, the lens can easily be integrated in an experimental setup.

The geometrical size of X-ray refractive lenses is perfectly matched to the XFEL beam. The acceptance of a lens is limited by absorption to a diameter of $\approx$ 1 mm for low-Z materials like Be, B_4C or C. A focal length ranging from 0.1 m to 100 m seems feasible. The focal size is determined by the coherence, the natural collimation of the beam, and the numerical aperture of the lens. In Fig. 5.2.6, the diffraction-limited focal size for a stack of 500 Be-lenses is shown as a function of the source-to-lens distance. The calculated minimal focal size ($\approx$ 500Å) is larger than given by the geometrical demagnification and will further increase due to small-angle scattering in the lens material (which has been neglected here). The transmission of such a lens at 1Å will be in the few percent region, depending on the lens material.

Further detailed studies of the application of refractive lenses for XFEL experiments and the fundamental limits of coherent beam focusing are necessary. The main topics will be small-angle and Compton scattering, wavefront distortions, temporal issues, and the choice of the appropriate material and related manufacturing processes.

5.2.4. Optical delay lines

Using single-crystal diffraction, it should be feasible to build X-ray delay lines with variable delay times analogous to what is done with mirrors in the visible. In these devices, part of the XFEL beam is transmitted through a beam splitter, for example a thin diamond crystal, then doubly reflected by a pair of crystals at 90° and recombined with the direct beam through a second beam splitter. The delay time can be adjusted by sliding the pair of crystals in a direction parallel to the incident beam. This scheme requires an adjustment of the energy, but suitable crystal reflections can be found so that the wavelength is quite close to 1.5-1.0 Å. Other schemes can be imagined for time-tunable, very fast pump-probe experiments where the divergent beam from an asymmetrically cut crystal is refocused onto the sample by a symmetric, curved crystal, maybe with a lattice parameter gradient. Here, the delay and the pulse length could be varied independently, typically between 1 and 200 fs.

5.3. Experimental Techniques

5.3.1. Time-resolved experiments

The section describes state-of-the-art time-resolved experiments that could be performed at an XFEL and determines what instrumentation developments will be required to bring these experiments to fruition. The scientific justifications and impact of such experiments have been discussed in the scientific case. The following sections describe pump–probe schemes, synchronization of these sources and a proposal for a photon pulse echo experiment employing pulse delay techniques. Furthermore an attempt is made to examine the instrumentation research and development (R&D) needed to ensure the success of time-resolved experiments. Here three areas are critical, namely the synchronization of pump and probe pulses on a subpicosecond timescale, timing detectors to determine the relative arrival time between pump and probe pulses, and X-ray optical components to effectively and efficiently split and delay X-ray beams.

Clearly, the unique aspect of an FEL source is its short pulse duration and high instantaneous flux. It will be possible to perform subpicosecond-resolution experiments with X-rays. X-ray scattering in general is a snapshot technique which gives us information on atomic positions on a time scale determined by the bandwidth of the monochromator. This is typically a few fs. In a real present-day experiment, however, we observe not a single snapshot, but an average over a macroscopic number of individual pictures. This average has to be taken over the time and the spatial coordinates. With the XFEL we will have a tool at hand allowing this averaging procedure to be largely overcome. The coherence allows observation of the structure of the illuminated individual sample volume rather than the average structure. The extremely short pulse duration of only 100 fs together with the high brilliance, restricts the temporal average to processes faster than this time.

In fact, pulse durations even shorter than 100 femtoseconds may be useful for some scientific applications. The pursuit of shorter pulses should be explored through both accelerator techniques and optical techniques or a combination of both (i.e., pulse compression via optics of a chirped beam). Single pulse operations are a must for the FEL (i.e., a mode where

a single pulse of X-rays is delivered at a user-specified repetition rate), as this will benefit a large number of pump–probe experiments, in particular when femtosecond visible lasers, which run at a repetition rate of few kHz, are used as pumps. As the proposed fill pattern of bunch trains contains 11500 pulses with a gap of 93 ns between them, data processing (reading out of the data acquisition detectors, timing detector, etc.) should be completed in less than 93 nanoseconds in order to fully utilize the delivered beam. Since detectors with such high-speed readouts may not be available on day one of the FEL operations, flexibility in the time structure of the X-ray pulses is essential. Variably spaced pulses to better match detector readout times, decay times of sample excitations, etc., will be a very valuable asset of the FEL.

5.3.1.1. Pump-probe techniques

To take full advantage of the extremely short X-ray bursts from the FEL, the sample excitation must also be very rapid; otherwise a temporal blurring will occur. This implies that in all likelihood the pump should also be a photon beam. Mechanical excitation seems very unlikely at these time scales, and even electrical stimulation seems marginal at best. Three types of photon-pump – photon-probe techniques are proposed here (see Fig. 5.3.1):

- separate (independent) pump and probe light sources (such as a visible light laser and the XFEL beam),
- pump and probe light sources originating from the splitting of a single beam produced by an insertion device (with one partial beam delayed relative to the other)
- pump and probe beams that are generated by the same electron bunch but from two insertion devices (again with one beam delayed with respect to the other).

In addition, other pump techniques could be applied at longer time-scales by making use of the high flux of the XFEL in investigating long irreversible processes. In most of these processes the excitation of the sample is limited to timescales longer than picoseconds. Electrical or mechanical stimulation may be used here, but shock-waves produced by lasers are also diffusion limited and require several picoseconds. In these cases no problem of synchronization between sources occurs. It will nevertheless be important to determine the time window of investigation, as the pulse structure of the present design of the XFEL does not provide a high continuous repetition rate in the Hz to kHz range. These experiments may better be carried out at storage rings offering continuous repetition rates of several MHz.

5.3.1.2. Synchronization

Independent pumps and probes will require synchronization to enable standard time-delay schemes, where the arrival time of the probe relative to the pump can be predetermined through the use of delay lines. At present the best achievable synchronization between the two sources is of the order of a few picoseconds. Picosecond time-resolved work can be performed using known techniques. Subpicosecond synchronization, on the other hand, needs further R&D. Possibilities using the photocathode laser [26] or other pick-up signals from the

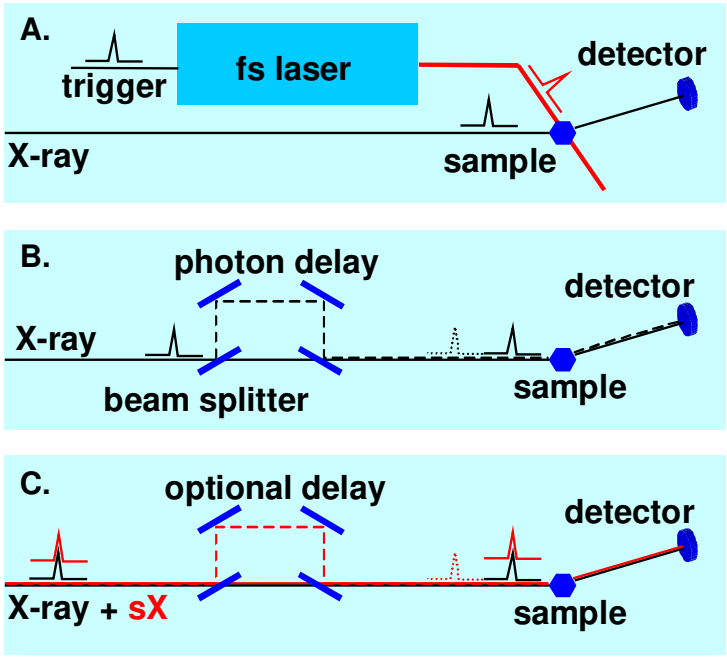

Figure 5.3.1.: *Three schemes for pump–probe experiments employing light as a pump. Either external (femtosecond) laser sources (A) could be used, or split-beam techniques using FEL light at same wavelength (B) or different wavelengths (C) are proposed. In the last scheme, photons labelled "sX" are generated with a different wavelength than photons labelled "X-ray" by an additional insertion device using the same electron bunch.*

electron beam have to be investigated. Furthermore, the temporal jitter between pump and probe can be used to randomly sample various time delays in subpicosecond time-resolution experiments. In this case, a post-processing of the relative arrival time of the pump and probe for every excitation is required. To achieve subpicosecond resolution, the detector will need to have very good time resolution on the order of 100 fs or below.

Using beam splitting techniques (as is almost always done in visible laser pump–probe experiments), precisely controlled temporal resolution down to several tens of femtoseconds should be achievable, limited only by the stability of the optics used to delay one of the X-ray pulses relative to the other. To delay the beam, crystal optics has to be applied, which will split the beam into two beams, delay one of them, and recombine both beams on one path. Although proposals for X-ray beam-splitter schemes can be found in the literature [27], considerable work will need to be undertaken to make them into to a routinely used optical element. If perfect single crystals are to be used as splitters and/or delays, a detailed understanding of the time response of dynamically diffracting crystals needs to be developed [28, 29] (see also Sec. 5.2 and the next paragraph on "Photon pulse echo"). To calibrate the delay line, timing techniques need to be developed to ensure that accurate timing can be achieved.

The technique to use two different frequencies generated by the same electron bunch may

be a more novel approach to the area of photon-pump – photon-probe experimentation. The concept is very interesting in view of the critical synchronization of beams of two "colors" or wavelengths. It may be an alternative to the optical laser – XFEL approach, which is felt to be limited in the level of synchronization that can be achieved (see above). In fact, the approach itself should most probably be considered as an R&D activity in and of itself: FEL accelerator physicists need to determine if a high-quality X-ray beam and visible light beam can be generated from a *single* electron pulse (in one or two separate insertion devices) with subpicosecond timing between the two light pulses. The electron beam could, e.g., be passed through a second set of undulators (after passing through the FEL undulator) to produce another frequency radiation. If that radiation is in the visible region of the spectrum, its intensity might be enhanced by a single-pass laser amplification scheme. Clearly, R&D will be needed to explore the timing jitter between radiation pulses generated by the same particle beam in separate insertion devices. In addition to the accelerator R&D required for this approach, X-ray delay lines and timing detectors will again be required for this technique.

R&D efforts for time-resolved experiments The most important and critical R&D activity will be the development of a detector that will allow measurements of the relative arrival times of the two photon beams with a resolution below 100 fs. This device may be called a *timing detector*. This brings up a second critical area of R&D for time-resolved experiments utilizing the X-ray FEL, namely, the design, construction, and development of X-ray beam splitters and delay lines.

5.3.1.3. Photon pulse echo

Because thermal neutrons match both the energy and the wavelength of thermal excitations in solids, experiments probing atomic dynamics with atomic spatial and energy resolution have been a domain of neutron scattering for several decades. Only in the last few years has the overwhelming increase in spectral flux offered by synchrotron radiation sources made inelastic X-ray scattering experiments with the required monochromaticity of 10^{-6} to 10^{-7} feasible. Inelastic scattering measurements are now performed using a triple-axis set-up in backscattering geometry [30], photo-correlation spectroscopy [31] and nuclear resonant techniques [32]. While energy domain techniques benefit mainly from the increase in brilliance at an XFEL, time-domain techniques will in addition profit from the unique beam time structure. In order to fully benefit from the improvement in pulse length, most experiments require a corresponding improvement in detector resolution.

An experiment is proposed that makes use of the extreme reduction of the bunch length to study microscopic dynamics directly as a function of time. The idea is to transfer the scheme of the (resonant) neutron spin echo technique [33] to the X-ray case. Information on the sample dynamics is obtained by recombining two pulses which have been elastically scattered by the sample with a time delay τ and observing the interference pattern of the two pulses. As in the NSE case, information on the intermediate scattering function S(q,t) is obtained by a steady state experiment, without the need for fast detection.

The experiment consists of two X-ray delay lines D1 and D2 located before and after the

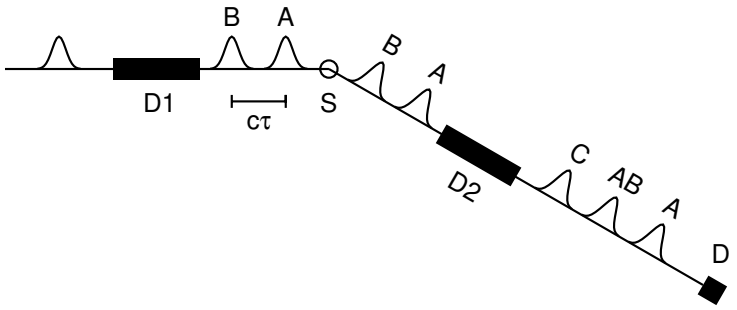

Figure 5.3.2.: *Schematic experimental set-up. The primary spectrometer (D1) splits an XFEL pulse into two pulses separated by the delay time τ (c is the speed of light). After scattering off the sample (S), the two pulses travel through the secondary spectrometer (D2) where either pulse may be delayed. The detector (D) receives three separated pulses A, AB and C as described in the text.*

sample, respectively (Fig. 5.3.2). The first part prepares two pulses, A and B, separated by a fixed delay so that both pulses probe the sample structure at different times. The second delay line D2 adds a second delay of exactly the same quantity so that the pulse delayed in D1 and the one delayed in D2 exactly overlap. Consequently, three pulses arrive at the detector:

- pulse A, which is not delayed at all.
- pulse C, which is delayed in both parts of the spectrometer.
- pulse AB, which is a coherent sum of that part of the reference pulse A which is delayed in the second part and the pulse B delayed in the first part, but not in the second. This contains the information on the structural changes during τ.

Pulses A and C contain no information on the sample dynamics and provide an inherent background. If one assumes that the separation of the pulses τ is much larger than the width of a pulse (which corresponds to a path difference in the delay unit of some 24 μm) the intensity is simply the square of the three terms - cross-interference terms are negligible. If the transmissions of the spectrometer branches are equal, the amplitude in the pulse AB is proportional to S(q,t), and the intensity reads

$$I(q,\tau) = I_0(S(q) + 4S(q,\tau) + S(q)) \,, \tag{5.3.1}$$

where $S(q)$ is the static structure factor and $S(q,t)$ is the intermediate scattering law or relaxation function. Up to this point the experiment does not require a time resolving detector to extract the dynamic information. Time resolution is merely given by the delay time τ. A fast detector will nevertheless be beneficial to reduce the background.

The problem remains to design a delay unit, with the option to copy it with high precision. A rectangular geometry may be realized for example using a silicon (553) reflection at 0.9974 Å. Certainly the requirements on stability are challenging. In order to achieve a coherent superposition of the delayed pulses the two delay units must be perfectly identical (modulo wavelength). Moreover the path length of the beams in the delay units must be stable during data acquisition to fractions of the wavelength. It should be noted, however, that the sub-Å precision is required only on a relative scale. To relax the requirements even more, a dynamical mode of operation may be used. By changing the path length in one delay unit by a fraction of the wavelength from bunch to bunch, a signal perfectly similar to a resonant spin echo signal is created.

In the following, the range of dynamical parameters covered by a X-ray pulse echo experiment will be estimated. If one assumes a wavelength of 1 Å and a maximum scattering angle of roughly 160°, the maximum wavevector transfer q is 12 Å^{-1}. The lower limit is determined by the divergence of the beam, which is again extremely low for an XFEL beam. The minimum wavevector transfer is then $6 \cdot 10^{-5} \text{Å}^{-1}$, well within the small angle scattering regime. Even if some further imperfections of the real experiment are allowed for, this range covers the entire microscopic length-scale up to the range of light scattering techniques. Concerning the range of relaxation times (and corresponding energy transfers in Fourier space), one certainly has to consider first the timing of the XFEL. A range from the bunch length (100 fs) to the bunch repetition (93 ns) is accessible. Expressed in delay line path differences this corresponds to 30 μm and 30 m, respectively. The first value will be difficult to achieve because of limitations of the beam size and the crystal sizes. However, a value of 100 fs, corresponding to an energy transfer of 40 meV (or a path difference of 30 μm), is a typical value for optical phonons in simple metals. So it seems worth the effort to work on the realization of such small path differences. On the other extreme, 30 m may be accessible by increasing the number of reflections in the delay unit. However, the maximum length of the delay path is also limited by the increasing path difference, even with a beam collimated to micro-radians.

Possible applications will cover quasielastic scattering to probe diffusive motions or relaxation and inelastic measurements with high resolution. The wide time-interval offered by this technique is particularly valuable for systems showing non-exponential behavior of the relaxation function, like glasses or bio-molecules. In the inelastic (short time, few ps) regime, the phonon density of states in particular that of low-lying excitations, will be accessible. In this field there is still a controversy about the influence of disorder on phonon propagation. Damping mechanisms determining phonon lifetime play a dominant role in this time range.

5.3.2. Coherence experiments

5.3.2.1. Imaging

Hard X-ray radiation from the XFEL source enables development of novel methods for imaging of objects and processes in materials science, biology, and microelectronics. It also opens a way for significant developments in existing imaging techniques and promises an improve-

ment in resolution and application range of the well established methods. The main novel properties of the XFEL imaging techniques will rely on the high intensity and full transverse coherence of the diffraction-limited source and on the short pulsed time structure, which allows time resolved measurements. These very properties, however, present a great challenge for the experimental techniques and the apparatus used.

In general, imaging techniques can be classified as full-field or scanning. Among the full-field techniques are absorption radiography and tomography, phase-contrast tomography, phase contrast imaging, tomography in holographic geometry, and diffraction topography, to name just a few. They can be implemented at the XFEL at various levels of resolution by direct (coherent) illumination of the sample or by adding magnifying optical elements: beam expanders (asymmetric crystals), Fresnel zone plates (FZP), or Bragg-Fresnel optics (BFO). With fully coherent beams, the diffractive optics promises to reach a resolution of 10 nm for 10 keV radiation, compared to the 100 nm limit at third generation synchrotron sources.

Very promising is flash imaging for time-resolved studies of processes. The high brilliance of the source and the time structure of the beam also open ways to image new classes of objects, like laser-generated plasma, that could not be studied on existing X-ray sources. Scanning methods, on the other hand, require focusing optics to provide a small beam cross-section at the sample position and microstages for mechanical movements of the sample. There are wide prospects of combining scanning imaging techniques with other methods of X-ray analysis (chemical mapping, trace element mapping, magnetic circular dichroism, magnetic diffraction, microspectroscopy, etc). The main problems of both classes of imaging methods will be radiation damage in the sample and high load on the detector. Thus one will need to attenuate the beam with absorbers to control this damage.

Novel imaging techniques with coherent radiation The full transverse coherence of the beam allows the development of novel methods for the investigation of crystalline and non-crystalline matter. Many of these methods are already known from the domain explored by optical lasers, but the use of short-wavelength radiation in the Å regime will improve the resolution and expand the range of applications. Methods to be mentioned here are off-line holography, interferometric methods and speckle interferometry.

The use of coherent beams will enable the development of new techniques like lensless imaging, where the information about wave front form and intensity distribution provides phase information and allows the image of the object to be reconstructed with holographic methods. In the case of a fully coherent beam, the boundary between holography and diffraction vanishes, so that the same approach can be used to obtain unambiguous structural information from diffraction patterns. The new convergent-beam X-ray diffraction method [34] has an analogy in convergent electron diffraction. In contrast to most modern X-ray scattering methods, which use plane waves in the far field (Fraunhofer diffraction), the proposed method takes the curvature of the wavefront into account and is based on the Fresnel formalism. Its advantage is the unambiguously obtained phase information.

Another way to access phase information is based on oversampling of the image in scattering (diffraction) patterns of non-crystalline objects and nanocrystals. It has already been developed and was described in Ref. [35]. This method requires in addition the scattering data information about the boundaries of the sample in real space.

Single molecules often scatter too weakly to produce patterns with sufficient statistics for applications in imaging or scattering, even with an XFEL. On the other hand, it will be possible to obtain relevant data from small clusters or other arrays of molecules. The possible technical ways are either to organize arrays of $10^4 - 10^5$ equivalently oriented identical single molecules frozen in a substrate, or to add up scattering patterns from single molecules oriented means of e.g. laser light or a magnetic field. The images obtained in this way will most probably need additional treatment with image analysis and transformation methods known from cryo electron microscopy [36].

5.3.2.2. X-Ray Photon Correlation Spectroscopy

Complex relaxations in disordered systems have been studied successfully by scattering of both visible light and neutrons. Neutron-based techniques (inelastic and quasi-elastic neutron scattering, neutron spin-echo) can probe the dynamic properties of matter at high frequencies from 10^{14} Hz down to about 10^8 Hz and achieve atomic resolution. Scattering vectors $0.02 - 10\text{Å}^{-1}$ are usually accessible in these experiments. Visible-light photon correlation spectroscopy covers the low frequency dynamics ($\omega < 10^6$ Hz), but probes only the long wavelength ($q < 4 \cdot 10^{-3}\text{Å}^{-1}$) region in materials which do not absorb visible light. For several years, partly coherent X-ray beams at third generation synchrotron radiation sources have offered the possibility of q- and time-domain speckle spectroscopy. X-ray Photon Correlation Spectroscopy (XPCS) is capable at present of probing the low-frequency dynamics (10^6 Hz to 10^{-3} Hz) in a q range from $1 \cdot 10^{-3}\text{Å}^{-1}$ up to several Å^{-1}, thus providing atomic resolution. At the XFEL the unprecedented coherent flux and time resolution will allow time-domain studies using this technique as a complement to inelastic scattering. Thus the time domain for XPCS could be stretched to up to 10^{13} Hz at XFEL sources. The different domains are illustrated in Fig. 5.3.3 in frequency–wave vector space showing how use of XPCS techniques at XFEL's could close the gap between present day possibilities and inelastic X-ray and neutron scattering.

Basics X-Ray Photon Correlation Spectroscopy probes the dynamical properties of matter by analyzing the temporal correlations between photons scattered by a material. Correlations of the scattered intensity can be quantified via the normalized time correlation function

$$g(\tau) =< n(\tau)n(\tau + t) > / < n >^2 \tag{5.3.2}$$

where $n(t)$ is the number of scattered photons at time t and the brackets denote the time average. XPCS requires the sample to be illuminated coherently. Thus an intense X-ray beam with sufficiently large transverse (ξ_t) and longitudinal (ξ_l) coherence length is necessary. The longitudinal coherence length $\xi_l = \lambda \cdot \lambda / 2\Delta\lambda$ depends on the monochromaticity of the beam. The intrinsic bandwidth of $\approx 0.1\%$ for the SASE line yields $\xi_l = 100$ nm. Larger longitudinal coherence lengths can be achieved by further monochromatization. For example, $\xi_l = 1\mu$m is feasible using the diamond (111) reflection with a bandwidth of $6{\cdot}10^{-5}$. The longitudinal coherence length must be larger than or equal to the maximum path length difference in the sample under investigation. This is equal to $2h \cdot sin\,\theta \cdot tan\,\theta$ in transmission geometry or

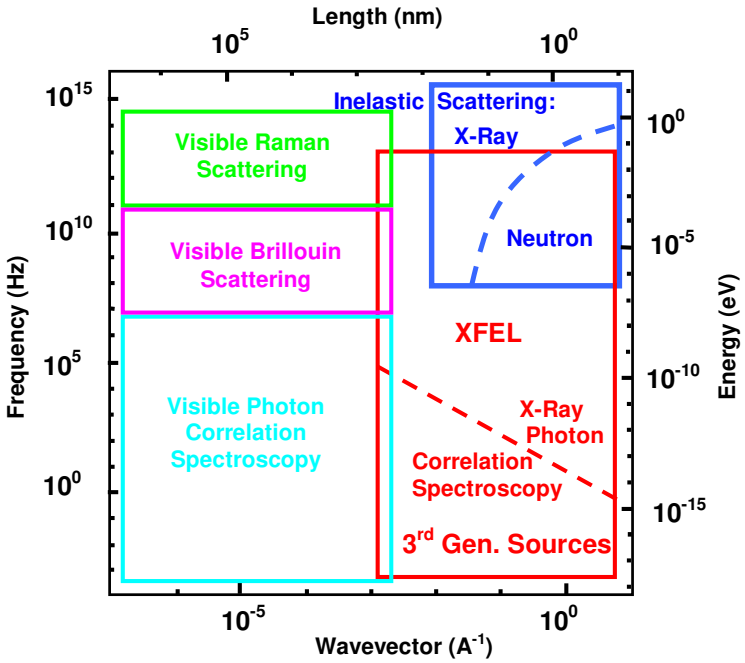

Figure 5.3.3.: *Plot of the frequency–wave vector space important for condensed matter processes. Areas covered by the various methods are indicated.*

$sin(2\theta)/\mu$ in reflection geometry. Here h is the sample thickness and μ^{-1} the absorption length. Thus ξ_l sets a limit for the largest usable scattering vector q. The transverse coherence length $\xi_t = (\lambda/2)(R/\sigma)$ is usually determined by the source size σ of an incoherent source and the distance R from the source. For the fully transverse coherent XFEL beam, the longitudinal and transverse coherence length at the position of the sample is on the order of 100 nm and 400-800 μm, respectively. Typical values for the transverse coherence length at third generation synchrotron sources are on the order of 10 μm. The transverse coherence furthermore determines the angular size λ/ξ_t of an individual speckle when the aperture is matched to the transverse coherence length and thus defines the required spatial resolution of the detection system.

Application of the XPCS technique The XFEL bunch-trains (1 ms long) consist of at most 11500 bunches with a length of 100 fs and a separation of 93 ns. This time structure opens two important time windows for spectroscopy with coherent X-rays. First, XPCS experiments similar to those performed today at third generation sources can be performed with a timing given by the bunch-train repetition rate (5 Hz), thus giving access to the regime of very slow relaxations with correlation times below 1 second. The significantly larger coherent flux will allow the study of a greater variety of systems. In particular, systems with small (atomic) correlation lengths could be studied. Access to correlation times above 1 sec is obviously of utmost importance. One could in principle imagine performing experiments

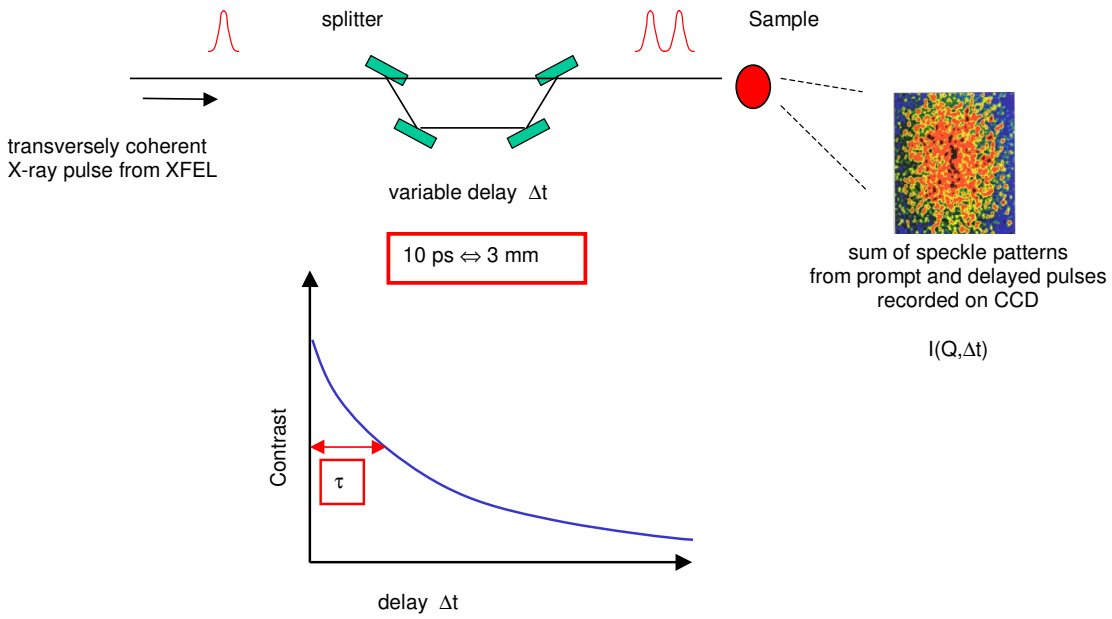

Figure 5.3.4.: *A single XFEL pulse passes a beam splitter, generating two pulses travelling different paths. After the two paths are recombined, the two pulses impinge on the sample at a time difference Δt which can be varied by changing the relative crystal position. The two individual scattering patterns are integrated with a CCD detector, resulting in the sum of the speckle patterns from the prompt and the delayed pulse.*

at the repetition rate of individual bunches (1/93 ns) within a bunch-train, limited only by the maximum length of a single bunch-train (1 ms). A second, very exciting regime is that of the 100 fs pulses. A time resolution equivalent to or larger than the pulse width could, in principle, be achieved, giving access to frequencies up to 10^{13} Hz. This would allow time-domain studies complementary to inelastic scattering. New spectroscopic techniques need to be explored in this time range. Alternative schemes taking advantage of the time structure of the XFEL could consist of splitting a 100 fs pulse and introducing a variable time delay in one of the beam paths [37]. This is depicted in Fig. 5.3.4. A time-delay of $\Delta t = 1$ps would require a path length difference of 300 μm. The dynamics of a system could be mapped by recording two "speckle" patterns at time t and $t + \Delta t$. Repeating this procedure for a series of different delays might allow the measurement and analysis of correlation functions. Path length differences between 300μm and 300 mm appear feasible. These would allow dynamics between 10^{13} Hz and 10^{9} Hz to be traced. The study of fast dynamics clearly requires appropriate detection systems. The recording of a two-dimensional speckle pattern with an angular speckle size of $\lambda/\xi_t = 2\mu$rad and a time resolution of 1 ps would require a major effort in detector development.

5.3.3. X-ray diffraction

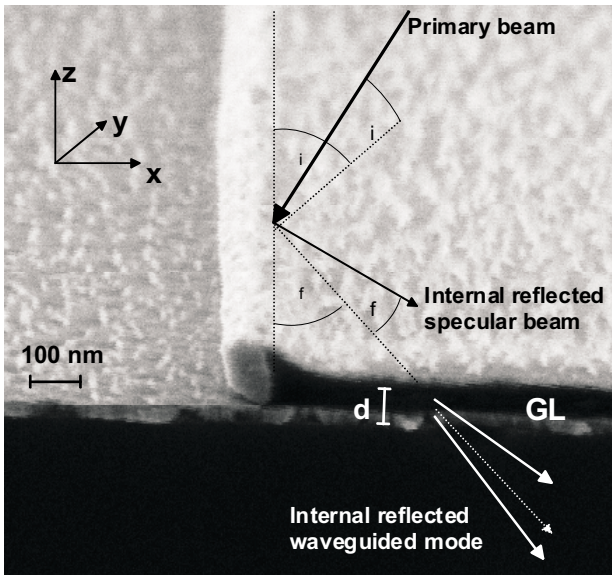

Figure 5.3.5.: *Electron micrograph of a sample structure with defined nano-channel. The waveguided mode trapped in the vertical (z) direction impinges at grazing angles on the one-dimensional edge and is reflected along x (see ref. [39]).*

5.3.3.1. Diffraction and imaging from nanoparticles

Currently, X-ray nanobeam production by waveguide optics has been developed to achieve a two-dimensionally confined X-ray beam with a cross-section well below the μm range (Fig. 5.3.5). The first results indicate that present-day optics with one dimension in the range of 10-100 nm [38] can be generalized to a point source [39], which may be used to scan a sample in order to map out heterogeneous macromolecular assemblies, in particular within a living cell, by a combination of a two-dimensional waveguide setup and a micropipette sample fixation. Flux estimates show that this setup is beyond the capabilities of present day-sources for the most interesting (e.g. weakly ordered) systems. The advent of the XFEL may give rise to significant advances.

Beyond space-resolved diffraction and spectroscopy with spot-sizes in the nm-range, imaging of individual macromolecular assemblies may become possible with phase contrast projection microscopy, as sketched in Fig. 5.3.6. Radiation damage might limit the achievable resolution. In view of recent advances in the reconstruction of sample images from continuous diffraction patterns [35] and the emerging possibilities of nanometer sized X-ray beams, it is anticipated that this will evolve into a productive field in the near future.

Surfaces and Clusters The XFEL beam source size and divergence are very suitable for diffraction studies of surfaces and clusters as long as the focussing can be achieved faithfully, with a reasonable demagnification (around 100:1). The required instrumentation would be a diffractometer with a very long detector arm, able to reach the 2Θ-angles for diffraction from

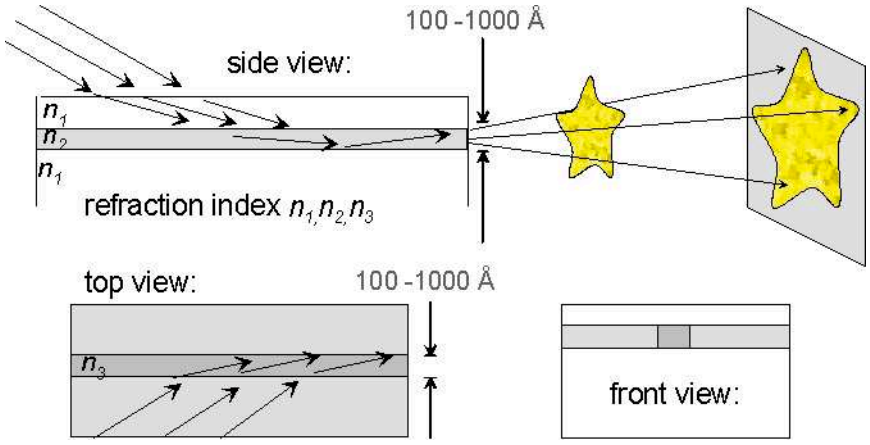

Figure 5.3.6.: *Sketch of an X-ray waveguide device with laterally defined guiding channel. At the side of the structure, a fully coherent and divergent beam exits the channel. The phase contrast created by passing a macromolecular sample is projected and recorded in the far-field pattern. Only a short pulsed and coherent beam such as that from an XFEL can be used to image macromolecular entities rapidly moving on the nanometer scale.*

small-unit-cell crystals. The length of the arm depends on the pixel size of the detector. It is necessary to have several pixels within each "speckle" of the diffraction pattern. The speckle size is the inverse of the particle size under investigation, so the length of the detector arm can be used to adjust the angular acceptance for each pixel. If the pixels are a few millimeters in size, the arm may have to be tens of meters long.

Most of the technical difficulties envisaged concern the detector. The goal is to have a 2D array with 100 ns time resolution. Energy resolution, although desirable, has a lower priority because a monochromator can be used before the sample. It is not clear now whether a CCD can be developed with sufficient readout speed, although this might be possible with a 1D linear array shifted at high speed into a 2D readout array. A better solution would be to develop a new detector based on pixels that are scintillators or avalanche photodiodes (APD's), each with an electronic readout chain. To accept very high count rates, the measurement should be analog, proportional to the number of photons. The detector would need to operate in at least two different modes: The first mode measures the temporal correlation function, pixel by pixel, without storing the full time sequence. The second mode would be triggered by an "event", as a particle-physics detector would be triggered. The event would be either a larger-than-threshold intensity, caused by a fluctuation in the sample, or an external trigger from the arrival of an irradiating ion. Full frames of pixels would only need to be saved around the time of the triggering event for later analysis. Since the experiments envisaged require seeking a small signal on a high background, the background subtraction should be an integral part of the signal processing in each pixel.

5.3.3.2. Surface experiments

Surface- and interface-related applications have been discussed in the scientific case. Here, the feasibility of the proposed time-resolved experiments is shown. Considering the XFEL properties, estimates will be given for experimental parameters based on the experience from present surface X-ray diffraction experiments.

Single pulse experiments on single-crystal surfaces A single 100 fs XFEL pulse contains about $2 \cdot 10^{12}$ photons within a bandwidth of 0.1 %. It is realistic to assume that the beam can be focussed to a spot size of about 1 μm^2 having a divergence of about 0.1 mrad.

At present, the BW2 wiggler beamline at HASYLAB delivers about $5 \cdot 10^{12}$ photons/sec within a bandwidth of 0.02 %. For diffraction experiments, the beam size is about 0.5 mm (V) x 3 mm (H). At comparable ESRF beamlines, the flux is about the same, but the beam-sizes are considerably smaller due to the lower electron emittance and the use of undulators. In a solid surface diffraction experiment, the sample is normally mounted vertically with a typical grazing angle relative to the surface of $\approx 1^o$. That means that only $\sin(1^o) \cdot$ 3 mm = 0.05 mm of the beam in the horizontal direction is used in the BW2 experiment, which is equivalent to $\approx 10^{11}$ photons/sec. Typical counting rates in a diffraction signal from a surface are 100-10000 counts/sec, depending on the surface. The XFEL would provide a 1 μm^2 beam at the sample so that all the photons would be used. Hence the number of diffracted photons in a *single* 100 fs XFEL pulse is about 50 times larger than the accumulated number in 1 sec from a present source.

The sample will presumably suffer from radiation damage, but with the small focal spot on the sample and the bunch-to-bunch distance of 100 ns, the sample could be translated with a speed of 10 cm/sec in order to probe a fresh surface region with each pulse. Then, in one pulse train (11500 pulses), a total area of 1 cm x $1\mu m/\sin(1^o)$ = 1 cm $\cdot$ 0.057 mm would have been damaged. This could presumably be handled as standard surfaces are of the order 1 cm^2 and samples under ultra high vacuum can be re-prepared by e.g. sputtering and annealing. However, it is important to consider the effects of sample damage *during* the X-ray pulse duration, as they may influence the diffraction signal. Such effects, however, may be minimized by using a short X-ray pulse since this limits the time the sample has to undergo a structural transition. Molecular dynamic simulations for interactions between conventional fs-laser and materials show that significant structural changes might occur [40] on time scales as short as 40 fs. For small beam sizes this effect may be significant.

Single pulse experiments on liquid surfaces Much faster time resolution can be obtained on two-dimensional powder samples like Langmuir layers or artificial lipid membranes. This will allow studies of structural changes during light-induced reactions in Langmuir layers or even artificial membranes. By performing pump-probe experiments, a reaction can be followed step by step in time. By reconstructing that information, it will be possible to obtain molecular movies of the intermediate steps. One application is the study of structural changes in azobenzene liquid crystalline side chain polymers, materials that are potential candidates for optical storage devices. These molecules undergo a light-induced cis-trans conformational change, and major structural changes of the entire material surface

are known to occur on time scales shorter than 5 ns. Another application is the study of light-induced structural changes in membrane proteins. A model system of this kind is the purple-membrane molecule bacteriorhodopsin. The molecule has a light sensitive group, a chromophore retinal, that changes its configuration when activated by light. This again causes changes in the protein that allow proton transport through the membrane. These structural processes are believed to happen on picosecond time scales, which are accessible by the XFEL.

At the BW1 undulator beamline at HASYLAB, where scattering experiments from liquid surfaces currently are being performed, the photon flux is about $2 \cdot 10^{11}$/sec into a beam spot of 0.1 mm (V) $\cdot$ 2 mm (H) (within a 0.1% BW of the Be monochromator). At a typical 0.1^o angle of incidence, the footprint along the surface is 57 mm, of which only about 1/5 is used in a diffraction experiment. The diffraction signal is measured by scanning the detector horizontally using a position-sensitive detector (PSD) and Soller slits giving 0.1^o resolution for the in-plane scattering. The PSD is used to collect the scattering out of the surface plane. Typically, counting times of 10 sec are needed, meaning that $4 \cdot 10^{11}$ incoming photons are used/measured per in-plane scattering angle.

By focussing the XFEL beam to $1\mu\text{m}^2$, the footprint would be only 0.6 mm. The same in-plane resolution could be achieved by using an area detector where the footprint itself acts as a slit. Then a full diffraction pattern may be recorded within a single 100 fs XFEL pulse at the same resolution and even with 10 times more signal intensity than is possible today.

Crossed beam setup As has been discussed above, the XFEL brilliance allows for structural studies with a single pulse, e.g. pump-probe experiments. In order for such experiments to be carried out, it is necessary to have two pulses that are time-locked with an accuracy which exceeds any time-resolution that is aimed for in the experiment. It is required that a second exciting (or probing) pulse be available and locked to the X-ray pulse to better than 100 fs. One could envision using the light from a second undulator or a time-locked ultrashort laser for this purpose. In the first experiments, this second light source would presumably serve as a pump, which initiates a structural change that can be probed in a time-resolved manner by the short X-ray pulse. An example of such an experiment is ultrafast melting probed by time-resolved diffraction [41]. For a certain class of experiments carried out on reasonably large uniform samples, another approach to the time-resolved studies can be taken. Instead of focussing the X-ray beam to a small spot on the sample, millimeter-sized quasi-parallel beams are used (Fig. 5.3.7). By having the pump and the probe beams strike the sample under a small angle relative to each other, a range of different time delays are probed across the sample. Typically the experiment is arranged such that this temporal walk-off occurs perpendicular to the diffraction direction. Thus, in the two-dimensional X-ray image, one direction indicates the diffraction angle while the perpendicular direction is associated with different time-delays between the pump and the probe. This allows a full time-resolved experiment in a single pulse. This may be useful in experiments where the sample preparation is time-consuming. In addition, by using large beams on the sample, the X-ray intensity is minimized, thus reducing the effects of radiation damage (of course at the expense of a larger footprint). At this point it is worth noting that the number of X-ray photons available from a single XFEL pulse is orders of magnitude higher than the useful

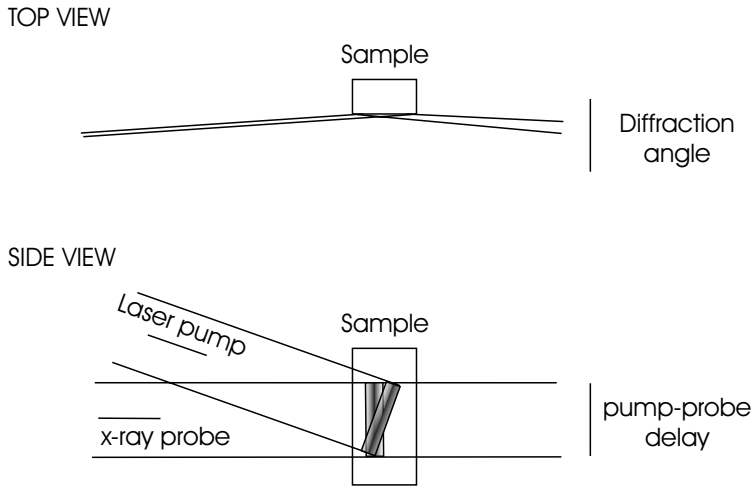

Figure 5.3.7.: *A schematic of the inclined-beams setup. The small angle between the laser and X-ray beams results in a variable pump-probe delay across the sample (side view). A two-dimensional image of a* single *X-ray pulse thus contains information about the diffraction pattern at a range of time-delays.*

flux per second in previous time-resolved diffraction experiments, which shows that single shot experiments indeed are a realistic option.

5.3.3.3. Polymer Scattering Experiments

The basic set-up for a scattering experiment at an XFEL is outlined in Fig. 5.3.8. Since the scattering reflections in polymer systems are usually relatively broad, no monochromatization of the SASE line is required; the line width $\Delta E/E \approx 0.1\%$ is sufficient. The contribution of the spontaneous undulator radiation will be negligible because it is more than five orders of magnitude less intense than the SASE line. In addition, the main contribution of spontaneous emission is also confined to a wavelength band of a few percent around the location of the SASE line. For most applications in polymer science, the SASE line should be tuned to a wavelength between 0.1 nm and 0.15 nm. If the sample and detector set-up is about 500 m from the source (this is a very reasonable assumption), a 60:1 demagnification of the source can be achieved at the sample position by placing a focusing element ≈ 8 m in front of the sample. This focusing element could be e.g. a refractive lens. The resulting focus at the sample has a diameter of ≈ 1 μm (FWHM), a divergence of 100 μrad (FWHM), and contains about 10^{12} photons in a single 100 fs photon pulse. Given the 100 μrad divergence, a rough estimate for the largest correlation distances observable in the scattering experiment yields 1000 nm, corresponding to the smallest observable scattering angles. The limit towards large scattering angles is defined only by the detector geometry. In principle, the classical wide-angle regime will be accessible with scattering angles up to about 50^o and corresponding correlation distances down to less than 0.2 nm. The observable correlation lengths thus cover the whole range from classical wide-angle x-ray scattering to ultra-small-angle x-ray scattering, and the actual observed angular range depends only on the size and

spatial resolution of the detector and its distance from the sample. Due to the extremely small size and divergence of the beam at the focus, the classical distinction between SAXS and WAXS becomes obsolete from the experimental point of view. The brilliant beam allows the use of position-sensitive detectors with small pixel size. Detectors with 30 μm pixel size and 1000 pixels for a given direction would be sufficient for most applications. Therefore, systems based on CCD technology would be appropriate. For fragile polymer samples, it

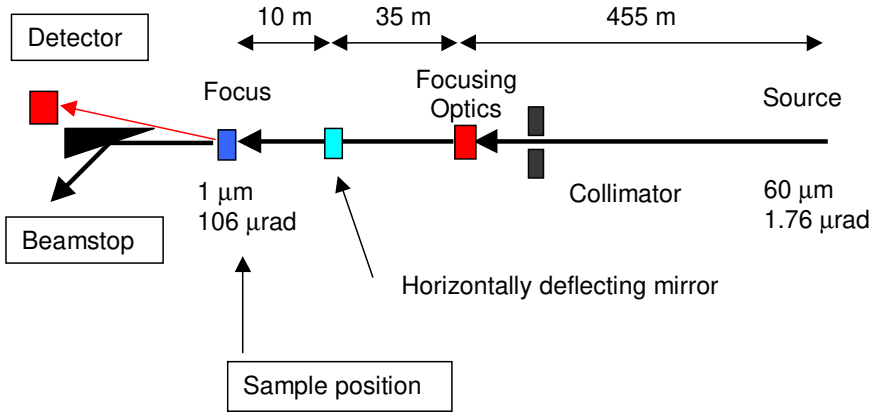

Figure 5.3.8.: *Schematic layout of a scanning microfocus experiment.*

may be necessary to expose a new sample area for each subsequent pulse of the bunch train. Therefore, a raster scan along the sample with sufficient speed is proposed by deflecting the beam periodically in the horizontal direction and, if necessary, by further superimposing this beam motion with a vertical motion of the sample itself. For the horizontal deflection, an oscillating mirror can be placed behind the focusing optics. The distance between this mirror and the sample is close to 10 m. If the mirror oscillates with a frequency of 100 kHz over an angular range of 10 μrad, the first 100 pulses of a full bunch train would be distributed over a 200 μm long line scan on the sample, i.e. the mean spatial distance between two adjacent pulses would be 2 μm.

If the sample performs an additional oscillatory motion in the vertical direction with a frequency of 1 kHz and 200 μm amplitude, the pulses of a complete bunch train could be distributed over a $200 \cdot 200\ \mu\text{m}^2$ sample area on a $100 \cdot 100$ pixel raster. The mirror could be e.g. a specially designed piezo-device with the reflecting surface directly evaporated onto it. Note that this scanning scheme is intended only to serve as an example. It could be widely modified by changing the frequency and amplitude of the oscillatory motions of mirror and sample, depending on the experimental conditions and requirements, on the technical feasibility, and on the time structure realized in the bunch train.

Single-pulse, stroboscopic, and pump-probe experiments It is considered that a two-dimensional scattering pattern is acquired with a single pulse. After the exposure, sufficient time is available to read out the detector. With this kind of experiment, conventional in-

tegrating detectors like CCD cameras or image plates can be used. Due to the short exposure time (≈ 100 fs), snapshots of rapidly changing structures can be obtained, i.e. the scattering patterns are not averaged over time when structural changes on a picosecond time scale or above are involved. If the structural changes are reversibly periodic, like for example segment reorientation in liquid crystalline polymers in response to a periodically changing external electric field, changes that occur during rapidly oscillating external mechanical forces, or laser induced conformational changes at optically active polymer sites, stroboscopic or pump-probe techniques could be used to resolve the time evolution of these changes. The moment at which the exposure takes place has to be synchronized to the phase of the external field or to the moment of external excitation. Then, a series of scattering patterns can be obtained as a function of the phase of the external field or of the elapsed time after excitation. This technique might be used to study the temporal behavior of new polymer systems for electronic devices.

Raster imaging An inhomogeneous sample may be scanned on a one- or two-dimensional grid with μm spatial resolution. Certain information in the scattering patterns can be used to reconstruct an image of the sample which visualizes the spatial distribution of structural properties. One possible application is the observation of structural changes along the cross section of a polymer fiber during melt spinning. Present techniques only allow the collection of scattering patterns which average over the whole cross section. Surface effects on the structure formation cannot be resolved [42]–[44]. If a periodic line scan is performed across the fiber during the continuously running fiber spinning experiment, a 100 μm thick fiber could be spatially resolved into about 100 distinct regions. This gives information on structural differences (crystalline structure, chain orientation) between material in the center of the fiber and that close to the surface.

Fast time-resolved measurement on homogeneous samples In the case of homogeneous samples, raster scanning can be used during structural changes on the nanosecond or microsecond time scale to obtain time resolved scattering patterns of these changes in real time, as already discussed above. The shortest time resolution is given by the time delay between subsequent pulses in the bunch train, i.e. 93 ns. On the other hand, the longest time available to follow the process is given by the duration of a complete bunch train, i.e. 1 ms. This may be relevant if irreversible processes are involved or if radiation damage caused by a single pulse exposure does not allow stroboscopic or pump-probe experiments.

Fast time-resolved measurement on inhomogeneous samples In some cases, structures are formed which are randomly distributed in the sample, such as micro-cracks (crazes) during elongation of a polymer sample. Scattering experiments with a micro-focus beam allow the observation of a single craze and the time evolution of its formation. However, the problem is that one does not know the locations at which crazes will appear. Rapid periodic scanning along a line can help to circumvent this problem. With the scanning scheme discussed above, each point in the line-scan can be observed with a time resolution of about 10 μs. In this experiment the sample can either be elongated continuously or

subjected to a periodic external force.

X-Ray Transient Grating Spectroscopy (XTGS) At an XFEL source the transient grating technique presently used for visible light studies [45] can be extended into the X-ray regime. With this technique the incoming beam is split into two transversely coherent beams which are crossed under an angle *s* to produce a standing wave field with periodicity $d = k_0 sin(s/2)$, where k_0 is the wavevector of the incident beams. The value of d can be in the range from one to several hundred nanometers. If a sample is placed in the standing wave field it will produce a periodic density modulation in the sample which has the same periodicity as the standing wave. If an XFEL is used, this modulation is formed during a single laser pulse, and after the pulse, relaxation will occur. A second pulse with a delay $Delta\ t$ to the first one forming the standing wave pulse can now be used to probe the periodic modulations within the sample by means of X-ray scattering. If the modulations relax, the scattered intensity will increase. Therefore, if the measurement is repeated with different $Delta\ t$, the time course of the relaxation can be followed. This can reveal valuable information about the local dynamics within the sample on a nanometer length scale.

5.3.4. Spectroscopy

5.3.4.1. Soft X-ray spectroscopy

The energy range from 500 to 3100 eV, covered by the SASE 5 undulator, is particularly interesting for several reasons. In this energy range, element-specific core level spectroscopy is possible under conditions where the depth sensitivity with respect to solid samples can be tuned from highly surface-sensitive to more or less bulk-sensitive. The available energy range covers the K-edges of the low Z-elements up to argon, the important L-edges of the 3d transition-metals, and the M-edges up to platinum and gold. Hence, a large variety of material science problems can be tackled using element specific core level spectroscopy.

Quite generally one can distinguish two classes of experiments which can be performed by exploiting the extraordinary source parameters. Firstly, spectroscopic experiments (e.g. photoemission, resonant absorption and resonant inelastic scattering, X-ray emission) already performed at third generation synchrotron sources could be carried out with much higher spectral and/or spatial and/or temporal resolution, respectively, sacrificing flux to gain resolution. Alternatively, samples which are much more dilute than those used to today may be investigated. Secondly, the source will make feasible new kinds of experiments in the XUV regime which so far have been only possible with conventional lasers in the visible or the UV range. Among those are correlated two-pulse pump-probe experiments, which will enable us to investigate ultrafast dynamical processes using element-specific spectroscopic techniques, as well as nonlinear spectroscopic experiments like two photon absorption processes.

Photo-electron spectroscopy Element-specific high-resolution core level photoelectron spectroscopy (XPS) with a spatial resolution in the range of a few nanometers may

become possible in the proposed spectral regime. This technique should provide unique information on the electronic structure and the chemical composition of single nanostructures or even large single organic molecules. To achieve this goal, technologies developed for scanning microscopy may be combined with photoelectron spectroscopy. Due to the high coherent XFEL photon density, it should be possible through the use of special optics based on photon sieves to illuminate only sample areas in the nanometer range with a sufficient amount of photons to perform spectroscopic investigations. A prototype instrument is currently under construction. It will be tested at the DESY VUV-FEL.

Photon sieves are diffraction optics consisting of a quasi random distribution of a large number of pinholes. The distance between the center of the pinholes and the desired focal spot has to equal a multiple of the wavelength. Higher-order reflections are effectively suppressed by the statistical distribution of the pinholes on circles around the center. Spatial resolution well below 0.5 μm, the diameter of the smallest pinhole available, can be achieved.

Time-resolved photoelectron spectroscopy: *in-situ* XPS The advantages to use photoelectron spectroscopy to study catalysts under *in-situ* conditions have been described in Sec. 3.6.3.1. Here a short summary of the proposed instrument and its usage is given. It is proposed to combine for these investigations the "Temporal Analysis of Products" (TAP) principle (see also Sec. 3.6.3.1 for further explanations) with the XPS technique so that XPS analysis will be possible under conditions close to those of the TAP experiment. In the TAP technique, the catalyst is placed in a vacuum system, and small feed quantities are pulsed onto the catalyst by high-speed pulse valves (typical opening time 0.5 ms). The product from the reactor is skimmed through a differential pumping system and finally analyzed by a quantitative mass analysis (QMA). A possible experimental setup is shown in Fig. 5.3.9, and the inset shows an alternative arrangement. The X-ray source is the SASE-FEL. It illuminates a sample that is placed in the mouth of a reactor tube that leads to the differentially-pumped analysis system of the TAP. After sample introduction, a reactant tube, which is connected to the pulse valves, is lowered to get in touch with the sample holder. The reactant tube has apertures for the X-rays to enter and for the photoelectrons to leave the sample. These apertures may be covered by a shield. Upon pulsing, most of the feed will diffuse through the catalyst when the apertures are covered. The product mixture can be analyzed in the TAP section. When the apertures are open, the catalyst sample will also be charged with the feed pulses. Most of the reaction mixture will now be pumped away through the apertures, which may include some feed that may not have had contact with the catalyst. It will be possible, however, to induce the adsorptive and reactive interactions characteristic for the conditions selected in the catalyst layers seen by XPS.

For this arrangement, it is essential that the relation between the incoming bunch train(s) and the handling of the pulse valves can be accurately timed. It is desirable that the instant for XPS analysis is variable along the time coordinate of the pulse (see Fig. 3.6.8), which usually lasts some 100 ms. In case that the detectors cannot record the whole spectrum from a single bunch train repetitions are necessary. These also require accurate timing between the incoming bunch train and the feed pulse. One bunch train per feed pulse will be singled out to perform the analysis. Feed pulses are typically dosed at a frequency of 1 per 3-10 seconds. For *in-situ*-XPS it is essential to avoid sample damage, since the technique relies

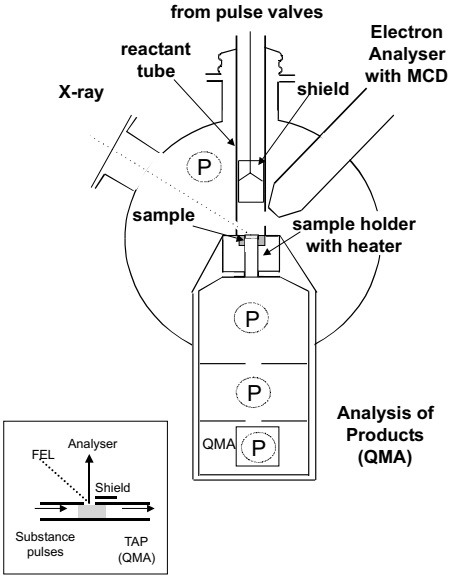

Figure 5.3.9.: *Schematic representation of a setup for in-situ-XPS (for detailed explanation see text). The inset shows an alternative arrangement.*

on repetitive analysis. The beam will have to be used in a defocused mode (mm size). On the other hand, photon-induced desorption will not be a problem as long as the reactants desorb completely. The surface will be re-populated by each reactant pulse, and in the interaction with the X-ray bunches, photo-emission precedes desorption, which will be, most likely, a heat effect.

As a general prerequisite for the proposed investigations, the high photon fluxes can be utilized appropriately only if multichannel electron detectors with a high number of channels and a high dynamic range are available. At present, there are detectors with 400 parallel channels (Scienta), which allow the acquisition of simple spectra in one shot. Therefore it is assumed that the required detector technology will be available in time. Such detectors would be exploited using dwell times dictated by the bunch train frequency (5 Hz). The bunch train structure (number of bunches) will have to be modified to keep the power load on the sample low enough to avoid heat damage and detector overflow. The energy bandwidth should be as small as possible. Typical excitation energies will not exceed 1200 eV. In many cases, however, it will be desirable to use 600-800 eV. With this low excitation energy, the width of the exciting radiation corresponds to that of typical laboratory instruments at a bandwidth of 0.1 %. A bandwidth of 0.2 % would already allow meaningful XPS with the lowest excitation energies.

5.3.4.2. Inelastic X-ray scattering

The XFEL opens the possibility to use so-called meV in-line monochromators in analyzing the scattering signal. At present, back-reflection Si monochromators are used, but the new approach offers a number of significant advantages. With the application of in-line

monochromators, one is not restricted to the energies given by the Si back reflections. It is then possible to perform inelastic scattering at (almost) arbitrary energies, e.g., around the absorption edge of a particular element. This allows one to discriminate the inelastic signal from this element by using the anomalous dispersion around the absorption edge. The subtraction of two measurements above and below the edge yields the inelastic signal from that particular element. If that element is confined e.g. in a thin film, the difference signal is free of contributions from adjacent layers, and one can perform spectroscopy on just those atoms. Thus, a similar elemental sensitivity, as in the case of nuclear resonant scattering, is obtained and vibrational properties of single films and particles can be studied. The energy resolution is not fixed as it would be for a particular Si back-reflection geometry. In principle, any appropriate high-order reflection can be used that results in the desired energy resolution. If the beamline is operated at 14.4 keV, e.g., the best energy resolution that can be obtained is 0.3 meV [46]. This aspect is of particular importance if a seeding option is used that keeps the operating energy essentially fixed. Due to the narrow angular acceptance, a very high resolution in momentum space can be reached. This is very relevant for studies at very low momentum transfers. The momentum transfer q in an X-ray scattering experiment probes correlations over a length scale of $L = 2\pi/q$ in the sample.

Momentum transfers of $q = 0.006\text{Å}^{-1}$ have to be employed for the investigation of correlations on length scales of about 100 nm. This range is of interest for the study of dynamics in disordered systems with low-energy excitations that are confined in large structural units. Extremely high energy resolution and momentum resolution are mandatory, e.g., to unambiguously decide whether a low-energy excitation exhibits a dispersion or not. Only under those conditions is it possible to resolve the nature of that particular excitation, i.e., propagating or localized. It should be noted that for X-ray inelastic scattering there are no kinematical restrictions as for neutron scattering. Energy resolution and momentum resolution are therefore completely decoupled. Thus, arbitrary energy transfers can be probed even at very small momentum transfers.

It should also be mentioned that the sample geometry can be used to create interference effects that concentrate the radiation field in particular regions of the sample by the formation of standing waves [47]–[49]. In those cases, a significant amplification of the signal from certain regions in the film can be obtained, e.g., if the layer system is designed as an X-ray waveguide.

Thin film and surface applications In general, the application of this method to thin films suffers from the difficulty of separating the inelastic signal of the film from the signal of the adjacent layers and the substrate. A certain control of this effect can be achieved by adjusting the angle of incidence, but this is not a perfect solution since one cannot restrict the radiation field to single layers exclusively. The XFEL opens a very interesting option to solve this problem due to its enormous brilliance. Using the in-line analyzing techniques described before along with selective δ-doping of thin films, one could access vibrational properties of buried interfaces with atomic resolution.

5.3.4.3. X-ray absorption spectroscopy

X-ray absorption spectroscopy (XAS) is a well-established and most powerful technique in use at SR sources world-wide. XAS finds widespread application in almost all areas of science: physics, chemistry, biology, materials and environmental science. This method is also frequently applied in industrial research using synchrotron radiation, e.g. for *in-situ* studies for the optimization of catalysts. Whereas most current applications of XAS exploit the (monochromatized) continuous spectrum of synchrotron radiation, the XFEL will make novel techniques routine for applications, that are currently only in their infancy.

Raman XAS This new technique, which utilizes the fine structure that occurs in inelastic X-ray scattering, has the potential to revolutionize structural studies by using monochromatic, *hard X-rays* to measure absorption fine-structure spectra of *low-energy edges*. Many interesting absorption edges are well below 1 keV, e.g. the L- and M-edges of first row transition metals and the K-edges of light elements, especially carbon, nitrogen and oxygen. Conventional XAS-measurements at these low energies encounter experimental difficulties, such as a small probing depth and the need for a good vacuum environment, thus limiting the range of applications to those materials that are vacuum-compatible and stable. Complex systems, liquids, reactive specimens, samples under extreme conditions (temperature, pressure) or in situ studies of materials in a gas atmosphere (e.g. catalysts) defy XAS measurements at low energies. These difficulties can be overcome by using hard X-rays. The ability to carry out Raman XAS experiments on these samples under ambient conditions opens new fields in chemistry and materials science. Inelastic X-ray Raman scattering is a technique having its largest cross section at low-energy transfers ($< 500\,\mathrm{eV}$). Already noted several decades ago, the phenomenon was not observed unambiguously until the 1960s [50] and even today, besides some feasibility studies, there have been only very few applications [51, 52] due to the extremely small cross section and the demanding instrumentation. Figure 5.3.10 shows the inelastic scattering process in which the core electrons are excited into empty valence and continuum states. The energy transfer spectrum reflects the absorption edge structure of the corresponding core electron in great detail. Besides its inherent bulk sensitivity due to the hard X-rays, Raman XAS, unlike conventional XAS, is not restricted by dipole selection rules and has a q dependence which can reveal the symmetry of unoccupied states [53, 54]. Furthermore, the Raman spectrum is shifted away from the primary excitation peak, enabling a good background discrimination. Fast single-shot experiments may be carried out using bent crystal techniques for the analyzer. Wavelength-dispersive analyzers may use either spherically or cylindrically bent crystals and one- and two-dimensional detectors, respectively (see A.1.5). Up to 5% of the full solid angle could be covered at best. The incident bandwidth has to be on the order of 10^{-4}. These devices would enable one to obtain Raman XAS spectra, both near-edge and extended, from an XFEL bunch train consisting of 10^4 bunches. Spherically curved crystals would yield a slightly better performance for a near-edge XAS spectrum if the required energy range is less than 100 eV. It does not seems possible, though, to obtain a Raman XAS spectrum from a single bunch with either device. However, one could construct a "crystal ball" type instrument by restricting the energy range, but capturing a very large faction of 4π. In that case, a single XFEL bunch could be suffi-

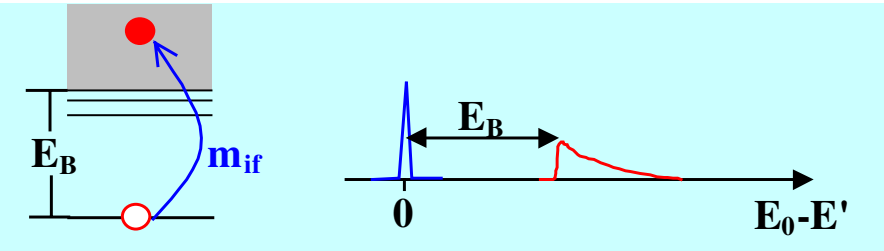

Figure 5.3.10.: *Illustration of inelastic X-ray Raman scattering. The energy scheme shows the excitation leading to the energy transfer spectrum shown on the right.*

cient to obtain a Raman XAS spectrum. The XFEL will take the time scale for Raman XAS experiments to fractions of a second per spectrum for typical samples, with the potential of making Raman XAS a routine method for materials research, similar to conventional XAS today.

Energy scanning Today, major efforts are also being made to study time-dependent processes by XAS spectroscopy. The aim is to acquire atomic structure information during chemical reactions and phase transformations, e.g. on surfaces during heterogeneous catalysis. In addition, a time-dependent change of the valence state of selected elements can be monitored. Using circularly polarized X-rays, even changes in the magnetic short range order can be followed. For time-resolved studies, the XFEL offers photon flux and time resolution exceeding those available with current sources by several orders of magnitude. The photon energy range up to 12 keV, the pulse length of 100 fs, and the time structure of the pulse train have to be considered when selecting an appropriate sample system or experimental method. At a photon energy of 12 keV, 10^{12} photons are available per bunch, and the natural beamsize at the sample position (< 800 μm) can be reduced considerably by focusing optical elements. The relatively narrow bandwidth of the SASE line, $\Delta E/E = 10^{-3}$, allows direct absorption measurements without further monochromatization in several cases, at the expense of energy resolution. For time-resolved measurements, a sequential "QEXAFS-method" would be applicable [55]. An elegant approach would be the combination with an energy tuning of the electron beam. Within one bunch train, an electron energy tuning range of $\approx$ 1-2% seems possible, corresponding to a photon energy range of 90-180 eV at the Cu K-edge. Thus, high precision XAS measurements would be feasible within 1 ms.

5.3.5. Nuclear resonant scattering

Due to the extraordinary narrow linewidth of nuclear resonances, nuclear scattering experiments using synchrotron radiation offer the option to perform inelastic measurements. This may be done in the energy regime, where generally a Bragg monochromator with meV resolution and a nuclear analyzer are used. For even better resolution in the μeV or even sub-μeV range, time-domain experiments are favorable. The present techniques will benefit from the unique XFEL properties in terms of unprecedented resolution in both energy and momentum,

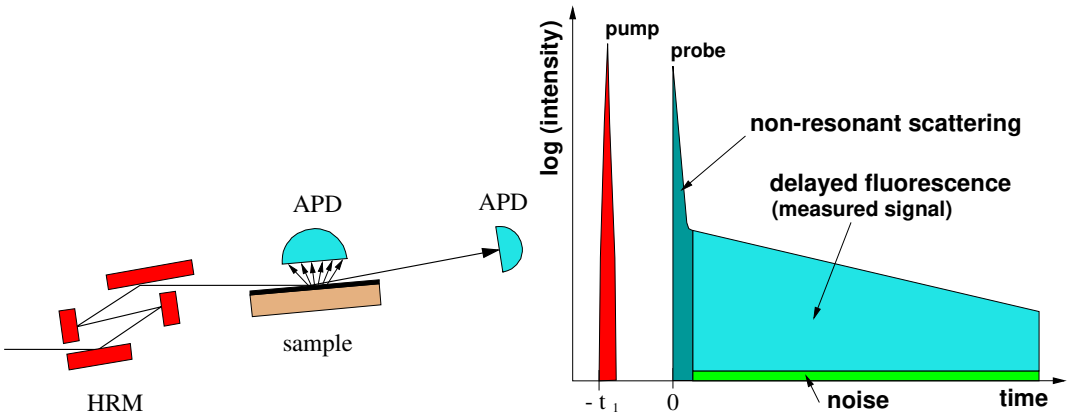

Figure 5.3.11.: *Illustration of an inelastic nuclear resonant scattering experiment :*
a) Experimental setup with high-resolution monochromator (HRM, $\Delta E \approx 1$ meV) and fluorescence detection using a large-area avalanche photodiode (APD).
b) Time discrimination of the delayed nuclear fluorescence after excitation at $t = 0$. If a pump pulse hits the sample at a time $-t_1$, the X-ray pulse probes the phonon states that have developed during the time interval between pump and probe pulse.

which not only opens new areas of research but also allows the development of completely new techniques.

5.3.5.1. Inelastic scattering

This method uses Mössbauer nuclei in the sample as the analyzer for the energy transfer in a resonant absorption process. A synopsis of this method is shown in Fig. 5.3.11. The experimental scheme employs a high-resolution monochromator to extract a meV-wide energy band around the nuclear resonance out of the incident radiation. If the energy of the incident photon is off-resonance, a nuclear excitation may proceed via excitation or annihilation of phonons. These events are detected by recording nuclear decay products like fluorescence photons, which are detected with a time delay according to the finite lifetime of the nuclear transition. Monitoring the yield of the delayed events as a function of incident energy gives a direct measure of the phonon occupation number and the phonon density of states which is derived thereof.

The enormous brilliance of the XFEL radiation will allow the crystal monochromators to be pushed to their theoretical resolution limit. Considering dynamical theory of X-ray diffraction, it was shown that the resolution limit for crystal optics is given essentially by the photo-absorption cross-section (provided the crystal is perfect enough). For the 14.4 keV resonance of ^{57}Fe, this limit is ≈ 0.3 meV. If we also consider diamond as a material for high-resolution monochromators, the limit will be shifted to ≈ 0.06 meV. This requires, however, a crystal perfection of Δd/d = $4 \cdot 10^{-9}$, which seems unrealistic at the moment.

It is evident from the above statement that, for resonances with lower energies, it will not be possible to obtain such a narrow bandwidth. The resolution will remain above 1 meV. Only resonances with higher transition energies (see below) will allow beams with narrower

Isotope	E_0/keV	τ_0/ns	rel. yield
^{181}Ta	6.2	9800	0.002
^{169}Tm	8.4	7.6	0.22
^{83}Kr	9.4	121	0.062
^{73}Ge	13.3	20	0.0001
^{57}Fe	14.4	141	1.0

Table 5.3.1.: *All stable Mössbauer isotopes with transition energies in the range of the XFEL SASE 2 undulator. E_0 is the transition energy and τ_0 is the natural lifetime. The last column gives the yield of delayed fluorescence, normalized to that of ^{57}Fe.*

bandwidth.

One topic which has to be addressed in the near future is the heat load on the crystal faces, even *after* a high-heat-load monochromator. Estimates show that the surface of a silicon monochromator crystal will be heated by several K during a bunch train. In the interval between two bunch trains, the temperature will decrease. Obviously such a treatment will cause strain in the crystals, degrading their performance as ideal Bragg-reflectors. Cryogenic cooling schemes have to be developed. These can take advantage of the zero thermal expansion coefficient of silicon at 123 K.

The brilliance and femtosecond time structure of the XFEL radiation open unique applications in the following fields :

Equilibrium Lattice Dynamics of Thin Films Since this method yields the *partial* vibrational density-of-states of the Mössbauer atoms in the sample, it offers the unique possibility to selectively obtain the vibrational properties of nanoparticles and thin films that contain the resonant isotope. There is no need to discriminate against inelastic signals from surrounding materials. The sensitivity of the method to thin films has been proven already in a number of experiments [47]–[49]. However, the statistical quality of the data obtained at present-day sources does not allow the investigation of single monolayers. On the other hand, flux estimates for the SASE line of the XFEL at 14.4 keV indicate that a vibrational spectrum from a single monolayer of ^{57}Fe can be obtained in a few minutes. This allows to δ-doping layers to be selectively introduced into the sample, so that vibrational properties with atomic resolution can be obtained. It is an inherent advantage of X-ray spectroscopy over other methods such as inelastic electron or He–scattering that dynamical properties can be probed *inside* solids, i.e. at interfaces or grain boundaries.

At the XFEL, this method can be applied to Mössbauer isotopes with transition energies up to 14.4 keV, as listed in Table 5.3.1. These isotopes can be used as local probes for vibrational properties of low-dimensional structures. The last column of this table gives the yield of delayed fluorescence relative to the value for ^{57}Fe as a basis for count rate estimates.

Non-Equilibrium Lattice Dynamics of Thin Films Using the short-pulsed time structure of the XFEL, the above method can be applied to study time-resolved lattice dynamics : Since the incoherent signal reflects the phonon occupation number *at the very moment of excitation*, it is possible to set up a pump-probe scheme, as sketched in Fig. 5.3.11. A high occupation number of phonons can be created by a short pump pulse of a conventional laser. The spectral phonon distribution and the corresponding phonon lifetime are determined by the coupling mechanism of the pump laser radiation to the sample. A simple heat pulse creates thermal phonons with lifetimes in the ps range or below. Highly monochromatic phonons with lifetimes of several 100 ns can be created by coupling the laser pulse to impurity resonances that decay via electronic relaxation [56]. The decay of such non-equilibrium phonon states provides valuable information about the thermal transport properties of the sample.

The spectral and temporal evolution of these phonon states can then be determined with the XFEL. If the photon energy of the X-ray probe pulse is tuned around the nuclear resonance for a fixed pump-probe delay, one obtains the phonon spectrum that has developed during this time interval. On the other hand, tuning the pump-probe time delay at a fixed off-resonance X-ray energy allows the time evolution of particular vibrational states to be monitored. The time resolution is given by the pulse length. Note that the energy resolution ΔE and the time resolution Δt are linked according to $\Delta E \Delta t > \hbar = 0.66$ meV $\cdot$ ps.

Using a meV monochromator, it should thus be possible to study non-equilibrium lattice dynamics on a ps time scale. Time resolution well below 1 ps can be obtained by sacrificing energy resolution, taking full advantage of the short-pulse XFEL time structure. An immediate application would be to study the dynamics of heat transfer on nanoscopic length scales. Due to the isotopic sensitivity of the absorption process, an extremely high spatial resolution can be obtained by the use of probe layers, making this technique a rather XFEL-specific application. Since it relies on the unique time structure of the XFEL beam, it can also be used with the *spontaneous* emission of the XFEL and is therefore is not restricted to the isotopes mentioned in the above table.

As described above, the minimum energy bandwidth ΔE that can be obtained via electronic Bragg scattering using Si crystals is limited to a few hundred μeV. To go beyond that limit, other scattering mechanisms have to be applied. Here we propose to use nuclear resonant scattering to achieve energy resolutions in the μeV range. The corresponding spectrometer is shown in Fig. 5.3.12. It has been described already in a number of publications [47, 57, 58]. However, due to the strong bandwidth reduction, the flux delivered by this instrument at existing sources is not yet enough to perform inelastic scattering experiments. With the availability of SASE radiation from the XFEL, this spectrometer will deliver a μeV - wide beam that is tunable over several meV.

The spectrometer relies on grazing-incidence reflection from a thin α - ^{57}Fe film, magnetized along $\vec{k}_0$, in combination with a polarization-filtering technique. Two Si(840) polarizer - analyzer crystals in crossed setting provide a polarization suppression of 10^{-8}. The optical activity that is associated with the reflection in this magnetization geometry leads to strong off-diagonal elements in the reflectivity matrix. This off-diagonal reflectivity is transmitted by the crystal optics. Measurements have already shown that an integrated bandwidth of ΔE = 50 Γ_0 can be obtained [57].

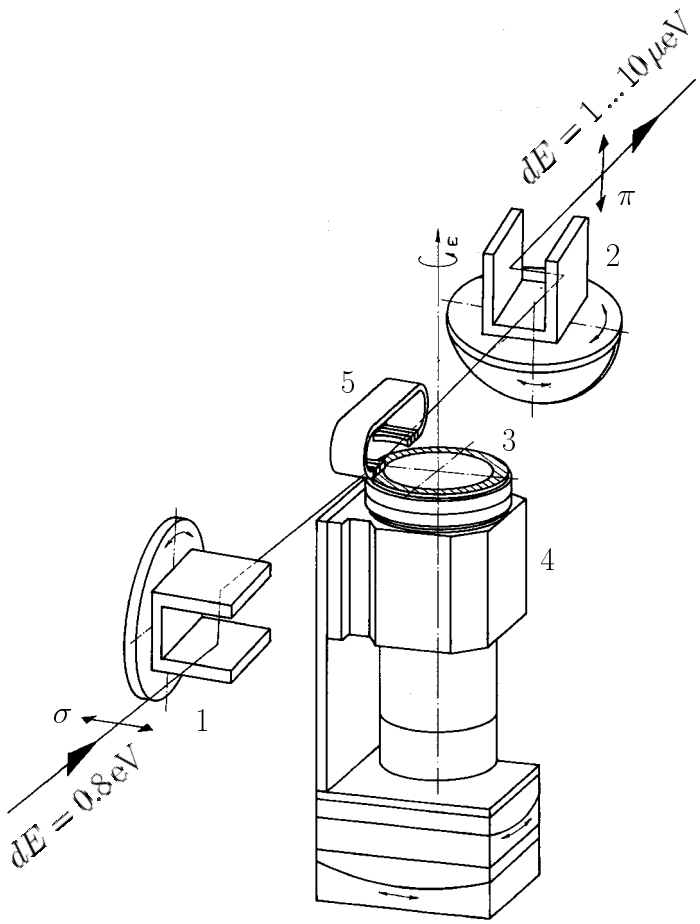

Figure 5.3.12.: *Schematic setup of a spectrometer for μeV-resolved x-ray scattering based on elastic nuclear resonant scattering. 1: Si(840)-Polarizer, 2: Si(840)-Analyzer, 3: Superpolished mirror coated with ^{57}Fe, 4: Drive for mirror rotation with up to 8000 min $^{-1}$, 5: Permanent magnet for magnetization of the Fe - film parallel to $\vec{k}_0$. Polarizer and analyzer are channel-cut crystals with scattering planes tilted by 90 ° (crossed polarizers).*

With the expected flux of 10^7 ph/(s Γ_0) at the XFEL one obtains a meV-tunable, μeV-wide X-ray beam with an average flux of $5{\cdot}10^8$ ph/s (this is a value that is used in present-day inelastic X-ray scattering experiments with meV-resolution). Such a beam can be used for the determination of the phonon density of states of samples that contain resonant nuclei [59] or for coherent inelastic scattering experiments [60]. In the latter case one needs an energy analyzer with the same energy resolution as the monochromator. For this purpose one uses a resonant analyzer like a static α - ^{57}Fe foil, as proposed by Chumakov et al. [61].

5.3.5.2. Nuclear lighthouse effect

Nuclear resonant scattering from a fast rotating sample leads to a mapping of the time response to an angular scale [62]. This is shown schematically in Fig. 5.3.13. Due to its

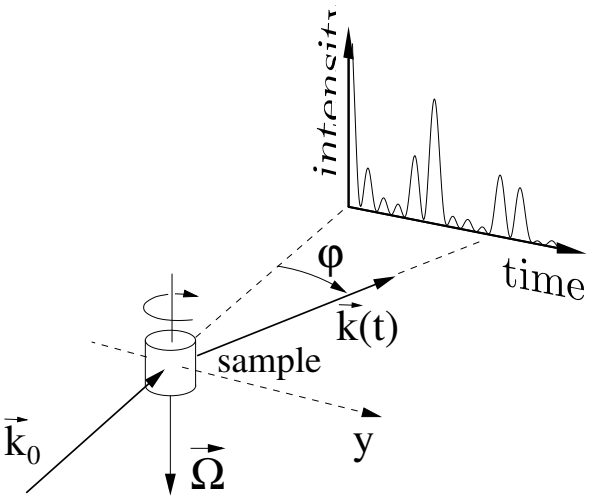

Figure 5.3.13.: *Scattering geometry of nuclear resonant scattering at a sample rotating with angular velocity $\vec{\Omega}$. The time spectrum of the radiative nuclear decay is mapped to an angular scale.*

apparent resemblance to a sweeping ray of light this effect has been called the *"Nuclear Lighthouse Effect"*. Employing rotational frequencies of up to 35 kHz, time spectra of nuclear resonant scattering can be conveniently recorded with a position-sensitive detector.

In the following, we want to show that the use of the nuclear lighthouse effect at an XFEL beamline enables a time resolution of a few ps. Since the deflection of the resonant radiation from the rotating sample is due to the change of spatial phase factors of the radiating nuclei during the lifetime of the exited state, the lighthouse effect can be described as a diffraction phenomenon. The transverse coherence of the radiation introduces a finite resolution function in reciprocal space if the mutual coherence function varies significantly over the length scale of the diffracting objects [63, 64]. The time resolution Δt is given by the width of this resolution function as $\Delta t = 1/(k_0\,\xi\,\Omega)$ [62], where ξ is the transverse coherence length of the radiation and Ω is the angular velocity. For a completely coherent illumination, as in the case of the SASE radiation from XFEL, the transverse coherence length is practically infinite. The time resolution is then limited only by the angular resolution $\Delta\varphi$ of the system, determined by the angular spread of the beam and the angular resolution of the analyzer (e.g. a Bragg reflection). For a perfect analyzer, this results in a time resolution of $\Delta t = \Delta\varphi/\Omega$. Assuming a rotational frequency of 35 kHz and taking $\Delta\varphi$ = 1 μrad, we obtain Δt = 4.5 ps.

While this value is already way below the limit of present techniques, even values below 1 ps can be achieved by implementing an appropriate focusing scheme. The experimental setup is shown in Fig. 5.3.14. The beam is focused towards a position-sensitive detector by a lens or a mirror to record the time spectrum as a function of a spatial coordinate. In order to reduce the nonresonant background, a meV high-resolution monochromator should be introduced after the rotor. Its horizontal acceptance of a few mrad matches the range of deflection angles of the resonant radiation.

For a given source size a, a source-to-lens distance S, and a lens-to-detector distance

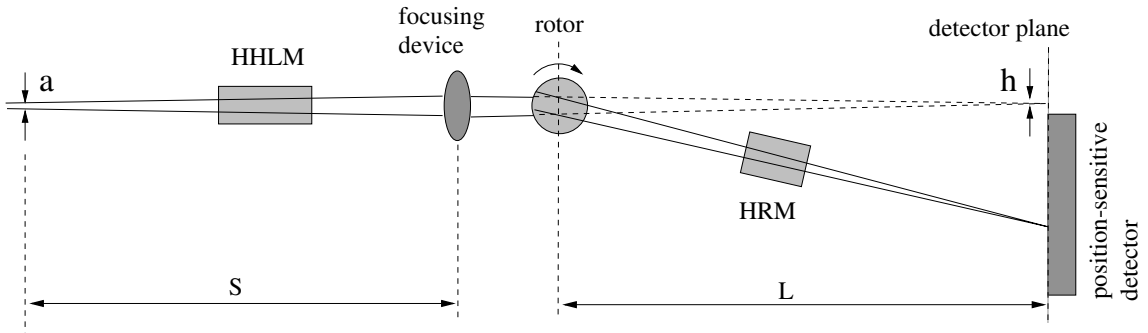

Figure 5.3.14.: *Experimental setup (top view) to obtain picosecond time resolution in nuclear resonant scattering at the XFEL. The setup contains the high-heat-load monochromator (HHLM) and a focusing device (mirror or lens) that focuses the beam on the detector plane. The distance between the lens and the rotor (a few m) is small compared to S (500 m) and L (up to 100 m). The radiation resonantly scattered at the rotor is deflected due to the Nuclear Lighthouse Effect. For suppression of the nonresonant background, a monochromator with meV-resolution (HRM) is introduced.*

L, the demagnified image of the source at the detector position has the size $h = a\,L/S$. Because h/L is the angle that the focal spot subtends as seen from the rotor, the effective time resolution is given by $\Delta t = h/(\Omega\,L) = a/(\Omega\,S)$. For a = 60 μm and S = 500 m, and a rotational frequency of $\Omega/(2\pi)$ = 35 kHz, we obtain Δt = 540 fs. Since rotational frequencies of up to 100 kHz seem feasible in the near future, a time resolution close to 200 fs may be reached. Even though the pulse length of the XFEL radiation is in that range, such time resolution is not currently possible with existing x-ray detectors. By mapping the time response to a spatial scale, the nuclear lighthouse effect allows access to sub-ps time resolution with existing detector technology. In addition, the method is intrinsically free of any time jitter that is often encountered in conventional timing schemes.

This technique is also very attractive for use with the spontaneous radiation at high photon energies. The energy range around 80 keV is very interesting for nuclear resonant spectroscopy, because there are many resonances among the rare-earths with lifetimes of 3 – 5 ns [65]. Moreover, the background due to small-angle scattering will be significantly reduced compared to the 10 keV range, because its angular distribution typically scales with a power-law as $I(\varphi) \sim (k_0\,\varphi)^{-n}$ with n = 3 – 4. Due to the long baseline S, time resolutions can be reached that are not possible at third generation sources, even though the average photon flux at those energies may be comparable.

In particular, applications in the following fields can be envisaged:

- **Dynamics of magnetic switching**
  The dynamics of magnetization reversal is of great technical relevance for the development of high-speed magnetic storage devices and spin electronics. The experimental method proposed here offers the possibility to study magnetic phenomena with an outstanding time resolution, using resonant nuclei as a probe. This is particularly interesting in the case of rare-earth magnetism, because most of these elements exhibit

nuclear resonances with transition energies around 80 keV. The theory of nuclear resonant scattering in the presence of hyperfine-field switching has already been developed and tested to a great extent [66, 67].

- **Isotopes with large hyperfine splittings**
  Large hyperfine splittings lead to very small quantum-beat periods. An example is magnetic ordering in Dy metal that orders ferromagnetically below 85 K with magnetic hyperfine fields of up to 600 T. Due to the large magnetic moments of the Dy nucleus, the quantum beats of the magnetic hyperfine interactions are around 100 ps.

5.3.5.3. Time-domain interferometry

These experiments [68] will turn to a routine technique (Fig. 5.3.15) to study the q - dependence of relaxational motion. At present sources, this technique is flux-limited. Count rates under optimum conditions amount to some 10 Hz only. Thus time-domain interferometry will directly benefit from the increase in brilliance. Due to the high degree of monochromatization, radiation damage in the sample will be a minor problem in this case.

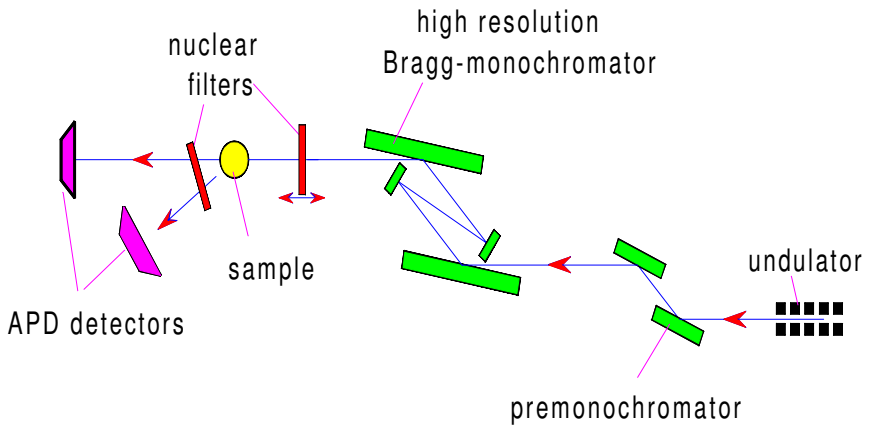

Figure 5.3.15.: *Setup for time domain interferometry experiments.*

This method has the option to extend the q-range of present high-resolution inelastic scattering techniques. While neutron spin echo covers the range of low-momentum transfer with similar (neV) energy resolution, it is limited to $\approx 2\,\text{Å}^{-1}$ in q–space. Time-domain interferometry will be able to reach $q \approx 12\,\text{Å}^{-1}$. This area is particularly interesting for studies of diffuse scattering (where the scattering cross-section scales with the momentum transfer) and for disordered systems where new information on the scaling behavior of the relaxation times may be obtained. All this is not possible with present-day sources.

5.3.5.4. Nuclear speckle scattering

A particularly interesting subject would be nuclear resonant speckle interferometry. This would provide information about the correlation of hyperfine interaction parameters in the sample, for example the correlation of magnetic field directions, quadrupolar interactions etc. Due to flux limitations at present-day sources, this kind of spectroscopy will only be possible at the XFEL. Since nuclear resonant scattering is a time-resolved technique, it is clear that one has to use a 2D detector with ns - time resolution.

5.4. Detectors for XFEL experiments

The unique challenges for detectors posed by the XFEL, as compared to third generation x-ray sources, will be the very high dose rate at the detector entrance window, and the extremely fast timing of the pulse and bunch structure. As at third generation x-ray sources, detectors at the XFEL will be used both for aligning the experiment, and for final data recording in a wide variety of applications, including diffraction and scattering, imaging and spectroscopy. The kinetic or time-resolved counterparts of each of these methods may require additional features for detection. Each experimental method has its own special requirements for its detector. In general, an acceptable detector must be optimized for a specific application with respect to numerous criteria, including detective quantum efficiency (DQE) at a given energy, event rate. linearity, saturation, signal-to-noise, dynamic range, detector size and number of pixels, spatial resolution, energy resolution, stability of calibration, residual non-uniformity, radiation damage susceptibility, readout speed, availability, ease of use and finally cost. In Tab. 5.4.1 the requirements by the XFEL source to an ideal detector system are listed. In addition, the corresponding parameters for several established detection techniques are indicated. Present-day X-ray detection utilizes either scintillators or pn–junctions in semiconductor material. As can be seen from Tab. 5.4.1 both detectors will be limited in time resolution to about 100 ps, which fits exactly the time distance of two adjacent pulses. Semiconductors based photo-conductor schemes and photo-cathodes will reach a time resolution < 1 ps, yet these detection schemes have other intrinsic limitations.

It is strongly emphasized that soon after the initial investigations to be performed at the XFEL are identified, the detector requirements needed to accomplish those experiments should be evaluated, and an appropriate development effort should be initiated, where necessary. The time-structure of the XFEL radiation presents severe constraints for existing detector technology. In the following we describe the situation and possibilities for these technologies and furthermore the steps one has to anticipate in order to provide detectors with the required features when the XFEL will come into operation. The requirements to detectors for XFEL application may also require completely new developments and in the last part we will present such a proposal for a femtosecond X-ray detector.

Very few technologies have the potential to resolve the individual bunches, which would require characteristic times less than 50 fs. Photoconducting detectors and streak cameras are the fastest detectors available so far, but are still an order of magnitude too slow for this time scale. Only optical pre-processing of the data before recording has the potential to reach this time scale, and for such methods detector developers should look into the optical

	XFEL requirements	Scintillators		Semiconductors		Photocathodes
		inorganic	plastic	pn–junction 3 μm Si	photo-conductors 12 μm CdTe	100 nm CsI
time resolution	fs - ms	> 10 ns	> 1 ns	> 100 ps	6 ps	20 ps
expected					0.8 ps	1 ps
absorption (10 keV)	> 50%	100%	100%	2%	60%	1%
readout noise	low	-	-	low	low	low
intensity	10^{13} phot/100 fs	ok	ok	rad. damage? *	rad. damage?	rad. damage?
DQE (10 keV)	high	high	high	low	high	low
dynamic range	$\approx 10^{-4}$	ok	ok	ok	ok	ok
energy range	0.4-15 keV	ok	ok	ok	ok	ok
energy resolution		low	low	ok	ok	low
N-dim. detection	0-D, 1-D, 2-D	ok	ok	0-D	0-D	0-D, 1-D

* Radiation damage mechanisms may appear for these detectors at too high count rate per time interval.

Table 5.4.1.: *Detector requirements for experiments at the XFEL. Parameters provided by A. Koch (Thomson Tube Electroniques).*

and telecommunications fields. Optical pre-processing, like correlation detection, however, is not equivalent to direct time resolved detection because the phase information is lost. If the individual pulses cannot be resolved, then associated detector development should concentrate on the next time point, the 93 ns inter-bunch time, which seems to be an attainable goal. A one-dimensional data set, from perhaps a 100 pixel strip detector with a pipeline architecture, every 93 ns would be very useful for some spectroscopic applications, such as XANES.

Time-resolved experiments also need to be able to measure the delay between a pump and a probe to better than 100 fs. If such delays cannot be controlled to this accuracy, they can at least be measured and recorded for later interpretation.

Large area, fine resolution, but relatively slow area detectors would also have a place at the XFEL. Such a pattern every millisecond would be a very useful detector. Resolving the 93 ns interval for a short imaging burst with an area detector may also be feasible.

Pixel size is deemed not a major factor for most experiments because most experiments can be scaled to the size of the detector if there is sufficient space for a flight tube. But some experiments are constrained with respect to detector placement: Fresnel patterns must be recorded at the point of maximum contrast and holography needs small pixels.

For radiographic imaging, both direct recording and magnified imaging using refractive lenses, it is concluded that the requirements of most applications can be met with detectors whose performance characteristics are similar to present CCD-based systems. But, it is emphasized that the major challenge may not be to improve the performance of present systems, but to ensure that the same performance is available under the conditions of such a novel source as the XFEL, especially with respect to the high energy deposition in all components exposed to the beam.

One note of caution, concerns the possibility of an electromagnetic pulse (EMP). The predicted fields from the flux densities at the XFEL are sufficiently high that an EMP large enough to destroy nearby sensitive electronics could be produced. Measurements are being undertaken at the APS to assess the magnitude of this effect.

In any case, radiation damage to specimens will certainly be a problem at the XFEL. One bunch train (1 ms) from the XFEL will equal the exposure from 10 s of an undulator beam at the ESRF. If it is not possible to protect specimens adequately, it will be necessary to acquire

full data sets from single "shots", a significant constraint on detector design.

It is suggested that effort should be made to design several detectors tailored to some of the specific requirements of the XFEL. This should be a European-wide collaboration with a realistically large budget. It is noted, for example, that detector budgets at other accelerators (for physics) are a significant fraction of the overall facility cost. It was also noted that this collaboration should be undertaken relatively soon, as there are significant problems to be solved. We should try to understand why such collaborative efforts could not be established in the past, despite similar situations and discussions, e.g. for the third generation sources. Points to be discussed include: management and control of large development groups and acceptance by beamline groups of such projects.

Detector technologies divide into two groups with fundamentally different technological approaches: counting technology, in which individual photons are recorded, perhaps with energy resolution; and integrating technology, in which only the total dose during an exposure is measured.

Counting detectors for x-rays include several designs of multi-wire proportional counters (MWPCs), and solid-state counters. Each type can be configured as point, linear or area detectors. MWPCs utilize the ionization produced in a gaseous medium by the conversion of an x-ray, and are limited by the ionization recovery time to about 1 MHz/pixel [69]. Solid state counters include scintillator/photomultiplier detectors, and semiconductor counters. Scintillating crystal detectors are generally configured as point detectors, or area detectors with very few pixels, and are frequently configured with a multi-channel analyzer to provide energy-resolved counting at event rates up to 10 Mhz. Semiconductor counting detectors using silicon, germanium or gallium arsenide sensors are currently under development in several laboratories, but they too are limited in counting frequency to below 5-10 MHz/pixel [70]. Since many experiments with the XFEL are expected to produce several photons per pixel during each bunch time (100 fs), counting detectors are generally too slow to handle the expected flux.

An exception to this would be experiments with very low cross-sections, such as those using highly coherent photons, where the expected event rate is quite low. In fact, such experiments are prime candidates for the XFEL, since experiments which result in large numbers of photons at the detector probably can be done with more conventional sources. For low event rates, counting detectors would be the best choice, since many counting detectors have no background, and so provide true quantum-limited statistics for analysis. Scintillating crystal counters may also find application in several spectroscopic experiments at the XFEL.

Arrays of avalanche photodiodes (APDs) may also be applicable in low cross-section experiments, and are especially promising for Mössbauer spectroscopy. APDs are relatively fast, with counting rates up to 40 MHz in commercial units. Currently, such detectors are still quite small, consisting of small arrays of $1 \times 1\text{mm}^2$ pixels [71].

Photoconductive detectors have the potential to be very fast (~ 1 ps), and should be investigated for application to the XFEL experiments. To date, such detectors are also quite small, have a low DQE, and are susceptible to radiation damage.

By contrast, integrating detectors are well suited to the XFEL requirements. A number of proven designs have been developed, and several types are commercially available, including storage phosphor systems, charge-couple device (CCD) based detectors, and amorphous

silicon flat-panel detectors. Integrating silicon sensor detectors have also been demonstrated. Amorphous silicon detectors are primarily designed for medical imaging, and presently are not suited to the low-noise imaging requirements of XFEL experiments.

Storage phosphors, also called image plates, are sheets of BaFBr:Eu phosphor material that can be handled much like x-ray film. This phosphor stores a fraction of incident x-ray energy in deep traps that can be subsequently released as photo-stimulated radiation when the sheet is scanned with a laser. The sheet is exposed to x-rays, then either physically removed for off-line scanning, or scanned in place in an integrated unit. Storage phosphors have, in principle, a very wide dynamic range (which may not be reproduced by the scanner) and a high stopping power, but they have limited spatial resolution (typically 100-150 μm) and can have a relatively low DQE at lower energies [72]. However, their main disadvantage is the experimental dead-time associated with the scanning step, which typically takes 3 minutes. This limits their usefulness for high repetition-rate experiments.

CCD-based detectors have been designed in several different forms, and are excellent candidates for XFEL experiments. Most designs use an energy-converting phosphor screen (typically Gd_2O_2S:Tb) to convert the incoming x-rays into a light pattern which is then imaged onto the CCD for readout. The speed of such detectors is constrained to $\sim 100\,\mu$s by the lag in photoemission of the phosphor. In large aperture detectors, several of which are commercially available, the light image is coupled to the CCD by means of a fiber-optic taper. In such demagnifying applications, where the detector pixels are larger than the CCD pixels, lens coupling is too energy-inefficient to give a detector with a satisfactory DQE [73]. Pixel sizes at the incident plane of such detectors are in the range of 50 to 150 μm, and readout times are generally from 0.05 to 5 s [74]. Video rate cameras have also been designed, and there is a special purpose CCD that reads 10^6 frames/s [75]. Well-designed systems have DQE > 0.5 for the normal range of incident dose, and intensity can be recorded with 0.5% error in favorable cases.

Designs with untapered fiber-optic plates permit detector pixels to be the same size as the CCD pixels (9 to 26 μm, typically), and inverted tapers give detector pixels smaller than the CCD pixels. In these cases, the granularity of the phosphor can become the limiting factor for image sharpness. Thus, for very small images, the light from a fluorescent crystal can be focussed on a CCD camera by means of a lens [76]. In this situation, lens coupling is energy-efficient because the magnification is > 1. Readout can be by a video camera, or a low-noise scientific camera controller can be used.

Of theoretical concern in the XFEL application is possible non-linearity in the response of phosphors and scintillators at high dose rate. This phenomenon is predicted, but has not yet been observed experimentally.

Integrating detectors with silicon (or other semiconductor) sensors are one of the most attractive detector technologies for the XFEL. In these two-layer devices, a pixelated silicon sensor is bump-bonded ("flip-chip" technology) to a custom-designed CMOS readout chip. X-rays are converted in the sensor layer, and the resulting charge is swept into the readout chip by the applied electric field. One such detector with 92×100 pixels of 150 μm $\times$ 150 μm has been extensively characterized as a prototype [77]. In this detector, each pixel contained 8 storage capacitors and the necessary switching circuits to permit rapid storage of 8 frames of data. This device has demonstrated framing times as short as 150 ns, with 450 ns dead-

time between frames. After the 8 frames are stored, the detector is stopped and read out. Readout of the prototype was slow, but this could be shortened significantly with a different design. The device has a "full-well" of 23000 8-keV x-rays, with a readout error of 2-3 8-keV x-rays. It seems likely that with more development, such a detector could resolve the 93 ns bunch interval of the XFEL, permitting data to be gathered from single bunches. However, this development will be difficult.

An attractive feature of the silicon sensor pixel detectors is that they can be specifically designed for special tasks. All one must do is redesign the readout pixel in the CMOS array. Sensor, interconnections, mechanical design, and much of the electronics can remain unchanged, greatly facilitating the fabrication of the detector. One potential application that has aroused considerable interest is the possibility of in-pixel autocorrelation for recording speckle interference patterns. An in-pixel analog-to-digital converter would also be highly desirable. Either of these developments would require significant resources.

Another class of detectors that should be borne in mind is direct exposure CCDs, which are capable of highly accurate dose measurements with low energy x-rays. Of course, radiation damage to such a device will be a major design concern for an XFEL detector.

Silicon drift chambers are another technology that should be evaluated. They are capable of very accurate time measurement, and energy resolution. A design at Brookhaven National Laboratory is 5 cm x 5 cm, and features excellent spatial resolution and low noise. Five millimeter hexagonal cells also with very low noise are commercially available, and a "bucky-ball" detector of these covering most of a spherical surface has been proposed at DESY and is under development. These cells are, however, quite susceptible to radiation damage.

In summary X-ray detectors that take advantage of the unique characteristics of the XFEL will be specialized devices that are much more advanced than detectors available today. Encouragingly, several technologies appear to be applicable, though not without significant effort. The specific experimental requirements for detectors should be identified as early as possible and international collaborative development programs should be established to meet these needs. The development efforts will be time-consuming, and so should be started soon.

A femtosecond X-ray detector A scheme for time resolved X-ray detection with a resolution better than 10fs is presented where the central idea is to use intense fs-laser pulses to depopulate the valence band of a semiconductor and thus switch the absorption of X-rays. Such device could be used as a fast detector by recording secondary processes such as x-ray fluorescence or resonant Raman scattering or as a fast shutter, employing the variation of transmission [78].

The operating principle of the detector is based on optical switching of a semiconductor material like GaAs. Using a femtosecond laser a massive transfer of charges from a deep-lying part of the valence band to the conduction band is induced. X-rays monochromatized to match a transition from a core level (i.e. Ga K) to that part of the valence band can then induce X-ray absorption and subsequent X-ray fluorescence (i.e. Ga K_α by the transition from Ga L to Ga K). A schematic, illustrating these processes, is shown in Fig. 5.4.1. The part of the valence band that is accessible to the x-ray transition is determined by the x-ray photon energy and the momentum relative to the semiconductor crystal orientation.

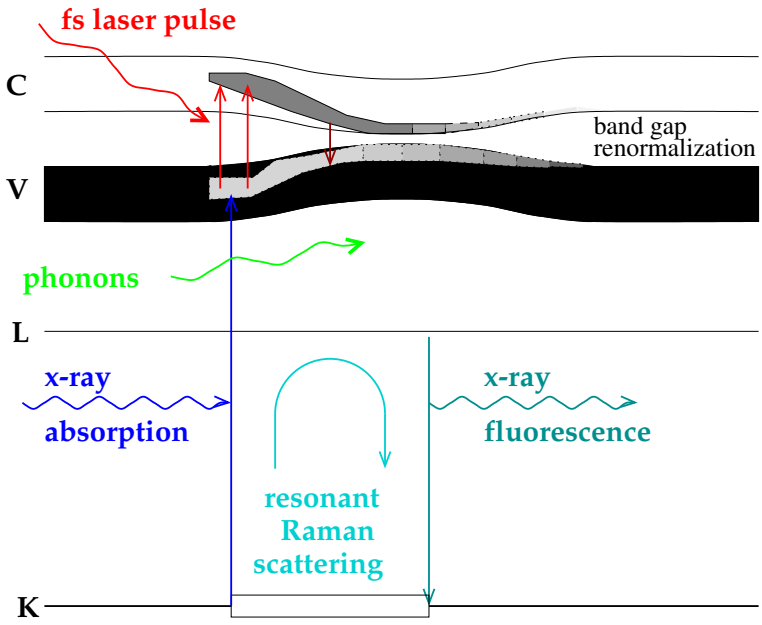

Figure 5.4.1.: *Schematic of the detector principle with time on the abscissa and energy on the ordinate. Labels K, L, V and C indicate K- and L-shell, valence and conduction band. The device is activated by an optical laser pulse generating electron transfer from the valence to the conduction band. Now X-ray photons tuned to the energy difference for K-shell to valence band transition can be absorbed. The device is no more transparent for these X-rays and X-ray fluorescence occurs. X-ray absorption and fluorescence may also occur coherently as resonant Raman scattering.*

As shown in Fig. 5.4.2 such a device could be used in two ways. Firstly, the relaxation processes of the x-ray transition, such as x-ray fluorescence or Auger electron emission, may be used to indicate that the X-ray transition has taken place and the device operates as an X-ray detector delivering a signal proportional to the X-ray intensity incident on the detector. Secondly, it becomes opaque immediately after the optical laser pulse and the device can be used as an X-ray shutter. Here the band relaxation processes will re-establish transparency on a time scale of 100 to 150 fs. One can imagine to combine these two principles to obtain a time window with sharp opening and closing edges of the order of femtoseconds (see Fig. 5.4.2).

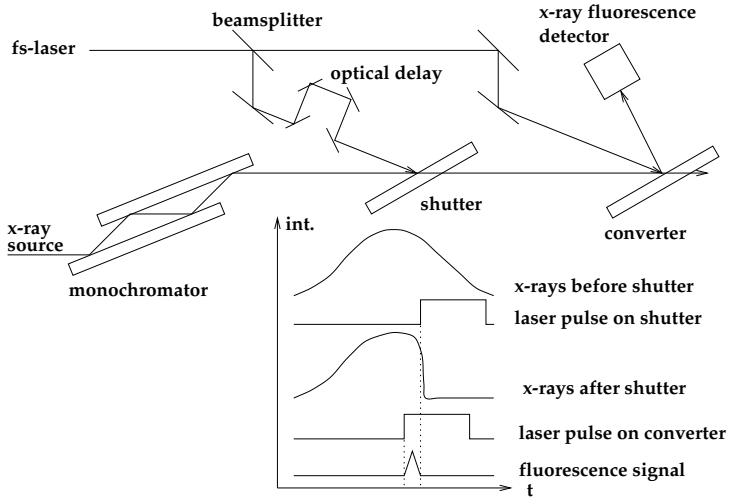

Figure 5.4.2.: *A schematic of the detector setup, showing the two modes of operation as a photon shutter and, in combination with a fluorescence detector, as a femtosecond detector. Indicated are further the monochromatization by a 4-bounce Bragg reflection, the optical laser needed for depopulation of the valence band, and a optical delay unit for time adjustment. The retarded time scale shows the sequence of X-ray and optical pulses.*

Bibliography

[1] E. Gluskin, P. Ilinski, N. Vinokurov, *Predicted Performance of the LCLS X-Ray Diagnostics*, LCLS reports LCLS-TN-00-13, Stanford (2000).

[2] J.S. Wark and H. He, Laser and Particle Beams **12**, 507 (1994).

[3] I. Uschmann et al., Rev. Sci. Instrum. **66**, 733 (1995).

[4] T. Missalla, I. Uschmann, E. Förster, G. Jenke, D. von der Linde, Rev. Sci. Instr. **70**, 1288 (1999).

[5] R. Tatchyn etal., Nucl. Instrum. Meth. A**429**, 397 (1999).

[6] S.D. Shastri, P. Zambianchi, D.M. Mills, SPIE proc. 4143, (2001) in press.

[7] S.D. Shastri, P. Zambianchi, D.M. Mills, *Dynamical diffraction of ultrashort X-ray free-electron laser pulses*, to be published.

[8] W. Graeff, *Short X-ray pulses in a crystal*, to be published.

[9] M. Born and E. Wolff, *Principles of Optics*, Pergamon Press, Oxford (1993).

[10] W. Lauterborn, T. Kurz, M. Wiesenfeldt, *Coherent Optics*, Springer, Berlin-Heidelberg (1993).

[11] V.M. Kaganer, B. Jenichen, K.H. Ploog, Physica B**283**, 268 (2000).

[12] A. Souvorov, M. Drakopoulos, I. Snigireva, A. Snigirev, J. Phys. D: Appl. Phys. **32**, A184 (1999).

[13] K. Tamasaku and T. Ishikawa, SPIE proc. 3773, (1999).

[14] R. Follath and F. Senf, Nucl. Instrum. Meth. A**390**, 388 (1997).

[15] D. H. Bilderback et al., J. Synchrotron Rad.**7**, 53 (2000).

[16] A.K. Freund, Opt. Eng. **34**, 432 (1995).

[17] J. Hoszowska et al., Proc. Conf. XTOP-2000, Ustron-Jaszowiec, September 13-15 (2000), J. Phys. D, in press.

[18] H. Yamaoka et al., Nucl. Instrum. Meth. A**364**, 581 (1995).

[19] C. Giles et al., J. Appl. Cryst. **27**, 232 (1994).

[20] A.K. Freund, private communication .

[21] M.R. Howells et al., Opt. Eng. **39**, 2748 (2000).

[22] E. Church and P.Z. Takacs, Opt. Eng. **34**, 353 (1995); see also the erratum, (ibid.), p.3348.

[23] G. Derst, H. Handschuh, M. Schmidt, K. Werner, SPIE proc. 3152, 51 (1997).

[24] The LCLS Design Study Group, *LCLS Design Study Report* SLAC reports SLAC-R-521, Stanford (1998), Chap. 10 .

[25] B. Lengeler et al., Appl. Phys. Lett. **74**, 3924 (1999).

[26] M. Uesaka et al., Jour. of Nuc. Mats. **248**, 380 (1997); M. Uesaka et al, Proc. of the Asian Particle Accelerator Conference (APAC98).

[27] S. Joksch et al., Rev. Sci. Instrum. **63**, 1114 (1992).

[28] J. Wark and H. He, Laser and Particle Beams **12**, 507 (1994).

[29] J.N. Chukhovskii, E. Förster, Acta Cryst. A**51**, 668 (1995).

[30] F. Sette et al., Phys. Rev. Lett. **77**, 83 (1996).

[31] T. Thun-Albrecht et al., Phys. Rev. Lett. **77**, 5437 (1996).

[32] E. Gerdau and H. de Waardt, Hyperfine Inter. **123/124**, (1999).

[33] R. Gähler and R. Golub, Z. Phys. B **65**, 269 (1987).

[34] J.B. Tiller, A. Barty, D. Paganin, K.A. Nugent, Optics. Comm. **183**, 7 (2000).

[35] J. Miao, P. Charalambous, J. Kirz, D. Sayre, Nature **400**, 342 (1999).

[36] R. Nuetze, R. Wouts, D. van der Spoel, E. Weckert, J. Hajdu, Nature **406**, 752 (2000).

[37] J. Arthur, in Proc. of the workshop on "Perspectives of X-Ray Photon Correlation Spectroscopy", June 1996, ESRF, Grenoble, G. Grübel, D. Abernathy (eds.) .

[38] S. DiFonzo et al., Nature **403**, 683 (2000).

[39] F. Pfeiffer, C. David, T. Salditt, to be published.

[40] H.-P. Cheng and J.D. Gillaspy, Phys. Rev. B**55**, 2628 (1997).

[41] A.H. Chin et al., Phys. Rev. Lett. **83**, 336 (1999).

[42] J.M. Samon et al., J. Polym. Sci. Phys. **37**, 1277 (1999).

[43] J.M. Samon et al., Macromolecules **32**, 8121 (1999).

[44] J.W.H. Kolnaar, A. Keller, S. Seifert, C. Zschunke, H-G. Zachmann, Polymer **36**, 3969 (1995).

[45] Y.-X. Yan and K.A. Nelson, J. Chem. Phys. 87, 6240 (1987).

[46] A.I. Chumakov, private communication .

[47] R. Röhlsberger et al., Physica B **263-264**, 581 (1999).

[48] W. Sturhahn et al., J. Magn. Magn. Mat. **198-199**, 590 (1999).

[49] R. Röhlsberger et al., J. Appl. Phys. **86**, 584 (1999).

[50] T. Suzuki, J. Phys. Soc. Jap. **22**, 1139 (1967).

[51] N. Watanabe, H. Hayashi, Y. Udagawa, K. Takeshita, H. Kawata, App. Phys. Lett. **69**, 1370 (1996).

[52] U. Bergmann, O.C. Mullins, S.P. Cramer, Anal. Chem. **72**, 2609 (2000).

[53] W. Schülke, U. Bonse, H. Nagasawa, A. Kaprolat, A. Berthold, Phys. Rev. B**38**, 2112 (1988).

[54] M.H. Krisch, F. Sette, C. Masciovecchio, R. Verbeni, Phys. Rev. Lett. **78**, 2843 (1997).

[55] M. Richwin, R. Zaeper, D. Lützenkirchen-Hecht, R. Frahm, J. Synchrotron Rad., in press (2001).

[56] W.A. Tolbert, W.M. Dennis, W.M. Yen, Phys. Rev. Lett. **65**, 607 (1990).

[57] R. Röhlsberger et al., Nucl. Instrum. Meth. A**394**, 251 (1997).

[58] R. Röhlsberger, in *Nuclear Resonant Scattering of Synchrotron Radiation*, E. Gerdau, H. de Waard (eds.), Hyperfine Inter. **125**, (2000).

[59] W. Sturhahn et al., Phys. Rev. Lett. **74**, 3832 (1995).

[60] E. Burkel, *Inelastic Scattering of X-Rays with Very High Energy Resolution*, Springer-Verlag, New York, (1991).

[61] A.I. Chumakov et al., Phys. Rev. Lett. **76**, 4258 (1996).

[62] R. Röhlsberger et al., Phys. Rev. Lett. **84**, 1007 (2000).

[63] L. Mandel and E. Wolf, *Optical Coherence and Quantum Optics*, Cambridge University Press (1995); S.K. Sinha, M. Tolan, A. Gibaud, Phys. Rev. B**57**, 2740 (1998).

[64] M. Tolan, *X-ray Scattering from Soft-Matter Thin Films*, Springer, Berlin (1999).

[65] J.G. Stevens and V.E. Stevens, *Mössbauer Effect Data Index*, Plenum Press, New York (1973).

[66] Yu.V. Shvyd'ko et al., Phys. Rev. Lett. **77**, 3232 (1996).

[67] Yu.V. Shvyd'ko, Phys.Rev. B**59**, 9132 (1999).

[68] A.Q.R. Baron et al., Phys. Rev. Lett. **79**, 2823 (1997).

[69] R. Fourme, Nucl. Instrum. Meth. A**392**, 1 (1997).

[70] C. Broennimann et al., Nucl. Instrum. Meth., in press.

[71] A.Q.R. Baron, Hyperfine Inter. **125**, 29 (2000).

[72] R.H. Templer, N.A. Warrender, J.M. Seddon, J.M. Davis, A. Harrison, Nucl. Instrum. Meth. A**310**, 232 (1991).

[73] E.M. Westbrook and I. Naday, Meth. Enzymology **276**, 244 (1997).

[74] S.M. Gruner, M.W. Tate, E.F. Eikenberry, *CCD Detectors*, *International Tables for Crystallography, vol. F: Macromolecular Crystallography*, Kluwer Academic Publishers, Dordrecht. in press.

[75] J. Lowrance, personal communication, Princeton New Jersey, 1999.

[76] A. Koch et al., Proc. SPIE **3659**, 170 (1999).

[77] G. Rossi, J. Synchrotron Rad. **6**, 1096 (1999).

[78] B. Adams, Nucl. Instrum. Meth. A**459**, 339 (2001).

6. Beam Line Design and Instrumentation

The proposal for beamlines in this chapter has been written on the basis of contributions to the report of the workshop "Methods and Instrumentation for an XFEL" edited by J. Hastings (BNL Brookhaven) and Th. Tschentscher (HASYLAB, Hamburg) and of explicit design proposals for a beamline for time-resolved studies by D. Mills, et al. (APS, Argonne, U.S.A) and for a soft X-ray beamline by R. Follath, F. Senf, W. Gudat (BESSY Berlin). In the report (see A.1.5), more detailed description and further references can be found.

In this chapter we present details for the beamline design and give a principle distribution of different experimental methods. The general beamline design will be based on a generic layout, presented in the first part of this chapter. It comprises all elements needed for the design of one specific layout. Since the detailed request for the special experiments can not be foreseen at this present state we made sure that the generic design is flexible enough to incorporate the demands of the beamlines and experiments requested. The second part of the chapter considers the assignment of experimental techniques to the various XFEL beamlines. Five beamline proposals and considerations are presented here in more detail, each optimized to use a different characteristics of the XFELs, namely time resolution, high energy and momentum resolution, imaging, spectroscopic applications, and soft X-rays. Depending on the proposal, details concerning optical elements or the instruments to be installed at this beamline may be omitted. With respect to costing we have chosen four representative experiments, namely atomic and cluster research, biological studies, nuclear resonance scattering and time-resolved studies as representatives for the large variety of methods. From this an average cost per experimental station is deduced. No detailed distribution of the experimental techniques discussed in Chapter 5 has been attempted. No special assignment has been done for the beamlines and experiments using the radiation from spontaneous undulators.

6.1. Generic Photon Beamline Layout

For the beam transport between undulator and experimental hall, a generic beamline, which contains all needed elements to guide the XFEL photon beam to the experiment, is defined. This generic beamline consists of the estimated maximum number of components for this purpose. Special experimental needs may reduce the number of proposed devices in the generic part and add special optical devices close to the experiment. The elements in the generic beamline will provide the following functions:

- Transport of the photon beam from the undulator to the experiment, conservation of the beam properties, especially of the transverse coherence

- Filtering
- Beam position monitoring
- Beam shaping
- Focussing
- Monochromatization
- Radiation safety, collimator, beamshutter
- Vacuum system, hydrocarbon-free, dust-free

In addition, especially the SASE beamlines depend on a photon diagnostic station to ensure an operation of the segmented undulators in the SASE regime.

6.1.0.5. Filtering

The purpose of filters is the reduction of the intensity (flux) of the SASE line by several orders of magnitude down to the level of the incoherent radiation from the same undulator. The proposed solution consists of a 100 m long absorption cell [1, 2] with an average Xenon pressure of between 10^{-4} and 0.2 mbar. The differential pumping scheme of the beam position monitors (BPM) at the entrance and at the end of this section can be adapted to allow operation at these pressure levels. To minimize the Xe consumption, a gas recirculation scheme will be used.

6.1.0.6. Beam position monitors

Beam position monitors will measure the photon beam position in the beamline along the beam path. They are also needed for aligning the photon beam emitted by single undulator segments during the set up phase of SASE and spontaneous undulators. A precision of 10% of the beam parameters, i.e. for 1 Å a resolution of 10 μm and 0.1 μrad is needed. With a distance of 100 m between the monitors, this specification can be reached by measuring the intensity center with split electrodes ionization chambers [3, 4]. An average pressure of 0.1 mbar should be sufficient for a filling with nitrogen gas. The operation of the monitors with Xe gas should also be possible. Since the monitors are integrated in the absorption cell, it needs a special differential pumping scheme.

To measure the relative position of buildings and components, the installation of a global levelling system with a resolution of 0.1 mm relative to a line connecting undulator and experiment is mandatory. A possible implementation of such a system can be built following the SLAC final focus beam alignment proposal [5].

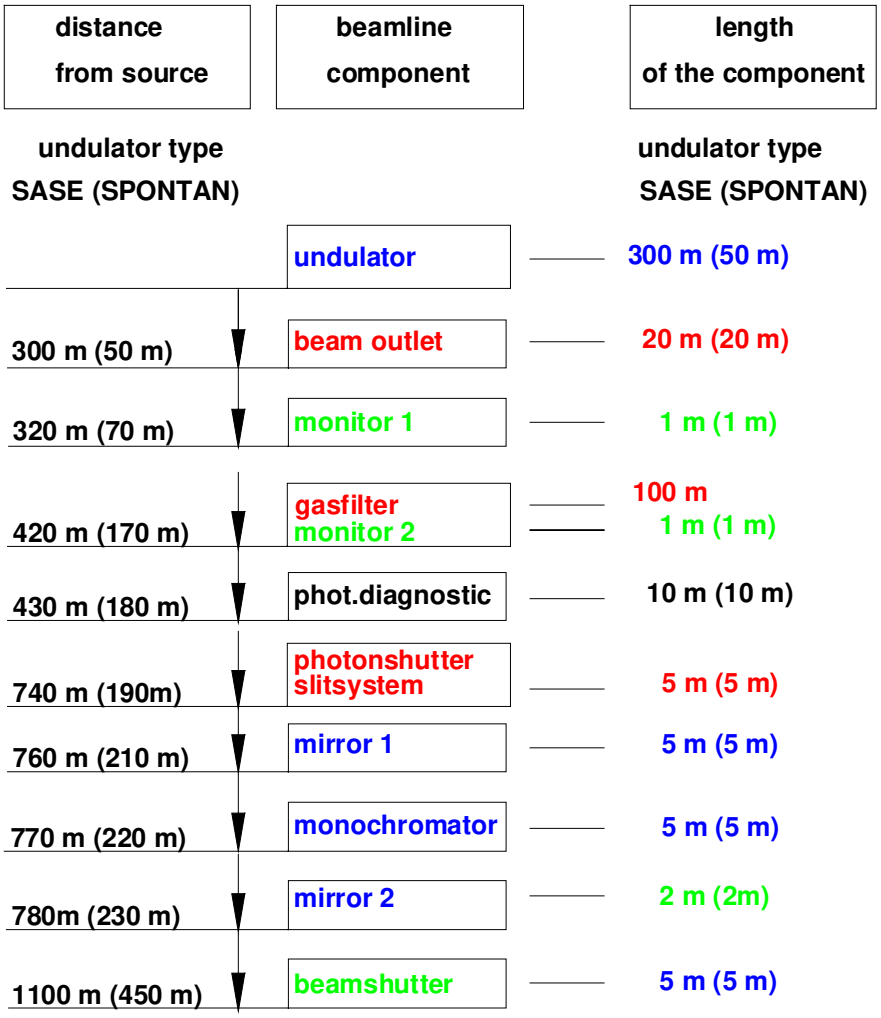

Figure 6.1.1.: *Schematic of a generic beamline for the XFEL laboratory.*

6.1.1. Beam shaping and photon shutter

The first harmonic of the spontaneously emitted undulator spectrum has the same divergence as the coherent amplified XFEL line. Because both lines overlap in space, only even harmonics and the off-axis intensity of odd harmonics will be stopped in apertures. As any edge interfering with the coherent XFEL beam will lead to diffraction patterns [6] and thereby reduce the homogeneity of the beam profile, any aperture size should be 2-3 times larger than the coherent beam size at that position. A similar condition applies to the primary slit system. As a solution, a slit system is foreseen which allows absorption of off-axis radiation of the undulator combined with a power absorber to shut off the photon beam. The realization of this slit system will follow the design of devices built for PETRA beamlines, modified according to the increased power of the XFEL photon beam [7, 8]. The total power in the incoherent beam will be as high as 20 kW and 0.2 – 1 kW in the SASE line.

6.1.2. Mirror systems

Two one-meter long mirrors provide a fixed offset of the beam and keep the size of the beamline tunnel on a reasonable level. The mirrors will provide a separation from the bremsstrahlung background and a suppression of incoherent high energy radiation. >From average power load considerations a Si mirror substrate is the best available choice. To minimize the absorbed power, a coating with Be or C is the most likely solution. At a glancing angle of 2 mrad the full coherent photon beam will be accepted by a 1 m long mirror. An open question arises for the low energy regime below 3 keV due to large photon cross sections.

A special issue for all mirrors is coherence preservation. The necessary precision of the mirror surface with figure errors in the nm range is reached by ion beam figuring. Ultra-small glancing angles will lower the precision requirements and the power density on the mirror surface at the expense of drastically enlarged mirrors with lengths close to 5 m. The space for such large devices should be available in the tunnel. Ultra micro focusing schemes in Kirkpatrick-Baez configuration with bent plane mirrors and mirror lengths of 5 m require further R&D (see also A.1.5 and Ref. [9]).

6.1.3. Monochromators

A fixed-exit double-crystal monochromator set up with the option of either Laue- or Bragg-geometry will be used. Preservation of coherence will require the use of silicon monochromator crystals due to the ultimate perfection of single crystal silicon. Isotopically enriched ^{28}Si should be able to accept the average power density due to the enhanced thermal conductivity compared to natural Si. For all experiments not depending on the transverse coherence properties of the photon beam, diamond crystals will be used, either at room temperature or cryogenically cooled. The decision between the use of Laue-cases and Bragg-cases and possible combinations of both depends on the tolerance to chromatic aberrations. Due to the small size of the perfect area of synthetic diamond crystals in the 5×5 mm^2 range, a C (100) cut diamond in a Laue-case setup is favorable. Other means of beam conditioning, like the use of asymmetric crystals, have to be explored carefully in order to preserve the quality of the beam. Directly connected to monochromatization is the bunch length in time. The overall length of the photon pulse of 100 fs will not be affected, but the spike structure inside the bunch on a 0.1 fs scale will be affected according to the degree of monochromatization [10]–[17].

6.1.4. Vacuum components

6.1.4.1. General requirements

An average pressure of 10^{-7} mbar is targeted. This pressure range is determined by the acceptable absorption of the photon beam and by the operation and lifetime of ion-pumps. Differential pumping for a windowless operation of the beamline is mandatory. A vacuum system free of dust particles is necessary to avoid destructive coherence effects at the surfaces of mirrors and monochromators. This means all cleaning and mounting of devices has to be done in a class 100 clean room environment. The design and assembling of the beamline

instruments have to take this requirement into account. To avoid contamination of surfaces, a hydrocarbon free vacuum (partial pressures of Hydrocarbons < 10^{-3} of the total pressure) is needed.

Device	Distance to source (SASE)	Length	Distance to source (spont. radiator)	Length	Tube diameter	Remarks
Units	[m]	[m]	[m]	[m]	[mm]	
Beam outlet	300	20	50	20	60	
Linac valve					60	all metal
1^{st} beam position monitor	320	1	70	1	60	
Differential pumping step	320	10	70	10	10-100	
Gas filter	321	100	71	100	100	
Differential pumping step	410	10	160	10	10-100	
2^{nd} beam position monitor	420	1	170	1	60	
Beampipe		9		9	100	
1^{st} photon diagnostic	430	10	180	10	100	
Beampipe		310		-		
Photon shutter	740	5	190	5	100	
1^{st} valve					60	Fast, particle free, Viton sealed
Beampipe		15		15	100	
1^{st} mirror chamber	760	5	210	5		additional pumping
2^{nd} valve					60	particle free, Viton sealed
Beampipe		5		5	100	
Monochromator	770	10	220	10		additional pumping
2^{nd} mirror chamber	780	5	230	5		additional pumping
4^{th} valve					60	particle free, Viton sealed
Beampipe		315		115		
Safety beamshutter	1100	1	350	1	60	
5^{th} valve					60	Fast, particle free, Viton sealed

Table 6.1.1.: *Vacuum layout of SASE (columns 2 and 3) and spontaneous radiation (columns 4 and 5) beamlines.*

6.1.4.2. Layout of the beamline vacuum system

Table 6.1.1 shows the vacuum structure of the different beamline types. Distinction is made between SASE beamlines, which are longer and carry beams with high peak powers, and beamlines for spontaneous radiation. In Tab. 6.1.1 the position of the various devices to be installed in the photon beamline are listed with their respective position and length. The diameter of the vacuum beam tube between devices, as well as special remarks, are added where needed. Five vacuum sections, separated by valves, are proposed. The first valve close to the particle beam should be an all-metal valve, while for the others Viton sealed valves are preferred. This is because of simplicity, the particle-free operation, and possible short closing times of these devices. The pressure demand for mirror and monochromator chambers will be in the 10^{-9} mbar range to minimize contamination. A beampipe diameter of 100 mm is chosen to reduce the number of pumps along the beamline. Ion pumps with a

nominal pumping speed of 75 l/sec installed at a distance of 30 m will result in an average pressure of $<10^{-7}$ mbar. The pressure difference at mirror and monochromator chambers will result from the differential pumping.

6.1.4.3. Operation of the beamline vacuum system

The first valve in the beamline (linac valve) has no protection against synchrotron radiation. This means it can only be closed when the related undulator is not radiating, e.g. the magnetic gap of all undulator elements are open or no electron beam is accelerated. All other section valves and the beamshutter are protected by the photon shutter. The two differential pumping stages of the absorption cell need a special operation and safety system. The accidental venting of large beamline parts with a long pumping time to restore the vacuum has to be excluded.

6.2. Beamline Assignment and Instruments

6.2.1. Time-resolved experiments : SASE 1

In the following, the beamline design foreseen for time-resolved experiments with a particular focus on subpicosecond investigations is presented. Applications of this technique have been described in the scientific case. In Sec. 5.3 some considerations for time-resolved scattering techniques are given.

6.2.1.1. Requirements for the experiments station

For pump and probe experiments it holds true that, whatever the source of the pump is, the pump and probe beam must be as collinear as possible in order to achieve the highest temporal resolution. This is the first requirement placed on the general layout for a time-resolved experiment station. White beam operation (or more likely "pink" beam operation, where mirrors are used to reduce the high energy component of the spontaneous spectrum) will be required for Laue diffraction techniques. Experimental stations and optics must be designed to permit this mode of operation. Additionally, a standard double-crystal monochromator (ΔE/E $\sim 10^{-4}$) will be required for scattering and spectroscopy experiments. Flux per pulse is an issue for one-shot experiments and will continue to be a concern even for an x-ray FEL. At currently operating synchrotron radiation sources, increased flux can be realized through the use of multilayer optics. However, wide bandpass optics may not be necessary at FEL's, since the x-ray first harmonic line has a natural energy spread of 10^{-3} and can be isolated with a small aperture. Even if this approach is taken, mirrors will still be required to remove the high-energy components that remain in the collimated beam. Focusing will undoubtedly be required on a time-resolved beamline. Clearly all these x-ray optical components will require considerable R&D in order to perform effectively and efficiently under the very high instantaneous power loads that will be generated by the x-ray FEL. Those issues will be addressed in more detail in the section on x-ray optics. The following layout considerations

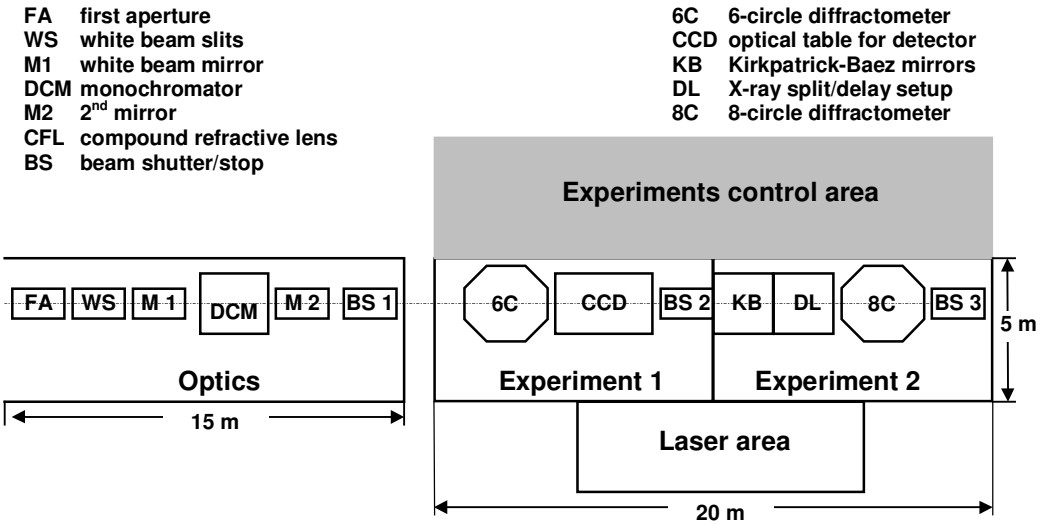

Figure 6.2.1.: *Proposed beamline for time-resolved studies (see A.1.5). A description of the different items is given in the drawing.*

contain some of the reasoning and motivation behind the conceptual design developed for a time-resolved beamline at an XFEL laboratory.

6.2.1.2. Desired beam properties

The beamline design reflects the fact that preservation of the temporal properties of the beam and/or synchronization capabilities are high priorities. Both monochromatic and white beam capabilities were considered a necessity to cover the widest possible range of experiments. These two requirements, short pulse/synchronization and mono/white beam capability, define much of the optics and beamline layout. Coherence preservation was not considered a high priority for this beamline.

6.2.1.3. Detailed layout

As can be seen from the layout drawing in Fig. 6.2.1, the basic setup is a tandem experiment station arrangement with a control cabin for researcher workspace and a laser control area for the installation of visible light lasers for pump/probe experiments. (Due to the size of the experiment hall floor space, only two tandem stations could be incorporated into the design.) The tandem configuration was chosen rather than a "tanzboden" arrangement because it allows the primary instruments (6- or 8-circle diffractometer, CCD set ups, etc.) to remain fixed (no hooking and unhooking cabling in order to move them), thereby minimizing set-up time. In addition, fixed instrumentation permits alignment of a laser with respect to the goniometer (for instance) in Station 2 while x-ray experiments are being performed in Station 1. If possible a shielded beam pipe can be inserted in Station 1 to allow access in that station while beam is passed to Station 2. That arrangement would then provide access to either station while the other takes beam.

The layout drawing includes a laser control area designed to house a laser that can be synchronized to the x-ray beam. The exact location is not critical, but it is a requirement for a time resolution below a few picoseconds that the pump and probe beams have to be collinear. This requirement may have some bearing on the final location of the pump laser. Rather than having a laser in close proximity to the stations, an alternative approach may be to derive the pump pulse from the same laser used for the photocathode gun or from some other centrally located laser. This would require laser-beam transport from the laser source to these stations.

Another potential pump source for a two-color pump/probe experiment could be a second undulator through which the electron pulse from the XFEL could be passed. If this approach, essentially a second ID, is considered, then an additional front-end, radiation safety system, optical system and beam transport system would need to be installed.

First optics and first optics enclosure The optics enclosure should be placed as far from the source as possible and as close to the experiment stations as possible. (This area does not fit within the current experiment hall floor space and hence must be in an enlarged part of the beam transport tunnel.) Non-optical components in the optics area include fixed apertures, user-controlled white-beam slits, a filter for power reduction, and a combined or integral beam stop to prevent passage of the white/pink beam but control the passage of monochromatic beam into Station 1 or 2. (Note that there is a similar component in Station 1.) This will allow the white beam to enter Station 1 but allow safe access for setup in Station 2. The proposed optics include a double-crystal monochromator (DCM) flanked on either side by two flat mirrors to keep the outgoing beam, whether it be monochromatic or "pink" (white beam with the high energy component removed), parallel with the incoming beam. The beamline could be run in four different modes: (a) no optics in place (white beam mode), (b) two mirrors and DCM (mirrors for harmonic rejection- mono mode), (c) two mirrors (pink beam mode or with narrow slits, sort of a pseudo-monochromatic mode) or (d) with just the DCM (high-energy mono mode). Due to the very high effective critical energy of the radiated spectrum, space is also provided for a compound refractive lens for focusing in the horizontal and/or vertical directions.

Experiment stations Since the spontaneous spectrum from an XFEL can extend well in to the MeV range, and Bremsstrahlung radiation could be more intense than at third generation sources, considerably more shielding will be necessary than at e.g. the APS.

Experiment instruments and control Station 1 is equipped with more or less routine synchrotron radiation instruments, a 6-circle diffractometer, an optical table, and CCD system. Station 2 has been outfitted with an 8-circle along with a Kirkpatrick-Baez mirror set-up (when small beams and microfocusing capabilities are required) and space for an x-ray beam splitter/delay line arrangement. Laser beams can enter either station from the laser control area, which will house various lasers for pump/probe experiment. The experiment is controlled through computers and electronics located in the control cabin.

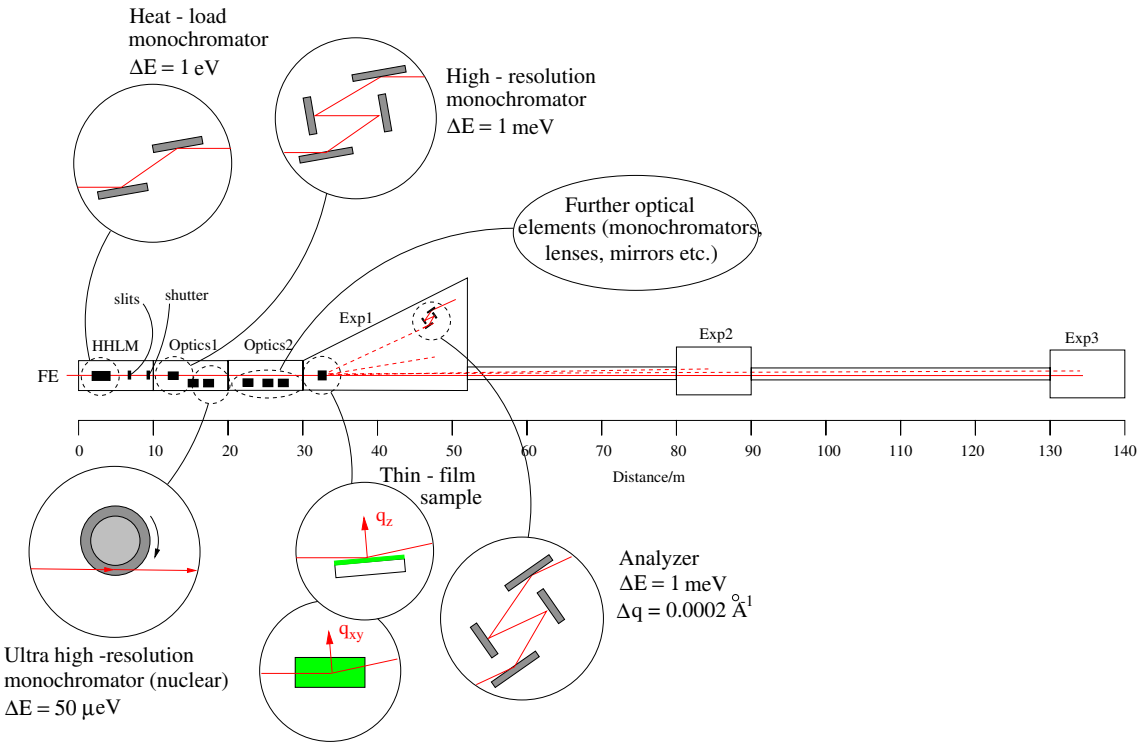

Figure 6.2.2.: *Schematic layout for a beamline at the XFEL, incorporating experiments at small momentum transfers and inelastic x-ray scattering experiments as well as examples of nuclear resonant scattering and scattering from thin films.*

6.2.2. High resolution scattering : SASE 2

The beamline discussed here should use the SASE 2 undulator at the nuclear transition energies listed in Tab. 5.3.1. The beamline layout allows the performance of nuclear resonance scattering experiments in various fields of natural sciences as well as surface science experiments in particular. The schematic design of the beamline in Fig. 6.2.2 includes a station with a horizontal spectrometer for coherent inelastic scattering and a long section with two experimental stations at distances of 50 m and 100 m from the sample, respectively. The long baseline is mainly motivated by the desire to access very small momentum transfers. This is particularly important for methods which require an additional time-resolution like speckle correlation interferometry, where the detector pixel size cannot be made arbitrarily small while maintaining a good time resolution.

Arguments for a long experimental arrangement A beamline of about 100 m length is needed for experiments that rely on the analysis of very small momentum transfers. This is particularly true for the case that not only spatial information has to be recorded, but other parameters have to monitored too, e.g., the time evolution of the scattering process or the energy of the scattered radiation. In those cases the pixel size of the detector cannot be made arbitrarily small. Consequently, one has to move away from the scattering center to ensure a

sufficient q - resolution.

Besides applications in the field of nuclear resonant scattering there are also other areas in condensed matter research that will benefit from such a beamline. In particular, inelastic X-ray scattering and time-correlation spectroscopy applications will benefit. The nuclear lighthouse effect is the main application that requires a long baseline. When the time response of the scattering is mapped to an angular scale, very short times are located very close to the direct beam.

6.2.3. Imaging and coherence experiments : SASE 3

The general layout of an imaging beamline at the XFEL must provide beams conditioned for all classical and most of the emerging techniques. Obviously, the optical hutch must include elements for:

- beam focusing with Fresnel zone plates, Bragg-Fresnel diffraction plates, compound lenses. This class of optics profits most from the diffraction limited source, as the footprint of the beam on the optical elements becomes equal to the transverse coherence length. These microfocusing optics can work most effectively under such conditions.
- beam focusing with bent mirrors and multilayers. The focused beams will be used for low-resolution scanning microscopy, as such optics destroys the coherence of the beam.
- monochromatization (standard double-crystal monochromators, most probably thin-film single crystal diamond, double-crystal back-scattering secondary monochromator to achieve large longitudinal coherence lengths);
- mirrors (flat, double-mirror arrangement);
- beam splitters and intensity attenuators.

Additional optics in the experimental hutch add short focus capillaries, an attenuator for scattered beams, and magnifying elements and choppers for time resolved measurements. Slits inside the coherent beam should be avoided as far as possible. The requirements on the detector side correspond to those of already available CCD-based cameras (1000 X 1000 pixels, 25 μm resolution). The cameras should be significantly more tolerant to high intensities. At the moment there are no area detectors available with acquisition speeds comparable with the $\sim$ 100 fs time scale of the XFEL light bunches. Therefore the experimental approach for time resolved measurements can be based on choppers and/or pump and probe techniques.

6.2.4. Raman Spectroscopy : SASE 4

Here we describe one particular instrumentation this beamline will be suitable for: Inelastic X-ray Raman scattering has the potential to provide information like today absorption spectroscopy does. In particular, it enables to investigate low Z materials at photon energies of 8 to 12 keV. The beamline design is based on the generic beamline concept and options

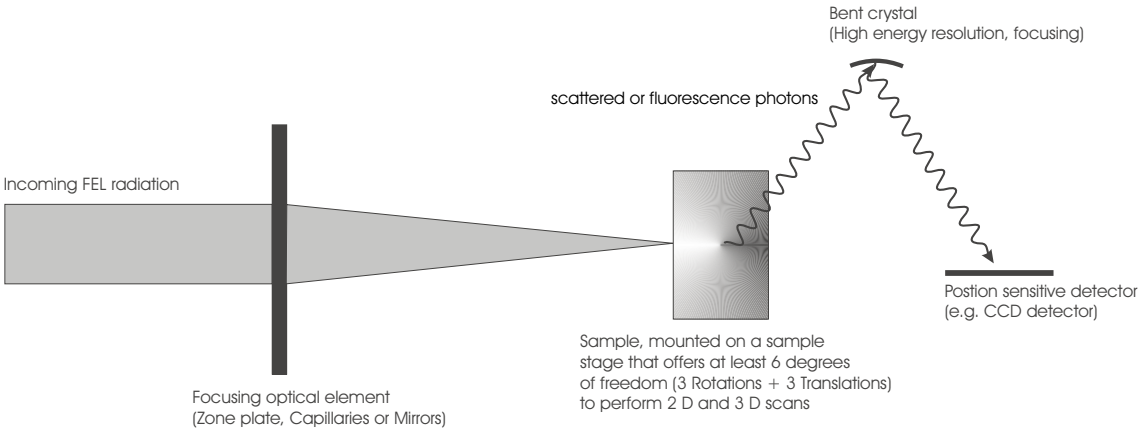

Figure 6.2.3.: *Proposed experimental setup for X-ray absorption and X-ray fluorescence spectroscopy with sub-micrometer spatial resolution at the XFEL.*

for monochromatization and focussing will be available. The SASE 4 undulator will provide FEL radiation from 1 to 10 Å wavelength. Also use of the spontaneous radiation above 15 keV has to be foreseen. Figure 6.2.3 shows the principle of the beamline layout employing focussing to enable good spatial resolution. The monochromatization to a bandwidth $< 10^{-4}$ will reduce at the same time the power in the beam.

6.2.4.1. Spectrometer for inelastic X-ray Raman scattering

While at third generation sources this technique starts to become accessible, at an XFEL X-ray Raman spectroscopy could be performed on a time frame below 1 s, using a few bunch trains. We describe here two wavelength dispersive spectrometers to be installed at this beamline. Both can collect Raman spectral data without scanning the incident wavelength.

Arrays of spherically curved analyzers This system is based on arrays of Johann type crystals aligned in Rowland geometry. It is a one-to-one imaging device and requires a one-dimensional position sensitive detector (PSD) and a line shaped incident beam. Figure 6.2.4 shows the schematic setup of a version using eight crystals. In an advanced setup a total of $\approx$ 80 crystals in four arrays could cover a solid angle of $\approx$5% of 4π sr. In a typical X-ray Raman experiment with a concentrated low Z system (Li, C), the edge jump (scattered into 4π sr) accounts for $1 - 2 \cdot 10^{-8}$ of the incident photons. An XFEL flux of $5 \cdot 10^{11}$ photons/bunch in a 0.5 eV bandpass would result in a total of at most 10^4 photons/bunch/4π sr distributed over the x-ray Raman spectrum. This is not sufficient for a single bunch experiment with the device discussed here. However, a few millisecond long bunch trains consisting of 10^4 bunches would give enough signal for high quality Raman XANES.

Arrays of cylindrically curved analyzers Sagittal focusing of a cylindrically curved analyzer has only a second-order effect on its energy resolution and is therefore well suited

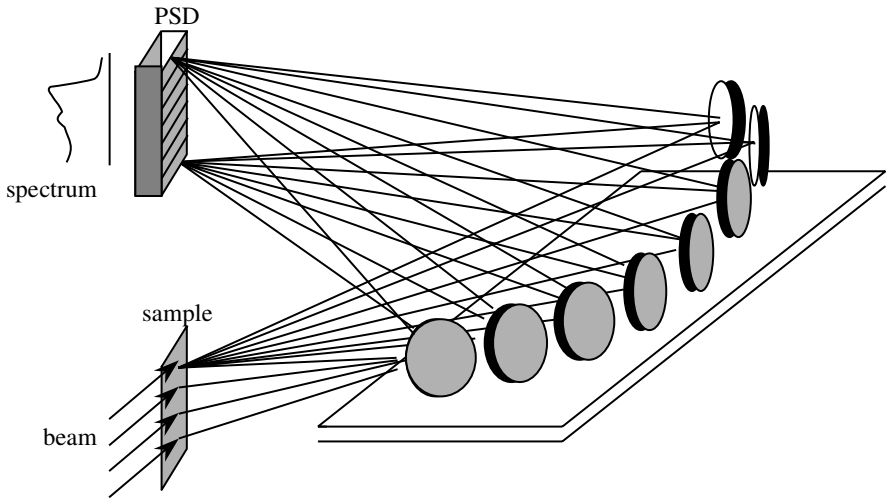

Figure 6.2.4.: *Schematic setup of an array of spherically curved crystals in Rowland geometry. Scattering of a vertically defocused beam is analyzed at different energies resulting in a spectrum on the PSD.*

for a wavelength dispersive device with good energy resolution. Figure 6.2.5 shows a possible design. Each of the four quarter-circles consists of four crystals with a radius of curvature of order 30 cm (depending on the required resolution). The solid angle Ω of such a device can be calculated with the following equation:

$$\Omega[4\pi\ sr] = 1/2\,[cos\theta - cos(\theta - \Delta\theta)] \approx 1/2\ \Delta E/E\ sin\theta\ tan\theta.$$

For a Si(444) reflection (backscattering energy 7.9 keV) the Bragg angles in a XANES region ($\approx$ 100 eV) could range from 81° to 88° and the total solid angle would be 6% of 4π sr. If an energy resolution of ΔE=0.5 eV is chosen, the solid angle per ΔE ranges from $2{\cdot}10^{-4}$ at 81° to $9{\cdot}10^{-4}$ at 88°. This results in a Raman XANES signal of $\approx\ 10^4 - 10^5$ photons/bunchtrain/ΔE. For a Raman EXAFS experiment the typical energy range is < 800 eV. The range of Bragg angles in this case is $65° - 88°$ resulting in a total solid angle of 19% of 4π sr. With an energy resolution of $\Delta E = 10$ eV, the solid angle per ΔE ranges from $1.1 \cdot 10^{-3}$ at 65° to $1.8 \cdot 10^{-2}$ at 88°. The incident photon flux in a 10 eV band would be essentially the total number of photons coming from the XFEL or $\approx 5 \cdot 10^{15}$ per bunch train, resulting in a Raman EXAFS signal of $\approx\ 10^6 - 3 \cdot 10^7$ photons/bunchtrain/ΔE.

Such an array of cylindrically curved analyzers in combination with a position sensitive detector would capture a sufficient solid angle to obtain both Raman XANES and EXAFS spectra from an XFEL bunch train consisting of 10^4 bunches. The array of spherically curved crystals would yield a similar or slightly better performance for a XANES spectrum if the required energy range is less than 100 eV. The advantage of the spherically bent crystal optics is the fact that a line shaped beam causes less radiation damage, but it requires a much larger and homogenous sample. For very small energy ranges (< 50 eV) the solid angle might be

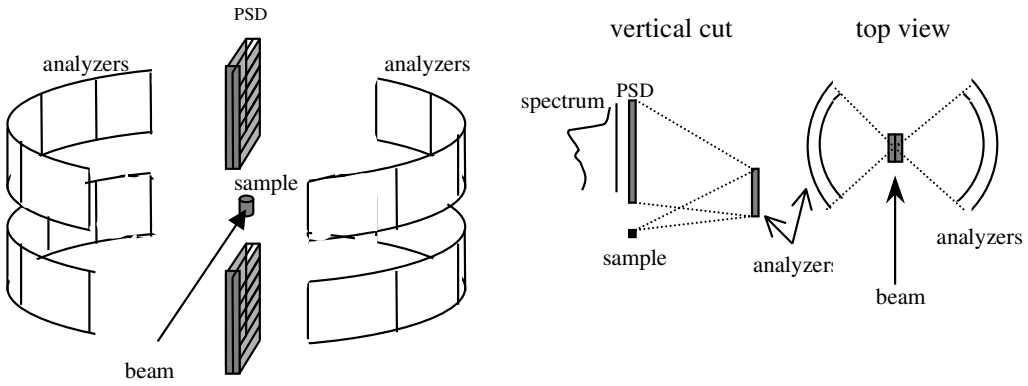

Figure 6.2.5.: *Schematic setup of four arrays of cylindrically curved crystals in sagittal focusing mode. Scattering of a point source beam is analyzed at different energies (see vertical cut) resulting in spectra on the PSD.*

also somewhat larger in this setup.

Obtaining a Raman XANES from a single bunch is not possible with either of the devices. However, one could possibly construct a crystal ball type instrument specialized to a smaller energy range, but capturing a very large fraction of 4π sr. In that case, a single XFEL bunch could be sufficient to obtain a Raman XANES spectrum. The XFEL will take the time scale for Raman XAS experiments to fractions of a second per spectrum for typical samples, making Raman XAS almost as routine as conventional XAS is today.

6.2.5. Soft X-rays : SASE 5

The energy range from 500 to 3000 eV, to be opened by this beamline, is particularly interesting for several reasons. It bridges the gap between the VUV-FEL currently under construction at DESY and the other X-ray beamlines planned at the TESLA facility. In this energy range, element specific core level spectroscopy is possible under conditions where the depth sensitivity with respect to solid samples can be tuned from highly surface sensitive to more or less bulk sensitive. The available energy range covers the K-edges of the low Z-elements up to Ar, the important L-edges of the 3d transition-metals as well as the M-edges up to Pt and Au. Hence, a large variety of material science problems can be tackled using element specific core level spectroscopy.

6.2.5.1. Introduction to the monochromator design

Based on an undulator with 107 mm period length and an electron energy of 23 GeV, the SASE 5 XUV-FEL will generate coherent radiation of several hundred GW peak power in an energy range from 500 eV to 3100 eV with an intrinsic line width of approximately 0.5%. For various experiments and spectroscopic examinations a higher degree of spectral resolution is required. To meet this demand, a monochromator has to reduce the bandwidth of the

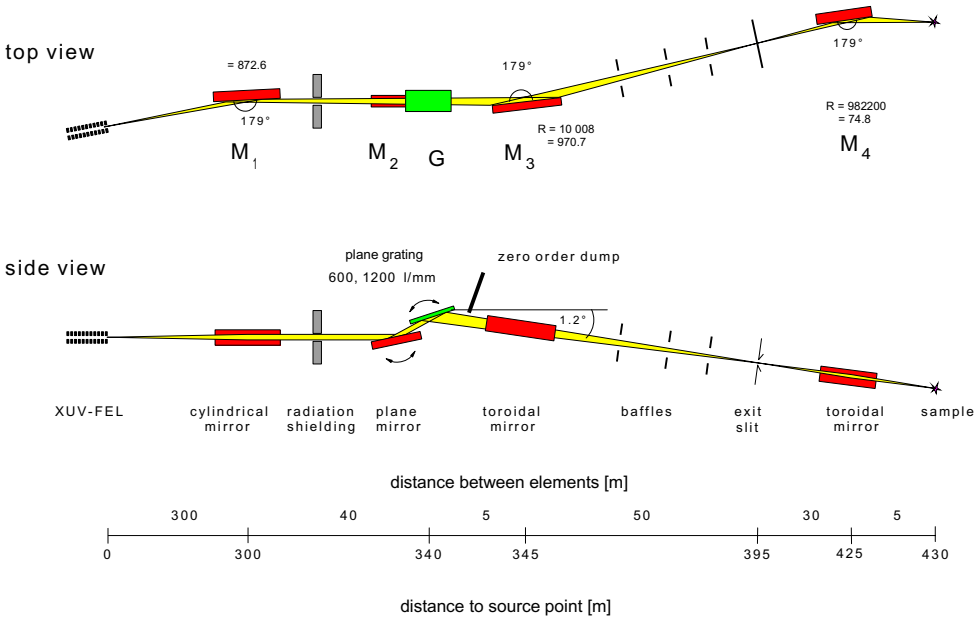

Figure 6.2.6.: *Optical design of the XUV-plane grating monochromator. See also A.2.3 for a more detailed description of this design.*

radiation.The monochromator should achieve a resolving power E/ΔE of 10.000 across the whole spectral range with relatively high transmittance.

A challenge is the high brilliance of the XUV-FEL. The optical elements will be exposed to tremendous photon densities. Especially in the XUV energy range atoms exhibit a high absorption cross section which could lead to a continuous evaporation of surface atoms. On the other hand, taking advantage of the high brilliance, very small angles of incidence can be chosen at still tolerable lengths of the optical elements. The large distance between the FEL and the first optical element can reduce the density to a reasonable level. As will be shown below, also the grating problem can be solved by using the same advantage of the FEL and appropriate coatings. However, the high photon densities, the total amount of absorbed power and a good performance in the desired energy range push the proposed design to the limits of existing technology.

6.2.5.2. Beamline design

The proposed beamline design takes pattern of the very successful line of plane grating monochromators of BESSY II [18]. The existing PGMs at BESSY operate in parallel light, which, together with a rotatable plane mirror in front of the grating, allows for a free choice of the incidence and diffraction angles. At the FEL the high photon density prohibits this operational mode. The collimated beam — generated by the first mirror — would require a grating length of 600 mm (4σ–value of the beam cross section), which is not feasible.

However, the first mirror can also be used to generate a convergent beam. In this design

a vertical demagnification of 5:1 was chosen with a vertical image located 20 m downstream of the grating. A 200 mm long grating then accepts nearly all (4σ) of the FEL beam. Two gratings G1 and G2 with line densities of 600 l/mm and 1200 l/mm, respectively, have been optimized to cover the energy ranges of 500 – 1200 eV and 1200 – 3100 eV. The final optical scheme is shown in Fig. 6.2.6 and the parameters of the optical elements are listed in Tab. 6.2.3.

The plane mirror M2 in front of the grating allows for a variable deflection angle so that the angles of incidence and diffraction at the grating, α and β, can be set independently. Since the plane grating is now illuminated in convergent light, its focusing properties must be taken into account [19]. The grating generates a virtual image of the source, with a source distance r, in an image distance $r' = c^2 \cdot r$. The fix-focus constant c is related to the angles of incidence and diffraction (measured to the surface) by $c = \sin\beta / \sin\alpha$. For high energy resolution its value has to be kept constant for the whole energy range. In contrast to the SX700 design (c=2.25), the fix-focus constant had to be increased in order to reduce the angle of incidence on a 200 mm long grating and hence reduce the photon density. In order to achieve a good compromise between resolving power ($\sim$ 10000) and transmission a c value of 5 was chosen. With c=5 the virtual image then is located 500 m downstream of the grating.

Mirror M3 focuses the virtual image onto the exit slit which is located 50 m downstream yielding a total vertical demagnification of 10:1. The diffracted beam declines vertically with 1.2° in order to achieve a high transmission. By declining the diffracted beam the angle of incidence on the mirror M2 can be reduced and its reflectivity will increase (A.2.3). Horizontally, the beam is unaffected by the deflection of M1 and propagates with its natural divergence until M3. The toroidal mirror M3 focuses onto the exit slit, making a 7:1 horizontal demagnification. A heat dump between the gratings and M3 removes the specularly reflected zero order of the grating. Baffles between M3 and the exit slit reduce stray light caused by reflections of the dispersed light at the tube walls of the beamline. A horizontally deflecting toroidal mirror provides a 6:1 demagnified image of the exit slit at an image distance of 5 m. The distance of 40 m between M1 and grating and a deflection angle of 1° should be sufficient to install radiation shields against the against background from spontaneous radiation or Bremsstrahlung. With a c-value of 5 from the grating a slope error of up to 0.5" (FWHM), including thermal deformation is tolerable for the pre-optic without deteriorating the resolving power.

To enable the so called fix-focus operation mode, the deviation angle at the grating is varied with photon energy by the plane mirror M2. For this, in principle it has to rotate and translate along the incident beam. This combined motion can be approximated by a single rotation around a particular axis which is located outside the mirror surface [20, 21]. Since the rotation axis of the plane grating is not in the intersection of the incident beam and the mirror surface, the illuminated area on the plane mirror moves along the mirror surface during an energy scan. This implies an increased length of the mirror compared to the operation with decoupled motions.

The vertical distance y_0 between the incident beam and the grating rotation axis is chosen to be only 8 mm in order to get an acceptable length of the mirror M2 (see Fig. 6.2.7).

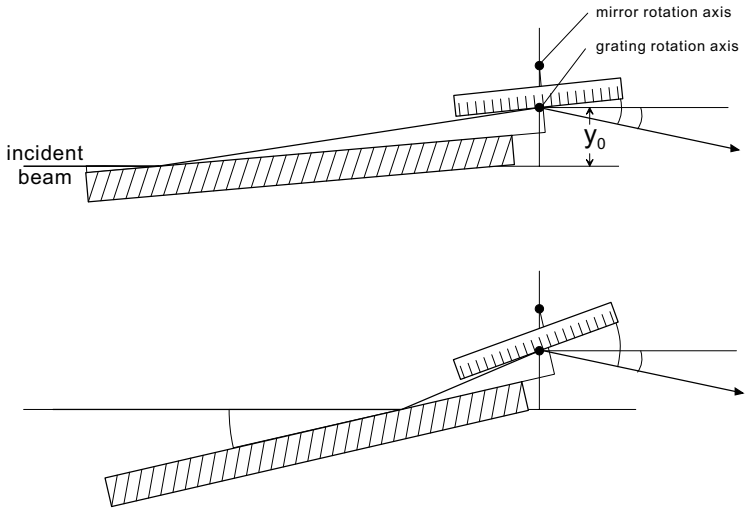

Figure 6.2.7.: *The vertical distance y_0 between the incident beam and the grating rotation axis is chosen to be only 8 mm because the 510 mm length of the plane mirror is proportional to this value. An even smaller value of y_0 in principle allows for a shorter mirror length without restricting the energy range. On the other hand, the grating would cut off a part of the incident beam at low energies. The value of 8 mm has been optimized for a grating length of 250 mm instead of 210 mm allowing for an additional heat load shielding. This prevents damage of the grating in case of a misteered incident beam.*

6.2.5.3. Bulk material and coating of the optical elements

Due to the extremely high photon densities and corresponding heat loads on the optical elements, the thermal properties of the mirror substrate and coating material are of crucial importance for the performance of the beamline. Experiences at high energy third generation synchrotron light sources with crystal monochromators showed, that a cryogenic cooling (studied at liquid nitrogen cooled silicon crystals) is best suited to cope with high heat loads. Even absorbed power densities of several W/mm^2 did not deteriorate the performance of crystal monochromators [11]. The slope errors induced by the thermal load seemed to be far below 1 arcsec. Moreover, at lower photon energies and for grating applications, silicon single crystal material is already well established. Thus we propose to use silicon as bulk material and a cryogenic cooling technology for the mirrors and gratings of the XUV-FEL-monochromator.

The bulk silicon material has to be covered with an appropriate thin film coating in order to avoid a strong absorption at its K-edge at 1840 eV. Concerning coating properties two coating materials seem to be optimal, carbon and chromium. Chromium is a well proven coating material, which forms very smooth layers, adheres very tightly to the bulk material and is often used as contact layer. Its disadvantage are strong absorption edges at 574 eV and 584 eV corresponding to the $2p_{3/2}$ and $2p_{1/2}$ excitations.

Carbon is a very light element showing no absorbtion edges above 285 eV (K-edge). It has excellent thermal properties when used in its diamond modification. On the other

energy [eV]	diverg. [μrad]	average flux phts/s	bw [eV]	spectral flux density [phts./s/eV]	[phts./bunch/eV]
500	14.3	$1.9 \cdot 10^{19}$	3.4	$5.6 \cdot 10^{18}$	$1.0 \cdot 10^{14}$
1200	7.7	$3.5 \cdot 10^{18}$	5.8	$6.2 \cdot 10^{17}$	$1.1 \cdot 10^{13}$
3100	4.0	$1.3 \cdot 10^{18}$	11.2	$1.1 \cdot 10^{17}$	$2.1 \cdot 10^{12}$

Table 6.2.1.: *Source parameters of the TESLA XUV-FEL as function of energy. The divergence is given as FWHM and the spectral flux density as average value. The peak flux is therefore* 1.77×10^8 *times the average value. The last column gives the number of photons per laser pulse.*

hand, the coating quality of diamond layers on silicon is not yet as good as for chromium. Assuming a declination angle of the diffracted beam of 1.2° the angle of incidence on the mirror M2 can be as small as $\approx 0.5^\circ$. As a result, its reflectivity varies between 80 and 95% in the energy range 1000 to 3000 eV for carbon and chromium coating. For the envisaged range from 500 to 3000 eV a carbon coating seems advantageous due to its better performance below 1000 eV.

With respect to power considerations the penetration depth of the radiation is very important. In the regime of total external reflection the penetration depth $d_{1/2}$ perpendicular to the surface, in which the intensity drops to half of its initial value can be calculated according to

$$d_{1/2} = \frac{\lambda}{4\pi} \frac{\ln 2}{\sqrt{\cos^2 \phi / \cos^2 \phi_c - 1}} , \tag{6.2.1}$$

where ϕ_c is the critical angle of total external reflection for wavelength λ. ϕ_c is related to the index of refraction by $n = \cos \phi_c$. For the carbon coating of M2 the penetration depth is 2.4 nm at 500 eV, meaning that half of the intensity is absorbed in a very thin surface layer.

6.2.5.4. Expected performance

The performance of the beamline is calculated with realistic assumptions on the surface quality of the optical components. It is optimized for both gratings by using the BESSY computer codes RAY and REFLEC [22, 23]. For the raytracing code RAY the FEL is modelled as a source with a gaussian intensity distribution of 100 μm (FWHM) diameter laterally and zero depth. The angular distribution is also assumed to be gaussian with a wavelength dependent divergence according to Tab. 6.2.1.

The raytracing was carried out for the beamline design as given in Fig. 6.2.6. The parameters of the optical elements such as geometric size, surface quality and grating profiles are summarized in Tab. 6.2.3. The monochromatic source image in the exit slit plane is approximately 75 μm. Consequently, the raytracing was done with a continuous energy distribution of the source and an adapted exit slit width of 75 μm. The results for the lowest and highest energies for each grating are summarized in Tab. 6.2.2.

In the fix-focus mode, the resolving power scales like $E/\Delta E \propto 1/\sqrt{E}$. The variation of the resolving power is shown for both gratings in Fig. 6.2.8. In addition, the monochromator transmission was calculated using the BESSY code REFLEC.

energy [eV]	bw [eV]	resolving power	T %	flux average [phts/s]	flux bunch [phts.]
500	0.034	15000	4.4	$8.5 \cdot 10^{15}$	$1.5 \cdot 10^{11}$
1200 (G1)	0.121	10000	4.0	$3.0 \cdot 10^{15}$	$5.3 \cdot 10^{10}$
1200 (G2)	0.087	14000	3.5	$1.9 \cdot 10^{15}$	$3.3 \cdot 10^{10}$
3100	0.370	8400	2.6	$1.1 \cdot 10^{15}$	$1.9 \cdot 10^{10}$

Table 6.2.2.: *Raytrace results for the beamline. Given are the values for bandwidth (bw), transmission (T) with respect to the resolving power (energy/bw), bandwidth, and photon flux. At 1200 eV the values are given for grating 1 (G1) with 600 l/mm and grating 2 (G2) with 1200 l/mm, respectively.*

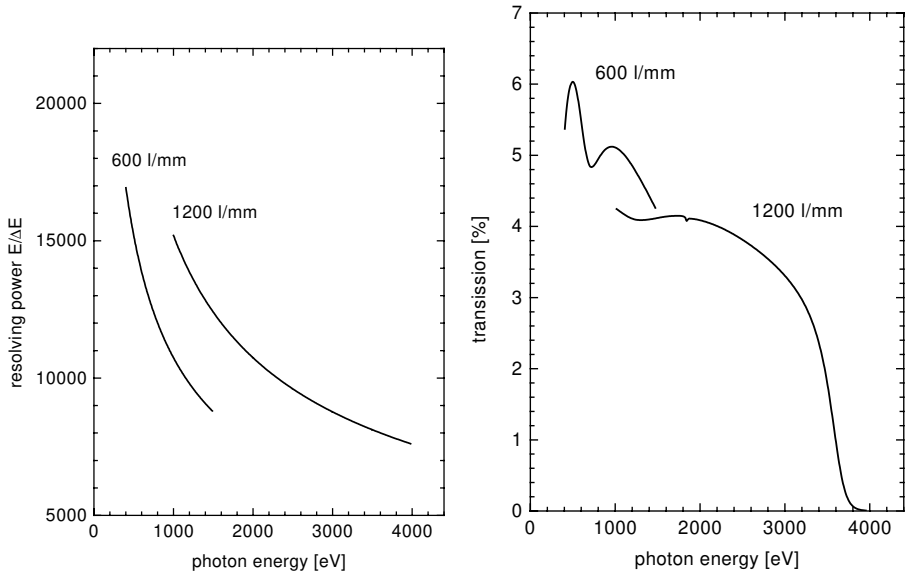

Figure 6.2.8.: *Resolving power and monochromatic transmission of the beamline. Only the reflectivities of the optical elements are considered for the calculation of the transmission.*

The photon flux is given as average value of photons per second and as number of photons per electron bunch. Typical flux values for current insertion device beamlines at third generation synchrotron sources, normalized to 100 mA ring current, are in the order of 10^{13} phts./s/0.1%BW. The average photon flux of the FEL is four orders of magnitude larger and the number of photons per bunch (100 fs bunch length) is comparable to the number of monochromatic photons in 0.1–0.01 s of modern insertion device beamlines.

The refocusing is performed with a horizontally deflecting toroidal mirror. This configuration delivers higher photon densities at small exit slit settings compared to a vertical deflection. A spot size of approximately 150×15 μm^2 (FWHM) can be obtained. As a result the average flux density varies between $6.6 \cdot 10^{17}$ and $2.7 \cdot 10^{18}$ phts/s/mm^2.

element	illum. area (FWHM) [mm^2]	ave. absorbed power total [W]	ave. absorbed power density [W/mm^2]	photon density per bunch incident [phts./mm^2]	photon density per bunch absorbed [phts./mm^2]
M1	470×4.2	146	0.08	$1.7 \cdot 10^{11}$	$1.8 \cdot 10^{10}$
M2	64×4.6	300	1.02	$1.0 \cdot 10^{12}$	$2.2 \cdot 10^{11}$
G1	112×4.6	163	0.32	$4.7 \cdot 10^{11}$	$1.0 \cdot 10^{11}$
M3	520×6.3	8.5	0.003	$6.4 \cdot 10^{9}$	$5.5 \cdot 10^{8}$

Table 6.2.3.: *Illuminated areas (FWHM-values) and absorbed power on the optical elements at a monochromator setting of 500 eV. For the absorbed power density the maximum value is given. The last two columns show the maximum incident and absorbed photon density per bunch.*

6.2.5.5. Heat load and power densities

The illuminated areas of the optical elements and the incident and absorbed power densities have been calculated for all optical elements using the raytracing program RAY. The highest absorbed power density occurs at low photon energies where the emitted power is maximal and the grazing incidence angle at M2 is large. Table 6.2.3 shows the thermal loads of the optical elements for a photon energy of 500 eV.

The highest power densities occur at mirror M2 (1 W/mm^2) and at the grating (0.3 W/mm^2). However, since the radiation arrives in 1 ms long bunch trains every 200 ms, the surface temperature will rise steeply for 1 ms and then decrease for 200 ms until the next bunch train arrives. Therefore, the relevant power density is a factor of 200 higher than the average value given in Tab. 6.2.3. Interestingly, similar values are also observed and can be handled at existing synchrotron sources. For comparison, a group at APS [24] reported for crystal monochromators, that it is possible to handle an absorbed power density of up to 83 W/mm^2 and a total absorbed power of 134 W by internal cryogenic nitrogen cooling without an increase in the Bragg peak width of 2" (FWHM). This demonstrates the feasibility to handle the average power load as well as the power densities of the TESLA-XUV grating monochromator by cryogenic cooling without damaging the optical elements. It should also be mentioned that most experiments do not rely on full average power, and a moderate reduction by a factor 2 to 5 should not be a problem.

Another challenge is the high peak photon density occurring during one single laser pulse. As shown above, a significant amount of energy is deposited into a thin surface layer at a time scale where thermal conductivity does not take place. For this situation and under the assumption of the proposed optical design of the beamline, it is important to know whether the surface atoms will stay in place or will ablate. For a rough estimation we can calculate the number of atoms N_A, that absorb a photon by assuming, that half of the absorbed photon flux is absorbed within the penetration depth $d_{1/2}$. With the particle density n of the layer material, N_A can be calculated by

$$N_A = \frac{\mathrm{n} \cdot d_{1/2}}{0.5 \cdot \Phi_{abs}} \tag{6.2.2}$$

(for carbon n $\approx 1 \cdot 10^{20}$/mm^3). Table 6.2.3 gives for mirror M2 at 500 eV a total number of $2.2 \cdot 10^{11}$ photons/bunch/mm^2 absorbed within the whole depth. With a penetration depth of

2.4 nm we find that an average number of 2200 atoms would absorb one photon per bunch, which makes approximately 0.22 eV per atom. This value is just between thermal binding energies such that damage may or may not occur depending on the mechanism of electronic energy transport and relaxation in to the lattice of the specific coating material. Research and development in this field has already started and is an integrated part of the FEL program at the TESLA test facility.

The slope error of the pre–optic surface should not exceed 0.5" (FWHM) and for this reason, mirror M2 and the gratings should have an intrinsic cryogenic cooling. For mirror M1 a cryogenic side cooling may be sufficient. In the regular user operation, mirror M3 and M4 should stand the heat load with a conventional side water-cooling. But if the zero order has to be transmitted through the monochromator, at least M3 needs a cryogenical side cooling too.

6.2.5.6. Seeding option

The small value of average photon flux at the end of the beamline with high resolving power compared to the total flux produced by the FEL is due to the fact, that the radiation emitted by the FEL has a rather broad bandwidth. As the monochromator selects a much smaller bandwidth, most of the photons generated by the FEL are discarded. Although the monochromatic transmission of the beamline is in the order of a few percent, the transmission referred to the total number of photons produced, as given in Tab. 6.2.2, is two orders of magnitude lower.

The seeding scheme improves this ratio drastically [25]. If a FEL is seeded with already monochromatic radiation, all of the emitted radiation is within the seeded bandwidth and no subsequent monochromator has to discard the radiation with unwanted wavelength. For 500 eV, the monochromatic flux at the experiment could thus increase by three orders of magnitude compared to the presented design where the monochromator is located behind the FEL.

Although the seeding option requires a more sophisticated monochromator design, a complicated electron bypass and a second undulator to produce the input for the seeding monochromator, precaution should be made, to allow for a future seeding upgrade.

6.2.6. Experiments infrastructure

The XFEL beamlines and the experiments will be complemented by laboratories for sample preparation. Sufficient space and instrumentation must be foreseen here in the areas of chemistry, biochemistry, and nanoparticle handling. Analytical means for characterization and orientation of these specimen have further to be foreseen in order to make efficient use of the XFEL instruments possible.

Ancillary instrumentation for the experiments such as femtosecond laser setups for pump/-probe experiments need to be established and require sufficient space and infrastructure. For example laser environments require clean room conditions and accurate temperature control in order to achieve highest stable operation. For the preparation and analysis of X-ray optical elements a metrology laboratory will have to be set up with the apparatuses for precise characterization of mirrors and surfaces. Again clean room environment is mandatory in order to

achieve stable operation at the performance needed for the XFEL.

Finally, reliable computerized control of beamlines, instruments and experiments will be established. Although forecasts of computing power are difficult due to the rapid development in the field of information technology schemes based on PC farms are already today powerful enough to fulfil the requirements for the XFEL laboratory. For the computing at the experiments the tasks of real-time instrument control, data acquisition, data monitoring have to be achieved. Further a rather high capacity will be needed for data recording, archiving and transfer due to the amount of data provided. An estimate for a 2k $\times$ 2k pixel detectors with a depth of 16 bit taking 100 frames per bunch train leads to a peak data rate of 8 GB/s. Although the mean rate is probably 100 times smaller storage capacity of > 100 Terabyte has to be foreseen if data is kept for 1 month.

Bibliography

[1] P.A. Heimann, SPIE proc. **2856**, 90 (1996).

[2] D. Ryutov and A. Torr, LCLS reports LCLS-TN-00-10, Stanford (2000).

[3] K. Sato, T. Kudo, M. Suzuki, T. Ishikawa, 1998 Ann. report SPring-8, Harima (1999), 181.

[4] K. Sato, H. Tanida, S. Adachi, 1999 Ann. report SPring-8, Harima (2001), 146.

[5] G.E. Fischer and R.E. Ruland, Proc. 1^{st} Int. Workshop on Accelerator Alignment, Stanford reports SLAC-375, Stanford (1990), 296.

[6] H. Schulte-Schrepping, *Photon Beamlines at TESLA XFEL Undulators*, SPIE proc. **4143**, in print.

[7] U. Hahn, L. Bittner, M. Hesse, E.W. Weiner, SPIE proc. **1997**, 392 (1993).

[8] U. Hahn and Z. Wang, SPIE proc. **2856**, 268 (1996).

[9] A.K. Freund, D.M. Mills, T. Ishikawa, Proc. SRI'2000, Berlin, to appear in Nucl. Instrum. Meth. A.

[10] A.K. Freund, Opt. Eng. **34**, 432 (1995).

[11] D. Bilderback, A.K. Freund, G.S. Knapp, D.M. Mills, J. Synchrotron Rad. **7**, 53 (2000).

[12] T. Missalla, I. Uschmann, E. Förster, G. Jenke, D. von der Linde, Rev. Sci. Instrum. **70**, 1288 (1999).

[13] S. Brauer et al., Rev. Sci. Instrum. **66**, 1506 (1995).

[14] A. Souvorov, M. Drakopolous, I. Snigireva, A. Snigirev, J. Phys. D: Appl. Phys. **32**, A184 (1999).

[15] S.D. Shastri, P. Zambianchi, D.M. Mills, SPIE proc. **4143**, in print.

[16] J.S. Wark, SPIE proc. **4143**, in print.

[17] J.N. Chukhovskii, E. Förster, Acta Cryst. A**51**, 668 (1995).

[18] R. Follath and F. Senf, Nucl. Instrum. Meth. A**390**, 388 (1997).

[19] M. Murty, J. Opt. Soc. Am. **52**, 768 (1962).

[20] F. Riemer and R. Torge, Nucl. Instrum. Meth. A**208**, 313 (1983).

[21] A.V. Pimpale, S.K. Deshpande, V.G. Bhide, Appl. Opt. **30**, 1591 (1991).

[22] F. Schäfers, BESSY Tech. Ber. 202/96, 1 (1996).

[23] F. Schäfers and M. Krumrey, BESSY Tech. Ber. 201/96, 1 (1996).

[24] C.S. Rogers et al., Rev. Sci. Instrum. **66**, 3494 (1995).

[25] J. Feldhaus et al., Optics Comm. **140**, 341 (1997).

7. Civil Engineering

The civil engineering for TESLA and the XFEL laboratory is described in detail in Part II, Chap.8. Here we only give a brief summary.

7.1. XFEL Buildings

The XFEL laboratory consists of different buildings. The main building for photon generation and beam transport is a tunnel system extending over 1.3 km in length. The tunnel system connects the "electron switchyard" on one end with the main experimental hall and several beam dump halls on the other end. The XFEL site in Ellerhoop is about 17 km away from the DESY site. An overview of the area is shown in Fig.7.1.1. It is mandatory that central facilities which are provided at the DESY site are also available at the XFEL site. In addition, enough office space for the staff and the users as well as necessary facilities for a lively scientific environment should be available. Many of them can be combined with the high energy physics activities. In the following, a realization of the XFEL buildings is presented.

7.1.1. Switchyard and tunnels

7.1.1.1. Introduction

Figure 7.1.2 shows the schematic layout of the switchyard and the undulator beamlines together with the TESLA facility. The two electron branches with 13–27 GeV and 20–50 GeV, separated from the main linac, split into four branches which feed the four SASE XFELs. In the SASE 2 line, additional place for a seeding scheme is reserved. The SASE 3 undulator is followed by the soft X-ray FEL SASE 5. The electron beams of SASE 1, SASE 2, and SASE 4 are further used to drive undulators which produce spontaneous radiation (U1 – U5). After passing all undulators, the electrons are stopped in beam dumps D1 – D4. Bending magnets separate the photon beams from the particle beams. All photon beamlines can be operated in parallel. The angular separation is designed for a distance of 17 m between beamlines in the experimental hall.

A transfer tunnel connects the main linac with the XFEL tunnel system. To separate the XFEL buildings from the HEP buildings, a horizontal angle of 8.4° between main linac and transfer lines is required. In order to preserve the quality of the electron beams, a smooth bend of $\approx$ 2000 m curvature is necessary, resulting in a rather long tunnel of $\approx$ 900 m length. At the beginning of the transfer tunnel, both transfer lines are separated vertically by 40 cm

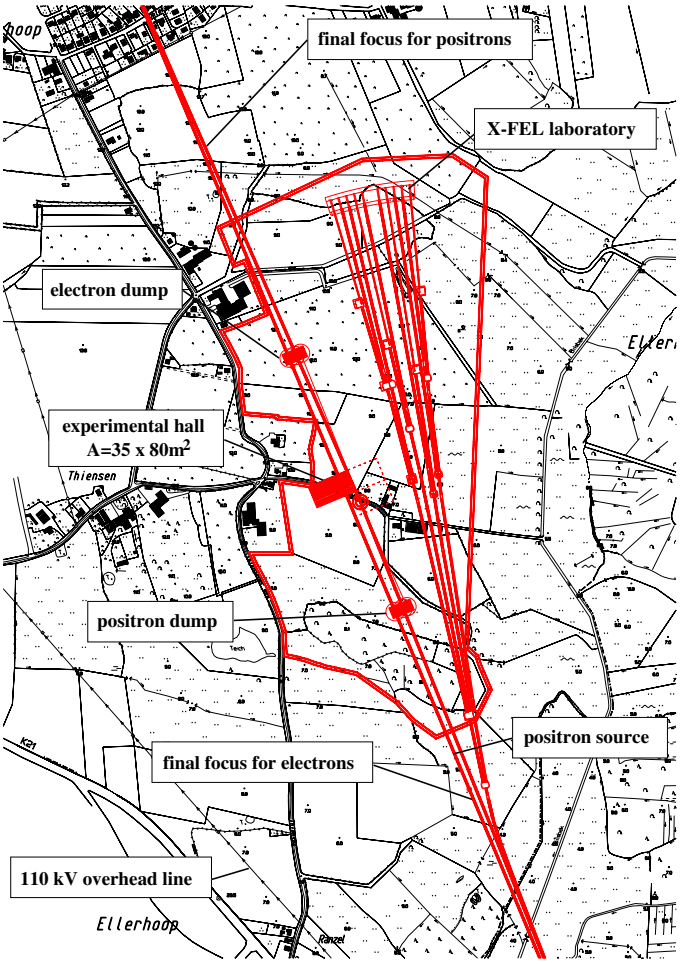

Figure 7.1.1.: *Overview of the campus area in Ellerhoop*

and run in parallel. At the end they are horizontally separated by 2.5m and run under an angle of 2.9°.

The main linac tunnel and the electron transfer lines are about 14 m below the ground level. The experimental hall should lie close to the surface. To connect the switchyard with the experimental hall, a tunnel system will be used. Different geometries of placing and building the tunnel system have been investigated [1]. Environmental and building constraints have been taken into account. As a result of these investigations, an inclined tunnel system with 10 mrad (or 1%) slope is the favorable solution. The whole building structure consists out of tunnels and shafts. The shafts are placed in the crotches of the tunnels. The tunnels need a minimum distance of 1 m at the crotch for the drilling machines.

The main advantage of the inclined tunnel version is the optimum exploitation of the available space. This results in the longest photon beamlines and a sufficient separation between dumps and experimental hall. Enough room for handling the extremely high power densities of the XFEL beams is available, and additional sand shielding is not required. Moreover, the surrounding landscape is preserved from major changes. Fig. 7.1.3 shows an artist's view of the tunnel system integrated in the Ellerhoop area.

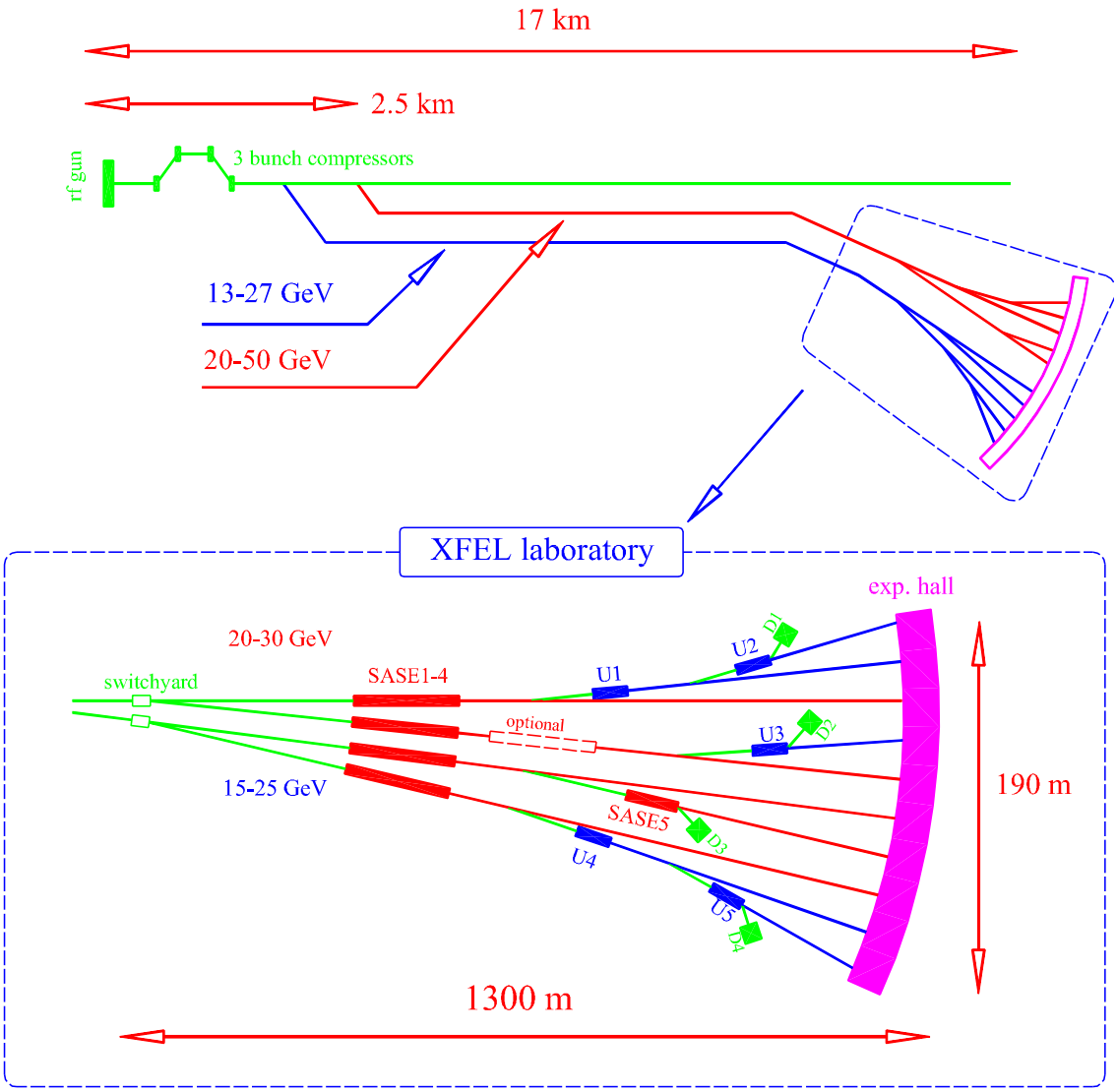

Figure 7.1.2.: *Schematic view of the TESLA XFEL electron beam transport (top) and the XFEL laboratory. At about 2.5 km from the starting point of the main linac (or 3 km from the rf gun), the XFEL electron beams are extracted into two transfer lines running parallel to the linac. The electron transfer lines cover the tuning ranges 13–27 GeV and 20–50 GeV. For the operation of the XFELs 15–25 GeV and 20–30 GeV are needed. The XFEL laboratory consists of the electron switchyard, SASE undulators SASE 1–5, undulators U1–U5, beamdumps D1–D4, photon beamlines and the experimental hall.*

7.1.1.2. Layout of the switchyard and tunnel system

The actual realization of the tunnel system is sketched in Fig. 7.1.4. The buildings belonging to the FEL area start with the transfer tunnel. At the end of the transfer tunnel, the two

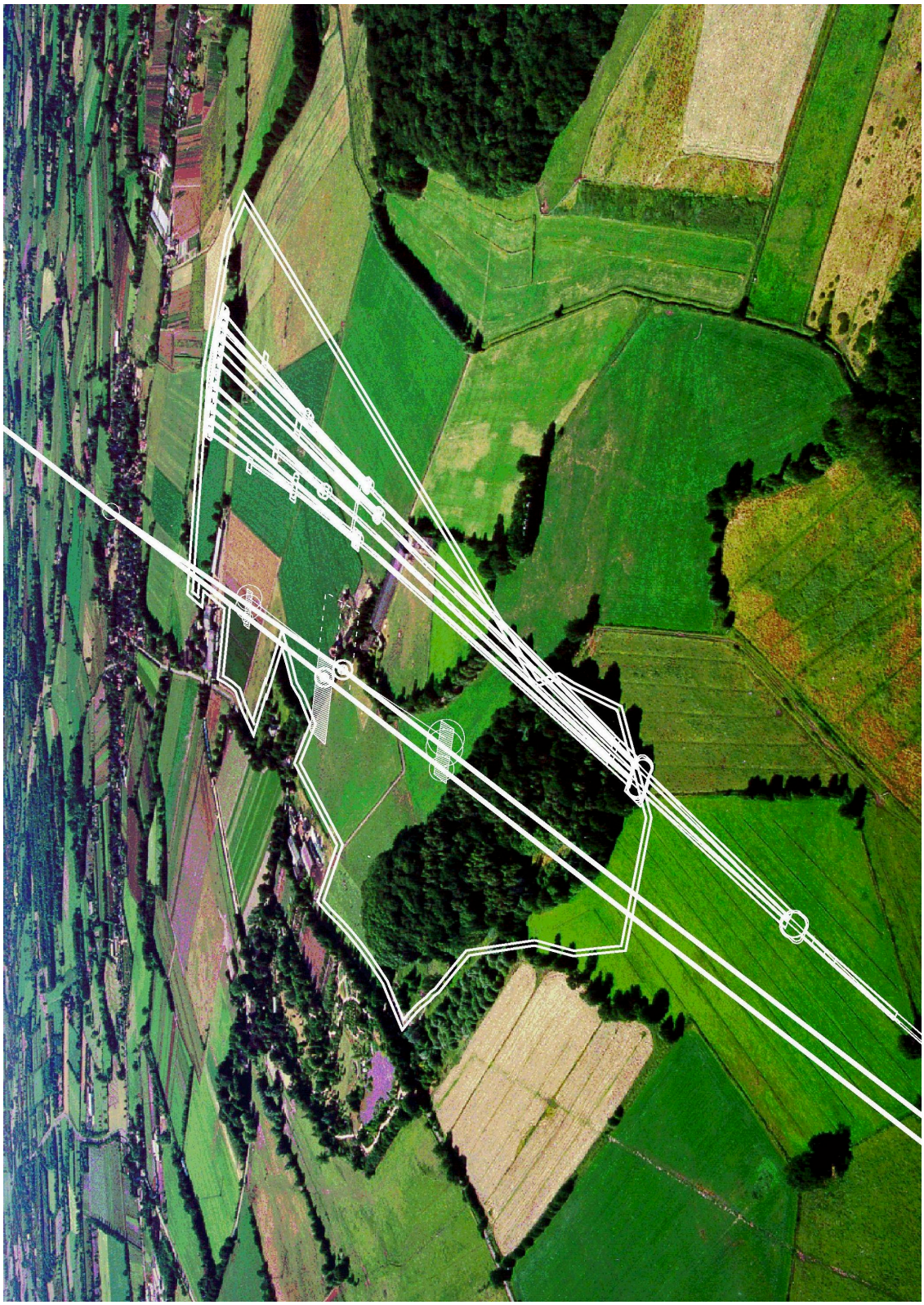

Figure 7.1.3.: *Artist's view of the XFEL site integrated in the Ellerhoop landscape*

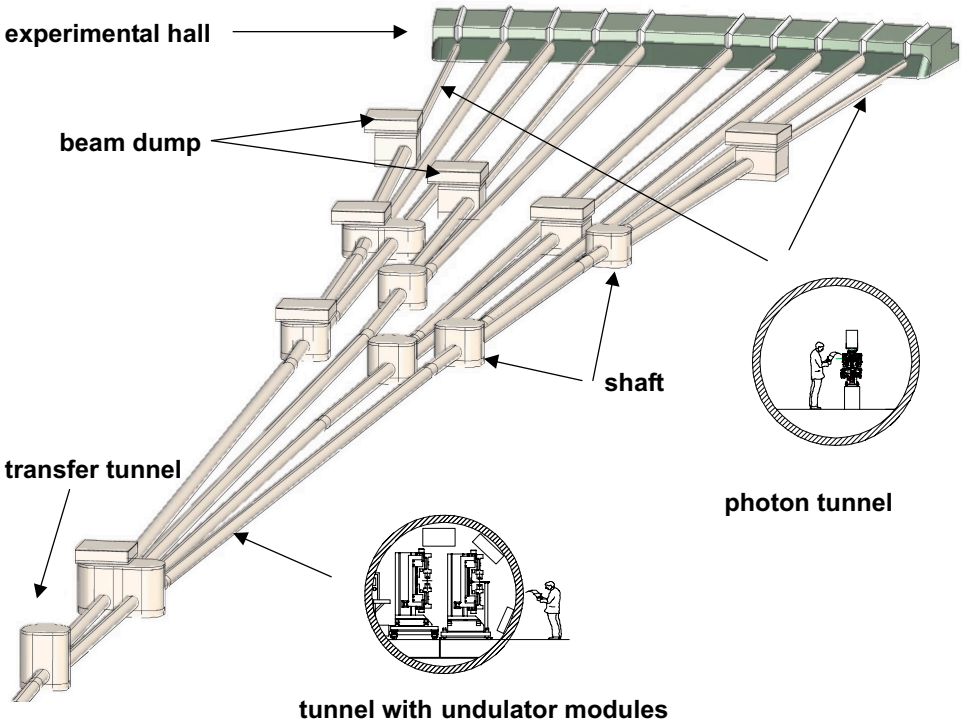

Figure 7.1.4.: *The XFEL tunnel system with insets showing enlarged cross sections of the two tunnel types. The electron beams enter the switchyard from the bottom left and will be absorbed in the electron beam dumps. The experimental hall is at the end of the photon tunnels. In the first cross section two undulator modules are shown side by side, one permanently installed, the other being transported*

electron beams are separated by an angle of 2.9° and a distance of 2.5 m. Two tunnels of 140 m length follow which house the switches (15 m long pulsed dipole magnets) to split the incoming electron beams and lead to the undulator section. The shaft between these tunnels and the transfer tunnel is directly accessible from the surface only during the construction phase. Afterwards it will be closed by a ceiling and covered with sand. In this part the tunnel is smoothly bent with a radius of 400 m in order to let the photon beam travel on a straight line and to separate electrons from photons.

These bends need a length of 63 m. The drift sections necessary to get a separation of at least 3.2 m (resulting from the 4 m inner diameter of the tunnel minus the safety margins of 0.5 m for electron beams and 0.3 m for photon beams) determine the length of the tunnels. After the SASE undulators the electrons pass undulators to generate spontaneous radiation or another SASE undulator (SASE5) according to the scheme in Fig. 7.1.2. The electrons are then stopped in the beam dumps while the photons are transferred to the experimental hall. The photon beamlines need a tunnel with 4 m diameter. This gives good accessibility and flexibility to the optical and experimental components of these lines.

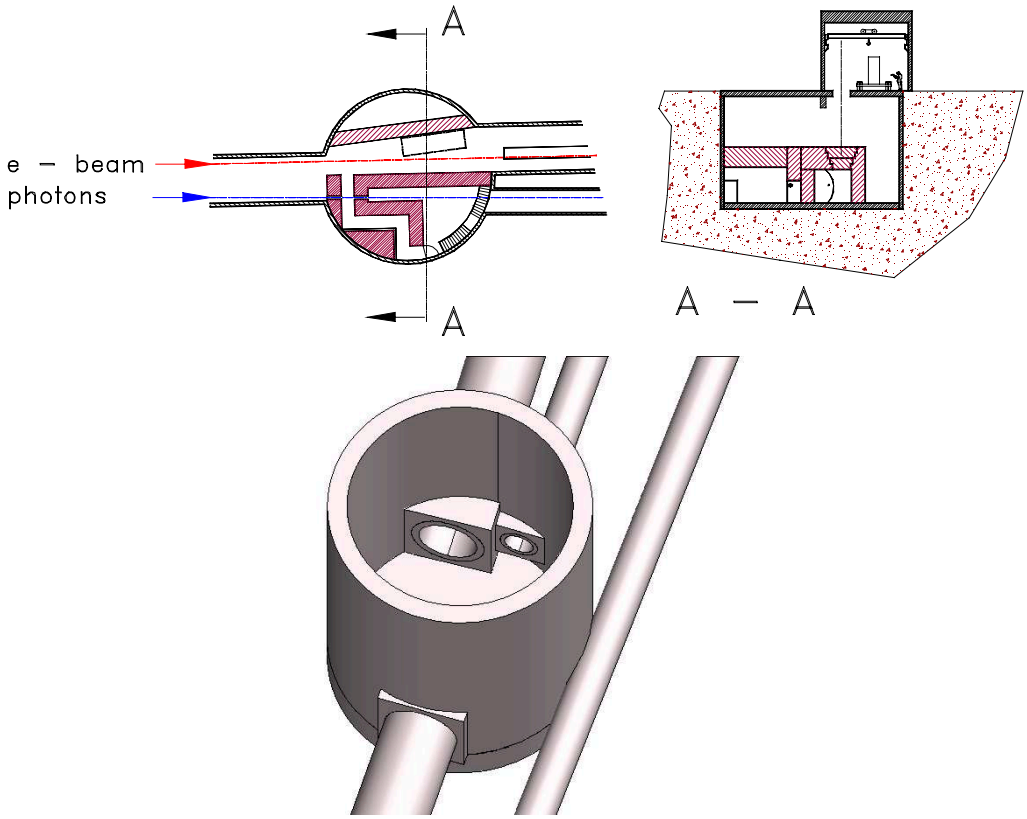

Figure 7.1.5.: *Different views of a shaft. In the upper row, a top view (left) and a cross section (right) are sketched. The 3D graphics below gives an impression of the ensemble. In the top view, the electron beam enters the shaft from the left and leaves through the upper right tunnel. The photon beam enters from the left and leaves the shaft through the lower right tunnel. The side elevation shows how heavy elements can reach the tunnels from the surface.*

7.1.1.3. Tunnel design

The demand for position stability of all components related to the X-ray laser beam is very high. Therefore all undulator modules and especially the quadrupole magnets between them are located on a thick solid block. This block is isolated from the tunnel by vertical cuts and horizontally by a damping material like rubber or plastics. These blocks are too long - some of them will exceed 300 m - not to deform elastically. They will follow the motion of the tunnel system with a time constant in the order of weeks. Due to the weight of the undulator modules, the floor should have a bearing capacity of 4 t/m^2.

The first and the last shafts are used temporarily during the drilling phase and will be permanently closed afterwards. All others are used as entrances for the tunnel system. They must be permanently accessible as a transport route for heavy components like undulator modules. This makes special shielding precautions necessary. A shielding of 2 m concrete on top of the electron beam and 1.2 m in the vertical direction is necessary [2]. Figure 7.1.5 shows a top and a side view together with a 3D image of a shaft used as an entrance. The

2 m thick shielding of the ceiling can be opened. A hatch of 5.4 × 1.4 m^2 is necessary to handle the undulator modules. The hatches are normally closed by two layers of 1 m thick concrete blocks. The weight of the blocks must not exceed the weight of an undulator module. The lifting capacity of the crane in the access building at the surface is matched to these loads. The access building is large enough to leave space for trucks to transport the undulator modules and shielding blocks. A stair case leads to the bottom of the shaft, where a radiation-safe labyrinth gives access to the tunnels for personnel.

The outside of all buildings has to be safe for the public. Therefore, sand shielding of the tunnels containing electrons is required. A conservative estimate assumes a beam loss of 1% on a length of 100 m of the beamline over a time interval of 1/10 of the total beam time per year (600 h/a). To stay far below the natural radiation dose 5.1 m of sand as lateral shielding is needed. As the XFEL fan starts at about 14 m below ground level (the height of the electron beams in the main tunnel), the coverage of the tunnels by the soil, even at the end where the tunnels approach the surface, is sufficient. Raising the starting point of the switchyard, for instance by an additional inclination of the transfer tunnel, will require additional shielding.

At the end of each electron beamline, i.e. behind the last undulator, the electrons must be dumped in special beam dumps. The dumps are housed in special buildings which also give access to the undulators. A detailed description of the dumps is given in Part II, Chap. 9.9.

7.1.2. Experimental hall

The cross section of the experimental hall is seen in Fig. 7.1.6. The hall contains a section with a larger height equipped with a crane. The section with the lower height is needed for ancillary laboratories and control rooms. The hall is slightly curved with its center in the origin of the whole XFEL layout. This ensures a nearly perpendicular entry of each beam into the experimental area.

At the experimental hall 10 photon beams, five from SASE-undulators and five from conventional undulators are used in 30 experiments as shown in Fig. 7.1.7. The experiments are housed in experimental hutches. There will be prohibited access during experiments with beam. If the experiment is a side station, a monochromator in a central optics hutch distributes the photons to the side. In the case of end stations the beam is directly used. Here the optics hutch can be omitted. If the beam is only used by an end station, a so called "Tanzboden" (a smooth surface for moving heavy components by air cushions) may be installed. Three experiments can make use of the same beam. Two of them are set up and adjusted outside the beam. The third one is moved into the beam for measurements. Space for transportation and a walking way is behind the experiments.

The dimensions of the experimental hall are estimated as follows: The typical experimental hutch has a space requirement of 4×6 m^2 at a height of 3.5 m. The roof is removable for crane access to heavy components (3.5 t). Standardized elements for the hutch design are available. A central optics hutch with side hutches on either side requires a width of 12 m and 5 m space for transportation between the beams. That results in a necessary spacing between beams of 17 m. The undulators SASE 1 through SASE 4 must serve the photon lines 3, 5, 6 and 8. To keep the angular spacing between these beamlines constant, the distance

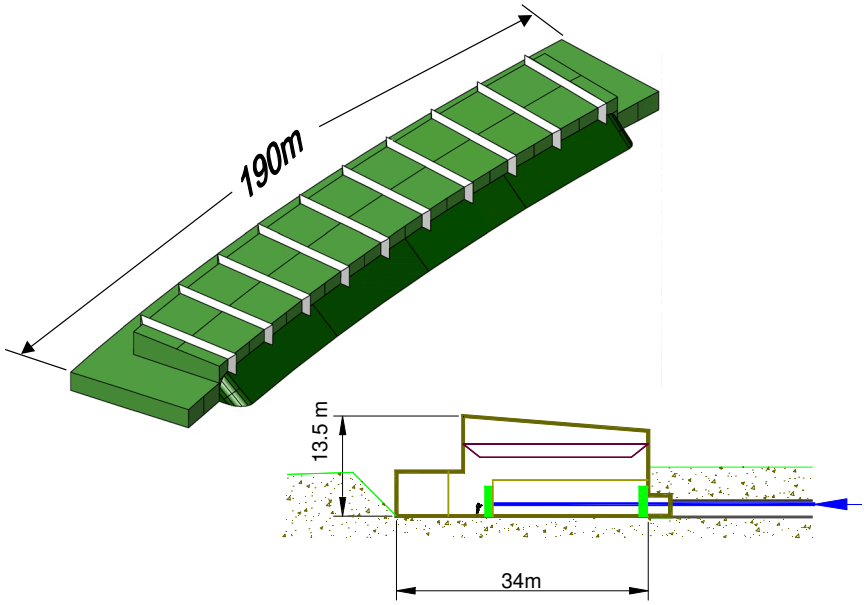

Figure 7.1.6.: *Artist's view and cross section of the experimental hall. Although the hall floor is well below the surface, the side laboratories receive daylight through their windows. Elongated windows in the roof provide illumination for the experimental areas.*

between line 5 and 6 at the experimental hall is 34 m. This extra space is used by four central laboratories. 10 beams with 12 transport ways, two central laboratories of 6 m, and two outer walls yield a total length of the hall of 192.6 m at the front and 197.4 m at the back. In most cases three experimental hutches may be arranged behind each other. A beamstop for the direct beam needs a 1 m depth. A transportation area accessible by the crane (3.5 tons capacity) of 6 m width is added. This gives the total width of 25 m for the experimental area. The lower laboratory and control room section contains a transport way of 2 m width. This is a safe walking lane for the hall users, as it is not accessible by the crane. The ancillary laboratories will be 5 m deep. Adding twice the outer walls dimensions of 0.3 m, and a 0.2 m thick separation to the side rooms, the total width of the experimental hall is 32.8 m. Thus the gross surface of the experimental hall is 6396 m^2.

The laboratory section comprises 1477 m^2 including all walls. The low-height part of the transport way, which is also an access to the laboratories, takes up 393 m^2. As gross surface for the side rooms, 1084 m^2 are available. Assuming 13% for the walls a net surface of 960 m^2 can be used. For each experiment a laboratory is foreseen. These laboratories have different sizes, so that the distribution to the individual experiment is flexible. A total area of 830 m^2 should be reserved for them. 200 m^2 are realized by central laboratories. The hall service needs 70 m^2 for storage purposes. Clean rooms are set up on 70 m^2. An access area suitable for trucks takes 33 m^2. An additional emergency exit needs 11 m^2. Four sanitary units of 25 m^2 each are necessary. At least one should be equipped for handicapped persons. Showers should also be incorporated. The remaining rest of 46 m^2 is used for technical equipment like central electrical supply, ventilation, etc.

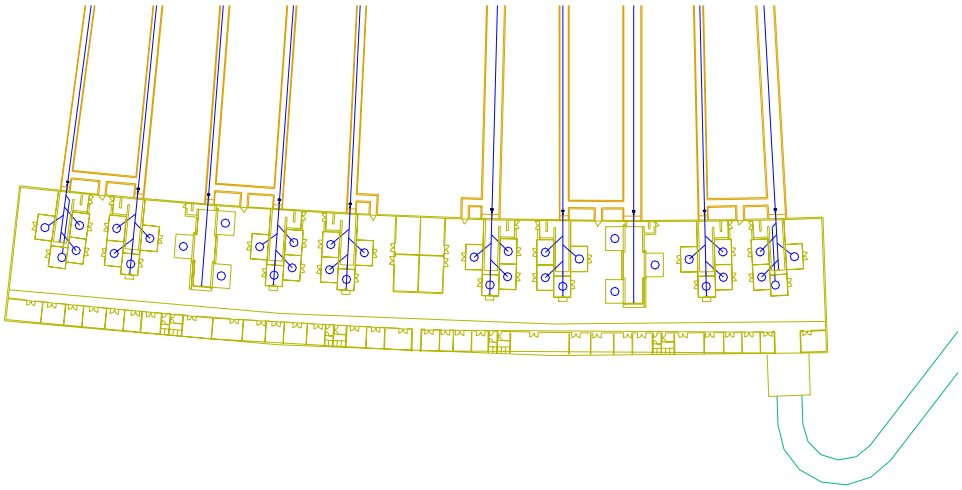

Figure 7.1.7.: *A bird's view of the experimental hall showing a possible layout. The arrangement of the experiments is very flexible as all walls and shielding blocks are modular.*

7.2. Infrastructure and General Supplies

The area will provide the necessary infrastructure to support the XFEL laboratory. This infrastructure includes offices, workshops, storage, canteen, guest apartments, access roads, parking areas, central services (such as computing, electricity, heating), etc. . More details are given in Part II, Chap. 8.

Bibliography

[1] L. Hänisch, W. Henkel, J. Mittag, Zwischenbericht zur Bewertung verschiedener Strahlführungsvarianten für die XFEL Anlagen von TESLA in Ellerhoop/Kreis Pinneberg, DESY report, Hamburg (2000)

[2] H. Dinter, *Abschirmung des Linear Colliders TESLA im Bereich der Kryohallen*, DESY report D3-99, Hamburg (1999).

8. Time schedule, Cost and Personnel

The time schedule to build, commission and start user operation of the XFEL laboratory is closely connected to the overall schedule of the main linac construction and the commissioning of the machine. Since the construction time needed for the laser part is shorter than for the main linac we have not attempted to present a separate time schedule but assume that operation will start together with the main linac.

The cost distribution is linked to this time schedule so that we will only give the total cost here, for the photon related components, namely the undulators, the beamlines, the optical components, and the experiments. This amounts to *290 - 345 MEUR* depending on whether 20 or 30 experimental stations will go into operation.

The costs for Civil Engineering and the electron related components can be found in Part II. We are assuming that the XFEL laboratory will finally be operated similar to the ESRF so that personnel has to be provided for construction, commissioning, infrastructure, maintenance, and experimental service to the XFEL users.

We estimate that 1150 FTE man-years are needed for the construction of the undulators, the photon beamlines and the first four experimental stations. At the subsequent start of the operation of the XFEL laboratory a manpower of 230 is needed for operation of the then existing experimental stations and for building further installations. After construction and commissioning of all together 30 experimental stations over a period of 10 years the final manpower requirement for operation of the XFEL laboratory is 360.

A. Additional Material on CD-Rom

In addition to the section of the technical design report concerning the X-ray free electron laser laboratory we provide material of interest to the reader on a cd-rom, attached to this report. This material has not been included directly into the TDR due to space restrictions, but documents nicely the work in the various fields. Nevertheless, some of the conclusion in the main part are based on the work presented here and it is therefore our aim to provide this material to the reader. In this appendix we describe very briefly the different documents and their contents. Two main groups can be found: reports of workshops and meetings to define the scientific case for the XFEL and technical documents underlying the technical design of the laboratory.

A.1. Scientific Workshop Reports

The scientific case for the X-ray free electron laser laboratory is mostly based on a series of seven workshops and two working group meetings addressing several fields of science and the application of the XFEL in these fields. In addition one workshop addressed the requirements for beam line instrumentation and experimental techniques for XFEL laboratories. Reports have been compiled in each field to demonstrate the possibilities emerging from the fully new machines. The reports are composed on the attached CD-ROM in pdf-format.

The reports contain detailed proposals of experiments and their requirements. Several figures illustrate how the measurements should be carried out and how the system of investigation may look like on the atomic scale. The following list indicates the titles of the reports ordered alphabetically.

A.1.1. Atomic, molecular and cluster phenomena

A.1.2. Chemistry applications of XFELs

A.1.3. Hard condensed matter physics

A.1.4. Life sciences with XFELs

A.1.5. Methods and instrumentation for XFELs

A.1.6. Nonlinear, quantum and atom optics and ultrafast phenomena

A.1.7. Nuclear resonance scattering at an XFEL

A.1.8. Small angle scattering

A.1.9. Surface, interfaces and nanomaterials

A.2. Other Scientific Contributions

A.2.1. Nonlinear optics with X-rays

A.2.2. XFEL with a meV bandwidth : seeding option

A.2.3. Monochromator concept for a soft X-ray XFEL beamline

A.3. Technical documents

A.3.1. A prototype phase shifter for the undulator systems at the XFEL

A.3.2. Manufacturing considerations of the magnetic structures for the undulators for the XFEL at TESLA

A.3.3. Conceptual design of a planar helical undulator for the XFEL

A.3.4. Influence of different focusing solutions for the XFELs on debunching of the electron beam

A.3.5. Field accuracy requirements for the undulator systems of the XFELs at TESLA

A.3.6. Design considerations for a 1 Ångstroem SASE undulator

A.3.7. A prototype gap separation system for the TESLA undulator

A.3.8. Manufacturing Considerations of the magnetic structures for the Undulators for the XFEL at TESLA

A.3.9. Magnet design of a prototype structure for the XFELs at TESLA

A.3.10. A SIMATIC based control system for XFEL undulators (in german)

A.3.11. Magnet sorting by simulated annealing